R-05-32

Regional hydrogeological simulations for Forsmark – numerical modelling using CONNECTFLOW

Preliminary site description Forsmark area – version 1.2

Lee Hartley, Ian Cox, Fiona Hunter,
Peter Jackson, Steve Joyce, Ben Swift
Serco Assurance

Björn Gylling, Niko Marsic
Kemakta Konsult AB

May 2005

Svensk Kärnbränslehantering AB
Swedish Nuclear Fuel
and Waste Management Co
Box 5864
SE-102 40 Stockholm Sweden
Tel 08-459 84 00
+46 8 459 84 00
Fax 08-661 57 19
+46 8 661 57 19

ISSN 1402-3091
SKB Rapport R-05-32

Regional hydrogeological simulations for Forsmark – numerical modelling using CONNECTFLOW

Preliminary site description Forsmark area – version 1.2

Lee Hartley, Ian Cox, Fiona Hunter,
Peter Jackson, Steve Joyce, Ben Swift
Serco Assurance

Björn Gylling, Niko Marsic
Kemakta Konsult AB

May 2005

Summary

The Swedish Nuclear Fuel and Waste Management Company (SKB) carries out site investigations in two different candidate areas in Sweden with the objective of describing the in-situ conditions for a bedrock repository for spent nuclear fuel. The two candidate areas are named Forsmark and Simpevarp. The site characterisation work is divided into two phases, an initial site investigation phase (IPLU) and a complete site investigation phase (KPLU). The results of IPLU are used as a basis for deciding on a subsequent KPLU phase. On the basis of the KPLU investigations a decision is made as to whether detailed characterisation will be performed (including sinking of a shaft).

An integrated component in the site characterisation work is the development of site descriptive models. These comprise basic models in three dimensions with an accompanying text description. Central in the modelling work is the geological model, which provides the geometrical context in terms of a model of deformation zones and the rock mass between the zones. Using the geological and geometrical description models as a basis, descriptive models for other geo-disciplines (hydrogeology, hydro-geochemistry, rock mechanics, thermal properties and transport properties) will be developed. Great care is taken to arrive at a general consistency in the description of the various models and assessment of uncertainty and possible needs of alternative models.

Here, a numerical model is developed on a regional-scale (hundreds of square kilometres) to understand the zone of influence for groundwater flow that affects the Forsmark area. Transport calculations are then performed by particle tracking from a local-scale release area (a few square kilometres) to identify potential discharge areas for the site and using greater grid resolution.

The main objective of this study is to support the development of a preliminary Site Description of the Forsmark area on a regional-scale based on the available data of 30 June 2004 (Data Freeze F1.2) and the previous Site Description. A more specific objective of this study is to assess the role of known and unknown hydrogeological conditions for the present-day distribution of saline groundwater in the Forsmark area on a regional scale. An improved understanding of the palaeo-hydrogeology is necessary in order to gain credibility for the Site Description in general and the hydrogeological description in particular. The latter will serve as a basis for describing the present-day hydrogeological conditions on a local scale as well as predictions of future hydrogeological conditions. Finally, this study aims to identify some of the issues that may impact the SR-Can Performance Safety Assessment (PSA) project, and where possible provide a preliminary evaluation of sensitivities to such issues. In particular, recommendations are made as to which uncertainties need to be addressed as part of SR-Can.

A number of new aspects to the scope of modelling have been included for F1.2. One of the most important is the representation and treatment of uncertainty of the deformation zones (DZs). Three new alternative geological models were produced for Version 1.2 based on different levels of confidence in interpretation. A base case (BC) was provided based on high confidence structures local to the site between the Singö DZ and Eckarfjärden DZ. One of the key features of this model is the presence of several extensive sub-horizontal DZs within the candidate area. A variant case (VC) was developed that considers an extension of some sub-horizontal zones beyond the candidate area. Finally, an alternative case (AC) case was proposed with the inclusion of many low confidence sub-vertical lineaments outside

the candidate area. In addition to these considerations of the sensitivity to various structural models, the concept that hydrogeological properties for the hydraulic conductor domains (HCDs) should vary with depth and according to the dip of structures was introduced.

Another key difference from F1.1 is the increased effort invested in conditioning the hydrogeological properties for the hydraulic rock domain (HRD) to the fracture boremap and hydraulic data. A new methodology was applied for interpreting the discrete fracture network (DFN) by integrating the geological description of the DFN (Geo-DFN) with the hydraulic test data from Posiva flow-log (PFL) and Pipe-string system (PSS) double-packer techniques to produce a conditioned Hydro-DFN model. This was done in a systematic way that addressed uncertainties associated with the assumptions made in interpreting the data, such as the relationship between fracture transmissivity and length. PSS and PFL data were both available for only three boreholes, KFM01A–KFM03A. PFL anomaly data were also available for KFM04A–KFM05A. Considerable spatial variations in fracture occurrence and flow were observed within and between boreholes. However, it was felt there were insufficient data to substantiate anything more than relatively simplistic fracture spatial models, although it was believed important to differentiate rock properties inside Rock Domain 29 (the so-called 'tectonic lens' that spans the candidate area) from those outside.

Significantly, far greater quantities of hydro-geochemical data were available for calibration in the Version 1.2 data freeze for Forsmark. These were provided for cored boreholes KFM01A, KFM02A, KFM03A, KFM04A, and KFM05A and for a series of shallower percussion drilled boreholes. Further, the data were provided in terms of interpreted mixing fractions for reference waters, concentrations of major ions, stable isotope ratios and tritium concentrations in addition to the salinity data that had been supplied previously. This enabled a more widespread and comprehensive calibration of the groundwater flow models than was possible previously. However, data at elevations below –500 m were still sparse, and hence there remains uncertainty in interpreting and modelling the deep groundwaters.

The numerical modelling was performed by two separate modelling teams. The work presented in this report was conducted by The CONNECTFLOW Team involving modelling experts from Serco Assurance, Kemakta Konsult and Golder Associates.

The main conclusions from the groundwater modelling are:

- It is possible to calibrate several possible models for fracture transmissivity, although the direct correlation between transmissivity and length is perhaps easier to match to the borehole flow data;
- There were some difficulties in applying the Geo-DFN. The primary difficult stemmed from significant variations in fracture intensities and the proportions of sets between boreholes making it hard to use an averaged model such as the Geo-DFN when matching hydraulic tests at a specific borehole. Another major problem was that the uncertainty in the fracture length PDF in terms of the slope, k_r, and reference fracture length, L_0. This was addressed by considering a variant Geo-DFN with a uniform slope $k_r = 2.75$ as a sensitivity test and calibrating a alternative Hydro-DFN based on this length PDF;
- The variant Geo-DFN makes a more conceptually feasible Hydro-DFN based on KFM03A since the original Geo-DFN requires the fracture intensity of open fractures to be increased by about 30% above that observed in the borehole to match the hydraulic responses, requiring all the fractures judged as possibly sealed and about half the probably sealed fractured to actually be open, which seems unlikely. Whereas the variant Geo-DFN requires it to be reduced by 30%, which is within the recorded uncertainty range on open fractures. This is because it is less dominated by small fractures and hence better connected;

- Due to the spatial variability of the fracture properties a number of bedrock volumes were defined jointly with the DarcyTools Team. For CONNECTFLOW the following were defined: Volume E – below Zone A2 and above 400 m depth, Volume F – above Zone A2, Volume G – below Zone A2 and below 400 m depth;
- For a 100 m block for both Volume E and Volume F, the median effective hydraulic conductivity is much more similar for all three T models, with $\log(K_{eff})$ varying between –8.9 and –9.4. For the 100 m block the variant Geo-DFN parameters show similar median K_{eff} to the original Geo-DFN input parameters ($\log(K_{eff})$ of –9.1 and –9.5 for the correlated and uncorrelated models). For both rock volumes, the hydraulic conductivity is similar in x, y and z directions, suggesting little regional anisotropy. There is only a weak regional anisotropy between the horizontal and vertical hydraulic conductivity with median ratio Kh_{max}/Kz of about 1 to 1.5;
- The regional model from F1.1 ~ 15 km (SW-NE) by 11 km (NW-SE) was more than sufficient for reference water calculation for site areas since flow in the candidate area is quite localised. The large area was retained to allow the evolution of flow and transport in to the future to be considered when the shoreline is likely to retreat to the north. A refined grid of at least 50 m element size is required throughout a local area that covers the release-area and the calibration boreholes to represent flow and transport due to a large number of sub-horizontal zones within the candidate area;
- Calibration of hydraulic and hydro-geochemical properties is most sensitive to the width and transmissivity of deformation zones that intersect the boreholes. This leads to depth dependent HCD property model that differentiates between gently and steeply dipping deformations zones. The presence and properties of deformation zones outside the candidate area have little effect on flow and transport, and hence the regional geological model cannot be calibrated currently;
- A Base Case model has been developed for F1.2 that gives a reasonable match to the hydro-geochemistry data using reference water mixing fractions, major ion concentrations and environmental isotopes at KFM01A–KFM04A. However, the hydro-geochemical data are sparse, especially at depth, so it was difficult to constrain model variants and parameters with confidence;
- HRD and HCD properties outside the candidate area had little effect on flow and transport inside since flow is relatively localised in the local-area. In fact, HRD block-scale properties of the DFN in rock domains RFM017/029 are most sensitive to the fracture transmissivity model rather than the fracture length distribution providing the other fracture parameters are calibrated to the hydraulic data in a consistent methodology;
- The results were not sensitive to surface property variants considered. Both a specified topographic head and a specified flux type boundary condition was considered, but for the infiltration and surface properties considered, the water table was close to ground surface so there was very little difference in results;
- Sensitivities to transport parameters such as flow-wetted surface, matrix porosity and diffusivity that affect RMD have been investigated. Matrix porosity was found to potentially influence the results, but not for the relative tight range of values supplied for this parameter. Hence, transport is probably most uncertain with respect to flow-wetted surface. The results here suggest a difference in groundwater concentrations between fracture and matrix systems if a_r is less than or around 0.25 m^2/m^3.

A series of transport calculations were performed for each of the variants considered to provide guidance for the Preliminary Safety Evaluation (PSE). Based on these results the following conclusions are drawn:

- The variations in the performance measures between the variants considered is generally low, around 5–10%. This perhaps should not be a surprise since all the cases considered have been calibrated against the same hydraulic data in the case of the Hydro-DFN variants, and against the same hydro-geochemistry data in the case of regional flow and solute transport.
- The F-quotient for most of the local-scale area is of order 10^6y m^{-1}, with the 5th percentile at about 10^5y m^{-1} and the 95th percentile at about 10^7y m^{-1}.
- The median path lengths stays around 1 km for all cases considered with only a few particles reaching further than 4 km. This indicates much localised flows in the modelled area.
- The uncertainties around the value of the flow-wetted surface should be addressed further since this has a significant impact mainly on the F-quotient.

This study has suggested some issues on which to focus further acquisition of site data:

- The PSS data helped reduce uncertainty in the intensity of flowing features at the low end of the transmissivity distribution. This was important in the relatively tight rock at Forsmark and will improve the constraint of hydraulic properties of fractures affecting canister-scale flows in the SR-Can safety assessment;
- This study suggests that efforts should focus on the locations and properties of deformation zones local to the site. This may involve further drilling to confirm seismic reflectors to establish the extent of zones, and also interference test within zones to investigate large scale flow and connectivity;
- Hydraulic properties in the top 100 m are uncertain as the cored boreholes are cased. However, the models have struggled to match a high Cl concentration near surface in some boreholes. To improve our understanding, hydraulic tests such as single-hole interference test in the top 200 m, say, would be useful;
- There is considerable variability in fracture intensity and flowing features within and between boreholes. In particular, KFM01A is very tight while KFM03A has flowing features at depth. Additional boreholes will be required to confirm any trends and their spatial extent. Hydraulic data outside RFM017/029 would also help set the hydraulic properties better in a regional-scale context. Although the result here suggest a low sensitivity;
- The hydro-geochemistry data available for Forsmark 1.2 were very limited, especially at or below –400 m (the provisional repository depth for Forsmark). Additional data would provide a better calibration target and assist constraining the hydrogeological models;
- The hydro-geochemistry data for the top 100 m is especially uncertain in the top 100 m of boreholes due to different water sampling techniques and contamination. Greater effort to acquire representative water samples in the top 100–150 m would significantly help focus the near-surface hydrogeological model calibration efforts;
- The groundwater model calibration has suggested that groundwater chemistry in the fracture system should be similar to that in the matrix if the flow wetted surface area is around 1 m^2/m^3, but different if it is less than 0.25 m^2/m^3. If the former value is valid it suggests groundwater infiltrates a network of small but connected fractures that give access to significant matrix diffusion, and hence potential retardation of radionuclides in the host rock. Experiments would be useful to verify this finding, e.g. porewater composition in cores far from flowing features or as a profile over a 20 m section, say, of borehole.

Some key uncertainties that should be considered within the SR-Can Safety Assessment based on F1.2 include:

- Some additional simulations need to be performed for the HCD properties. In particular, a gentler slope in the depth trend of transmissivity should be considered as this is will likely to lead to deeper flows, which may in turn lead to more regional flows. It may result in longer flow-paths and hence a positive effect on safety assessment. However, it should be considered to evaluate the sensitivity to the interpretation of a depth trend. Stochastic variations of transmissivity within deformation zones should also be considered;
- Transport properties, kinematic porosity and flow-wetted surface, of the HCD are another issue that requires further attention. It is suggested that one order of magnitude higher and lower be tried;
- Depth variations in the HRD hydraulic conductivity should be considered by variants with an order of magnitude higher and an order of magnitude lower in the top 100 m;
- DFN variants with an uncorrelated and semi-correlated transmissivity model should be considered since the results seemed to be sensitive to this, although the uncorrelated model gave a poorer correlation to the hydro-geochemistry data;
- The variant Geo-DFN should be considered in SR-Can as it may have a stronger impact on canister-scale flows than was seen here on regional-scale flows;
- A variant should be considered with lower open P32 below A2;
- Additional variants need to be considered with lower values of the flow-wetted surface, a_r, in the HRD, although it may be possible to discount them if they do not calibrate to the hydro-geochemistry data;
- Flow-paths need to be considered at future times, once the shoreline has retreated north from the site, as this will modify hydraulic gradients.

Contents

1 Introduction

1.1 Background

The Swedish Nuclear Fuel and Waste Management Company (SKB) is carrying out site investigations in two different candidate areas in Sweden with the objective of describing the in-situ conditions for a bedrock repository for spent nuclear fuel. The two candidate areas are named Forsmark and Simpevarp. The site characterisation work is divided into two phases, an initial site investigation phase (IPLU) and a complete site investigation phase (KPLU) /1/. The results of the IPLU are used as a basis for deciding on a subsequent KPLU phase. On the basis of the KPLU investigations, a decision is made as to whether detailed characterisation will be performed (including sinking of a shaft).

An integrated component of the site characterisation work is the development of descriptive site models (SDM). These comprise basic models in three dimensions with an accompanying text description. Central to the modelling work is the geological model, which provides the geometrical context in terms of a model of deformation zones and the rock mass between these zones. Using the geological and geometrical description models as a basis, descriptive models for other geo-disciplines (hydrogeology, hydro-geochemistry, rock mechanics, thermal properties and transport properties) will be developed /2/. In addition, a description is provided of the surface ecological system, which partly constitutes the interface between the geosphere and the biosphere. Great care is taken to arrive at a general consistency in the description of the various models, the assessment of uncertainty and possible data requirements of alternative models /3/.

A numerical model is developed on a regional-scale (hundreds of square kilometres) to understand the zone of influence for groundwater flow that affects the Forsmark area. Transport calculations are then performed by particle tracking from a site-scale release-area (a few square kilometres) to identify potential discharge areas for the site. A finer grid discretisation is used around the site-scale area to improve resolution of surface boundaries, geological structures, and hence flow pathways in this key model sub-domain.

Descriptive model versions are produced at specified times that are adapted to the needs of the primary users, i.e. repository design and safety assessment. These specified times define a “data freeze”, which identifies the database that should inform the model version in question. The results of the descriptive modelling also serve to produce feedback to, and set the priorities for, the ongoing site characterisation.

1.2 Scope and objectives

The main objective of this study is to support the development of a preliminary Site Description of the Forsmark area on a regional scale based on the data available as at June 30, 2004 (Data Freeze 1.2) and the previous Site Description /4/.

A more specific objective of this study is to assess the role of known and unknown hydrogeological conditions for the present-day distribution of saline groundwater in the Forsmark area on a regional scale. An improved understanding of the palaeo-hydrogeology is necessary in order to gain credibility for the Site Description in general and the

hydrogeological description in particular. The latter will serve as a basis for describing the present-day hydrogeological conditions on a local scale as well as predictions of future hydrogeological conditions.

Finally, this study aims to identify some of the issues that may impact the SR-Can Performance Safety Assessment (PSA) project, and where possible provide a preliminary evaluation of sensitivities to such issues. In particular, recommendations are made as to which uncertainties need to be addressed as part of SR-Can.

1.3 Setting and limitations

A number of new aspects to the scope of modelling have been included for F1.2. One of the most important is the representation and treatment of uncertainty of the deformation zones (DZs). Three new alternative geological models were produced for Version 1.2 based on different levels of confidence in interpretation. A base case (BC) was provided based on high confidence structures local to the site between the Singö DZ and Eckarfjärden DZ. One of the key features of this model is the presence of several extensive sub-horizontal DZs within the candidate area. A variant case (VC) was developed that considers an extension of some sub-horizontal zones beyond the candidate area. Finally, an alternative case (AC) case was proposed with the inclusion of many low confidence sub-vertical lineaments outside the candidate area. In addition to these considerations of the sensitivity to various structural models, the concept that hydrogeological properties for the hydraulic conductor domains (HCDs) should vary with depth and according to the dip of structures was introduced.
To address these new issues it is necessary not only to consider sensitivities to the HCDs themselves, but also to the size and discretisation of the model required to accurately represent them. The suggested regional model area is oriented 45° NE and has an area of 15 km by 11 km as shown in Figure 1-1. The local-area in which the high confidence DZs has been interpreted is 3.1 km by 9.3 km. A release-area for particles is required that is 2 km by 2.5 km around KFM01A.

Another key difference from F1.1 is the increased effort invested in conditioning the hydrogeological properties for the hydraulic rock domain (HRD) to the fracture boremap and hydraulic data. A new methodology was developed for interpreting the discrete fracture network (DFN) by integrating the geological description of the DFN (Geo-DFN) /5/ with the hydraulic test data from Posiva flow-log (PFL) and Pipe-string system (PSS) double-packer techniques to produce a conditioned Hydro-DFN model. This was done in a systematic way that addressed uncertainties associated with the assumptions made in interpreting the data, such as the relationship between fracture transmissivity and length.
PSS and PFL data were both available for only three boreholes, KFM01A–KFM03A. PFL anomaly data were also available for KFM04A–KFM05A. Considerable spatial variations in fracture occurrence and flow were observed within and between boreholes. However, it was felt there were insufficient data to substantiate anything more than relatively simplistic fracture spatial models, although it was believed important to differentiate rock properties inside Rock Domain 29 (the so-called ‘tectonic lens’ that spans the candidate area) from those outside.

Significantly, far greater quantities of hydro-geochemical data were available for calibration in the Version 1.2 data freeze for Forsmark. These were provided for cored boreholes KFM01A, KFM02A, KFM03A, KFM04A, and KFM05A and for a series of shallower percussion drilled boreholes. Further, the data were provided in terms of interpreted mixing fractions for reference waters, concentrations of major ions, stable isotope ratios and tritium concentrations in addition to the salinity data that had been supplied previously. This

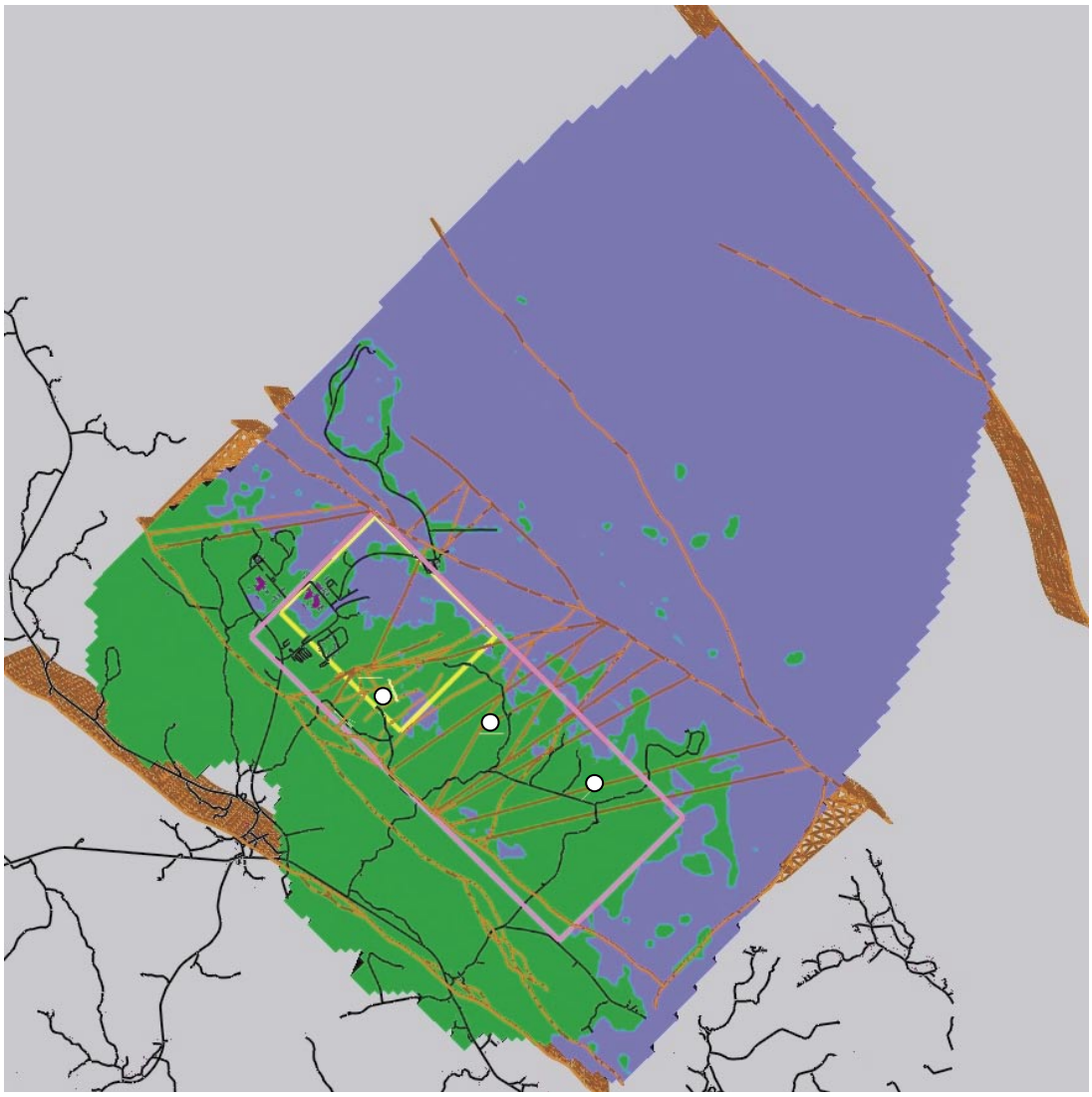

Figure 1-1. *Setting of regional scale area (green = land, blue = sea), roads (black), DZs (orange), local-scale area (pink), and particle release area (yellow) along with position of KFM01A (NW), KFM02A (middle) and KFM03A (SE).*

enabled a more widespread and comprehensive calibration of the groundwater flow models than was possible previously. However, data at elevations below –500 m were still sparse, and hence there remains uncertainty in interpreting and modelling the deep groundwaters.

The number of modelling cases that can be considered has to be limited so the reporting can be made according to the time schedule with the POM and PFM site modelling projects.

1.4 Organisation of work and structure of report

The numerical modelling was performed by two separate modelling teams. The focus of the simulations is in part different between the two modelling teams, CONNECTFLOW (CF) and DarcyTools (DT), although both teams have agreed a common initial regional model setup. While exploring the sensitivity of simulated hydro-geochemistry distributions to different geometric alternatives, variations in the initial and boundary conditions

and parameter uncertainties, CF have concentrated on confidence issues relating to the needs of Safety performance, whereas DT has focused on confidence issues of general hydrogeological character, e.g. model domain size and boundary conditions. It is recognised, however, that there is not a clear cut distinction between the two foci. Indeed, it is necessary to maintain some overlap on behalf of the objectives of SDM F1.2.

The work presented in this report was conducted by The CONNECTFLOW Team involving modelling experts from Serco Assurance, Kemakta Konsult and Golder Associates. The CONNECTFLOW code is developed and maintained by Serco Assurance /6, 7 and 8/.

This report presents the development of a Hydro-DFN for Forsmark, simulations of regional-scale variable-density groundwater flow, and transport calculations. Each phase of the modelling was specified a priori in a brief Task Description (TD), which was used to guide the modelling. Many variants were considered for the regional-scale groundwater flow to investigate the influence of conceptual and parameter uncertainties relating to initial and boundary conditions, DFN data interpretation, and background rock properties including some of the properties known to affect the rock matrix diffusion. Section 2 presents the overall modelling methodology, the model specifications and the deliverables on groundwater flow and particle tracking. Section 3 and Appendix B describe the methodology for deriving the Hydro-DFN parameters and its application to Forsmark. In Section 4 these parameters are used to study block-scale hydraulic properties required by Design and the regional-scale modelling. Section 5 gives more specific information on the overall approach to modelling groundwater flow at Forsmark and the various assumptions and uncertainties. The methods and data available for calibrating the regional flow models are detailed in Section 6. Section 7 presents the results for the calibration of the regional flow model and variants against the hydro-geochemistry and hydraulic data in boreholes. The results for the simulations of reference waters at the present-day are illustrated in Section 8. Further results for the groundwater flow patterns, discharge areas and reference water distributions for each variant considered are included in Section 9. Finally, Section 10 concludes the study.

A glossary of abbreviations used in the report is included in Appendix A. A series of transport calculations for particles released in the local-scale and site-scale release areas were performed for each of the variants considered to provide guidance for the Preliminary Safety Evaluation (PSE) and are presented in Appendix C.

2 Model set-up and specifications

2.1 Modelling methodology

The modelling methodology used in this study is based on the use of the discrete fracture network (DFN) concept, which explicitly represents fractures within a rock mass and calculates flows through the individual fractures and between fractures at intersections. Using DFN models it is possible to integrate statistically-generated, smaller-scale fracture sets with large-scale deterministic features. From these DFN models, it is then possible to generate equivalent porous medium (EPM) models by converting the flow properties of blocks of the fracture network into the equivalent properties for a porous medium block of the same size. This effectively 'smears' the flow from the fractures intersecting a block boundary across the whole of the block face. Serco Assurance's CONNECTFLOW software was used to carry out the modelling as it allows both DFN and EPM representations to be used independently or combined in a single model.

The models generated in this study have been used to calculate the flow of groundwater at Forsmark and also the transport of dissolved species in the groundwater. This latter facility has enabled density dependent calculations to be undertaken using an option in CONNECTFLOW that allows the mixing of various groundwater 'end members' (groundwaters with defined compositions) to be tracked. From these models, the flow field at the present day has been used to track particles released from potential repository locations at Forsmark to the model boundary, from which transport performance measures are derived.

The regional groundwater models are constructed from the following three hydro-geological units:

HCD Hydraulic conductor domains – deterministically represented fracture zones of generally relatively high conductivity;

HRD Hydraulic rock domains – the bedrock between the fracture zones;

HSD Hydraulic surface domains – the surface hydrological units.

This distinction is made since different modelling concepts, field investigations, and interpretation techniques are applied to each.

The following subsections describe the main concepts and assumptions used in the Forsmark 1.2 modelling study.

2.2 DFN model representation

The discrete fracture network (DFN) concept assumes flow though a fractured rock is predominantly through an inter-connected network of flow-conductive fractures with groundwater moving from one fracture to another at the intersections between them. The properties of the network are usually characterized in terms of:

- Spatial distribution (e.g. Poisson, fractal, clustered around points or lineaments);
- Fracture intensity (and its spatial variation);
- Number of fracture orientation sets.

The properties of individual fractures are primarily:

- Either deterministic or stochastic;
- Length;
- Orientation (strike and dip);
- Transmissivity (and possibly spatial variability within the plane);
- Transport aperture;
- Storativity.

In CONNECTFLOW, fractures are rectangular, or may be right-angle triangles where a complex surface has been triangulated into many pieces. For stochastic fractures, the properties are sampled from probability distribution functions (PDFs) specified for each fracture set. The properties may be sampled independently or correlated.

The purposes of the Hydro-DFN modelling exercise were:

- Checking the fracture distributions in the boreholes based on the Geo-DFN;
- Deriving transmissivity distributions to match the observed flows in the Posiva flow-log (PFL) and Pipe-string system (PSS) data;
- Deriving the statistical distributions of equivalent porous medium (EPM) properties on specified block scales for addressing design issues using flux-based upscaling;
- Creating realisations of the regional-scale EPM model based on upscaling regional-scale DFN models.

The DFN concept is very useful since it naturally reflects the individual flow conduits in fractured rock, and the available field data. However, to understand flow and transport on the regional-scale it is often necessary to consider larger-scale bulk properties in the context of an EPM continuum concept. This requires methods (i) to convert the properties of a network of discrete fractures of lengths less than the continuum blocks into equivalent continuum porous medium (CPM) block properties, known as upscaling, and (ii) to represent larger scale features such as fracture zones by appropriate properties in a series of continuum blocks, i.e. a downscaling method. The implementation of upscaling and downscaling in CONNECTFLOW is described in subsections 2.3 and 2.4, respectively.

2.3 Fracture representation as equivalent EPM flow properties

In order to assess the implications of the DFN model on flow and transport on the regional-scale, it is often necessary for practical reasons to convert the DFN model to an EPM model with appropriate properties. The resulting parameters are a directional hydraulic conductivity tensor, fracture kinematic porosity and other transport properties (such as the fracture surface area per unit volume). In CONNECTFLOW a flux-based upscaling method is used that requires several flow calculations through a DFN model in different directions.

Figure 2-1 shows an illustration of how flow is calculated in a DFN model (a 2D network is shown for simplicity). To calculate equivalent hydraulic conductivity for the block shown, the flux through the network is calculated for a linear head gradient in each of the axial directions. Due to the variety of connections across the network, several flow paths are possible, and may result in cross-flows non-parallel to the head gradient. Cross-flows are a common characteristic of DFN models and can be approximated in an EPM by

an anisotropic hydraulic conductivity. In 3D, CONNECTFLOW uses a six component symmetric hydraulic conductivity tensor. Using the DFN flow simulations, the fluxes through each face of the block are calculated for each head gradient direction. The hydraulic conductivity tensor is then derived by a least-squares fit to these flux responses for the fixed head gradients. Other authors /9/ have only considered the components of the equivalent hydraulic conductivity parallel to the coordinate axes using a head difference between opposite faces and no-flow on the other faces. This leads to a very poor representation of blocks in which the network connections, and hence flow, are mostly between adjacent faces rather than between opposite faces. The effective permeability assigned to such blocks may be essentially zero, even though the flow paths through the block may contribute significantly to the overall flow through the network.

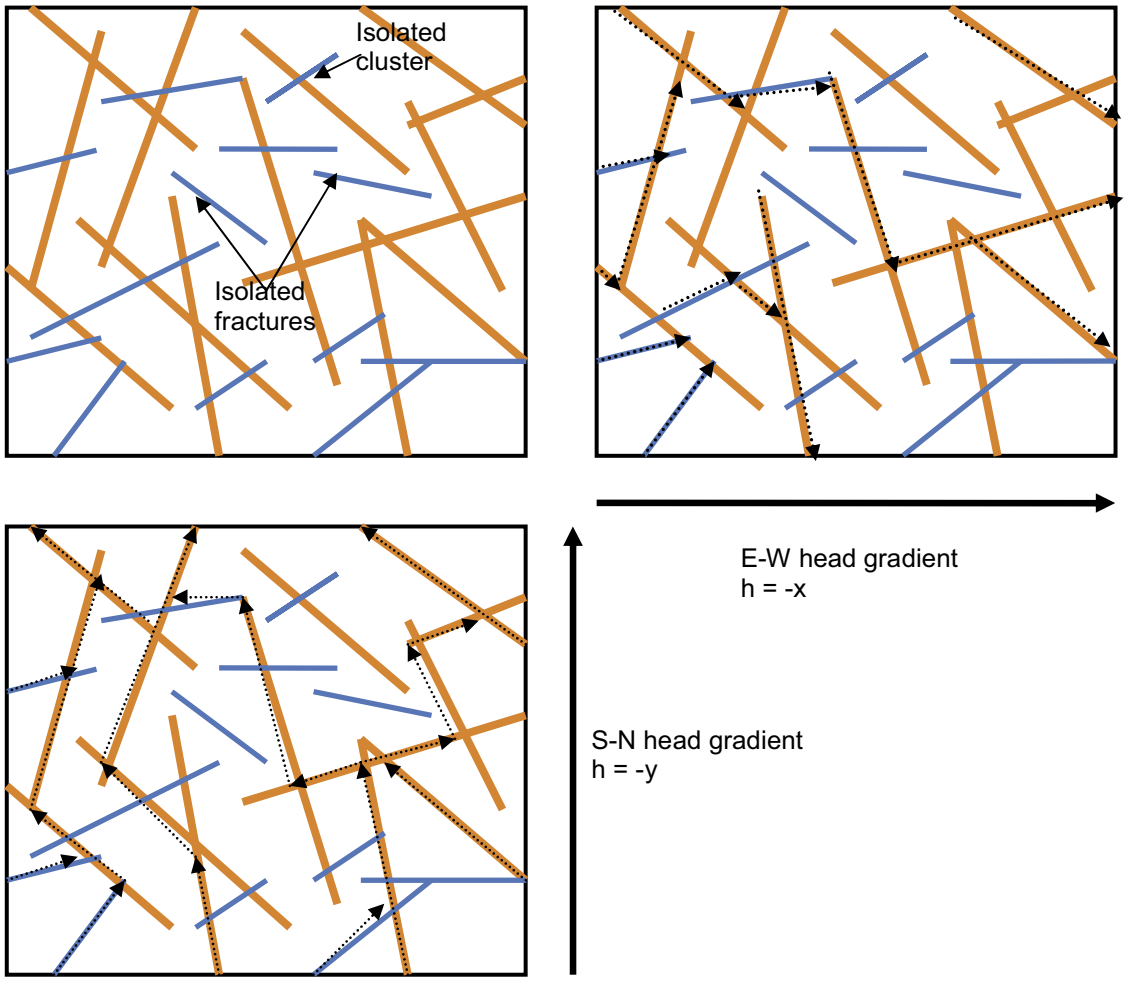

Figure 2-1. *2D illustration of flow through a network of fractures. A random network of fractures with variable length and transmissivity is shown top left (orange fractures are large transmissivity, blue are low). Top right: flow paths for a linear head gradient E-W decreasing along the x-axis. Bottom left: flow paths through the network for a linear head gradient S-N decreasing along the y-axis.*

In 3D, the blocks have to be hexahedra (cuboids), but the upscaling method can be applied to an array of sub-blocks within a much larger DFN domain by performing the upscaling on each sub-block in sequence. The upscaling method is typically used in one of two ways:

1. To obtain the statistical distribution of hydraulic conductivity on a given block scale a DFN model is generated for a much larger domain, and then EPM properties are calculated for an array of sub-blocks of equal size and shape to give an ensemble of properties;
2. To obtain an EPM model for a local- or regional-scale grid, a DFN model is generated within the grid domain, and the upscaling is performed within each grid element to derive the EPM properties element by element.

A detailed description of the upscaling method to calculate the EPM hydraulic conductivity tensor is given in Reference /10/. Briefly, the method can be summarised by the following steps:

- Define a sub-block within a DFN model;
- Identify the fractures that are either completely inside or cut the block;
- Calculate the connections between these fractures and their connection to the faces of the block;
- Specify a linear head gradient parallel to each coordinate axis on all the faces of the block;
- Calculate the flow through the network and the flux through each face of the block for each axial head gradient;
- Fit a symmetric anisotropic hydraulic conductivity tensor that best fits (least-squares) the flux response of the network;
- Fracture kinematic porosity is calculated as the sum (over all fractures that are connected on the scale of the block) of fracture area within the block multiplied by the transport aperture of the fracture.

Hence, to calculate the EPM properties for a finite-element grid with 1 million elements, say, involves 3 times 1 million DFN flow calculations. One important aspect of this approach is that the properties are calculated on a particular scale, that of the blocks, and that a connectivity analysis of the network is performed only on the scale of the block. Bulk flows across many blocks will depend on the correlation and variability of properties between blocks.

One refinement of the upscaling methodology is to simulate flow through a slightly larger domain than the block size required for the EPM properties, but then calculate the flux responses through the correct block size. The reason for this is to avoid over-prediction of hydraulic conductivity from flows through fractures that just cut the corner of the block but that are unrepresentative of flows through the in-situ fracture network. This is the method used in this study and is illustrated in Figure 2-2. The area around the block is known as a ‘guard-zone’, and an appropriate choice for its thickness is about half a fracture length. The problem is most significant in sparse heterogeneous networks in which the flux through the network of fractures is affected by ‘bottlenecks’ through low transmissivity fractures, and is quite different to the flux through single fractures.

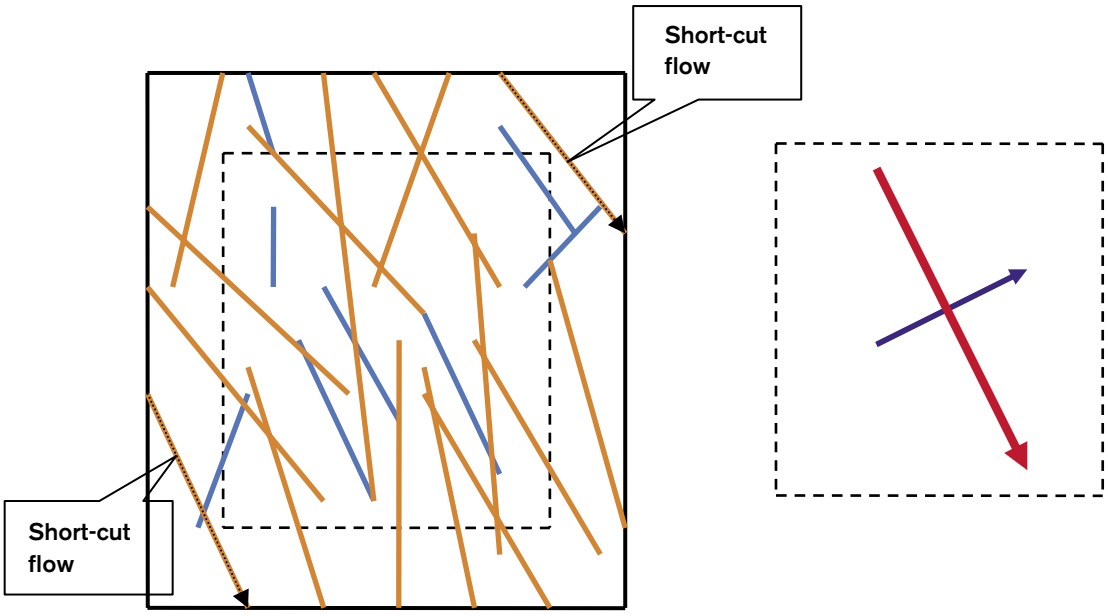

Figure 2-2. *2D sketch of how block-scale hydraulic conductivity can be over-estimated using a linear head gradient by high transmissivity fractures that cut across a corner of the block. By simulating flow through a larger domain, but only calculating the flux through the required block size (dashed block) then fluxes more consistent with flow through an in-situ network are obtained. The EPM hydraulic conductivities are then calculated for the dashed block to give principal components (right). The red arrow is the maximum component, blue the minimum.*

2.4 Implicit representation of fracture zones (the 'IFZ' method)

For Forsmark 1.2, the basic concept is that fractures exist on a continuous range of length scales, which motivates a methodology to generate sub-lineament-scale fractures stochastically on scales between tens of metres and about 1 km, and then combine this DFN by superposition with the larger scale deterministic deformation zones. In CONNECTFLOW, the approach taken was to create one or more realisations of the stochastic network on the regional-scale and then, using the upscaling methods described above, to convert this to a realisation of the EPM model, minus the deformation zones. That is, at this point the EPM model was only an equivalent representation of the stochastic network. The EPM model was then modified to incorporate the structural model in terms of the geometry and properties of a set of large-scale deformation zones using the Implicit Fracture Zone (IFZ) method in CONNECTFLOW as described in Reference /11/. The reason for this approach was that it was then relatively quick to combine different scenarios for the deformation zones with the stochastic DFN model without having to repeat the computationally expensive upscaling step.

The IFZ downscaling method identifies which elements are crossed by a fracture zone and combines a hydraulic conductivity tensor associated with the fracture zone with a hydraulic conductivity tensor for the background stochastic network. For each element crossed by the fracture zone the following steps are performed:

- The volume of intersection between the fracture zone and the element is determined;
- The hydraulic conductivity tensor of the background rock is calculated in the coordinate system of the fracture zone;

- The combined conductivity tensor of the background rock and the fracture zone is calculated in the coordinate system of fracture zone;
- The effective hydraulic conductivity tensor that includes the effect of the fracture zone is determined in the original coordinate system.

The methodology is illustrated diagrammatically in Figure 2-3. In 3D, the resultant hydraulic conductivity is a 6-component symmetric tensor in the Cartesian coordinate system. The tensor can be diagonalised to give the principal components and directions of anisotropy.

Similarly, a combined scalar block-sale porosity is calculated for the element based on combining the fracture zone porosity and the background block-sale porosity using a weighting either based simply on either the relative volume or on relative transmissibility (total channel flow capacity, which is transmissivity times flow length (m^3s^{-1})). The latter weighting can be suitable for transport since it weights the combined porosity toward the fracture zone porosity if this is of a relatively high hydraulic conductivity. The result of this step is to produce a spatial distribution of CPM element properties (hydraulic conductivity tensor and porosity) that represent the combined influence of both the deterministic fractures zones and background stochastic fractures.

It may be noted the term “background conductivity” here means the equivalent conductivity of the stochastic fracture network. No extra component for matrix conductivity or micro-fracturing is added. However, the stochastic DFN is necessarily truncated in some way e.g. based on fracture length which consequence means that some elements may include a connected network of fractures or may only be connected in some directions. To avoid this just being a result of the choice of truncation limit and chance, a minimum block

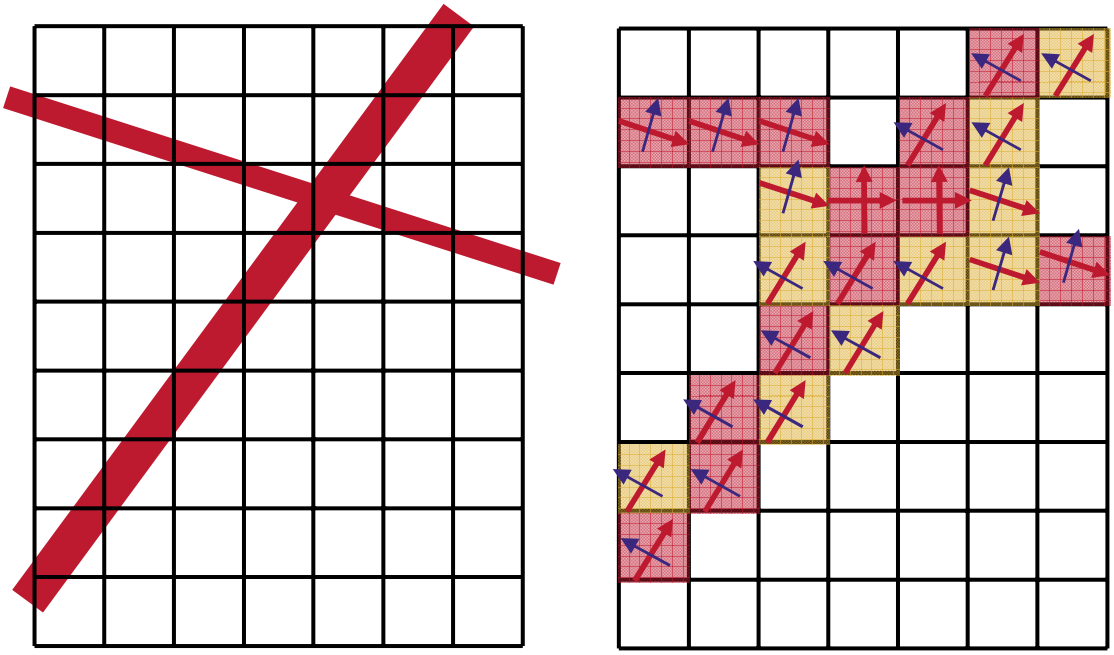

Figure 2-3. *Schematic illustration of the modification of the hydraulic conductivity tensor by the IFZ method. A finite-element grid crossed obliquely by two fracture zones of different thickness (left). The effect on the equivalent porous medium hydraulic conductivity (right). Elements with a large IFZ effect are coloured pink. Ones with a lesser effect, where the fracture zone only crosses one corner, are coloured orange. The principal directions of the resultant anisotropic hydraulic conductivity tensor are shown by arrows (red for major component, blue for minor).*

conductivity and porosity is set for any elements that have zero properties following the fracture upscaling and IFZ methods. Appropriate minimum properties are derived from the block-scale property studies by calculating the minimum values seen when the DFN is truncated only at very small fractures relative to the block size, and so are essentially free from the truncation effect.

2.5 Variable density groundwater flow and salt transport

An option has been added to CONNECTFLOW for the Version F 1.2 modelling to model flow in a porous medium for groundwater of variable salinity, where the salinity arises from a number of groundwater constituents. This can be modelled either in terms of transport of mass fractions each of the basic hydro-geochemical constituents (such as chloride, sodium, oxygen isotope ratio), which are taken to be conservative, or in terms of transport of fractions of selected reference waters. Either way, the transport equations are coupled with the overall mass conservation equation for groundwater.

The first approach would to be solve transport equations for each of the major ions and isotopic values with the transient groundwater flow and including a coupling back to the flow via spatial variations in groundwater density due is varying composition. Since the raw hydro-geochemical is analysed in terms of concentrations of major ions then this option appears attractive as it models what is measured. However, the model would need to be formulated in terms of individual ion concentration of the initial groundwaters and the surface waters as they evolve in time. This would not be straightforward since the hydro-geochemical conceptual understanding and data have been developed in terms of the mixing of fractions of well defined reference waters. In consequence it is more practical to use the option for transport of reference water fractions since the boundary conditions for the flow modelling are most naturally expressed in the terms of the reference waters. This option makes the approximation that the geochemical composition of a mixture of reference waters can be related linearly to the compositions of the individual reference waters (i.e. no reactions), and that transport properties of the major ions (e.g. diffusivities) are similar. The option also provides a very user-friendly way of presenting the results of multi-component groundwater flow calculations, which are given directly in terms of the selected reference waters for direct comparison with the Mixing and mass-balance modelling (M3) geochemical analysis. In addition, the assumed linear relationship between reference water mixing fractions and groundwater composition can be used to obtain the concentrations of the basic geochemical constituents for direct comparison with measurements of groundwater chemistry. This option has been used in the EPM regional-scale model. A simplified representation in terms of four reference waters (Rain 1960, Marine, Glacial, and Brine) was used (see subsection 5.3).

Transport of fractions of reference waters can be modelled using the same equations used to model transport of groundwater constituents (the various ionic species, oxygen and hydrogen isotope ratios) provided that it is assumed that the constituents have the same dispersion, matrix diffusion and sorption properties. This may be a good approximation for dispersion, which may be largely determined by the variations in groundwater velocity within and between pores. However, the self-diffusion coefficients for the various constituents differ by a factor of about two, and so the effective (or intrinsic) diffusion coefficients would be expected to differ by a similar factor, or even more, if anion exclusion is significant. If differences of this order are considered important, then the standard transport equations can only be used to model the transport of constituents. For this work it has been assumed that these factor differences in diffusion rates are relatively unimportant, and hence we can work in terms of mixing fractions.

However, the following point should be noted. Because of the linearity of the transport equations (in the assumed absence of reactions), linear combinations of the constituents also satisfy transport equations. Transport equations for the fractions of reference waters can still be written down, therefore, even if the diffusion coefficients for the different constituents are different. However, the key point is that each equation no longer involves only a single reference water, but the equations are coupled. In this case, it would probably be best to carry out the transport calculations in terms of constituents, translating between reference waters and constituents before and after the calculations if necessary.

It should also be noted that if the constituents have different transport properties, it is also necessary to account for the constraint of electro-neutrality.

It is also possible to model diffusion of the reference waters, or constituents, between groundwater flowing in fractures and immobile water in the rock matrix between the fractures (rock-matrix diffusion or RMD). The numerical approach used /12/ is based on a method developed by Carrera et al. /13/ enhanced to enable potentially larger time steps to be taken. The approach combines an approximation that is accurate for small times with one that is accurate for long times, to give a representation of the diffusion into the rock matrix that is accurate for all times. At early times, the diffusion is represented in terms of the inverse of the square root of time, and at long times it is represented as a series of decaying exponentials. The approach is very efficient computationally, although it is necessary to make the assumption that the groundwater density does not vary in the rock matrix at each location.

2.6 Boundary condition concepts

Simulating the palaeo-hydrogeology for Forsmark 1.2 requires modelling of the evolution of groundwater flow and solute transport during the post-glacial period up to the present day. A key issue in this exercise is how to represent the time-varying boundary conditions for both flow and solutes or reference waters.

For flow, there are two main possibilities onshore: either specified head, or a flux type boundary condition. For specified head, the model is assumed to be fully saturated, and hence head is equal to the height of the topographic surface at that time according to the sea-level transgression. Offshore it is most natural to use a specified head type boundary condition. Here, the head is equal to the depth of the sea multiplied by the relative salinity of the Baltic Sea, and both the salinity of the Baltic and sea depth alter in time.

Specified head boundary conditions are straightforward to implement numerically by setting the value at nodes on the surface to the required head at each time-step. For the flux type boundary condition is more complicated because in reality the flux through the top surface will vary spatially both in magnitude and direction since in some areas groundwater is recharging and other it is discharging. This distribution of flux varies according to the amount of potential infiltration and the hydraulic properties it is also going to change in time as the shoreline retreats. The approach taken in CONNECTFLOW is to define the recharge flux, R, into or out of the model as a function of the current head, h, in the model, the topographic surface height, z, and the potential infiltration, I. Appropriate functions for the flux, R, must have certain characteristics. For recharge areas the head, or water table, is below ground surface and so the recharge must be equal to the full infiltration, I. In discharge areas, the water table is just above ground surface so head is just above ground surface, which can be achieved by having a taking a suitably large flux out of the model, i.e. negative value of R, whenever the head goes above ground surface. The standard function used in CONNECTFLOW is:

$$R = \begin{cases} I & h \le z - \varepsilon \\ -I(h-z)/\varepsilon & h > z - \varepsilon \end{cases},$$

where ε is a small number. This function implies that if the water table is more than ε below the topographic surface then recharge equals the full potential infiltration. Above that, the recharge reduces until the water table is at the surface. If the water table is above the topographic surface, then recharge becomes negative, i.e. discharge, and an appropriate flux of groundwater is taken from the model to reduce the head until the water table is restored to the topographic height. Hence, this boundary condition is a non-linear equation (the flux depends on the free-variable head) that ensures a specified flux if the water table is low and a specified head where the water table is at or above ground surface. The non-linearity requires that multiple iterations of the groundwater flow equations be performed at each time-step to reach convergence, which implies longer run times for this boundary condition. The topographic surface is not constant in time due to post-glacial rebound and marine transgressions, and hence z = z(t). Newton-Raphson iteration was used to achieve convergence of the non-linear equations at each time-step. This technique works best for systems with smooth gradients. The standard function given above for flux has a discontinuous derivative at h = z-ε and this led to a slow rate of convergence; typically 3–5 Newton-Raphson iterations were required at each time-step. Hence, an alternative smooth function for recharge was tried:

$$R = I \times \left(\exp\left(\frac{h-z}{0.5} \right) - 1 \right).$$

This has similar characteristics to the standard function, but has smooth derivatives around h = z. It was found to always converge in 2 Newton-Raphson iterations for the time-step used, and hence gave quicker and more robust solutions. There are other candidates for this function such as a modification to the standard function but using a hyperbola to give a smooth transition around h = z.

For solutes, the boundary conditions are generally a specified value where there is an advective flow into the model (recharge area), or an outflow condition where there is flow out (discharge). Because the flows are transient, the areas of recharge and discharge evolve in time, and hence it is important to have an automatic way of determining the recharge and discharge areas automatically. The problems in achieving this are that it requires mixing a Neumann, or flux, type boundary on outflow with a Dirichlet, or value, type boundary condition on inflow; and since the recharge/discharge areas change in time, then the type of boundary condition has to be changed in time. Hence, we use a trick to specify a flux of solute over the top surface that changes depending on the direction of flow across the model boundary with the Dirichlet condition on inflow being achieved as a penalty weight function of the difference between solute concentration in the model and the required input concentration. The flux of solute out of the model, F_c, is then given by the equation:

$$F_c = \begin{cases} (q \cdot n)c & q \cdot n \ge 0 \\ (c - c_0)/\delta & q \cdot n < 0 \end{cases},$$

where q·n is the advective flux out of the model, i.e. the groundwater flow, q, in the direction parallel to the outward normal to the surface, n, c is the solute concentration or mixing fraction, and δ is a small number. For $q \cdot n \ge 0$ the flux corresponds an outflow condition, for $q \cdot n < 0$ a specified value condition, $c = c_0$, is implemented as a penalty function such that solute is removed if $c > c_0$, and injected if $c < c_0$ this effectively ensures that $c \approx c_0$.

2.7 Transport performance measures: Canister flux (q), Travel time (t_w), Pathlength (L) and F-quotient (F)

One objective of the site descriptive modelling is to understand groundwater pathways from a local-scale area to the surface. The approach taken is to track particles moving with the advective flow velocity from a range of release points until they reach the top surface. Although it would be possible in CONNECTFLOW to track particles as they move through a velocity field that evolves in time, it is preferred here to only use the velocity field from the present day. This is mainly because particle tracks released in a transient velocity field would be sensitive to the release time and the kinematic porosity, making it more difficult to interpret the results due to the added uncertainties. One uncertainty that it is important to address here is the effect of the stochastic DFN on regional-scale pathways. Hence, several realizations of the DFN model, and hence the EPM model, will be considered here to quantify the sensitivity of transport performance measures to particular realizations. The four performance measures required are:

- Travel time, $t_w = \sum_l \frac{\phi \delta l}{q}$, where δl is a step in distance along the path, for example through one finite-element, Φ is the kinematic porosity, and q the Darcy velocity;
- Canister flux, $q = q_0$, the initial Darcy velocity at the release point;
- Pathlength, $L = \sum_l \delta l$;
- F-quotient, $F = \sum_l \frac{a_r \delta l}{q}$, where a_r is the fracture surface area per unit volume.

The approach to calculating the performance measures is to release a large number of particles distributed evenly (fixed spacing) over the local-scale area and use these to produce ensemble statistics for the performance measures, as well as locating the discharge areas. No attempt is made to avoid starting particles in either deterministic fracture zones or high transmissivity stochastic fractures. In reality such features are likely to be avoided during repository construction, and hence the model may tend to see particles start in a wider range of possible fracture transmissivities than might be encountered in reality.

2.8 Modelling strategy

A key philosophy in developing the groundwater models described here has been to calibrate model parameters against field data within a margin appropriate to the quality and availability of the data. Equally, it is important that any variants considered in order to quantify uncertainties are also calibrated to data, rather than being arbitrary parameter variations, so than in a sense they are equally possible realisations. As such, many models have been created during this study, but in the reporting we focus on the combinations of parameters and conditions that give predictions consistent with field data. The variants reported here are therefore the ones that have been constructed to demonstrate the uncertainties that remain in the model concepts and parameters, and consequent model predictions, due to the lack of constraint by the available data. These variants are used to quantify sensitivities and form the basis for recommending important uncertainties that should be propagated to the SR-Can Assessment calculations.

3 Assessment of hydraulic Discrete Fracture Network (DFN) model

The current site characterisation of Forsmark, F1.2, has provided a Geo-DFN model of fracture geometrical data (orientation and intensities) based on outcrop and borehole data. However, for the hydrogeological modelling it is necessary to integrate the hydraulic data, namely the Posiva flow log (PFL) data and double packer injection test data, known as Pipe-string system (PSS) data. In doing so, it may be necessary to make some practical simplifications to derive a complete Hydro-DFN fit for modelling. Having derived a Hydro-DFN, block-scale properties on 100 m and 20 m scales are required for regional groundwater flow (GWF) property assignment, and also for repository design issues.

A Task description PFM_1 2_Hydro-DFN_1.1.doc has been issued to specify these tasks. The work reported here on the Hydro-DFN includes:

- Simulating the discrete fracture network (DFN) model(s) based on delivery by Geology (Geo-DFN) and testing different relationships between transmissivity models, fracture (feature) size and fracture (feature) intensities. Then comparing with borehole fracture statistics and hydraulic data from borehole tests and evaluating the transmissivities and comparing with measured transmissivities (PFL and PSS hydraulic test data). This is achieved by performing flow simulations based on flow through a fracture network for radial flow boundary conditions and then calibrating the interpreted transmissivities based on simulated and measured flow-rates.
- For each borehole (KFM01A, KFM02A, KFM03A, KFM04A and KFM05A), the fracture analysis and DFN parameterisation based on core-logs is summarised. In the case of KFM01A and KFM03A, DFN simulations of the PFL and PSS tests were carried out for various transmissivity models to compare modelled transmissivities with the measurements. For the PFL tests, the interpreted transmissivities from flow anomalies were grouped into 5 m intervals to give a distribution, and then compared with the equivalent interval transmissivities interpreted from the flow-rates in the simulations. For the PSS tests, the model predictions of the transmissivities of 5 m intervals were compared with the 5 m interval tests. The flow simulations considered alternative transmissivity models and are used to identify parameter ranges that can reproduce the observed flows.
- Based on a collation of the information from the group of Forsmark boreholes, recommendations are made for the DFN definition to be applied in the regional and site-scale GWF modelling.

The work reported here on the block properties in the Forsmark area includes:

- Estimation of the anisotropy in horizontal and vertical directions;
- Calculation of the statistics of the hydraulic conductivity of 100 m and 20 m blocks;
- Evaluating the effects of size-truncation of stochastic features and cell-background properties for the forthcoming Regional-Scale GWF modelling;
- Calculation of the kinematic porosity based on the ‘aperture = function(Transmissivity)’ relationship from Äspö Task Force 6c /14/;
- Calculation of the block properties for the alternative transmissivity models;
- Comparison of block properties derived from the DarcyTools Team and the CONNECTFLOW Team to quantify uncertainties.

3.1 Methodology

A methodology was developed and tested using data from Simpevarp as part of the Pre-S1.2 and the S1.2 /15/ modelling exercises. The approach had to be modified slightly for Forsmark to address some site-specific issues. The current workflow used in F1.2 can be summarised by the following steps:

1. Group fractures using the borehole core-log according to whether they are inside or outside Deformation Zones (DZs), and into rock domains for fractures outside of a DZ;
2. Generate stereonets for each DZ that are Terzaghi-corrected for borehole and fracture orientation. Check fracture orientations against Geo-DFN orientation sets (focus on brittle DZs). Calculate fracture intensity in each zone;
3. Within a borehole, compare the mean poles of dominant fracture sets within each DZ, and fracture intensity within each DZ;
4. Calculate the linear fracture intensity[1], P10, and Terzaghi-corrected $P10_{corr}$ (and range of values according to confidence indicator [certain/probable/possible]) for rock domains outside of DZs, and mark according to the orientation sets defined in the Geo-DFN. Use Terzaghi correction for borehole data to compare $P10_{corr}$ with that obtained in Geo-DFN;
5. Fit orientation statistics for sets in rock domains outside of DZs. Derive borehole-specific Geo-DFN set statistics (mean azimuth, mean dip, Fisher concentration, open $P10_{corr}$) for each of the Geo-DFN sets. Note that fracture intensity is based on both confidence indicators 'open' and 'partly-open', although for simplicity, this is denoted as '$P10_{corr}$, open' in this text;
6. Analyse fracture intensity for depth trend;
7. Use length distribution from Geo-DFN;
8. Assume a reference length, L_0, for the $P10_{corr}$ model (either borehole diameter (76 mm) or outcrop minimum (0.5 m))
9. Generate five realisations of the DFN model around the borehole and check the modelled P10open in the borehole against that in the field data. Adjust $P10_{corr}$ if necessary. (Note: the actual number of open fractures is not known. We only have an estimated range based on the confidence indicator $P10_{corr}$, open/certain to $P10_{corr}$, open);
10. Cross check the area density P21 distribution qualitatively with outcrop maps;
11. Define alternative transmissivity concepts (uncorrelated; log-normal: correlated; direct T vs L correlation: semi-correlated; correlated but with log-normal perturbation);
12. For each T concept, use DFN flow simulations to match the interpreted distribution of transmissivity for 5 m intervals. For the PFL data, this requires that the transmissivity of each flow anomaly be grouped into 5 m intervals. This gives distributions of T for 5 m intervals consistent with the data format from the PSS tests. Intervals associated with DZs have to be removed from the data when calibrating the transmissivity of the background fractures;
13. For each T concept, identify possible ranges of parameters, i.e. uncertainties;
14. Analyse PFL data for orientations of flow anomalies. Compare with regional stress field;
15. For each T concept, calculate block-scale directional permeability and porosity.

[1] The linear fracture intensity is the number of fractures per metre along a defined line.

The objective of this modelling is to demonstrate one or more matches to the observations in the boreholes in a statistical sense, i.e. based on distributions of quantities such as transmissivity, rather than to reproduce very specific and perhaps localised characteristics seen in each borehole. The rationale behind this approach is that we are aiming to make conclusions that can be applied over the whole Forsmark area and also for the regional-scale GWF models, and hence it is most important to understand the DFN characteristics in a broad sense and also the associated uncertainties.

3.2 Modelling assumptions and input data

The available data that have been used in this study include:

- The borehole core logs that record all the fractures identified in the cores (cross-checked with the BIPS borehole image logs) along with a comprehensive set of fracture classifications (KFM01A, KFM02A, KFM03A, KFM04A and KFM05A);
- The PFL flow anomalies, including the flow rates and head changes for each feature (KFM01A, KFM02A, KFM03A, KFM04A and KFM05A);
- Rock domain data in boreholes, including Deformation Zones for each borehole;
- The outcrop maps (AFM000053, AFM000054, AFM001097 and AFM100201);
- The preliminary Geo-DFN fracture characterisation based on all outcrops and boreholes;
- Double-packer injection test data (PSS) for 5 m intervals in KFM01A, KFM02A and KSH03A.

The following assumptions have been made:

- L_0 for open fractures is either the borehole diameter (0.076 m) or the minimum measured length in outcrop (~ 0.5 m);
- Deformation Zones represent a swarm of fractures, but these are modelled and characterised as a single large stochastic feature;
- Fractures exist on all scales with stochastic fractures ranging in lengths from L_0 to 1 km;
- Fracture sets can be categorised based on orientation and length groupings (based on Geo-DFN);
- Fracture dip $\geq 50°$ for sub-vertical sets. Fractures with dips $< 50°$ are assigned to the 'sub-horizontal' set.

3.3 Conceptual models with potential alternatives

Few characteristics of the DFN can be determined uniquely and directly, so it is necessary to assume a framework of conceptual models, and then derive parameters that best match observed data.

3.3.1 Continuous power-law length distribution

One of the most difficult fracture characteristics to measure directly in the sub-surface is fracture length. Fracture lengths can be measured on outcrops for fractures on the scale of metres to tens of metres, and data are available for lineaments on the scale of 500 m to

several kilometres, but this leaves a gap between the scales. A widely used assumption is one of a continuum of fracturing that spans all scales and that can be described by a power-law relationship between fracture intensity and length. A schematic illustration of such a relationship is shown in Figure 3-1 and is compared with a lognormal distribution, which is another commonly used model for fracture length. The key parameters for the power-law distribution are the slope and reference length, L_0. The distribution is often defined only in a truncated range, $L_{min} < L < L_{max}$.

It should be noted that CONNECTFLOW represents fractures as squares, rectangles or triangulated surfaces. For this particular modelling squares are use, and the length of a side is denoted by L. Elsewhere in SKB's programme fractures are represented by discs of radius. Assuming a consistent area between both representations implies a conversion $r = L/\sqrt{\pi}$.

In the groundwater flow modelling for Forsmark 1.2, it will be assumed that fractures of length greater than 1 km will be modelled deterministically having been detected as lineaments or fracture zones, whereas fractures less than 1,000 m in length will have to be modelled stochastically based on the Hydro-DFN model developed here.

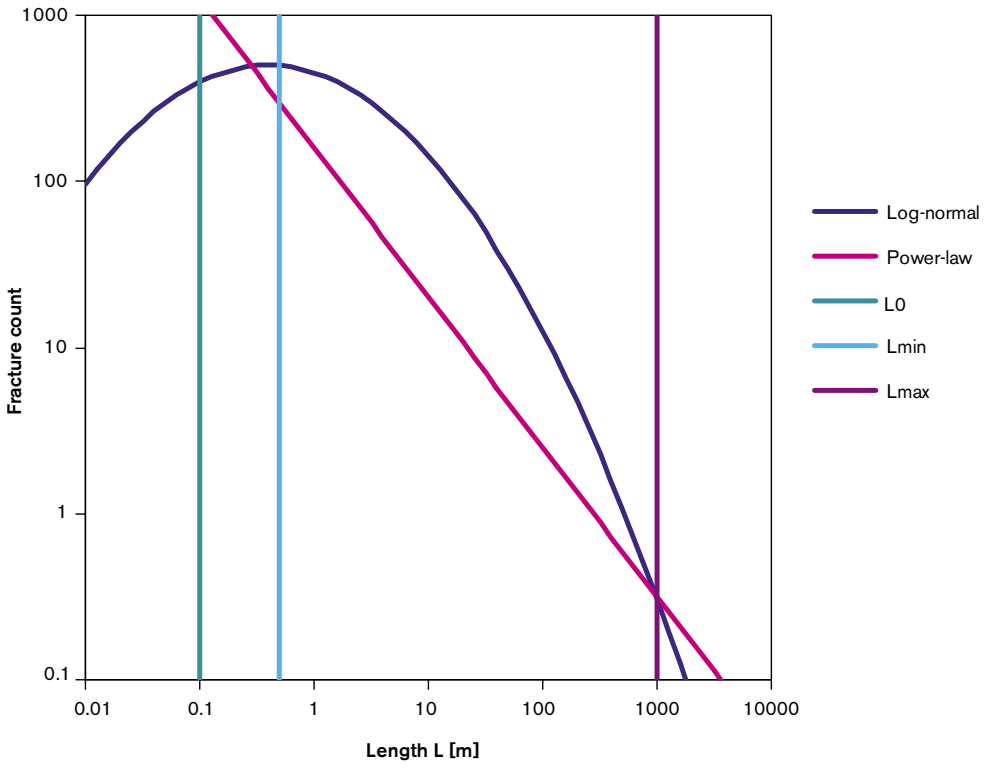

Figure 3-1. *Example of a power-law and lognormal model of fracture length distribution. Also shown is an example of the reference length, L_0, which depends on the resolution of the fracture observation technique. When a fracture network is simulated, it is often necessary for practical reasons to truncate the power-law distribution and these limits will be referred to as L_{min} and L_{max}.*

3.3.2 Stochastic lineament swarms represented as planar features

Large fractures of lengths on the order of 100 m may exist as single breaks. However, it is more common that discontinuities of lengths greater than about 50 m exist as Deformation Zones or 'lineament swarms'. A number of Deformation Zones are observed in the boreholes, and hence it is useful to characterise these features to get some indication of the width and fracture intensities within these zones. However, at this stage, Deformation Zones will be approximated as large stochastic fracture planes in a continuous range of fracture sizes as shown in Figure 3-2. It is important that data such as fracture intensity and the PFL flow anomalies are handled in a manner consistent with this concept. Also, transport parameters such as fracture kinematic porosity and flow-wetted surface may have to be enhanced in the larger fractures to reflect their zone characteristic.

3.3.3 Fracture intensity and Terzaghi correction

The potential bias arising from observing fractures cutting boreholes of varying trajectory was removed by correcting for the orientation of fractures relative to the trajectory of the borehole in which they were observed. The sketch in Figure 3-3 illustrates the issue in an idealised case. For sub-vertical fractures, a vertical borehole will cut fractures at an average separation of s that is much larger than the true separation, t. The ratio of $s/t = 1/\cos(\vartheta)$, where ϑ is the angle between the fracture pole and the borehole trajectory. For an inclined borehole near orthogonal to the fractures, the angle is much smaller and so s/t is close to 1. However, for a horizontal borehole parallel to the fracture strike, s/t would again be large.

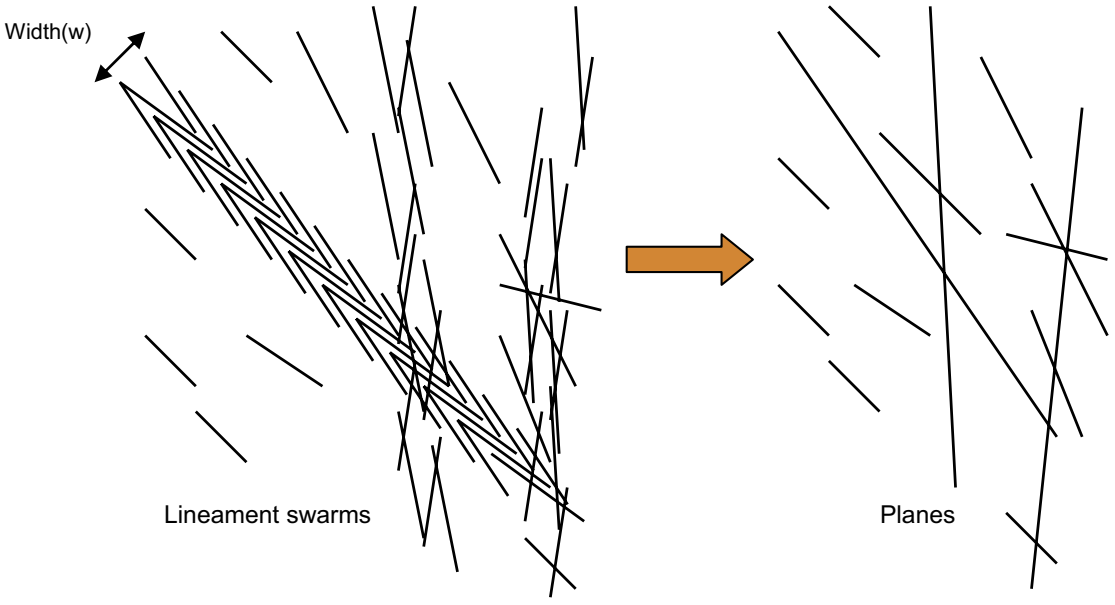

Figure 3-2. *Representation of lineament swarms as stochastic planar features using the power-law distribution.*

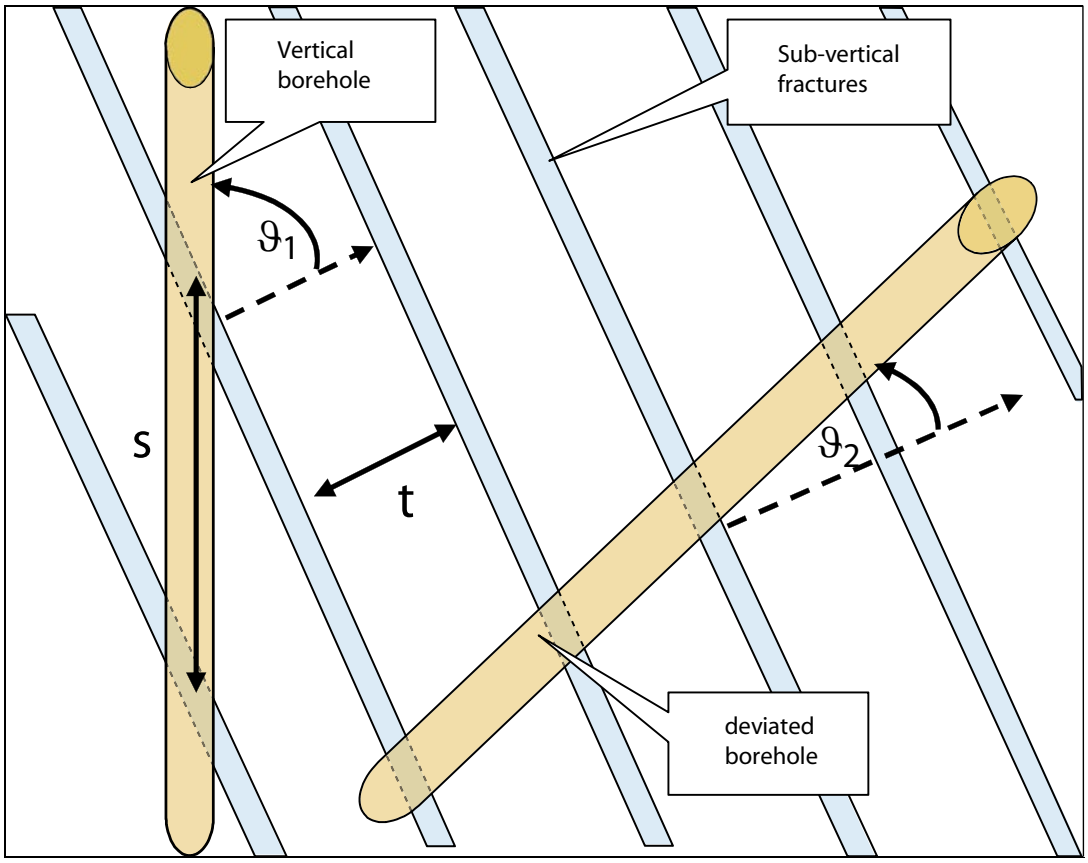

Figure 3-3. *Example of Terzaghi correction for different borehole orientations. The angles ϑ_1 and ϑ_2 are shown between the fracture pole (dotted arrow) and two different borehole orientations. The Terzaghi correction is proportional to 1/cos(ϑ).*

The implication is that care has to be used when combining fracture statistics, e.g. fracture intensities or counts from boreholes of varying orientation. In this illustration, P10 is 1/s, and $P10_{corr}$ is 1/t. In reality, each fracture has a different orientation and the borehole trajectory may vary downhole. Hence, a correction 1/cos(ϑ) is calculated for every fracture and this correction is used as a weighting when calculating statistics such as mean fracture poles, $P10_{corr}$, and when plotting density contours on stereonets. In addition, the orientation correction is used when calculating the percentage of fractures in each orientation set. Rather than just counting the number of fractures in each set, a weighted percentage is calculated by weighting each fracture by 1/cos(ϑ) (but using a maximum weight of 5 where ϑ is near to 90°).

An alternative correction factor is proposed by Darcel et al. /16/ for the case where the fractures encountered in the borehole are dominated by small ones, the lengths of which are comparable to the borehole diameter. Based on a power-law length model they propose a correction factor around $1/(\cos(\vartheta))^3$ for Simpevarp, which emphasises the sub-vertical fractures more, and would perhaps give more consistency when comparing the relative intensity of fracture sets when measured in boreholes against outcrops. However, this approach has not been used in this study.

3.3.4 Fracture transmissivity models

In the Forsmark Version 1.1 modelling, a direct correlation between fracture transmissivity and length was assumed. For F1.2 the uncertainty associated with this assumption was explored. Three alternative transmissivity concepts were considered for F1.2 (as shown in Figure 3-4):

1. Uncorrelated log-normal (mean, μ, and standard deviation, σ);
2. Directly correlated (factor, a, and exponent, b);
3. Semi-correlated T versus L: random log-normal spread about a mean based on a correlated function (factor, a, exponent, b, and standard deviation, σ).

All three cases were simulated in the development of a Hydro-DFN with Case 2 as the base case. Each of these concepts has an associated set of parameters, as given in parentheses above, and it is the objective of Hydro-DFN to explore what ranges of parameters required in the DFN simulations to give a match to hydrogeological data.

The second relationship was proposed in Reference /14/. One argument for it is that, at least for deformation zones, the zone width often increases with length, and thus generally the number of individual conductive fractures associated with zone. If the transmissivity distribution for individual fracture is the same, then based on the above assumption it follows that the effective transmissivity for the fracture zone should increase with the length of the fracture zone.

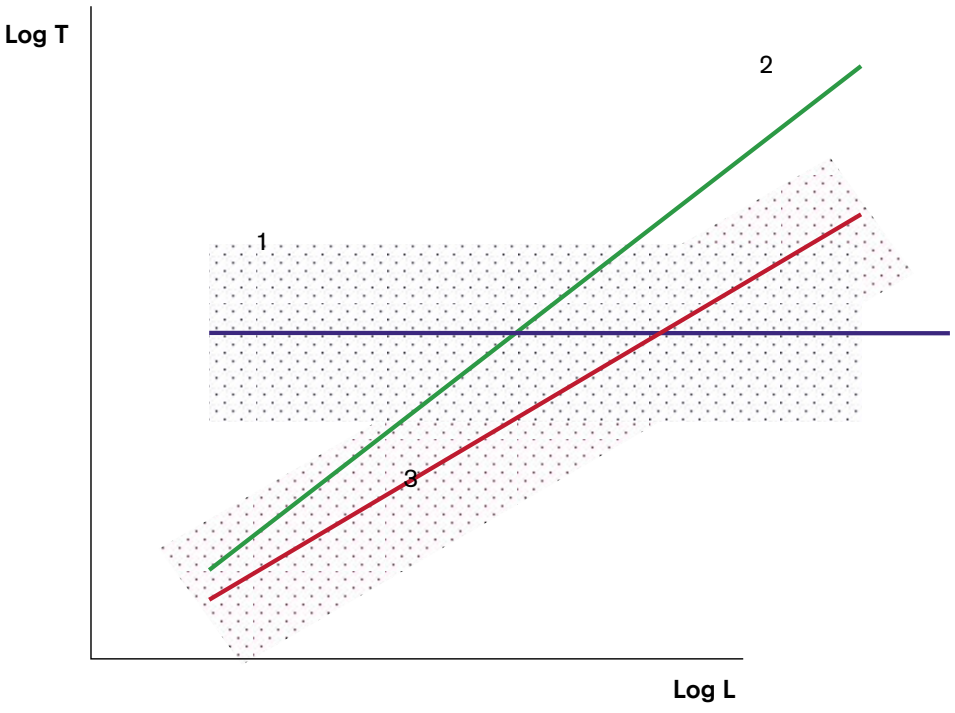

Figure 3-4. *Schematic of transmissivity models: 1) Uncorrelated, 2) Correlated, and 3) Semi-correlated.*

3.3.5 Fracture kinematic porosity models

As part of the modelling, it is intended to derive fracture kinematic porosity as part of the block properties, as these will be needed in the regional GWF modelling. There are no new data such as tracer tests to try to interpret, so the model for the porosity of an individual fracture will be based on Äspö Task Force 6c results /14/. This approximates a direct correlation between the transport aperture e_t, and the transmissivity, such that:

$$e_t = aT^b$$

The values for the constants suggested from Äspö Task Force 6c are a = 0.46 and b = 0.5.

3.4 Analysis of geological data and Geo-DFN model

3.4.1 Calculation of $P10_{corr}$

The first step in the analysis of the geological data was to group the fractures according to whether they lie inside or outside a DZ and then divide them into fracture sets for each DZ and for the background rock. The purpose is to see whether each DZ has a clearly dominant set. If such a set exists, then it may be expected that this will coincide with the general orientation of the DZ. It may be possible to verify this by comparing with, for example, reflection seismics. Sub-vertical boreholes will tend to have a bias toward intersecting sub-horizontal fractures. To mitigate against under-predicting the intensity of sub-vertical fractures, the Terzaghi correction was used. This was applied by calculating a weighting factor, f_T, for each fracture based on the angle, ϑ, between the pole to the fracture plane and the borehole trajectory:

$$f_T = \min(1/\cos(\vartheta), 5) .$$

A maximum factor of 5 was used. This weighting was used when calculating density contours on stereonets, and also for estimating $P10_{corr}$. That is, the linear fracture intensity, P10, is calculated as the number of fractures in an interval divided by the interval length, whereas the Terzaghi-corrected fracture intensity, $P10_{corr}$, is estimated as the sum of weight factors divided by the interval length. It is our experience that this gives an accurate prediction of the $P10_{corr}$ that can be used as an estimate for P32 (fracture area per unit volume) in a DFN model to simulate the observed P10.

In this analysis, the $P10_{corr}$ has been calculated for open and partly-open background fractures for each borehole, and for subsections of each borehole where there are very apparent differences in fracture intensity.

The analysis for each of the five cored boreholes at Forsmark is presented in Section B.1 of Appendix B for both DZs and background rock. The following illustrates the process for fracture intensities in DZs in borehole KFM01A.

KFM01A contains two Deformation Zones. In terms of the length down the boreholes, these are found at 386 m to 412 m (DZ2), and 639 m to 683 m (DZ3). The orientations of the open and partly-open fractures associated with these DZs appear distinctly on the stereonet within the NE sub-vertical and HZ sub-horizontal sets (see Figure 3-5). Both sets occur in both DZs, although the mean strike for the NE set is slightly less for DZ3 than in DZ2. KFM01A is a near-vertical borehole, with trend of around 304° and plunge of around 80°.

The fracture intensity within each DZ is recorded in Table 3-1. The mean length is the length down the borehole for the DZ. $P10_{corr}$ is relatively high in the DZs compared to the background fracturing where it is about 0.4 m^{-1} below about 400 m, or 1.4 m^{-1} taken over the whole borehole.

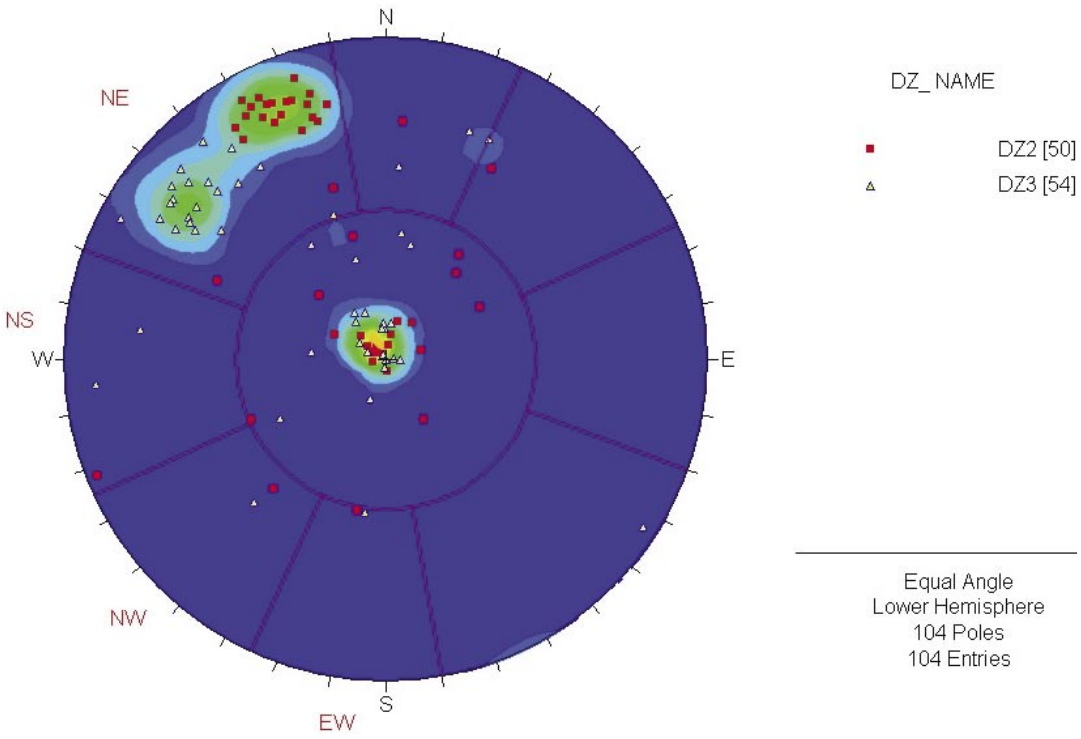

Figure 3-5. *Poles of open and partly-open fractures associated with Deformation Zones in KFM01A. The individual features are plotted as points, whereas the coloured contours show a Terzaghi-corrected density plot.*

Table 3-1. Positions, interval lengths and fracture intensity for Deformation Zones in KFM01A.

KFM01A	HCD Domain	Mean length (m)	Interval length in borehole (m)	all P10 (m^{-1})	open P10 (m^{-1})	open $P10_{corr}$ (m^{-1})
DZ2	ZFMNE1192	398.91	25.8	4.42	1.94	4.42
DZ3	ZFMNE0061	661.21	44.4	5.56	1.22	2.49

3.4.2 Variation in fracture intensity with rock domain

Fracture intensity varies widely within and between boreholes KFM01A to KFM05A (see Section B.1 of Appendix B). To help provide an overall understanding, the fracture intensity has been considered within the different rock domains sampled by the boreholes.

There are four different rock domains intercepted by the F1.2 boreholes. The rock domain within the tectonic lens is RFM029. In boreholes KFM01A, KFM02A and KFM05A this is the only rock domain encountered. KFM03A intercepts a section of RFM017 from 223 m to 292 m, sandwiched between RFM029 above and below. KFM04A originates outside the tectonic lens, first intercepting rock domain RFM018 (109 m to 177 m), then RFM012 (177 m to 500 m) and at depth enters the tectonic lens (RFM029, at lengths deeper than 500 m). Table 3-2 starts with a cross-comparison of fracture intensity within RFM029. This indicates considerable variation within a single rock domain, with values between 0.3 m^{-1} and 1.4 m^{-1}. Note that the open $P10_{corr}$ value given here for KFM01A has been calculated along the whole borehole, but there is a much higher fracture intensity in the upper section (< 400 m) of KFM01A than at depth (see subsection B.1.2 of Appendix B).

Table 3-3 summarises the fracture intensity in other domains, suggesting much higher fracture intensity in some of the rock domains in KFM04A outside the tectonic lens. However, since the interval lengths in these domains are short, apart from RFM012, the dependence of fracture intensity on rock domain suggested in the Geo-DFN seems speculative.

Table 3-2. Summary of variation in open $P10_{corr}$ between different boreholes for RFM029.

Borehole	Thickness (m)	open $P10_{corr}$ (m^{-1})	Length position
KFM01A	820.62	1.36	all borehole
KFM02A	656.95	0.28	all borehole
KFM03A	749.74	0.74	top 120 m, bottom 707 m
KFM04A	447.53	0.68	bottom 447 m
KFM05A	803.94	1.08	all borehole

Table 3-3. Summary of variation in open $P10_{corr}$ between different boreholes for RFM017, RFM018 and RFM012.

Borehole	Rock domain	Thickness (m)	open $P10_{corr}$ (m^{-1})	Length position
KFM03A	RFM017	68.19	0.20	223 to 292 m
KFM04A	RFM018	60.88	5.21	109 to 177 m
KFM04A	RFM012	251.83	4.01	177 to 500 m

3.4.3 Variation in fracture intensity above and below Deformation Zone ZFMNE00A2

Deformation Zone ZFMNE00A2 was highlighted by the Geo-DFN as being of particular importance within Forsmark as a divider between areas of relatively intense and less intense fractured rock. Hence, the fracture intensity in each of the boreholes has been considered in relation to ZFMNE00A2. ZFMNE00A2 cuts KFM01B at 36 m to 48 m length, hence is found wholly below KFM01A; KFM02A is cut by ZFMNE00A2 between 416 m and 600 m; KFM03A is found wholly above ZFMNE00A2; KFM04A is cut by ZFMNE00A2 between 169 m and 242 m; and KFM05A is found wholly below ZFMNE00A2. Considering borehole KFM04A in more detail shows that rock domain RFM018 is above ZFMNE00A2 (above 169 m, i.e. above DZ1), whereas domains RFM012 and RFM029 are below ZFMNE00A2. A schematic of the relationship of ZFMNE00A2 to each borehole is shown in Figure 3-6.

The fracture intensity above and below ZFMNE00A2 is shown in Table 3-4 and Table 3-5. There is no consistent pattern of fracture intensity based solely on position relative to ZFMNE00A2. The two data points for KFM02A and KFM03A show open $P10_{corr}$ of 0.4 to 0.7 m^{-1} while KFM04A shows much greater fracture intensity for rock domain RFM018 above ZFMNE00A2 (open $P10_{corr}$ = 5.3 m^{-1}). Similarly, the fracture intensity below ZFMNE00A2 does not show a consistent pattern, with variation from open $P10_{corr}$ of 0.2 m^{-1} in KFM02A to 1.6 m^{-1} in KFM04A.

Table 3-4. Summary of fracture intensity above ZFMNE00A2.

Borehole	Section	all P10 (m^{-1})	open P10 (m^{-1})	open $P10_{corr}$ (m^{-1})
KFM02A	fractures above 416 m	1.95	0.18	0.38
KFM03A	complete borehole	1.77	0.30	0.69
KFM04A	fractures above 169 m	7.22	3.02	5.25

Table 3-5. Summary of fracture intensity below ZFMNE00A2.

Borehole	Section	all P10 (m^{-1})	open P10 (m^{-1})	open $P10_{corr}$ (m^{-1})
KFM01A	complete borehole	1.41	0.79	1.36
KFM02A	fractures below 600 m	0.91	0.07	0.22
KFM04A	fractures below 242 m	3.89	0.98	1.63
KFM05A	complete borehole	2.79	0.58	1.08

3.4.4 Variation in classification of fracture confidence

Each type of fracture (open, partly open and sealed) has been classified in the Geo-DFN as ‘certain’, ‘probable’ or ‘possible’. Table 3-6 and Table 3-7 summarise the percentages of each confidence class for each borehole. Sealed fractures are mostly certain or probable with an average of about 50% certain, and around 10% or less possibly sealed apart from KFM01A. The uncertainty with identifying open fractures is higher and more variable between boreholes. It is not clear if the differences are “true geological differences” or more indicative of bias in the mapping process.

Table 3-6. Fracture confidence for open and partly open fractures for KFM01A to KFM05A.

Borehole	Open, certain	Open, probable	Open, possible
KFM01A	25%	19%	56%
Upper section of KFM01A (< 386 m)	26%	17%	57%
Lower section of KFM01A (> 412 m)	22%	28%	50%
KFM02A	28%	60%	12%
KFM03A	29%	41%	30%
KFM04A	57%	30%	13%
KFM05A	8%	30%	62%

Table 3-7. Fracture confidence for sealed fractures for KFM01A to KFM05A.

Borehole	Sealed, certain	Sealed, probable	Sealed, possible
KFM01A	58%	11%	31%
KFM02A	29%	70%	1%
KFM03A	42%	53%	5%
KFM04A	57%	30%	13%
KFM05A	63%	22%	15%

3.4.5 Summary of fracture intensities

A summary of the fracture intensities $P10_{corr}$ for open and partly-open fractures is given in Table 3-8 for all boreholes, split into rock domains, and inside or outside of DZs. Based on this summary some observations can be made:

- There is a wide range of fracture intensities both within and between boreholes. The lowest measured background fracture intensity shows open $P10_{corr} = 0.2\ m^{-1}$ below 600 m in KFM02A, while the highest measured fracture intensity has open $P10_{corr} = 4.6\ m^{-1}$ above 412 m in KFM04A;
- Fracture intensity tends to be greater in DZs than in the background rock. For example, KFM02A shows a much greater (around 6 times) fracture intensity in its DZs than in the background rock. Overall $P10_{corr}$ averages about $3\ m^{-1}$ in DZs. KFM01A in the upper background rock has a similar mean intensity to its two DZs;

- Fracture intensity, $P10_{corr,}$ for open and partly-open fractures in the background rock domain RFM029 varies between about 0.2 to 3.3 m^{-1}. The upper section of KFM04A passes through rock domains RFM018 and RFM012 giving a higher background fracture intensity, $P10_{corr,}$ of 5.2 m^{-1} and 4.0 m^{-1} respectively. A section of RFM017 found within KFM03A has $P10_{corr}$ of 0.2 m^{-1}. Anyway, it seems there are too few data to establish a correlation between rock domain and fracture intensity (see subsection 3.4.2);
- Based on one borehole section (rock above 412 m in KFM04A), fracture intensity is much greater outside the tectonic lens (open $P10_{corr}$ = 4.6 m^{-1}).

Due to the wide variation in fracture intensity, coupled with flow measurements found at varying depth (see subsection 3.5), it is suggested that different volumes of rock should be considered separately, depending on the fracture intensity measured in different regions within the study area. Hence, a conceptual model is presented in Figure 3-6 with the rock sub-divided into volumes according to both depth and position relative to DZ ZFMNE00A2. (Note the volume labels have been chosen for comparison with a similar concept proposed by the DarcyTools Team that uses Volumes A–D.)

Table 3-8. Summary table of fracture intensity of open and partly open fractures. A weighted mean is given for the Deformation Zones and the total fracture intensity for the background rock.

Borehole	Details	open P10 (m^{-1})	open $P10_{corr}$ (m^{-1})	Rock domain	Volume
KFM01A	upper fractures (< 386.01 m)	1.90	3.27	RFM029	F
	lower fractures (> 411.81 m)	0.21	0.36	RFM029	G
	DZ	1.58	3.20	RFM029	–
KFM02A	upper fractures (< 415.48 m)	0.18	0.38	RFM029	E
	lower fractures (> 599.59 m)	0.07	0.22	RFM029	G
	DZ	3.91	2.39	RFM029	–
KFM03A	complete borehole	0.30	0.69	RFM029 (some RFM017)	E
	DZ	1.37	2.38	RFM029 (some RFM017)	–
KFM04A	upper fractures (< 412.01 m)	2.61	4.61	RFM018, RFM012	E
	lower fractures (below 461.94 m)	0.51	0.73	RFM029 (some RFM012)	G
	DZ	6.01	6.67	RFM018, RFM012, RFM029	–
KFM05A	complete borehole	0.58	1.08	RFM029	F and G
	DZ	2.30	6.68	RFM029	–

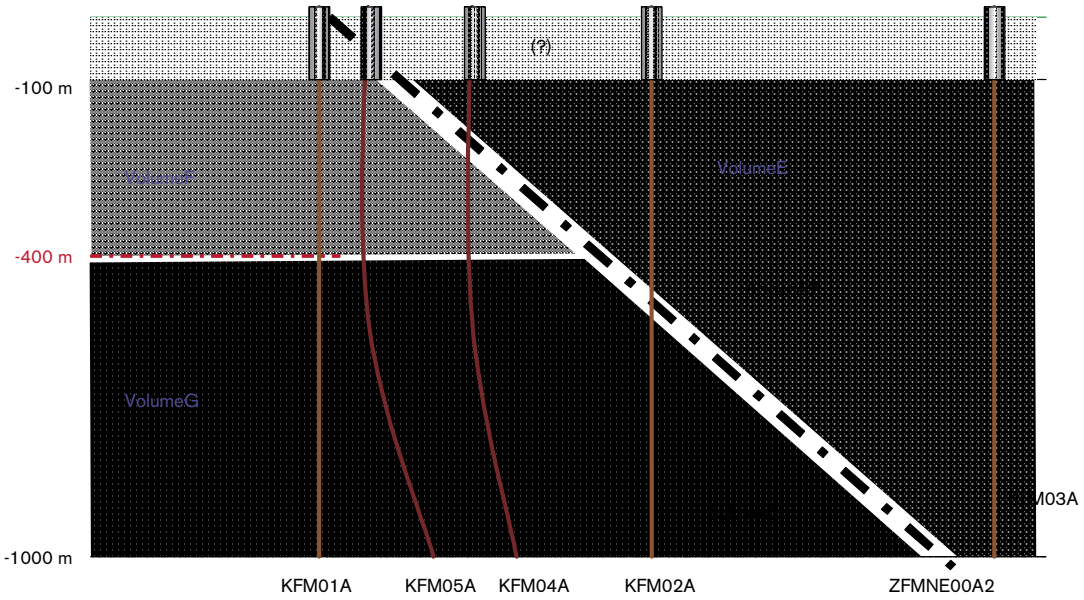

Figure 3-6. *Conceptual model of the different rock volumes for Forsmark as divided by Deformation Zone ZFMNE00A2 and at a depth of 400 m.*

Volume E is found above ZFMNE00A2 and is characterised by a fracture intensity of open fractures around $P10_{corr} = 0.7$ m^{-1}, based on KFM03A. This borehole is used since flow anomalies have been measured along the whole length of KFM03A (see subsection B.2.3 of Appendix B). The section of KFM02A above ZFMNE00A2 also exhibits flow and is considered to be within Volume E. Here, the background rock fracture intensity ($P10_{corr} = 0.4$ m^{-1}) is the lowest observed in F1.2, but KFM02A is cut by many DZs where flow is observed (subsection B.2.2 of Appendix B).

Volume F is described as the upper section of rock, below ZFMNE00A2. It is characterised by a high fracture intensity (e.g. open $P10_{corr} = 3.3$ m^{-1} for fractures above 386 m in KFM01A). Flow anomalies have been observed in Volume F, e.g. the upper 386 m of KFM01A shows much flow (subsection B.2.1 of Appendix B). KFM05A has PFL flow anomalies restricted to only about the top 200 m, suggesting the base of Volume F is uncertain or variable. The upper 412 m of KFM04A is found outside the tectonic lens, and also exhibits high fracture intensity (open $P10_{corr} = 4.61$ m^{-1}). It is suggested that the background rock outside the tectonic lens should be analogous to the Volume F conceptual model. The reasons for this are two-fold: firstly, the high fracture intensity outside the tectonic lens is most similar to that found in Volume F, such as upper KFM01A; and secondly, since there are limited data available outside the tectonic lens in the F1.2 data freeze, a conservative assumption that the rock has high fracture intensity is appropriate, i.e. significant groundwater flow-rates, a hypothesis that can be tested in the regional flow modelling.

Volume G is described as the deeper rock that is also found below ZFMNE00A2. It is characterised by low fracture intensity with measurement of almost no flow anomalies. For example, the deeper section of KFM01A (> 412 m) shows a fracture intensity of open $P10_{corr} = 0.4$ m^{-1}, and the deeper section of KFM02A (> 600 m) shows a fracture intensity of open $P10_{corr} = 0.2$ m^{-1}; both of these boreholes exhibit almost no measured flow anomalies in Volume G. Equally, KFM04A shows almost no measured flow anomalies despite a slightly higher fracture intensity of open $P10_{corr} = 0.7$ m^{-1}.

The top 100 m of the model is labelled '?' since there are no boremap data or hydraulic data available. The properties of this layer should be considered by sensitivity analyses in the regional groundwater flow modelling.

3.5 Analysis of hydrogeological data

Brief summaries of the hydraulic data in the boreholes and how these vary between the identified hydraulic volumes are given for the PFL data in Table 3-9 and PSS in Table 3-10. Table 3-9 suggest intensity for PFL anomalies $P10_{PFL}$ of 0.40–0.48 in DZ ZFMNE00A2, 0.06–0.38 m^{-1} in Volume E, 0.13–0.48 m^{-1} in Volume F, and 0.002–0.02 m^{-1} in Volume G. This confirms the Volume G is exceptionally low below A2, intermediate in Volume E, and higher in Volume F. The PSS data in Table 3-10 confirms that there is only one flowing interval in Volume G, while there are about an even number of flowing and non-flowing in the other volumes. The total transmissivities and mean hydraulic conductivities are also given, but these show no clear link to the hydraulic volume. They are subject to the chance of including one high transmissivity feature that dominates all flow.

Table 3-9. Summary table of PFL anomalies. $P10_{PFL}$ is the number of flowing PFL anomalies per unit length of borehole.

		Number of PFL anomalies	$P10_{PFL}$ (m^{-1})	Total transmissivity ($m^2\ s^{-1}$)	Mean K (m/s)
KFM01A	Volume F (< 400 m)	34	0.13	2.0E–07	7.7E–10
	Volume G (> 400 m)	0	0.00	–	–
KFM02A	Volume E (< 414 m, above A2)	75	0.38	1.2E–04	6.2E–07
	ZFMNE00A2 (414 m to 514 m, DZ6)	49	0.48	7.8E–06	7.6E–08
	Volume G (> 514 m, below A2)	1	0.002	2.6E–09	–
KFM03A	Volume E	52	0.06	1.1E–04	1.2E–07
KFM04A	Volume F (< 169 m, above A2)	29	0.48	6.4E–05	1.1E–06
	ZFMNE00A2 (169 m to 242 m, DZ1, DZ2 and DZ3)	26	0.40	8.9E–05	1.4E–06
	Volume G (> 242 m, below A2)	16	0.02	1.5E–06	2.1E–09
KFM05A	Volume F (< 400 m)	25	0.16	1.3E–03	8.0E–06
	Volume G (> 400 m)	2	0.12	1.0E–08	5.9E–10

Table 3-10. Summary table of PSS anomalies for 5 m intervals. $P10_{PSS}$ is the number of flowing PSS 5 m intervals per unit length, assuming one fracture per 5 m interval.

		Number of flowing PSS 5 m intervals	Number of non-flowing PSS 5 m intervals	$P10_{PSS}$ (m^{-1})	Total T ($m^2\ s^{-1}$)	Mean K (m/s)
KFM01A	Volume F (< 400 m)	25	25	0.09	3.3E–07	1.2E–09
	Volume G (> 400 m)	0	0	0.00	–	–
KFM02A	Volume E (< 414 m, above A2)	31	11	0.15	7.1E–04	3.4E–06
	ZFMNE00A2 (414 m to 514 m, DZ6)	20	4	0.17	4.9E–06	4.3E–08
	Volume G (> 514 m, below A2)	1	3	0.07	2.7E–09	1.8E–10
KFM03A	Volume E	50	50	0.06	1.9E–04	2.1E–07

To help interpret the flow data measured by the Posiva Flow Log (PFL), borehole fractures that correspond to the depths at which flow anomalies have been measured in the PFL tests have been identified. The orientation of poles to the fractures seen in each core that correspond to these anomalies are then plotted on a stereonet to indicate preferred orientations for high flow features. For each anomaly, the fracture (or fractures) most 'consistent' with the anomaly is (are) selected. Consistency is judged primarily on the distance between the depth of the fracture and the depth of the anomaly. However, a fracture slightly further away may be preferred if it has a higher open confidence indicator. To ensure all anomalies are associated with at least one fracture, in regions of sparse fracturing, a fracture up to 1 m away occasionally had to be selected. If there are more than one equally consistent fractures associated with an anomaly, then the orientations of each fracture are used. Generally, there are only one or two consistent fractures, but sometimes there are 3–5 equally consistent fractures. The final step is to plot flow anomaly orientations on a stereonet and colour them according to the magnitude of the transmissivity associated with the anomaly.

Details of this analysis for each of the boreholes KFM01A–KFM05A are given in section B.2 of Appendix B. Data for borehole KFM01A are presented below as an example of the analysis.

Flowing features in KFM01A are predominantly in the HZ and NE sets based on the PFL anomalies (see Figure 3-7). This corresponds well with the dominant background fracture orientation. PSS flow is measured over 5 m intervals, in which there may be several fractures, and therefore it is difficult to match these to individual features. For KFM01A, no flowing features within DZs are recorded in either PFL or PSS data. In fact, all flowing features are found within the top 400 m of KFM01A as shown in Figure 3-8. Note that the transmissivity plotted here is for 5 m intervals for both PFL and PSS data, so that both sets of data can be compared in a consistent way. This is because the PSS data are given as the transmissivity of contiguous 5 m intervals whereas the PFL data are given as the transmissivity of individual fractures, and hence it is necessary to convert the PFL data into a compatible format. This is achieved by grouping the PFL anomalies according to the same 5 m intervals for which the PSS data are provided. In some instances there are a few anomalies in an interval, in others there are none. In KFM01A the detection limit is about $10^{-9}\ m^2 s^{-1}$ for both PFL and PSS data, and so the PSS does not supplement the PFL data in this case.

It is useful to investigate the consistency between the transmissivities interpreted from the PFL and PSS anomalies. Figure 3-9 shows a cross-plot of the PFL and PSS data for KFM01A. The agreement is generally good, though there are a few intervals with order of magnitude differences.

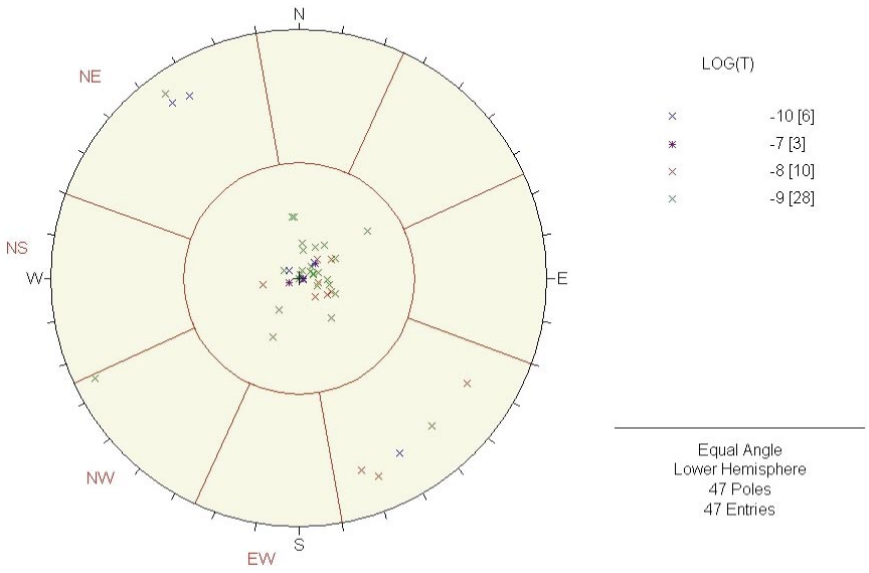

Figure 3-7. *Orientations of the pole to fractures associated with PFL anomalies in KFM01A. Fractures are coloured by magnitude of the transmissivity of the PFL anomaly. The set divisions and the names of each set are superimposed in red.*

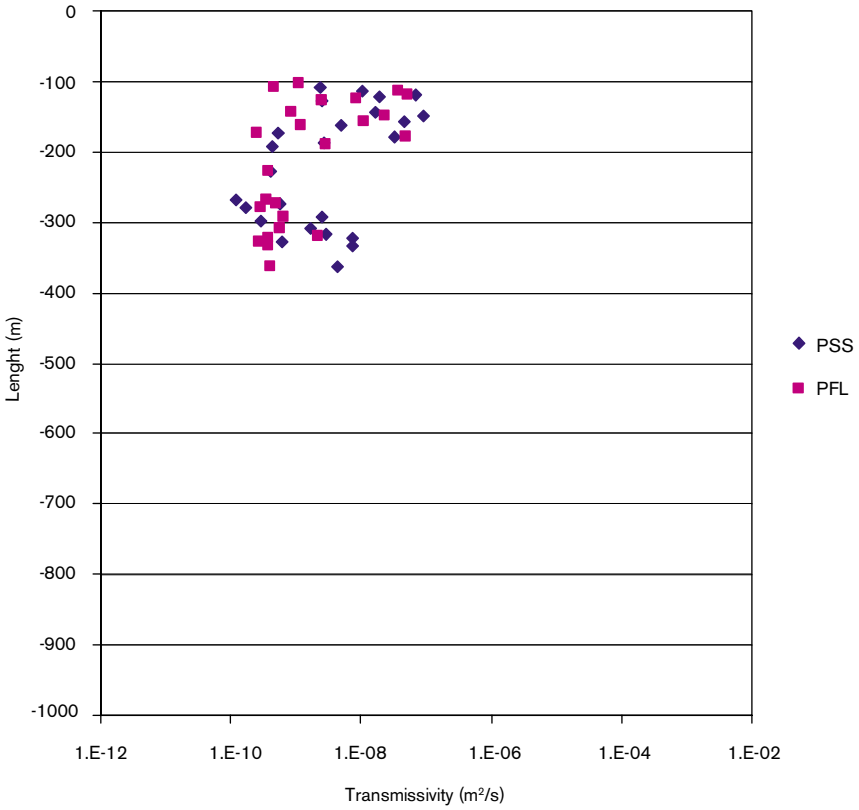

Figure 3-8. *Transmissivity of 5 m borehole intervals with measurable flow recorded by PFL and PSS in KFM01A. The measurement limit is around 10^{-9} m^2s^{-1} for PFL and PSS.*

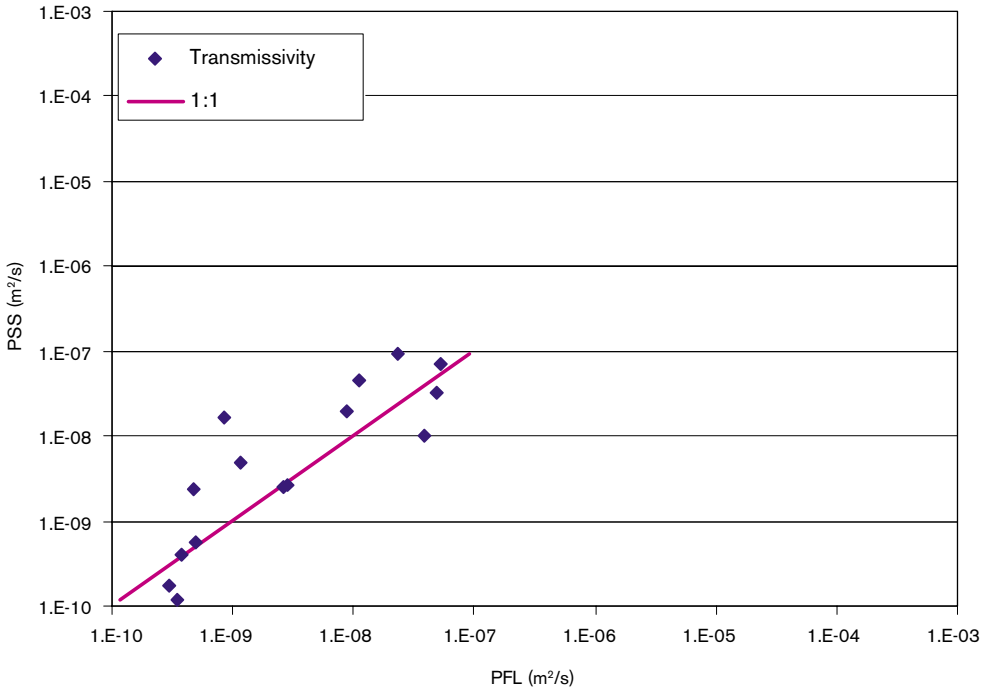

Figure 3-9. *Cross-plot of PFL and PSS measurements for KFM01A. A 1:1 correlation is shown for comparison.*

3.6 Simulations for assessment of DFN properties

The primary reasons for performing DFN simulations are:

1. Check that the fracture intensities, $P10_{corr}$, and fracture set definitions derived from the boremap data can be applied in a DFN model to reproduce the observed P10 seen in the boreholes, and the relative intensities between the sets. This may require calibration of the fracture intensity P32, and the proportions of each set;
2. Condition the P32 for open conductive fractures and fracture transmissivity parameters against the PFL and PSS 5 m interval transmissivity data using DFN flow simulations;
3. For the PFL data, compare both the distribution of transmissivity and flow-rate for flowing features.

The initial step is to use a DFN model to simulate the fracturing around a borehole and check the modelled open P10 against that in the core-log. To do this, several realisations of the Hydro-DFN model of all open and partly-open fractures in each borehole are generated. Initially, the fracture intensity P32 (m^2m^{-3}) input to the DFN model is estimate using the analysed value of $P10_{corr}$. Then the simulated frequency of open fractures is used to check against the observation to see whether this open $P10_{corr}$ is an accurate estimate of P32. If not, then P32 can be adjusted to get a better match. This 'fine-tuning' is considered for the overall fracture intensity and for the individual sets where the relative proportion of fractures intercepted by the borehole in each set differs significantly between the model and the measurement. This step is described in section B.3 of Appendix B.

The second step, to condition the DFN models based on transmissivity distributions from PFL and PSS data, is discussed in section B.4 of Appendix B. The final step, to compare flow-rates from PFL data, is described in section B.5 of the same Appendix. In

F1.2 a complete set of PFL and PSS data was only available for KFM01A, KFM02A and KFM03A. However, hydraulic responses in KFM02A are dominated by ZFMNE00A2 making it of limited use, and hence the simulations of hydraulic data focuses necessarily on KFM01A and KFM03A. Flow responses in these boreholes are very different in nature. KFM01A is located within the candidate area and has no measurable flow at depth which is both useful information and encouraging from a safety assessment viewpoint. However, one should ask whether all the rock within the candidate area is likely to be this good. KFM03A in contrast has PFL flow anomalies at various depths to the bottom at 1 km, but this 3–4 km from the candidate area, so although it perhaps indicates the possibility of more conductive rock it may not be representative of the candidate rock.

3.7 Model parameters of the Hydro-DFN Models with uncertainties

To aid consideration of design issues, calculations of block properties such as hydraulic conductivity are required over the whole Forsmark area. Hence, a Hydro-DFN model needs to be derived that captures the broad features of the whole area, but not necessarily all the localised characteristics of particular boreholes. To this end, the following pragmatic assumptions were made in producing a Hydro-DFN for the Forsmark area:

1. The fracture intensity of flowing fractures is not controlled significantly by rock domain;
2. There is wide variation in the fracture intensity within and between boreholes;
3. The three proposed transmissivity models can be used as alternative cases with the parameterisation derived for the analysis of the PFL and PSS data;
4. Localised effects associated with large deterministic DZs will be captured by the geological model and definition of hydraulic conductor domains.

Assumption 1 is based on the data in Table 3-2 and Table 3-3. Assumption 2 is based on subsection 3.4. Assumption 3 is based on the fact that the PFL and PSS anomaly data for both Volume E and Volume F could be matched with the same parameter values for each transmissivity model. Assumption 4 is based on the observation that large localised effects seen in the boreholes seem to correspond to the presence of large DZs that have been identified in the regional-scale geological model.

3.7.1 Model parameters

On the basis of the above assumptions, parameters for the Hydro-DFN were derived for Volume E (intermediate fracture intensity) using KFM03A, Volume F (high fracture intensity) using the upper section of KFM01A and Volume G (no flow) using the lower section of KFM01A. Each of the three transmissivity models was considered. In order to match the measured flow anomalies, the P32 had to be adjusted: in the case of Volume E, the best match was shown with a P32 of 0.9 m^2m^{-3} (30% higher than the observed intensity of open fractures), whereas in the case of Volume F the P32 had to be reduced to 1.2 m^2m^{-3} to provide the best fit. This suggests that the near surface rock (Volume E and Volume F) could be considered as having flow anomalies through similar amounts of fracture intensity, while deeper rock below zone A2 (Volume G) illustrated by the lower section of KFM01A is much less fractured and exhibits little or no flow.

A summary of the best-fit parameters, using the Geo-DFN fracture set orientations, for Volume E, Volume F and Volume G is given in Table 3-11, Table 3-12 and Table 3-13, respectively. The percolation threshold for the Geo-DFN below which there is no flow is considered to be a fracture intensity of around 0.4 m^2m^{-3}, as shown in Volume G (subsection B.4.4 of Appendix B).

In order to quantify uncertainties the variant Geo-DFN ($k_r = 2.75$ for all fracture sets) with a bias toward slightly more long fractures requires a lower open fracture intensity for the best fit parameters as shown in Table 3-14.

Table 3-11. Description of DFN parameters and global Geo-DFN fracture set orientations used for simulation of fractures to fit the PFL anomalies and PSS data for KFM03A. P32 and the transmissivity model parameters are given for each of the cases, denoted in italics. (This table is also included as Table B-24 in Appendix B.)

Rock domain	Fracture set name	Orientation set pole: (trend, plunge), concentration	Length model, constants: power-law (L_0, k_r) (m)	Intensity, (P_{32}), valid length interval: L_0, L_{max} (m^2 m^{-3})	Relative intensity of P32	Transmissivity model Eq no, constants T (m^2 s^{-1})
RFM029 (177 m)	NS	(87, 2) 21.7	(0.5, 2.88)	*130% of open:* 0.903, (0.5, 1,000)	0.124	*Correlated (excl DZs):* (a,b) (1.0 10^{-9}, 1.0)
	NE	(135, 3) 21.5	(0.5, 3.02)		0.291	*Uncorrelated (excl DZs):* (μ,σ) (–6.5, 0.9)
RFM017 (68 m)	NW	(41, 2) 23.9	(0.5, 2.81)		0.191	*Semi-correlated (excl DZs):* (a,b,σ) (3.0 10^{-8}, 0.6, 1.0)
	EW	(190, 1) 30.6	(0.5, 2.95)		0.100	*Alternative: Correlated, L < 100 m:* (a,b) (1.0 10^{-9}, 1.5); *L > 100 m:* (a,b) (1.0 10^{-10}, 2.0)
RFM029 (707 m)	HZ	(343, 80) 8.2	(0.5, 2.92)		0.294	

Table 3-12. Description of DFN parameters and Geo-DFN set orientations used for simulation of fractures to fit the PFL anomalies and PSS data for Volume F (upper section of KFM01A). P32 and the transmissivity model parameters are given for each of the cases, denoted in italics. (This table is also included as Table B-27 in Appendix B.)

Rock domain	Fracture set name	Orientation set pole: (trend, plunge), concentration	Length model, power-law (L_0, k_r) (m)	Intensity, (P_{32}), valid length interval: L_0, L_{max} (m^2 m^{-3})	Relative intensity of P32	Transmissivity model Eq no, constants T (m^2 s^{-1})
RFM029	NS	(87, 2) 21.7	(0.5, 2.88)	26% of open: 1.2 (0.5, 1,000)	0.110	*Correlated: (a,b) (1 10^{-9}, 1.0)*
	NE	(135, 3) 21.5	(0.5, 3.02)		0.449	*Uncorrelated: (μ, σ) (–6.5, 0.9)*
	NW	(41, 2) 23.9	(0.5, 2.81)		0.085	*Semi-correlated: (a,b,σ) (3 10^{-8}, 0.6, 1.0)*
	EW	(190, 1) 30.6	(0.5, 2.95)		0.049	
	HZ	(343, 80) 8.2	(0.5, 2.92)		0.306	

Table 3-13. Description of DFN parameters and Geo-DFN set orientations used for simulation of fractures to fit the PFL anomalies and PSS data for Volume G (lower section of KFM01A). P32 and the transmissivity model parameters are given for each of the cases, denoted in italics (See Section B.4.4 in Appendix B.)

Rock domain	Fracture set name	Orientation set pole: (trend, plunge), concentration	Length model, power-law (L_0, k_r) (m)	Intensity, (P_{32}), valid length interval: L_0, L_{max} (m^2 m^{-3})	Relative intensity of P32	Transmissivity model Eq no, constants T (m^2 s^{-1})
RFM029	NS	(87, 2) 21.7	(0.5, 2.88)	*100% of open:* 0.36, (0.5, 1,000)	0.110	Correlated: (a,b) (1 10^{-9}, 1.0)
	NE	(135, 3) 21.5	(0.5, 3.02)		0.449	Uncorrelated: (μ, σ) (–6.5, 0.9)
	NW	(41, 2) 23.9	(0.5, 2.81)		0.085	Semi-correlated: (a,b,σ) (3 10^{-8}, 0.6, 1.0)
	EW	(190, 1) 30.6	(0.5, 2.95)		0.049	
	HZ	(343, 80) 8.2	(0.5, 2.92)		0.306	

Table 3-14. Description of variant Geo-DFN parameters used for simulation of fractures to fit the PFL anomalies and PSS data for Volume E (KFM03A). P32 and the transmissivity model parameters are given for each of the cases, denoted in italics. (This table is also included as Table B–25 in Appendix B.)

Rock domain	Fracture set name	Orientation set pole: (trend, plunge), concentration	Length model, power-law (L_0, k_r) (m)	Intensity, (P_{32}), valid length interval: L_0, L_{max} (m^2 m^{-3})	Relative intensity of P32	Transmissivity model Eq no, constants T (m^2 s^{-1})
RFM029 (177 m) RFM017 (68 m) RFM029 (707 m)	NS	(87, 2) 21.7	(0.5, 2.75)	*70% of open:* 0.53, (0.5, 1,000)	0.161	*Correlated, (excl DZ):* (a,b) (1.0 10^{-9}, 1.0)
	NE	(135, 3) 21.5	(0.5, 2.75)		0.319	*Uncorrelated (excl DZs):* (μ, σ) (–6.9, 0.9)
	NW	(41, 2) 23.9	(0.5, 2.75)		0.164	*Semi-correlated (excl DZs):* (a,b, σ) (1 10^{-8}, 0.3, 1.0)
	EW	(190, 1) 30.6	(0.5, 2.75)		0.076	
	HZ	(343, 80) 8.2	(0.5, 2.75)		0.280	

3.7.2 Evaluation of uncertainties

The key uncertainties in the Hydro-DFN model and the manner in which it has been addressed can be summarised as follows:

- The correlation between transmissivity and length. This has been addressed here by considering three alternative transmissivity models;
- The slope of the power-law distribution, k_r, and hence the need for the variant Geo-DFN model;
- The spatial variability between boreholes making it hard to derive statistics that can be extrapolated away from the borehole.

It is possible there is a higher fracture intensity of conductive fractures outside of the tectonic lens area. The F1.2 data only include one borehole outside the tectonic lens, which limits the scope for accurate regional modelling outside the tectonic lens.

4 Assessment of hydraulic block properties

The objectives for the hydraulic block property task can be summarised as follows:

- Estimate anisotropy and calculate the statistics of the hydraulic conductivity of 100 m and 20 m blocks using the results of the TD PFM 1.2 – Hydro-DFN;
- Calculate the statistics of the hydraulic conductivity of 100 m and 20 m blocks;
- Include DFN porosity based on 'aperture = function(Transmissivity)' relationship from Äspö Task 6;
- Evaluate effects of size-truncation of stochastic features and cell-background properties (to be added to cells after applying Hydro-DFN) to motivate the minimum fracture length that can be used in the regional DFN models.

4.1 Methodology

To calculate equivalent continuum porous medium (CPM) block properties (directional hydraulic conductivity and porosity) based on an underlying DFN model, the following modelling steps are performed:

1. A fracture network is calculated stochastically by generating fractures within a domain that is much larger than the required block size (1,000 m for a 100 m block and 200 m for a 20 m block was used here).
2. The fracture domain is split into sub-blocks of a selected scale. For greatest accuracy it is best to divide the domain of fractures into blocks larger than the size on which the properties are required. Using larger blocks has the advantage that flows are calculated through the fractures 'in situ', i.e. within a network, and avoids overestimating hydraulic conductivity due to flows through fractures that cut across edges or corners of the block and do not represent flows within a network. Here, the domain was subdivided into overlapping 200 m blocks, but block properties were calculated only for the central 100 m block.
3. Perform flow simulations through each block of DFN in each of the 3 axial directions. For the flow simulations, a linear pressure gradient is specified parallel to each of the axial directions and imposed on all six faces of a cube to allow a general symmetric hydraulic conductivity tensor (6 components) to be calculated.
4. For each set of the three axial pressure gradients, compute the flux through each of the six faces of the central 100 m block. Based on these 18 flux responses for the 3 pressure gradients, a full symmetric 3D hydraulic conductivity tensor is fitted based on a least-squares optimisation.
5. The hydraulic conductivity was calculated for 100 m and 20 m blocks and different fracture length truncations were considered. For calculating the 100 m block hydraulic conductivity, fractures were generated in a 1,000 m cube that was split into an array of 9×9×9 (729 blocks in total) overlapping cubes of side 200 m for use in the flow simulations. The hydraulic conductivity was then calculated based on the flux through the central 100 m block, so as to avoid problems with high flows through the corner or edge of a cube unrepresentative of flow in a network.

6. Hydraulic conductivities were then calculated as a cumulative distribution function (CDF) of the values for an ensemble of 729 blocks to give a geometric mean and standard deviation ($Log_{10}(K)$).
7. For a 20 m block, fractures were generated in a 200 m cube and an array of 9×9×9 (729 blocks in total) cubes of side 40 m.
8. Anisotropy was studied in several ways. The geometric mean of the axial components was to give effective block conductivities. A principal component analysis was used to derive the maximum and minimum horizontal hydraulic conductivities together with the strike of the maximum hydraulic conductivity for each of the 729 blocks. This shows how much anisotropy can be expected in any given block and whether there is a general trend toward certain directions over all blocks.
9. Fracture kinematic porosity was calculated by summing the fracture area multiplied by transport aperture for each connected fracture within each block and dividing by the block volume.

4.2 Modelling assumptions and input data

The remit for this study, as specified by SKB's Design Team, was to calculate the statistics of the hydraulic conductivity tensor of 20 m and 100 m blocks using the results of the TD PFM1.2 – Hydro-DFN as described in subsection 3.7.1.

The main modelling assumptions in the study performed here are:

1. The hydraulic conductivity in the host rock is completely dominated by the connected fracture system and hence can be modelled by the DFN concept;
2. Flow within fractures can be approximated by Darcy's law;
3. The heterogeneity between blocks on a specified scale can be modelled by calculating the hydraulic conductivity of an array of sub-blocks within a much larger domain (as big as the largest stochastic fracture, and ten times the block size) and use this as an ensemble;
4. Forsmark release area can be represented by three volumes of rock, as described in subsection 3.4.5. These are Volume E (characterised by KFM03A), Volume F (characterised by the upper section (< 386 m) of KFM01A) and Volume G (characterised by the lower section (> 412 m) of KFM01A);
5. Fracture transmissivity can be described by one of three alternative models;
6. Fracture kinematic porosity (transport aperture) is correlated to fracture transmissivity.

4.3 Simulations for assessment of hydraulic block properties

An example of the DFN model used to calculate hydraulic properties for a 20 m block, Volume F, for the case with a correlated transmissivity is shown in Figure 4-1. Here, the DFN is created within a 200 m domain and then sub-divided into 20 m blocks for flow simulations. Clearly, blocks cut by a large fracture, coloured red here, will have a high hydraulic conductivity. A corresponding example of the DFN used for the 100 m block properties for Volume F is shown in Figure 4-2. Overall, there are very few large fractures,

with the fracture length distribution dominated by small fractures. This is a function of the power law fracture size distribution from the Geo-DFN, which uses a large k_r value. In particular, the fracture sets with the greatest fracture intensity, sub-HZ and NE, have k_r of 3.92 and 4.02. As a result, this fracture size distribution, which is determined by k_r, may not be realistic to simulate the correct number of observed (large) regional-scale lineaments.

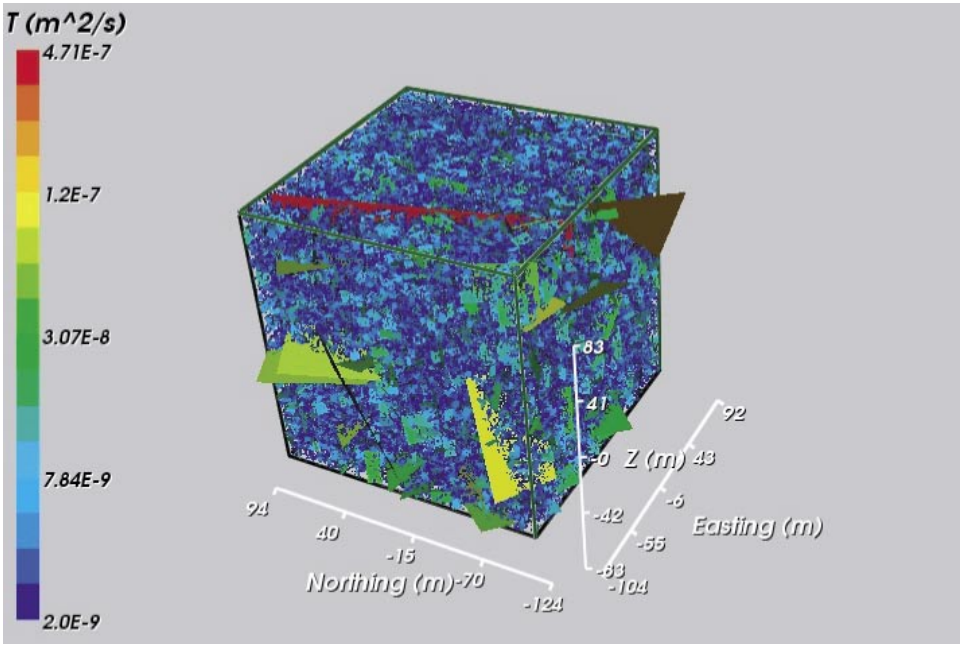

Figure 4-1. *Volume F DFN model simulation for a 200 m domain used to calculate hydraulic block properties for 20 m blocks and the correlated T model. Model input parameters shown in Table B-26.*

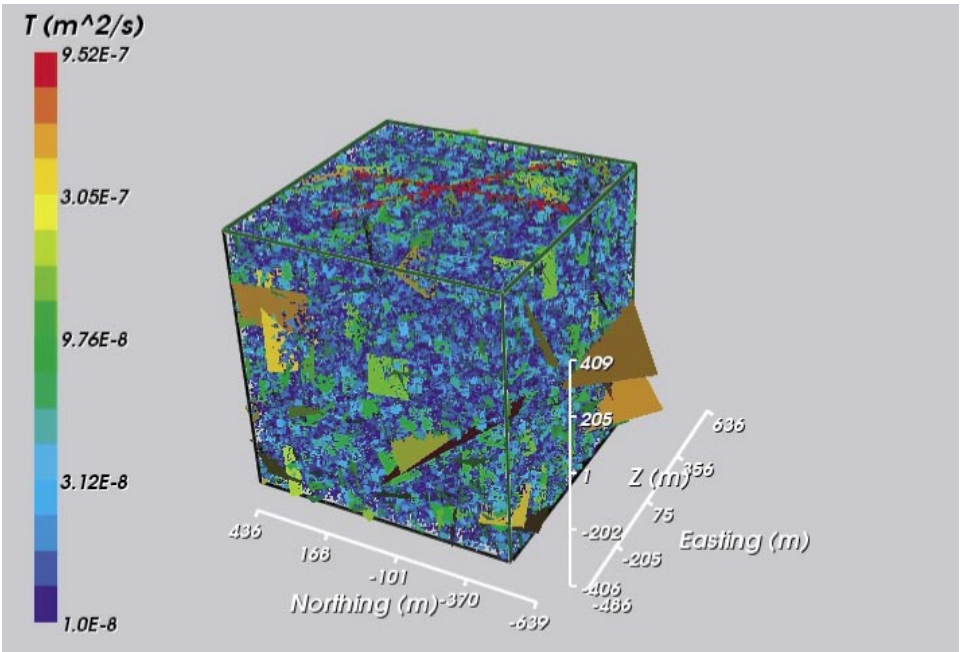

Figure 4-2. *Volume F DFN model simulation for a 1,000 m domain used to calculate hydraulic block properties for 100 m blocks and the correlated T model. Model input parameters shown in Table B-26.*

4.4 Model parameters for block properties with uncertainties

For both Volume E and Volume F, simulations were performed for the 100 m and 20 m block sizes and for the three different transmissivity models, for the DFN models described by the parameters in Table B–24, Table B–25 and Table B–27. All three transmissivity models were propagated to the block scale modelling in order to quantify the sensitivity to the assumption of a relationship between fracture transmissivity and length, and see if there are any distinct differences between the models that may point toward one model being more realistic. None of the hydro-tests, PFL or PSS, detected measurable flow in Volume G. Hence, all that can be said is that block hydraulic conductivity is at or below the detection limit of about 1.1 10^{-11} m/s based on 100 m PSS tests.

4.4.1 Resultant model parameters for Volume E (complete length of KFM03A)

Some examples of the calculations of the resultant model parameters for the hydraulic block properties are shown in Figure 4-3 to Figure 4-6 for the 100 m block. Figure 4-3 shows the x (East-West) hydraulic conductivity for the uncorrelated T model case. Figure 4-4 shows the same properties, but with fractures with a relatively high transmissivity superimposed ($> 10^{-7}$ m^2/s). This case demonstrates some characteristic features particular to the uncorrelated model. There is considerable heterogeneity, and there is little correlation between adjacent blocks. This stems from the fact that high transmissivity fractures can be any length, and because of the power-law length distribution for the larger sets, then many of the high T fractures are relatively small, and so only affect 1 or 2 blocks. It is rare that a large fracture is generated with a high T, so there are few, if any, continuous lineaments of high hydraulic conductivity. In addition, there are few large fractures due to the power law distribution of fracture length, which exhibits a high k_r value.

Figure 4-5 and Figure 4-6 show the corresponding plots for the case with a correlated T model. A clear difference here is the much greater correlation between blocks due to the effect of larger fractures with higher transmissivity. The median conductivity and porosity is far more stable than for the uncorrelated model as the latter cases converges very slowly, if at all, with respect to the minimum fracture size. This is evident in the porosity values for the 20 m block being much higher than in the 100 m block for the uncorrelated model.

Statistics for 20 m and 100 m blocks for Volume E for each T model and L_{min} truncation are included in Table 4-1. The results are given in terms of percentiles (10, 25, 50, 75 and 90), as well as one standard deviation of the sample, to capture the distribution of K_{eff}, the geometric mean of the axial components of the hydraulic conductivity tensor. For a 20 m block, the median (50-percentile) is similar for the uncorrelated and semi-correlated case, giving Log(K_{eff}) of around –8.5 and –8.8 respectively. However, the correlated case (excluding matching to DZs) shows a lower Log(K_{eff}) of –9.8, although it rises to –9.3 if a discontinuous correlated transmissivity model is matched to small and large fracture lengths separately (Corr 2Tmodel). The variant Geo-DFN (using $K_r = 2.75$ for all fracture sets) shows median Log(K_{eff}) of –10.2 and –9.16 for the 20 m block for the correlated and uncorrelated cases respectively. For the 100 m block there is less difference in the median hydraulic conductivity, with all three cases showing Log(K_{eff}) of –9.1 to –9.4. The variant Geo-DFN input parameters show similar log(Keff) to the original Geo-DFN for the 100 m block, with log(K_{eff}) of –9.1 and –9.5 for the correlated and uncorrelated cases.

The results for these cases are also presented in Table 4-2 in terms of the individual axial components of hydraulic conductivity (Kx, Ky and Kz). Using the full conductivity tensor, the magnitude and direction of the maximum and minimum horizontal conductivities were also calculated for each block. Then considering the ensemble of 729 blocks, the median ratios maximum horizontal and minimum horizontal conductivities were calculated, together with the median ratios of maximum horizontal and vertical conductivities. The directions of maximum horizontal conductivity within each block were used to search for any general trend in the strike of maximum horizontal conductivity. On the local scale, the ratio of Kh_{max} to Kh_{min} is generally around 4 to 9, showing clear local anisotropy. However, a different picture is observed on the regional scale. The ratio between Kh_{max} to Kz is between 1 and 1.5, showing only a very slight regional anisotropy. For the correlated and semi-correlated cases, this regional anisotropy is orientated towards a strike direction between about 120° to 150°, as shown by the horizontal Kh_{max}. In contrast, there is no obvious regional anisotropy orientation for the uncorrelated case. The corresponding fracture kinematic porosity percentiles (10, 25, 50, 75 and 90) are given in Table 4-3. In a 20 m block, the median log(porosity) is greatest for an uncorrelated case (log(porosity) = –3.7) and lowest for a correlated case (log(porosity) = –4.9). For a 100 m block, a similar trend is followed with up to one order of magnitude lower porosity than in the 20 m blocks, due to the different truncation of L_{min} used and hence much lower fracture volume. L_{min} has the greatest effect in the uncorrelated case on both hydraulic conductivity and fracture kinematic porosity.

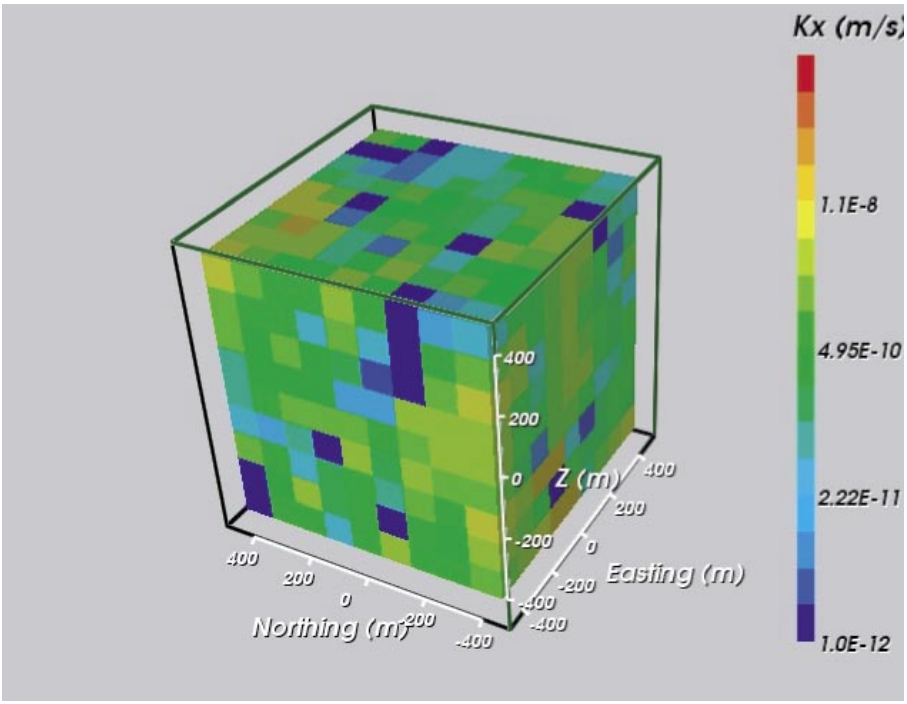

Figure 4-3. *Calculated hydraulic conductivity in the East-West direction for a 9×9×9 array of 100 m blocks for the Volume E DFN with an uncorrelated T model. Model input parameters shown in Table B-24.*

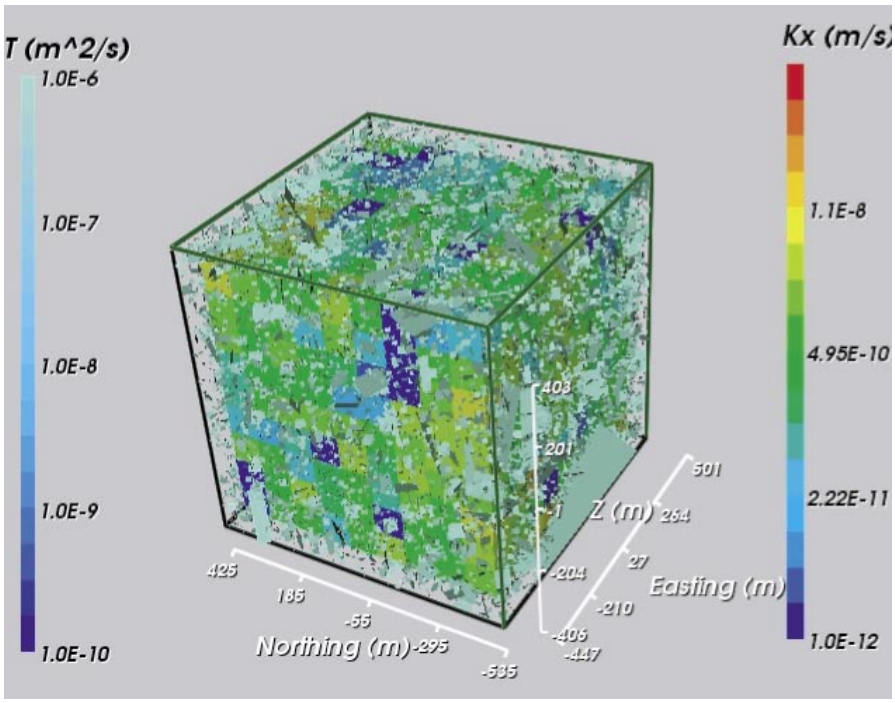

Figure 4-4. *Calculated hydraulic conductivity in the East-West direction for a 9×9×9 array of 100 m blocks for the Volume E DFN with an uncorrelated T model. Fractures with large transmissivity are superimposed. Model input parameters shown in Table B-24.*

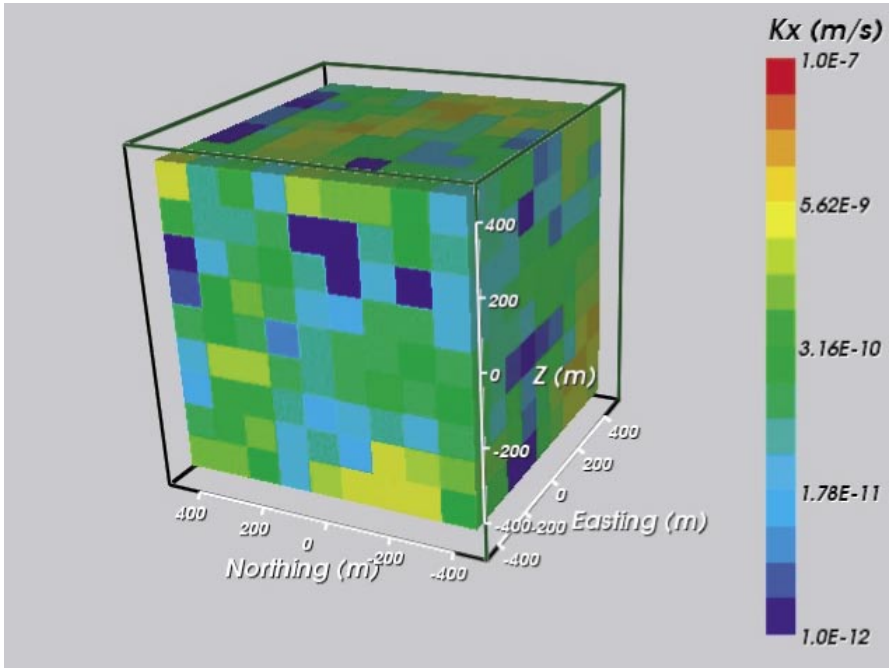

Figure 4-5. *Calculated hydraulic conductivity in the East-West direction for a 9×9×9 array of 100 m blocks for the Volume E DFN with a correlated T model. Model input parameters shown in Table B-24.*

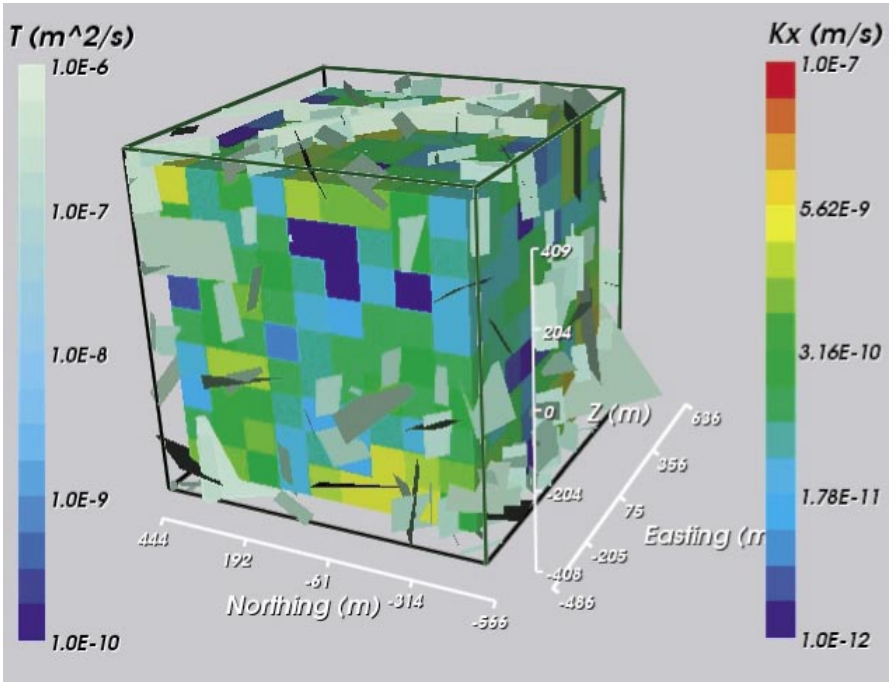

Figure 4-6. *Calculated hydraulic conductivity in the East-West direction for a 9×9×9 array of 100 m blocks for the Volume E DFN with a correlated T model. Fractures with large transmissivity are superimposed. Model input parameters are shown in Table B–24.*

Table 4-1. Effective hydraulic conductivity for correlated, uncorrelated, semi-correlated transmissivity concepts for Volume E. Scale (cell size) and L_{min} are recorded in metres. A correlated transmissivity case with different parameters for small and large fracture length scales is also included (Corr 2 T model). Cases are shown for the correlated and uncorrelated variant Geo-DFN parameters (e.g. Corr, variant Geoff (k_r = 2.75)). The case names correspond to the Hydro-DFN (see Table B-24 and Table B-25).

T model	Scale	L_{min}	Log10 (K_{eff}) (m s^{-1})					
			10-percentile	25-percentile	50-percentile	75-percentile	90-percentile	Std Dev (1σ)
Corr (excl DZs, using Geoff)	20	0.5	–11.07	–10.44	–9.77	–9.07	–8.49	0.93
Corr (excl DZs, using Geo-DFN)	100	10	–10.87	–10.12	–9.42	–8.78	–8.39	0.89
Corr (excl DZs, using Geo-DFN)	100	25	–23.00	–10.68	–9.58	–8.79	–8.33	0.92
Uncorr (excl DZs, using Geo-DFN)	20	0.5	–9.62	–9.00	–8.47	–7.99	–7.61	0.84
Uncorr (excl DZs, using Geo-DFN)	100	10	–10.61	–9.84	–9.35	–8.81	–8.40	0.91
Uncorr (excl DZs, using Geo-DFN)	100	25	–23.00	–12.04	–9.93	–9.07	–8.58	0.95
Semi-corr (excl DZs, using Geo-DFN)	20	0.5	–9.99	–9.35	–8.76	–8.16	–7.84	0.85
Semi-corr (excl DZs, using Geo-DFN)	100	10	–10.32	–9.61	–9.12	–8.64	–8.23	0.79
Corr 2Tmodel (incl DZs, Geo-DFN)	20	0.5	–11.63	–10.12	–9.25	–8.03	–5.83	1.75
Corr 2Tmodel (incl DZs, Geo-DFN)	100	10	–9.93	–9.27	–8.59	–7.94	–7.33	0.99

T model	Scale	L_{min}	Log10 (K_{eff}) (m s^{-1})					
			10-percentile	25-percentile	50-percentile	75-percentile	90-percentile	Std Dev (1σ)
Corr, variant Geo-DFN (k_r = 2.75)	20	0.5	–13.20	–11.13	–10.19	–9.41	–8.82	1.00
Corr, variant Geo-DFN (k_r = 2.75)	100	10	–10.77	–9.93	–9.13	–8.57	–8.31	0.93
Uncorr, variant Geo-DFN (k_r = 2.75)	20	0.5	–10.90	–9.93	–9.16	–8.47	–7.67	1.12
Uncorr, variant Geo-DFN (k_r = 2.75)	100	10	–10.49	–9.94	–9.48	–9.02	–8.63	0.77

Table 4-2. Comparison of anisotropy for correlated, uncorrelated and semi-correlated transmissivity concepts for Volume E. Scale (cell size) and L_{min} are recorded in metres. A correlated transmissivity case with different parameters for small and large fracture length scales is also included (Corr 2 Tmodel). Cases are shown for the correlated and uncorrelated variant Geo-DFN parameters (e.g. Corr, variant Geo-DFN (k_r = 2.75)). The case names correspond to the Hydro-DFN (see Table B-24 and Table B-25).

T model	Scale (m)	L_{min} (m)	Median (Log10 (Kx)) (m s^{-1})	Median (Log10 (Ky)) (m s^{-1})	Median (Log10 (Kz)) (m s^{-1})	Median ratio Khmax/ Khmin	Median ratio Khmax/Kz	Strike of Khmax
Corr (excl DZs, using Geo-DFN)	20	0.5	–9.90	–9.74	–9.77	6.26	1.39	170–180
Corr (excl DZs, using Geo-DFN)	100	10	–9.47	–9.46	–9.36	6.63	1.35	120–150
Corr (excl DZs, using Geo-DFN)	100	25	–9.67	–9.67	–9.49	7.38	1.14	120–150
Uncorr (excl DZs, using Geo-DFN)	20	0.5	–8.53	–8.49	–8.39	5.36	1.34	120–150
Uncorr (excl DZs, using Geo-DFN)	100	10	–9.32	–9.32	–9.27	6.30	1.44	no trend
Uncorr (excl DZs, using Geo-DFN)	100	25	–9.93	–9.90	–9.87	6.25	1.18	no trend
Semi-corr (excl DZs, using Geo-DFN)	20	0.5	–8.80	–8.75	–8.63	6.29	1.25	40–60, 120–150
Semi-corr (excl DZs, using Geo-DFN)	100	10	–9.10	–9.10	–9.03	5.88	1.38	120–150
Corr 2Tmodel (incl DZs, Geo-DFN)	20	0.5	–9.26	–9.19	–9.21	9.91	1.44	120–140
Corr 2Tmodel (incl DZs, Geo-DFN)	100	10	–8.64	–8.60	–8.57	6.98	1.41	120–150
Corr, variant Geo-DFN (k_r = 2.75)	20	0.5	–10.28	–10.15	–10.16	7.24	1.32	30–60
Corr, variant Geo-DFN (k_r = 2.75)	100	10	–9.23	–9.23	–9.10	6.20	1.23	120–140
Uncorr, variant Geo-DFN (k_r = 2.75)	20	0.5	–9.11	–9.29	–9.06	7.99	1.25	90–100
Uncorr, variant Geo-DFN (k_r = 2.75)	100	10	–9.49	–9.45	–9.45	4.35	1.42	no trend

Table 4-3. Porosity for correlated, uncorrelated and semi-correlated transmissivity concepts for Volume E. Scale (cell size) and L_{min} are recorded in metres. A correlated transmissivity case with different parameters for small and large fracture length scales is also included (Corr 2 T model). Cases are shown for the correlated and uncorrelated variant Geo-DFN parameters (e.g. Corr, variant Geo-DFN (k_r = 2.75)). The case names correspond to the Hydro-DFN (see Table B-24 and Table B-25).

T model	Scale (m)	L_{min} (m)	Log10 (n_e) (–) 10-percentile	25-percentile	50-percentile	75-percentile	90-percentile
Corr (excl DZs, using Geo-DFN)	20	0.5	–4.93	–4.90	–4.85	–4.78	–4.70
Corr (excl DZs, using Geo-DFN)	100	10	–5.39	–5.33	–5.25	–5.16	–5.09
Corr (excl DZs, using Geo-DFN)	100	25	–5.66	–5.55	–5.42	–5.28	–5.16
Uncorr (excl DZs, using Geo-DFN)	20	0.5	–3.73	–3.72	–3.70	–3.69	–3.67
Uncorr (excl DZs, using Geo-DFN)	100	10	–4.69	–4.66	–4.64	–4.61	–4.57
Uncorr (excl DZs, using Geo-DFN)	100	25	–5.13	–5.08	–5.02	–4.95	–4.87
Semi-corr (excl DZs, using Geo-DFN)	20	0.5	–4.25	–4.24	–4.21	–4.18	–4.15
Semi-corr (excl DZs, using Geo-DFN)	100	10	–4.91	–4.89	–4.85	–4.81	–4.77
Corr 2Tmodel (incl DZs, Geo-DFN)	20	0.5	–4.90	–4.84	–4.71	–4.17	–3.89
Corr 2Tmodel (incl DZs, Geo-DFN)	100	0.5	–4.97	–4.91	–4.83	–4.72	–4.61
Corr, variant Geo-DFN (k_r = 2.75)	20	0.5	–5.12	–5.08	–5.02	–4.95	–4.88
Corr, variant Geo-DFN (k_r = 2.75)	100	10	–5.38	–5.31	–5.21	–5.13	–5.06
Uncorr, variant Geo-DFN (k_r = 2.75)	20	0.5	–4.14	–4.12	–4.10	–4.07	–4.01
Uncorr, variant Geo-DFN (k_r = 2.75)	100	10	–4.92	–4.89	–4.86	–4.82	–4.78

These block-scale hydraulic conductivities are also presented as CDF distributions in Figure 4-7 for the uncorrelated case, Figure 4-8 for the correlated case, and Figure 4-9 for the semi-correlated case. For the uncorrelated case, the spread is greater and the median higher for the 20 m blocks than the 100 m blocks since properties are averaged over a greater volume in the 100 m blocks. For example, the likelihood of one fracture dominating a 20 m block is much greater than for a 100 m block, leading to greater heterogeneity and therefore increased spread. For the correlated case, the spread and median are more similar for the 20 m blocks and the 100 m blocks, due to the greater likelihood of a 100 m block capturing several highly transmissive fractures. Both cases show similar Kx, Ky and Kz and can therefore be considered regionally isotropic. The semi-correlated case lies between the two other cases. Corresponding plots for the uncorrelated and correlated cases for the distribution of the strike of the maximum horizontal hydraulic conductivity are shown in Figure 4-10 and Figure 4-11.

The minimum fracture truncation length that still produces reasonably accurate results has been considered, and the block properties for L_{min} = 10 m and 25 m for the 100 m block has been calculated for all cases. Using L_{min} of 25 m produces the best compromise between computational feasibility and accuracy for Volume E, as explained in subsection 4.4.2.

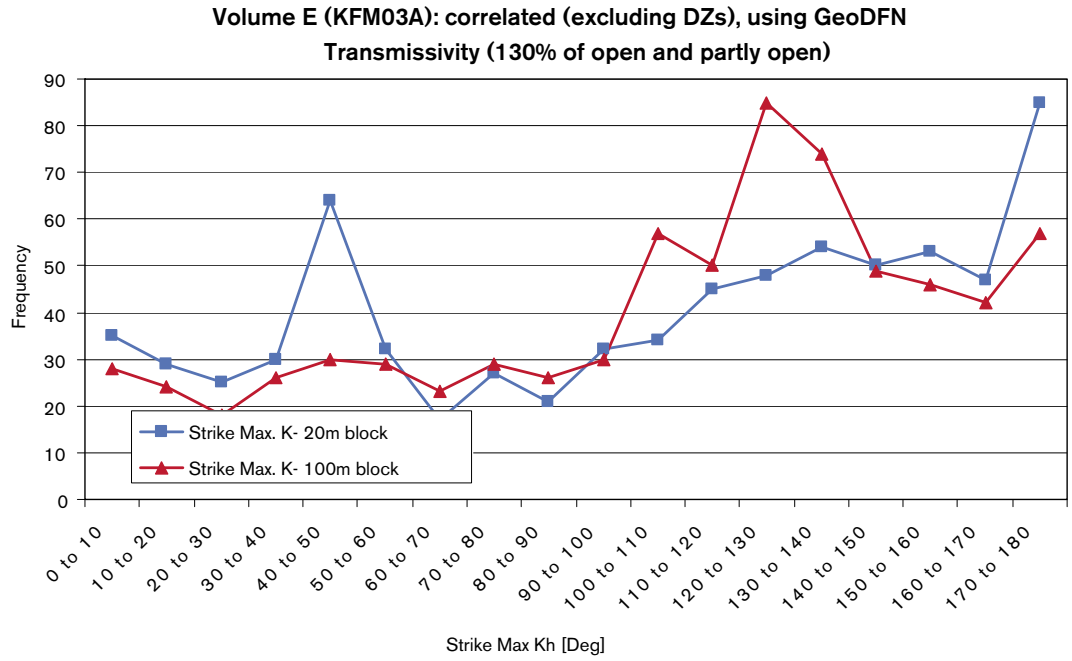

Figure 4-7. *Hydraulic conductivity distribution for an uncorrelated transmissivity, for Volume E. K11, K22, K33 correspond to Kx (Easting), Ky (Northing) and Kz (vertical), respectively. Model input parameters shown in Table B-24.*

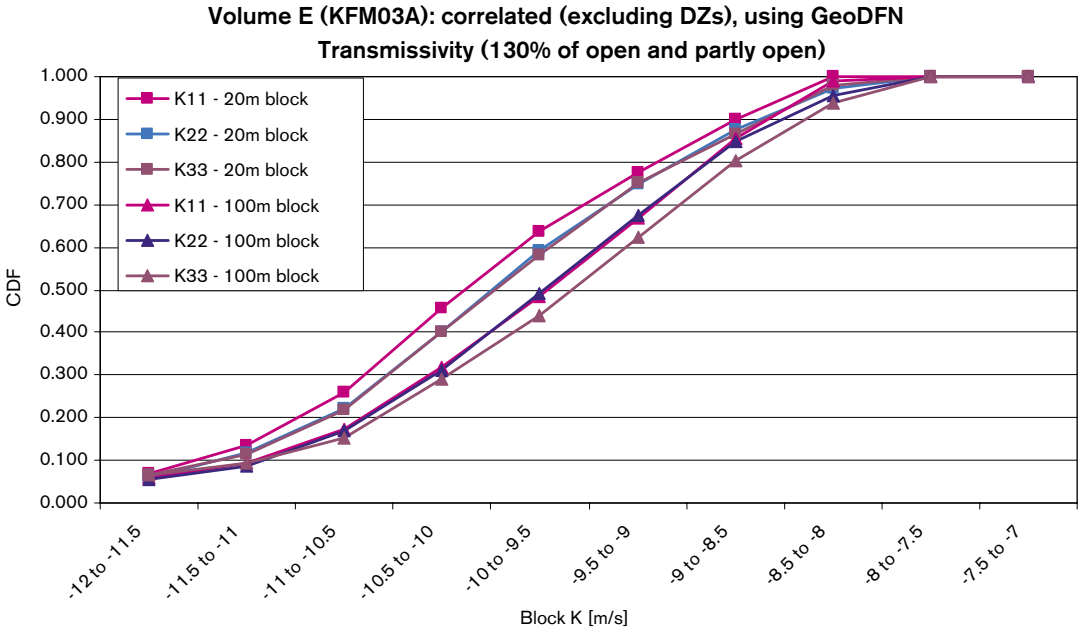

Figure 4-8. *Hydraulic conductivity distribution for a correlated transmissivity, for Volume E. K11, K22, K33 correspond to Kx (Easting), Ky (Northing) and Kz (vertical), respectively. Model input parameters shown in Table B-24.*

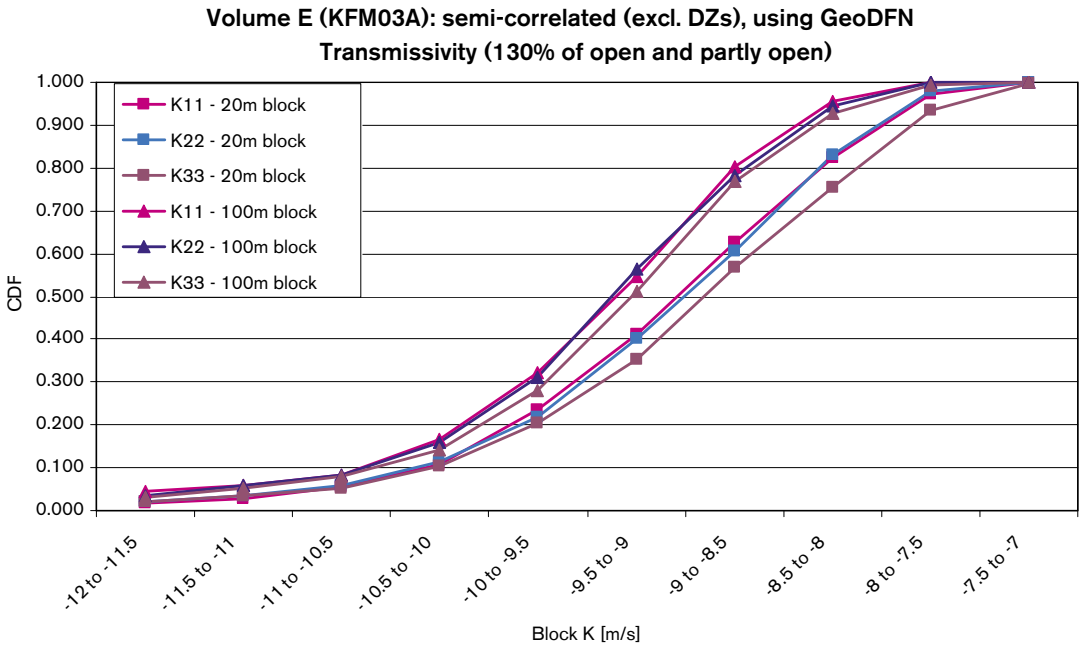

Figure 4-9. *Hydraulic conductivity distribution for a semi-correlated transmissivity, for Volume E. K11, K22, K33 correspond to Kx (Easting), Ky (Northing) and Kz (vertical), respectively. Model input parameters shown in Table B-24.*

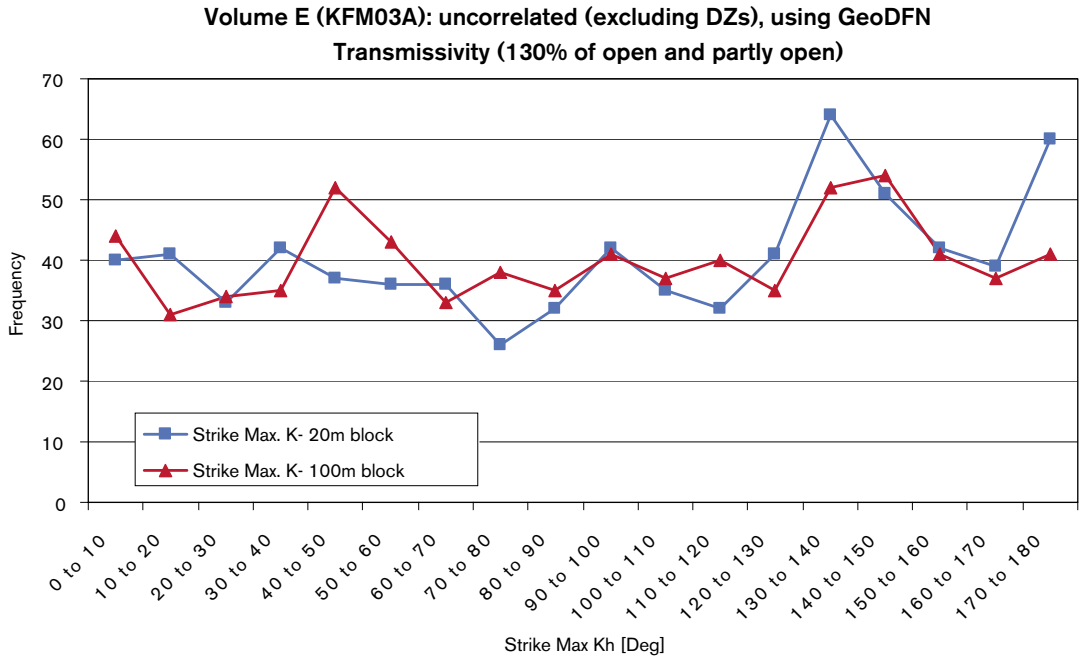

Figure 4-10. *Distribution of the maximum horizontal hydraulic conductivity for an uncorrelated transmissivity model for Volume E. Model input parameters shown in Table B-24.*

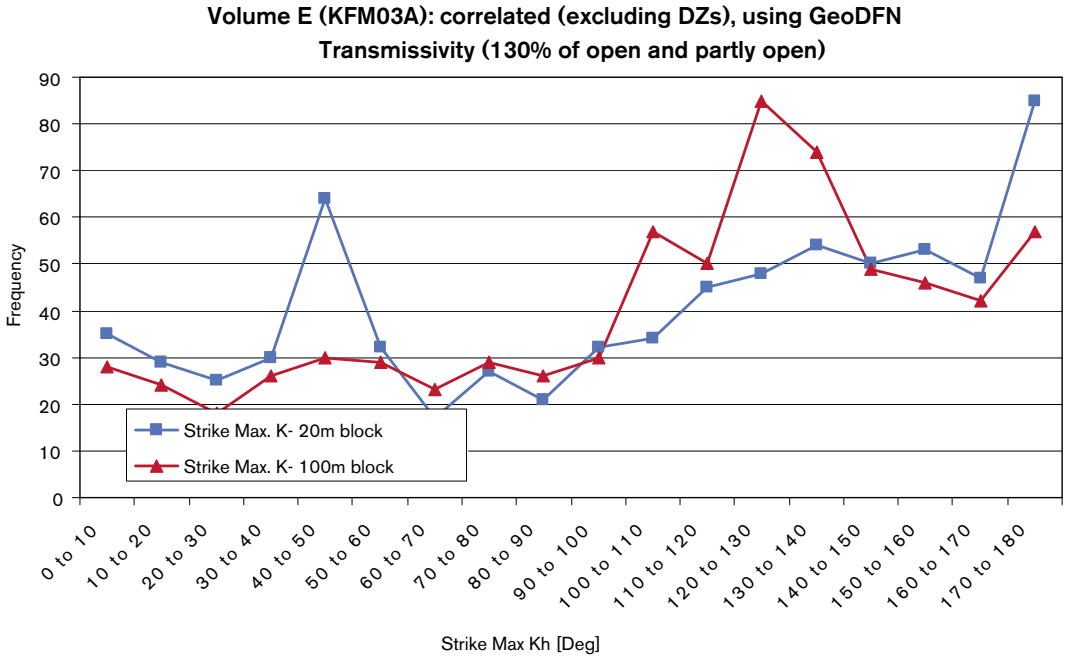

Figure 4-11. *Distribution of the maximum horizontal hydraulic conductivity for a correlated transmissivity model for Volume E. Model input parameters shown in Table B-24.*

4.4.2 Resultant model parameters for Volume F (upper section of KFM01A)

Some examples of the calculations of the resultant model parameters for the hydraulic block properties are shown in Figure 4-12 to Figure 4-15 for the 100 m block. Figure 4-12 shows the x (East-West) hydraulic conductivity for the uncorrelated T model case. Figure 4-13 shows the same properties, but with fractures with large transmissivity superimposed. Figure 4-14 and Figure 4-15 show the corresponding plots for the case with a correlated T model.

Statistics for 20 m and 100 m blocks for Volume F for each T model and L_{min} truncations are included in Table 4-4. The results are given in terms of percentiles (10, 25, 50, 75 and 90), as well as one standard deviation of the sample, to capture the distribution of K_{eff}, the geometric mean of the axial components of the hydraulic conductivity tensor. For a 20 m block, the median (50-percentile) is similar for the uncorrelated and semi-correlated case giving $\log(K_{eff})$ of around –8.6. However, the correlated case (excluding matching to DZs) shows a lower $\log(K_{eff})$ of –9.5. In contrast, the 100 m block shows more similar values for all three cases, varying between $\log(K_{eff})$ of 8.9 and 9.3.

The results for these cases are also presented in Table 4-5 in terms of the individual axial components of hydraulic conductivity (Kx, Ky and Kz); the median ratios of maximum horizontal and minimum horizontal conductivities; the median ratios of maximum horizontal and vertical conductivities; and the strike of any general trend in the maximum horizontal conductivity. The ratios of anisotropy are calculated block-by-block and then the median is computed over the ensemble of 729 blocks. Similar to Volume E, there is local anisotropy shown clearly by the ratio of Kh_{max} to Kh_{min} between 3 to 7. In contrast, there is only slight regional anisotropy with the ratio between Kh_{max} to Kz being around 1.4. For all three cases there is a trend in the horizontal regional anisotropy with a direction of strike between about 30° to 60°.

The corresponding fracture kinematic porosity percentiles (10, 25, 50, 75 and 90) are given in Table 4-6. The median log(porosity) in a 20 m block for the uncorrelated and semi-correlated cases is very similar (–4.2), with the correlated case slightly less at median log(porosity) of –4.9. In a 100 m block, the median porosities are log(porosity) is lower (between –4.7 to –5.2) for all cases.

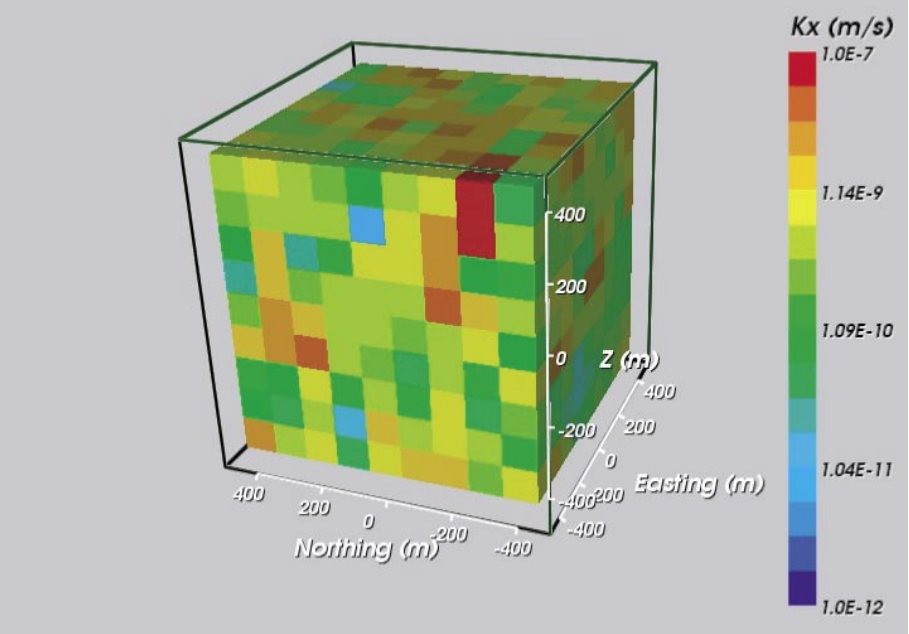

Figure 4-12. *Calculated hydraulic conductivity in the East-West direction for a 9×9×9 array of 100 m blocks for the Volume F DFN with an uncorrelated T model. Model input parameters shown in Table B–27.*

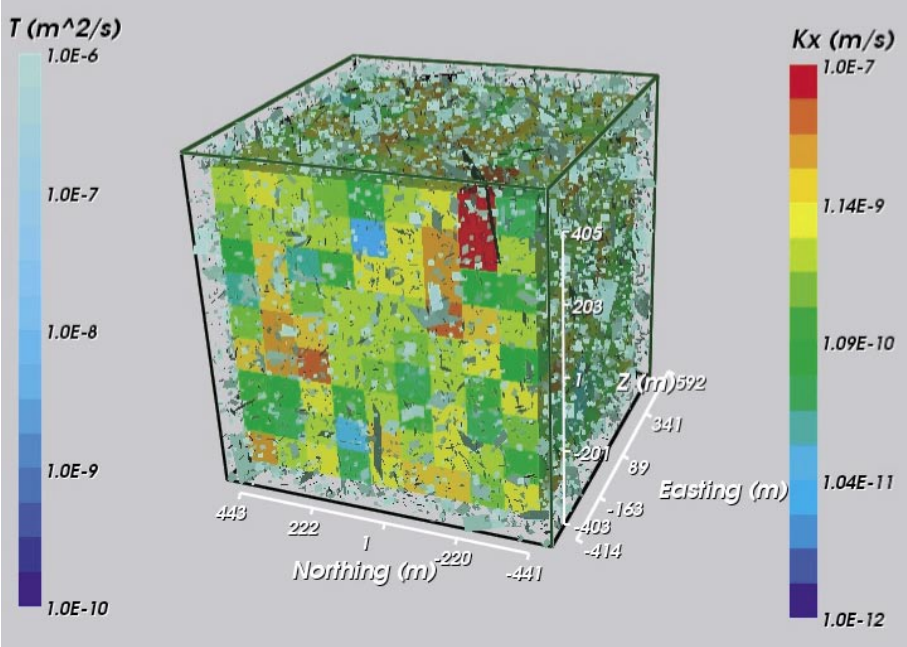

Figure 4-13. *Calculated hydraulic conductivity in the East-West direction for a 9×9×9 array of 100 m blocks for the Volume E DFN with an uncorrelated T model. Fractures with large transmissivity are superimposed. Model input parameters shown in Table B–27.*

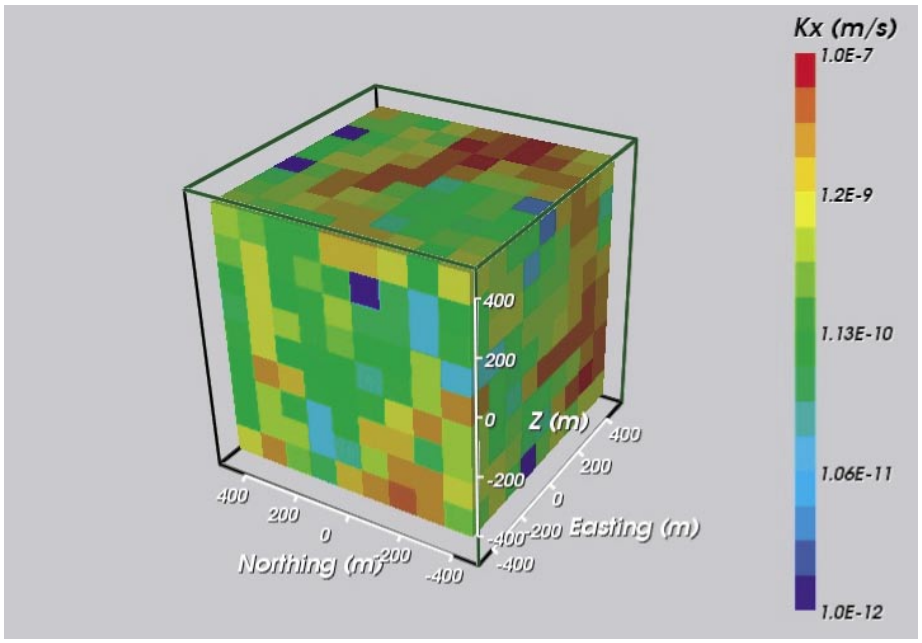

Figure 4-14. *Calculated hydraulic conductivity in the East-West direction for a 9×9×9 array of 100 m blocks for the Volume F DFN with a correlated T model. Model input parameters shown in Table B–27.*

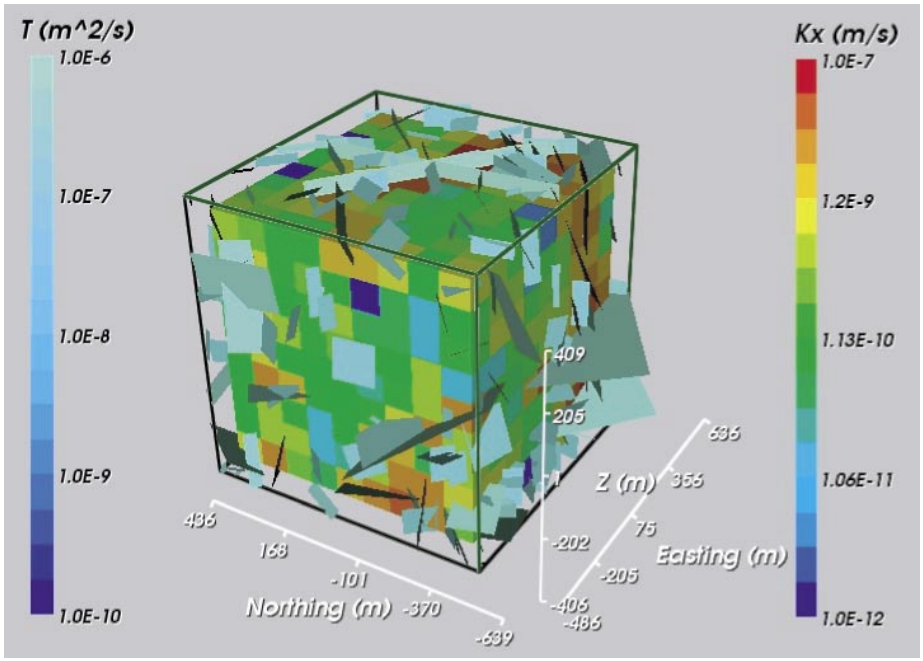

Figure 4-15. *Calculated hydraulic conductivity in the East-West direction for a 9×9×9 array of 100 m blocks for the Volume E DFN with a correlated T model. Fractures with large transmissivity are superimposed. Model input parameters shown in Table B–27.*

Table 4-4. Effective hydraulic conductivity for correlated, uncorrelated and semi-correlated transmissivity concepts for Volume F. Scale (cell size) and L_{min} are recorded in metres. (The P32 used was 26% of open and partly open fractures.) The case names correspond to the Hydro-DFN (see Table B-27).

T model	Scale (m)	L_{min} (m)	Log10 (K_{eff}) (m s^{-1}) 10-percentile	25-percentile	50-percentile	75-percentile	90-percentile	Std Dev (1σ)
Corr, Geo-DFN	20	0.5	–10.56	–10.10	–9.54	–8.96	–8.48	0.79
Corr, Geo-DFN	100	10	–10.19	–9.73	–9.15	–8.62	–8.31	0.75
Corr, Geo-DFN	100	20	–10.84	–9.96	–9.19	–8.58	–8.28	0.88
Corr, Geo-DFN	100	25	–11.19	–10.06	–9.27	–8.66	–8.32	0.84
Corr, Geo-DFN	100	50	–23.00	–18.85	–9.52	–8.76	–8.33	0.83
Uncorr, Geo-DFN	20	0.5	–9.56	–9.04	–8.62	–8.20	–7.94	0.63
Uncorr, Geo-DFN	100	10	–10.01	–9.63	–9.29	–9.01	–8.77	0.49
Uncorr, Geo-DFN	100	25	–11.67	–10.30	–9.69	–9.25	–8.96	0.71
Uncorr, Geo-DFN	100	50	–23.00	–23.00	–10.36	–9.53	–9.08	0.76
Semi-corr, Geo-DFN	20	0.5	–10.02	–9.36	–8.64	–7.89	–7.49	0.97
Semi-corr, Geo-DFN	100	10	–10.09	–9.58	–8.93	–8.33	–7.85	0.89

Table 4-5. Comparison of anisotropy for correlated, uncorrelated and semi-correlated Transmissivity concepts for Volume F. Scale (cell size) and L_{min} are recorded in metres. The case names correspond to the Hydro-DFN (see Table B-27).

T model	Scale (m)	L_{min} (m)	Median (Log10 (K_x)) (m s^{-1})	Median (Log10 (Ky)) (m s^{-1})	Median (Log10 (Kz)) (m s^{-1})	Median ratio Khmax/ Khmin	Median ratio Khmax/ Kz	Strike of Khmax
Corr, Geo-DFN	20	0.5	–9.65	–9.50	–9.55	5.17	1.36	30–60
Corr, Geo-DFN	100	10	–9.24	–9.15	–9.10	4.68	1.33	130–140
Corr, Geo-DFN	100	20	–9.31	–9.19	–9.17	6.05	1.30	30–60, 120–150
Corr, Geo-DFN	100	25	–9.39	–9.28	–9.21	6.21	1.26	120–140
Corr, Geo-DFN	100	50	–9.60	–9.51	–9.49	4.04	1.00	120–140
Uncorr, Geo-DFN	20	0.5	–8.62	–8.57	–8.62	3.61	1.45	30–60
Uncorr, Geo-DFN	100	10	–9.31	–9.25	–9.26	3.42	1.38	30–60
Uncorr, Geo-DFN	100	25	–9.69	–9.63	–9.63	5.73	1.39	30–60
Uncorr, Geo-DFN	100	50	–10.35	–10.35	–10.31	4.05	1.00	30–60
Semi-corr, Geo-DFN	20	0.5	–8.69	–8.64	–8.55	6.98	1.32	30–60
Semi-corr, Geo-DFN	100	10	–9.04	–8.95	–8.89	6.52	1.30	30–60

Table 4-6. Porosity for correlated, uncorrelated and semi-correlated transmissivity concepts for Volume F. Scale (cell size) and L_{min} are recorded in metres. The case names correspond to the Hydro-DFN (see Table B-27).

T model	Scale (m)	L_{min} (m)	Log10 (n_e) (–) 10-percentile	25-percentile	50-percentile	75-percentile	90-percentile
Corr, Geo-DFN	20	2	–4.98	–4.94	–4.89	–4.82	–4.73
Corr, Geo-DFN	100	10	–5.27	–5.22	–5.16	–5.07	–4.99
Corr, Geo-DFN	100	20	–5.47	–5.38	–5.29	–5.16	–5.05
Corr, Geo-DFN	100	25	–5.54	–5.43	–5.34	–5.22	–5.10
Corr, Geo-DFN	100	50	–5.78	–5.63	–5.48	–5.32	–5.18
Uncorr, Geo-DFN	20	2	–4.21	–4.19	–4.17	–4.14	–4.12
Uncorr, Geo-DFN	100	10	–4.88	–4.87	–4.85	–4.83	–4.81
Uncorr, Geo-DFN	100	25	–5.31	–5.27	–5.23	–5.18	–5.14
Uncorr, Geo-DFN	100	50	–5.70	–5.61	–5.52	–5.44	–5.37
Semi-corr, Geo-DFN	20	2	–4.22	–4.19	–4.16	–4.11	–4.06
Semi-corr, Geo-DFN	100	10	–4.77	–4.74	–4.70	–4.65	–4.59

These block-scale hydraulic conductivities are also presented as CDF distributions in Figure 4-16 for the uncorrelated case, Figure 4-17 for the correlated case, and Figure 4-18 for the semi-correlated case. Similar to Volume E, for the uncorrelated case (Volume F), the mean is higher and the spread greater for the 20 m blocks than the 100 m blocks since properties are averaged over a greater volume in the 100 m blocks. For the correlated case, the spread and median are more similar for the 20 m blocks and the 100 m blocks, with the 20 m blocks showing slightly lower median value. Both cases show similar Kx, Ky and Kz showing a regional isotropic nature. The semi-correlated case lies between the two other cases. Corresponding plots for the uncorrelated and correlated cases for the distribution of the strike of the maximum horizontal hydraulic conductivity are shown in Figure 4-20 and Figure 4-21.

The next issue to be addressed is how sensitive the calculated block properties are to the fracture length truncation L_{min}. This is important for the follow-on project of Forsmark (F1.2) regional modelling. Block-scale hydraulic properties were calculated for Volume F for values of L_{min} = 10 m, 25 m and 50 m for 100 m blocks. An example for the correlated transmissivity case is shown in Figure 4-19. For a truncation at 50 m, there are about 28% of blocks without a connected network. This improves with a 25 m truncation, with 90% of cells that have some hydraulic conductivity. There is a trade off between using the best fit truncation length and the limit of the simulation that is possible to run computationally. The best compromise uses L_{min} of about 25 m for all transmissivity cases; any smaller truncation size and it is not possible to run the model. As a general rule of thumb, fractures down to a length at least as small as a quarter of the block-size need to be included. Block-scale hydraulic properties have also been calculated for L_{min} = 10 m and 25 m for 100 m blocks for Volume E. A similar trend is observed, and the best compromise uses L_{min} of 25 m for the 100 m block for all three transmissivity cases.

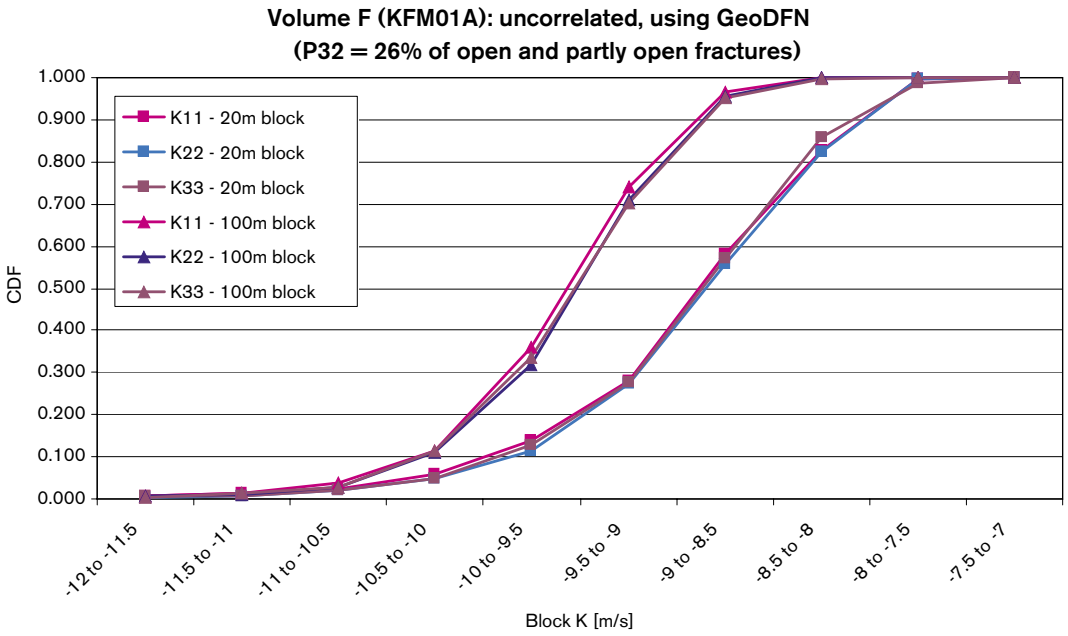

Figure 4-16. *Hydraulic conductivity distribution for an uncorrelated transmissivity, for Volume F. K11, K22, K33 correspond to Kx (Easting), Ky (Northing) and Kz (vertical), respectively. Model input parameters shown in Table B-27.*

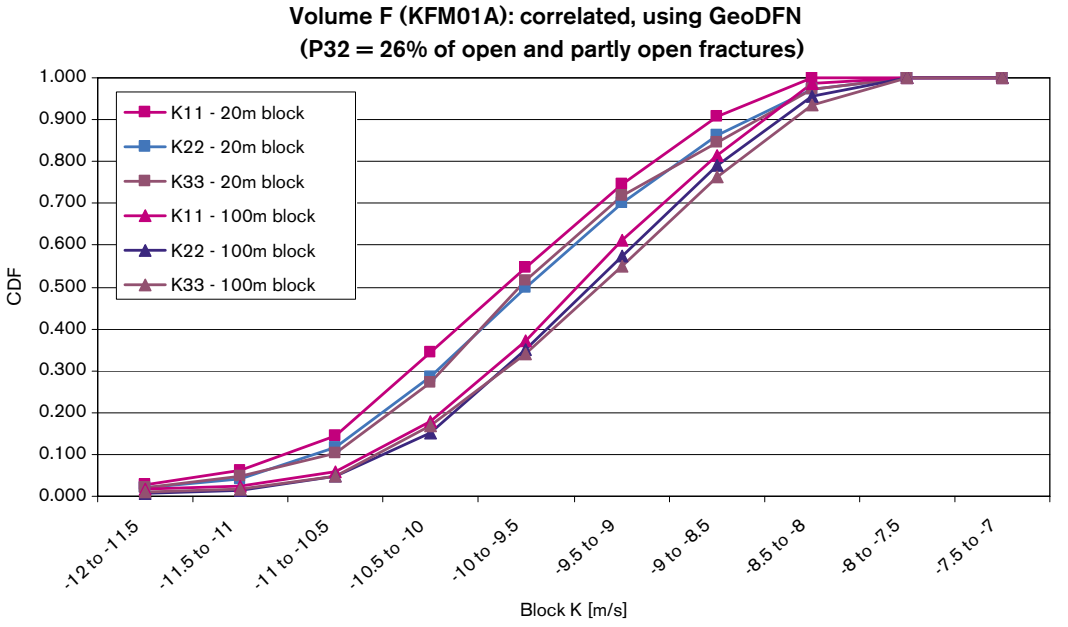

Figure 4-17. *Hydraulic conductivity distribution for a correlated transmissivity, for Volume F. K11, K22, K33 correspond to Kx (Easting), Ky (Northing) and Kz (vertical), respectively. Model input parameters shown in Table B-27.*

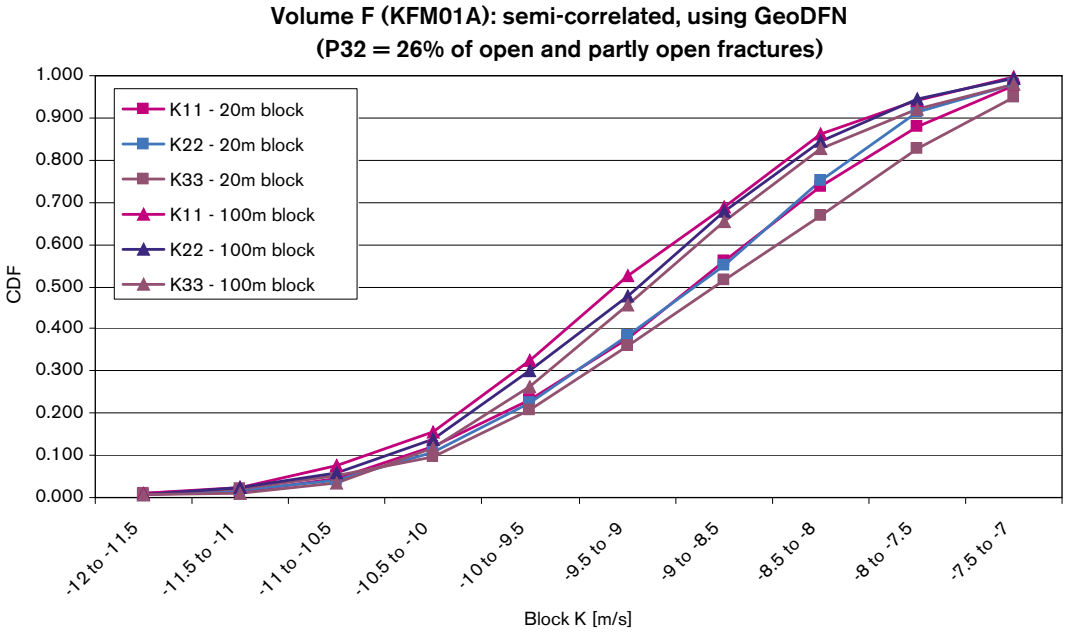

Figure 4-18. *Hydraulic conductivity distribution for a semi-correlated transmissivity, for Volume F. K11, K22, K33 correspond to Kx (Easting), Ky (Northing) and Kz (vertical), respectively. Model input parameters shown in Table B-27.*

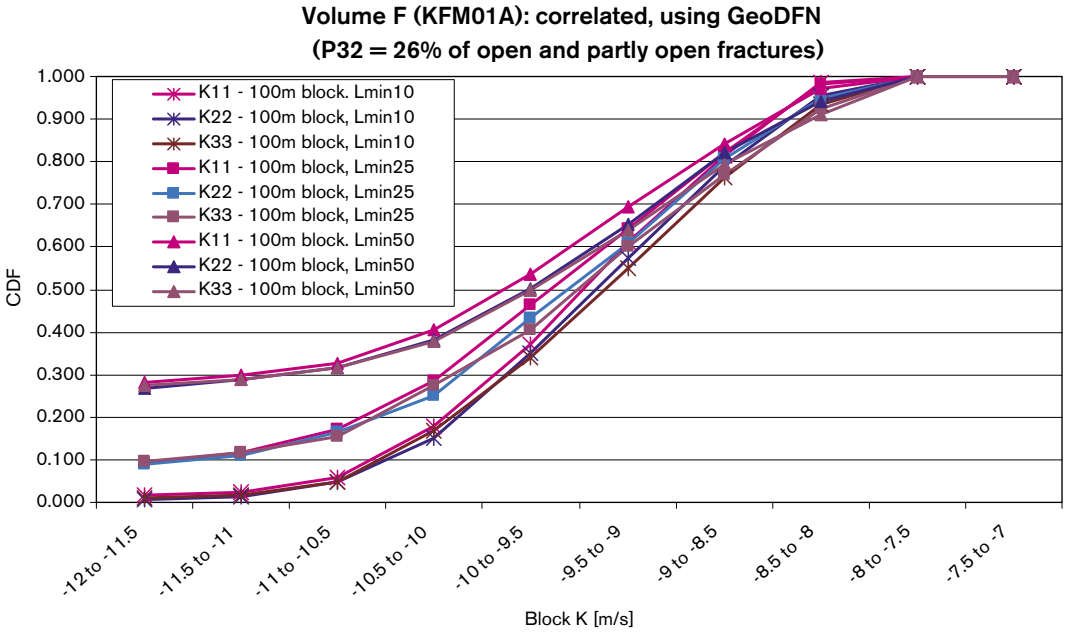

Figure 4-19. *Hydraulic conductivity distribution for a correlated transmissivity, for Volume F. Different L_{min} are used for the 100 m block. K11, K22, K33 correspond to Kx (Easting), Ky (Northing) and Kz (vertical), respectively. Model input parameters shown in Table B-27.*

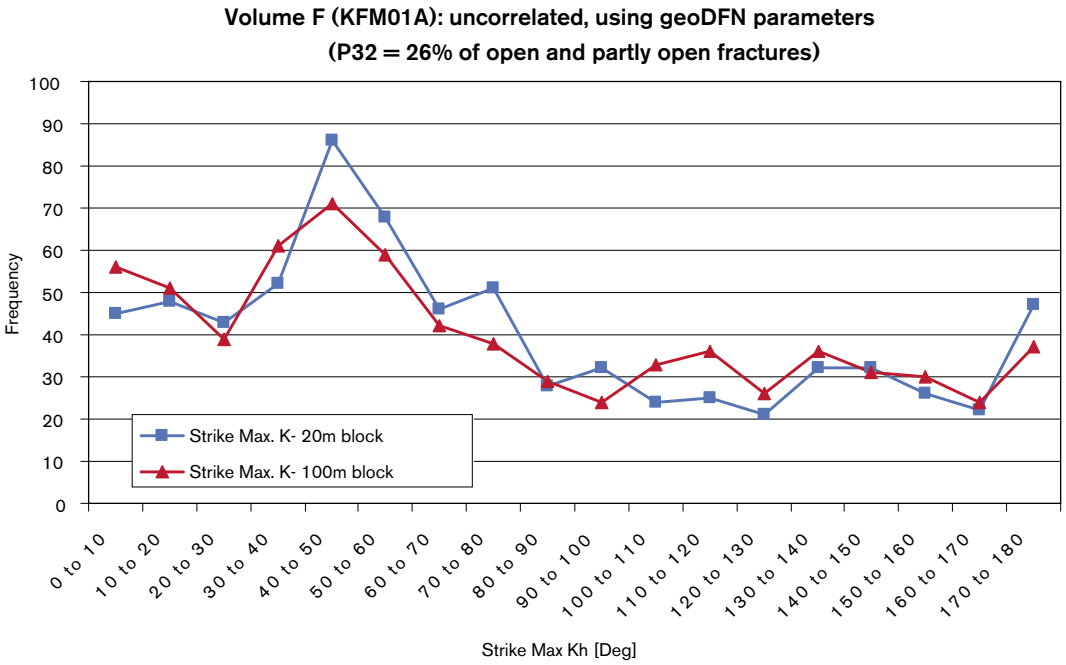

Figure 4-20. *Distribution of the maximum horizontal hydraulic conductivity for an uncorrelated transmissivity model for Volume F. Model input parameters shown in Table B-27.*

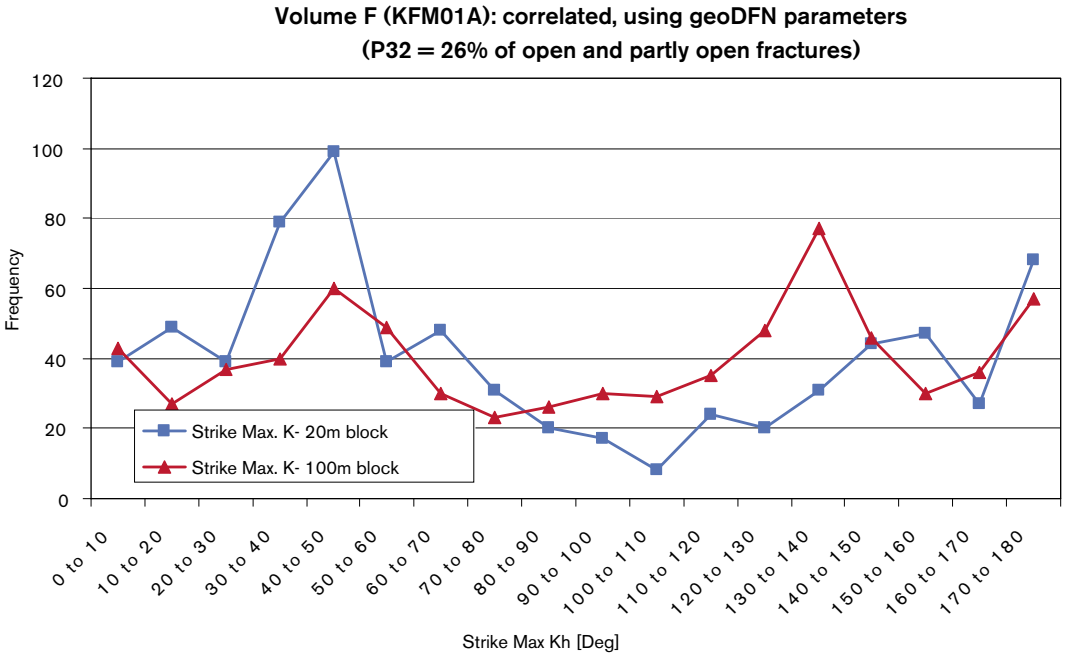

Figure 4-21. *Distribution of the maximum horizontal hydraulic conductivity for a correlated transmissivity model for Volume F.*

4.4.3 Evaluation of uncertainties

The sensitivity of the block-scale properties with regard to all the assumptions listed in subsection 4.2 has been considered. The effect of truncation of lower fracture size limit has been considered, a requirement of the regional modelling (subsections 4.4.1 and 4.4.2). A better match to the observed numbers of regional scale lineaments has been considered by using the variant Geo-DFN input parameters for Volume E with $k_r = 2.75$ (subsection 4.4.1).

4.5 Conclusions from block property study

The following conclusions can be drawn from the study of block properties:

- For both Volume E and Volume F for the 20 m block, the median for uncorrelated and semi-correlated transmissivity models is similar, around $\log(K_{eff})$ of –8.5 and –8.8 for Volume E, and –8.6 for both cases for Volume F. For the correlated case, for both Volume E and Volume F, the median effective hydraulic conductivity is around one order of magnitude lower ($\log(K_{eff}) = –9.8$ and –9.5, respectively).
- Use of the variant Geo-DFN parameters ($k_r = 2.75$) for the correlated and uncorrelated cases for Volume E shows lower median $\log(K_{eff})$ of –10.2 and –9.2 for the 20 m block than the original Geo-DFN.
- For a 100 m block for both Volume E and Volume F, the median effective hydraulic conductivity is much more similar for all three cases, with $\log(K_{eff})$ varying between –8.9 and –9.4 in all cases and for both rock volumes. For the 100 m block the variant Geo-DFN parameters show similar median K_{eff} to the original Geo-DFN input parameters ($\log(K_{eff})$ of –9.1 and –9.5 for the correlated and uncorrelated cases).
- There is localised horizontal anisotropy within a block for all cases due to the discrete nature of the DFN. The median horizontal anisotropy Kh_{max}/Kh_{min} for Volume E is generally around 6, although inclusion of large flows in DZs shows Kh_{max}/Kh_{min} of 7 to 10. For Volume F, Kh_{max}/Kh_{min} is observed to be in the range 3 to 7.
- For both rock volumes, the hydraulic conductivity is similar in x, y and z directions, suggesting only slight regional anisotropy. There is a weak regional anisotropy between the horizontal and vertical hydraulic conductivity with median ratio Kh_{max}/Kz of about 1 to 1.5.
- For Volume F, for all cases, there is a slight trend of regional anisotropy with an observed Kh_{max} with a strike direction of about 030°–060°. This is consistent with the PFL flow anomaly data. For Volume E, the direction of the slight regional anisotropy is less clear, with the uncorrelated case showing no directional trend, and the correlated and semi-correlated cases showing a trend in the direction with strike of 120°–150°. This is consistent with the NW-SE regional stress.
- Fracture kinematic porosity is more similar for the uncorrelated and semi-correlated cases. For example, for Volume E, $\log(n_e)$ is around –4.7 for the 100 m block for the uncorrelated and semi-correlated models. In contrast, the correlated case shows around half an order of magnitude lower fracture kinematic porosity for both rock volumes. For Volume F, the uncorrelated and semi-correlated 100 m block cases show $\log(n_e)$ of –4.9 and –4.7, whereas the uncorrelated case has $\log(n_e)$ of –5.2.
- A minimum fracture truncation length (L_{min}) of 25 m is recommended for the regional modelling, since it produces the best compromise between computational feasibility and accuracy of block properties, for both Volume E and Volume F.

5 Regional model – general conditions

Regional modelling of groundwater flow and transport is required to assess the uncertainties of the hydrogeological properties and conditions at Forsmark. The primary objective is to assess the role of known and unknown hydrogeological conditions for the present-day distribution of saline groundwater at the Forsmark site. An improved understanding of the palaeo-hydrogeology is necessary in order to gain credibility for the Site Descriptive Model in general and the Site Hydrogeological Description in particular. The numerical models developed are therefore to serve as a basis for describing the present hydrogeological conditions as well as for predictions of future hydrogeological conditions and transport pathways.

The main objective implies a testing of following modelling components:

- Structural geology with geometrical alternatives;
- Bedrock fracturing;
- Initial and boundary condition variants;
- Parameter uncertainties (i.e. uncertainties in the hydraulic property assignment).

Another specific objective is to assess the flow-paths from the local-scale model domain, based on the present-day flow conditions, to assess the distribution of discharge and recharge areas associated with the flow at approximate repository depth. (The SR-Can Assessment calculations subsequent to this study will consider future flow conditions and more detailed selection of particle release points, which may of course show different results.) This aspect is necessary in order to evaluate the impact on the groundwater flow-field of the specified components and to promote proposals of further investigations of the hydrogeological conditions at the site.

5.1 Model assumptions and input data

The simulations of how flow and reference waters have evolved in the post-glacial period up to the present day are modelled using an EPM model with fixed hydraulic properties, but with boundary conditions that change with time. In the base case, the head on the top surface was set to the topographic height that evolves in time due to post-glacial rebound. Offshore, the head was equal to the depth of the sea multiplied by the relative salinity of the Baltic Sea, and here both the salinity of the Baltic and sea depth altered in time. Simulations were started at 8,000 BC (10,000 BP), after the glaciers in the area melted and during the Ancylus Lake period, with an assumed initial distribution of the reference water fractions, and were run until the present-day (2,000 AD).

The key assumptions in the modelling and the possible alternatives are:

- The deformation zone models provided by Geology represent hydraulically active features. In terms of property assignment, the deformation zones may be grouped into three classifications. Firstly, deformation zones between the Singö DZ and Eckarfjärden DZ, which are sub-horizontal. Secondly, deformation zones between the Singö DZ and Eckarfjärden DZ, which are sub-vertical. Thirdly, deformation zones outside the Singö DZ and Eckarfjärden DZ, which tend to be sub-vertical lineaments. For each DZ group, depth dependent properties (transmissivity and porosity) are used with a different trend being interpreted for each DZ group. The three alternative geological models need to be considered to scope sensitivities to the regional distribution of DZs;
- The hydraulic properties of the rock mass inside rock domains RFM029 and RFM017 (containing the candidate area) have distinct properties from those outside (see Figure B–2).
- Properties within rock domains RFM029 and RFM017 are either modelled as homogeneous (during the initial model development) or based on the Hydro-DFN as described in Section 4; For the case using a DFN model a few simplifications are made such as the fracture intensity is homogeneous within RFM029 and RFM017 and there is no depth trend. Other more sophisticated models that incorporate some of the variations seen in the boreholes may be incorporated later within SR-Can. Alternatives include several different Hydro-DFN models based on different assumptions about a transmissivity dependence on length, the Hydro-DFN models developed by the two modelling teams, or a depth dependency in the hydraulic properties;
- Properties in rock domains other than RFM029 and RFM017 are treated as homogeneous bulk continuum porous medium (CPM) properties due to a lack of fracture data (only a small section of KFM04A). Some hydraulic data are available from Finnsjön /17/ that are used as an indication of the general properties;
- Initial and boundary conditions for the hydro-geochemistry are best conceptualised in terms of 4 reference water types (Rain 1960, Brine, Marine and Glacial) with the water at any point being a mixture of fraction, by mass, of each the reference waters;
- An estimate of the reference water fractions in a borehole water sample is interpreted based on the Multivariate Mixing and Mass-balance (M3) analysis /18/. Hence, for the calibration targets there are a number of possible choices: to use the reference water fractions, or a selection of individual ions, and/or environmental isotope ratios ($\delta^{18}O$, δD);
- An appropriate time to start the simulations is 8,000 BC and the groundwater is a mixture of Glacial and Brine reference waters with specified mixing fraction spatial distributions. Variants include different distributions for initial mixing fractions;
- Surface groundwaters are appropriate mixtures of Glacial and Marine waters during the early Baltic Ice Lake, Yoldia Sea, and Ancylus Lake periods. The surface groundwaters then switch to a mixture of Rain 1960 and Marine during the Littorina Sea and current Baltic Sea phases. The history of sea-water salinity has been provided and this is used to determine the relative fractions of Marine and Rain 1960 reference waters at the top surface of the model offshore. The surface water composition is implemented as boundary conditions on the reference water transport equations. Alternatives are to include some dilution by the Rain 1960 reference water during the early pre-Littorina phases;
- The surface flow condition is that onshore the head equals the evolving topographic surface as provided by ice-sheet modelling. Alternatively, a specified flux type boundary condition is used, using a potential infiltration based on surface hydrology giving 200 mm y^{-1}.

5.2 Conceptual model

The primary concepts used in the regional-scale groundwater flow modelling are:

- The current hydrogeological and hydro-geochemical situation at Forsmark has arisen due to natural transient processes that have evolved over the post-glacial period;
- The hydro-geochemistry can be modelled in terms of four reference water (Rain 1960, Brine, Marine and Glacial) using the reference water fractions as conservative tracers;
- The natural transient processes (land-rise, marine transgressions, dilution/mixing of sea water) can be modelled by appropriate choice of flow and reference water boundary conditions;
- The spatial variability of hydraulic properties can be represented in an EPM model by appropriate upscaling of bedrock fracturing and downscaling of deformation zones on a suitable grid resolution;
- The properties of the hydraulic rock domain (HRD) within RFM029 and RFM017 are represented as EPM under-pinned by a regional-scale stochastic DFN model. The HRD properties (hydraulic conductivity tensor, and porosity) are calculated explicitly for each element in the EPM model by an upscaling method;
- The properties of the hydraulic rock domain (HRD) outside of RFM029 and RFM017 are represented as a homogeneous CPM model;
- For the hydraulic conductor domains (HCD) the properties (transmissivity, thickness, and porosity) have a depth dependency.
- For the hydraulic surface domains (HSD) the properties (hydraulic conductivity, thickness, and porosity) are constant over the whole top surface of the model.

Subsections 5.3–5.9 give details of the actual concepts, parameter values and variants considered in the regional-scale groundwater flow modelling.

5.3 Concepts for reference water transport

Based on the analysis of hydro-geochemistry /18/, groundwater compositions were described using a simplified system of four reference waters, which have been previously used in M3 geochemical modelling:

- Brine water: Represents the sampled deep brine type (Cl = 47,000 mg l^{-1}) of water found in KLX02. An old age for the Brine is suggested by the measured ^{36}Cl values indicating a minimum residence time of 1.5 Ma for the Cl component.
- Glacial water: Represents a possible melt-water composition from the last glaciation > 13,000 BP. Modern sampled glacial melt water from Norway was used for the major elements and the $\delta^{18}O$ isotope value (−21‰ SMOW) was based on measured values of $\delta^{18}O$ in calcite surface deposits. The δD value (−158‰ SMOW) is a calculated value based on the equation ($\delta D = 8 \times \delta^{18}O + 10$) for the global meteoric water line.
- Marine is a composite of Littorina Sea and a modified sea water (Sea sediment). Littorina represents old marine water. This water is used for modelling purposes to represent past Baltic Sea water composition. The Modified Sea water (Sea sediment): represents sea water affected by microbial sulphate reduction.

- Rain 1960: Corresponds to infiltration of meteoric water (the origin can be rain or snow) from 1960. Sampled modern meteoric water with modelled high tritium content was used to represent precipitation from that period.

The major ion components and stable isotope composition for the selected reference waters are given in Table 5-1.

In the modelling, the groundwater density and viscosity are taken to be functions of the total groundwater salinity (and pressure and temperature). The salinity for a given water composition is just the sum of the products of each reference water fraction with the salinity of that reference water. The salinities for the reference waters were calculated from the Total Dissolved Solids (TDS, g l^{-1}) using

Salinity = TDS/density,

where density is a function of salinity (and temperature, pressure). It was assumed that the data given in Table 5-1 were obtained under laboratory conditions. Therefore, it was assumed that the data correspond to a temperature of 20°C and pressure of one atmosphere. The density and viscosity were obtained using empirical correlations for NaCl brines (see References /20/ and /21/). This corresponds to representing transport of equivalent NaCl for each water. The approximation made is reasonable, but it will lead to the density and salinity being slightly under-estimated for a Ca-rich solution such as the Brine reference water. The references formulate density as a polynomial function of salinity (s), temperature (t) and total pressure (p):

$$\text{Density}(p,t,s) = 1/(A(t)–B(t)\times p –C(t)\times p^2+D(t)\times s+E(t)\times s^2–F(t)\times s\times p–G(t)\times s^2\times p–0.5H(t)\times s\times p^2),$$

where A(t), B(t), C(t), D(t), E(t),F(t),G(t) and H(t) are quadratic coefficients in temperature.

Assuming a pressure profile down-core (surface ~0.1 MPa to ~23 MPa at the base of the model, 2,300 m), a salinity profile (surface 0‰ to 72.3‰ (brine) at depth), and a temperature range (surface 6°C; geothermal gradient 0.01°C m^{-1}, i.e. ~30°C at bottom of model), the groundwater density (ρ) can be calculated from the equation of state. At the surface, the density is around 1,000 kg m^{-3}; and at depth the density is around 1,056 kg m^{-3} (the greatest model depth is 2,300 m). The groundwater viscosity (μ) can be similarly calculated. At the surface, the viscosity is around 1.3×10^{-3}Pa s, and at depth the viscosity is around 0.9×10^{-3}Pa s.

Table 5-1. Groundwater analytical or modelled data used as reference waters for Forsmark /19, Table 5-1/.

	Cl (g l^{-1})	Na (g l^{-1})	K (g l^{-1})	Ca (g l^{-1})	Mg (g l^{-1})	HCO_3 (g l^{-1})	SO_4 (g l^{-1})	δD (‰)	$\delta^{18}O$ (‰)
Brine	47.2	8.5	0.045	19.3	0.002	0.014	0.906	–44.9	–8.9
Marine	6.5	3.674	0.134	0.151	0.448	0.093	0.89	–38	–4.7
Rain 1960	0	0	0	0	0	0.012	0.001	–80	–10.5
Glacial	0.001	0	0	0	0	0	0.001	–158	–21

The equations used to represent the transport of fractions of reference waters, with rock-matrix diffusion, are:

$$\frac{\partial(\phi_f \rho)}{\partial t} + \nabla \cdot (\rho \mathbf{q}) = 0 \qquad \text{(Mass conservation for groundwater)}$$

$$\frac{\partial(\phi_f \rho \sigma_i)}{\partial t} + \nabla \cdot (\rho \sigma_i \mathbf{q}) = \nabla \cdot (\phi_f \rho D \nabla \sigma_i) + \zeta \rho D_{\text{int}} \left. \frac{\partial \sigma_i'}{\partial w} \right|_{w=0} \qquad \text{(Transport of reference waters)}$$

$$\alpha_i \frac{\partial \sigma_i}{\partial t} = D_{\text{int}} \frac{\partial^2 \sigma_i'}{\partial w^2} \qquad \text{(Rock-matrix diffusion)}$$

where σ_i is the mass fraction of reference water i in the water in the fracture system (mobile water); σ_i' is the mass fraction of reference water i in the water in the matrix (immobile water); $\boldsymbol{q}$ is the Darcy velocity:

$$q = -\frac{k}{\mu}(\nabla p + \rho g) \; ;$$

D is the dispersion tensor; ϕ_f is the fracture kinematic porosity, ρ is the groundwater density, ζ is the specific surface area of the fractures D_{int} is the intrinsic (or effective) diffusion coefficient, α_i is the capacity factor for the rock matrix (which allows for sorption), w is a coordinate into the rock matrix, k is the permeability, μ is the fluid viscosity, p is residual pressure, t is time, and g is gravitational acceleration. All parameters use SI units.

In fact, the transport equations for the fractions of reference waters are not all independent. Since the sum of the reference water fractions must add to one, then it is not necessary to solve explicitly the transport equation for the final reference water. It can simply be evaluated as the remaining water fraction once the other reference water fractions have been computed at each time-step.

In the above equations, the groundwater density and viscosity are taken to be functions of the salinity (and the temperature and pressure). The salinity is just the sum of the products of each reference water fraction and the salinity of that reference water. The density and viscosity were calculated from the salinity using empirical correlations for NaCl brines /21/.

5.4 Topography and model domain

Topographic data were supplied on two scales, 50 m and 10 m. Since the refined 10 m data covered the entire regional-scale model area defined in the Task Description (TD), these fine-scale data were used both to define the model area and to set boundary conditions on the top surface. In addition, a number of regional and local water divides had been identified. In CONNECTFLOW it is possible to construct unstructured meshes with irregular boundaries, and hence it is possible to choose boundaries that follow water divides. Figure 5-1 shows the extent of the topographic data and water divides along with the regional model domain as proposed in the TD. These data are unchanged from that available for F1.1.

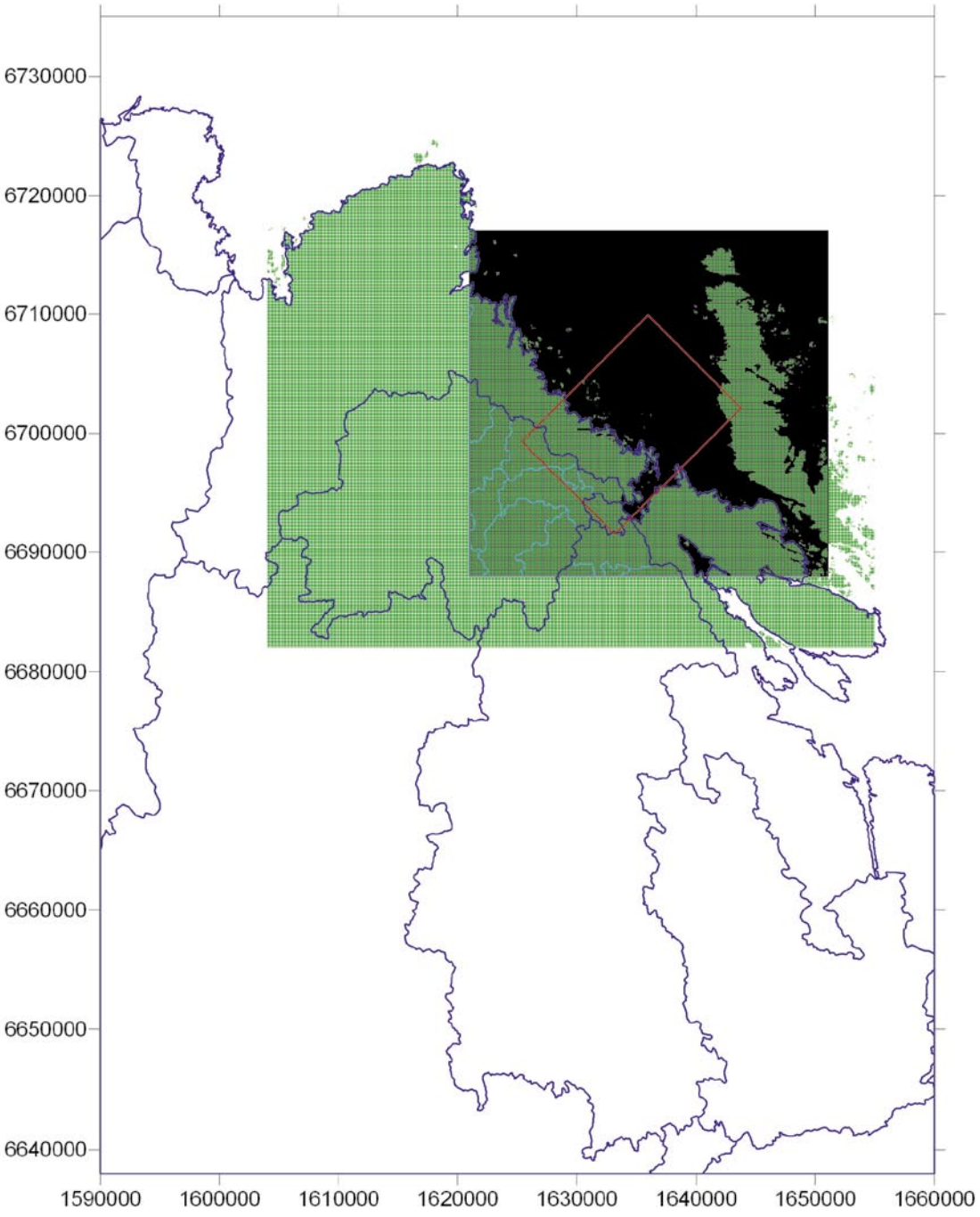

Figure 5-1. *Overview of available data: 10 m topographic data (dark green), 50 m topographic data (light green), regional water divides (dark blue), local water divides (light blue), and the suggested regional scale area (red).*

Modelling transient flow coupled to transport of four reference waters created significant computational demands, and hence it was important to limit the size of the model where possible The domain was chosen to follow regional-flow divides onshore to follow approximate trends of maximum depth in the sea floor and is the same as used Forsmark 1.1 /22/ (see Figure 5-2). This model domain covers a large area currently under the sea, which may be expected to have little influence on current groundwater flow at the site area.

However, this area was retained since for the SR-Can Assessment the model must consider flow conditions into the future when the shoreline is likely to retreat away from the site. The projection of the topographic data onto the CONNECTFLOW finite-element model is shown in Figure 5-3.

Figure 5-2 shows that although the model area onshore is relatively small it includes several areas bounded by water divides, which suggests that flow is compartmented into several localised flow cells. One of the objectives of the DT Team is to confirm whether this is the case by examining the sensitivities of results such as flow-paths to moving the upstream and downstream boundaries.

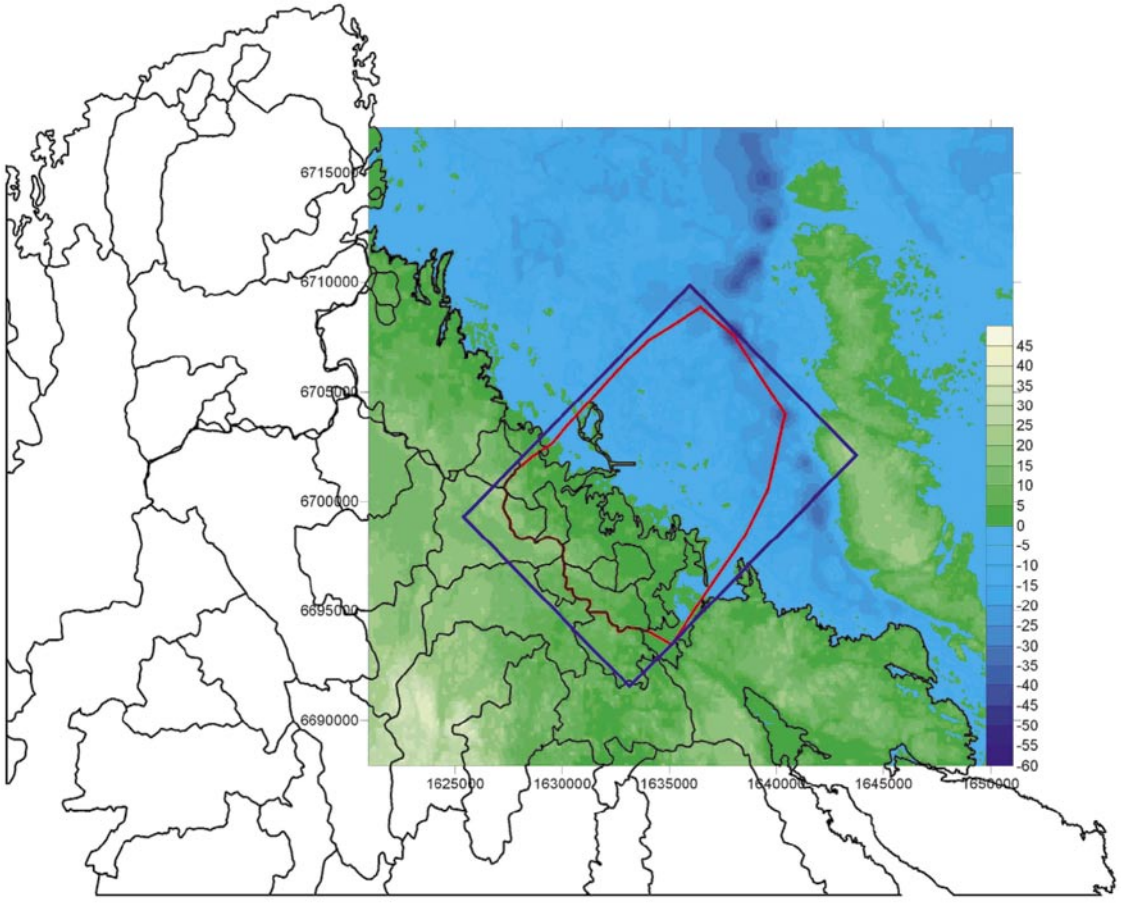

Figure 5-2. *Topographic data and water divides (black lines) from F1.1 together with the regional-model domain proposed in the Task Description (blue line), and the reduced domain used in the CONNECTFLOW F1.2 model (red line).*

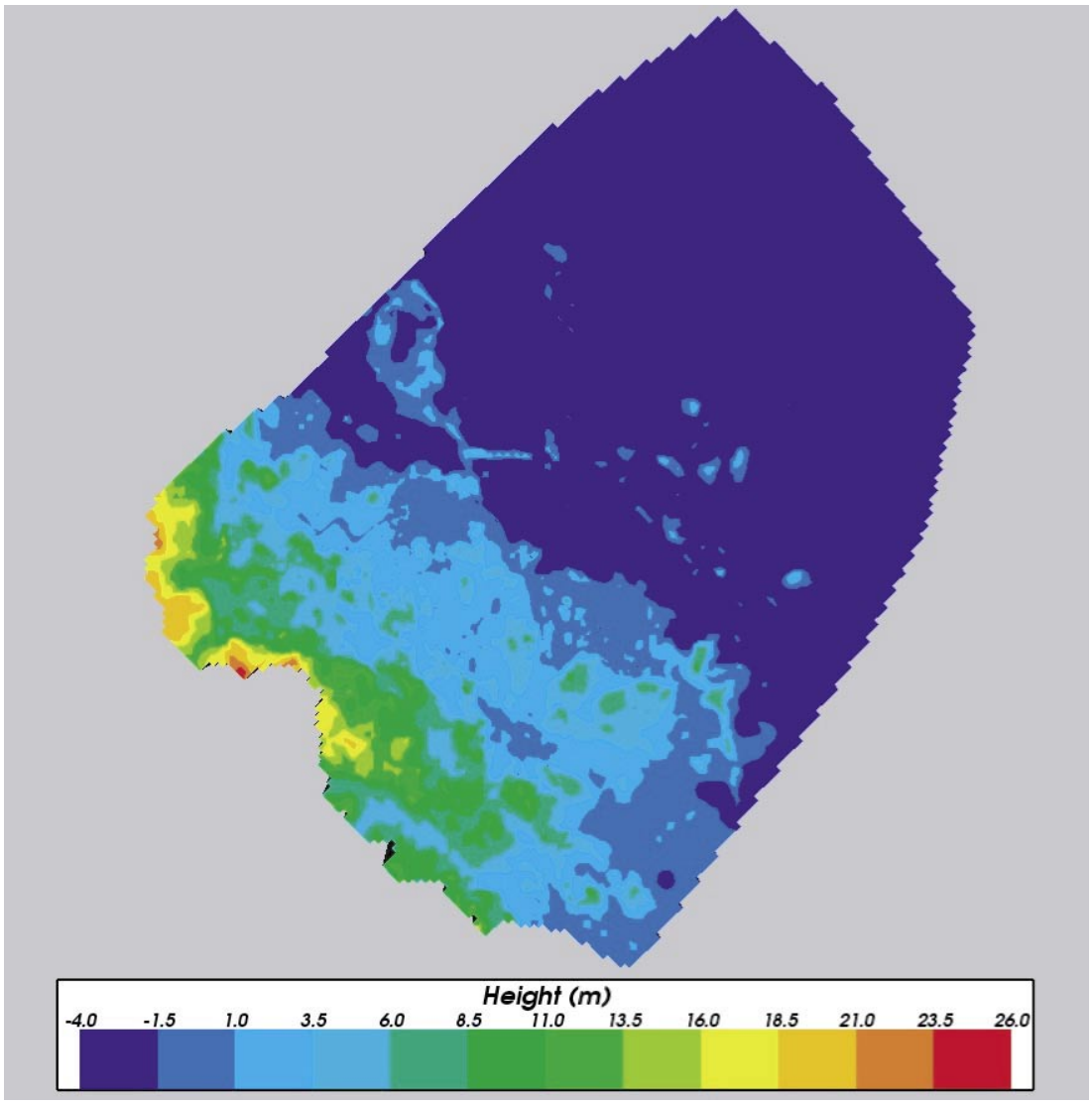

Figure 5-3. *Topographic height for the Forsmark Version 1.2 model domain. The domain boundaries are based on the water divides as were available for F1.1.*

5.5 Selection of grid resolution

Based on the requirements of Design, hydraulic properties were calculated on a 20 m and 100 m block-scale (see Section 4). The task description for the regional-scale modelling specified a 100 m grid resolution. For practical reasons of model size, greater resolution over the whole model domain would be prohibitive for transient multi-component reference water transport problems. However, in CONNECTFLOW it is possible to have embedded sub-grids with higher resolution, typically double or treble in each direction. This capability is used to attain greater resolution of properties and numerical accuracy within key areas of the model. Potential areas for greater grid refinement include: around the Forsmark release area for accurate flow-path calculations; the vicinity of the cored boreholes that are used for calibrating the model against hydraulic and hydro-geochemical data; and in the area south-east of the release-area where there is a need to resolve the large number of sub-horizontal DZs. These areas are shown in Figure 5-4.

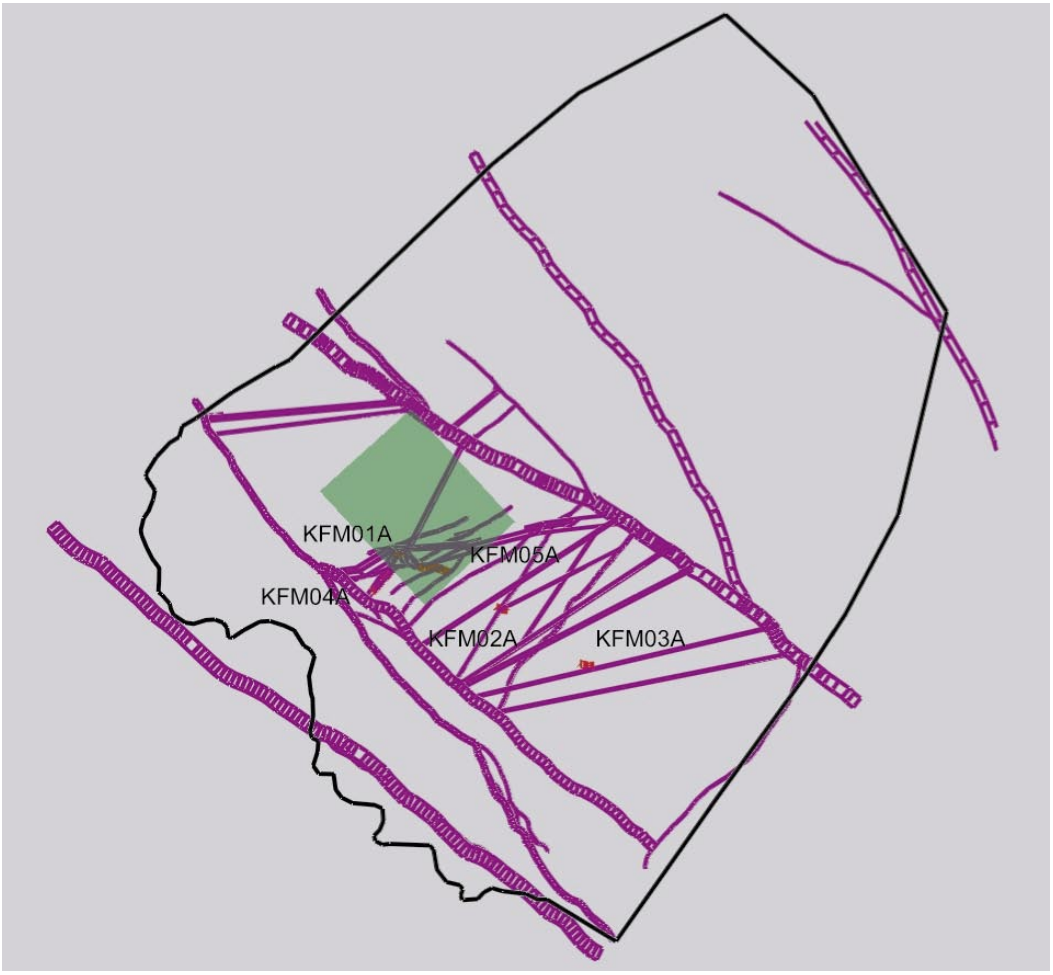

Figure 5-4. *Features that need to be considered in selecting a grid resolution: the position of the Forsmark release-area (green); the locations of 5 cored boreholes with calibration data; the geometry of the deformation zones on a slice at surface (purple). The boundary of model domain is shown in black.*

Due to the close spacing between DZs around boreholes KFM02A and KFM03A it was found that a finer grid was needed in this area to resolve the hydraulic properties of the DZs and the rock mass between. Hence, the regional model evolved to include an embedded 50 m mesh over a large part of the local-scale area. This proved to be important since the simulations of hydro-geochemistry in KFM02A and KFM03A were found to be sensitive to this increase in grid refinement, and hence avoided making incorrect conclusions in the model calibration due to a poor discretisation. As an example, Figure 5-5 shows the resolution of the hydraulic conductivity of both HRD and deterministic HCD features. The 50 m embedded grid covers an area 5.3 km by 2.6 km and extends down to a depth of 1,100 m. The band of high variability running through the centre corresponds to rock domains RFM029 and RFM017 where a DFN model is used. The assignment of properties for the HCD and HRD is described in detail in subsections 5.7 and 5.8, respectively. Here though, the purpose is just to show how the discretisation affects the representation of properties. Figure 5-6 shows a close-up of the embedded grid illustrating how the high conductivities associated with the HCD are much better resolved compared to the 100 m grid outside where DZs tend to smeared out and merge resulting in a connectivity between zones that is artificial. (The downscaling method used for mapping the DZ properties onto a grid is described in subsection 2.4.)

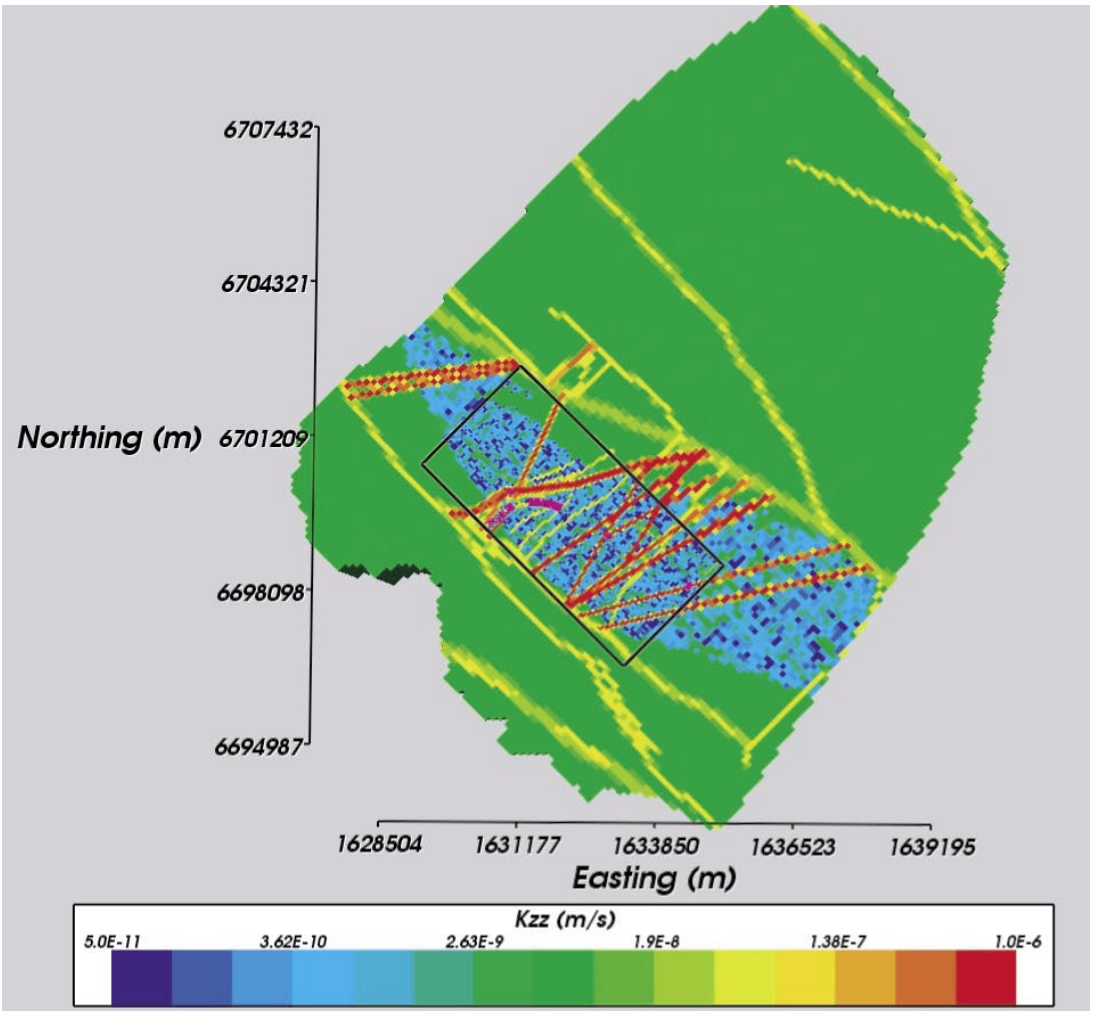

Figure 5-5. *Vertical hydraulic conductivity Kzz (m s^{-1}) showing the representation of the HRD and HCD on the regional-scale 100 m grid and 50 m embedded grid outlined by the black line.*

For all the models described in the remainder of this report the same 50 m embedded grid was used to give accurate results. At the interface between the two levels of refinement, internal boundary conditions are imposed to ensure continuity of variables (pressure and reference water fractions) and conservation of mass and reference water flux /11/. The improved refinement clearly gives a better representation of both the DZs and the heterogeneity of the HRD between them in the key areas of the Forsmark local-scale area.

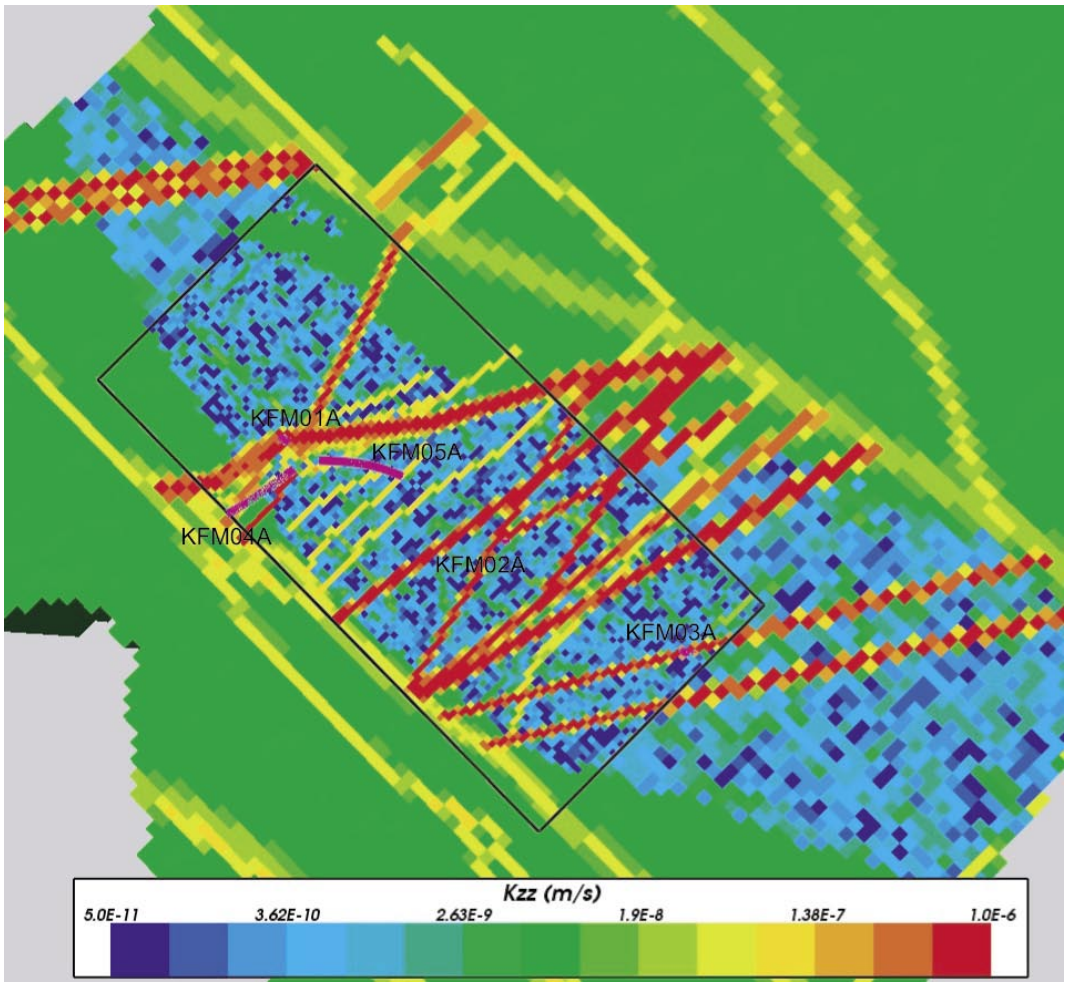

Figure 5-6. *Close-up of vertical hydraulic conductivity Kzz (m s^{-1}) showing the representation of the HRD and HCD on the regional-scale 100 m grid and 50 m embedded grid outlined by the black line. Borehole locations are shown in purple.*

5.6 Initial and boundary conditions

The boundary conditions definition has to represent the transient processes of shore displacement due to post-glacial rebound and the variations in the salinity of the Baltic Sea. The evolution of these two quantities over the post-glacial period is shown in Figure 5-7 and Figure 5-8. The shoreline displacement for F1.2 is very similar to F1.1, except between 8,000 BC to 6,000 BC when the land is about 5 m lower for F1.2. For the salinity, the main difference that the maximum marine salinity is reached later around 4,500 BC rather than 6,000 BC for F1.1. The general modelling approach was to hold the model domain fixed (i.e. same x, y and z coordinates), but modify the head and salinity on the top surface in time. The land-rise is fairly constant over the time period considered, although it is initially greater for about the first thousand years until 7,000 BC. The maximum current elevation in the regional-scale model is about 26 m, so the area has only emerged from sea in the last 3,000 years Salinity rises gradually at the start of the Littorina period about 7,500 BC, reaches a maximum at 4,500 BC, and then gradually starts to reduce toward modern salinity levels from 3,000 BC. It is also important to have a more general hypothesis of the evolution of surface and sub-surface reference waters. The current understanding of the evolution of the Forsmark site in the post-glacial period is illustrated in Figure 5-9. The simulations start during Phase c when the area is covered by the Ancylus Lake, which is

a mixture of glacial melt water and meteoric water. This is followed by the Littorina Sea Phase d, whose salinity gradually decreases, and eventually the land emerges from the sea and so becomes exposed to infiltration of modern meteoric water.

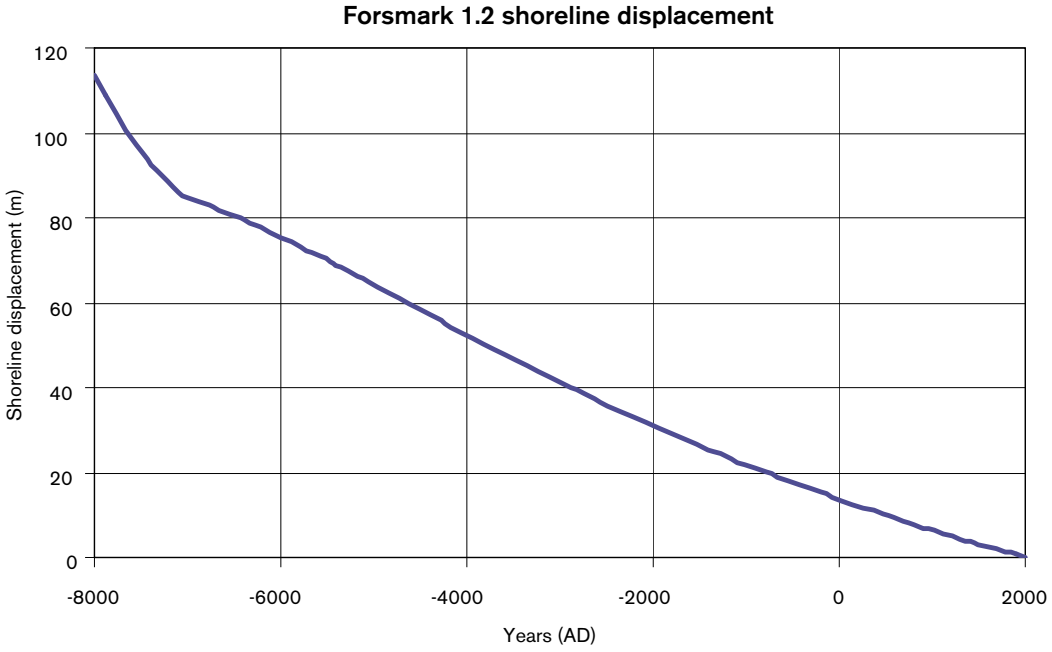

Figure 5-7. *The shoreline displacement at Forsmark Version 1.2 relative to the current sea-level for the time period considered in the simulations.*

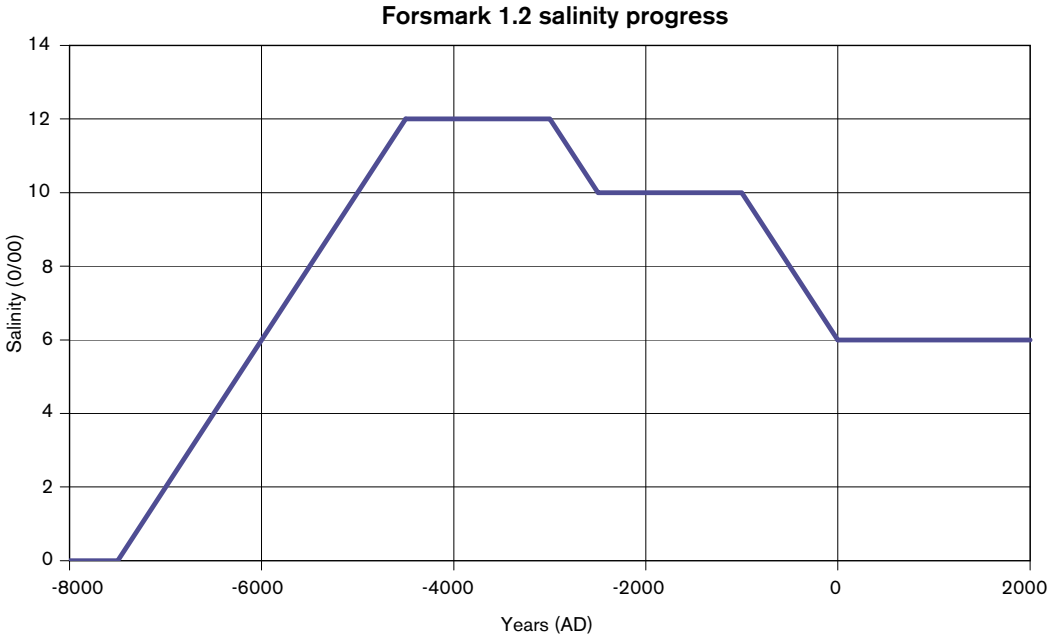

Figure 5-8. *The salinity progress in the Baltic Sea at Forsmark Version 1.2 for the time period considered in the simulations.*

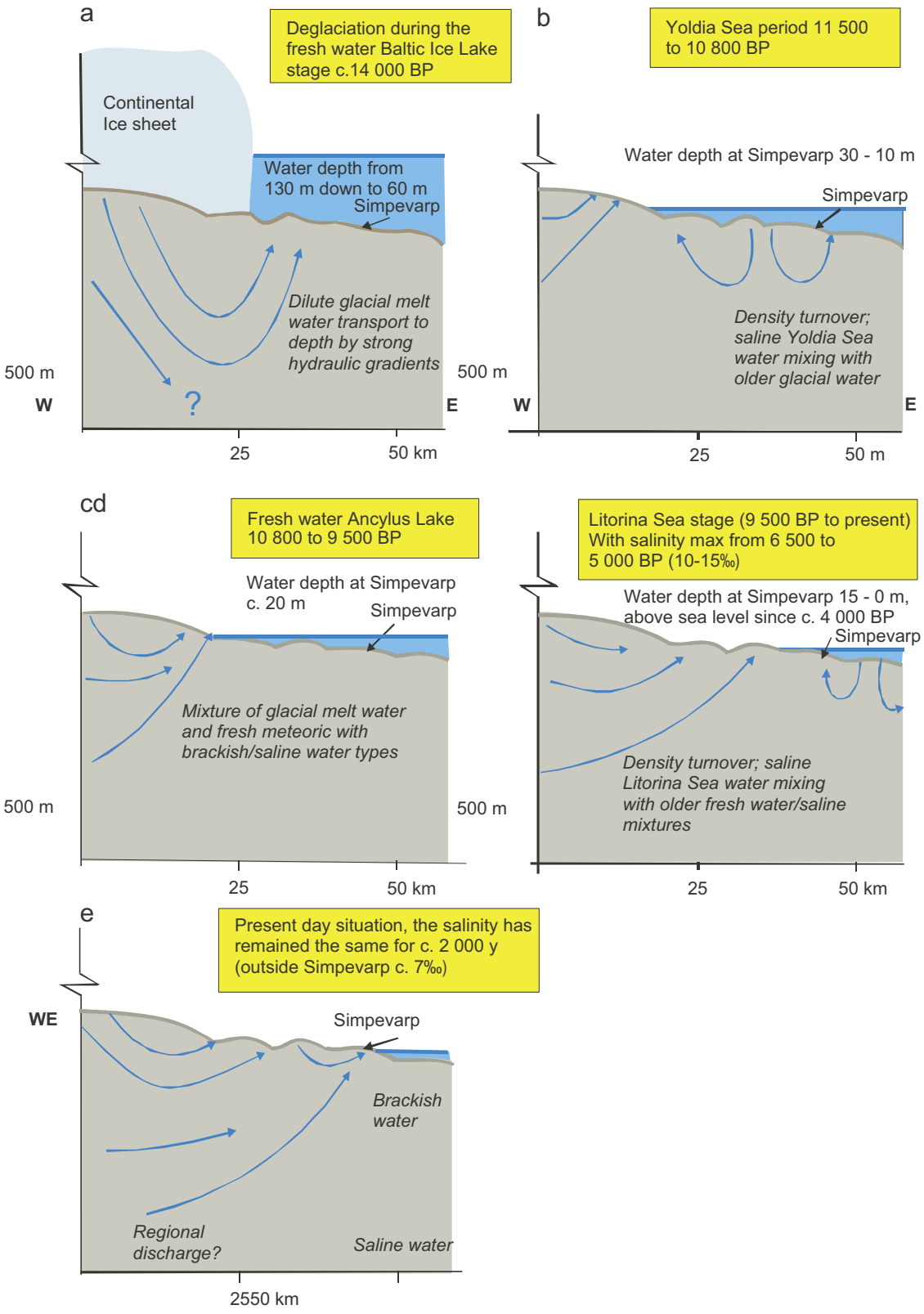

Figure 5-9. *Hydro-geochemistry scenario for evolution of reference water transport from 14,000 BP to present-day, showing 5 distinct phases. The simulations begin during phase c (Fresh water Ancylus Lake).*

For flow, the head on the top surface was set to the topographic height that evolves in time due to changes in the height relative to the shoreline (see Figure 5-7). Offshore, the head was equal to the depth of the sea multiplied by the relative density of the Baltic Sea to freshwater (i.e. $(\rho_{Baltic}-\rho_0)/\rho_0$). A variant that was considered was to use a flux-type boundary condition, as defined in subsection 2.6, with a potential infiltration of 200 mm per year (as specified in the Task Description).

Based on the surface hydro-geochemistry concept shown in Figure 5-9, the definition of reference water boundary conditions was specified according to the following phases:

- Ancylus Ice Lake: Full Glacial.
- Littorina Sea to present-day: Full Rain 1960 onshore; Offshore a mixture of Marine and Rain 1960 reference waters according to the ratio of TDS shown in Figure 5-8 to the TDS of the Marine reference water.

Setting the surface boundary condition to be full Glacial water was based on the modelling performed for S1.2 /15/ where deep boreholes suggested the presence of Glacial water to depths of 1 km and it was found that this could only be reproduced in the model if the Baltic and Ancylus Lakes were predominantly Glacial water. At Forsmark there fewer data at depth to confirm whether it is similar to Simpevarp in this respect, although 40–60% Glacial water has been interpreted at depths of 600 m–1 km in KFM03A, which would seem consistent with Simpevarp at these depths. Realistically, there are insufficient data at depth to confirm whether other scenarios such as 50% Glacial with 50% meteoric in the Ancylus Lake water matches the field data better.

The boundary conditions on the sides are no-flow and zero flux of reference waters. On the bottom of the model at z = –2,300 m, there is a no-flow condition and groundwater is set to pure Brine, i.e. Brine fraction = 1.0, all other fractions = 0.

The initial condition for the reference waters assumes a profile of Brine at depth and Glacial water at the surface, with a start time of 10,000 BP. In early models the initial condition derived in the S1.2 modelling /15/ was adopted that is piecewise linear with full Glacial to –700 m depth, then a gradual rise in Brine to full Brine at –1,500 m depth. This gave reasonable results, but was not entirely consistent with the only deep salinity data in KFM03A. KFM03A has three groups of data points at depth (there are groups of data relating to water samples that have been taken from the same location, but at several different times): one at about –640 m that has a salinity of around 9‰ and low magnesium content suggesting a predominantly Brine origin for the salinity; one at about –940 m that has a salinity of around 14‰ and very low magnesium suggesting the salinity is entirely of a Brine origin, and a similar sample at –990 m with around 16‰ salinity from Brine. Assuming a simple linear profile in Brine, KFM03A suggests Brine starts to occur at about –500 m and rises to about 22% at –1,000 m, which extrapolates to full Brine at about –2,700 m. Because of a reduced transmissivity in the HCD model (see in Section 5.7) at depth the simulated advective flows at depth are small. Together with the tendency toward stagnant flow within the dense Brine, the initial conditions for reference water composition tends to be preserved up to the present-day, and hence the measured hydro-geochemistry at depth is a good guide for choosing initial conditions at 10,000 BP. The ultimate initial condition used in the models reported here has full Glacial to –500 m, and then Brine rises linearly to full Brine at –2,000 m, as illustrated in Figure 5-10. This gradient is perhaps too large and gives an over-prediction of Brine at the base of KFM03A as will be seen later. The initial condition for flow is calculated by holding the reference water fractions instantaneously fixed, and calculating the flow field that represents hydrostatic equilibrium at the initial time of 10,000 BP. Having obtained these initial conditions for reference waters and flow, the simulations are then performed with the evolving situation of land-rise

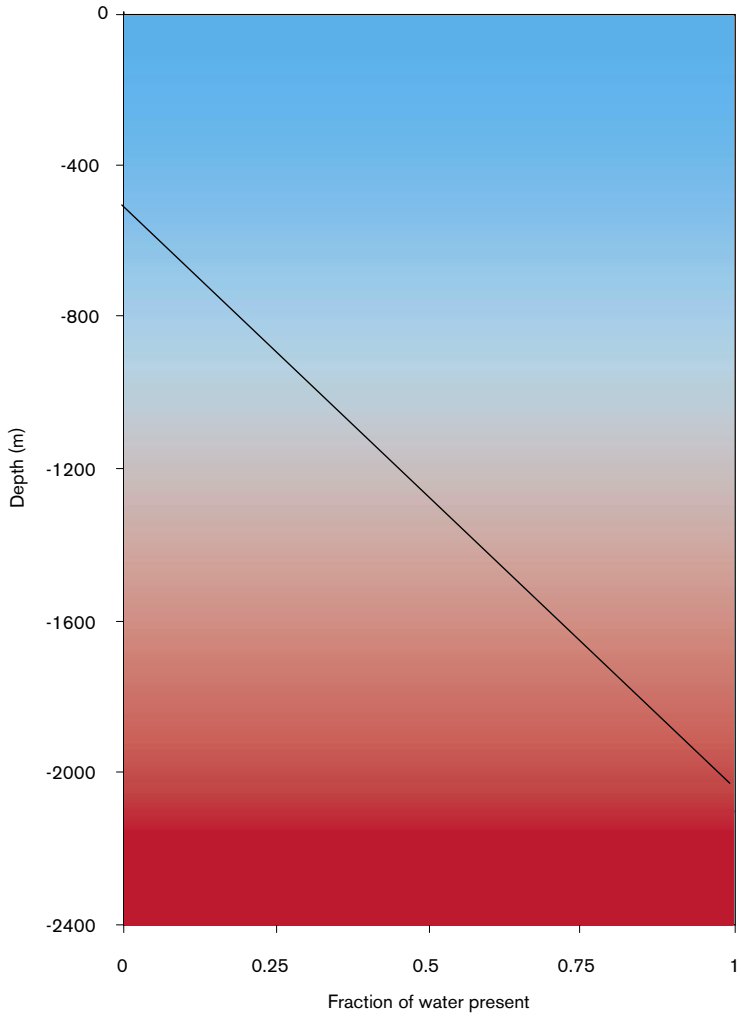

Figure 5-10. *Initial condition for reference water transport, at 10,000 BP. Above –500 m the water is pure Glacial (coloured cyan). There is then a linear transition between Glacial and Brine (coloured red) toward pure Brine below –2,000 m.*

and changes in surface water chemistry. Other initial conditions such as a non-linear rise in Brine at depth (becoming steeper with depth) could be advanced. However, there isn't data to confirm to such sophisticated profiles. Also because flow at depth is limited by not having conductive features extending to depth, as argued in Section 5.7, then it is not expected that profile of Brine below about 1 km will have much effect.

5.7 HCD model

Three alternative DZ geometries were supplied by the Geology Group as follows:

1. **Base Case (BC):** containing only high confidence DZs. This contains many sub-horizontal DZs between the Singö DZ and Eckarfjärden DZ that have been identified by drilling and/or reflection seismic techniques. Also it is assumed that DZs identified in the site area extend no further than the Singö DZ and Eckarfjärden DZ. Only the high confidence lineaments outside of this area are included, see Figure 5-11;
2. **Variant Case (VC):** is similar to the Base Case except a few large sub-horizontal zones are extended beyond the Eckarfjärden DZ, see Figure 5-12;

3. **Alternative Case (AC):** contains the DZs included in the Base Case with the addition of many regional-scale lineaments, based on lineament and comparison studies, that are potential hydraulic conductors but of lower confidence, see Figure 5-13.

The Base Case contains 44 distinct geological DZs, of which 23 are steeply dipping and 21 are gently dipping. The alternative model has an additional 171 DZs, which includes 36 steeply dipping zones DZs between the Singö DZ and Eckarfjärden DZ and 135 steeply dipping DZs outside. The lineaments are all assumed to be vertical. The VC and AC cases, in particular, give an indication of how much effect additional DZs outside of the Singö DZ and Eckarfjärden DZ can have on flow and transport in the local-scale area. One additional aspect considered by the DT Team was the potential effect of supplementing the HCD model with stochastically generated DZS outside of Singö and Eckarfjärden.

As part of the Task Description, an analysis of the measured transmissivity of DZs against the depth of test interval was provided. In this, DZs were categorised according to dip to give a correlation between transmissivity of sub-horizontal DZs:

$T_H = 4.1\ 10^{-4} \exp(-0.0116 \times \text{depth})\ m^2s^{-1}$;

where depth is in metres, and in sub-vertical DZs:

$T_V = 4.6\ 10^{-5} \exp(-0.0174 \times \text{depth})\ m^2s^{-1}$.

The basis of this analysis is shown in Figure 5-14. The coefficients of determination are around 0.7 for both cases in terms of log(T). The data exhibit a clear depth dependency; there are no high transmissivities at depth for example, but there is clearly uncertainty in determining this trend, especially in the top 200 m where values vary over 2–3 orders of magnitude. Therefore, it is worth considering other interpretations such as only considering the more transmissive DZs, which gives the pink line plotted:

$T_H = 7.2\ 10^{-3} \exp(-0.0154 \times \text{depth})\ m^2s^{-1}$.

This would give a more pessimistic case of higher flow rates. Another possibility is to use a stochastic model of fracture transmissivity:

$T_V = 10\text{^}\{\log[4.6\ 10^{-5} \exp(-0.0174 \times \text{depth})] + [1.2 \times (1 - \text{depth}/2{,}100)] \times N(0,1)\}\ m^2s^{-1}$,

where N(0,1) is a normally distributed random deviate with mean zero and standard deviation 1.0. Note the stochastic component decreases with depth due to less variability in the data (see Figure 5-14). Neither of these latter proposals was incorporated in the current CONNECTFLOW modelling due to time constraints, but should perhaps be considered for the SR-Can Assessment.

The basic depth trends above were used in the modelling such that gently dipping DZs between the Singö DZ and Eckarfjärden DZ transmissivities were set according to the depth trend for T_H; for steeply dipping DZs transmissivities were set according to the depth trend for T_H. Figure 5-11 to Figure 5-13 show example of this property assignment. This case was denoted property assignment **HCD1**. The case with stochastic variation (not implemented here) was denoted **HCD2**. It is important to note that by using these general trends then the transmissivity of particular borehole test intervals that intersect a DZ will not be equal to the measured value for the interval, and therefore the model will not be conditioned to the actual test interval data in the boreholes. During the calibration process this was found to be a significant problem as it was difficult to match both the hydraulic conductivity and hydro-geochemistry measurements without conditioning particular DZs to their measured values. The DZs whose properties were modified away from the basic trend are listed in Table 5-2. This locally conditioned deterministic case was denoted **HCD3**.

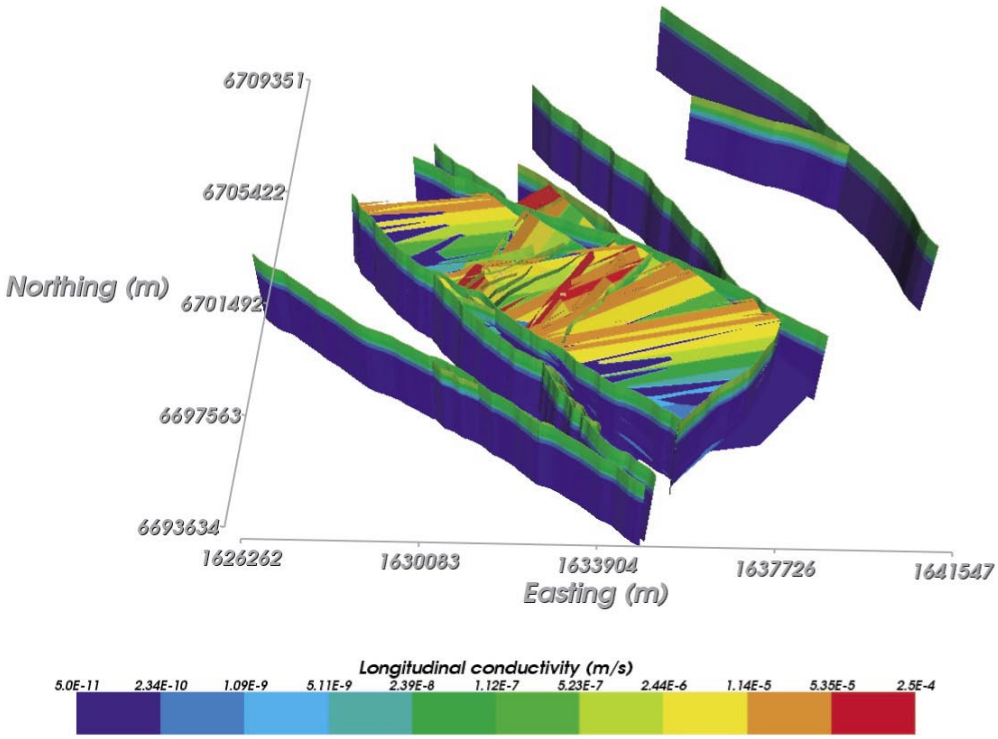

Figure 5-11. *Base Case (BC) HCD model that only includes high confidence zones. DZs are coloured by hydraulic conductivity, which shows the depth dependency of properties.*

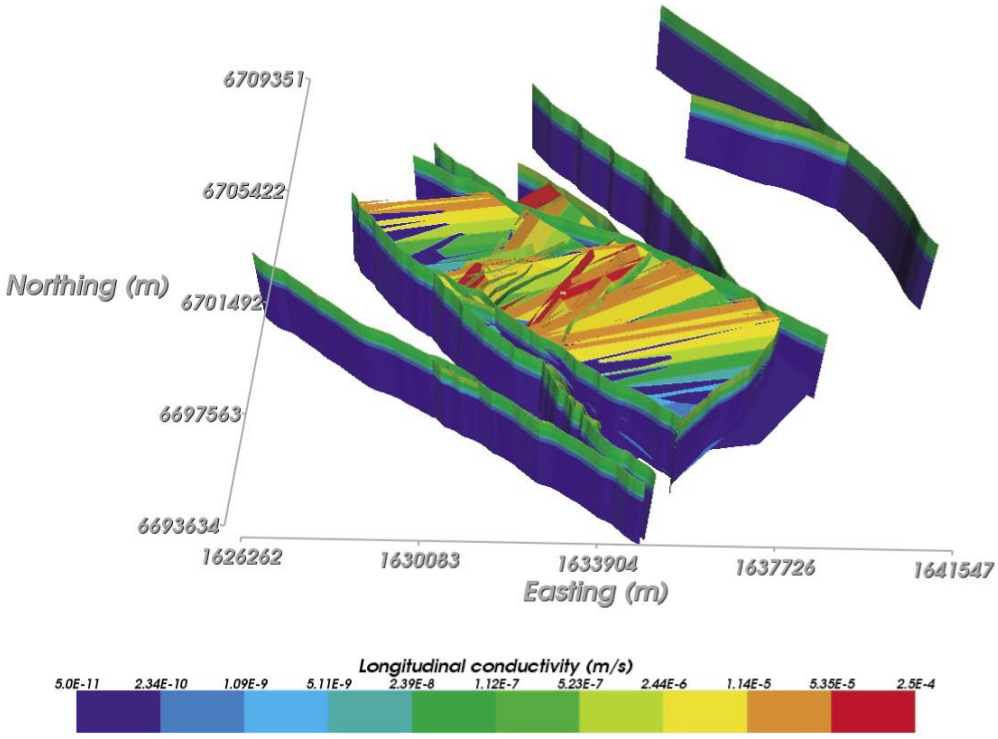

Figure 5-12. *Variant Case (VC) HCD model, which extends some large sub-horizontal DZs. DZs are coloured by hydraulic conductivity, which shows the depth dependency of properties.*

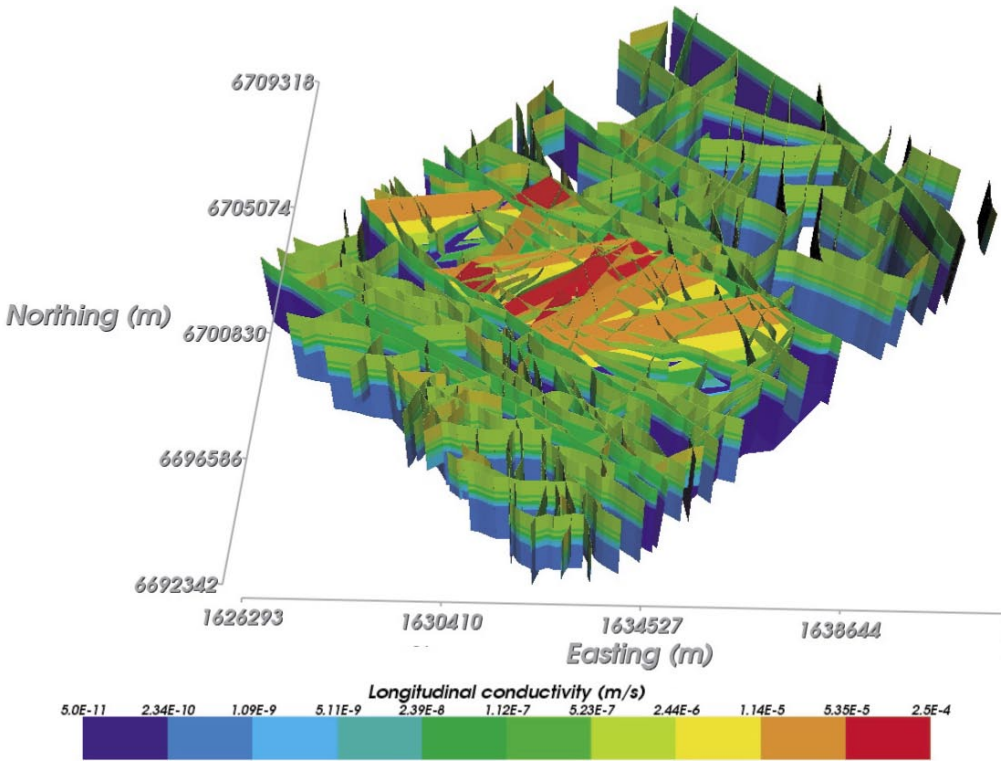

Figure 5-13. *Alternative Case (AC) HCD model, which includes many additional regional-scale lineaments that are of lower confidence. DZs are coloured by hydraulic conductivity, which shows the depth dependency of properties.*

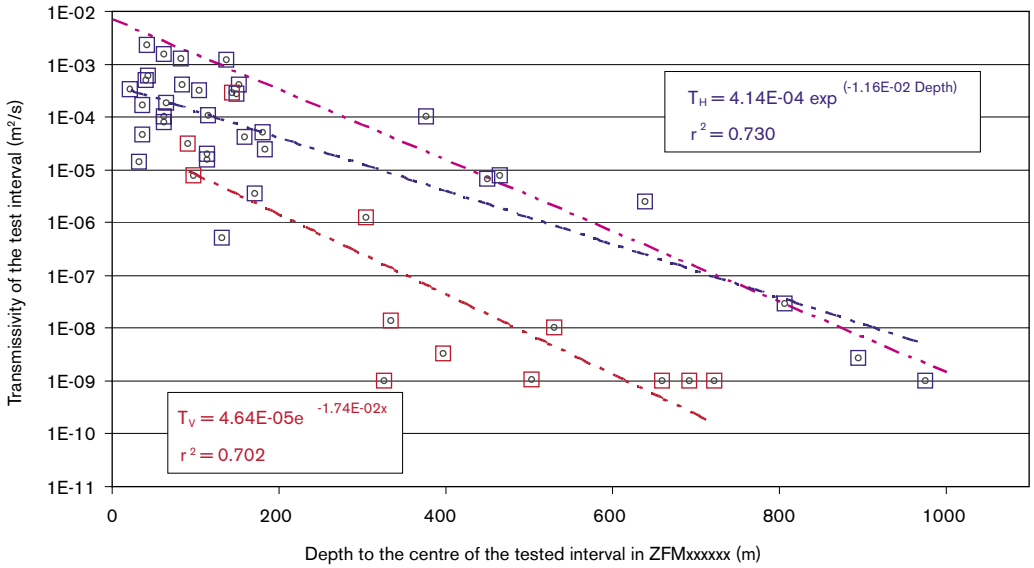

Figure 5-14. *Analysis of depth dependency of DZ transmissivity for gently dipping DZs (T_H and blue squares) and steeply dipping DZs (T_V and red squares). The trendlines and best least squares linear fit formulae are shown in the legends. A pink trendline is added to shown an alternative fit to the high T gently dipping DZs.*

Table 5-2. Hydraulic properties modified from overall trend based on hydraulic tests in the HCDs.

DZ-ID	Borehole measurement	Hydraulic thickness, b_{hyd} (m)	Transmissivity, T (m^2 s^{-1})
ZFMNE00A2	KFM01A, KFM02A, KFM04A, KFM05A	65	Min ($10T_H$, 10^{-3})
ZFMNE00A3	KFM02A, KFM03A	13	Min ($10T_H$, 10^{-3})
ZFMNE00A4	KFM03A	25	Min ($100T_H$, 10^{-3})
ZFMNE00B1	KFM03A	7	Min ($10T_H$, 10^{-3})
ZFMNE1188	KFM04A	1.5	Min ($10T_H$, 10^{-3})

Similar general formulae were used for assigning the hydraulic thickness, b_{hyd}, and effective fracture kinematic porosity for the zone ($n_e = 0.5\ T^{0.5}/b_{hyd}$). It is also stipulated that all DZs should be in hydraulic contact with the overburden (the modelled HSD).

5.8 HRD and DFN model

Due to the spatial variability in the derivation of DFN properties described in Section 3, and hence uncertainties in extrapolating the DFN model over the regional-scale, the treatment of HRD properties started with a simple homogeneous models and then gradually developed to include more sophisticated concepts such as DFN derived properties for Rock Domains RFM017 and RFM029. This strategy was adopted in order to develop the HRD initially with simple models and few parameters to gradually quantify parameter sensitivities prior to incorporating more complexity such as stochastic DFN models and dependence on rock domain. Three stages were considered:

- **HRD1:** the rock mass within the entire regional model domain is simulated with a fixed background conductivity in the range $5\ 10^{-11}$ m s^{-1} to $5\ 10^{-10}$ m s^{-1}. The purpose here is to do a simple sensitivity analysis to bulk properties for a simple homogeneous CPM model;
- **HRD2:** the rock mass outside RFM017/029 is simulated with elevated background conductivity about 10 times higher than the conductivity within RFM017/029. The purpose here is to do a simple sensitivity analysis to bulk properties for a simple heterogeneous CPM model;
- **HRD3:** the rock mass of the entire model domain is simulated as a heterogeneous DFN consisting of five fracture sets according to the Geo-DFN. This is a more sophisticated model that incorporates the details of the Hydro-DFN developed in Section 3 and Section 4.

Table 5-3. Hydraulic and transport properties used in the HRD1 case.

Property	Value	Comment
Block-scale hydraulic conductivity	$5\ 10^{-11}$–$5\ 10^{-10}$	Based on Table 4-1 and PSS 100 m intervals
Block-scale fracture kinematic porosity n_e	$1\ 10^{-4}$ z > –20 m $1\ 10^{-5}$ z < –20 m	Based on Table 4-3
Matrix porosity n_m	$4\ 10^{-3}$	2.8–6.6 10^{-3} for RFM017/029
Dispersion lengths	a_l = 40 m, a_t = 5 m	Minimal values for grid size
Flow wetted surface area per unit volume a_r (m^2 m^{-3})	~ 1.0 m^2/m^3	Based on $2*P32_c$
Intrinsic diffusivity, D_i (m^2 s^{-1})	$5\ 10^{-13}$	

For HRD1 the range of values considered, $5\ 10^{-11}$ m s^{-1} to $5\ 10^{-10}$ m s^{-1}, was chosen based partly on the PSS data for 100 m intervals away from deformation zones, and also because it is consistent with the range of 25-percentile to 50-percentile of 100 m block-scale conductivity calculated in Table 4-1 for Volume E (KFM03A). The hydraulic and transport parameters for this case are given in Table 5-3.

For HRD2 the original specification required that a higher hydraulic conductivity of about 10 times that used in RFM017/029 be used outside these rock domains. An alternative approach used data from investigations at Finnsjön /17/ as an analogue. This was based on 3 m test data and gave values in the approximate range $2\ 10^{-9}$–$1\ 10^{-7}$ m s^{-1} for the background rock with highest values in the top 100 m. The hydraulic conductivity considered here to analyse sensitivities were $5\ 10^{-9}$ and $3\ 10^{-8}$ m s^{-1}. The top 100 m was set to $1\ 10^{-7}$ m s^{-1}. This range is also consistent with values from wells drilled to about 100 m or more in the Forsmark and Östhammar area /23/. All other parameters remained homogeneous.

For HRD3 the concept was to generate stochastic realisations of DFN model on the regional-scale based on the Hydro-DFN with variants as described in Section B.4 of Appendix B and subsection 3.7, and using the upscaling method defined in subsection 2.3 to obtain EPM properties. Only the local-scale area composed of rock domains RFM017/029 are modelled by a DFN model, the rest of the regional model is treated as a homogeneous CPM as in HRD2. This is simply because there are few fracture data from outside the tectonic lens with which to parameterise a DFN in this region, although a section of borehole KFM04A suggests higher fracture intensity outside the tectonic lens. For RFM017/029 the conceptual DFN model proposed in Figure 3-6 is simplified for this study to use uniform statistics over the whole the rock domain based on Volume E, and hence spatial variations of EPM properties in the tectonic lens only occur due to the stochastic nature of the DFN parameters. It was not possible to consider a multi-faceted EPM model based on the domain sub-divisions shown in Figure 3-6 within the timescale of this project. However, the DarcyTools Team have considered a similar multi-faceted CPM model, and multi-faceted DFN and EPM models will be assessed as part of the SR-Can Safety Assessment F1.2.

Figure 5-15 shows the different areas in the F1.2 relating to different rock domains and grid refinement. In the local-scale area the element-size was 50 m compared to 100 m everywhere else. Based on the findings of block-scale upscaling in Section 4, L_{min} (the minimum fracture length sampled) should ideally be no more than one quarter the element size. This motivated using L_{min} = 25 m. In fact, a statistically uniform DFN model was constructed for the whole regional-domain and upscaled to give EPM properties. However, only the properties within rock domains RFM017/029 were used. One realisation of the regional-scale DFN model is shown in Figure 5-16 as the full 3D model in map view, and as a horizontal cross-section at z = –500 m (i.e. a trace map) in Figure 5-17. The equivalent plot with the deterministic Base Case HCD model superimposed is shown in Figure 5-18.

As an illustration of how the DFN fits onto the EPM grid, Figure 5-19 shows a close-up map view of a slice through the DFN and finite-element grid. The finite-elements are cubes, but the visualisation tool draws a slice through them as 2 triangles. It can be seen that some elements are not cut by a fracture (at least in this 2D view), some have several fractures and some larger stochastic fractures cut many elements. This is all due to the stochastic nature of the DFN model. Where an element does not contain a connected network a zero EPM hydraulic conductivity will be calculated. This may be realistic, or it may simply result from imposing a fracture length truncation Lmin. Either way zero conductivity would lead to numerical problems, so we have to ensure no cell has a value less than some minimum. A value $5\ 10^{-11}$ m s^{-1} was used as the minimum hydraulic conductivity based on values around the 10–25 percentiles in Table 4-1.

The value of flow wetted surface area per unit volume, a_r, was initially set to 1 m^2/m^3 base on 0.5 m^2/m^3 being a representative P32 value for a connected network (after removal of isolated fractures and clusters). As a variant a_r = 0.25 m^2/m^3 was considered to scope a case with poorer access to the matrix. This value is of interest since it is around the transition from a situation where the reference water mixture is the same in the fracture and matrix systems (around a_r = 1.0) on the timescales of interest, and where they are different. The sensitivity to a_r will be considered further in the SR-Can Assessment calculations.

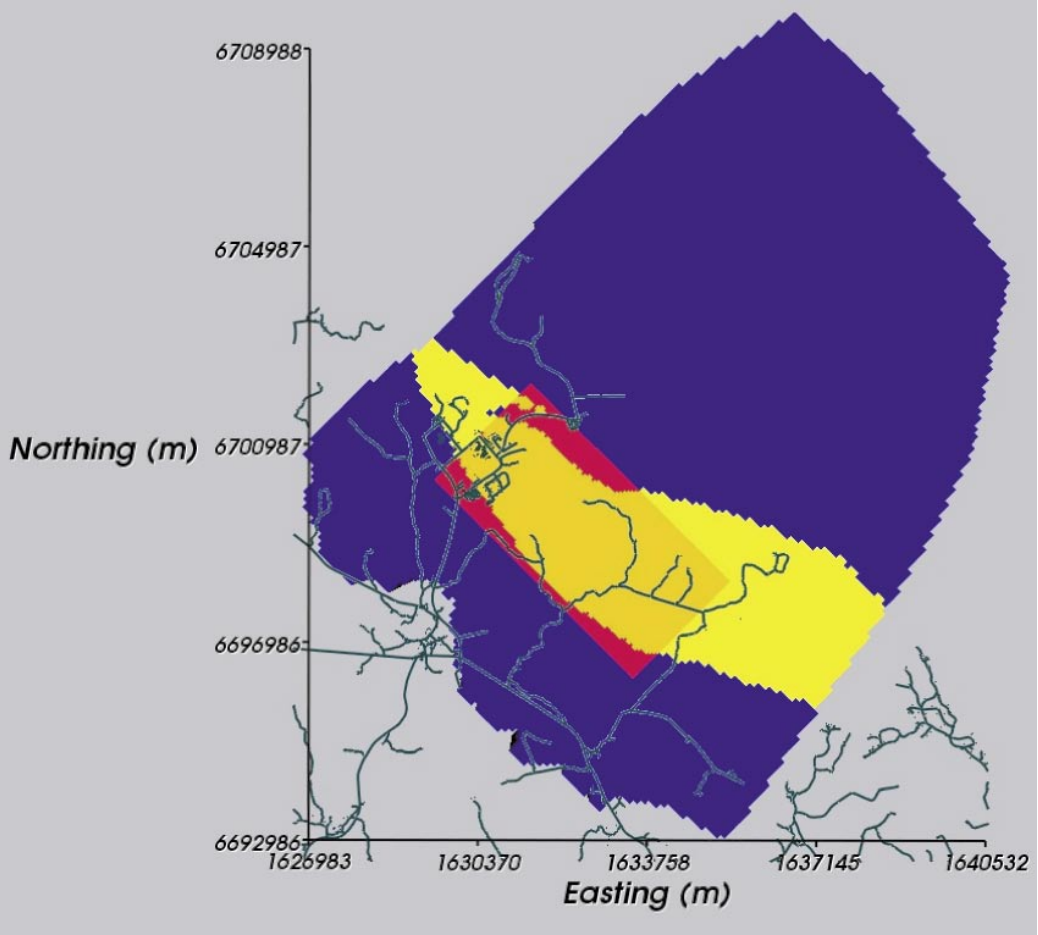

Figure 5-15. *Model areas in regional-scale model. The refined local-scale area (red and orange) used a grid size of 50 m. Outside of that a grid size of 100 m was used in the regional-scale (blue and yellow). EPM properties were used based on an underlying DFN model in the tectonic lens: rock domains RFM017/029 (yellow and orange). Homogeneous CPM properties were used in the remaining domain (blue and red). Roads are superimposed in black.*

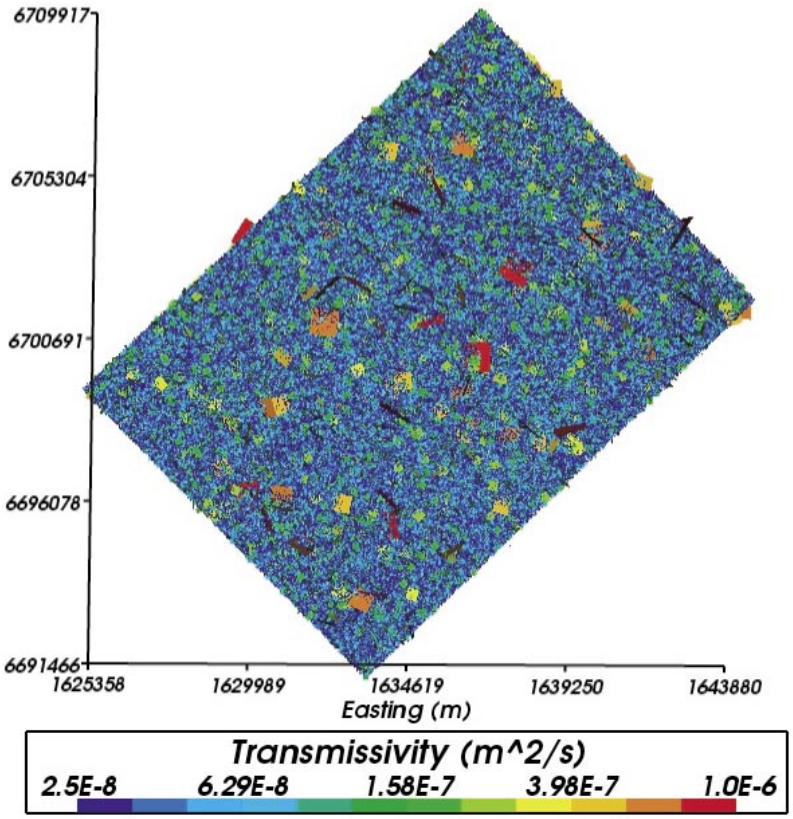

Figure 5-16. *Regional-scale DFN model showing all stochastic fractures (in 3D) coloured by log(transmissivity).*

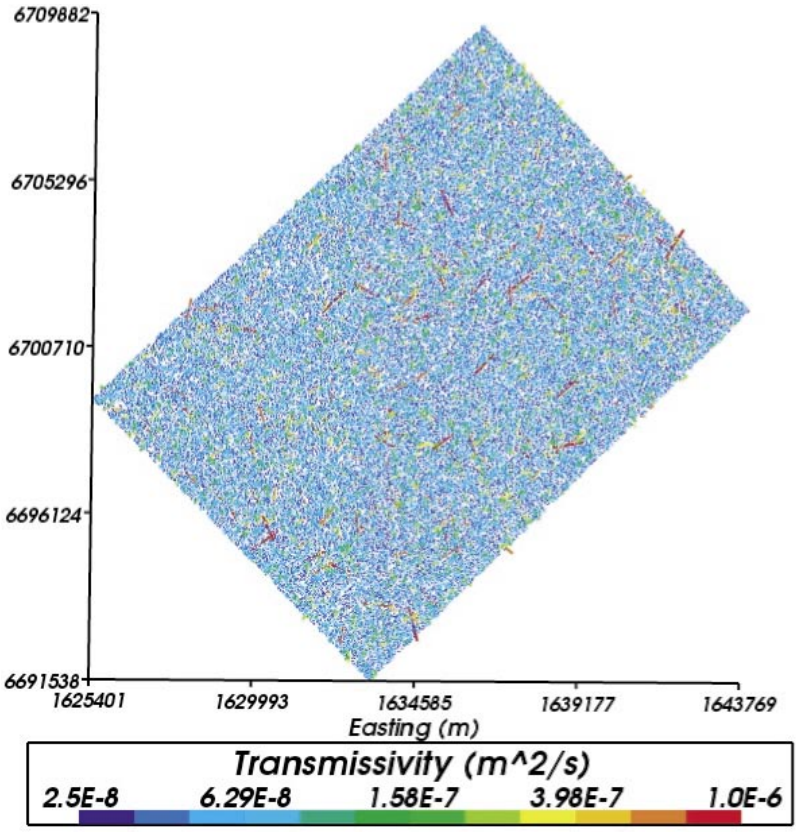

Figure 5-17. *Regional-scale DFN model showing stochastic fractures cutting a horizontal slice at z = –400 m coloured by log(transmissivity).*

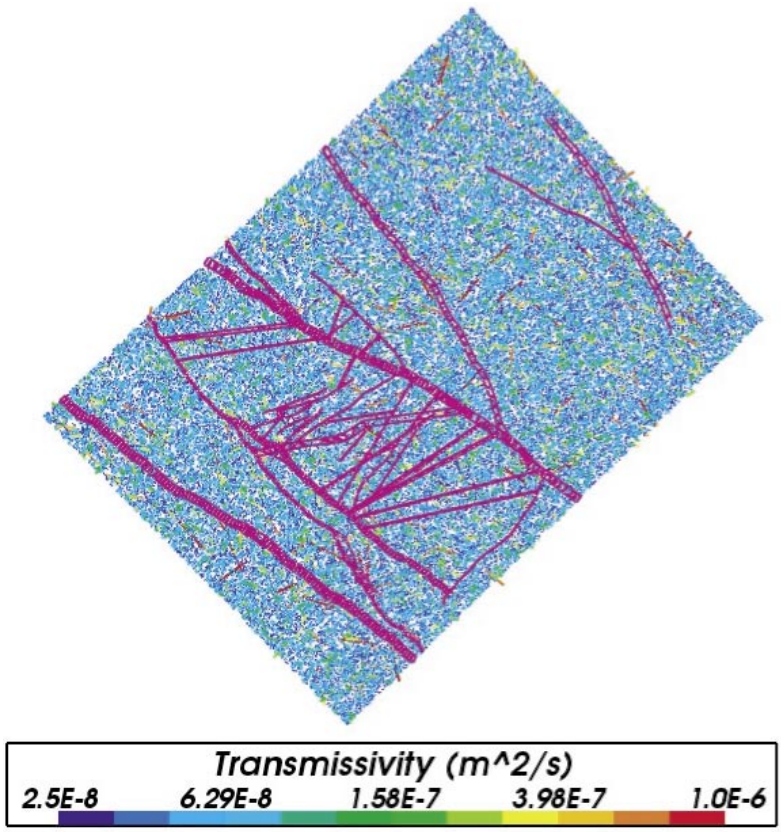

Figure 5-18. *Regional-scale DFN model showing stochastic fractures cutting a horizontal slice at z = –400 m coloured by log(transmissivity) and the BC geological model superimposed (purple).*

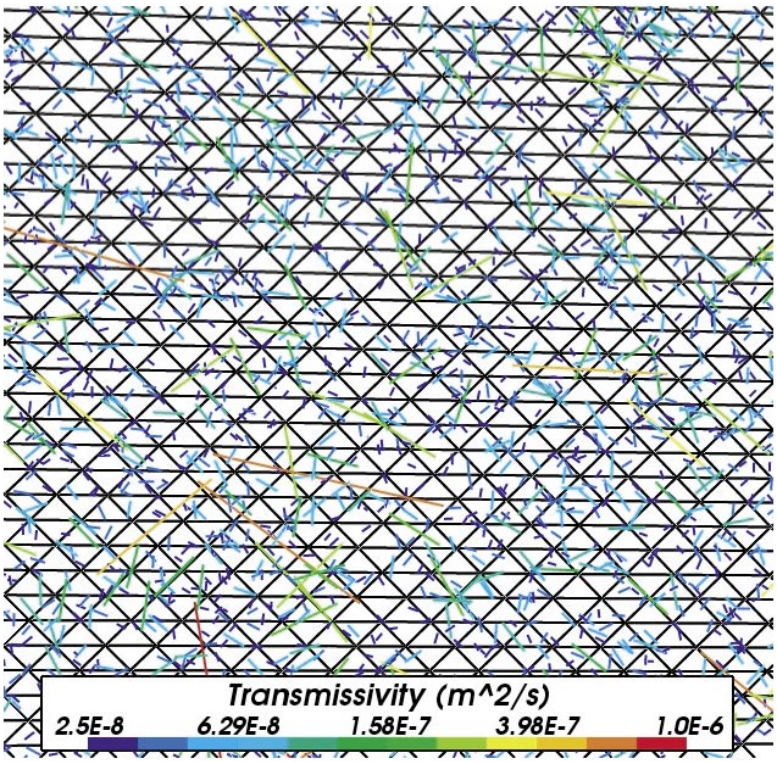

Figure 5-19. *A part of the DFN model as shown on a slice through the fractures coloured by log(transmissivity) and the 100 m finite-element grid (coloured black and each element drawn as 2 triangles).*

In order to perform sensitivity tests on the DFN input, several DFN models were created according to the cases parameterised in subsection 4.4. These are listed in Table 5-4 with names that denote the interpretation used in deriving the DFN, the transmissivity model used, and the realisation number. An example of the hydraulic conductivity used in the HRD3 model for the Base Case DFN is shown in Figure 5-5 and Figure 5-6.

In all cases, the transport aperture was calculated using $e_t = aT^b$, a = 0.5, b = 0.5, based on Reference /14/. The kinematic porosity, n_e, for a block was then calculated as the sum of products of fracture area within the block and the transport aperture, and then divided by the volume of the block. Figure 5-20 shows the block-scale kinematic porosity at the top of the HRD model (10 m below surface) and at z = –400 m. The HCD model gives kinematic porosities that decrease continuously with depth while in the HRD model the values are constant below 20 m from ground surface. At both depths the HCD model stands out as areas of relatively high kinematic porosity.

For the simulations of transient groundwater flow and reference water transport a flow-wetted surface is required for the coefficient ζ in the RMD process described in subsection 5.3. For simplicity this was set to a constant value for the whole domain (1.0 m^2m^{-3} in the Base Case). An alternative is to define the flow-wetted surface based on the DFN model as twice P32. Strictly, this should be the P32 of the connected network of fractures in which advective flow takes place. This is what is shown in Figure 5-21, although it is based on the regional DFN with a length truncation of L_{min} = 25 m and hence probably represents a low estimate. Typically values are around 0.1 m^2m^{-3} although some elements have values as low as 0.01 m^2m^{-3}. In the DZs the flow-wetted surface was equal to that specified in HRD outside of RFM017/029. The flow-wetted surface is a key transport parameter in this modelling not only because it affects RMD, but also because it is used in calculating the F-quotient along flow-paths, and hence it is important to investigate the possible ways of assigning this parameter. The approach taken was to test values of a_r = 1.0 m^2m^{-3} and 0.25 m^2m^{-3} as a variant in the reference water transport equations to quantify sensitivities in a simple way, but to use values based on the DFN for calculating the F-quotient in the flow-path analysis so as be conservative.

Table 5-4. DFN variants and their parameters. The Base Case DFN model is HRD3EC. For the other cases the differences from the Base Case are underlined.

DFN Case	Fracture model	Seed	L_{min}
HRD3EC	Volume E (KFM03A)	101	25 m
	Correlated T/L		
HRD3EU	Volume E (KFM03A)	101	25 m
	Uncorrelated T/L		
HRD3EC2	Volume E (KFM03A)	201	25 m
	Correlated T/L		
HRD3EC3	Volume E (KFM03A)	301	25 m
	Correlated T/L		
HRD3SFC	Volume E (KFM03A)	101	25 m
	Variant Geo-DFN		
	Correlated T/L		
HRD3SFU	Volume E (KFM03A)	101	25 m
	Variant Geo-DFN		
	Uncorrelated T/L		

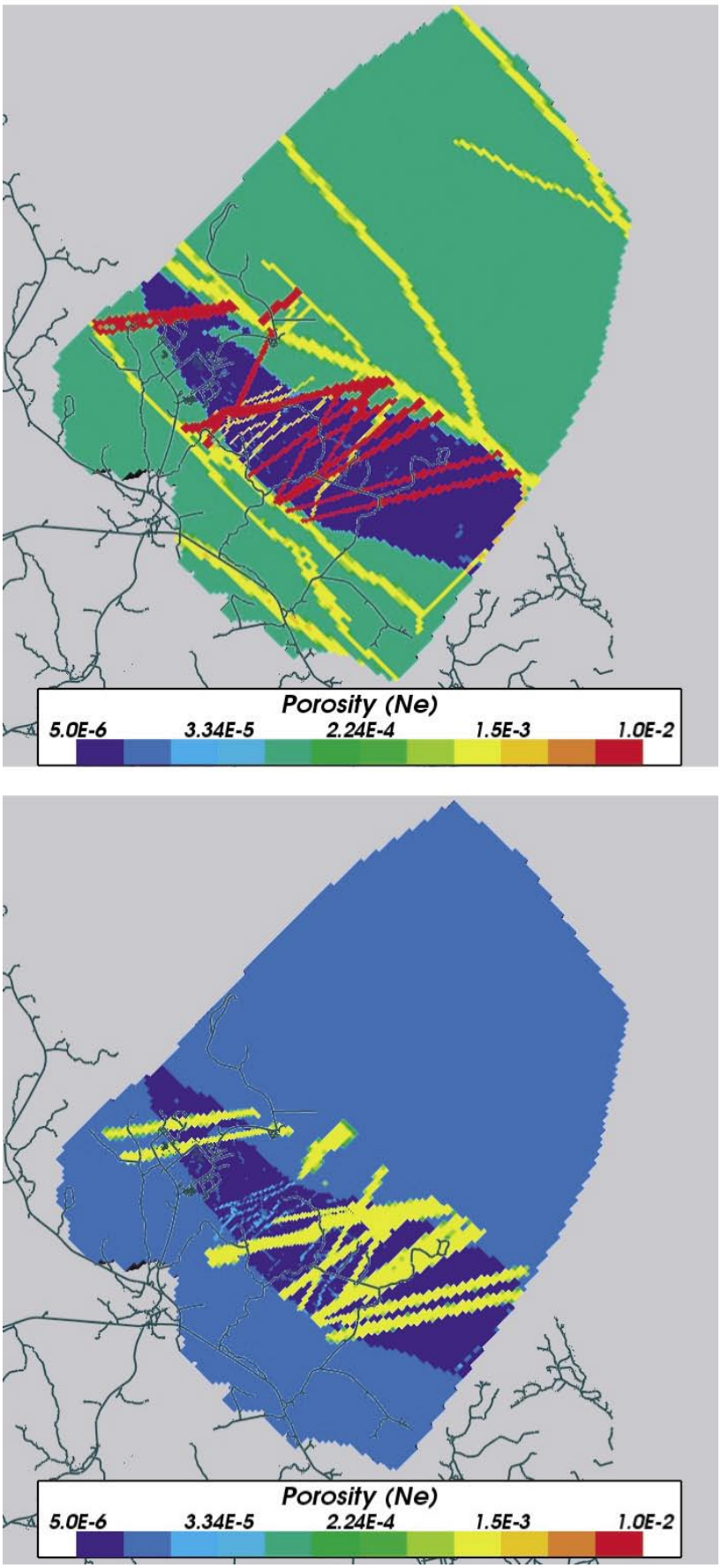

Figure 5-20. *The block-scale kinematic porosity in the Base Case model at z = –10 m (top) and z = –400 m (bottom). Roads are superimposed in black.*

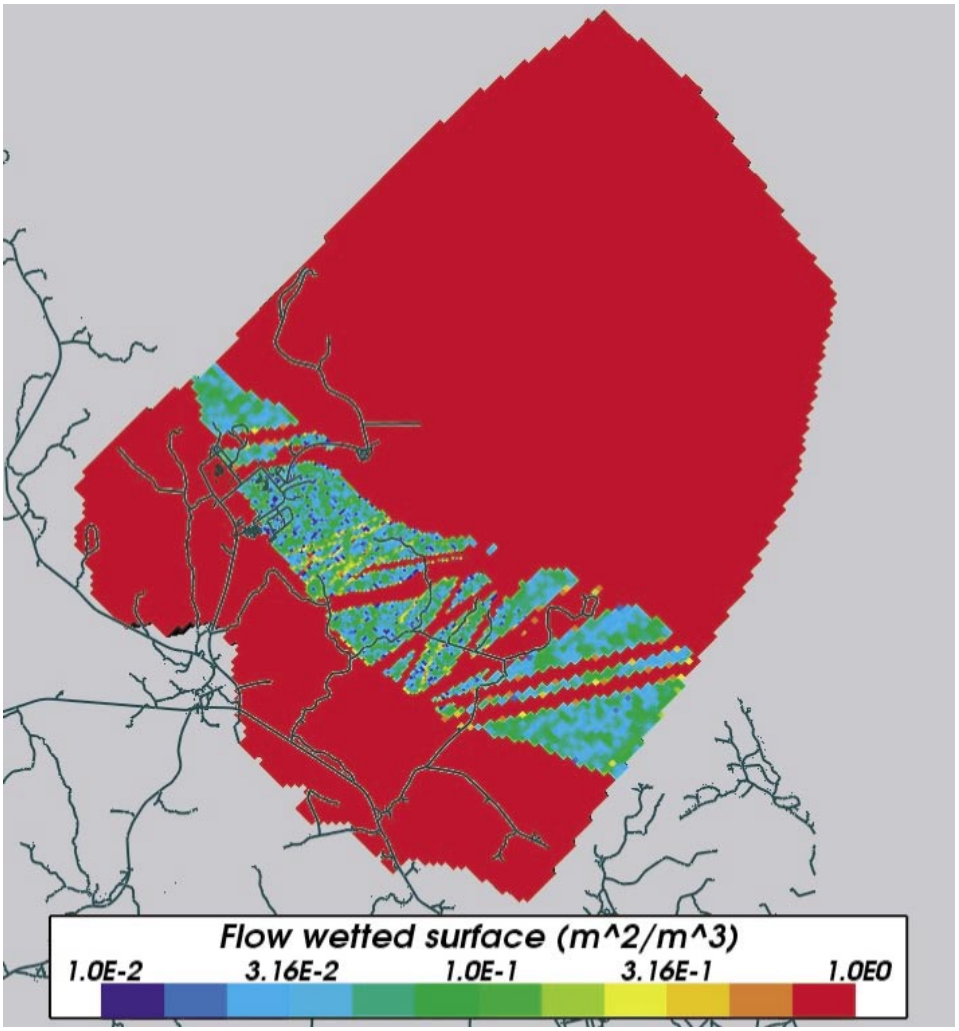

Figure 5-21. *The block-scale flow wetted surface a_r used in the flow-path calculations for the Base Case model at z = –400 m. Roads are superimposed in black.*

5.9 HSD model

The overburden in the Forsmark area is dominated by sandy till, but in raised areas or on small islands the thickness of the till is small or the rock is out-cropping. In small parts of the area, eskers with coarse grained material are found. It is assumed in this Forsmark 1.2 modelling that the majority of the area is covered by a 4 m thick sandy till with small discrete areas where the bedrock outcrops. The definition of the HSD model is summarised in Table 5-5. The surface properties are represented explicitly in the model as three very thin layers of finite-elements of thickness 1 m, 2 m and 1 m from the top. Properties are assigned to each element according to whether the element is predominantly covered by superficial deposits or outcrop to give the distribution shown in Figure 5-22. The outcrop map was provided on a 10 m resolution. In the Base Case homogeneous properties were used, HSD1, away from the outcrop. A variant, HSD2, was considered with a 2 m layer of less conductive fine grained till between two coarser grained layers. Rock matrix diffusion (RMD) was neglected for transport in these surface layers.

Table 5-5. Surface hydraulic domains and properties.

HSD case	Geological description	Hydraulic thickness (m)	Hydraulic conductivity (m s^{-1})	Kinematic porosity (–)
HSD1	Sandy till , near surface	4	$7.5\ 10^{-6}$	$5\ 10^{-2}$
HSD2	Coarser grained till	1	$1.5\ 10^{-5}$	$5\ 10^{-2}$
	Finer grained till	2	$1.5\ 10^{-6}$	
	Coarser grained till	1	$1.5\ 10^{-5}$	
HSDOC	Outcrop	4	$1.0\ 10^{-7}$	$1\ 10^{-4}$

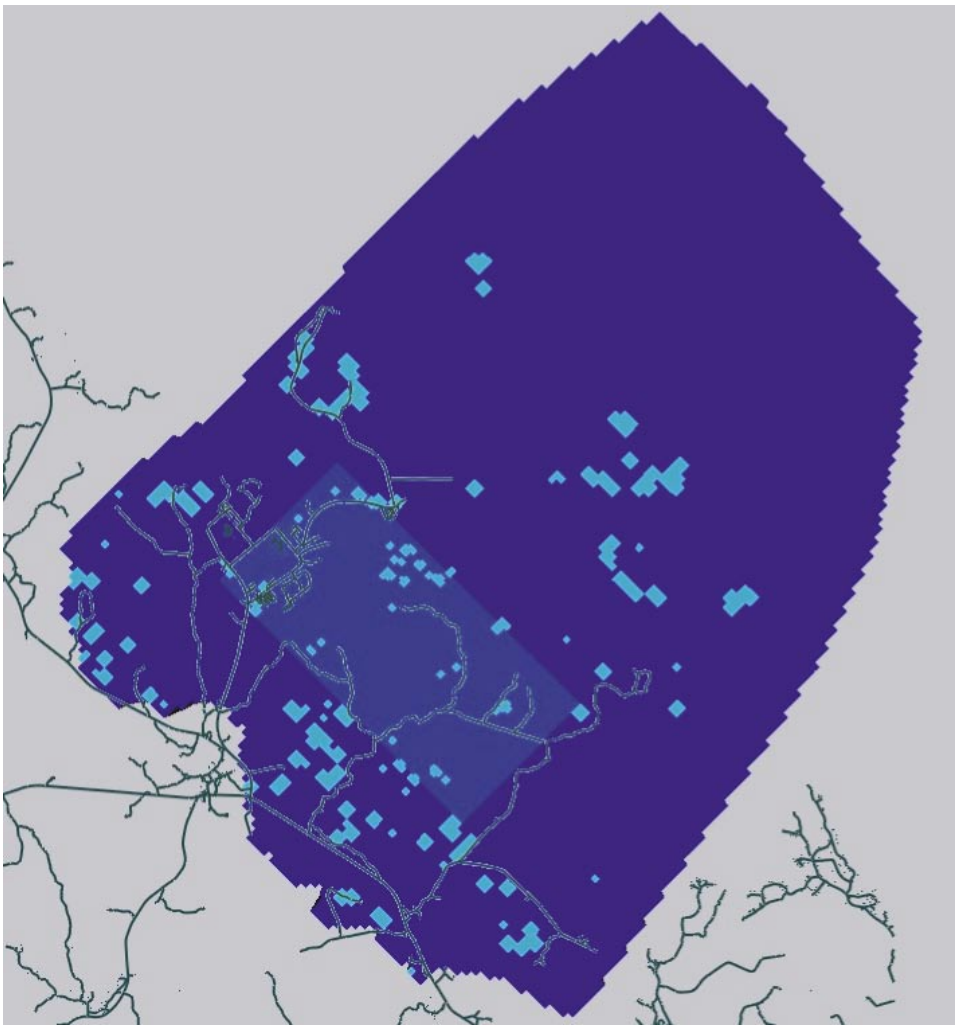

Figure 5-22. *Distribution of surface properties. Areas covered with superficial deposits are shown in dark blue, outcrop areas are shown in cyan. Roads are superimposed in black.*

5.10 Tritium migration model

The calculations of tritium migration were carried out by extending the models developed for simulating groundwater flow and reference water transport.

5.10.1 Period modelled

Tritium is formed naturally by cosmic rays in the upper atmosphere. The atomic bomb tests in the 1950's, 60's and 70's also produced large amounts of tritium, leading to much higher atmospheric concentrations than the natural background. There is a detailed record of atmospheric concentrations measured at Ottawa (see Figure 5-23). From this plot it appears that background levels of tritium are around 15 Tritium Units (TU). The bomb tests led to tritium levels that at their peak were about 100 times greater than this. Records for other locations are less detailed. However, the available measurements for locations in Sweden appear to be consistent with the measurements at Ottawa /18/, although some variation between locations might be expected, particularly for the bomb-test tritium.

Tritium is removed from the atmosphere in precipitation, and then enters the groundwater flow system. Tritium has a very short half-life (12.34 years), and hence tritium that entered the groundwater flow system more than fifty years ago will have been reduced in level by more than an order of magnitude (about a factor 16), and tritium that entered the groundwater flow system in precipitation more than a hundred years ago would have been reduced in level by more than two orders of magnitude (about a factor 256). Given the atmospheric concentrations shown in Figure 5-23, it is therefore really only necessary to consider migration of tritium since the 1950's. The natural background of tritium in precipitation prior to the bomb tests will now contribute less than 1 TU to the current groundwater concentrations, and so can be neglected. However, in order to facilitate a comparison of the levels of tritium in groundwater due to the bomb-test tritium with the levels due to the natural background, the calculations of tritium migration were carried out for a period of 120 years (about ten tritium half lives) starting from 1,890 AD. The results of the calculations therefore effectively provide results for an initial 60 year period with natural background levels of tritium in precipitation, and a 60 year period with the bomb-test tritium as well. (Carrying out the calculations in this way also ensured that the initial conditions for the calculations with the bomb-test tritium included are realistic, although this is not strictly necessary, for the reason discussed above.) It should be noted that the final time for the calculations is 2,005 AD, due to practical reasons relating to the range of time-steps considered. The final concentrations in the model will therefore be slightly lower than those for the present day, because the bomb-test tritium has had another 5 years of decay, which corresponds to a reduction to about 75% of the current contribution.

The time period modelled is short relative to the time-scale of natural evolutions of the regional groundwater flow such as sea-level and sea-water salinity changes that occur on time scales of thousands of years, and the results of the regional groundwater flow calculations were only saved every 1,000 years. Therefore, the flow and distributions of reference waters at the end of the transient regional groundwater flow calculation from 10,000 BC to the present day were used as the initial conditions for the calculations of tritium migration. This introduced a small error, in that the change in the flow since 1,890 AD and the present-day was effectively neglected. However, this change is small.

Using the conditions at the end of the transient regional groundwater flow as the initial conditions effectively takes the conditions in the rock matrix to be in equilibrium at the start of the tritium migration calculations. Provided that the distributions of the reference waters were not changing rapidly towards the end of the regional groundwater flow calculations, this will be a reasonable approximation.

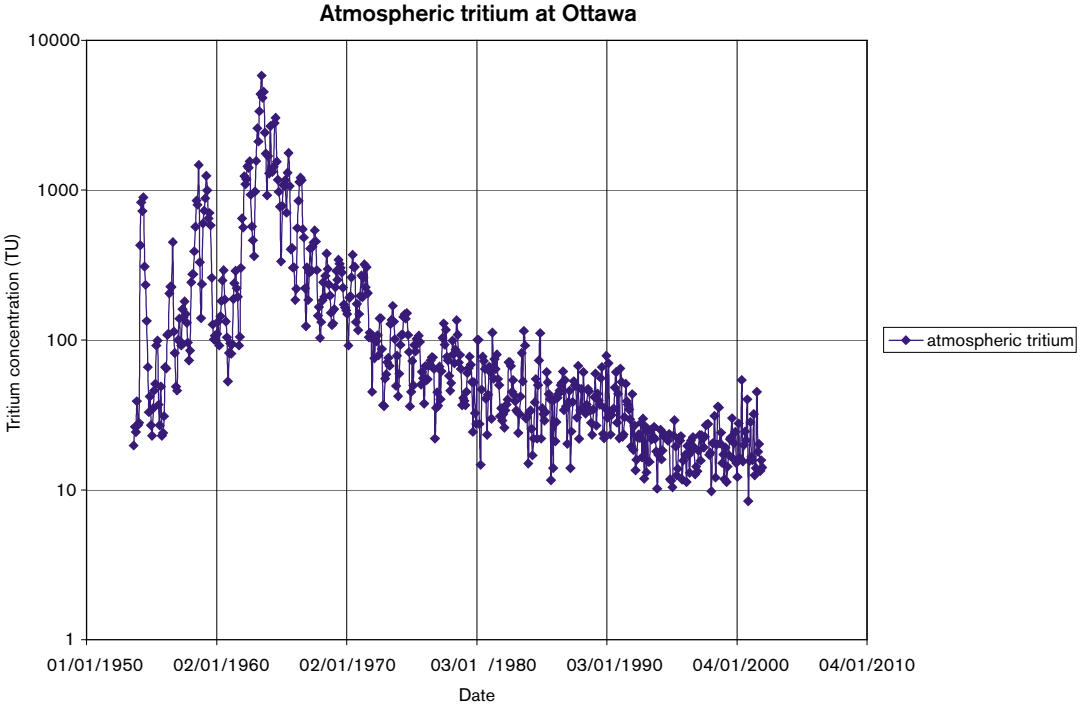

Figure 5-23. *Atmospheric concentrations of tritium measured at Ottawa.*

5.10.2 Boundary conditions

As indicated, calculations of tritium migration were carried out for the period since 1,890 AD. The calculations used multi-component groundwater flow, with rock-matrix diffusion. Tritium enters the model through the top surface, where the boundary condition was effectively specified such that the flux of tritium was equal to the recharge flux of groundwater multiplied by the concentration of tritium in precipitation, which was obtained from the data shown in Figure 5-23.

The option for modelling multi-component flow allows for modelling of tracers (e.g. $\delta^{18}O$, δD) as well as the main groundwater constituents (e.g. Na, Cl), but it does not currently allow for decay. All tracers are modelled as conservative, in the same way as the main groundwater constituents. However, it is straightforward to deal with this.

Since tritium must be transported as a non-decaying (i.e. conservative) tracer, then the 'undecayed' value of tritium is calculated, to give the required value of tritium in precipitation, at time, t. This 'undecayed' tritium is transported conservatively within the groundwater flow model. The value of tritium after transport must then be decayed to give the final tritium result. For instance, the background value of tritium in 1,890 AD (the reference time, t_{1890}) is given as 15 TU. Hence, the 'undecayed' input concentration for CONNECTFLOW (C_{input}) would be calculated as:

$$C_{input} = C_{ottawa}(t_{input}) \times \exp(\lambda [t_{input} - t_{1890}]),$$

where t_{input} is the time in years AD at the time under consideration, λ is ln(2)/12.34 years, C_{ottawa} is the atmospheric concentration of tritium at time, t. This example would give an 'undecayed' input concentration to CONNECTFLOW of 15 TU at 1,890 AD. Similarly, if at 1,950 AD the atmospheric tritium concentration is 2,000 TU, then the 'undecayed' input to CONNECTFLOW is 56,769 TU. After solute transport, the output tritium concentration from CONNECTFLOW must be decayed to give the final tritium result, C_{final}, using the formula:

$C_{final} = C_{model}(t_{output}) \times \exp(- \lambda [t_{output} - t_{1890}])$,

where C_{model} is the output tritium value from CONNECTFLOW, t_{output} is the time in years AD of the results, (generally 2,005 AD is used as the final time). For instance, a CONNECTFLOW, C_{model}, tritium value of 7,000 TU at 2,005 AD would be decayed to give a final tritium result of 11.5 TU at 2005.

Figure 5-24 shows the corrected tritium concentration in precipitation, given monthly, together with two simplified piecewise-constant approximations to this that were used in the modelling. In calculations with small time-steps, the finer temporal discretisation was used, taking the value corresponding to the end of a time-step. However, some calculations with carried out with a relatively long time-step of 20 years, and it was considered that using the value at the end of the time-step would not properly take into account the peak due to bomb tritium. For these calculations, the integrated value over the 20 year time-steps was used. Although a time-step of 20 years is very large for modelling the tritium migration, particularly in view of the tritium half life (12.34 years), this time-step was used for the initial tritium migration calculations since it was the time-step used for the groundwater flow calculations, and it was desired to avoid possible complications resulting from changing the time-step for the groundwater flow calculations.

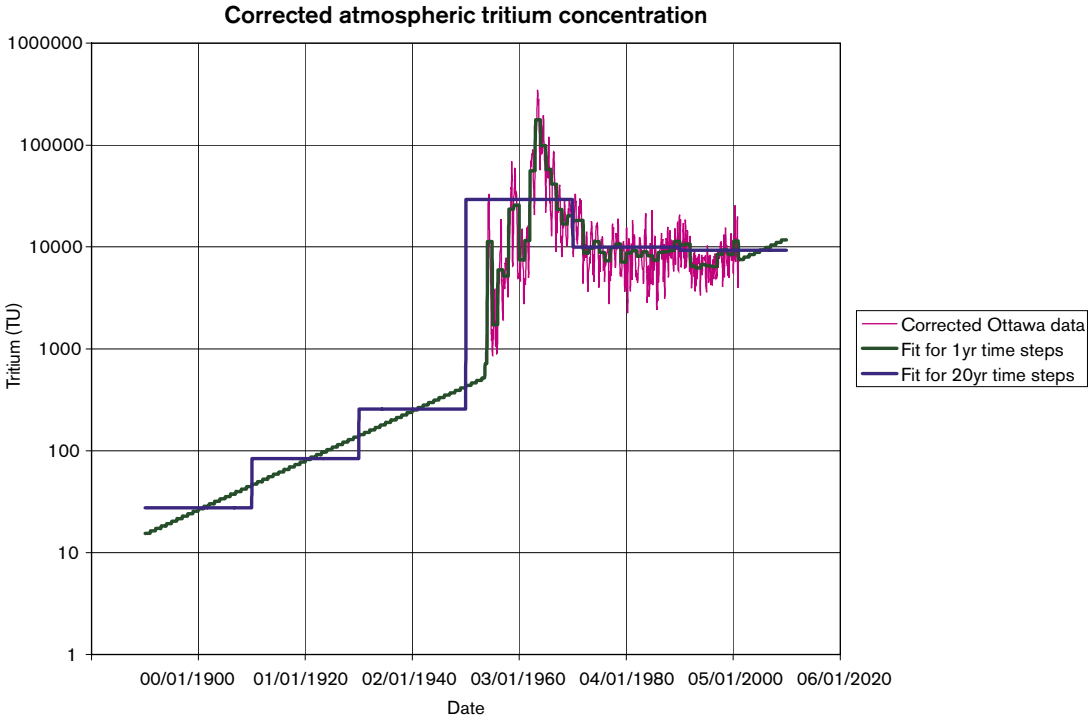

Figure 5-24. *The 'undecayed' input concentration for precipitation for CONNECTFLOW, shown between the 2,010 AD and the reference time of 1,890 AD.*

6 Regional model – calibration targets

The primary data used for calibration of the hydrogeological model concepts and parameters were the hydraulic and hydro-geochemical data available from boreholes in the regional model area. More precisely, these include the salinity profiles and mixing ratios along the trend and plunge of KFM01A, KFM02A, KFM03A, KFM04A, and KFM05A, under present-day conditions. It also includes concentrations of the major ions (e.g. Cl, Na, Ca, Mg) and ratios of environmental isotopes (Oxygen-18 and Deuterium). In addition, the F1.2 Task Description requested visualisation of the evolution of reference water fractions on a series of vertical sections through the model as a more qualitative calibration of the overall evolution of the hydrogeological situation. The new reference water transport modelling facility in CONNECTFLOW, when used in conjunction with RMD, calculates a mixing fraction for both the fracture system and the matrix. Hence, in theory it would be possible to calibrate the model against hydro-geochemistry data from both the flowing features (as is acquired currently) and that from the much tighter matrix. However, due to the obvious problems of sampling water from the rock matrix, there are currently no such data.

Another possible calibration test is to compare the hydraulic conductivity along the boreholes in the model with the long interval PSS data, or where these are not available, the PFL anomaly data upscaled to appropriate interval lengths.

6.1 Salinity profiles in boreholes

6.1.1 Data

The list of cored boreholes for which data are available is given in Table 6-1, and includes their positions and amount of data available. Figure B–1 shows the relative location of these boreholes together with percussion drilled boreholes in their vicinity. The number of data points specified in Table 6-1 represents the number of distinct depths at which water samples were collected, although there tend to be several samples associated with each depth corresponding to different samples taken at different times.

Table 6-1. Coordinates of the boreholes used as calibration targets. The amount and coverage of hydro-geochemistry data are also indicated.

Name	Easting	Northing	Adjacent percussion holes	Number of data points	Highest elevation of data (m)	Lowest elevation of data (m)
KFM01A	1631382	6699537	HFM01, HFM03	2	–115	–180
KFM02A	1633178	6698712	HFM04, HFM05	4	–59	–512
KFM03A	163462	6697845	HFM06, HFM08	9	–23	–990
KFM04A	1631052	6699005	HFM09, HFM10	4	–22	–270
KFM05A	1631710	6699344	HFM13, HFM14, HFM15, HFM19	0	–	–

The hydrogeochemical data are reported as either ‘representative’ or ‘unrepresentative’. A representative sample shows a complete set of element and isotopic analyses as well as having, for example, < 5% charge balance and contains < 1% drilling fluid. In the case of Forsmark F1.2 data, both representative and unrepresentative samples have been used for calibration purposes to increase the size of the otherwise sparse data set. Unrepresentative samples are not necessarily ‘bad’ samples simply that the representative samples have been picked as the best for chemical modelling purposes. Also, Table 6-1 gives a list of percussion drilled boreholes for which hydro-geochemical data were available close to the cored boreholes. These are included as an additional qualitative indication of near-surface data, typically in the top 100 m. However, the data from percussion holes have to be treated with caution since these water samples are taken from extracted water at relatively high pumped flow-rates compared with the cored boreholes.

6.1.2 Calibration targets

For Forsmark 1.1, the calibration target used was only the salinity in KFM01A supplemented with analogues drawn from salinity in deep boreholes at Olkiluoto and Laxemar. Hence, there are significantly more site specific salinity data available for F1.2 although it is still far from abundant with only KFM03A giving any data at depth.

Salinity gives an indication of the balance in driving forces between hydraulic gradients at the surface and buoyancy effects of the dense brine, and how this balance has changed over time due to land-rise. Hence, it acts as a natural tracer for transient variable-density flow. However, by including the mixing fractions of reference waters, a more stringent calibration of the hydrogeological properties and boundary conditions is possible since it introduces freshwater tracers of varying age, such as the Glacial and Rain 1960, and the less dense Marine waters. In the Forsmark 1.1 CONNECTFLOW modelling /22/, the salinity was found to be relatively insensitive to the initial condition for salinity. Hence, it is interesting to see if the uncertainties in initial conditions can be reduced by considering the individual reference waters.

The salinity for a given water composition in the model is calculated as the sum of the products of each reference water fraction with the salinity of that reference water. The salinities for the reference waters were calculated from the TDS based on Table 5-1.

6.1.3 Uncertainties in data

The salinity data in F1.2 are still quite limited in quantity and depth (see Table 6-1), only KFM03A has samples near 1 km where significant Brine is encountered. The next deepest is –512 m in KFM02A, which suggests a small proportion of Brine at the base, hence data on the dense saline water are quite sparse. Thus, there is a risk of bias if we base the calibration of salinity on just the one or two deep boreholes. In addition, most of the boreholes are near to the coast in very low topographic areas, and so there is additional risk of bias due to sampling essentially a single hydrogeological environment. This is one motivation for visualisation of the regional-scale salinity pattern using cross-sections.

6.2 Water types and major ions in boreholes

The reference water mixing fractions give us several different tracers that have entered the groundwater system at different times and with different densities. As such, they give the possibility to quantify sensitivities to initial conditions, boundary conditions and hydraulic properties not possible with salinity data alone.

6.2.1 Data

Transport of four reference waters (non-chemically reactive fluids) was simulated in the CONNECTFLOW groundwater flow model. These reference waters have been identified by the hydro-geochemistry group from previous site investigations as well as Forsmark site-specific data /18/ and their representative composition of element concentrations and isotopic values (e.g. Na, Cl, $\delta^{18}O$, δD, ^{3}H) has been analysed as given in Table 5-1. Using this information and assuming non-reactive mixing it is possible to make a linear conversion from mixing fractions to element concentrations and isotopic values at any point in the model. The main reason for performing simulations using the mixing fractions as the transported entities rather than element concentrations is that it is more straightforward to define boundary and initial conditions in terms of the evolution of different water types rather than chemical compositions. However, the output from a CONNECTFLOW simulation can readily be presented as either mixing fractions or as element concentrations and isotopic values for comparison with measured data from boreholes. For example, the fraction of each water type at a borehole can also be simulated using CONNECTFLOW and compared to the Multivariate Mixing and Mass-balance (M3) mixing fractions. The M3 approach takes samples from a borehole and uses 'principal component analysis' to calculate the fraction of each water type present in a sample /24/. However, this approach has at least a 10% margin of error on each M3 mixing fraction /24/. This margin is significant when several of the four reference waters are present since the cumulative error for all waters becomes large. Further, the error associated with a particular sample varies down boreholes depending which are the primary reference waters present, which leads to artificial spikes in the reference water profiles down the borehole. For this reason the major ions and environmental isotopes are also used in the calibration since they represent 'raw' data. However, caution has to be used here also since while some chemical constituents, like Cl and $\delta^{18}O$, are transported conservatively (i.e. no chemical reaction takes place during transport), others are likely to be non-conservative, like SO_4, which can be affected by sulphate reducing bacteria. Mg is not strictly a conservative element either, but it is a useful indicator to differentiate between Brine at depth (low Mg concentration) and shallower Marine water with high Mg concentration. The environmental isotopes δD and $\delta^{18}O$ help to differentiate between Glacial and Rain 1960 reference fresh waters, and to some extent $\delta^{18}O$ can be used to distinguish the saline reference waters (Brine from Marine).

6.2.2 Calibration targets

The main calibration target of coupled groundwater flow and reference water transport then is to compare the mixing fractions and selected constituents (Cl, $\delta^{18}O$, and Mg primarily) along the boreholes. The comparison is done in a visual way by comparing the trend for hydro-geochemistry along the whole length of borehole, and below, with the interpreted field data. It is done this way, rather than some sort of error norm only at the data points, to gain an understanding of the broader mixing pattern at a variety of depths.

6.2.3 Uncertainties in data

In view of the various uncertainties in the hydro-geochemical data, calibration of the CONNECTFLOW model is considered against as many of the measured data as possible. In particular, the calibration of CONNECTFLOW considers the most conservative, and representative, measured data (Cl, $\delta^{18}O$ and Mg), and the water types with larger fractions in the M3 mixing approach (where the 10% error margin is less significant). The measurement error on $\delta^{18}O$ is approximately ± 0.2‰, and ± 1‰ on δD.

To make best use of the limited number of data, all analyses have been plotted for comparison with the model, no matter whether the classification set by the geochemists is considered 'representative' or 'less representative but suitable when used with caution' /18/. This classification has been used by the geochemists to highlight their highest quality samples with a complete set of major ion and isotope analytical data, charge balance of ± 5%, less than 1% drilling water. It should be noted though that some of the data included for the cored drilled boreholes comes from the top 100 m which were percussion drilled. Data was provided for the upper 100 m in KFM02A which appears to be from a source in the percussion drilled part of the borehole while still open and appears to dilute modern to recent water. Later on tube sampling gave more saline water more in common with flushing water. In KFM03A and KFM04A water samples in the top 100 m could not be obtained during the open percussion drilled hole. Instead, data is supplied from tube samples that suggest brackish water, but these seem very unrepresentative, since KFM03A contains excessively high tritium for example. Hence, although we retain the data for the top 100 m it should be considered with particular caution.

6.3 Hydraulic conductivity in boreholes

In developing the Hydro-DFN, the DFN hydraulic properties were matched against relatively small scale measurements, i.e. individual flow anomalies from PFL or 5 m test intervals for PSS. A further testing of the models is possible by considering the EPM hydraulic properties on larger scales.

6.3.1 Data

Hence, an additional calibration test is to compare the hydraulic conductivity along the boreholes in the model with the long interval PSS data. The grid resolution is either 50 m or 100 m, and hence it is most appropriate to compare with the 100 m interval PSS data. PSS data on contiguous 100 m intervals are available for KFM01A, KFM02A and KFM03A. For KFM04A and KFM05A, only PFL flow anomaly data are available. However, the transmissivity inferred in flow anomalies can be grouped to approximate give bulk conductivities for 100 m intervals, although this is likely to have a higher measurement limit than the PSS data.

6.3.2 Calibration targets

The calibration on hydraulic data was focussed on the high flow intervals that are coincident with deformation zones in the HCD model. For the background rock in RFM017/029 a statistically uniform DFN model that has hydraulic conductivities similar to or less than the detection limit of the PSS data. Local conditioning of the background rock was not performed, mainly because it has only a secondary effect on regional-scale flow. Rather the objective was to ensure the overall magnitude of the background conductivity of the correct low magnitude.

6.3.3 Uncertainties in data

There are several uncertainties associated with the PSS data. Firstly, these are single-hole measurements, so there are issues relating to borehole skin or other localised effects like the test only evaluates part of the zone adjacent to the borehole. There are then interpretation uncertainties, for example two alternative methods used in the PSS interpretation are based on either the Moye or 2D radial transient flow assumptions have been used. For the PSS data, the transient evaluation is considered to "filter out" the effect of the skin factor. There are also some intervals in which there have been problems in making the single-hole test, and here a small hydraulic conductivity is given, so it is not always clear if this is a realistic value. Hence, in doing the comparison we might expect the overall magnitude of hydraulic conductivity to agree, with perhaps the high values to be in closer agreement, and lower values may indicate tighter areas although these are more uncertain.

6.4 Tritium in boreholes

Tritium provides a potential tracer for recent precipitation, because it only enters the groundwater flow system in precipitation and has a short half life (12.34 years).

6.4.1 Data

Tritium data are available for boreholes KFM01A, KFM02A, KFM03A and KFM04A. However only three of these boreholes have measurements of tritium of any significant level, and unfortunately all these samples have no reported amount of contamination by drilling water.

6.4.2 Calibration targets

The calibration against tritium was carried out by visually comparing the calculated concentrations of tritium down boreholes with measurements.

6.4.3 Uncertainties in data

Tritium samples for KFM01A were collected in January to April 2003, with one sample with no reported drilling water content collected in May 2002 (at –47 m elevation). KFM02A tritium samples were collected in June 2003 to Feb 2004, with two samples with no reported drilling water content collected in Nov 2002 (at –52 m elevation). KFM03A tritium samples were collected in Sept. 2003 to Feb. 2004, with five samples with no reported drilling water content collected in June 2003 (at –15 m, –137 m, –262 m, –362 m and –933 m elevation). KFM04A tritium samples were collected in December 2003 to January 2004.

To make best use of the limited number of tritium data, all analyses have been plotted for comparison with the model, no matter whether the classification set by the geochemists is considered 'representative' or 'less representative but suitable when used with caution' /18/. Instead, each data point has been marked on the figures with the percentage of contamination due to drilling fluid. The percentage of drilling water contained in each sample can affect the tritium analyses significantly, given that modern precipitation will have around 15 TU and most reported tritium analyses are low values or at the detection limit. The detection limit for tritium is 0.8 TU, hence a model predication of zero tritium, and an analysed value of 0.8 TU (i.e. below detection) can be considered a good match.

Due to the short half life of tritium (12.34 years), the sample collection date is important since decay will continue to occur after sample collection. (The sample analysis date has not been reported in this data set.) It was considered better to simulate the model at as close a match as possible to the sampling date, since this would best match the real data. The alternative method to correct the tritium value for radioactive decay to a particular date after analysis would not take in-situ mixing of different water masses into account. 2,005 AD has been used as the simulation date.

7 Regional model – flow simulations

The Task Description specified that modelling address two main objectives:

1. Palaeo-hydrogeological understanding: An improved understanding of known and unknown palaeo-hydrogeological conditions is necessary in order to gain credibility for the Site Descriptive Model in general and the hydrogeological description in particular. This requires modelling the groundwater flow from the last glaciation up to present-day with different boundary conditions and hydraulic properties, and compare with measured TDS and other hydro-geochemical measures.
2. Simulation of flow-paths: The simulation and visualisation of flow-paths from a tentative repository area is a means for describing the role of the current understanding of the modelled hydrogeological conditions from an engineering perspective. Of particular interest here is demonstration of the need for detailed far-field realism in the numerical simulations. The motivation for a particular model size (and resolution) and set of boundary conditions for a realistic description of the recharge and discharge connected to the flow at repository depth is an essential part of the groundwater simulations.

Both CONNECTFLOW and DarcyTools modelling teams considered both objectives, but CF has focussed on confidence issues relating to the needs of Safety performance, whereas DT focuses on confidence issues of general hydrogeological character, e.g., model domain size and boundary conditions. The CF Team has considered sensitivities to a refined local-scale stochastic DFN and transport parameters, for example. The DT Team considered extending the regional model approximately 5 km either south-west (upstream) or north-east (downstream) to illustrate the effects of significant increases in model size, and the effects of adding stochastic sub-horizontal DZs to the regional-scale. Both modelling teams considered what hydraulic properties, initial conditions and boundary conditions could give consistent simulations of the present-day salinity and mixing fractions.

This section describes the sensitivity analysis performed with CONNECTFLOW in matching the salinity and mixing fractions. The predictions of transient flow and groundwater flow-paths for some calibrated cases are given in Sections 8 and 9. A series of transport calculations were performed for each of the variants considered to provide guidance for the Preliminary Safety Evaluation (PSE) (see Appendix C).

7.1 Methodology

Figure 7-1 shows a schematic overview of the modelling workflow used in the project. The starting point is the Hydro-DFN conceptual model and the associated fracture properties. This can be used to obtain the statistics of block-scale properties or to construct a regional-scale DFN that is upscaled to produce an EPM model that has HRD hydraulic properties consistent with a realisation of the underlying DFN data. Within the EPM regional-model, the HCD and HSD properties are then combined with HRD. Finally, simulations of transient groundwater flow and reference water transport provide the calibration targets and required transport performance measures.

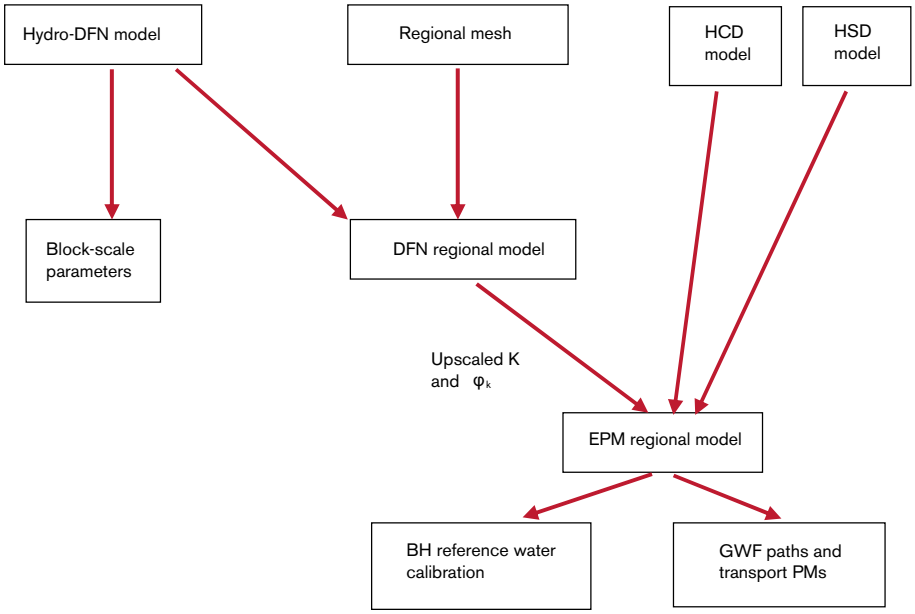

Figure 7-1. *A schematic workflow for the CONNECTFLOW modelling.*

The calibration is performed by plotting profiles of each of the salinity, 4 reference water fractions, major ions and isotope ratios down each borehole. The transport performance measures are processed as statistics over an ensemble of particles released from many points in the local-scale or site-scale areas to give histograms and tables. Several model variants were created to quantify the sensitivities to a number of key issues such as hydraulic properties, initial and boundary conditions.

7.2 Summary of applied regional model cases

The key issues simulated by CONNECTFLOW modelling were:

- Alternative geological models;
- Hydraulic properties of HCD (conductor domain), HRD (rock domain), and HSD (soil domain);
- Hydro-DFN parameters;
- Initial and boundary conditions for flow and reference water transport;
- Transport parameters for RMD and safety assessment calculations.

Several model cases were constructed to quantify the effects of and illustrate each of these issues. During the initial stages of the modelling, a significant number of other cases, including the simple rock domain model HRD1 and HRD2, were created on route to gaining an understanding of how individual model parameters affected the calibration, and ultimately to what ranges of parameters gave a reasonable match to the field data. Not all these steps are reported here since they are of limited interest. Instead, the approach was to define a base case that gives a reasonable match, and then consider variants from this to illustrate the sensitivity to the various issues. The variants considered are grouped by these key issues to give structure to the discussions.

The final Base Case properties and conditions arrived at were:

- Regional model (about 15×11 km, same as used for F1.1) with 50 m element-size embedded grid covering the potential repository area and the five boreholes KFM01A–KFM05A. A 100 m element-size was used elsewhere. Model boundaries aligned with natural boundaries such as regional water divides and large fracture zones;
- Initial Condition set to full Glacial 0–500 m; then linear gradient to no Glacial, full Brine at 2,000 m; full Brine below 2,000 m;
- Top-surface head equals topography;
- Top surface waters:
  - Before 4,500 BC – Baltic Ice Ancylus Ice Lake (Glacial),
  - Before 2,500 BC – Littorina Sea (Marine)
  - After 2,500 BC – Baltic Sea/Precipitation with land rise (Marine diluting with Rain 1960);
- HCD Base Case with Depth dependence on hydraulic conductivity modified as in Table 5-2;
- HRD3 with properties in RFM017/029 for Hydro-DFN model (HRD3EC, see Table 5-4) based on Volume E with correlated T vs L. This had block-scale properties of $K_{50\%} \sim 4\ 10^{-10}$ m s^{-1}, $K_{10\%} = 1\ 10^{-11}$ m s^{-1};
- HRD kinematic porosity $n_{etb} \geq 10^{-5}$ (based on DFN value, Table 4-3);
- HRD Matrix porosity $n_m = 3.7\ 10^{-3}$;
- Density and viscosity a function of salinity (transient), temperature (fixed) and total pressure (transient);
- Flow-wetted-surface (FWS) per unit volume for RMD $a_r = 1.0$ m^2 m^{-3};
- Matrix diffusion length into matrix blocks $L_D = 1.0$ m;
- Intrinsic diffusion coefficient into matrix $D_i = 5\ 10^{-13}$ m^{2}s^{-1}.

In Table 7-1 an explanation of the system used for naming the different cases is given. The names are constructed using a substring to specify the option used for each model component. All variants of each model component are also listed together with a brief description of the properties used. The names of the variants were chosen to denote the following components: hydraulic conductor domain (HCD); geological model; hydraulic rock domain (HRD); Hydro-DFN case; hydraulic soil domain (HSD); hydraulic or transport property; and boundary condition. Transmissivities for the HCD domains are split according to either steeply dipping (T_V), gently dipping (T_H), or outside the tectonic lens (T_O) and since they are vertical lineaments they equate to the T_V properties.

A list of the cases considered about the base case is given in Table 7-2 with a colour coding to highlight the key issue they were designed to address. HCD3_BC_HRD3EC_HSD1_BC1 is the overall base case.

Each of the key issues and associated variants are discussed in terms of the calibration results in the following sections.

Table 7-1. Explanation of the case naming and properties of variants.

Composition of the generic case name: AA_BB_CCDDEE_FF_GG	Variant	Description
AA (Hydraulic Conductor Domain)	HCD1	$T_V = 4.6\ 10^{-5}$ exp(–1.74 10^{-2} Depth), $T_V > 10^{-9}$ m^2 s^{-1} $T_H = 4.1\ 10^{-4}$ exp(–1.16 10^{-2} Depth), $T_H > 10^{-9}$ m^2 s^{-1} $T_o = 4.1\ 10^{-4}$ exp (–1.16 10^{-2} Depth), $T_o > 10^{-9}$ m^2 s^{-1} B = F1.2 b_{hyd} ne = F1.2 n_e AWS = 1 m^{2}m^{-3}
	HCD3	Modified b_{hyd} and T
BB (Geological Model)	BC	Base Case (geological)
	AC	Alternative Case (geological)
CC (Hydraulic Rock Domain)	HRD1	Inside RD29 K = 5 10^{-11} m s^{-1} $n_e = 1\ 10^{-5}$ $n_m = 4\ 10^{-3}$ $a_r = 1$ m^{2}m^{-3}
	HRD2	Outside RD29: K = 10^{-8}, 5 10^{-9} m s^{-1} (above, below 100 m)
	HRD3	DFN (Volume E) KFM03A $K_{min} = 5\ 10^{-11}$ m s^{-1} $n_{emin} = 5\ 10^{-6}$
DD (DFN Case)	EC EC2 EC3	Volume E (KFM03A), Correlated T/L; Realisation 1, 2 and 3
	EU	Volume E (KFM03A), Uncorrelated T/L
	SFC	DarcyTools Geo-DFN variant, Correlated T/L
	SFU	DarcyTools Geo-DFN variant, Uncorrelated T/L
EE (Hydraulic or transport property)	K1	Increased background conductivity outside RD29 (K = 10^{-7} m s^{-1}, K = 3 10^{-8} m s^{-1})
	F1	$a_r = 0.25$ for HRD and HCD
	N1	$n_m = 2.5\ 10^{-3}$
	D1	$D_i = 1.0\ 10^{-13}$ m^{2}s^{-1}
FF (Hydraulic Soil Domain)	HSD1	Top 4 m: K = 7.5 10^{-6} m s^{-1}, $n_e = 5\ 10^{-2}$ Outcrop: K = 1 10^{-7} top 4 m, $n_e = 1\ 10^{-4}$
	HSD2	Top 1 m: K = 1.5 10^{-5} m s^{-1}, $n_e = 1\ 10^{-1}$ Next 2 m: K = 1.5 10^{-6} m s^{-1}, $n_e = 5\ 10^{-2}$ Next 1 m: K = 1.5 10^{-5} m s^{-1}, $n_e = 5\ 10^{-2}$ Outcrop: K = 1 10^{-7} top 4 m, $n_e = 1\ 10^{-4}$
GG (Boundary Condition, Initial Condition)	BC1	Glacial to 500 m depth Linear increase in Brine to 100% at 2,000 m depth
	BC3	Flux BC on top

Table 7-2. Summary of the main regional-scale model cases performed. The cases are grouped by colour coding according to the sensitivities they quantify: surface boundary conditions and properties (orange); DFN cases (blue); HRD hydraulic and transport properties (yellow); geological model (green).

EPM Case	Properties	Comments
HCD3_BC_HRD3EC_HSD1_BC1	CF DFN – Correlated T/L	Base Case
HCD3_BC_HRD3EC_HSD1_BC3	CF DFN – Correlated T/L	Sensitivity to flow B.C. – Specified flux/infiltration
HCD3_BC_HRD3EC_HSD2_BC1	CF DFN – Correlated T/L	Sensitivity to refined HSD
HCD3_BC_HRD3EC2_HSD1_BC1	CF DFN – Correlated T/L DFN Realisation 2	Sensitivity to Stochastic DFN
HCD3_BC_HRD3EC3_HSD1_BC1	CF DFN – Correlated T/L DFN Realisation 3	Sensitivity to Stochastic DFN
HCD3_BC_HRD3EU_HSD1_BC1	CF DFN – Uncorrelated T/L	Sensitivity to DFN transmissivity model
HCD3_BC_HRD3SFC_HSD1_BC1	DT DFN – Correlated T/L	Sensitivity to DFN parameters (DarcyTools)
HCD3_BC_HRD3SFU_HSD1_BC1	DT DFN – Uncorrelated T/L	Sensitivity to DFN parameters (DarcyTools)
HCD3_BC_HRD3ECK1_HSD1_BC1	CF DFN – Correlated T/L Higher background outside RFM017/029: $K = 10^{-7}$, $K = 3\ 10^{-8}$ m s^{-1}	Sensitivity to hydraulic parameters outside of RFM017/029
HCD3_BC_HRD3ECF1_HSD1_BC1	CF DFN – Correlated T/L AWS = 0.25 for HRD and HCD	Sensitivity to RMD parameters
HCD3_BC_HRD3ECN1_HSD1_BC1	CF DFN – Correlated T/L $n_m = 2.5\ 10^{-3}$	Sensitivity to transport parameters
HCD3_BC_HRD3ECD1_HSD1_BC1	CF DFN – Correlated T/L $D_i = 1.0\ 10^{-13}$ m^{2}s^{-1}	Sensitivity to RMD parameters
HCD3_AC_HRD3EC_HSD1_BC1	CF DFN – Correlated T/L	Sensitivity to geological model Alternative Case
HCD3_AC_HRD3ECN1_HSD1_BC1	CF DFN – Correlated T/L $n_m = 2.5\ 10^{-3}$ m^{2}s^{-1}	Sensitivity to geological model and transport parameters Alternative Case

7.3 Reference water mixing fractions calibration of Base Case

Using the Regional model domain for transient coupled groundwater flow and reference water transport a calibration process resulted in the Base Case properties listed in subsection 7.2. Using the geological model together with the given HCD1 hydraulic properties, based on a fit to the overall depth trend for all DZs but not conditioned to the actual localised transmissivities measured in the single-hole interpretations, it was difficult to produce a reasonable match overall to the calibration targets by changing parameters globally. A better match for individual boreholes could only be achieved by making localised changes to the hydraulic and geometric properties of specific DZs intersected by boreholes to make their properties more consistent with the values actually measured. Such

'fine-tuning' was performed on zones A2, A3, A4, B1 and Zone 1,188 intersecting boreholes KFM02A, KFM03A and KFM04A. The transmissivities of these zones had to be increased a factor 10–100 above or below the overall trend in order to get a match (see Table 5-2). This is consistent with the variations seen in fit of T against depth shown in Figure 5-14.

7.3.1 Reference waters

Figure 7-2 to Figure 7-5 show the calibration of the Base Case against the interpreted 4 reference water profiles for the cored boreholes KFM01A to KFM05A. These calculations were performed with RMD, so the mixing fraction in both the fracture system and matrix are shown. The two sets of fractions are generally similar since $a_r = 1.0\ m^2m^{-3}$ gives good communication between the fracture and matrix (Note: $a_r = 2\times P32_c$, and hence we have set $P32_c = 0.5\ m^2m^{-3}$ in the RMD matrix parameter). The sensitivity to this parameter is discussed in subsection 7.8. It is very important to note that the hydro-geochemistry data have preferentially focused on sampling water from DZs. There is very little flow in the background rock between the DZs, and so the chemistry data represent discrete samples, and hence, although lines have been drawn linking up the data points down the boreholes, this continuity of water composition in the background rock is highly speculative. Therefore, the matching should only really be judged at depth where there are data.

Figure 7-2 shows that in KFM01A the hydro-geochemical samples are only between depths of 100 m and 200 m. This limited depth range the model predicts the reference water fractions very well with a sharp transition from Rain 1960 water to Marine and about 20% Glacial water. Below 200 m there are no data to support a calibration of the model. The model predicts a lens of Marine water between about 100 m and 500 m depth reaching a maximum of about 45% at 200 m depth. Below this it predicts a lens of Glacial water and a weak gradient toward Brine starting at 500 m. The match for KFM02A in Figure 7-3 is more interesting since the borehole has many more data and goes deeper. The model predicts a sharp transition from Rain 1960 to Marine water around 200–300 m depth, while the data suggest a more gradual transition between 100–500 m depth. Since the site only advanced from the sea about a thousand years ago, the data point to a faster transport of precipitation than in the model. The model predicts a lens of Marine water descending through the model between 200–600 m depth up to a fraction of 80%. Glacial water is simulated correctly to be in the range 10–20% until 500 m depth, and then rises sharply although there are no data to confirm it. KFM04A provides the greatest abundance of data as shown in Figure 7-4. The data for KFM03A near the surface are curious since they suggest 50% Marine water near the surface but the ground is at an elevation of about 8 m and so, based on land-rise rates, has been subject to precipitation for around 1,000 years. The percussion drilled boreholes give the expected precipitation near surface, but this under pumped conditions. According to the data, Marine gradually decreases to about 20% below 600 m. The model suggests a gradual rise in Marine water up to about 80% at 300 m and then falls-off at 700 m, with spikes corresponding to zones ZFMNE00A4 and ZFMNE00B1. The model gives a good prediction in the Glacial water composition at the data points. Even at the base of the borehole Brine is only just above the M3 resolution uncertainty, 10–15%, and so it is hard to calibrate Brine at Forsmark based on M3. KFM04A, seen in Figure 7-5, again only has data at 100–300 m depth. The 50% Marine, 20% Rain 1060, 15% Glacial at around 250 m depth is predicted very well by the model. The surface water composition of 40% Marine near the surface however, is again curious as this drill site is some 1.5 km form the sea and at 9 m elevation. The model predicts a lens of Marine water up to about 60% between 300 and 500 m depth. There are no hydro-geochemistry data in the KFM05A cored borehole, but data from nearby percussion drilled boreholes are compared with the model predictions (see Figure 7-6). A lens of Marine water up to about 30% is predicted between 200 and 500 m depth.

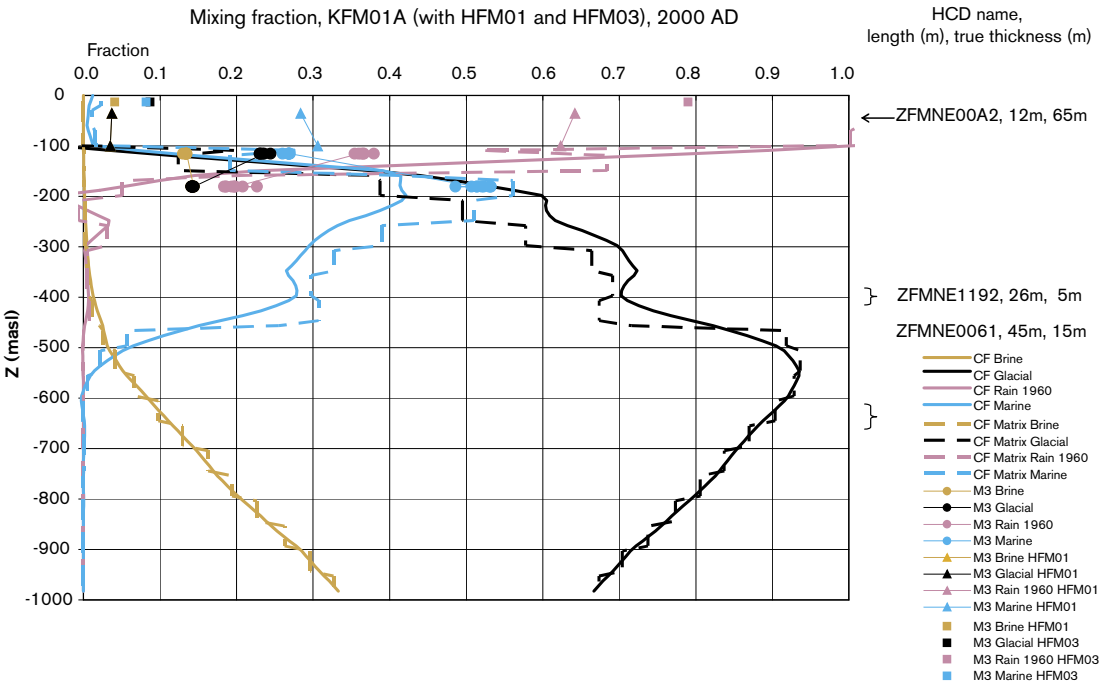

Figure 7-2. *Comparison of 4 reference water fractions in KFM01A for Base Case (HCD3_BC_HRD3EC_HSD1_BC1). The mixing fractions in the fracture system are shown by solid lines, in the matrix it is dashed, and the data by points.*

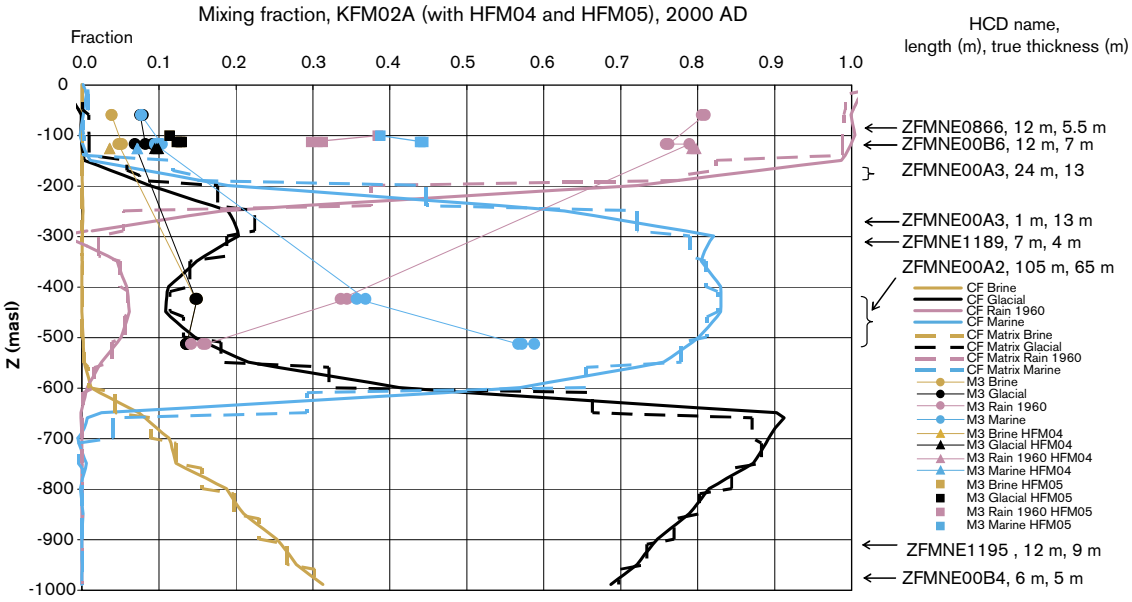

Figure 7-3. *Comparison of 4 reference water fractions in KFM02A for the Base Case (HCD3_BC_HRD3EC_HSD1_BC1). The mixing fractions in the fracture system are shown by solid lines, in the matrix it is dashed, and the data by points.*

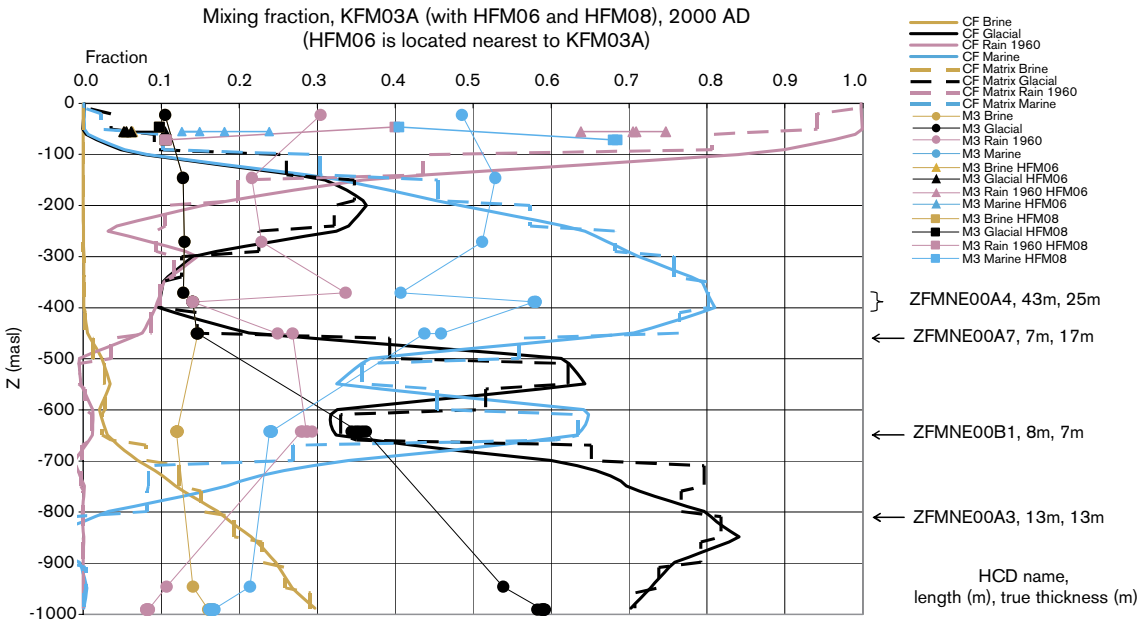

Figure 7-4. *Comparison of 4 reference water fractions in KFM03A for the Base Case (HCD3_BC_HRD3EC_HSD1_BC1). The mixing fractions in the fracture system are shown by solid lines, in the matrix it is dashed, and the data by points.*

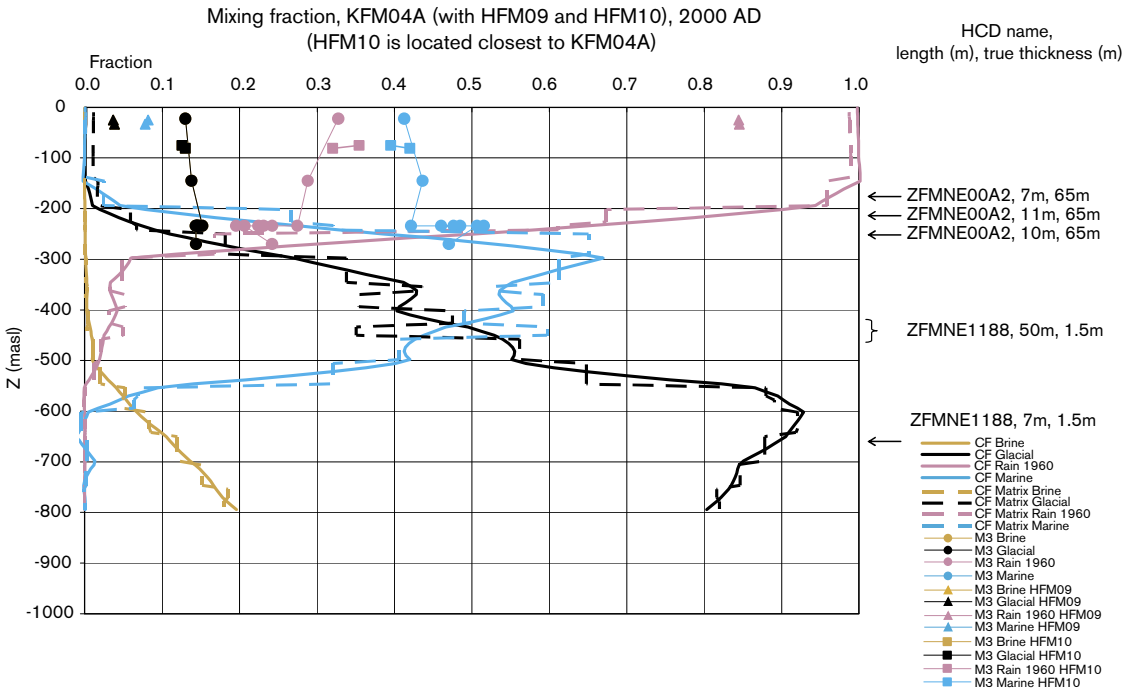

Figure 7-5. *Comparison of 4 reference water fractions in KFM04A for the Base Case (HCD3_BC_HRD3EC_HSD1_BC1). The mixing fractions in the fracture system are shown by solid lines, in the matrix it is dashed, and the data by points.*

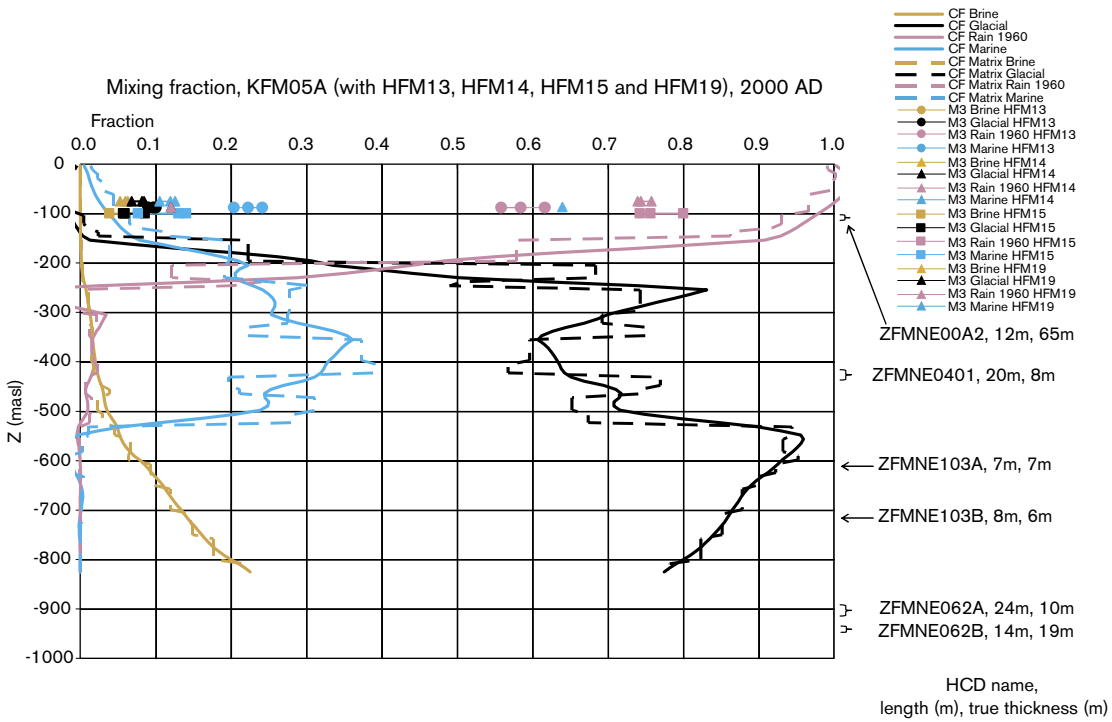

Figure 7-6. *Comparison of 4 reference water fractions in KFM05A for the Base Case (HCD3_BC_HRD3EC_HSD1_BC1). The mixing fractions in the fracture system are shown by solid lines, in the matrix it is dashed, and the data by points.*

7.3.2 Salinity

Salinity closely follows the profile of Brine, although there is also a contribution from the Marine reference water. Figure 7-7 shows the comparison for salinity between the Base Case simulation and the data for boreholes KFM01A, KFM02A, KFM04A and KFM04A to illustrate the performance of the model. By superimposing the data from the boreholes in this way it is interesting to observe a reasonably consistent and smooth trend of salinity with depth. The only significant anomaly is that freshwater is measured near the surface in KFM02A while salinities similar to that of sea water are measured in KFM01A, KFM03A and KFM04A. The model simulations also predict similar profiles down the boreholes, except KFM02A and KFM03A have perhaps higher salinity between depths of 200–700 m than KFM01A and KFM04A. This is interesting as KFM01A and KFM04A are in the less hydraulically conductive area below DZ ZFMN00A2.

Above 200 m the model under-predicts salinity except at KFM02A. As mentioned in Section 6.2.3 the data in the top 100 m tends to be particularly uncertain as it is sourced from quite different methods to the rest. Hence, it is not clear whether the top 100 m is generally brackish or there is a sharp transition in the top 100–150 m. If it is brackish, then it creates a conceptual problem since it is hard to reconcile having sufficient hydraulic conductivity to allow infiltration of a Littorina pulse without a following infiltration of freshwater once the site is exposed to precipitation about 1,000 years ago. This may just be a question of having to ‘fine-tune’ surface hydraulic, transport properties and boundary conditions to obtain a good match. Anyhow, greater effort to acquire representative water samples in the top 100–150 m would significantly help focus the model calibration efforts.

The salinity at 1 km as seen in KFM03A is over-predicted despite the very gradual rise in Brine specified in the initial condition that gives about 30% Brine at 1 km. It would suggest the Brine is even deeper.

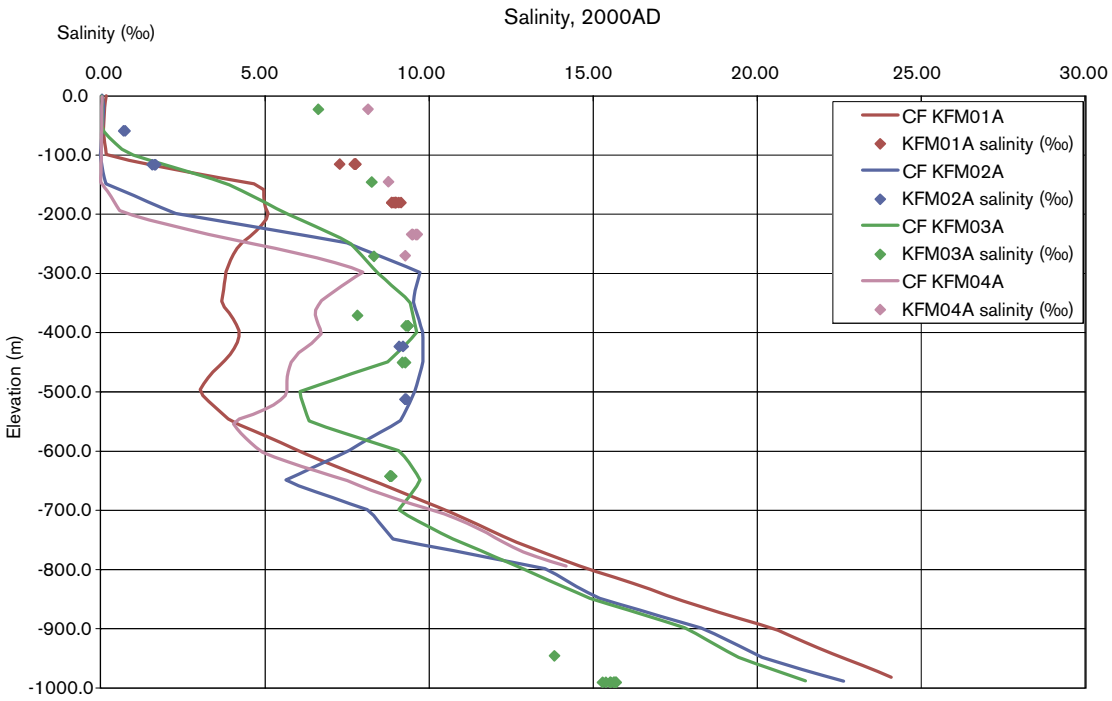

Figure 7-7. *Comparison of salinity (TDS) in KFM01A–KFM04A for the Base Case (HCD3_BC_HRD3EC_HSD1_BC1). The salinity in the fracture system is shown by solid lines, and the data by points.*

7.3.3 Major ions and environmental isotopes

Since there is an interpretation uncertainty present in the M3 analysis it was proposed to also consider a range of the basic constituents. The full range of major ions as well as the Oxygen-18 isotope ratio and Deuterium isotope ratios were considered. However, for presentation it is sufficient to just show $\delta^{18}O$, Cl and Mg as these are considered relatively conservative and representative. $\delta^{18}O$ allows the identification of Glacial water by a large negative ratio and differentiates between Rain 1960 and Glacial freshwaters; Cl indicates the presence of either Brine or Marine; and Mg differentiates between saline Marine (high) and Brine (low). Figure 7-8 shows the profiles of these three constituents in KFM01A–KFM04A for the Base Case. The error bars only indicate the laboratory analysis uncertainty of about 5%. It is again interesting to observe that the profiles are generally consistent between boreholes and generally suggest a smooth trend down the boreholes. They are less spiky than the M3 profiles, which are prone to being sensitive to which reference waters have been identified as the dominant waters, as this can change from point to point. For $\delta^{18}O$, the model predictions are generally good where there are corresponding data, but suggest Glacial spikes in the background rock where no data are available. Cl correlates to salinity, so the comments made in the previous section hold. Mg allows us to differentiate salinity from Brine below about 500 m from salinity from Marine water infiltration above 500 m. This transition from Marine to Brine originating salinity is correctly simulated in the model. Mg also gives evidence for water of Marine origin in the near surface for KFM01A, KFM03A and KFM04A.

Since these three basic constituents give smoother profiles and are less prone to uncertainty than the M3 interpretation, then these profiles will be used to compare and calibrate the variants in the following sections.

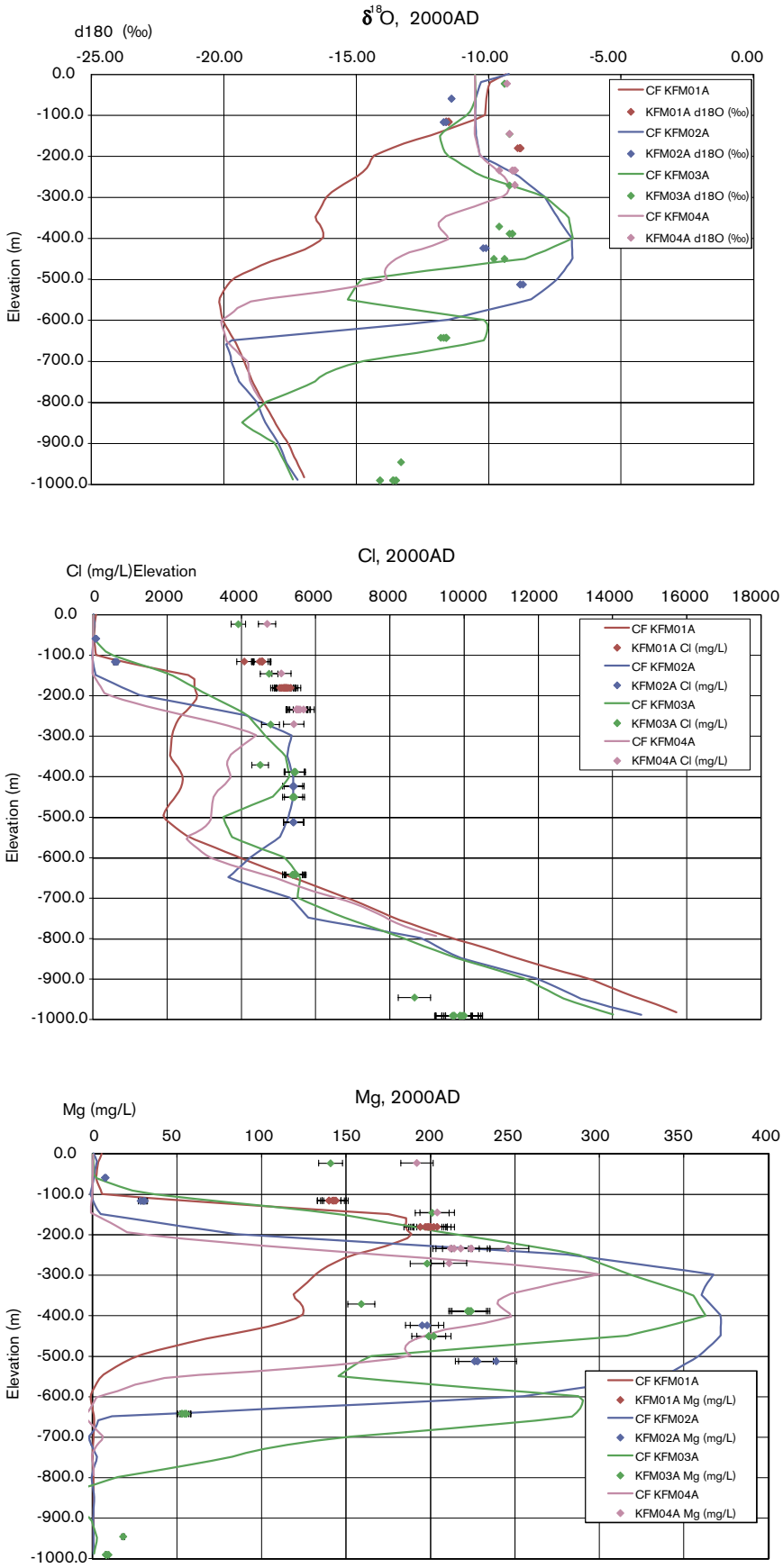

Figure 7-8. *Comparison of $\delta^{18}O$, Cl and Mg in KFM01A–KFM04A for the Base Case (HCD3_BC_HRD3EC_HSD1_BC1). Values in the simulated fracture system are shown by solid lines, and the data by points.*

7.4 Tritium modelling and comparison with measurements in boreholes

Tritium transport simulations were carried out for the Base Case (HCD3_BC_HRD3EC_HSD1_BC1_grid) and a case with low flow wetted surface area (AWS = 0.25 m^2m^{-3}; HCD3_BC_HRD3ECF1_HSD1_BC1_grid). In these calculations, the time-step was taken to be 5 years.

Modelled tritium concentrations are highest at the ground surface and decrease with depth, but are only seen at any significant concentration in the top 100 metres. All measurement values for all boreholes show tritium concentrations at or near the detection limit, (except for a couple of older measurements where contamination by drilling water has not been reported). Examples for the base case for the calculated distribution of tritium at 2,005 AD are shown for KFM01A, KFM02A and KFM03A (Figure 7-9 and Figure 7-10). The base case and the case with low flow wetted surface area (0.25 m^2 m^{-3}) show few differences in depth to which the modelled tritium penetrates.

Overall, tritium modelling at Forsmark shows little penetration of surface water into the rock, with a maximum of around –100 m elevation. This is contrast to modelled results from Simpevarp S1.2 where the tritium is shown to reach down to around 600 m elevation and the tritium measurements can help to calibrate an appropriate value of flow-wetted surface /15/.

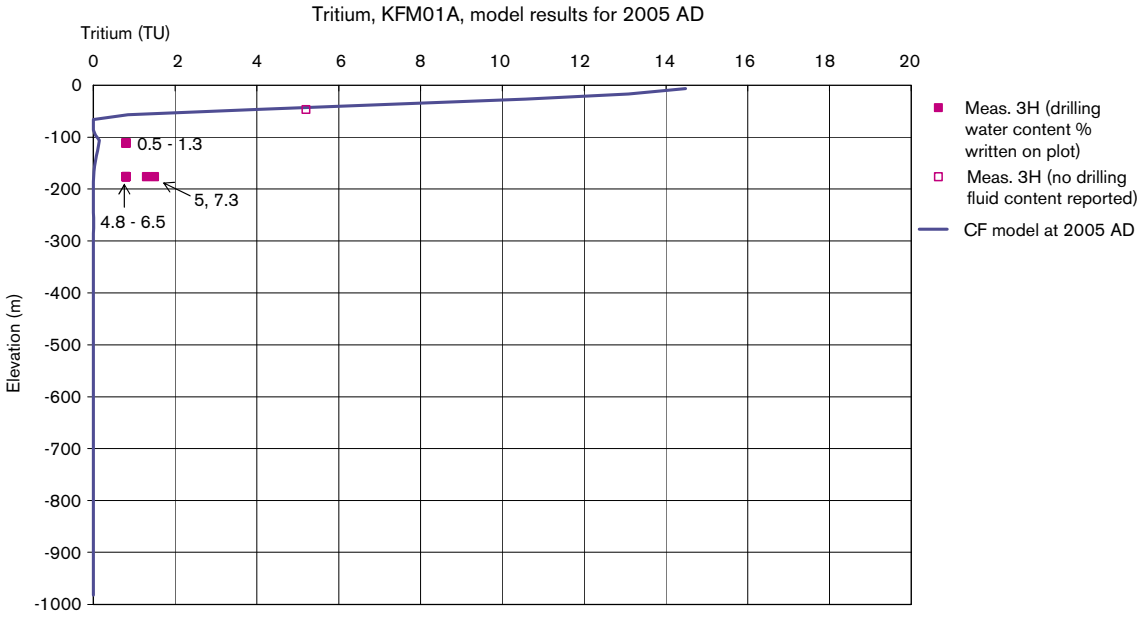

Figure 7-9. *Comparison of the calculated levels of tritium at 2,005 AD, with measurements in borehole KFM01A. The blue line represents the model results. Pink data points (filled) show measurement values, with the percentage contamination by drilling water written onto the figure next to each data point; unfilled pink data points are from earlier samples with no reported drilling water content.*

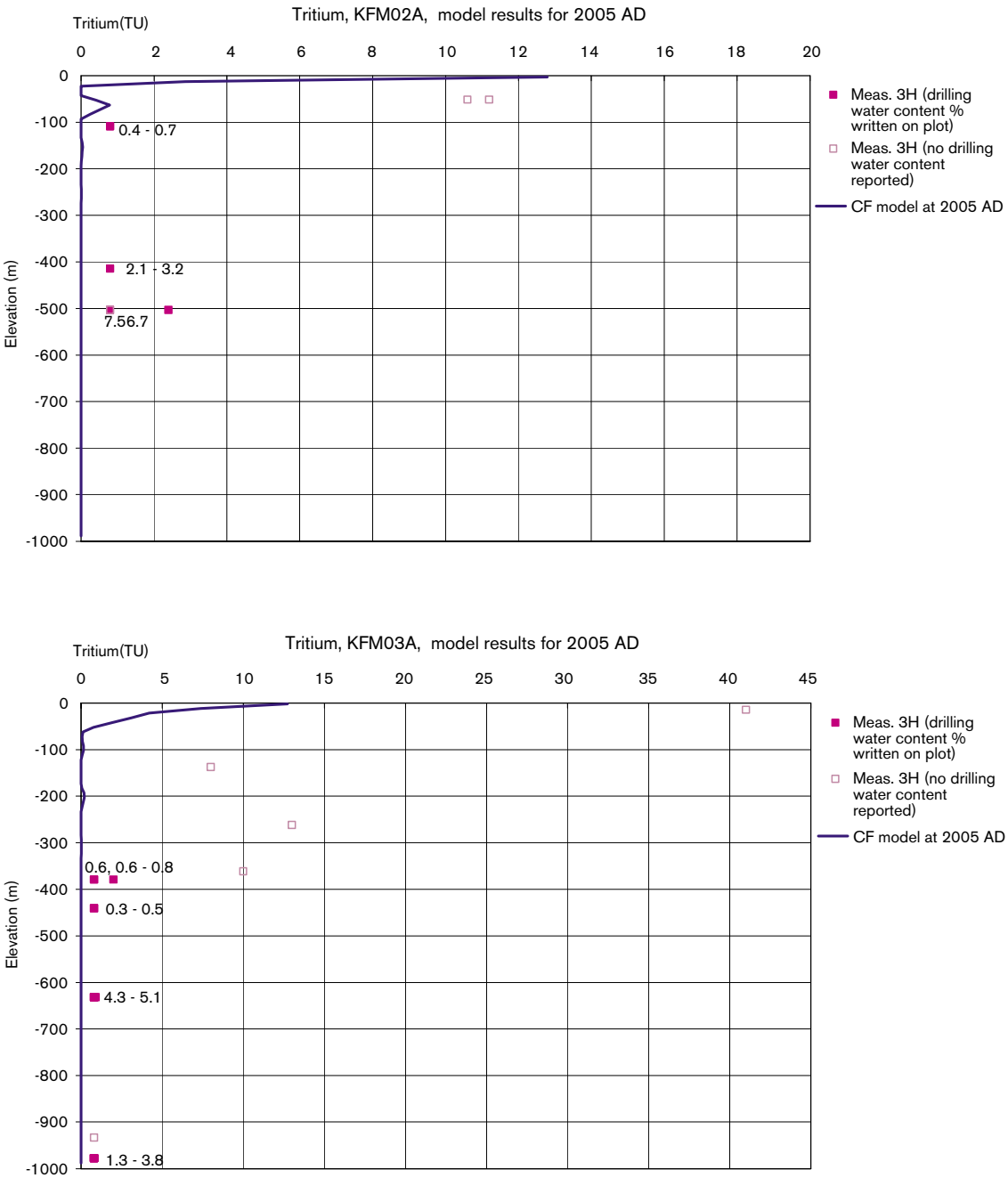

Figure 7-10. *Comparison of the calculated levels of tritium at 2,005 AD, with measurements in borehole KFM02A (top) KFM03A (bottom). The blue line represents the model results. Pink data points (filled) show measurement values, with the percentage contamination by drilling water written onto the figure next to each data point; unfilled pink data points are from earlier samples with no reported drilling water content.*

7.5 Comparison of hydraulic conductivities in boreholes

Another comparison that can be made at the boreholes is the modelled and measured hydraulic conductivity. The Hydro-DFN has been conditioned based on short interval flow measurements, i.e. the PFL anomalies or the PSS 5 m packer interval tests, but not directly to the longer interval PSS test performed for 100 m intervals that correspond to flows from several fractures or fracture zones. The EPM models represent upscaled stochastic DFN models with hydraulic properties based on either a 50 m or 100 m scale. Hence, it is

appropriate to compare the modelled hydraulic conductivity in finite-elements cut by the boreholes with the 100 m PSS intervals. The properties of the HCDs have been conditioned to these data, so one can expect is the intervals with large hydraulic conductivity to be reproduced by the model. For the lower conductivity background rock the stochastic DFN models have not been conditioned or screened based on the flow-test data and so only a broad simulation of the overall magnitude of background hydraulic conductivity can be expected.

Figure 7-11 and Figure 7-12 show the modelled and measured hydraulic conductivities for boreholes KFM01A, KFM02A, KFM03A, KFM04A, and KFM05A for the top 1,000 m of borehole. KFM01A, KFM02A and KFM03A are compared with the 100 m PSS data, while KFM04A, and KFM05A are compared with the PFL anomaly data converted to an average conductivity over 100 m intervals. Boreholes KFM01A, KFM04A and KFM05A are close together and all show exceptionally hydraulic conductivity in their lower sections. The values are often below the detection limit around 10^{-11} m s^{-1}, which is also used here for intervals with essentially no measurable flow. KFM02A and KFM03A have measurable flow even near the bottom of the boreholes at 1 km depth. The top parts of the boreholes are cased so there is no measurement for the top 100 m to compare with. In the figures the depths and thickness of DZs in the geological model are indicated since they correlate strongly with the high conductivity intervals. Note: the model uses a 50 m grid refinement throughout the area characterised by boreholes.

For KFM01A the model generally over-predicts hydraulic conductivity since ZFMNE1192 is a vertical DZ that cuts the finite-element within a few tens of metres of KFM01A and so affects the model properties, but does not actually cut the borehole in reality. Also the upscaled DFN model gives a hydraulic conductivity around 5 10^{-11} to 1 10^{-9} m s^{-1}, higher than suggested by the data. KFM02A has a lot more flow and the model predicts the measured features quite well, although again the tight intervals between 300–400 m and 600–700 m are higher in the model. KFM03A is about the best match, perhaps unsurprisingly since the Hydro-DFN is based on the PFL/PSS data for this borehole. The conductive intervals match very well, while the less conductive areas have about the correct average magnitude and variability, but not necessarily at consistent depths for this realisation. KFM04A is in good agreement for the top 500 m, but over-predicts in the tight area below 500 m. Similarly, KFM05A is good in the top 300 m, but over-predicts the very low hydraulic conductivity below ZFMNE00A2. The other DFN models give qualitatively similar results with similar mean hydraulic conductivities for the background rock. Cases based on the variant Geo-DFN give slightly more variability due to the presence of more long fractures.

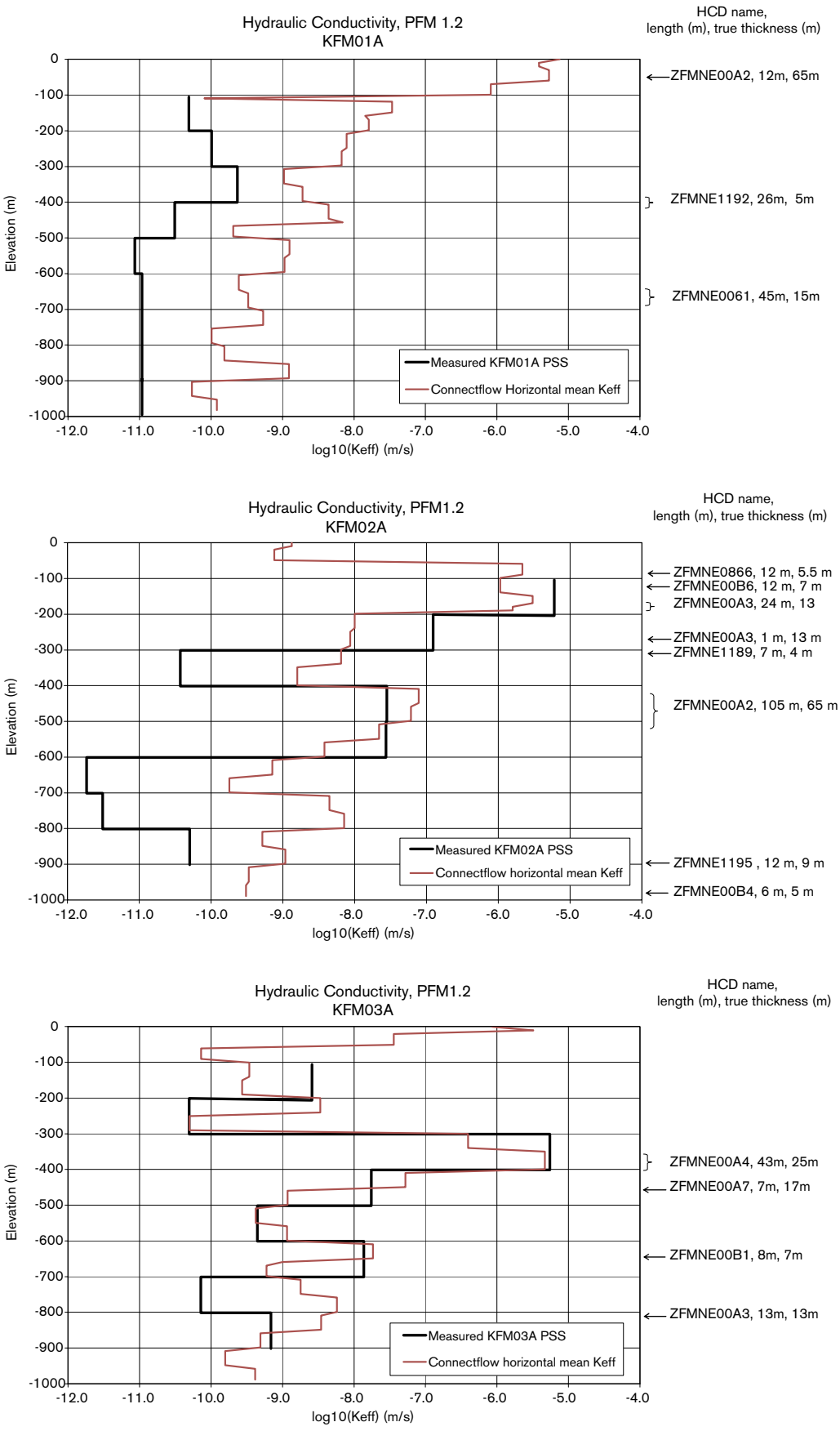

Figure 7-11. *Comparison of hydraulic conductivity in KFM01A–KFM03A for the Base Case (HCD3_BC_HRD3EC_HSD1_BC1). Values simulated in the model are shown by brown lines while the measured values in 100 m intervals are shown in black.*

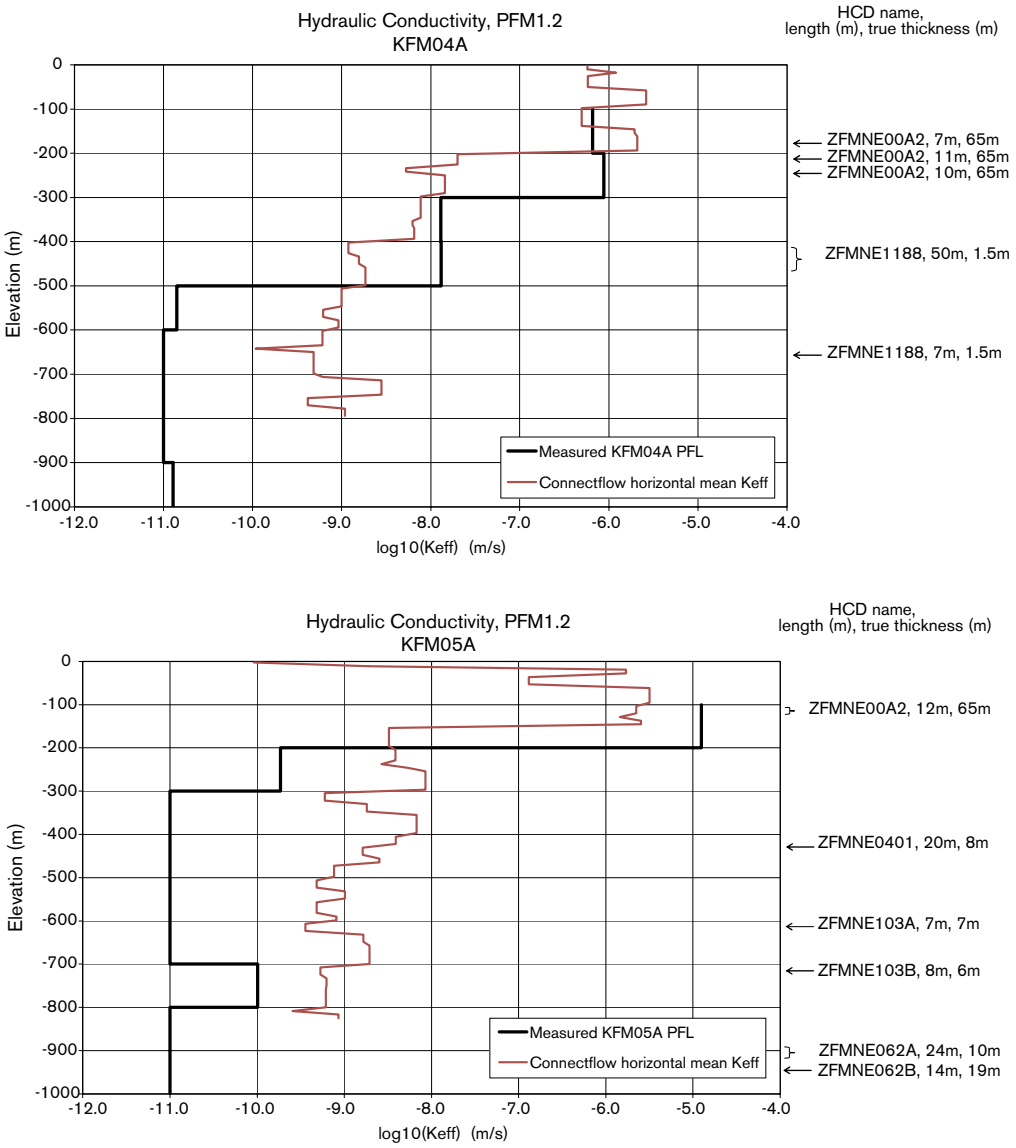

Figure 7-12. *Comparison of hydraulic conductivity in KFM04A–KFM05A for the Base Case (HCD3_BC_HRD3EC_HSD1_BC1). Values simulated in the model are shown by brown lines while the measured values in 100 m intervals are shown in black.*

7.6 Sensitivity to surface boundary conditions and properties

Surface boundary conditions and properties potentially affect flow at repository depth through their influence on the rate of infiltration of groundwater from the surface. Only a limited pair of variants was considered to scope sensitivities to surface aspects (see Table 7-2):

- **HCD3_BC_HRD3EC_HSD1_BC3:** a specified flux (non-linear recharge/discharge) condition for infiltration onshore;
- **HCD3_BC_HRD3EC_HSD2_BC1:** successive layers of high-low-high hydraulic conductivity for surface properties case HSD2;

For the variant with an alternative boundary condition for the top surface based on a specified flux or infiltration type boundary condition as described in subsection 2.6. The maximum potential infiltration on the top surface is set to 200 mm $year^{-1}$ and all other parameters are identical to the Base Case HCD3_BC_HRD3EC_HSD1_BC1. For the infiltration used and the hydraulic conductivity of the HSD layers the result was a phreatic surface close to ground surface and hence the results are expected to be similar to that for a specified head. For comparison with the Base Case the present-day profiles of $\delta^{18}O$, Cl and Mg are shown for KFM01A–KFM04A in Figure 7-13. The differences with the Base Case are generally small with only KFM01A showing only significant change. In KFM01A the spike of Marine water is higher and more pronounced due to a reduced infiltration and consequent flushing by precipitation. This leads an improved match of $\delta^{18}O$ and Cl in KFM01A. Other hydro-geochemistry in the other boreholes is far less sensitive, though the match for KFM02A is also slightly better for all three constituents.

The variant HCD3_BC_HRD3EC_HSD2_BC1 with an intermediate layer of lower conductivity in the surface domain exhibits almost no change from the Base Case as shown in Figure 7-14. Part of the purpose of this case was to investigate whether a lower conductive layer near the surface could affect the deeper hydro-geochemistry and perhaps improve the match against Cl near in the top 200 m, for example. This could motivate considering further cases such as lowering the conductivity to 10^{-7} m s^{-1} and/or coupling this with a specified flux case. Another possibility is to lower the hydraulic conductivity of the bedrock near the surface to reflect the observation that fine grained sediments has been injected into some near-surface fractures, and these could potentially inhibit flow from the surface. Further hydraulic tests such as single-hole interference tests may shed some light on the vertical communication near-surface.

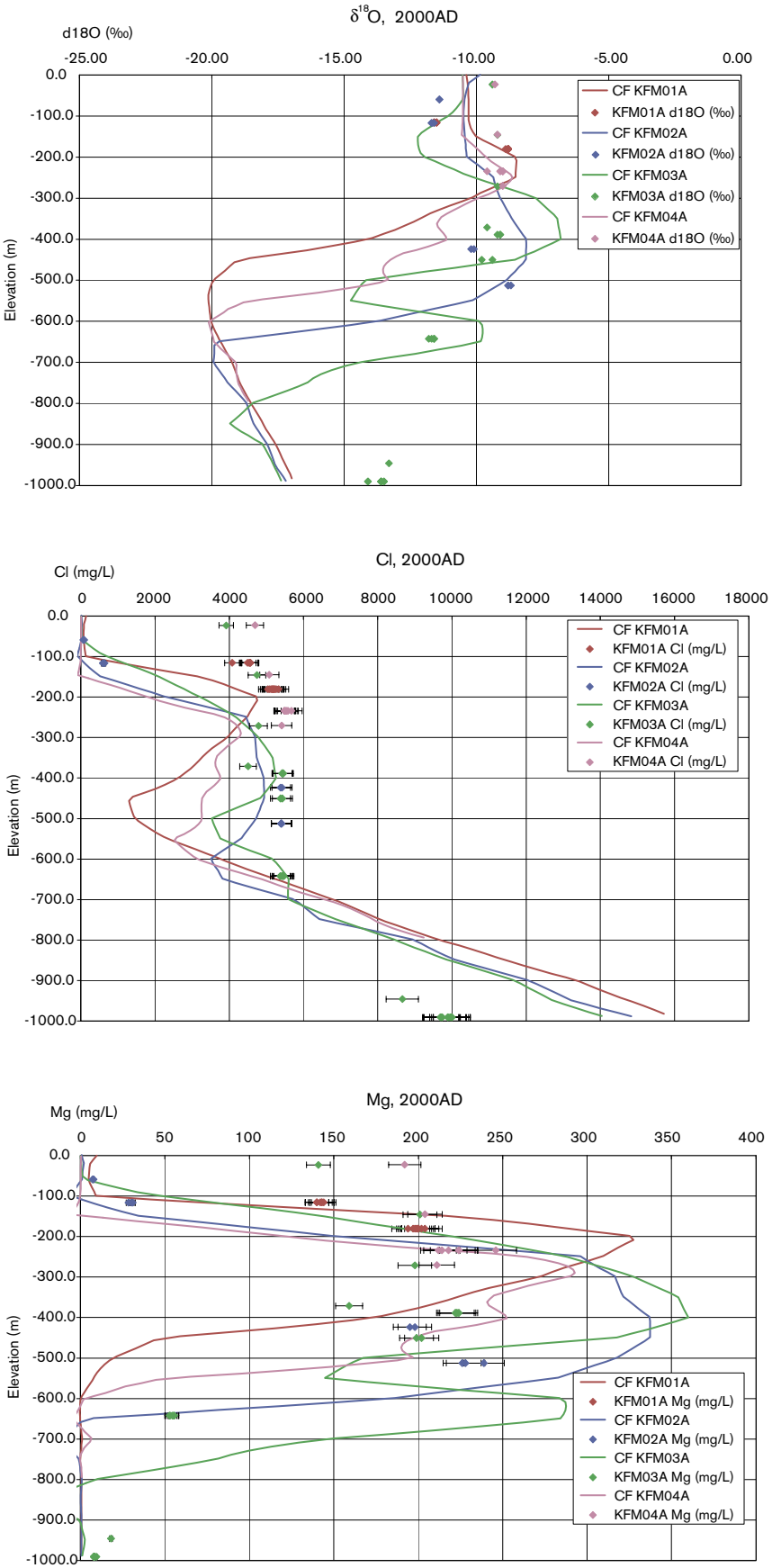

Figure 7-13. *Comparison of $\delta^{18}O$, Cl and Mg in KFM01A–KFM04A for the variant with a flux boundary condition (HCD3_BC_HRD3EC_HSD1_BC3). Values in the simulated fracture system are shown by solid lines, and the data by points.*

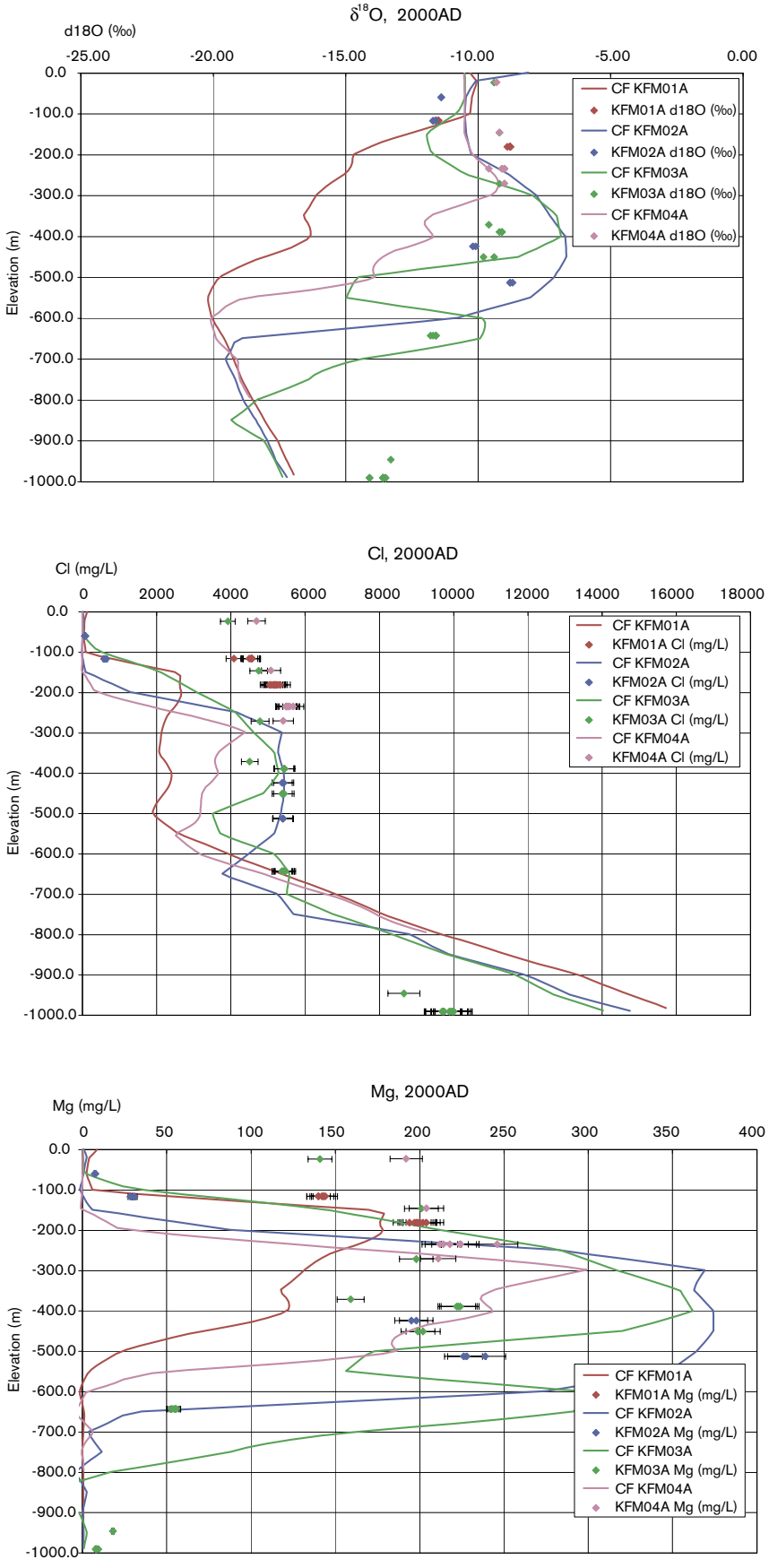

Figure 7-14. *Comparison of $\delta^{18}O$, Cl and Mg in KFM01A–KFM04A for the variant with HSD2 properties in the near-surface (HCD3_BC_HRD3EC_HSD2_BC1). Values in the simulated fracture system are shown by solid lines, and the data by points.*

7.7 Sensitivity to DFN model parameters and data interpretation

The variants that measure sensitivities to DFN model statistics, concepts and parameters include:

- **HCD3_BC_HRD3EC2_HSD1_BC1:** a second realisation of the Base Case;
- **HCD3_BC_HRD3EC3_HSD1_BC1:** a third realisation of the Base Case;
- **HCD3_BC_HRD3EU_HSD1_BC1:** an uncorrelated transmissivity model;
- **HCD3_BC_HRD3SFC_HSD1_BC1:** a realisation of the variant Geo-DFN with $k_r = 2.75$ and a correlated transmissivity model;
- **HCD3_BC_HRD3SFU_HSD1_BC1:** a realisation of the variant Geo-DFN with $k_r = 2.75$ and an uncorrelated transmissivity model.

The first two cases are intended to quantify how much affect the stochastic nature of the HRD properties has on the predicted borehole reference water profiles. The only change from the Base Case is to use a different random number seed in sampling all the DFN properties. This might be expected to give fractures in different positions in the boreholes, for example. Figure 7-15 shows the geochemical calibration constituents for Realisation 2, HCD3_BC_HRD3EC2_HSD1_BC1. Although there is a discernible difference between the two cases, all trends and features seen in the first realisation profiles area repeated for the second. The results for KFM01A and KFM04A are the most sensitive to the different realisation, showing similar sensitivities probably just because they are close together. The infiltration of Marine water is enhanced slightly in these two boreholes, which in turn displaces more Glacial water giving rise to the significant change in the simulated $\delta^{18}O$ in and KFM04A. Realisation 3, HCD3_BC_HRD3EC3_HSD1_BC1, also results in a discernible change in hydro-geochemistry with all four boreholes being affected for this case (see Figure 7-16). KFM01A shows a more pronounced spike of Marine water that leads to a better match for Cl and $\delta^{18}O$, but the model predicts more uniform infiltration of Marine water in KFM03A compared to Realisation 1, which has a more irregular profile, so Realisation 3 is worse for $\delta^{18}O$ and Mg than the Base Case. These extra realisations indicate some dependence on the stochastic nature of the EPM model, so it is interesting to consider the stochastic effect on flow-path performance measures as considered in Section 9.

The variant Hydro-DFN, HCD3_BC_HRD3EU_HSD1_BC1, with an uncorrelated transmissivity distribution has a strong impact on hydro-geochemistry as shown in Figure 7-17. The reason is that the EPM properties for this Hydro-DFN model are slightly more conductive especially around the 25- to 50-percentile as seen in Table 4-1. This was confirmed by the profiles of simulated background hydraulic conductivity in KFM01A–KFM04A. This leads a deeper penetration of the Littorina spike leading to a poorer match in KFM03A for Mg. Interestingly, the prediction of Cl in KFM01A is improved in the top 100–200 m with a slightly higher conductivity in the top 100–300 m for the uncorrelated case. This may suggest some sort of slight depth dependency, i.e. higher bedrock conductivity in the top 200 m compared to below, may improved the simulated results. The profiles are more similar between boreholes in this case since the uncorrelated transmissivity model gives more homogeneous background EPM properties.

Calibration chemical constituents for the case based on the variant Geo-DFN with a $k_r = 2.75$ and a correlated transmissivity model, HCD3_BC_HRD3SFC_HSD1_BC1, is given in Figure 7-18. Interestingly, this leads to very similar profiles to the Base Case based on the Geo-DFN. KFM01A and KFM04A have a narrower spike in Mg associated with Marine water, but we have no data to validate either simulation. This is not surprising since both Hydro-DFN models have been calibrated to the same hydraulic data, and hence share

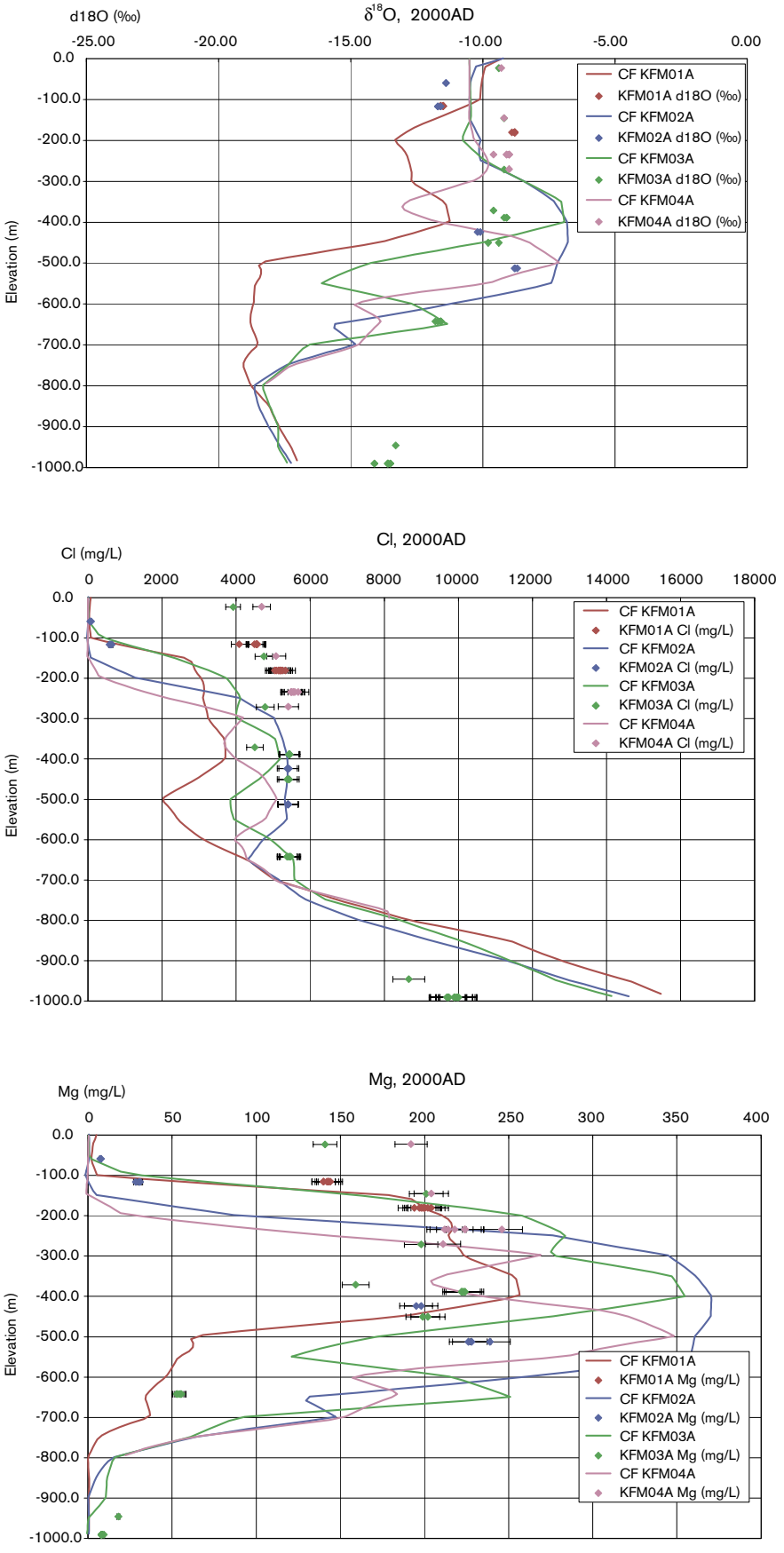

Figure 7-15. *Comparison of $\delta^{18}O$, Cl and Mg in KFM01A–KFM04A for Realisation 2 (HCD3_BC_HRD3EC2_HSD1_BC1). Values in the simulated fracture system are shown by solid lines, and the data by points.*

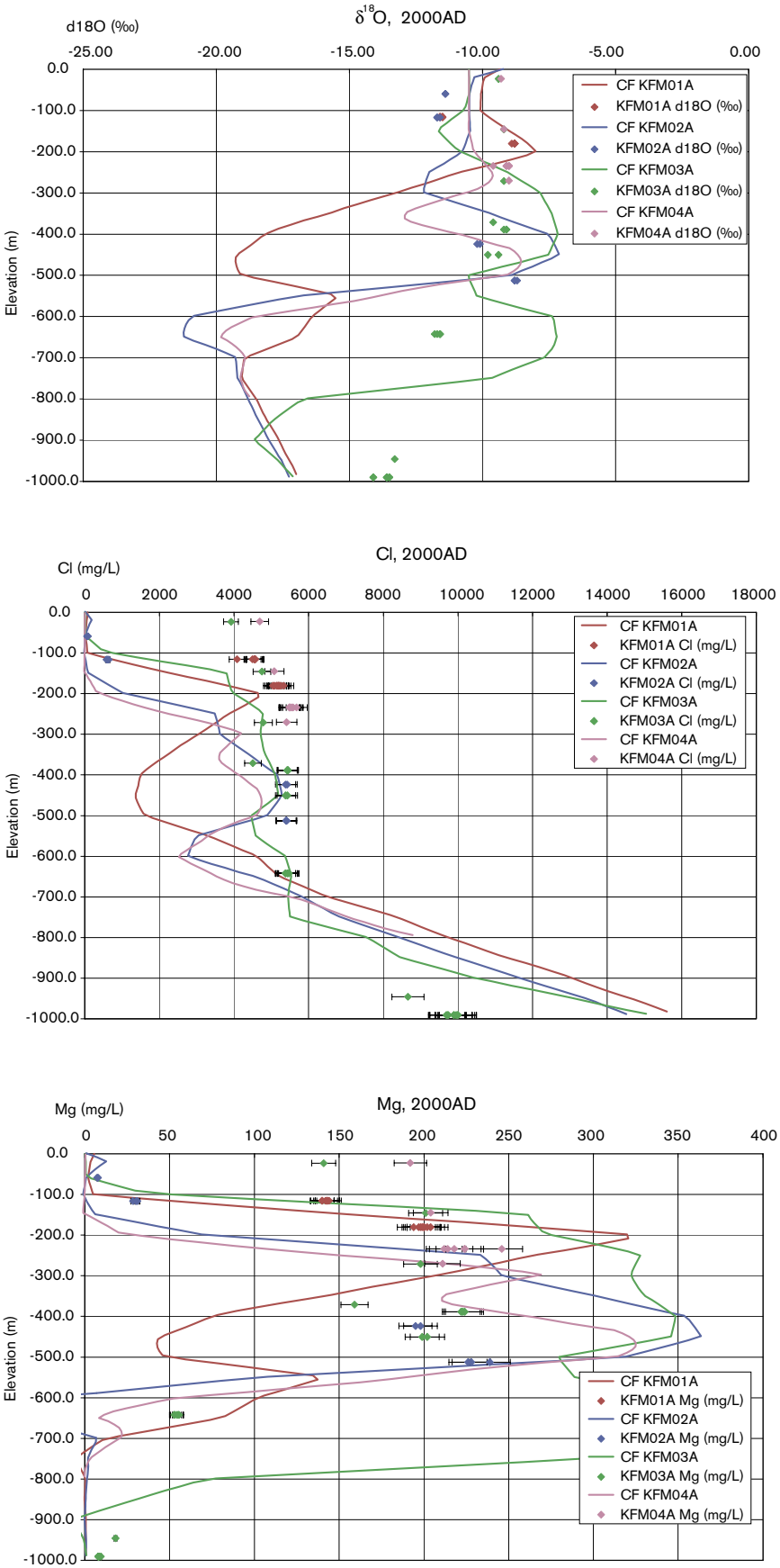

Figure 7-16. *Comparison of $\delta^{18}O$, Cl and Mg in KFM01A–KFM04A for Realisation 3 (HCD3_BC_HRD3EC3_HSD1_BC1). Values in the simulated fracture system are shown by solid lines, and the data by points.*

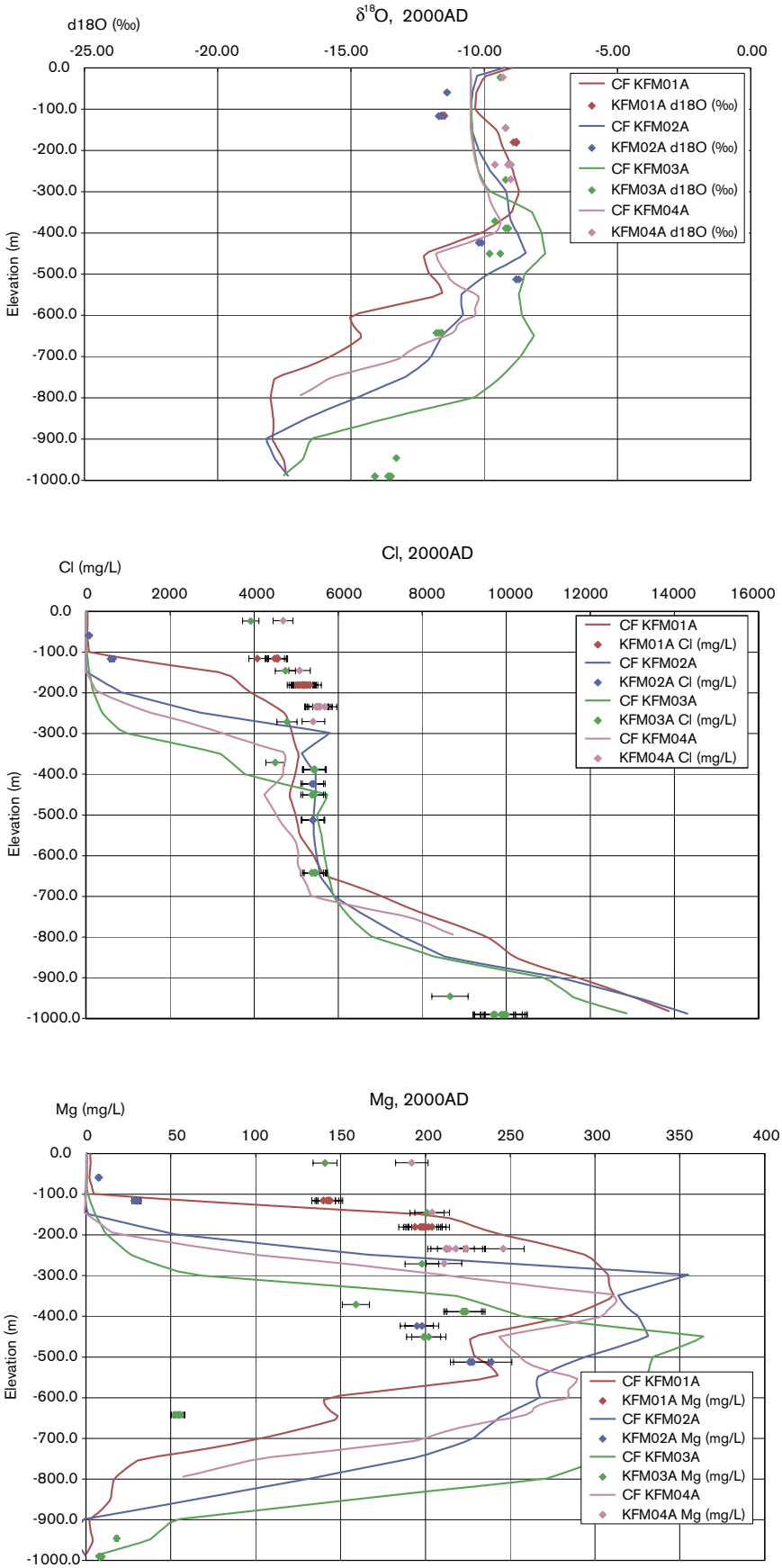

Figure 7-17. *Comparison of $\delta^{18}O$, Cl and Mg in KFM01A–KFM04A for the variant with uncorrelated T model (HCD3_BC_HRD3EU_HSD1_BC1). Values in the simulated fracture system are shown by solid lines, and the data by points.*

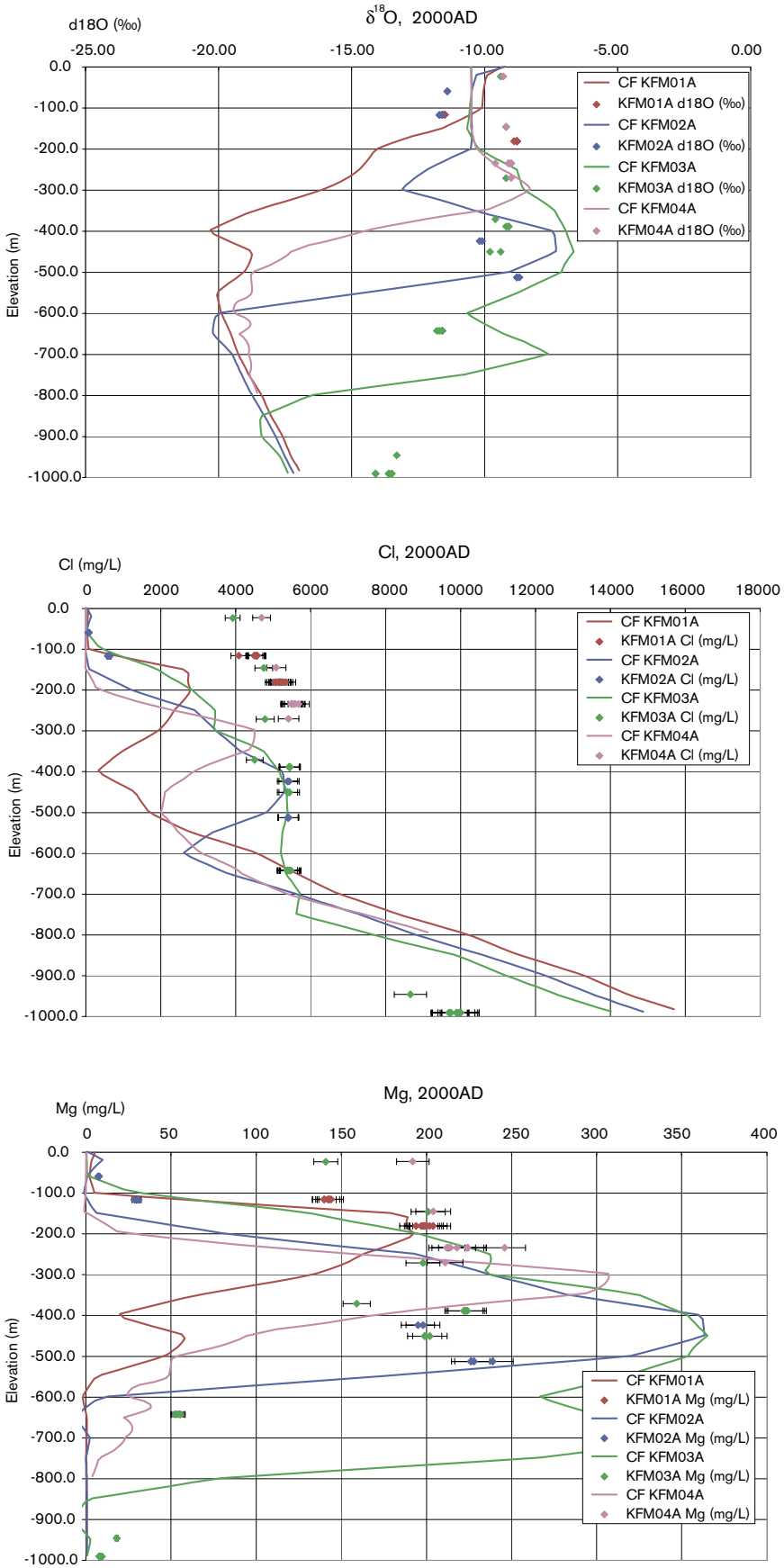

Figure 7-18. *Comparison of $\delta^{18}O$, Cl and Mg in KFM01A–KFM04A for the Geo-DFN with correlated T model (HCD3_BC_HRD3SFC_HSD1_BC1). Values in the simulated fracture system are shown by solid lines, and the data by points.*

similar overall properties. There is also more Mg and hence Marine in KFM03A, which is less consistent with the data. Still, the sparsity of hydro-geochemistry data makes it difficult to discern between either of the cases. Again, the comparison of flow-path performance measures for the variant Geo-DFN is of interest in Section 9.

Figure 7-19 shows the comparison for the variant Geo-DFN with an uncorrelated transmissivity model, HCD3_BC_HRD3SFC_HSD1_BC1, which shows a lot of similarity to the case based on the Geo-DFN with an uncorrelated transmissivity, HCD3_BC_HRD3SFU_HSD1_BC1. Hence, the model is more sensitive to the transmissivity model than the length distribution parameter k_r.

7.8 Sensitivity to HRD hydraulic and transport properties

The variants of the HRD hydraulic and transport parameters include:

- **HCD3_BC_HRD3ECK1_HSD1_BC1:** increased background conductivity outside RFM-017/029;
- **HCD3_BC_HRD3ECF1_HSD1_BC1:** reduced flow wetted surface;
- **HCD3_BC_HRD3ECN1_HSD1_BC1:** reduced matrix porosity;
- **HCD3_BC_HRD3ECD1_HSD1_BC1:** reduced diffusivity.

The reasons behind looking at the sensitivity to the hydraulic conductivity outside RFM017/029 are partly because there are few direct hydraulic data for this region, and to investigate a higher conductivity upstream could give rise to greater advection through the candidate area, if only through the DZs. The case HCD3_BC_HRD3ECK1_HSD1_BC1 has a hydraulic conductivity six times higher outside RFM017/029 at the base and ten times higher in the top 100 m giving the results shown in Figure 7-20. The constituent profiles show very little difference in any of the boreholes, only KFM01A and KFM04A show a perceptible change. This leads us to conclude that the properties outside the tectonic lens have little effect on flow and transport inside, i.e. the flow system is quite localised. The transport pathway study in Section 9 investigates whether pathlines enter and are affected by the downstream area outside of the tectonic lens.

The transport parameters of greatest interest are those that affect RMD since they affect retardation of radionuclides in groundwater flow. The timescales associated with the infiltration of surface groundwaters into the deep rock by natural transient processes are long enough, many thousands of years, to allow RMD. Hence, modelling transport and RMD of the reference waters can be a useful analogue for RMD of radionuclides. For safety assessment calculations the F-quotient is a useful concept since it allows retardation of radionuclide transport by sorption or RMD to be estimated. The formula used appropriate to an EPM is

$$F = \sum_{l} \frac{a_r \delta l}{q}$$ (see subsection 2.7),

and hence the unknown hydraulic parameter is a_r, or the flow-wetted surface. Conceptually, this equates to the fracture surface area (both faces of the fracture plane) of the connected network per unit volume of rock or twice $P32_c$. Due to the poor connectivity of the Hydro-DFN model, $P32_c$ is likely to be spatial variable and hence uncertain. From the Hydro-DFN parameterisation Table B–24 and Table B–25 suggested P32 values of 0.5–0.9 m^2m^{-3}. To be conservative though, slightly lower values of a_r = 1.0 and 0.25 m^2m^{-3} were considered to give an indication of the sensitivity. Yet smaller values could be realized, especially in

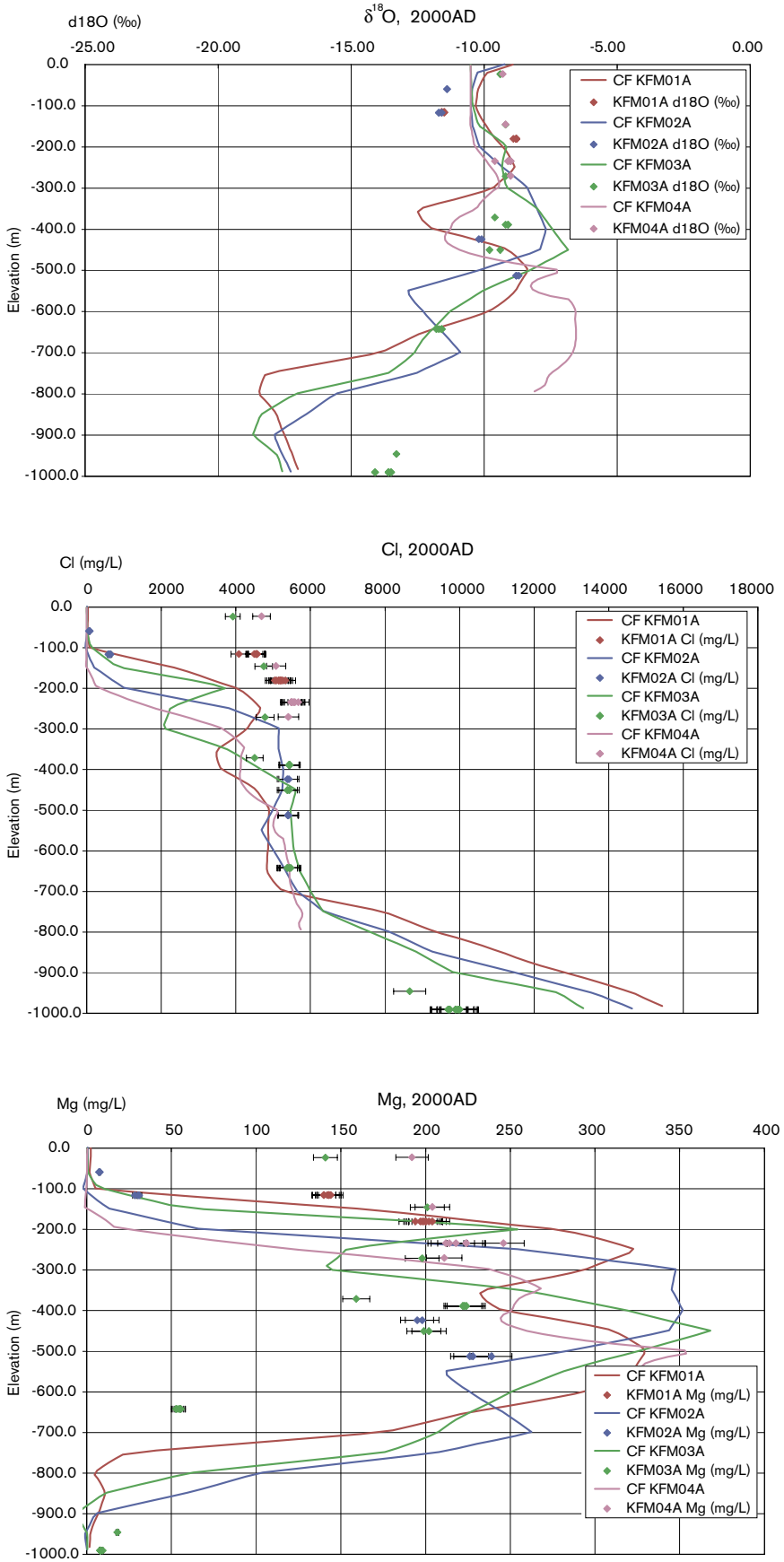

Figure 7-19. *Comparison of $\delta^{18}O$, Cl and Mg in KFM01A–KFM04A for the variant Geo-DFN with uncorrelated T model (HCD3_BC_HRD3SFU_HSD1_BC1). Values in the simulated fracture system are shown by solid lines, and the data by points.*

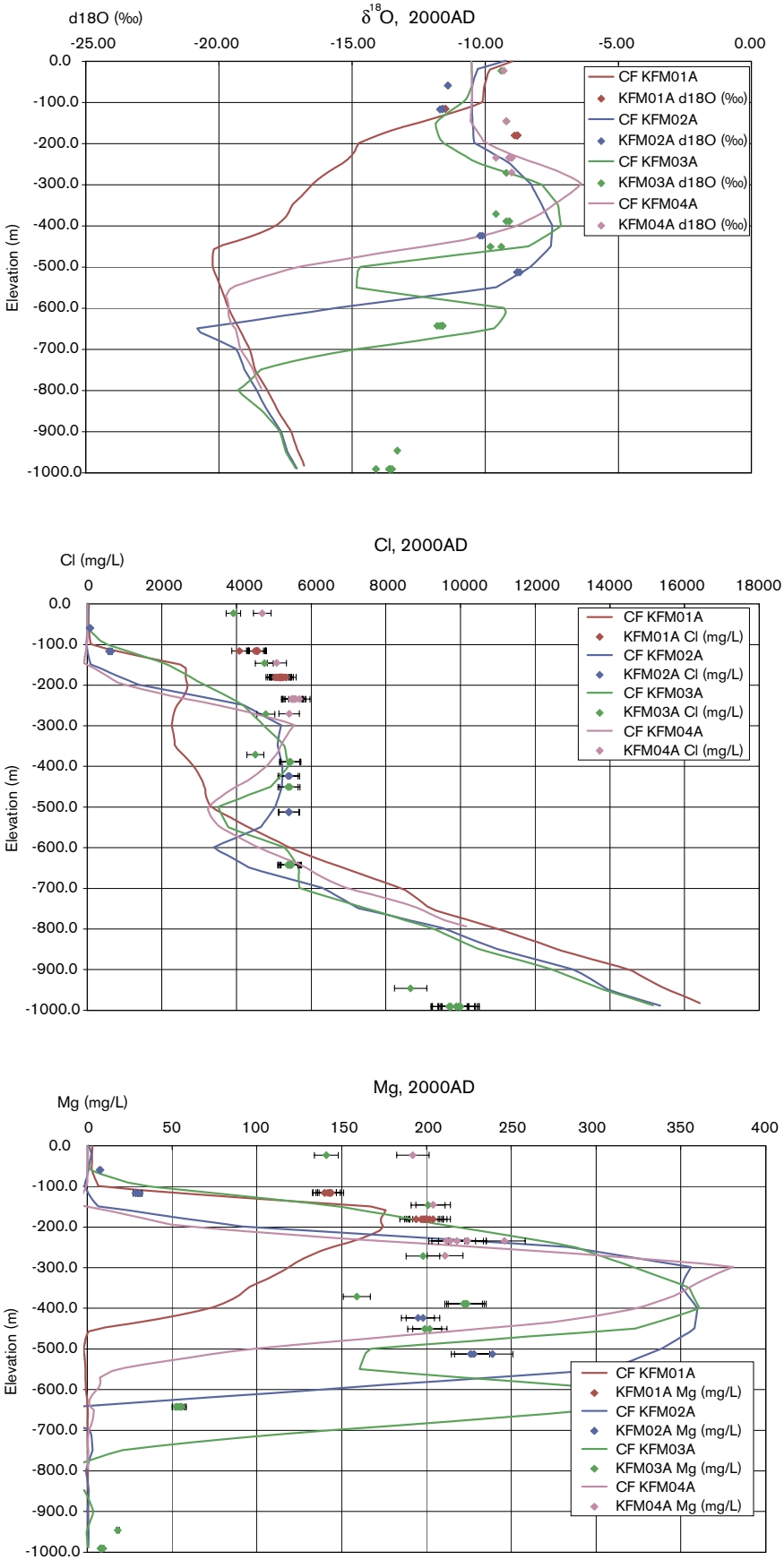

Figure 7-20. *Comparison of $\delta^{18}O$, Cl and Mg in KFM01A–KFM04A for the variant with higher K outside RFM017/029 (HCD3_BC_HRD3ECK1_HSD1_BC1). Values in the simulated fracture system are shown by solid lines, and the data by points.*

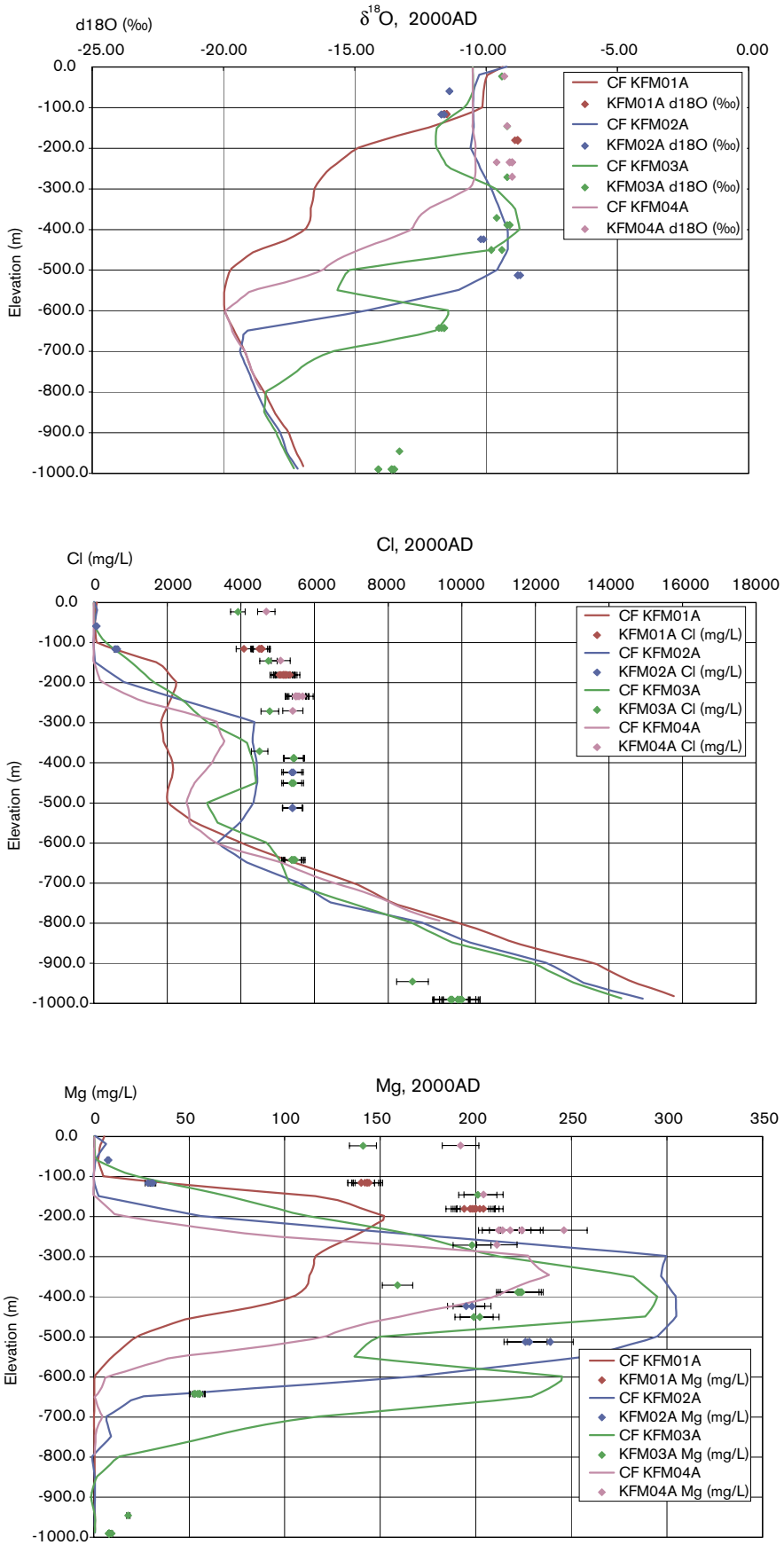

Figure 7-21. *Comparison of $\delta^{18}O$, Cl and Mg in KFM01A–KFM04A for the variant with a_r = 0.25 m^2m^{-3} (HCD3_BC_HRD3ECF1_HSD1_BC1). Values in the simulated fracture system are shown by solid lines, and the data by points.*

the very tight area around KFM01A. For the variant HCD3_BC_HRD3ECF1_HSD1_BC1 the value of a_r 0.25 m^2m^{-3} was set in the HCD and HRD. When considering the reference water profiles (not shown here) for this case it was clear that for a lower a_r there is a clear lag between constituent concentrations in the matrix system compare to the fractures in the vicinity of the surface where things are changing most rapidly. Figure 7-21 shows the constituent profiles for this case. The changes are slight, but there is a reduced penetration of Marine water in KFM02A and KFM03A. All that can be concluded is that the reduction in a_r means that Marine water is transported to slightly different places by the DZs. This case is expected to give rise to lower F-quotient values as it scales with a_r. Early scoping studies suggested that lower matrix porosity could have a strong influence on the groundwater chemistry since it controls the capacity fro RMD. In the scoping studies a very low value of $n_m = 1.0\ 10^{-3}$ was used, but this proved to be outside the measured range, which indicated a minimum of $2.5\ 10^{-3}$ and hence the variant HCD3_BC_HRD3ECN1_HSD1_BC1 used this value to see if such a small change could affect transport. Figure 7-22 suggests that within the parameter uncertainty associated with matrix porosity, transport is not significantly affected. Diffusivity of water into the matrix was also investigated by lower the value by a factor 5 in variant HCD3_BC_HRD3ECD1_HSD1_BC1, but again Figure 7-23 points to the results being insensitive to diffusivity also.

7.9 Sensitivity to geological model

During the initial scoping calculations it was found the simulations of present-day hydro-geochemistry was sensitive to changes in HCD properties associated with the Base Case geological model, but the changes considered were all localised to the candidate area and DZs that intersected the boreholes in particular, such as ZFMNE00A2. Beyond these local issues there is the question of whether the intensity and spatial distribution of DZs outside the Singö DZ and Eckarfjärden DZ has an effect on flow within the candidate area. This was the reason for considering three alternative interpretations of the geological model as described in subsection 5.7. Here, we only considered the Alternative Case (AC) geological model since it is the most different to the Base Case (BC). The DT Team made several simulations complimentary to this study considering aspects such as the sensitivity to stochastic sub-horizontal zones outside the Singö and Eckarfjärden DZs and varying the location of lineaments.

The variants considered here are:

- **HCD3_AC_HRD3EC_HSD1_BC1:** based on AC geological model;
- **HCD3_AC_HRD3EC_HSD1_BC1:** based AC geological mode and lower matrix porosity.

It is important to note that within the candidate area the AC geological model is identical to the BC geological model and in the simulations we have used exactly the same prescription for hydraulic and transport properties HCD3. The calibration chemical constituents shown in Figure 7-24 once again indicates very limited sensitivity to these seemingly large changes to the regional hydraulic properties, which confirms the findings of earlier variants that the hydro-geochemistry in the candidate area is insensitive to properties outside RFM017/029 as the flow here is quite localised. Still, it is important to consider this case for the transport pathway study in Section 9. For this case, matrix porosity has slightly more of an effect than in the Base Case, as shown in Figure 7-25, with a slightly greater Littorina pulse in KFM01A and KFM04A that leads to a small improvement in the match.

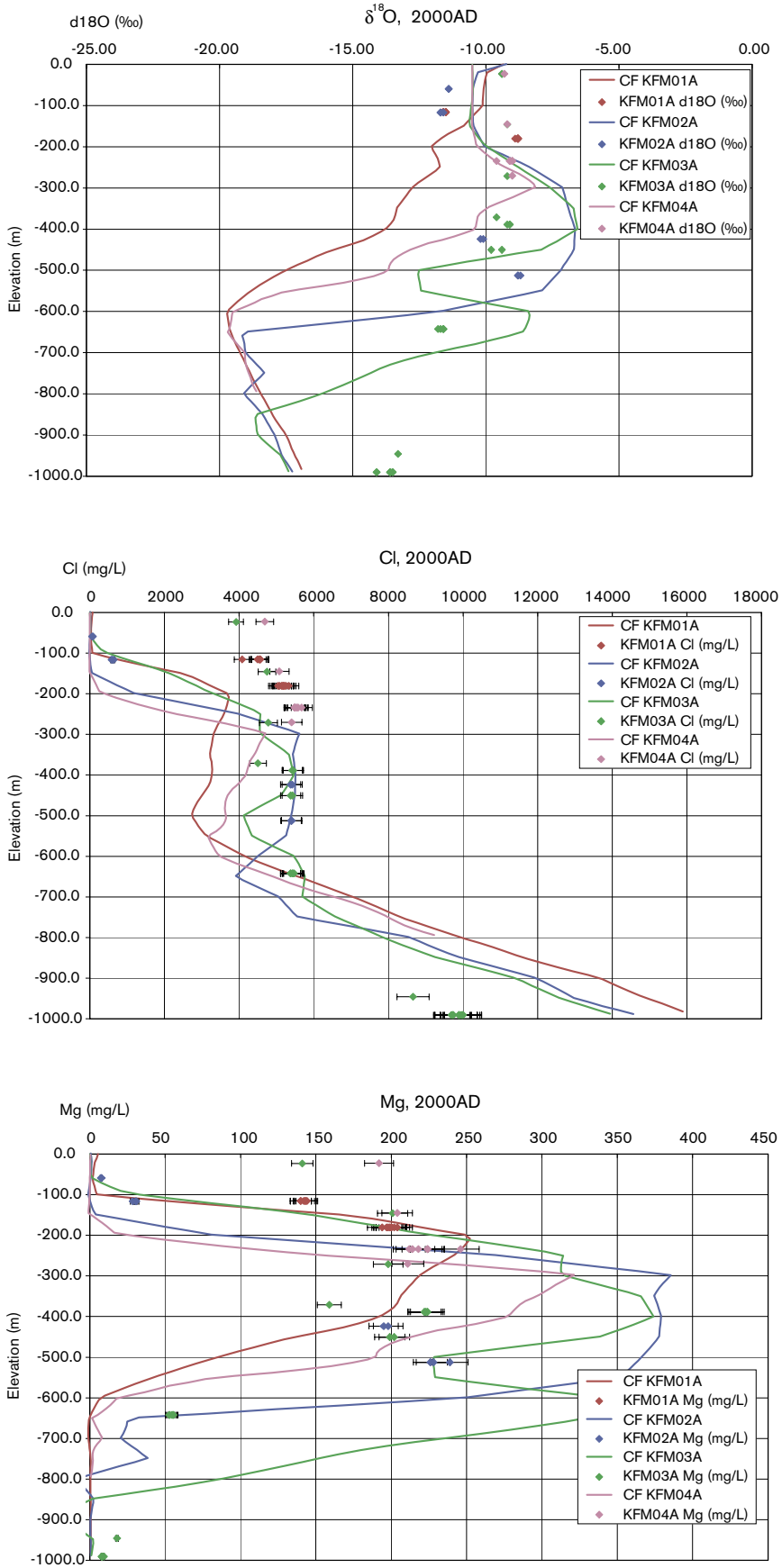

Figure 7-22. *Comparison of $\delta^{18}O$, Cl and Mg in KFM01A–KFM04A for the variant with $n_m = 2.5\ 10^{-3}$ (HCD3_BC_HRD3ECN1_HSD1_BC1). Values in the simulated fracture system are shown by solid lines, and the data by points.*

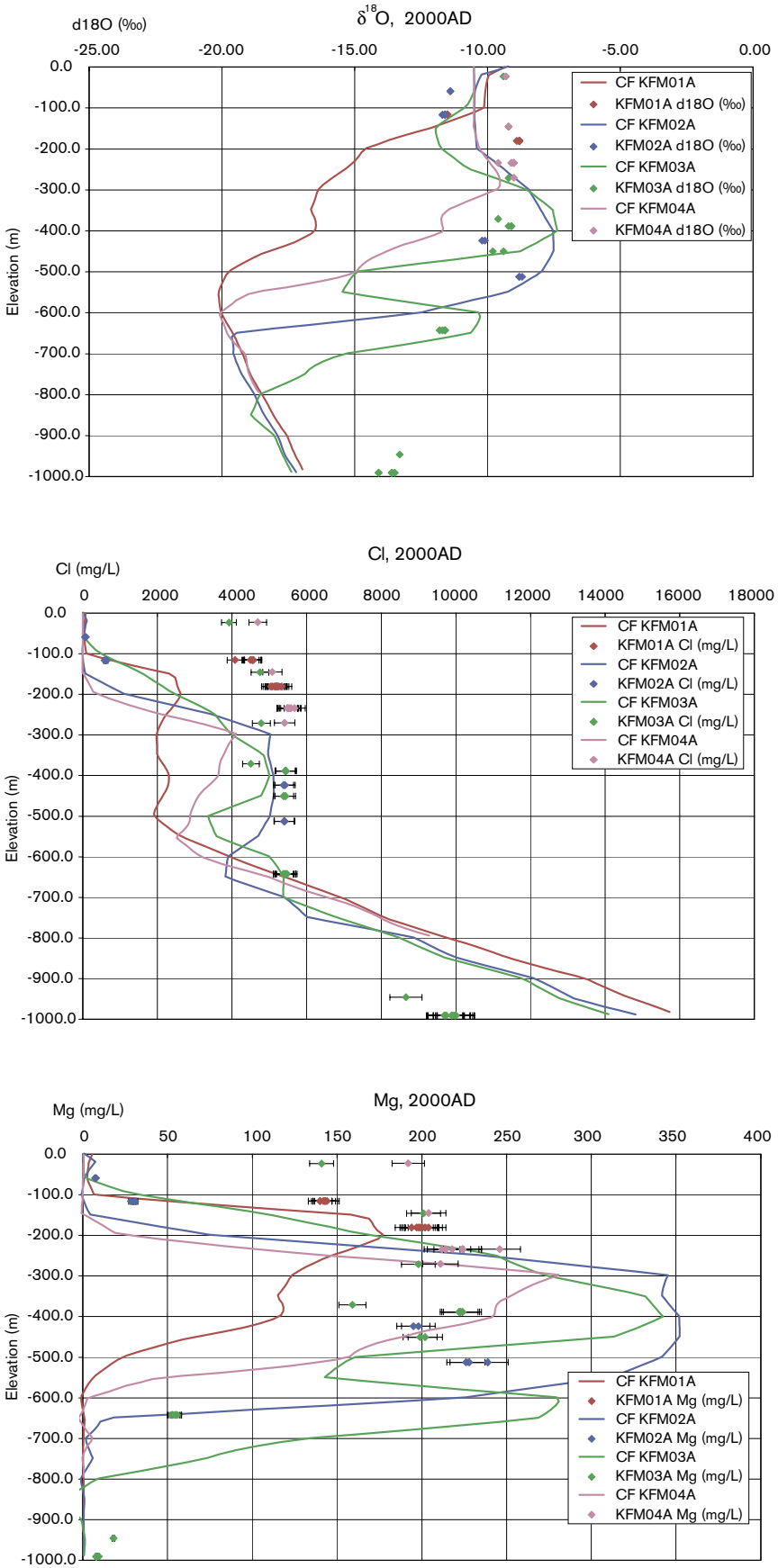

Figure 7-23. *Comparison of $\delta^{18}O$, Cl and Mg in KFM01A–KFM04A for the variant with $D_i = 1.0\ 10^{-13}\ m^2s^{-1}$ (HCD3_BC_HRD3ECD1_HSD1_BC1). Values in the simulated fracture system are shown by solid lines, and the data by points.*

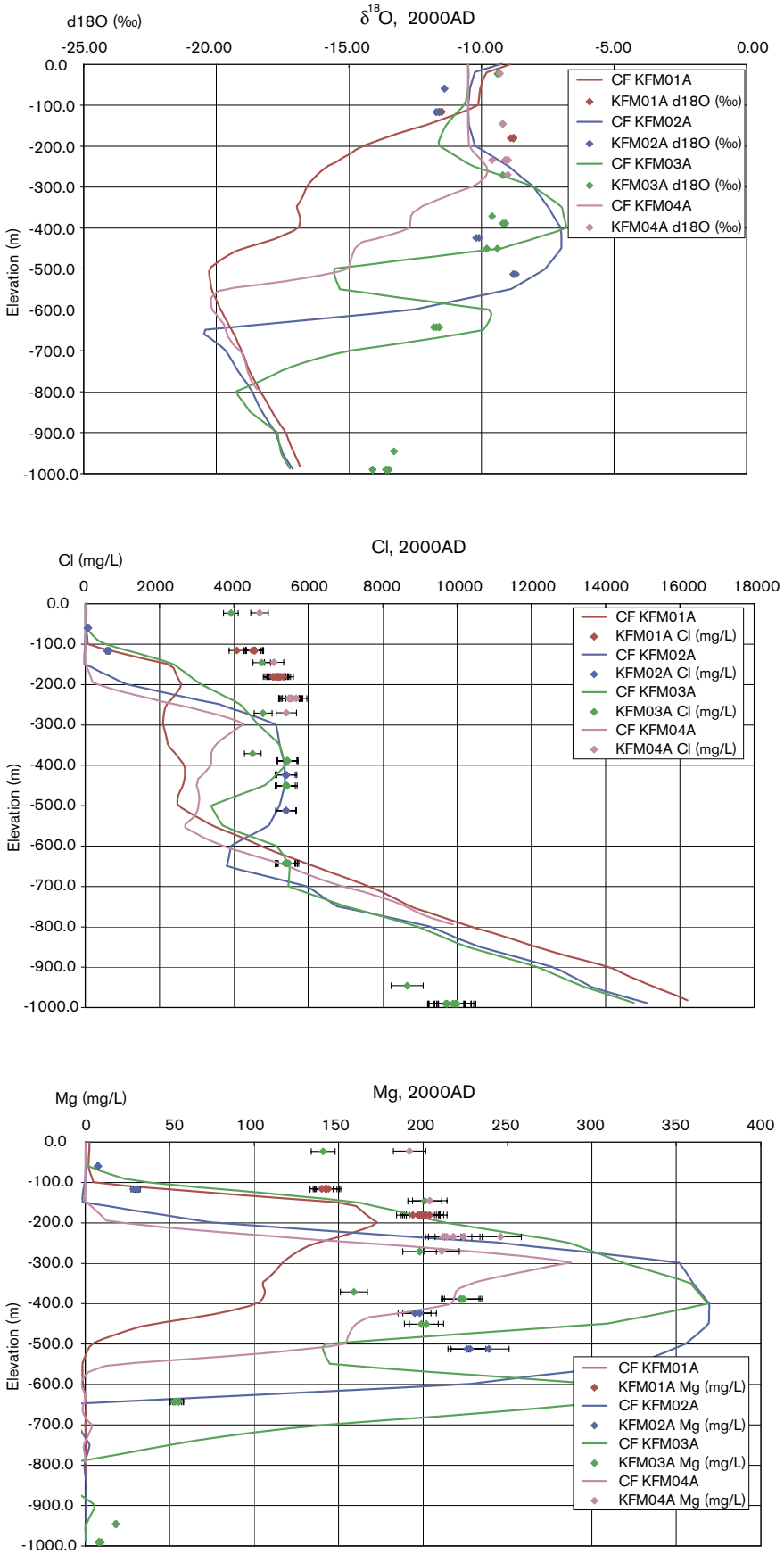

Figure 7-24. *Comparison of $\delta^{18}O$, Cl and Mg in KFM01A–KFM04A for the variant with the alternative case (AC) HCD model (HCD3_AC_HRD3EC_HSD1_BC1). Values in the simulated fracture system are shown by solid lines, and the data by points.*

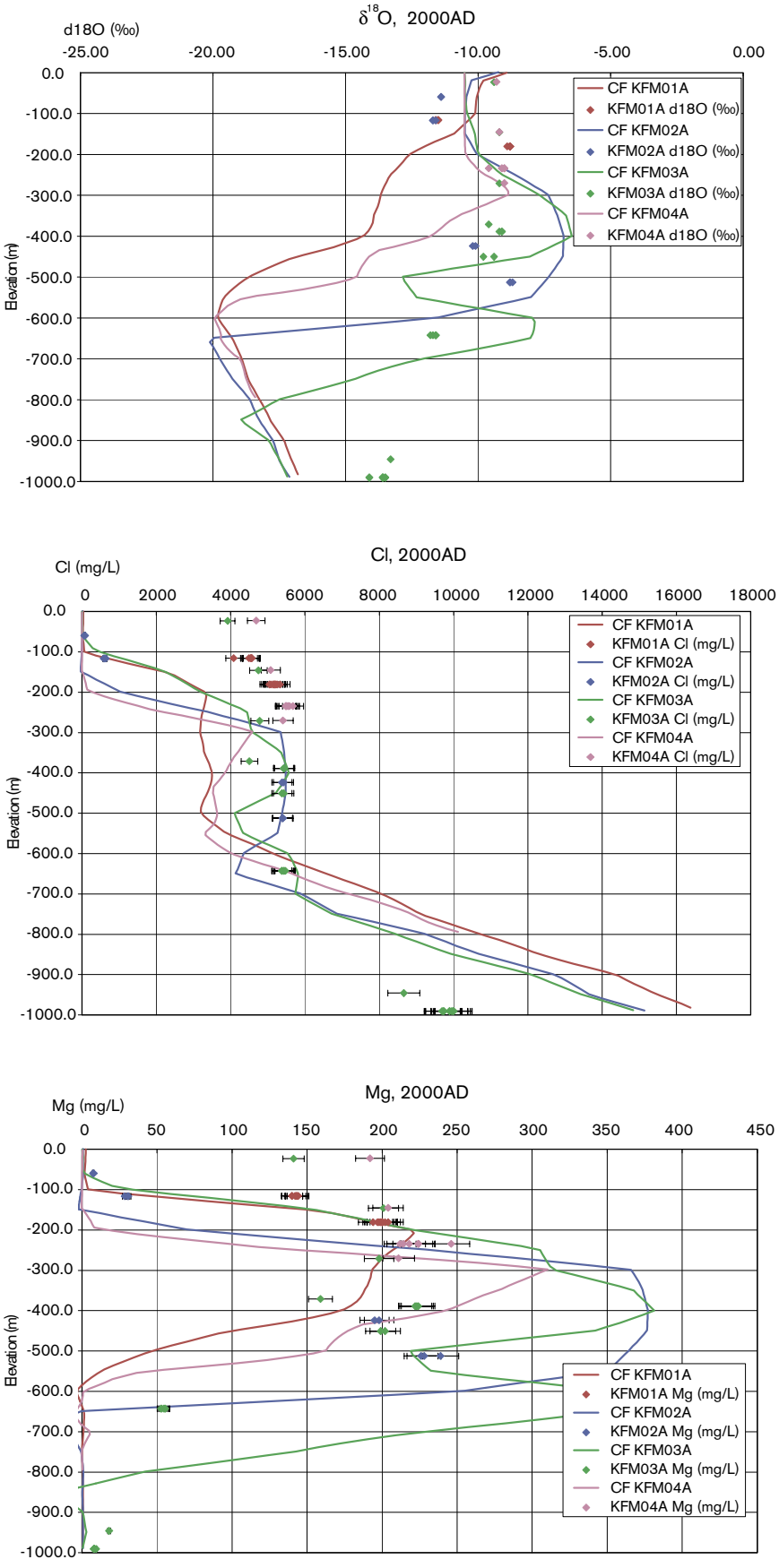

Figure 7-25. *Comparison of $\delta^{18}O$, Cl and Mg in KFM01A–KFM04A for the variant with AC HCD model and lower n_m (HCD3_AC_HRD3ECN1_HSD1_BC1). Values in the simulated fracture system are shown by solid lines, and the data by points.*

7.10 Summary of modelled cases and main monclusions from each case

An overview of the main conclusions from each of the variants presented in Section 7 is given in Table 7-3.

Table 7-3. Summary of the main conclusions for model cases. The cases are grouped by colour coding according to the sensitivities they quantify: model size (brown); initial and boundary conditions (green); DFN parameters (blue); HRD and HCD hydraulic properties (purple); Transport properties (yellow).

EPM case	Conclusions
HCD3_BC_HRD3EC_HSD1_BC1	Base Case resulting from calibration on reference waters and constituents. Hydraulic parameters for HCD and initial conditions identified for reasonable match.
HCD3_BC_HRD3EC_HSD1_BC3	Small differences mainly in KFM01A where the Littorina pulse is slightly higher giving a marginally better match.
HCD3_BC_HRD3EC_HSD2_BC1	No change in constituent profiles. Motivates trying modifications of the bedrock near the surface or a slight depth dependency in the HRD, and single-hole interference tests in top 100–200 m.
HCD3_BC_HRD3EC2_HSD1_BC1	There is a moderate stochastic effect from the HRD, but all no general change in the constituent profiles. KFM01A and KFM04A most sensitive having more Marine water.
HCD3_BC_HRD3EC3_HSD1_BC1	There is a moderate stochastic effect from the HRD. All four boreholes affected slightly. Worse match than Realisation 1.
HCD3_BC_HRD3EU_HSD1_BC1	Strong impact on constituents due to the EPM model having a slightly higher and homogeneous K for the uncorrelated T model. Deeper penetration of Littorina pulse. Indirectly suggests that a slight depth trend in K could improve KFM01A.
HCD3_BC_HRD3SFC_HSD1_BC1	Change in fracture length distribution with k_r = 2.75 does not impact constituent profiles, due to similar block-scale K.
HCD3_BC_HRD3SFU_HSD1_BC1	Much similarity to Base case with uncorrelated T model. Hence, more sensitive to T model than k_r.
HCD3_BC_HRD3ECK1_HSD1_BC1	Chemistry profiles in candidate area insensitive to hydraulic properties outside of RFM017/029. Suggests localised flow cells controlled by properties of local HCD and HRD.
HCD3_BC_HRD3ECF1_HSD1_BC1	Lower a_r = 0.25 m^2m^{-3} leads to a lag between fracture and matrix compositions, but not a large effect on the constituents below the surface as the timescales are large. KFM02A and KFM03A affected most.
HCD3_BC_HRD3ECN1_HSD1_BC1	Matrix porosity potential has a significant effect on transport, but not for the range of values measured at Forsmark 3–6 10^{-3}.
HCD3_BC_HRD3ECD1_HSD1_BC1	RMD is relatively insensitive to diffusivity unless it is reduced by an order of magnitude.
HCD3_AC_HRD3EC_HSD1_BC1	The alternative geological model with many lineaments outside the tectonic lens does not have a strong influence on the hydro-geochemistry inside. Hence, cannot calibrate the geological model outside lens based on chemistry in candidate area.
HCD3_AC_HRD3ECN1_HSD1_BC1	Matrix porosity affects the AC slightly more, but still not significant.

7.11 Conclusions on suitable hydraulic parameter representation with uncertainties

In deriving the Base Case, the parameters selected should not be considered as the only possibility for obtaining a match to the hydro-geochemistry data. Many other combinations of parameters may give a match since the data are relatively sparse, especially below 500 m depth. Hence, in Table 7-4 a summary is given of the parameters used to obtain a global calibration to the data, along with an estimate as to the range of the alternative parameters that might also result in a calibrated model. It would be useful to explore this parameter space more extensively in future modelling exercises to verify these estimates of uncertainty.

Table 7-4. Summary of hydraulic parameters and conditions used in calibration of Base Case model with an indication of the possible range of alternative parameters that may also give a match to the borehole hydro-geochemistry.

Parameter	**Calibration value**	**Range**
Model domain	Regional model – about 15 km (SW-NE)×11 km (NW-SE) is the minimum	Smaller models may give very similar results in the candidate area
Grid resolution	50 m necessary in site-scale	100 m sufficient on regional-scale
Initial condition	Full Glacial 0–500 m; then linear gradient to no Glacial, full Brine at –2,000 m; full Brine below –2,000 m	Full Brine could be even deeper: a linear profile suggests –2,700 m
Top surface flow BC	Topography	Specified infiltration 200 mm/y gives similar results for HSD1
Top surface waters	Ancylus Ice Lake (Glacial), Littorina Sea (Marine), Baltic Sea/Precipitation with land-rise (Marine diluting with Rain 1960);	Onshore – Ice Lakes could be mixture of Brine and Rain 1960. Offshore, Littorina could occur at slightly different time or strength
Hydro-DFN HRD K	Calibrated on short interval PSS and PFL data This had block-scale properties of $K_{50\%}$~ 4 10^{-10} m s^{-1}, $K_{10\%}$ = 1 10^{-11} m s^{-1}	All conditioned Hydro-DFN models are calibrated to hydro-testing, but the model is sensitive to changing K by a factor 10 or more
Depth dependence	None	2–10 higher K in top 100–200 m and/or 2–10 lower K below may improve calibration.
Kinematic HRD porosity n_e	Based on DFN value, Section 4.4, $e_t = 0.5T^{0.5}$	Fairly insensitive. Can increase by factor 10
Matrix porosity n_m	4 10^{-3}	2.5–6 10^{-3}
Geological model	BC	AC case and VC equally likely based on calibration possible here
HCD hydraulic properties	HCD3 = depth dependency but with local conditioning to PSS 100 m data	Consider different depth trend (less conservative) for gently dipping
Kinematic HCD porosity n_e	$n_e = 0.5T^{0.5}$	$n_e = 0.5T^{0.5}$ or $n_e = 0.5T^{0.5}/b$, where b is thickness
FWS, a_r, for RMD	1.0 m^2m^{-3}	0.25–2.0 m^2m^{-3}
Matrix diffusion length L_D	1.0 m	1–4 m
Intrinsic diffusion coefficient into matrix, D_e	5 10^{-13} m^2s^{-1}	1–5 10^{-13} m^2s^{-1}

7.11.1 Initial and boundary conditions

The initial and boundary conditions specified in Table 7-4 suggest the following:

- Glacial water injected under high pressures down to about 500 m–2.0 km during early post-glacial period;
- Large Glacial water composition in early freshwater in the Ancylus Lake period;
- A specified topographic head or specified infiltration give similar results for a maximum potential infiltration of 200 mm y^{-1} and the HSD properties considered.

7.11.2 HCD, HRD, HSD properties

Based on the variants considered and the calibration against reference water mixing the following observations is made:

- The Hydro-DFN properties give block-scale hydraulic conductivities of the correct order of magnitude to predict hydro-geochemistry. The uncorrelated T model suggests higher values do not give a match. Relaxing the minimum hydraulic conductivity to $1\ 10^{-11}$ m s^{-1} may improve the match though it may affect the numerics;
- DZs outside the tectonic lens do not affect hydro-geochemistry local to the site boreholes;
- The properties of DZs near the borehole have the strongest controls on the measured hydro-geochemistry and hence the properties of the HCD can be constrained using these measurements together with the hydraulic data;
- This motivates investigating more variants on the HCD properties such as other fits to the depth dependency and stochastic properties that are still conditioned to the boreholes locally.
- A variant with a slight depth dependency in the HRD would be of interest. Possibilities are a slightly higher conductivity (factor 2–10) in the top 100–200 m, and/or slightly lower below;
- More variants on the HSD properties need to be considered to see whether an improved match in salinity near the surface can be achieved. These variations should probably be coupled to a specified infiltration type boundary condition.

8 Description of past evolution

The simulations are started 8,000 BC and run for 10,000 years, i.e. to 2,000 AD, corresponding to present-day conditions. At 8,000 BC, the last glaciation had ended and the modelled area is assumed to be all covered with melted ice, here referred to as Glacial water. Initially, there are only two types of water in the model. The upper part of the model is filled with Glacial water and underneath this there is an increasing fraction of Brine.

8.1 Base Case (HCD3_BC_HRD3EC_HSD1_BC1)

The past evolution of the four reference waters Brine, Marine water, Rain 1960 and Glacial water, is shown in Figure 8-1 and Figure 8-2. The distributions of the different water types are presented in vertical slices at three times corresponding to: 5,000 BC, 0 BC and 2,000 AD (present day). The fraction of each water type is calculated and the sum of the fractions of the four water types equals one. The corresponding total dissolved solids (TDS) distributions are presented in Figure 8-3.

The Brine distribution is very stable for the whole simulation time due to the low hydraulic conductivity at depth that is a consequence of the depth dependency in HCD properties that approach the background conductivity below about 700 m depth. Therefore, the Brine profile just reflects the initial condition. Marine water enters the system when the land is covered by the Littorina and later Baltic seas up to about 1,000 years ago. The mechanism for infiltration of Marine water is from the fact that it is heavier than the underlying Glacial melt water and hence gradually sink downwards as a pulse through the system toward the dense Brine. The pulse will sink heterogeneously around the DZs since advection is more rapid. This effect can be seen in Figure 8-1, where the Marine water clearly enters some sub-horizontal zones sloping south-east. The Marine pulse is generally in the top 500 m.

Figure 8-2 shows Glacial water initially sits on top of Brine and gradually some parts of the top 500 m or so are flushed by Marine water especially in the sub-horizontal zones that dip south-east. Most of this flushing process has occurred by 0 BC probably due to a greater head of dense Marine water lying across the site in the early Littorina phase, partly because the water was denser and also the sea was deeper then. Precipitation (Rain 1960 water) only just starts to enter the very south-west of the model at 0 BC when parts of the site are just emerging from the sea. As the land continues to rise up to the present-day more of the site is exposed to infiltration precipitation that leads to a flushing of the preceding Marine water in the top 100–300 m in the south of the model. Again, it is possible to see that is happening most rapidly in the DZs that gently dip south-east.

The TDS distribution seen in Figure 8-3 is the result of mixing between Brine and Marine water, which has a time varying concentration of salt. The shape of the TDS distribution suggests that the dominant part of the salt originates from the Brine with a pulse of TDS of around 10g l^{-1} near the top associated with the Littorina pulse. The distribution of the vertical Darcy velocity, presented in Figure 8-3, shows a highly heterogeneous flow field confirming the presence of local flow cells. Flow in the sub-horizontal zones dipping south-east are generally downwards (negative q_z). There is an intuitive general trend of downward flow in the south where the higher ground is, and upward flow near the coast, although there are many local areas of downward flow near the coast also.

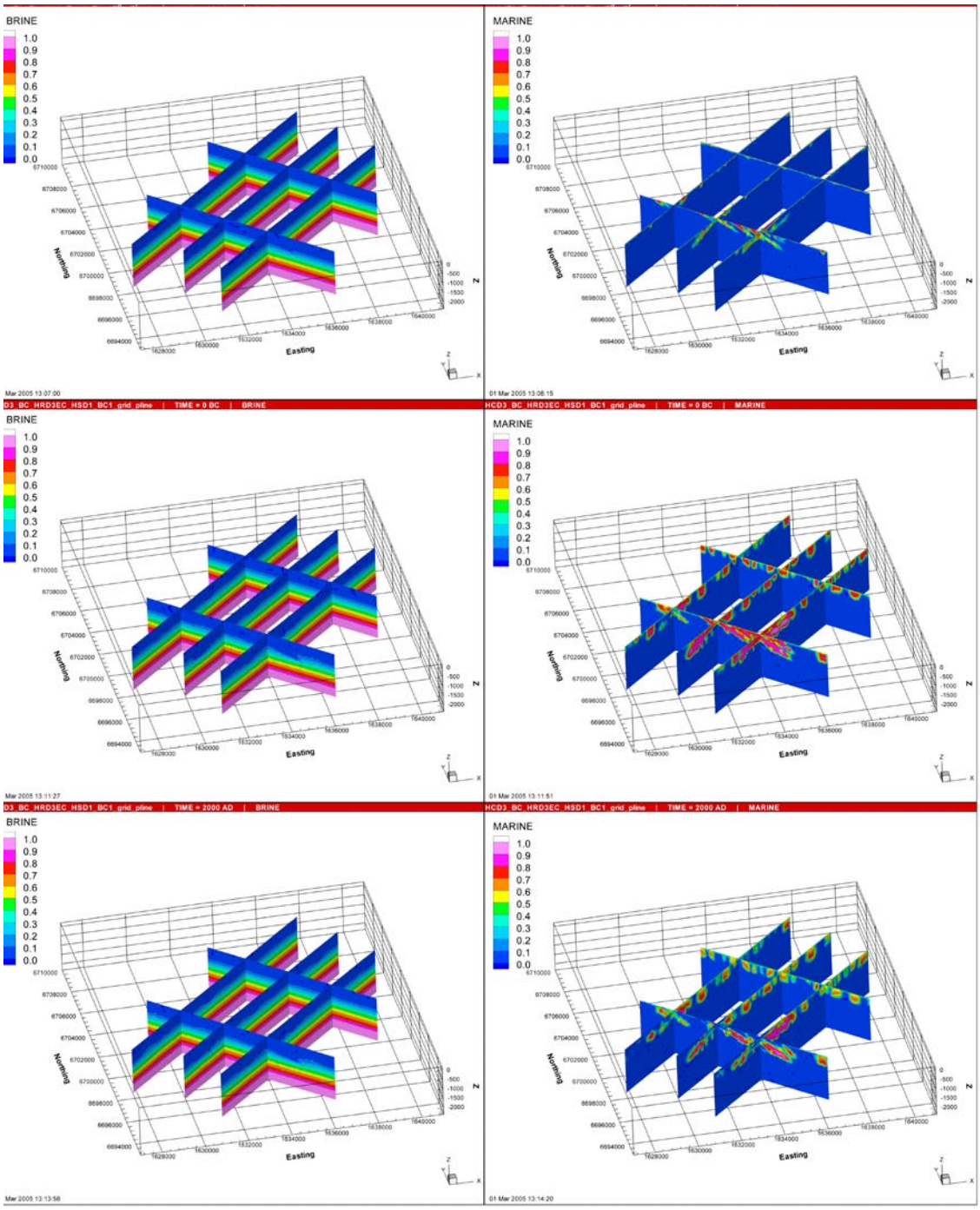

Figure 8-1. *Distribution of Brine (left) and Marine water (right) in vertical slices at times equal to (from top to bottom) 5,000 BC, 0 BC and 2,000 AD (present-day), for Base Case (HCD3_BC_ HRD3EC_HSD1_BC1).*

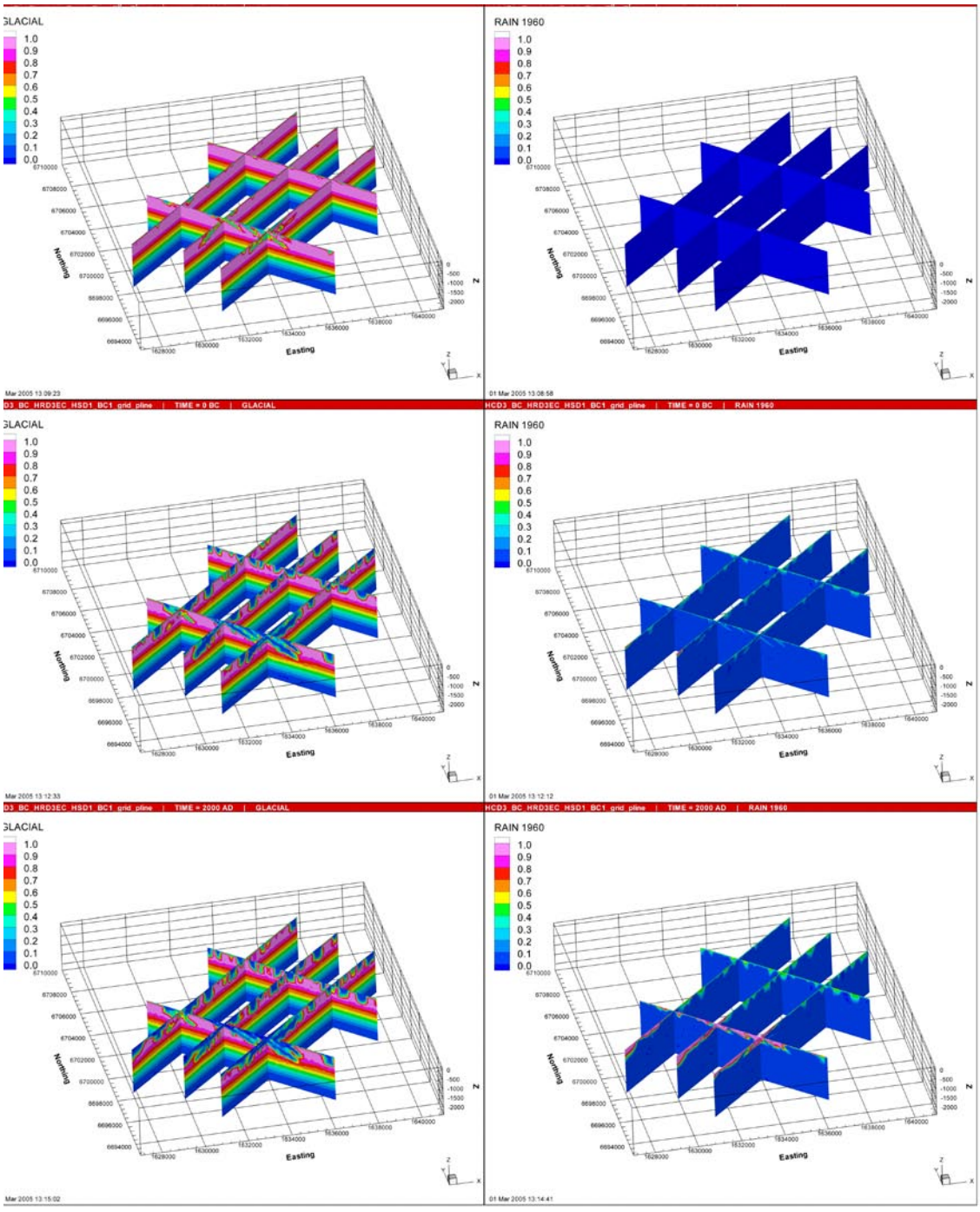

Figure 8-2. *Distribution of Glacial water (left) and Rain 1960 water (right) in vertical slices at times equal to (from top to bottom) 5,000 BC, 0 BC and 2,000 AD (present-day), for Base Case (HCD3_BC_HRD3EC_HSD1_BC1).*

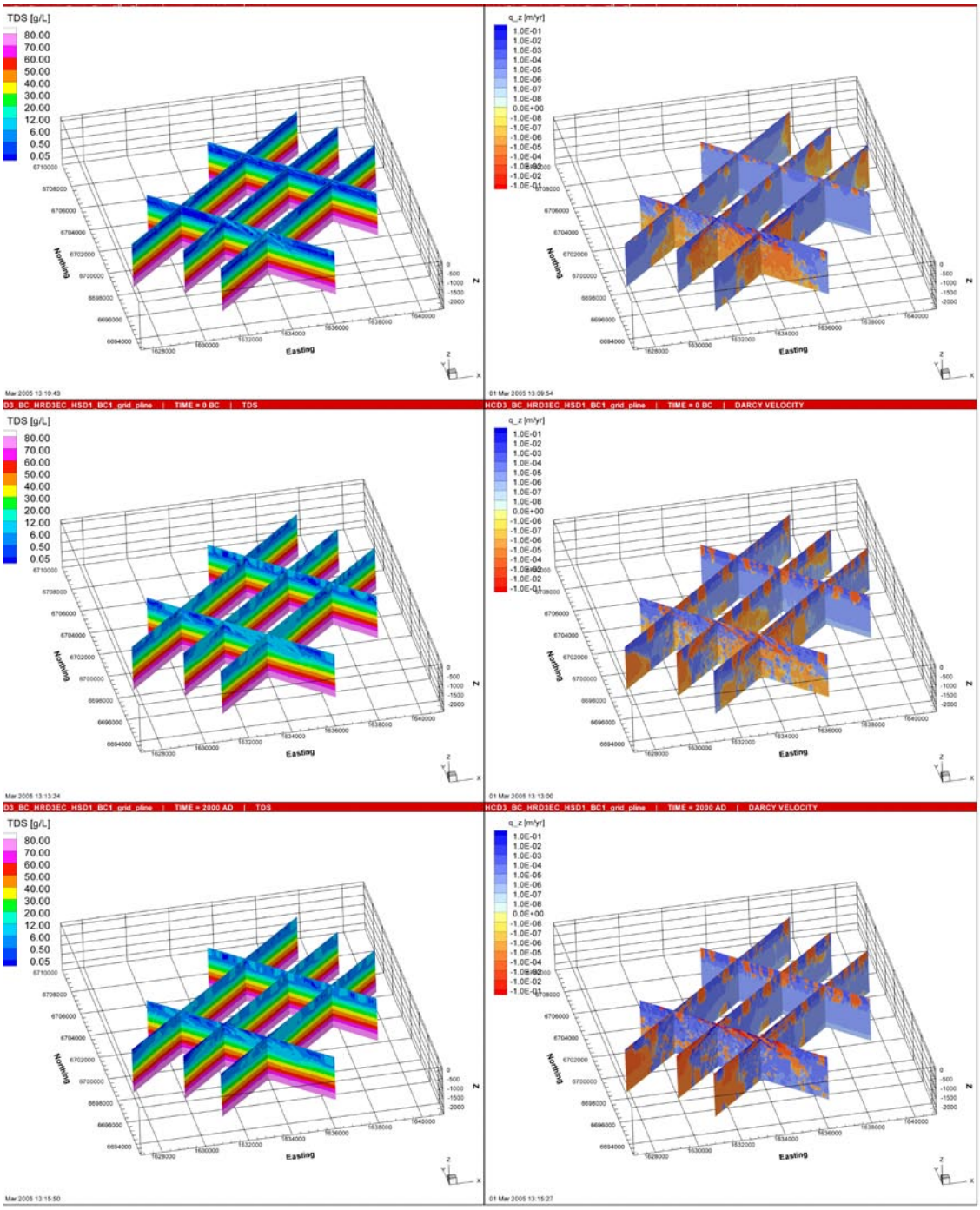

Figure 8-3. *Distribution of TDS (left) and the vertical Darcy velocity, q_z (right, positive is upward), in vertical slices at times equal to (from top to bottom) 5,000 BC, 0 BC and 2,000 AD (present-day), for Base Case (HCD3_BC_HRD3EC_HSD1_BC1).*

9 Description of the present-day flow conditions

9.1 Methodology

A selection of the most relevant modelled cases is presented in this section. Results representing the present-day flow conditions, i.e. 2,000 AD (the final time step in the simulations) will be shown in terms of flow paths (particles exit locations), distributions of F-quotient, regional distributions of reference waters, and recharge and discharge rates. The purpose of the flow-path analysis is two-fold. Firstly, it provides a set of performance measures for quantifying the current groundwater flow situation that can be used to compare variants and quantify uncertainties. Secondly, the identification of discharge areas is important for the Preliminary safety Evaluation (PSE). Due to a large amount of graphical output from the simulations, the number of figures presented in the report has been cut down to a minimum for each case. An exception is made for the Base Case, which is covered more thoroughly.

9.2 Base Case (HCD3_BC_HRD3EC_HSD1_BC1)

This subsection presents the results for the Base Case, which was developed from the calibration against the reference water mixing interpreted from borehole water samples to give a reasonable match in the global sense. Hydraulic parameters, initial conditions and boundary conditions obtained for the Base Case later on formed the basis for the sensitivity study performed.

9.2.1 Flow paths

In Figure 9-1 the distribution of the $\log_{10}$(F-quotient) at particle starting locations in the local-scale release-area for the Base Case is presented. Red colour indicates smaller F-quotient about 10^4y m^{-1} and blue means high 10^8y m^{-1}. The highest values are around 10^5 to 10^6y m^{-1} and occur in the centre of the release area where there is upwards flow and paths go almost straight up to the surface. The values of the F-quotient calculated are based on a conservative assumption about the value of a_r used for the particle transport as compared to the values used in RMD for reference water transport. Here a_r is chosen based on 2×P32, where P32 is based only on the fractures included in the regional-DFN, which is truncated at L_{min} = 25 m for the power-law fracture length distribution. This gives values of a_r perhaps an order of magnitude lower than those used in the RMD calculations. The reason for being so conservative was to assess how the F-quotient might be reduced if advective flow-paths are rapidly focused only into the longer fractures, since this was thought to be a legitimate scenario for flow in the very tight Forsmark bedrock. In the eastern and western parts of the release area higher values of F-quotient of about 10^7 to 10^8y m^{-1} are experienced, partly because flow-paths are initially downwards and hence paths are longer, but also because a value of a_r = 1.0 m^{2}m^{-3} is used in the HCD for the Base case. Perhaps smaller values of a_r need to be considered in the HCD also, but this depends on the concept of whether HCD features are single features or swarms of fractures that will give rise to a greater fracture surface area.

The discharge points are shown in Figure 9-2 and in Figure 9-3 with the position of the DZs on a horizontal section at z = –100 m. These show the exit points to be much localized to the site with discharge either directly above the release area or at the coast about 1 km to the north and around the Singö DZ. Considering Figure 5-5, the 50 m refined local-scale area covers most of the flow-paths to their discharge, so relatively good accuracy should be achieved in these transport calculations in terms of resolution of properties and DZs.

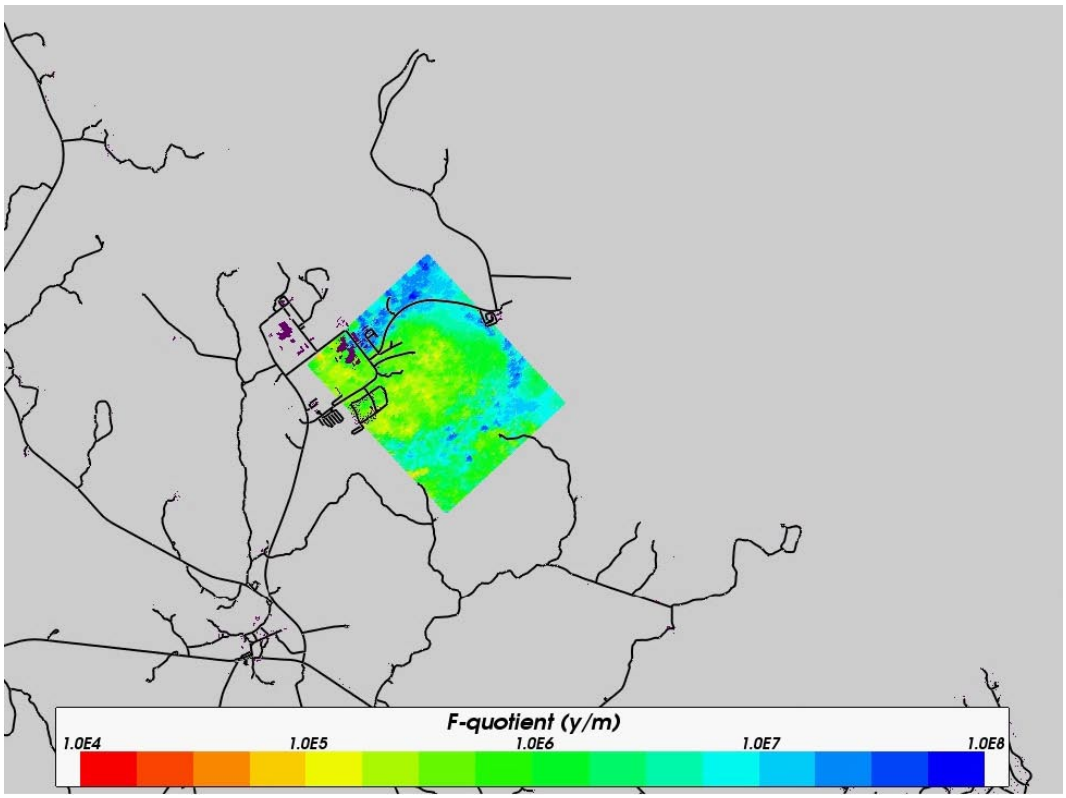

Figure 9-1. *Distribution of F-quotient (Log10) at particle starting locations in the local-scale release area for the Base Case (HCD3_BC_HRD3EC_HSD1_BC1). Roads are shown in black for context.*

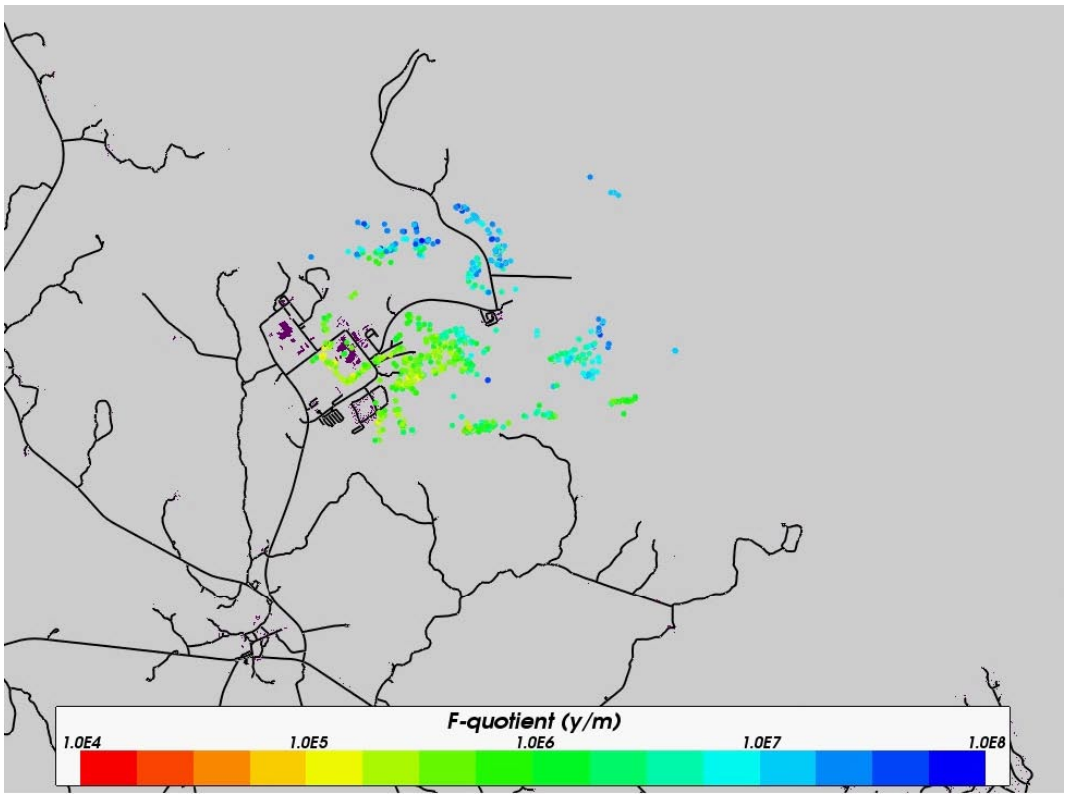

Figure 9-2. *Distribution of F-quotient (Log10) at particle exit locations in the local-scale release area for the Base Case (HCD3_BC_HRD3EC_HSD1_BC1). Roads are shown in black for context.*

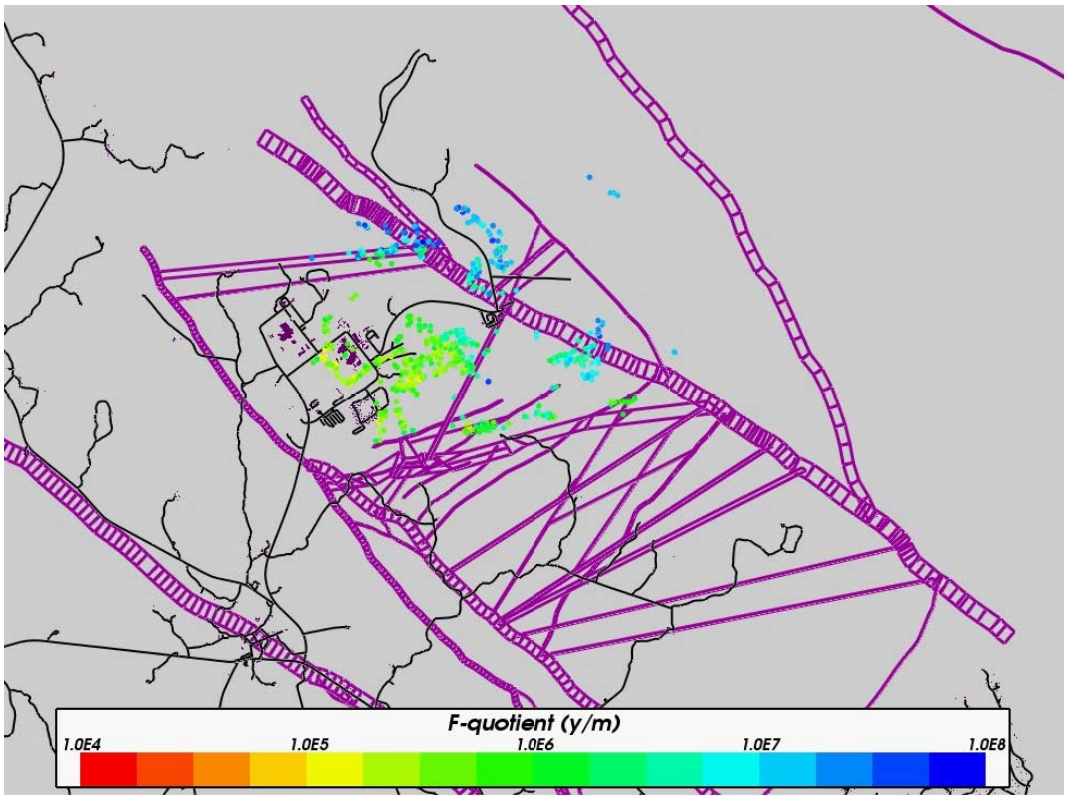

Figure 9-3. *Distribution of F-quotient (Log10) at particle exit locations in the local-scale release area for the Base Case (HCD3_BC_HRD3EC_HSD1_BC1). A section through the HCD model at z = –100 m is superimposed. Roads are shown in black for context.*

9.2.2 Regional distribution of reference waters

In Figure 9-4 to Figure 9-6, the present-day distributions of the four reference waters Brine, Marine water, Rain 1960 and Glacial water, are presented in vertical and horizontal slices. It is apparent that the Brine does not move very much from its initial state. Hence, at –400 m no Brine is found in the modelled area. At –1,000 m the Brine fraction is about 30–40%, which is approximately the same as the initial condition. Marine water penetrates the entire modelled area through the fracture zones down to –800 m. It is found enclosed into lenses with fractions of up to 100%. The impact from the sloping sub-horizontal fracture zones inside the candidate area is quite substantial. The Marine water clearly follows the slope of the fracture zones and stops where the fracture zones have been cut off in the model. These sloping fractures require a high degree of discretisation in the local-scale area in order to keep the fractures separated so that an unrealistic mixing of waters is avoided.

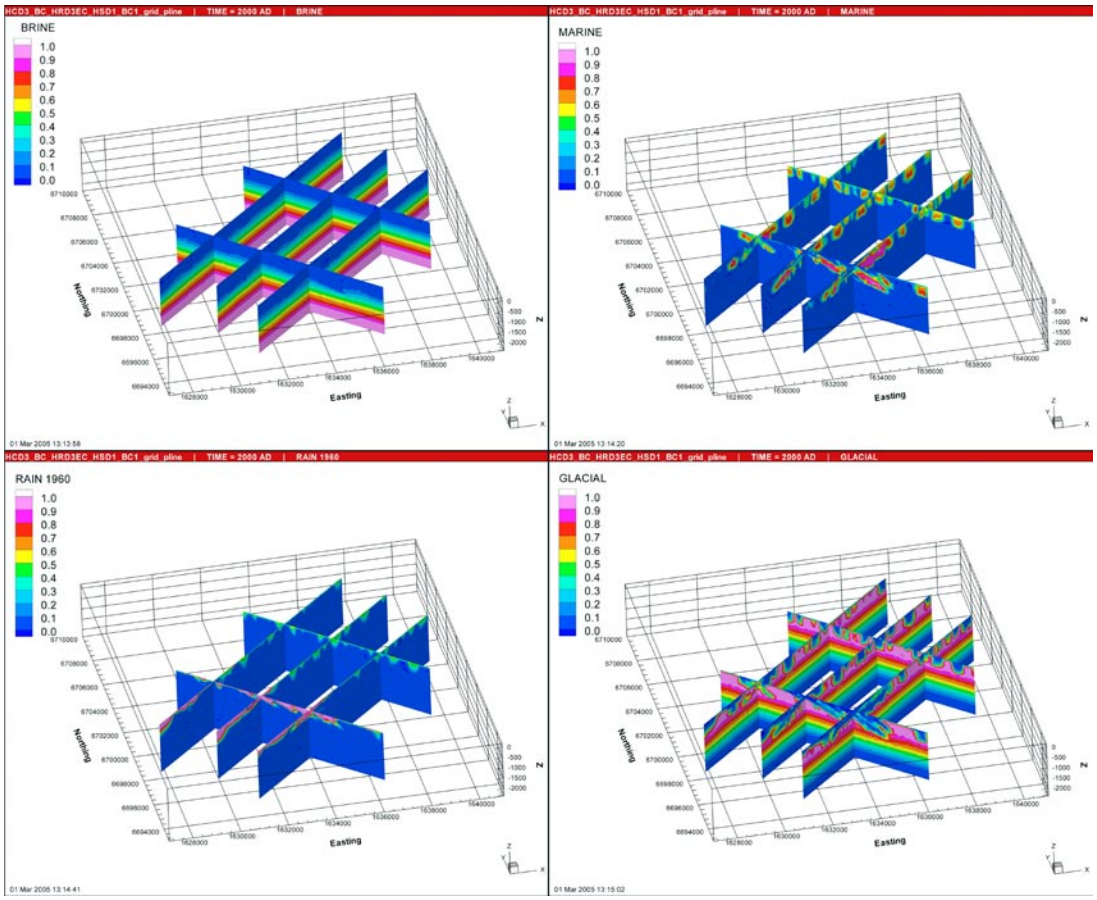

Figure 9-4. *Present-day distribution of the reference waters Brine (top left), Marine water (top right), Rain 1960 (bottom left) and Glacial water (bottom right) in vertical slices, for the Base Case (HCD3_BC_HRD3EC_HSD1_BC1).*

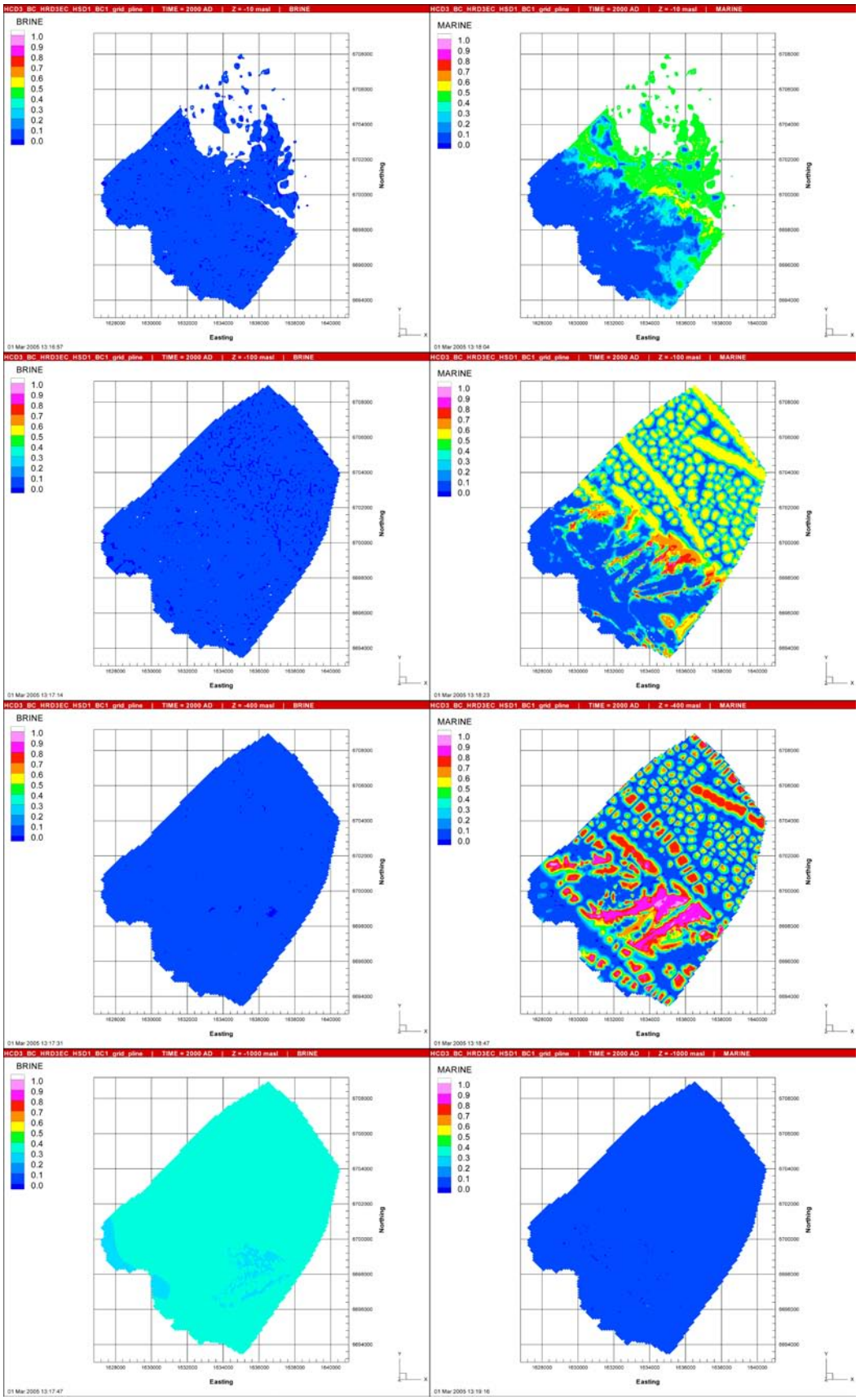

Figure 9-5. *Present-day distribution of Brine (left) and Marine water (right) in horizontal slices at elevations (from top to bottom) –10 m, –100 m, –400 m and –1,000 m, for the Base Case (HCD3_BC_HRD3EC_HSD1_BC1).*

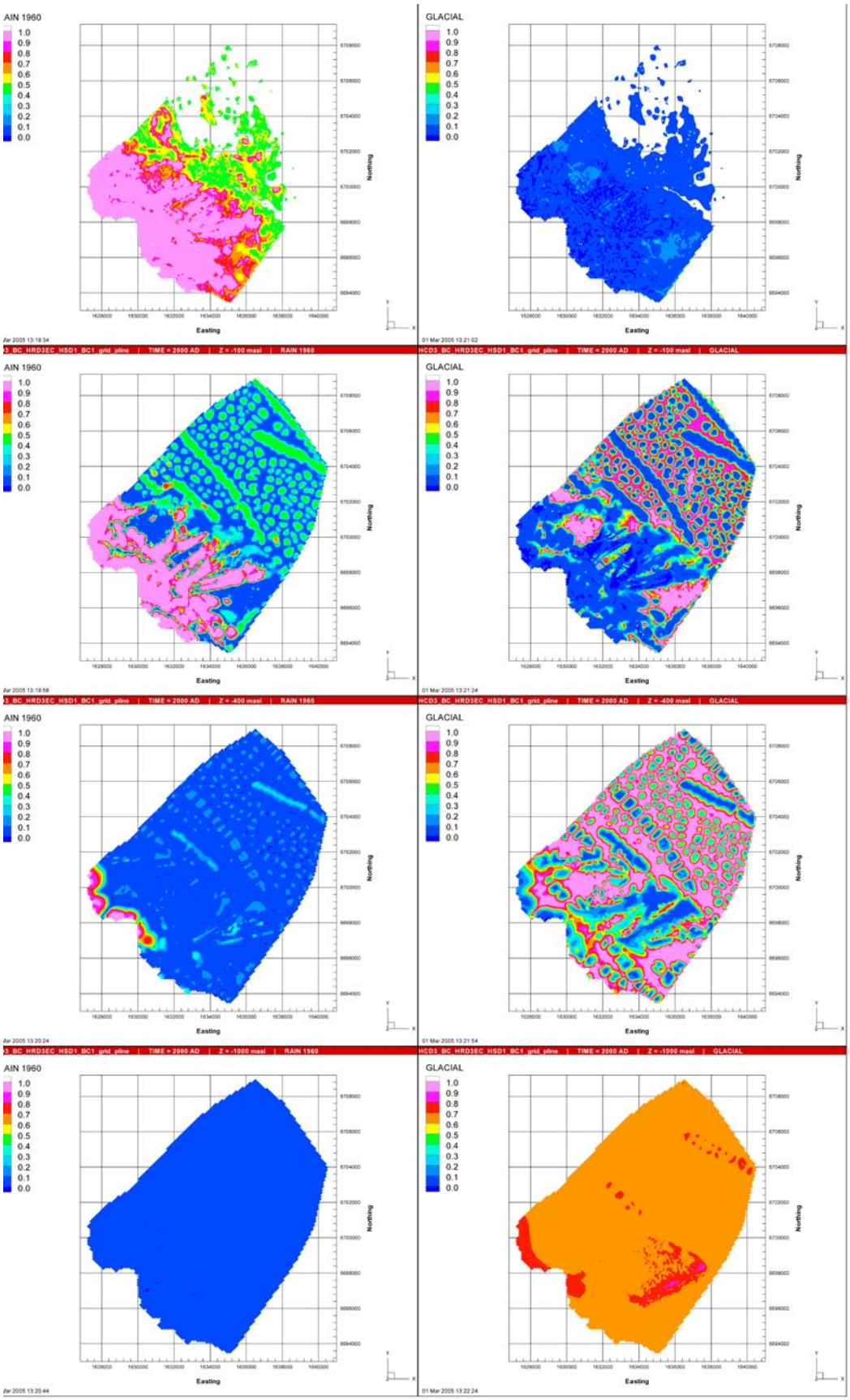

Figure 9-6. *Present-day distribution of Rain 1960 (left) and Glacial water (right) in horizontal slices at elevations (from top to bottom) –10 m, –100 m, –400 m and –1,000 m, for the Base Case (HCD3_BC_HRD3EC_HSD1_BC1).*

Marine water is slowly replaced by freshwater from the top in the areas above the sea. There is no Marine water found beneath –800 m at 2,000 AD. Water originating from the Rain 1960 penetrates the rock down to about –500 m in the western area where land first rose above the sea level. Since land rises above the sea very late in the modelled area there is Rain 1960 present only in the upper few hundred meters. The Glacial water that covered the upper part of the model at 8,000 BC has been flushed out mainly by Marine water down to about –800 m. During the last period of time also infiltrating Rain 1960 has flushed the western top part of the modelled area. However, Glacial water is still present in the tight rock between the fracture zones and can be found as high up as in the top 100 m. The fraction of Glacial water at –1,000 m is about 70%, indicating that only small movements of water occur at this depth.

9.2.3 Recharge and discharge rates

In Figure 9-7, the vertical Darcy velocity distribution under present-day flow conditions is presented in horizontal slices. Close to the surface, at –10 and –100 m, the downwards (recharge) flows are slightly dominating. The magnitude is around 0.001 to 0.1 m per year in the rock mass. It is clear that the flow pattern is very heterogeneous indicating localized flow cells. The discharge is located to the Baltic Sea in the eastern part of the modelled area. It is worth noting that the direction of flow underneath the sea is downward not only in the few very large fracture zones present in the model but also in the homogenous rock in between. This pattern is present down to about –800 m. The explanation for this behaviour is the bathymetry (sea bottom topography), which causes pressure differences due to a variable salt water pillar above the sea bottom. The result will be a specified head off-shore varying with the depth of the sea and causing localized flow cells to be established. At –400 m, the flow rates are around $1.0\ 10^{-5}$–$1.0\ 10^{-6}$ m per year in the recharge as well as in the discharge areas. At a depth of –1,000 m the flows are generally one order of magnitude lower. Also, the flow is more homogeneous and mainly upwards except from the western parts of the model that are above the sea.

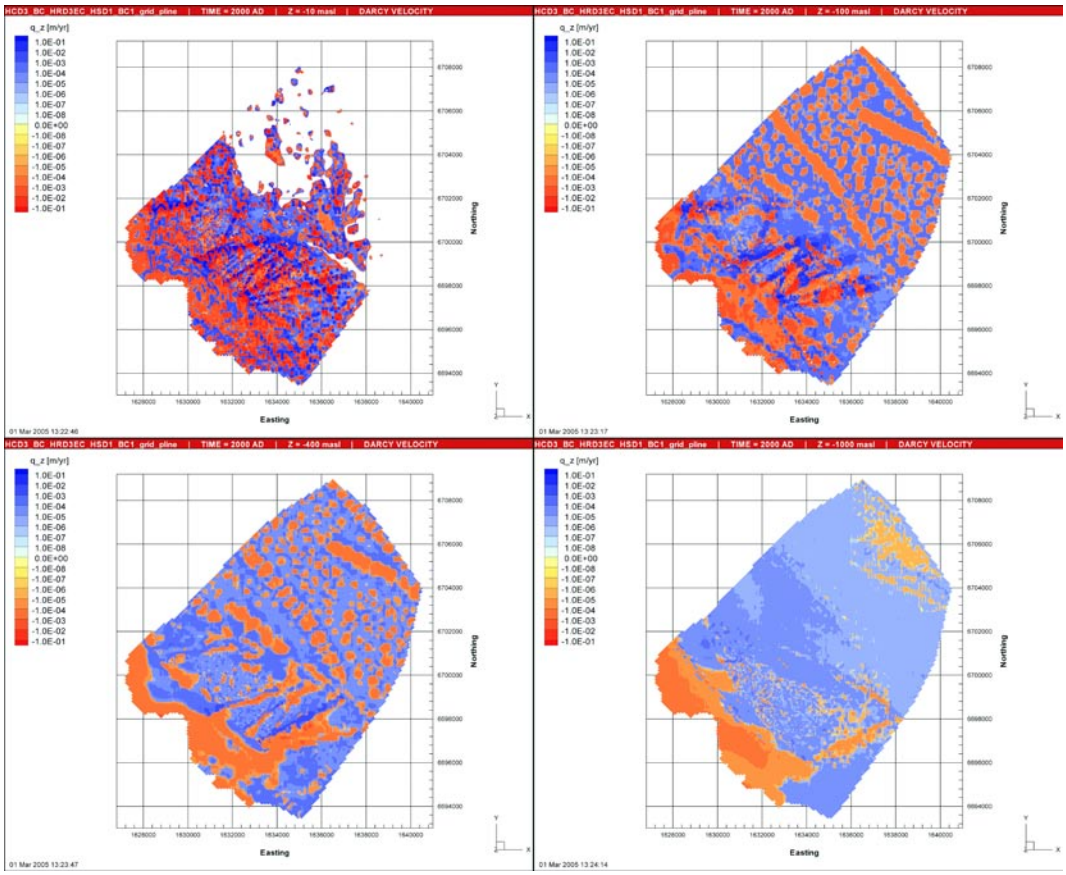

Figure 9-7. *Present-day distribution of the vertical Darcy velocity, q_z (positive is upward), in horizontal slices at elevations –10 m (top left), –100 m (top right), –400 m (bottom left) and –1,000 m (bottom right), for the Base Case (HCD3_BC_HRD3EC_HSD1_BC1).*

9.3 Sensitivity to surface boundary conditions and properties

9.3.1 Specified infiltration for flow (HCD3_BC_HRD3EC_HSD1_BC3)

This case uses a specified flux (non-linear recharge/discharge) boundary condition for flow onshore. Simulations for a specified infiltration of 200 mm y^{-1} and the HSD1 properties give a water table close to the surface and hence results are very similar to the base case. Transport results are shown as the F-quotient distribution at start and exit locations in Figure 9-8 and Figure 9-9, respectively. The distribution of F-quotient at the start locations is very similar while the exit locations change slightly with perhaps a few more long paths to the coast. Plots of reference water distributions and discharge patterns are visually identical to those in subsections 9.2.2 and 9.2.3.

9.3.2 Refined near-surface model using HSD2 properties (HCD3_BC_HRD3EC_HSD2_BC1)

This case has a refined near-surface model using HSD2 properties. The top four meters are split into three layers with the middle layer having an order of magnitude lower conductivity compared to the surrounding top layers. Results were found to be insensitive to these changes both in terms of reference water and particle transport as illustrated by the F-quotient distribution at the particle start locations shown in Figure 9-10. There were some small local differences found in the top 10 m but the magnitude of the velocity is the same as for the Base Case throughout the model domain. It can be concluded that the refined near-surface model, at least with the properties being used here, has little or no effect on the results.

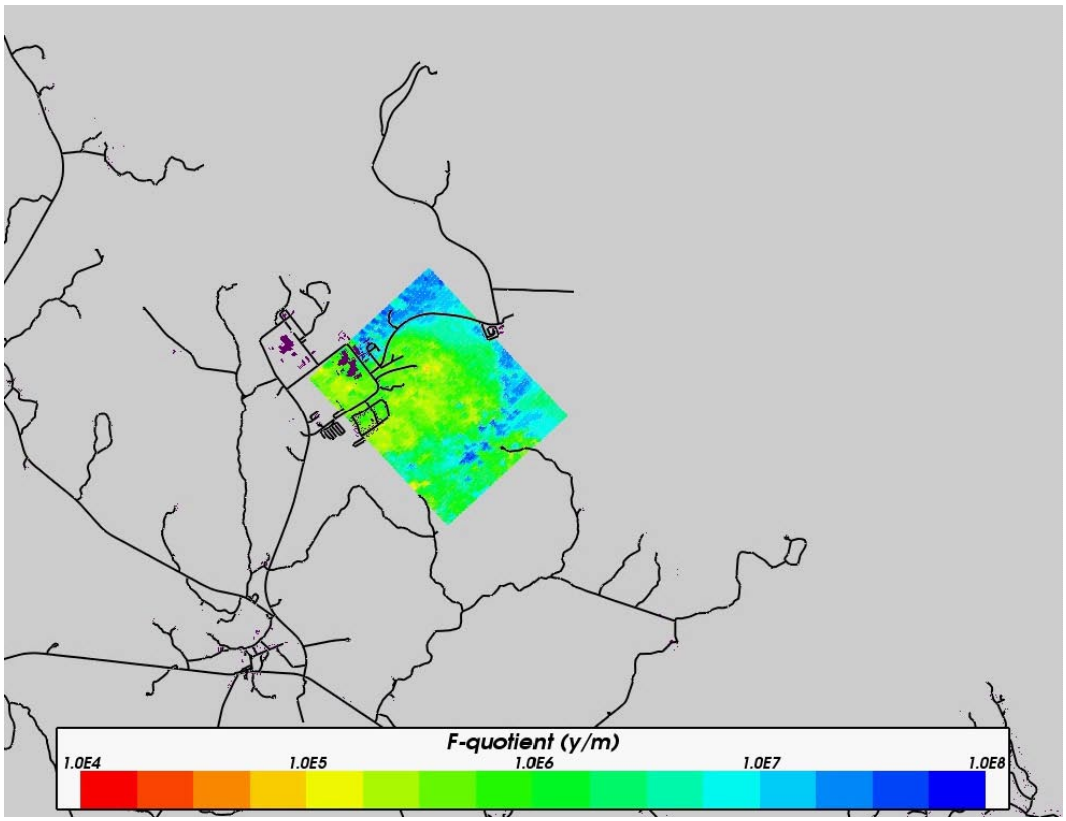

Figure 9-8. *Distribution of F-quotient (Log10) at particles starting locations in the local-scale release area for the variant with a specified infiltration onshore (HCD3_BC_HRD3EC_HSD1_BC3). Roads are shown in black for context.*

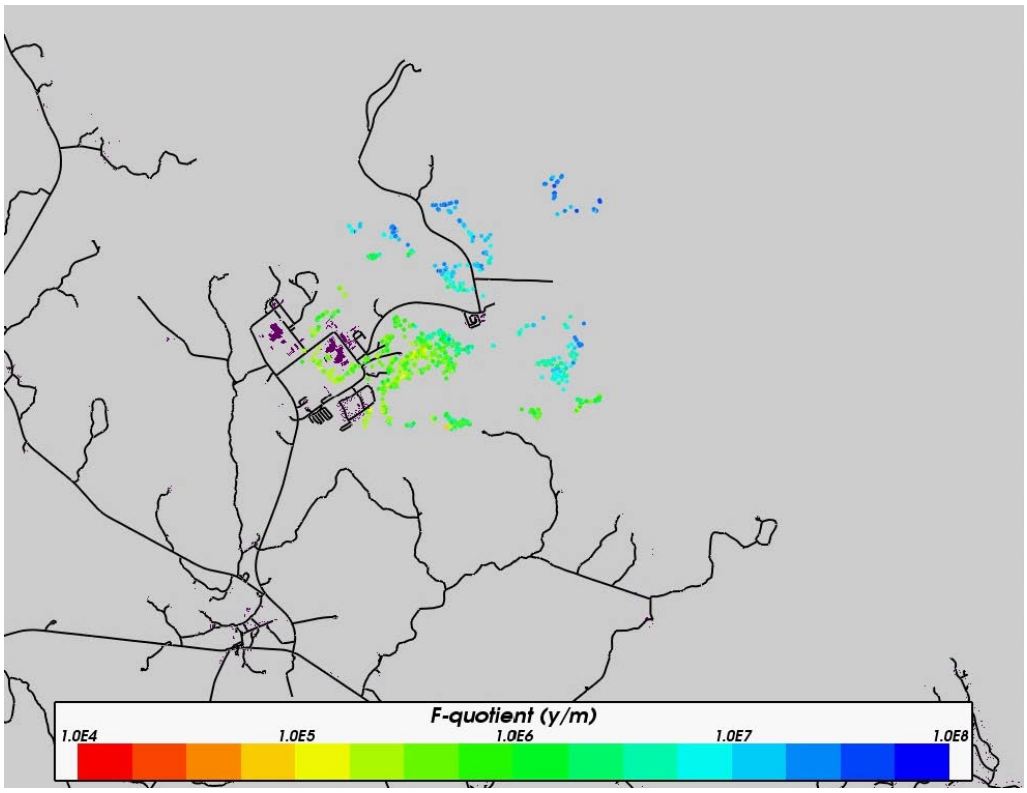

Figure 9-9. *Distribution of F-quotient (Log10) at particles exit locations in the local-scale release area for the variant with a specified infiltration onshore (HCD3_BC_HRD3EC_HSD1_BC3). Roads are shown in black for context.*

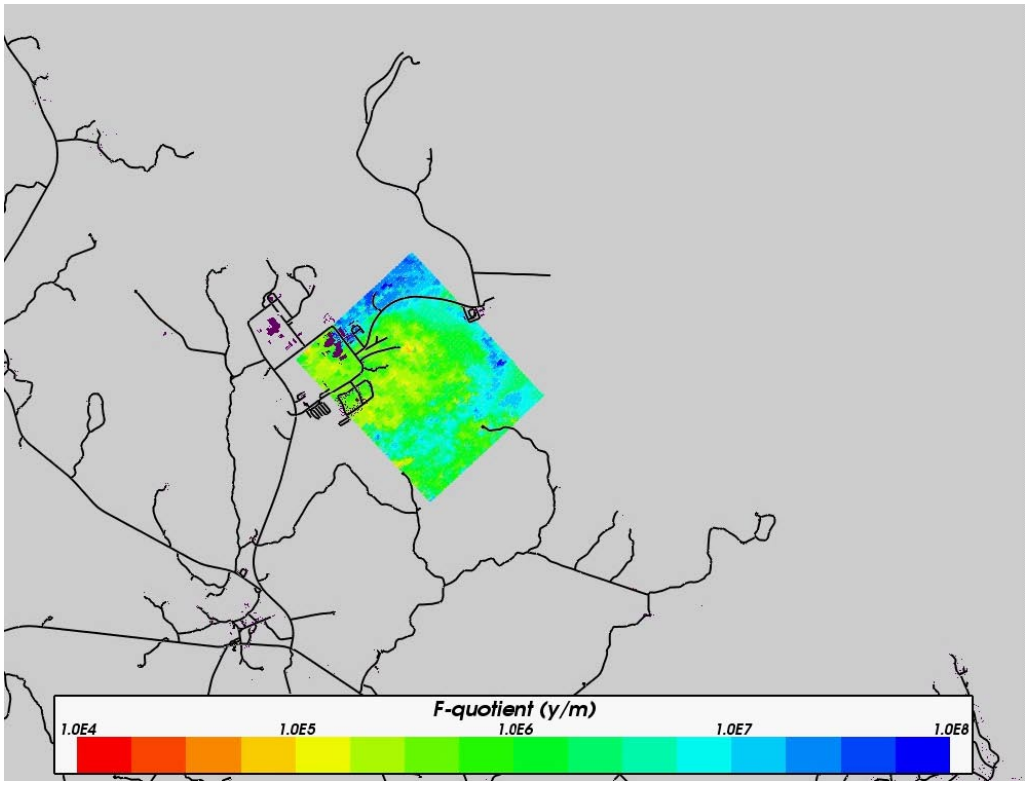

Figure 9-10. *Distribution of F-quotient (Log10) at particles starting locations in the local-scale release area for the variant with refined near surface properties (HCD3_BC_HRD3EC_HSD2_BC1). Roads are shown in black for context.*

9.4 Sensitivity to DFN model parameters and data interpretation

9.4.1 Stochastic DFN realisation 2 (HCD3_BC_HRD3EC2_HSD1_BC1)

This case represents the second stochastic realisation of the Base Case. The transport results are illustrated by the distribution of F-quotient at the start locations in Figure 9-11 demonstrating that the effect of the stochastic DFN is relatively small and localised, the overall trends being the same. There are perhaps slightly less areas of very low F-quotient in this realisation compared to the Base Case. Similar conclusions hold for the reference water and Darcy velocity distributions.

9.4.2 Stochastic DFN realisation 3 (HCD3_BC_HRD3EC3_HSD1_BC1)

This case represents the third stochastic realisation of the Base Case. The transport results are illustrated by the distribution of F-quotient at the start locations in Figure 9-12. Again there are some localised small differences with fewer very small F-quotient values than the Base Case. In conclusions, the stochastic influence of the DFN on transport statistics is likely to be small.

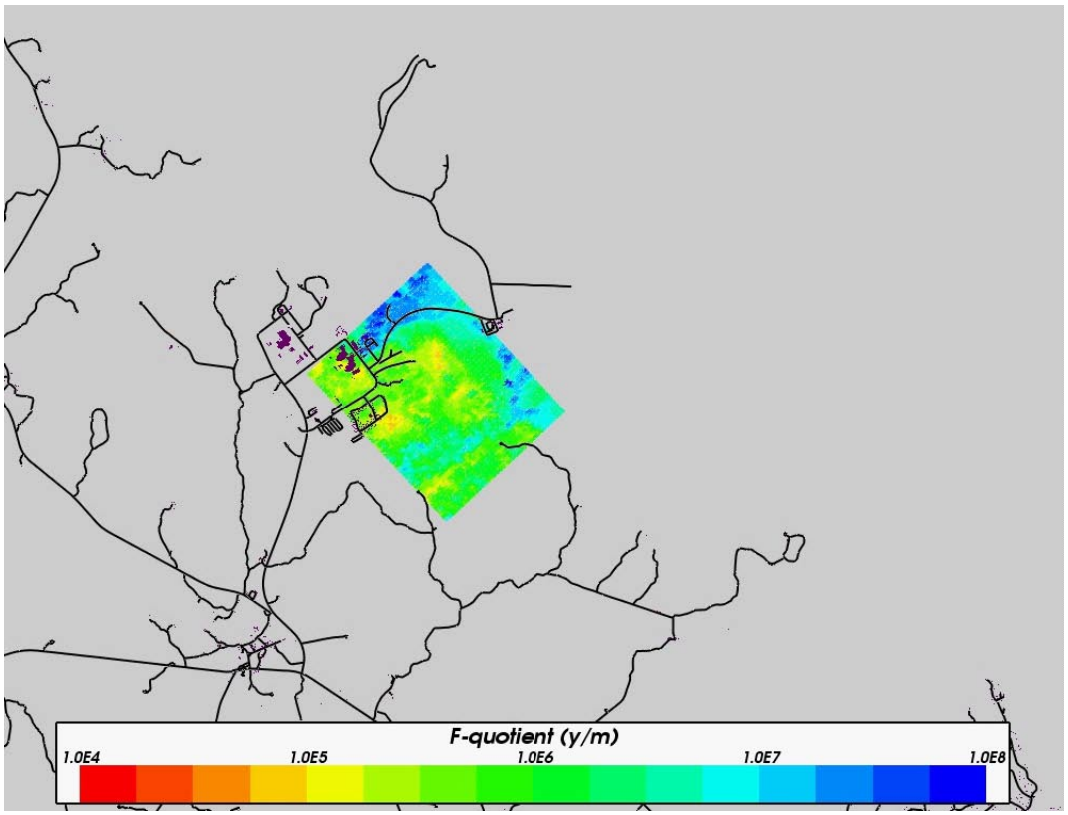

Figure 9-11. *Distribution of F-quotient (Log10) at particles starting locations in the local-scale release area for Realisation 2 (HCD3_BC_HRD3EC2_HSD1_BC1). Roads are shown in black for context.*

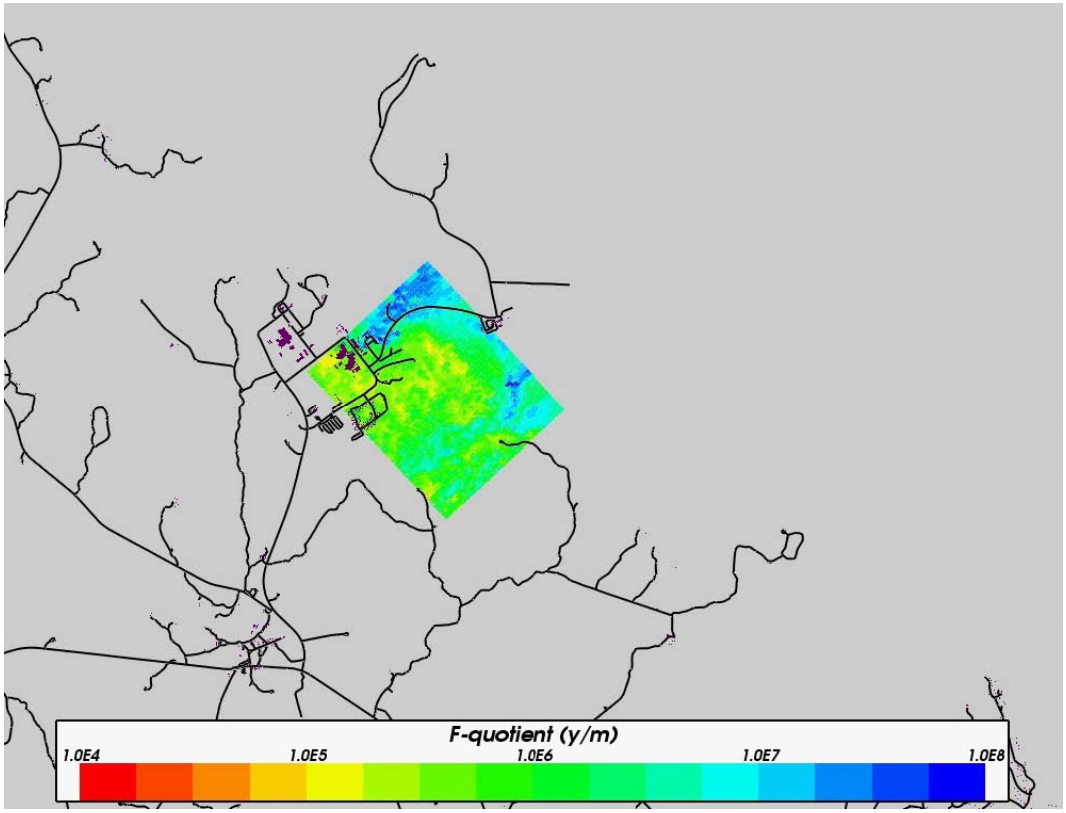

Figure 9-12. *Distribution of F-quotient (Log10) at particles starting locations in the local-scale release area for Realisation 3 (HCD3_BC_HRD3EC3_HSD1_BC1). Roads are shown in black for context.*

9.4.3 Uncorrelated transmissivity (HCD3_BC_HRD3EU_HSD1_BC1)

This case is a variant on the Base Case DFN with an uncorrelated transmissivity distribution model. Results for this case are more distinct than the other DFN variants. For example, Figure 9-13 shows that the F-quotient is generally lower for this case having a minimum approaching 10^4y m^{-1} and a maximum of 10^7y m^{-1}. This is probably due in part to the uncorrelated T model giving block-scale properties marginally higher than the correlate case, and also because the conductivity field has fewer low values in this case so there a less resistance from low K areas. The exit locations are qualitatively similar though as shown in Figure 9-14.

In Figure 9-15, the present-day distributions of the four reference waters Brine, Marine water, Rain 1960 and Glacial water, are presented in vertical slices. Compared to the Base Case there are some differences around the sub-horizontal fracture zones inside the candidate area. Using the uncorrelated transmissivity model results in a more connected network giving a more homogenous distribution of Marine water suggesting there is more leakage between the fracture zones. The Marine water also goes deeper into the model than for the correlated Base Case. The infiltrating freshwater, Rain 1960, penetrates deeper into the model replacing Glacial water to a higher extent compared to the Base Case. Apart from those differences, the distribution of reference waters very much resembles the Base Case. The differences in the distribution of the vertical Darcy velocity between the Base Case and the uncorrelated case are rather small and localised.

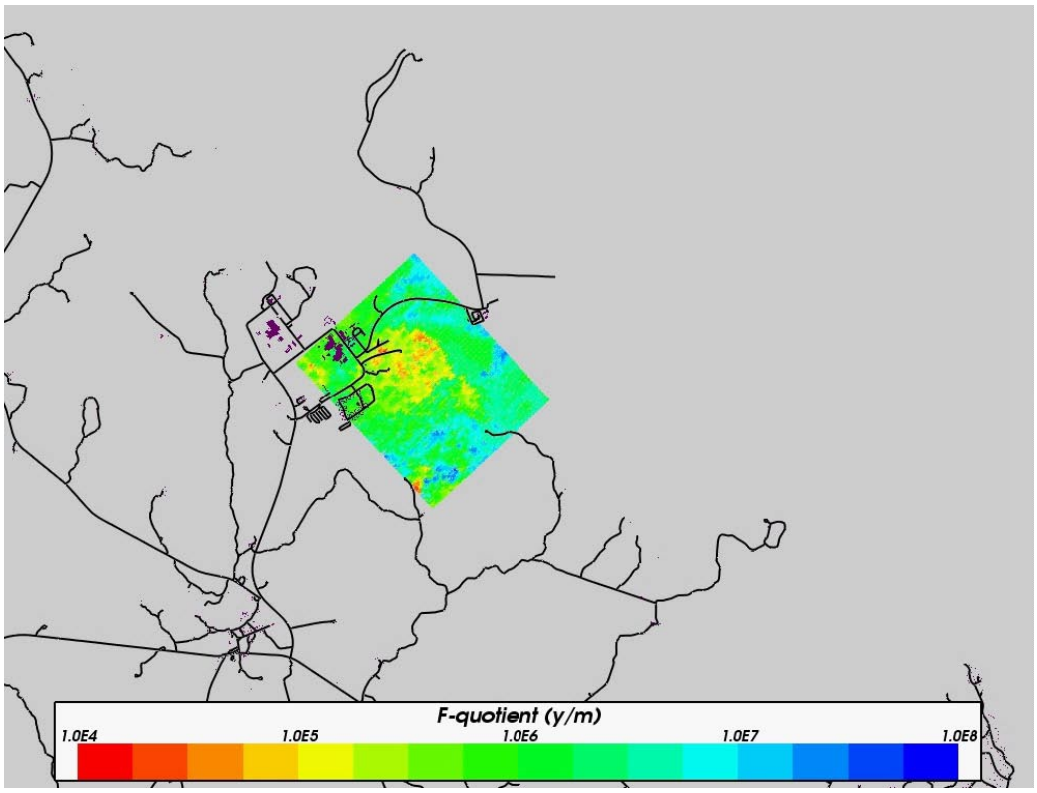

Figure 9-13. *Distribution of F-quotient (Log10) at particles starting locations in the local-scale release area for uncorrelated T (HCD3_BC_HRD3EU_HSD1_BC1). Roads are shown in black for context.*

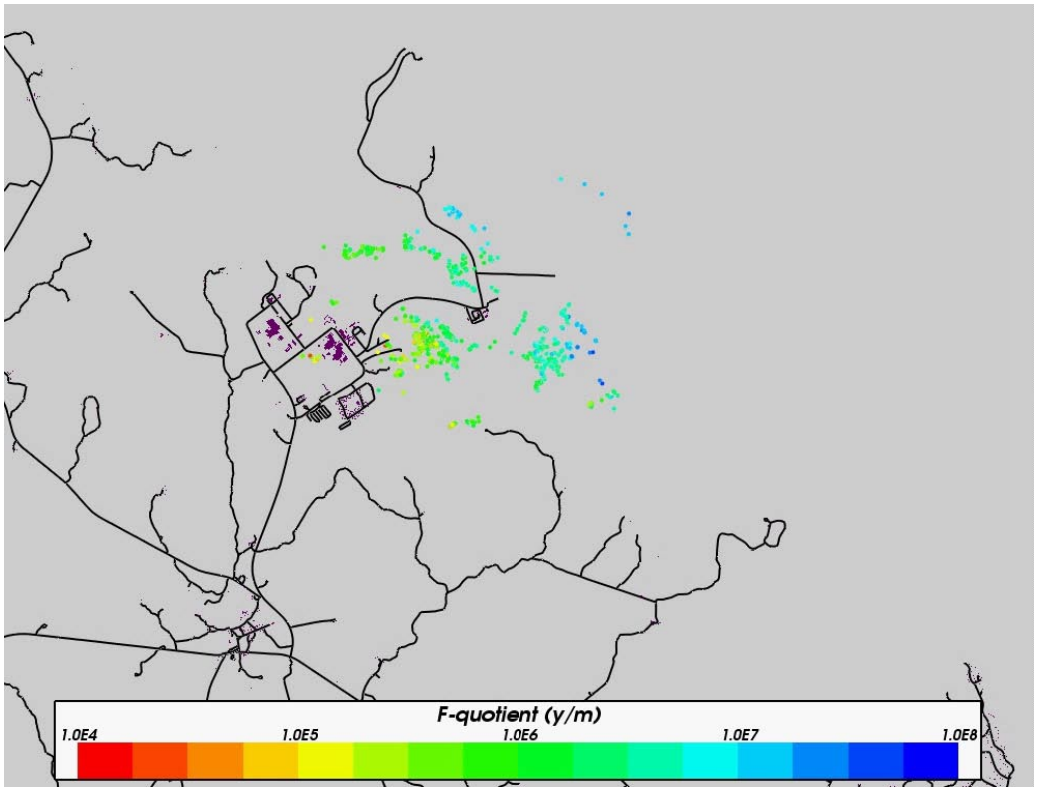

Figure 9-14. *Distribution of F-quotient (Log10) at particles exit locations in the local-scale release area for uncorrelated T (HCD3_BC_HRD3EU_HSD1_BC1). Roads are shown in black for context.*

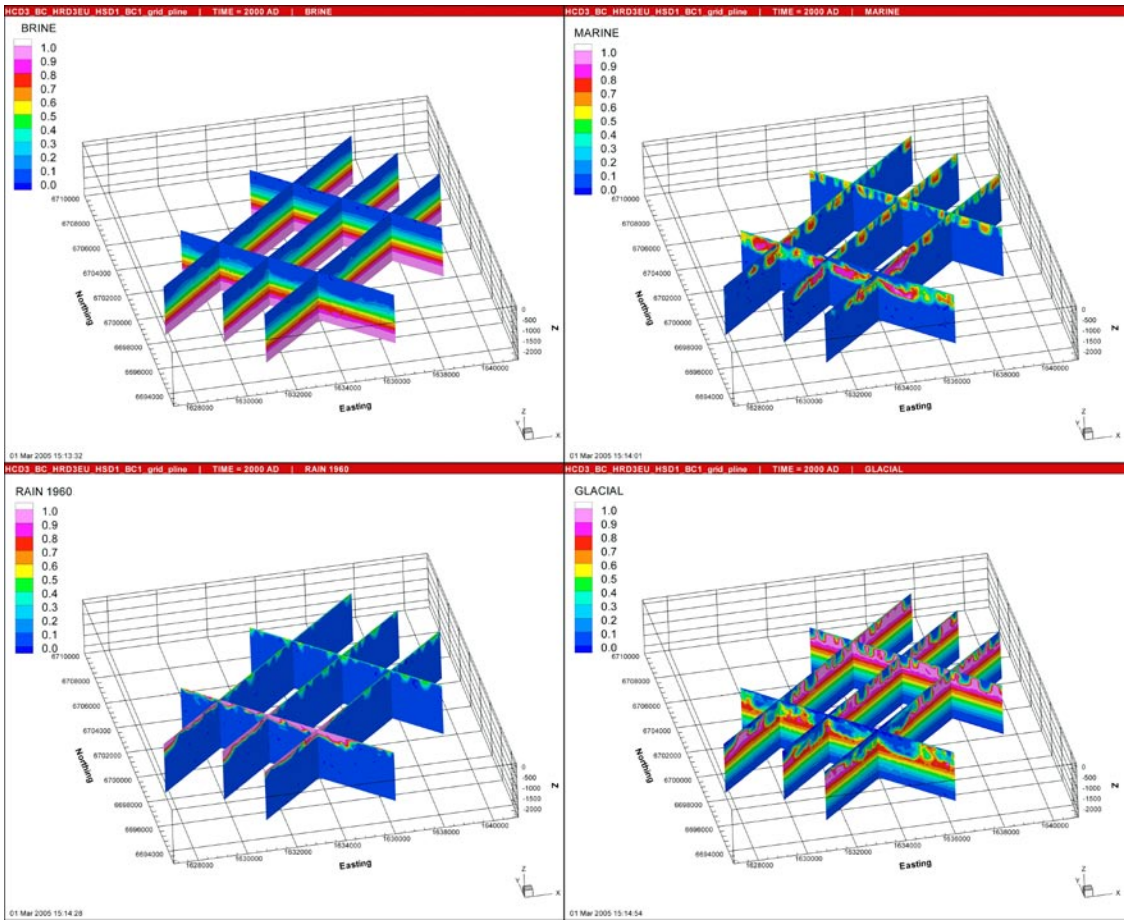

Figure 9-15. *Present-day distribution of the reference waters Brine (top left), Marine water (top right), Rain 1960 (bottom left) and Glacial water (bottom right) in vertical slices, for uncorrelated T (HCD3_BC_HRD3EU_HSD1_BC1).*

9.4.4 Variant Geo-DFN with different power-law fracture length PDF (kr = 2.75), correlated transmissivity model (HCD3_BC_HRD3SFC_HSD1_BC1)

This case uses a variant Geo-DFN with different power-law fracture length PDF ($k_r = 2.75$) derived using a correlated transmissivity model. In Figure 9-16 the distribution of the $\log_{10}$(F-quotient) at particles starting locations in the local scale area for the case using the Variant Geo-DFN with different power-law fracture length PDF is presented. The values for the F-quotient have a similar distribution and magnitude to the Base Case with a correlated distribution. Generally the differences for the distribution of reference waters compared to the Base Case are small. The distribution of the vertical Darcy velocity is also the same as in the Base Case. It can be concluded that changing the fracture length distribution while maintaining the match to the borehole hydraulic data does not significantly impact the results.

9.4.5 Variant Geo-DFN with different power-law fracture length PDF (kr = 2.75), uncorrelated transmissivity model (HCD3_BC_HRD3SFU_HSD1_BC1)

This case uses a variant Geo-DFN with different power-law fracture length PDF ($k_r = 2.75$) derived using an uncorrelated transmissivity model in DarcyTools. In Figure 9-17 the distribution of the $\log_{10}$(F-quotient) at particles starting locations in the local scale area for the case using the Variant Geo-DFN with different power-law fracture length PDF and an uncorrelated transmissivity model is presented. This case is very similar to the Base Case variant with an uncorrelated T model (HCD3_BC_HRD3EU_HSD1_BC1). The values for the F-quotient are slightly lower, but in line with the original uncorrelated variant. Generally the differences for the distribution of reference waters compared to the Base Case are small. The effects that can be seen are the same as was discussed for the previous uncorrelated case, i.e. some differences appear around the sub-horizontal fracture zones inside the candidate area. Using the uncorrelated transmissivity model results in a more connected network giving a more homogenous distribution of Marine water suggesting there is more leakage between the fracture zones. The Marine water also goes deeper into the model than for the correlated cases. The differences in the distribution of the vertical Darcy velocity between the Base Case and the uncorrelated case are very small and localised. Overall it can be concluded that model is more sensitive to the model used for fracture transmissivity than the length distribution for F1.2.

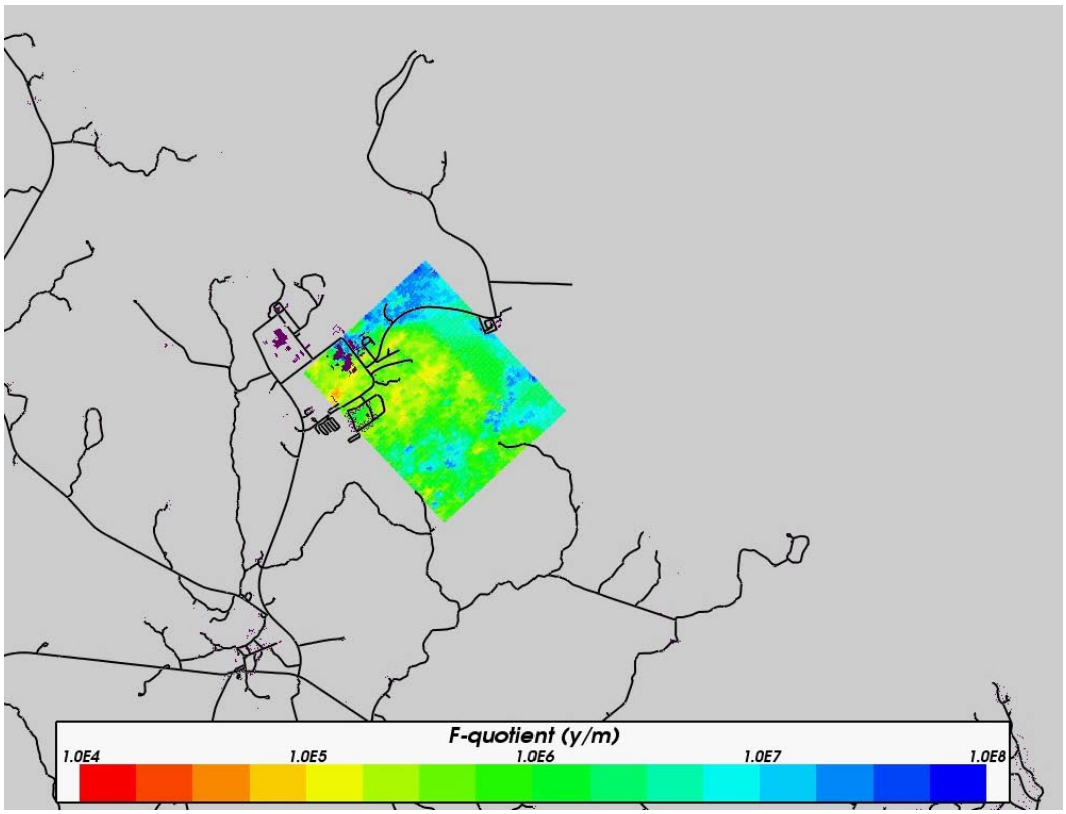

Figure 9-16. *Distribution of F-quotient (Log10) at particles starting locations in the local-scale release area for the Variant Geo-DFN using a correlated transmissivity model (HCD3_BC_ HRD3SFC_HSD1_BC1). Roads are shown in black for context.*

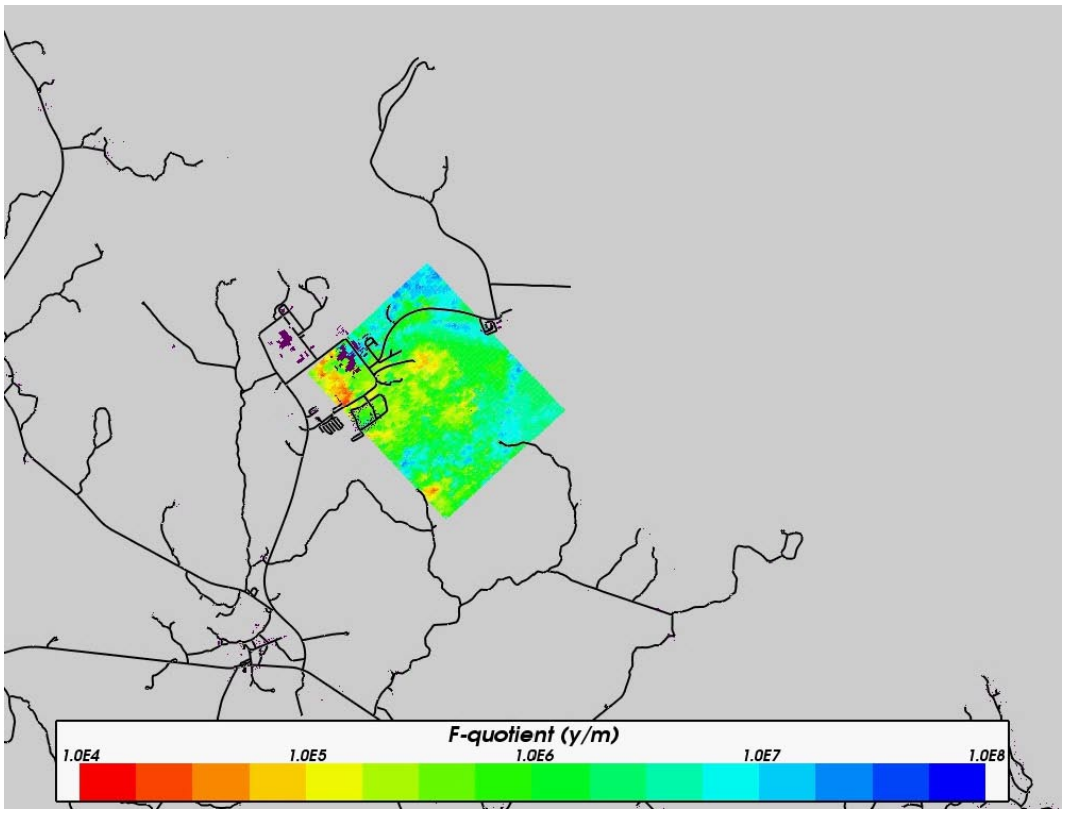

Figure 9-17. *Distribution of F-quotient (Log10) at particles starting locations in the local-scale release area for the Variant Geo-DFN using an uncorrelated transmissivity model (HCD3_BC_ HRD3SFU_HSD1_BC1). Roads are shown in black for context.*

9.5 Sensitivity to HRD hydraulic and transport properties

9.5.1 Increased background conductivity outside RFM017/029 (HCD3_BC_HRD3ECK1_HSD1_BC1)

This case uses a model with increased background conductivity outside RFM017/029. In Figure 9-21 the distribution of the $\log_{10}$(F-quotient) at particle starting locations in the local scale area for the case using increased background conductivity outside RFM017/029 is presented. Figure 9-22 presents the F-quotient at particles exit locations in the local-scale area. The values for the F-quotient are only slightly lower compared to the Base Case confirming that flow is localized within RFM017/029 and not affected strongly by upstream conditions. The exit locations are very similar for the two cases with a few more particles reaching further out in the Baltic Sea in the uncorrelated case. In Figure 9-20, the present-day distributions of the four reference waters Brine, Marine water, Rain 1960 and Glacial water, are presented in vertical slices. Increasing the conductivity outside RFM017/029 has a significant impact on the reference water distribution. The Brine water does not very much but the Marine water penetrates to a much larger extent outside RFM017/029. This results in Glacial water being flushed out from the top 600–700 m. Also infiltrating Rain 1960 reaches deeper into the model pushing Brine in the western part of the modelled area towards the Baltic Sea.

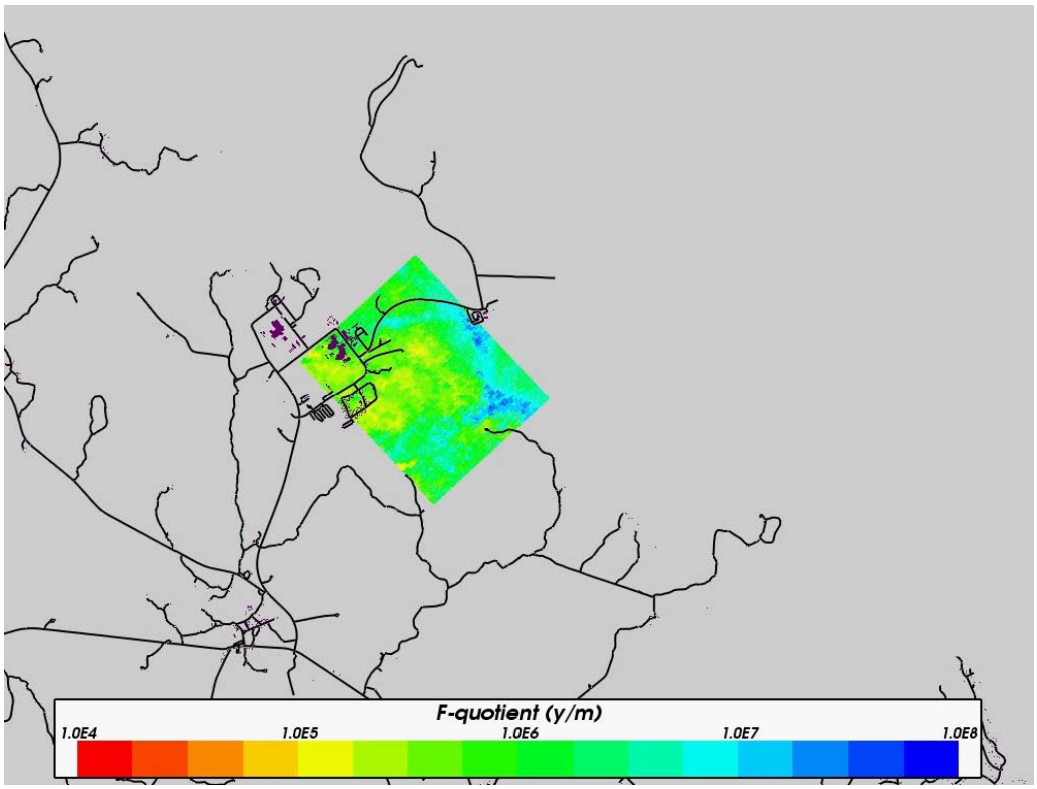

Figure 9-18. *Distribution of F-quotient (Log10) at particles starting locations in the local-scale release area for the model with increased K outside RFM017/029 (HCD3_BC_HRD3ECK1_HSD1_BC1). Roads are shown in black for context.*

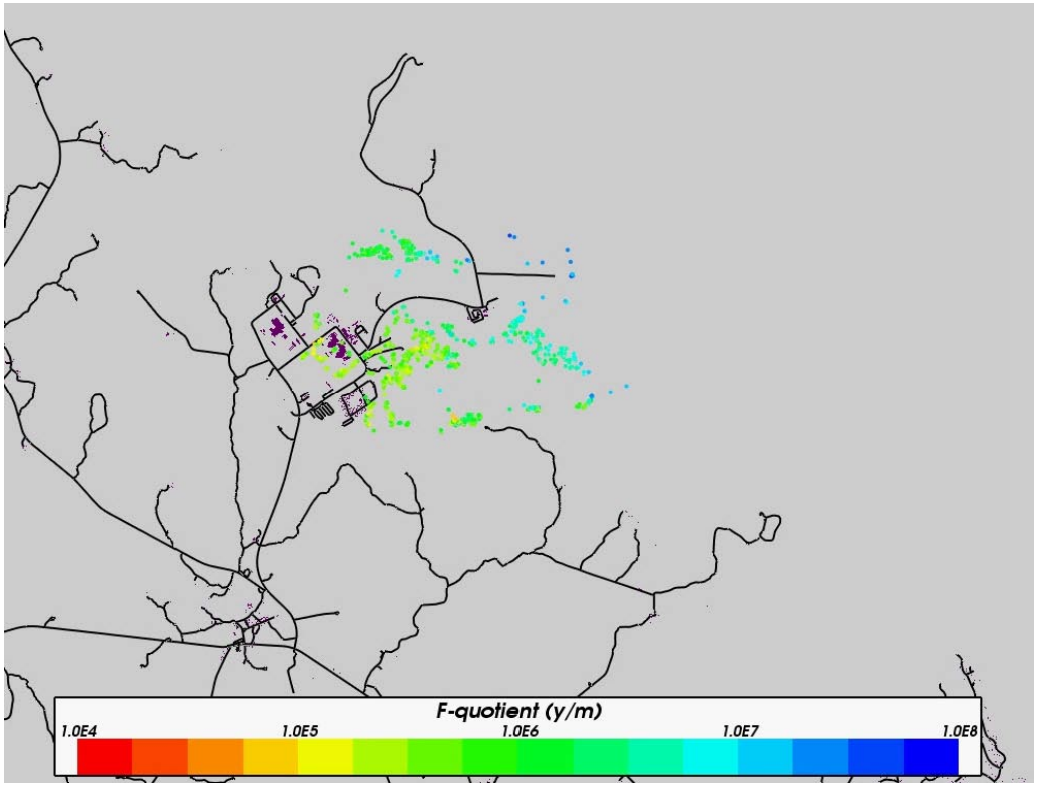

Figure 9-19. *Distribution of F-quotient (Log10) at particles exit locations in the local-scale release area for the model with increased K outside RFM017/029 (HCD3_BC_HRD3ECK1_HSD1_BC1). Roads are shown in black for context.*

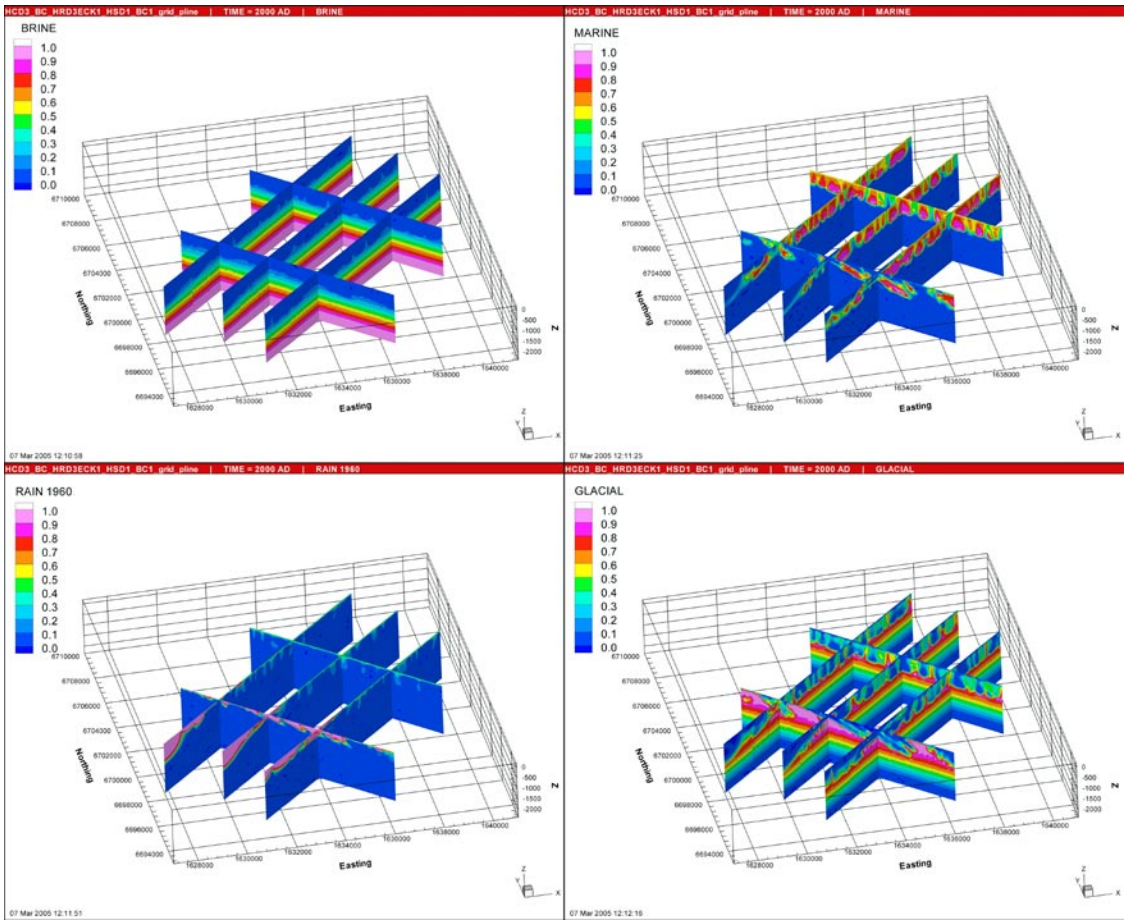

Figure 9-20. *Present-day distribution of the reference waters Brine (top left), Marine water (top right), Rain 1960 (bottom left) and Glacial water (bottom right) in vertical slices, for the model with increased K outside RFM017/029 (HCD3_BC_HRD3ECK1_HSD1_BC1).*

9.5.2 Lower flow-wetted-surface, a_r = 0.25 m^2m^{-3}, for RMD (HCD3_BC_HRD3ECF1_HSD1_BC1)

This case uses a model with reduced flow-wetted-surface, a_r = 0.25 m^2m^{-3}, to give reduced RMD. Potentially this will affect both the distribution of reference waters, as there is a slower access to the matrix, and also the F-quotient for transport in the HCD will be reduced directly by a quarter. Note that the flow wetted surface has been reduced for the reference water calculations in the HRD and HCD, by the same amount, whereas for the particle transport, a_r is unchanged in the HRD since it is based on the connected P32 in the underlying DFN model, and this has not been changed. In Figure 9-21 the distribution of the $\log_{10}$(F-quotient) at particles starting locations in the local scale release-area for the case with reduced flow-wetted-surface is presented. Figure 9-22 presents the F-quotient at particles exit locations in the local-scale area. The values for the F-quotient are slightly lowered compared to the Base Case and more homogeneous. The main reduction in F-quotient is coincident with where the HCDs cut the release-area. Overall, the changes are not large. The distribution of exit locations is almost identical to the Base Case. In Figure 9-23, the present-day distributions of the four reference waters Brine, Marine water, Rain 1960 and Glacial water, are presented in vertical slices. The penetration of Marine water in sub-horizontal zones is slightly greater than for the Base Case since it is retarded less by RMD.

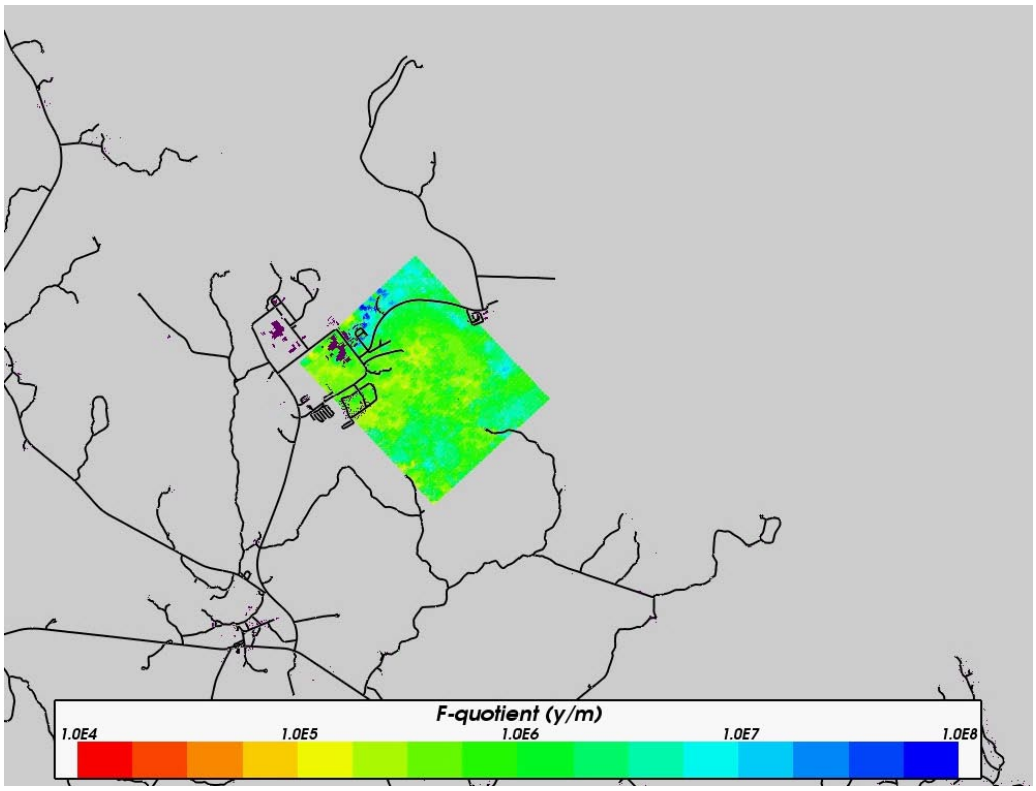

Figure 9-21. *Distribution of F-quotient (Log10) at particle start locations in the local-scale release area for the model with reduced RMD due to lower FWS a_r = 0.25 m^2m^{-3} (HCD3_BC_HRD3ECF1_HSD1_BC1). Roads are shown in black for context.*

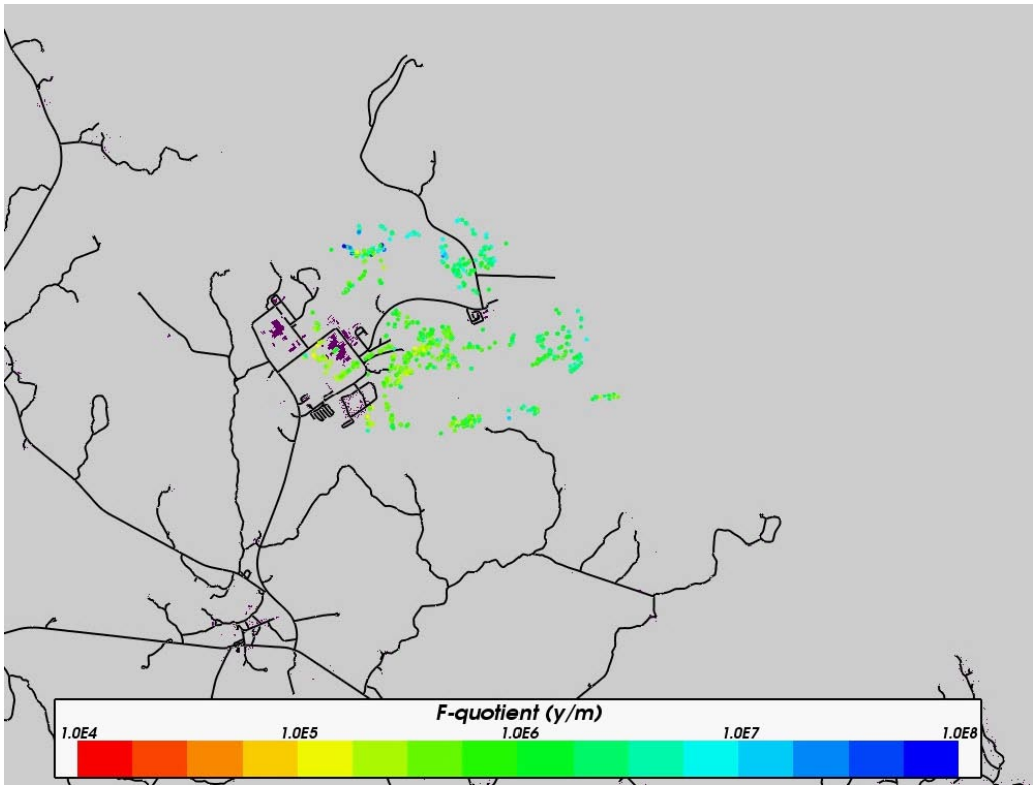

Figure 9-22. *Distribution of F-quotient (Log10) at particles exit locations in the local-scale release area for the model with reduced RMD due to lower FWS a_r = 0.25 m^2m^{-3} (HCD3_BC_HRD3ECF1_HSD1_BC1). Roads are shown in black for context.*

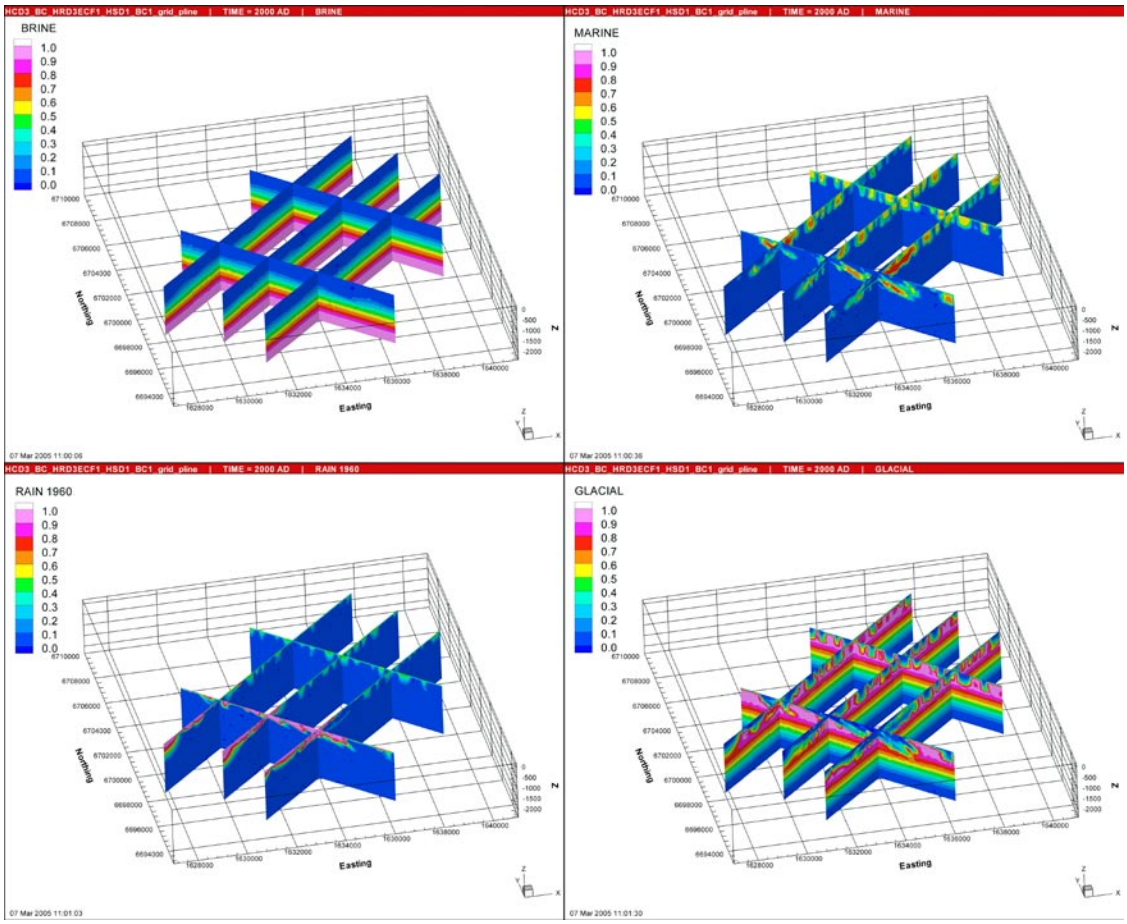

Figure 9-23. *Present-day distribution of the reference waters Brine (top left), Marine water (top right), Rain 1960 (bottom left) and Glacial water (bottom right) in vertical slices, for the model with* $a_r = 0.25\ m^2m^{-3}$ *(HCD3_BC_HRD3ECF1_HSD1_BC1).*

9.5.3 Lower matrix porosity, $n_m = 2.5\ 10^{-3}$ (HCD3_BC_HRD3ECN1_HSD1_BC1)

This case uses a model with reduced matrix porosity, $n_m = 2.5\ 10^{-3}$. In Figure 9-24 the distribution of the $\log_{10}$(F-quotient) at particles starting locations in the local scale area for the case with reduced matrix porosity is presented. The values for the F-quotient are very similar to the Base Case, perhaps slightly lower, since the reference water profiles were not significantly modified.

9.5.4 Lower diffusivity, $D_i = 1.0\ 10^{-13}\ m^2s^{-1}$ (HCD3_BC_HRD3ECD1_HSD1_BC1)

This case uses a model with reduced diffusivity, $D_i = 1.0\ 10^{-13}\ m^2s^{-1}$. The results for particle transport were virtually identical to the Base Case, and so it is not necessary to present results.

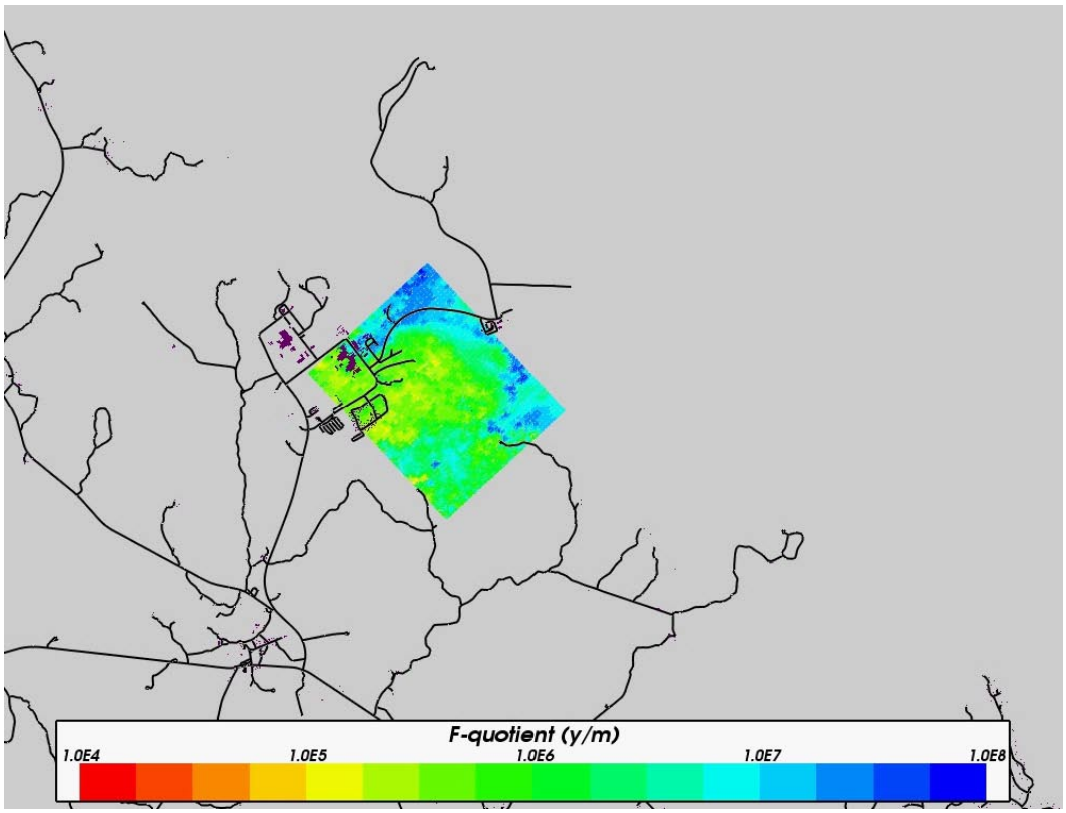

Figure 9-24. *Distribution of F-quotient (Log10) at particles starting locations in the local-scale release area for the model with matrix porosity n_m = 2.5 10^{-3} (HCD3_BC_HRD3ECN1_HSD1_ BC1). Roads are shown in black for context.*

9.6 Sensitivity to geological model

9.6.1 Alternative Case (AC) HCD model (HCD3_AC_HRD3EC_HSD1_BC1)

This case uses the Alternative Case (AC) geological model. In Figure 9-25 the distribution of the $\log_{10}$(F-quotient) at particles starting locations in the local scale area for the Alternative Case HCD model is presented. Figure 9-26 presents the F-quotient at particles exit locations in the local-scale area. The values for the F-quotient are only slightly lower compared to the Base Case confirming that presence of properties outside the candidate area do not significantly impact transport inside. The exit locations are very similar for the two cases with a few more particles reaching further out in the Baltic Sea in the AC case. In Figure 9-27, the present-day distributions of the four reference waters Brine, Marine water, Rain 1960 and Glacial water, are presented in vertical slices. Using the Alternative Case HCD model adds structures outside RFM017/029. The effect is similar to increasing the conductivity as demonstrated earlier. Marine water penetrates into the model through the fracture zones to a larger extent compared to the Base Case. The entering Marine water replaces the Glacial water in the top 600 m. The infiltrating Rain 1960 does not differ much from the Base Case. In Figure 9-28, the vertical Darcy velocity distribution under present-day flow conditions is presented in horizontal slices. The fracture zones added to the model is clearly visible in the flow pattern where the structures are shown as areas with downward flows in particular underneath the Baltic Sea. The magnitude of the vertical Darcy velocity in the top of the model is only slightly increased compared to the Base Case.

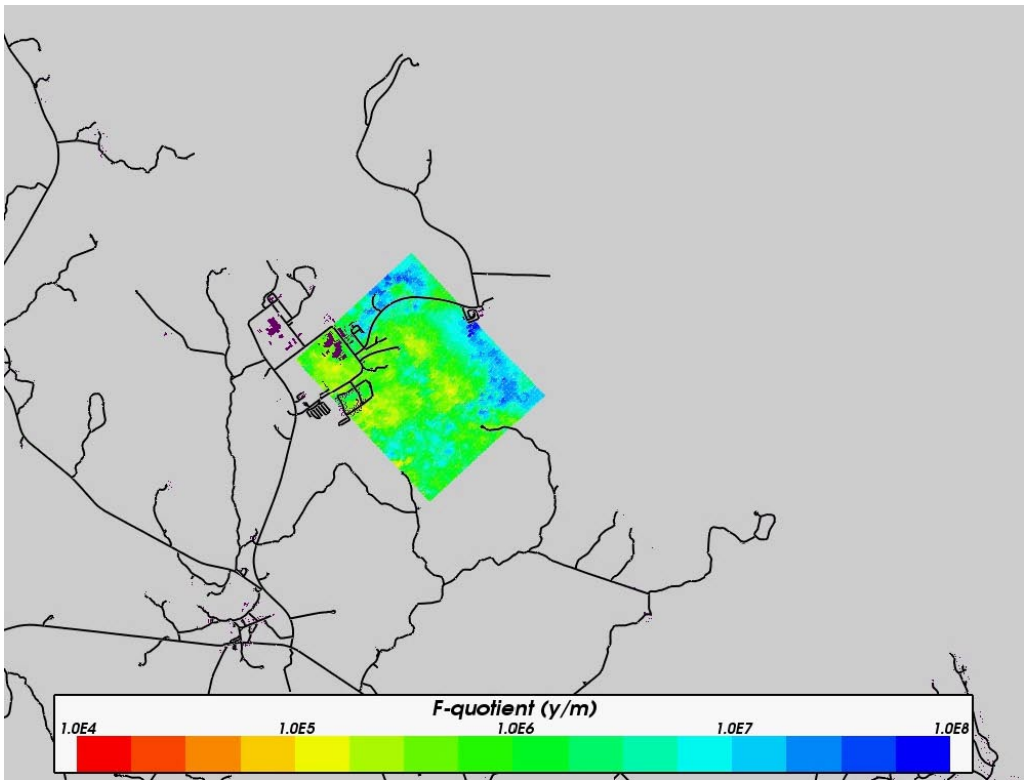

Figure 9-25. *Distribution of F-quotient (Log10) at particles starting locations in the local-scale release area for the alternative case (AC) HCD model (HCD3_AC_HRD3EC_HSD1_BC1). Roads are shown in black for context.*

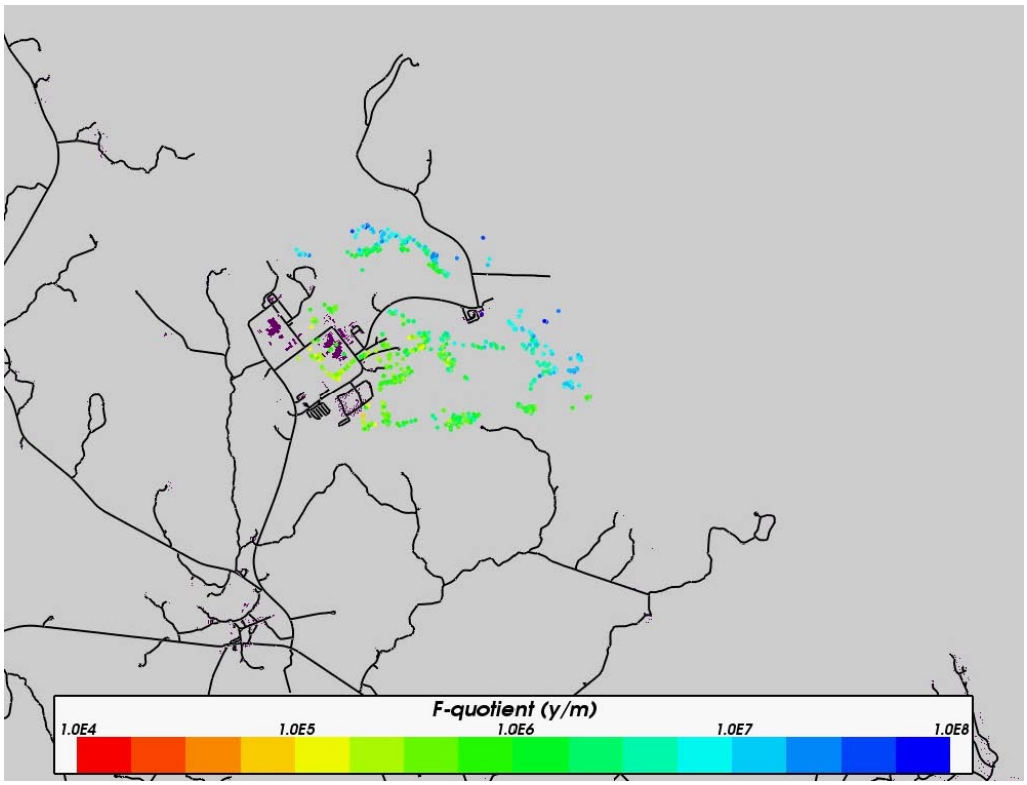

Figure 9-26. *Distribution of F-quotient (Log10) at particles exit locations in the local-scale release area for the alternative case (AC) HCD model (HCD3_AC_HRD3EC_HSD1_BC1). Roads are shown in black for context.*

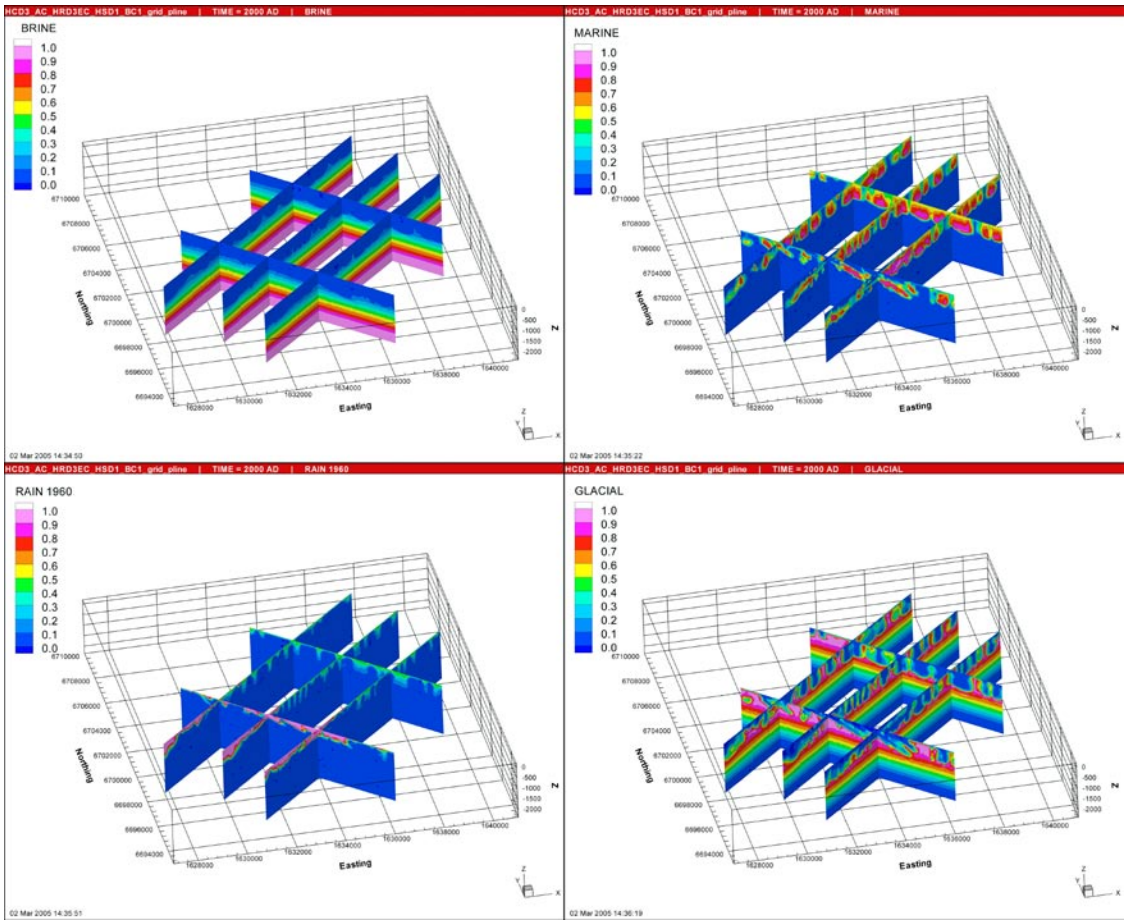

Figure 9-27. *Present-day distribution of the reference waters Brine (top left), Marine water (top right), Rain 1960 (bottom left) and Glacial water (bottom right) in vertical slices, for the alternative case (AC) HCD model (HCD3_AC_HRD3EC_HSD1_BC1).*

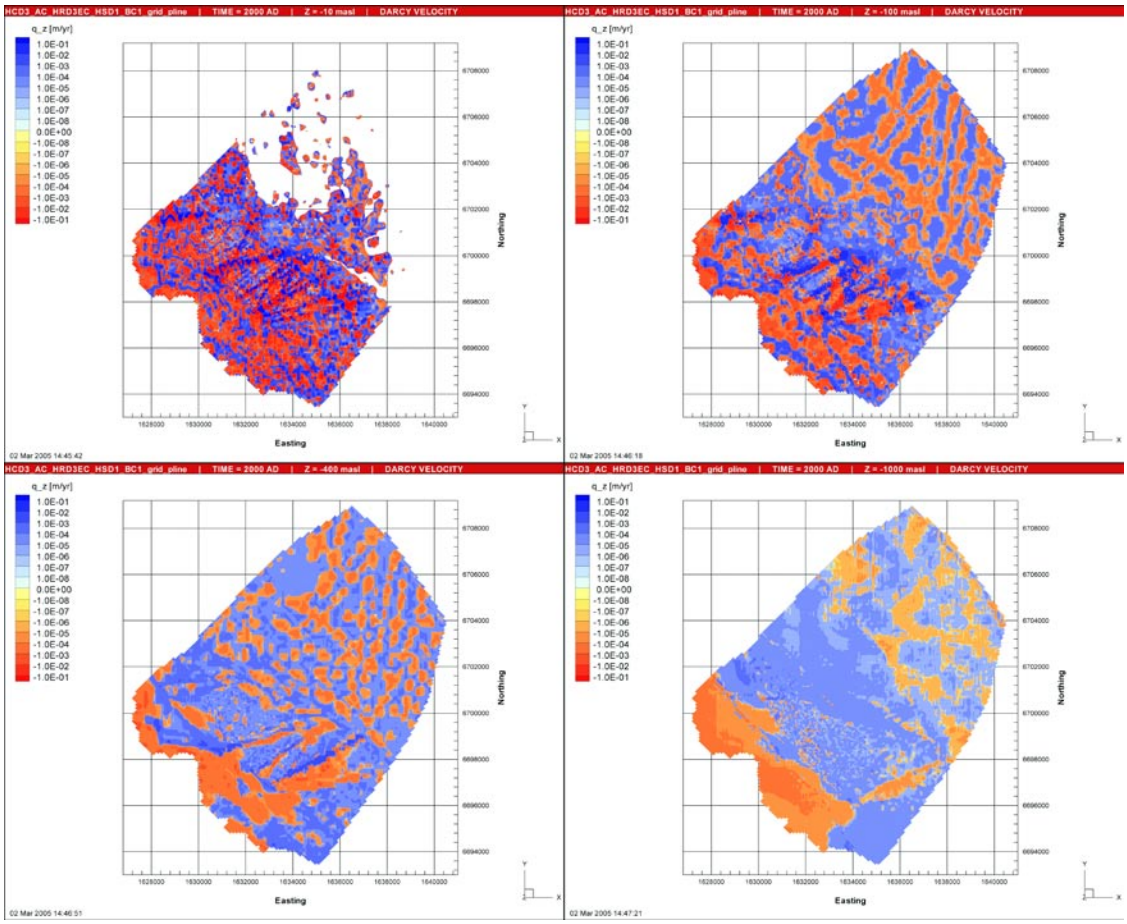

Figure 9-28. *Present-day distribution of the vertical Darcy velocity, q_z (positive is upward), in horizontal slices at elevations (from top to bottom) –10 m, –100 m, –400 m and –1,000 m, for the alternative case (AC) HCD model (HCD3_AC_HRD3EC_HSD1_BC1).*

9.6.2 Alternative Case (AC) HCD model with lower matrix porosity, $n_m = 10^{-3}$ m²s⁻¹ (HCD3_AC_HRD3ECN1_HSD1_BC1)

This case uses the Alternative Case (AC) HCD model with reduced matrix porosity, n_m, in HRD. The results are very similar to the previous case, HCD3_AC_HRD3EC_HSD1_BC1, so they are not described here.

10 Discussion and general conclusions

10.1 Summary of main conclusions and feedback to other disciplines

From the Hydro-DFN study:

- **A new methodology (developed for Simpevarp 1.2) has been used for integrating the PFL (KFM01A–KFM05A) and PSS (KFM01A–KFM03A) hydraulic data with the geological fracture interpretation to produce a conditioned Hydro-DFN model and to quantify the uncertainties to various assumptions.** This methodology uses flow simulations in DFN models to calibrate several alternative relationships between fracture transmissivity and length;
- **It is possible to calibrate several possible models for fracture transmissivity, although the direct correlation between transmissivity and length is perhaps easier to match to the borehole flow data;**
- There were some difficulties in applying the Geo-DFN. The primary difficult stemmed from significant variations in fracture intensities and the proportions of sets between boreholes making it hard to use an averaged model such as the Geo-DFN when matching hydraulic tests at a specific borehole. Another major problem was that the uncertainty in the fracture length PDF in terms of the slope k_r and reference fracture length, L_0. This was addressed by considering a variant Geo-DFN with a uniform slope $k_r = 2.75$ as a sensitivity test and calibrating a alternative Hydro-DFN based on this length PDF;
- The variant Geo-DFN makes a more conceptually feasible Hydro-DFN based on KFM03A since the original Geo-DFN requires the fracture intensity of open fractures to be increased by about 30% above the maximum of the range observed in the borehole to match the hydraulic responses, which is hard to justify. Whereas the variant Geo-DFN requires it to be reduced by 30%, which is within the recorded uncertainty range on open fractures;
- The PSS and PFL data were integrated as equivalent transmissivities of 5 m intervals to give two alternative calibration targets. This helped narrow uncertainties in some instances where there was a higher detection limit on the PFL data;
- Due to the spatial variability of the fracture properties a number of bedrock volumes were defined jointly with the DarcyTools Team. For CONNECTFLOW the following were defined: Volume E – below Zone A2 and above 400 m depth, Volume F – above Zone A2, Volume G – below Zone A2 and below 400 m depth;
- **For both Volume E and Volume F for the 20 m block, the median hydraulic conductivity for uncorrelated and semi-correlated transmissivity models is similar, around log(Keff) of –8.5 and –8.8 for Volume E, and –8.6 for both T models for Volume F. For the correlated model, for both Volume E and Volume F, the median effective hydraulic conductivity is nearly one order of magnitude lower ($\log(K_{eff}) = -9.8$ and –9.5, respectively);**
- Use of the variant Geo-DFN parameters ($k_r = 2.75$) for the correlated and uncorrelated models for Volume E shows lower median $\log(K_{eff})$ of –10.2 and –9.2 for the 20 m block compared to the original Geo-DFN;

- **For a 100 m block for both Volume E and Volume F, the median effective hydraulic conductivity is much more similar for all three T models, with log(K_{eff}) varying between –8.9 and –9.4 in all T models and for both rock volumes. For the 100 m block the variant Geo-DFN parameters show similar median K_{eff} to the original Geo-DFN input parameters (log(K_{eff}) of –9.1 and –9.5 for the correlated and uncorrelated models);**
- There is localised horizontal anisotropy within a block for all T models due to the discrete nature of the DFN. The median horizontal anisotropy Kh_{max}/Kh_{min} for Volume E is generally around 6. For Volume F, Kh_{max}/Kh_{min} is observed to be in the range 3 to 7;
- **For both rock volumes, the hydraulic conductivity is similar in x, y and z directions, suggesting little regional anisotropy. There is only a weak regional anisotropy between the horizontal and vertical hydraulic conductivity with median ratio Kh_{max}/Kz of about 1 to 1.5;**
- For Volume F, for all T models, there is a slight trend of regional anisotropy with an observed Kh_{max} with a strike direction of about 030°–060°. This is consistent with the PFL flow anomaly data. For Volume E, the direction of the slight regional anisotropy is less clear, with the uncorrelated model showing no directional trend, and the correlated and semi-correlated T models showing a trend in the direction with strike of 120°–150°. This is consistent with the NW-SE regional stress;
- **Fracture kinematic porosity is more similar for the uncorrelated and semi-correlated models. For example, for Volume E, log(n_e) is around –4.7 for the 100 m block for the uncorrelated and semi-correlated models. In contrast, the correlated model shows around half an order of magnitude lower fracture kinematic porosity for both rock volumes. For Volume F, the 100 m block for uncorrelated and semi-correlated T models show log(n_e) of –4.9 and –4.7, whereas the uncorrelated model has log(n_e) of –5.2;**
- **A minimum fracture truncation length (L_{min}) of 25 m is recommended for the regional modelling with a 100 m block,** since it produces the best compromise between computational feasibility and accuracy of block properties, for both Volume E and Volume F.

From the regional flow modelling and calibration against hydro-geochemistry:

- **The regional model from F1.1 ~15 km (SW-NE) by 11 km (NW-SE) was more than sufficient for reference water calculation for site areas since flow in the candidate area is quite localised.** The large area was retained to allow the evolution of flow and transport in to the future to be considered when the shoreline is likely to retreat to the north;
- A refined grid of at least 50 m element size is required throughout a local area that covers the release-area and the calibration boreholes to represent flow and transport due to a large number of sub-horizontal zones within the candidate area;
- **Calibration of hydraulic and hydro-geochemical properties is most sensitive to the width and transmissivity of deformation zones that intersect the boreholes;**
- This leads to depth dependent HCD property model that differentiates between gently and steeply dipping deformations zones;
- **The presence and properties of deformation zones outside the candidate area have little effect on present-day flow and transport, and hence the regional geological model cannot be calibrated currently;**
- The Hydro-DFN properties give background block-scale hydraulic conductivities of the correct order of magnitude to predict hydro-geochemistry although site data suggest rock volumes with conductivity below that predicted by the Hydro-DFN;

- A Base Case model has been developed for F1.2 that gives a reasonable match to the hydro-geochemistry data using reference water mixing fractions, major ion concentrations and environmental isotopes at KFM01A–KFM04A;
- **In terms of the use of hydro-geochemical information, it was found most convenient to define boundary and initial conditions in terms of reference water fraction, but then for the calibration to compare the simulations against borehole profiles for $\delta^{18}O$, Cl and Mg to avoid uncertainties associated with the M3 interpretation;**
- The hydro-geochemical data are sparse, especially at depth, so it was difficult to constrain model variants and parameters with confidence;
- The best initial condition was to impose Glacial water injected under high pressures down to about 500 m–2.0 km during early post-glacial period with a weak gradient for Brine below that from zero at 500 m to full Brine at 2.0 km;
- HRD and HCD properties outside the candidate area had little effect on flow and transport inside since flow is relatively localised in the local-area;
- HRD block-scale properties of the DFN in rock domains RFM017/029 are most sensitive to the fracture transmissivity model rather than the fracture length distribution providing the other fracture parameters are calibrated to the hydraulic data in a consistent methodology;
- Stochastic variations of the DFN have only a small influence on flow and transport compared to more important conditions such as the HCD positions and properties. This may justify the sufficiency of relatively few realisations of each HRD case;
- The calibrated uncorrelated transmissivity model gave higher block-scale hydraulic conductivities that gave a poorer match to the hydro-geochemical data than the correlated model;
- The results were not sensitive to surface property variants considered. However, the model matched the Cl concentration in the top 100 m of some boreholes. This motivates further investigation of alternative or spatial variable surface properties;
- **Both a specified topographic head and a specified flux type boundary condition was considered, but for the infiltration and surface properties considered the water table was close to ground surface so there was very little difference in results;**
- Sensitivities to transport parameters such as flow-wetted surface, matrix porosity and diffusivity that affect RMD have been investigated. Matrix porosity was found to potentially influence the results, but not for the relative tight range of values supplied for this parameter. Hence, transport is probably most uncertain with respect to flow-wetted surface. **The results here suggest a difference in groundwater concentrations between fracture and matrix systems if a_r is less than or around 0.25 m^2/m^3;**
- The seeming lack of sensitivity is partly a result of the conditioning of the models against both hydraulic and hydro-geochemical information that appears to give a range of parameter uncertainties that do not impact the regional flow results significantly;
- **Tritium modelling reinforces the concept of 'tight' rock at Forsmark, with penetration of surface tritium containing water down to a maximum of only –100 m elevation.** The lack of sensitivity in tritium due to the low values of tritium recorded and modelled makes it difficult to calibrate the modelling with flow-wetted surface area. This is in contrast to tritium modelling at Simpevarp /15/.

From the transport calculations:

- **The variations in the performance measures between the variants considered is generally low, around 5–10%. This perhaps should not be a surprise since all the cases considered have been calibrated against the same hydraulic data in the case of the Hydro-DFN variants, and against the same hydro-geochemistry data in the case of regional flow and solute transport.**
- **The F-quotient for most of the local-scale area is of order 10^6y m^{-1}, with the 5^{th} percentile at about 10^5y m^{-1} and the 95^{th} percentile at about 10^7y m^{-1}.**
- The median path lengths stays around 1 km for all cases considered with only a few particles reaching further than 4 km. This indicates much localised flows in the modelled area.
- Changing the hydraulic properties of the rock volume outside RFM017/029 does not have a significant impact on the present-day flow in the candidate area.
- **The uncertainties around the value of the flow-wetted surface should be addressed further within the SR-Can Assessment since this has a significant impact mainly on the F-quotient.**

10.2 Conclusions and recommendations for further investigations and simulations

10.2.1 Recommendations for further simulations

Important issues that should be addressed in future studies include:

- Since the results are most sensitive to the HCD model and properties, additional variants should be considered such as alternative depth dependency fits to transmissivity and stochastic variations within a zone. Varying the kinematic porosity of the HCD model should also be considered;
- Depth variations in the HRD properties may also be worth considering. Appropriate cases could be an order of magnitude higher or lower in the top 100–200 m;
- Another possible variation on the HRD properties is to construct a DFN with a lower fracture intensity below Zone A2 as suggested in the Hydro-DFN analysis;
- A greater number of variants on the HSD properties and surface infiltration are also desirable.

10.2.2 Recommendations for further investigations

This study has suggested some issues on which to focus further acquisition of site data:

- The PSS data helped reduce uncertainty in the intensity of flowing features at the low end of the transmissivity distribution. This was important in the relatively tight rock at Forsmark and will improve the constraint of hydraulic properties of fractures affecting canister-scale flows in the SR-Can safety assessment;
- In terms of flow and transport within the candidate areas, this study suggests that efforts should focus on the locations and properties of deformation zones local to the site. This may involve further drilling to confirm seismic reflectors to establish the extent of zones, and also interference test within zones to investigate large scale flow and connectivity;

- Hydraulic properties in the top 100 m are uncertain as the cored boreholes are cased. However, the models have struggled to match a high Cl concentration near surface in some boreholes. To improve our understanding, hydraulic tests such as single-hole interference test in the top 200 m, say, would be useful;
- There is considerable variability in fracture intensity and flowing features within and between boreholes. In particular, KFM01A is very tight while KFM03A has flowing features at depth. Additional boreholes will be required to confirm any trends and their spatial extent. Hydraulic data outside RFM017/029 would also help set the hydraulic properties better in a regional-scale context. Although the result here suggest a low sensitivity;
- The hydro-geochemistry data available for Forsmark 1.2 were very limited especially at or below 400 m (the provisional repository depth for Forsmark). Additional data would provide a better calibration target and assist constraining the hydrogeological models;
- The hydro-geochemistry data for the top 100 m is especially uncertain in the top 100 m of boreholes due to different water sampling techniques and contamination. Greater effort to acquire representative water samples in the top 100–150 m would significantly help focus the near-surface hydrogeological model calibration efforts;
- The models of the reference water transport suggest some pockets of Marine water near the coast. This motivates an integration of the borehole location selection and the groundwater modelling to confirm some of the model predictions;
- The groundwater model calibration has suggested that groundwater chemistry in the fracture system should be similar to that in the matrix. This is useful information since it suggests groundwater infiltrates a network of small but connected fractures that give access to significant matrix diffusion, and hence potential retardation of radionuclides in the host rock. Experiments would be useful to verify this finding, e.g. porewater composition in cores far from flowing features or as a profile over a 20 m section, say, of borehole;
- The tritium modelling could be improved with more high quality data, particularly near-surface data. In particular, each it would be helpful to have more details for every sample, including the date of sample analysis (sample collection date is already recorded), the detection limit, the analytical error on each measurement, the percentage of contamination present due to drilling fluid and the source of the drilling fluid. The half life of tritium is very short (12.34 years), which makes it a very sensitive measurement. Future measurements where significant tritium is measured could be considered for ^{3}He isotopic analysis. Tritium decays to stable ^{3}He, hence this would allow the depth of penetration of the atomic bomb tritium peak from the 1960's to be recorded.

10.2.3 Recommendations for the SR-Can Assessment

Some key uncertainties that should be considered within the SR-Can Safety Assessment based on F1.2 include:

- Some additional simulations need to be performed for the HCD properties. In particular, a gentler slope in the depth trend of transmissivity should be considered as this is will likely to lead to deeper flows, which may in turn lead to more regional flows. It may result in longer flow-paths and hence a positive effect on safety assessment. However, it should be considered to evaluate the sensitivity to the interpretation of a depth trend. Stochastic variations of transmissivity within deformation zones should also be considered;

- Transport properties, kinematic porosity and flow-wetted surface, of the HCD are another issue that requires further attention. It is suggested that one order of magnitude higher and lower be tried;
- Depth variations in the HRD hydraulic conductivity should be considered by variants with an order of magnitude higher and an order of magnitude lower in the top 100 m;
- DFN variants with an uncorrelated and semi-correlated transmissivity model should be considered since this the results seemed to be sensitive to this, although the uncorrelated model gave a poorer correlation to the hydro-geochemistry data;
- The variant Geo-DFN should be considered in SR-Can as it may have a stronger impact on canister-scale flows than was seen here on regional-scale flows;
- A variant should be considered with lower open P32 below A2;
- Additional variants need to be considered with lower values of the flow-wetted surface, a_r, in the HRD, although it may be possible to discount them if they do not calibrate to the hydro-geochemistry data;
- Flow-paths need to be considered at future times, once the shoreline has retreated north from the site, as this will modify hydraulic gradients.

References

1 **SKB, 2001.** Site Investigations. Investigation Methods and General Execution Programme, SKB TR-01-29, Svensk Kärnbränslehantering AB.

2 **SKB, 2000.** Geoscientific Programme for Investigation and Evaluation of Sites for the Deep Repository, SKB TR-00-20, Svensk Kärnbränslehantering AB.

3 **Andersson J, 2003.** Site Descriptive Modelling – Strategy for Integrated Evaluation, SKB R-03-05, Svensk Kärnbränslehantering AB.

4 **Skagius K (ed), 2004.** Preliminary Site Description: Forsmark Area – Version 1.1, SKB R-04-15, Svensk Kärnbränslehantering AB.

5 **La Pointe P R, Hermansson J, Olofsson I, 2005.** Statistical model of fractures and deformations zones for Forsmark. Preliminary site description Forsmark area – version 1.2. SKB R-05-26, Svensk Kärnbränslehantering AB.

6 **Hartley L J, Holton D, 2004.** CONNECTFLOW (Release 8.0) Technical Summary Document, Serco Assurance Report SERCO/ERRA C/TSD02V1.

7 **Hartley L J, Hoch A R, Cliffe K A, Jackson C P, Holton D, 2004.** NAMMU (Release 8.0) Technical Summary Document, Serco Assurance Report SA/ENV/0626.

8 **Hartley L J, Holton D, Hoch A R, 2004**. NAPSAC (Release 8.0) Technical Summary Document, Serco Assurance Report SERCO/ERRA-N/TSD02V1.

9 **La Pointe P R, Wallmann P, Follin S, 1995.** Estimation of Effective Block Conductivities Based on Discrete Network Analyses Using Data from the Äspö Site, SKB TR-95-15, Svensk Kärnbränslehantering AB.

10 **Jackson C P, Hoch A R, Todman S J, 2000.** Self-consistency of a Heterogeneous Continuum Porous Medium Representation of a Fractured Medium, Water Resources Research, 36, No. 1, pp 189–202.

11 **Marsic N, Hartley L J, Jackson C P, Poole M J, Morvik A, 2001.** Development of Hydrogeological Modelling Tools Based on NAMMU, SKB R-01-49, Svensk Kärnbränslehantering AB.

12 **Hoch A R, Jackson C P, 2004.** Rock-matrix Diffusion in Transport of Salinity. Implementation in CONNECTFLOW, SKB R-04-78, Svensk Kärnbränslehantering AB.

13 **Carrera J, Sanchez-Vila X, Benet I, Medina A, Galarza G, Guimera J, 1998.** On Matrix Diffusion: Formulations, Solution Methods and Quantitative Effects, Hydrogeology Journal, 6, No. 1, pp 178–190, (1998).

14 **Dershowitz W, Winberg A, Hermanson J, Byegård J, Tullborg E-L, Andersson P, Mazurek M, 2003.** Äspö Hard Rock Laboratory. Äspö Task Force on modelling of groundwater flow and transport of solutes – Task 6C – A semi-synthetic model of block scale conductive structures at the Äspö HRL. SKB IPR-03-13, Svensk Kärnbränslehantering AB.

15 **Hartley L J, Hoch A R, Hunter F M I, Jackson C P, Marsic N, 2005.** Regional hydrogeological simulations – Numerical modelling using CONNECTFLOW. Preliminary site description Simpevarp sub area – version 1.2:, SKB R-05-12, Svensk Kärnbränslehantering AB.

16 **Darcel C, Davy P, Bour O, De Dreuzy J-R, 2004.** Alternative DFN model based on initial site investigations at Simpevarp, SKB R-04-76, Svensk Kärnbränslehantering AB.

17 **Andersson J-E et al, 1989.** Hydrological Conditions in the Finnsjön Area: Compilation of Data and Conceptual Model, SKB Arbetsrapport 89–24, Svensk Kärnbränslehantering AB.

18 **Laaksoharju M et al, 2005.** Hydrogeochemical Evaluation for the Forsmark Model Version 1.2, SKB R-05-17, Svensk Kärnbränslehantering AB.

19 **Laaksoharju M et al, 2004.** Hydrogeochemical Evaluation of the Forsmark Site, Model Version 1.1, SKB R-04-05, Svensk Kärnbränslehantering AB.

20 **Adams J J, Bachu S, 2002.** Equations of State for Basin Geofluids: Algorithm Review and Intercomparison for Brines, Geofluids, 2, pp 257–271.

21 **Kestin J, Khalifa H E, Correia R J, 1981.** Tables of Dynamic and Kinematic Viscosity of Aqueous NaCl Solutions in the Temperature Range 20–150°C and the Pressure Range 0.1–35 MPa, J. Phys. Chem. Ref. Data Vol. 10, No. 1.

22 **Hartley L J, Worth D J, Gylling B, Marsic N, Holmen J, 2004.** Preliminary Site Description: Groundwater Flow Simulations. Simpevarp Area (Version 1.1) Modelled with CONNECTFLOW, SKB R-04-63, Svensk Kärnbränslehantering AB.

23 **Carlsson A, Olsson T, 1977.** Forsmark Power Plant Investigations, Bull. Geol. Inst. Univ. Uppsala, N.S.

24 **Laaksoharju M et al, 1999.** Multivariate Mixing and Mass Balance (M3) Calculations, A New Tool for Decoding Hydrogeochemical Information, Applied Geochemistry 14, 861–871.

Appendix A

Glossary of abbreviations

AC	Alternative case deformation zone model
a_r	Fracture surface area per unit volume (P32) ($m^2\,m^{-3}$)
BC	Base case deformation zone model
c	Solute concentration or mixing fraction
CDF	Cumulative density function
CF	CONNECTFLOW
CPM	Continuum porous medium
DFN	Discrete fracture network
DZ	Deformation zone
DT	DarcyTools
EPM	Equivalent porous medium
e_t	Fracture transport aperture (m)
F	F-quotient (y/m)
F_c	Solute flux
FWS	Flow-wetted surface
GWF	Groundwater flow
h	Groundwater head (m)
HCD	Hydraulic conductor domains
HRD	Hydraulic rock domains
HSD	Hydraulic surface domains
I	Potential infiltration (m/y)
IC	Initial condition
IFZ	Implicit fracture zone
K	Hydraulic conductivity (m^2s^{-1})
KFM	Cored borehole at Forsmark
L	Fracture length (m) or Pathlength (m)
M3	Mixing and mass-balance modelling
n_e	Kinematic porosity (–)
n_m	Matrix porosity (–)
P10	Linear fracture intensity: number of fractures per metre along a borehole (m^{-1})
P21	Area fracture intensity: total fracture lengths per square metre of outcrop ($m\,m^{-2}$)
P32	Volumetric fracture intensity: total fracture surface area per cubic metre of rock ($m^2\,m^{-3}$)
PDF	Probability distribution function

PFL Posiva flow-log

PM Performance measure

PSA Performance safety assessment

PSE Preliminary safety evaluation

PSS Pipe-string system

q Groundwater flow (m^3s^{-1}) or Darcy velocity ($m\ s^{-1}$)

R Recharge flux (m/y)

RD Rock domain

RMD Rock matrix diffusion

s Average separation of fractures in a vertical borehole (m)

SDM Site descriptive model

T Transmissivity (m^2s^{-1})

T_V Transmissivity model for steeply dipping DZs (m^2s^{-1})

T_H Transmissivity model for gently dipping DZs (m^2s^{-1})

T_O Transmissivity model for lineaments outside the tectonic lens (m^2s^{-1})

t True separation of fractures (m)

TD Task description

TDS Total dissolved solids

TU Tritium units

t_w Travel time

VC Variant case deformation zone model

z Topographic surface height (m)

Φ Kinematic porosity (–)

ϑ Angle between the fracture pole and the borehole trajectory (–)

Appendix B

Aspects of the analysis of the hydraulic DFN model

B.1 Analysis of geological data and Geo-DFN model

The first step in the analysis of the geological data was to group the fractures according to whether they lie inside or outside a DZ and then divide them into fracture sets for each DZ and for the background rock. The purpose is to see whether each DZ has a clearly dominant set. If such a set exists, then it may be expected that this will coincide with the general orientation of the DZ. It may be possible to verify this by comparing with, for example, reflection seismics. Sub-vertical boreholes will tend to have a bias toward intersecting sub-horizontal fractures. To mitigate against under-predicting the intensity of sub-vertical fractures, the Terzaghi correction was used. This was applied by calculating a weighting factor, f_T, for each fracture based on the angle, ∂, between the pole to the fracture plane and the borehole trajectory:

$$f_T = \min(1/\cos(\vartheta), 5) .$$

A maximum factor of 5 was used. This weighting was used when calculating density contours on stereonets, and also for estimating $P10_{corr}$. That is, the linear fracture intensity, P10, is calculated as the number of fractures in an interval divided by the interval length, whereas the Terzaghi-corrected fracture intensity, $P10_{corr}$, is estimated as the sum of weight factors divided by the interval length. It is our experience that this gives an accurate prediction of the $P10_{corr}$ that can be used as an estimate for P32 (fracture area per unit volume) in a DFN model to simulate the observed P10.

In this analysis, the $P10_{corr}$ has been calculated for open and partly-open background fractures for each borehole, and for subsections of each borehole where there are very apparent differences in fracture intensity.

The locations of the five cored boreholes, KFM01A–KFM05A, considered in the F1.2 data freeze are shown in Figure B-1 with respect to the outline of the candidate area. The locations of percussion drilled boreholes are also shown, but are not used in this analysis. The candidate area corresponds with the boundary of a ‘tectonic lens’ that is believed to be of exceptional mechanical strength and generally contains fewer fractures than the surrounding rock. Rock domains in the Forsmark area are illustrated in Figure B-2.

The fractures were classified according to set. This was provided by the Geo-DFN by analysis of lineaments, although the division between sub-vertical sets and the sub-horizontal set was not specified, and was taken to be 50° (Table B-1) based on a visual inspection of borehole stereonets.

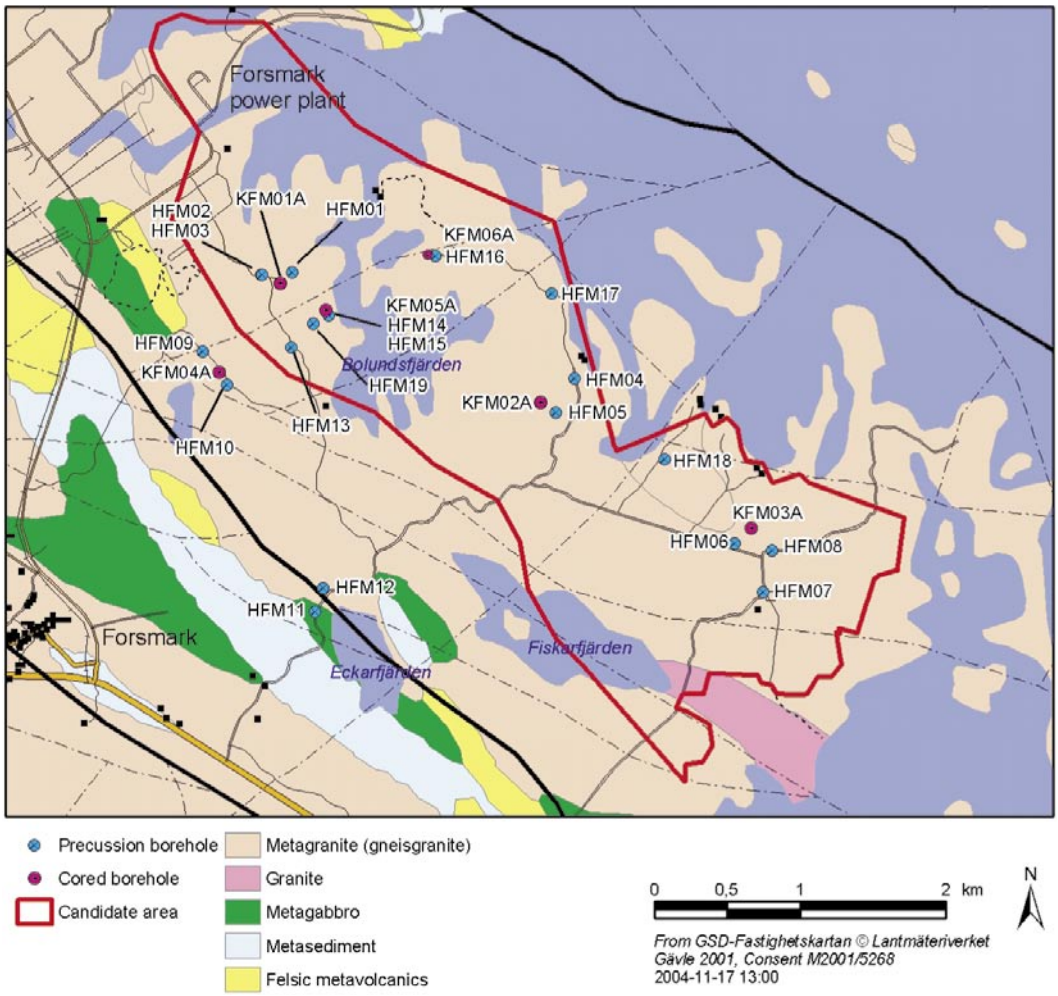

Figure B-1. *Geology of the Forsmark site showing the location of the evaluated boreholes KFM01A–KFM05A. Bounding NW-SE regional Deformation Zones are shown in black.*

Table B-1. Classification of the fractures into sets.

Set	Strike (°)	Azimuth (°)	Dip (°)
NS	0–20, 155–180	65–110, 245–290	50–90
NE	20–80	110–170, 290–350	50–90
NW	115–155	25–65, 205–245	50–90
EW	80–115	350–25, 170–205	50–90
HZ	0–180	0–360	0–50

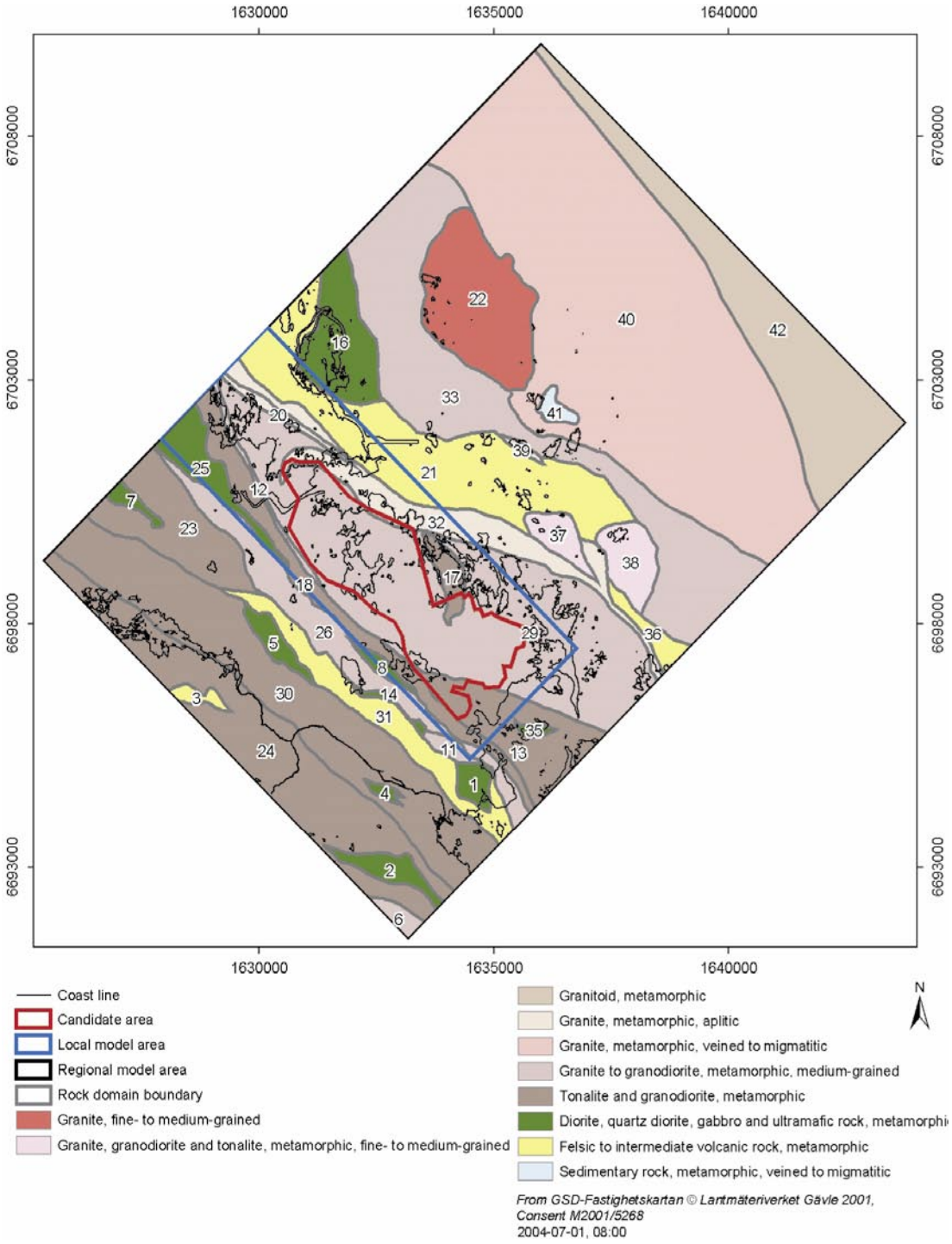

Figure B-2. *Rock Domains of Forsmark. The tectonic lens corresponds to RFM029 and RFM017.*

B.1.1 KFM01A: Deformation Zones and fracture intensities

KFM01A contains two Deformation Zones. In terms of the length down the boreholes, these are found at 386 m to 412 m (DZ2), and 639 m to 683 m (DZ3). The orientations of the open and partly-open fractures associated with these DZs appear distinctly on the stereonet within the NE sub-vertical and HZ sub-horizontal sets (see Figure B-3). Both sets occur in both DZs, although the mean strike for the NE set is slightly less for DZ3 than in DZ2. KFM01A is a near-vertical borehole, with trend of around 304° and plunge of around 80°.

The fracture intensity within each DZ is recorded in Table B-2. The mean length is the length down the borehole for the centre of the DZ. $P10_{corr}$ is relatively high in the DZs compared to the background fracturing where it is about 0.4 m^{-1} below about 400 m, or 1.4 m^{-1} taken over the whole borehole.

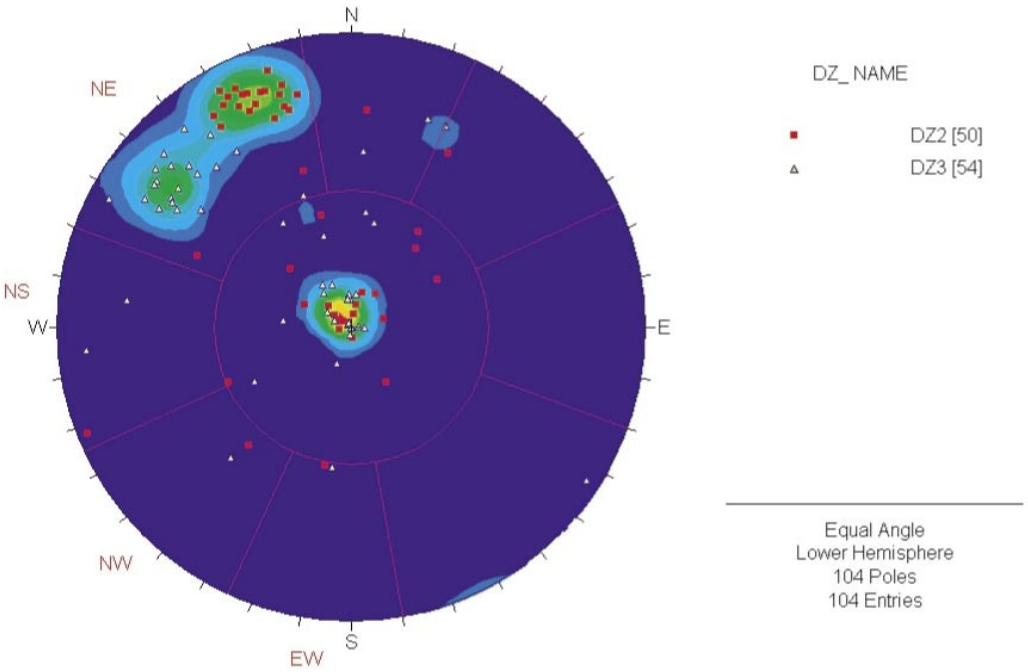

Figure B-3. *Poles of open and partly-open fractures associated with Deformation Zones in KFM01A. The individual features are plotted as points, whereas the coloured contours show a Terzaghi-corrected density plot.*

Table B-2. Positions‡, interval lengths and fracture intensity for Deformation Zones in KFM01A.

KFM01A	HCD domain	Mean length (m)	Interval length in borehole (m)	all P10 (m^{-1})	open P10 (m^{-1})	open $P10_{corr}$ (m^{-1})
DZ2	ZFMNE1192	398.91	25.8	4.42	1.94	4.42
DZ3	ZFMNE0061	661.21	44.4	5.56	1.22	2.49

‡ The Position is expressed as mean length (m), which gives the length down the borehole to the centre of the DZ.

B.1.2 KFM01A: Background fractures and fracture intensities

Each of the five boreholes was examined for the fracture intensity outside of Deformation Zones. This showed wide variation both between boreholes and within each borehole. For KFM01A, there is a clear reduction in the fracture intensity at around 400 m, as shown in Figure B-4 by the cumulative $P10_{corr}$ down the borehole starting from the top. Note: since it is a cumulative intensity, then it is the gradient in these plots that gives the value of fracture intensity at any depth. For example, the upper section of KFM01A (100 m to 386 m, i.e. above DZ2) shows much higher open fracture intensity of around $P10_{corr} = 3.3\ m^{-1}$ when compared to the lower section of KFM01A where $P10_{corr} = 0.36\ m^{-1}$ below 412 m (i.e. below DZ2), as seen in Table B-3 and Table B-4. About 72% of the total weighted fracture count in KFM01A is in the upper section, and HZ and NE are the dominant sets. In order to calculate the Terzaghi weighting, KFM01A has been approximated as a vertical borehole.

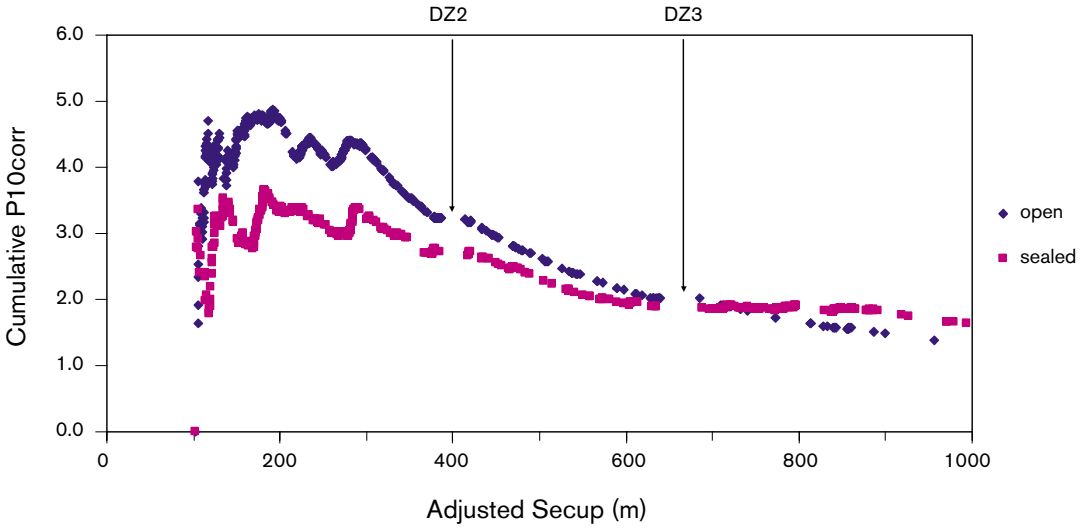

Figure B-4. *Cumulative $P10_{corr}$ (from the top) for open and partly-open fractures, and for sealed fractures for KFM01A. The apparent gaps in the data around 400 m and around 650 m correspond to DZ2 and DZ3.*

Table B-3. Background fracture intensity for the upper section of KFM01A (< 386 m). The interval length is 283 m.

KFM01A upper (< 386 m)	all P10 (m^{-1})	open P10 (m^{-1})	open $P10_{corr}$ (m^{-1})	open $P10_{corr}$ (%)
NS	0.24	0.10	0.29	8.83%
NE	0.80	0.35	1.21	37.12%
NW	0.21	0.11	0.25	7.75%
EW	0.09	0.06	0.16	4.94%
HZ	1.58	1.28	1.35	41.36%
Total	2.92	1.90	3.27	100.00%

Table B-4. Fracture intensity for the lower section of KFM01A (> 412 m). The interval length is 535 m.

KFM01A lower (> 412 m)	all P10 (m^{-1})	open P10 (m^{-1})	open $P10_{corr}$ (m^{-1})	open $P10_{corr}$ (%)
NS	0.21	0.032	0.103	28.54%
NE	0.18	0.026	0.089	24.60%
NW	0.02	0.006	0.018	5.04%
EW	0.01	0.000	0.000	0.00%
HZ	0.21	0.144	0.151	41.82%
Total	0.61	0.207	0.360	100.00%

After examination of the hydrogeological data (see subsection B.2.1), it was decided to focus separately on the upper section of KFM01A (above DZ2), where all the flow anomalies had been recorded, and the lower section of KFM01A (below DZ2), where no flow anomalies had been measured. Hence, the following stereonets of background fractures consider these length sections separately in Figure B-5 and Figure B-6, respectively. The background fractures in the upper section of KFM01A have dominant clusters in the HZ and NE sets, whereas those in the lower section of KFM01A have a dominant HZ cluster and two lesser NE and NS clusters.

The mean pole for each set in the upper section of KFM01A is compared to the global orientations for each set, defined in the Geo-DFN, in Figure B-7. The actual parameter values are compared in Table B-5 and Table B-6. The mean fracture pole is similar in both data sets. However, note the difference in the Fisher concentration in the Geo-DFN when compared to the upper section of KFM01A. For HZ, the Fisher concentration is a lot lower in the Geo-DFN, and in the NS, NW and EW sub-vertical sets it is much higher. (This may account for significant differences when later matching the P10 measured in the borehole, see subsection B.3.2).

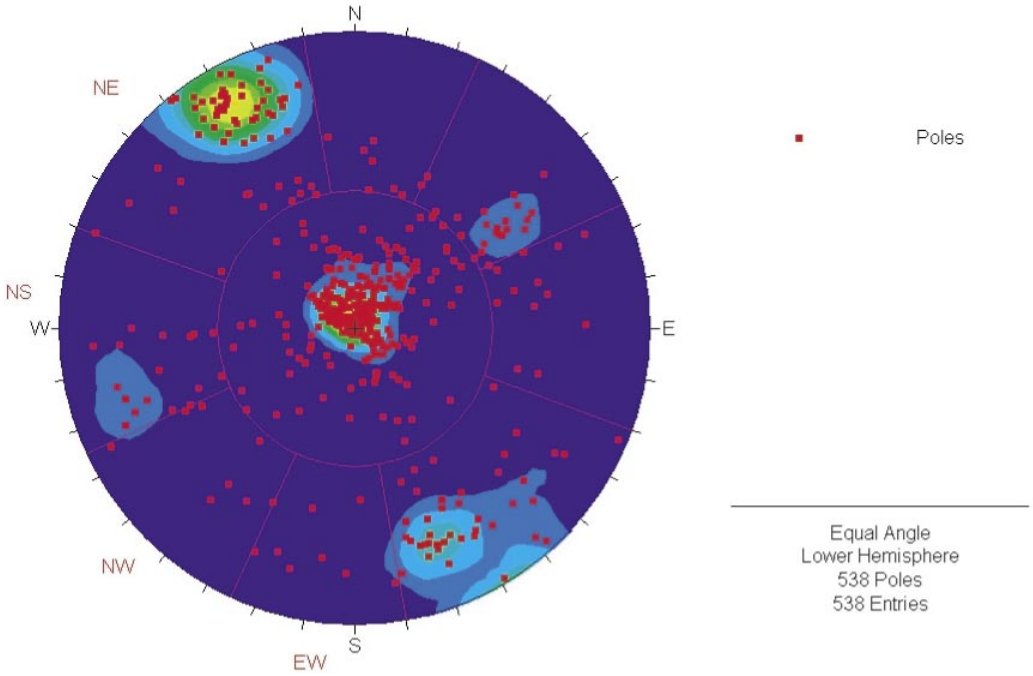

Figure B-5. *Open and partly-open background fractures in the upper section of KFM01A (above DZ2, i.e. above 386 m). The points show the poles to the individual fractures, and the coloured contours show a Terzaghi-corrected density plot.*

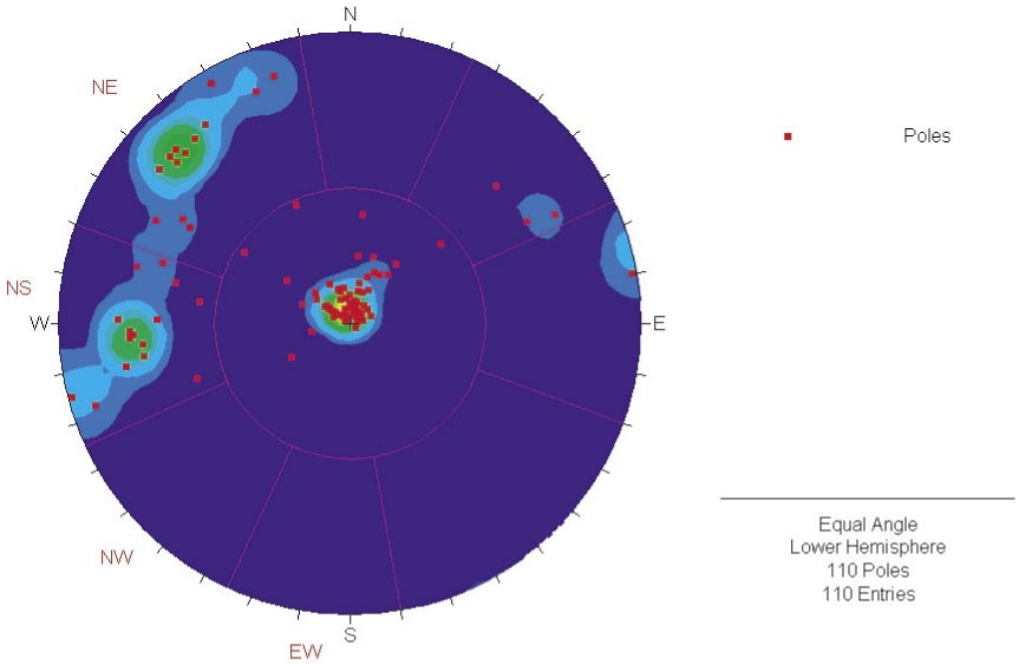

Figure B-6. *Open and partly-open background fractures in the lower section of KFM01A (below DZ2, i.e. below 412 m). The points show the poles to the individual fractures, and the coloured contours show a Terzaghi-corrected density plot.*

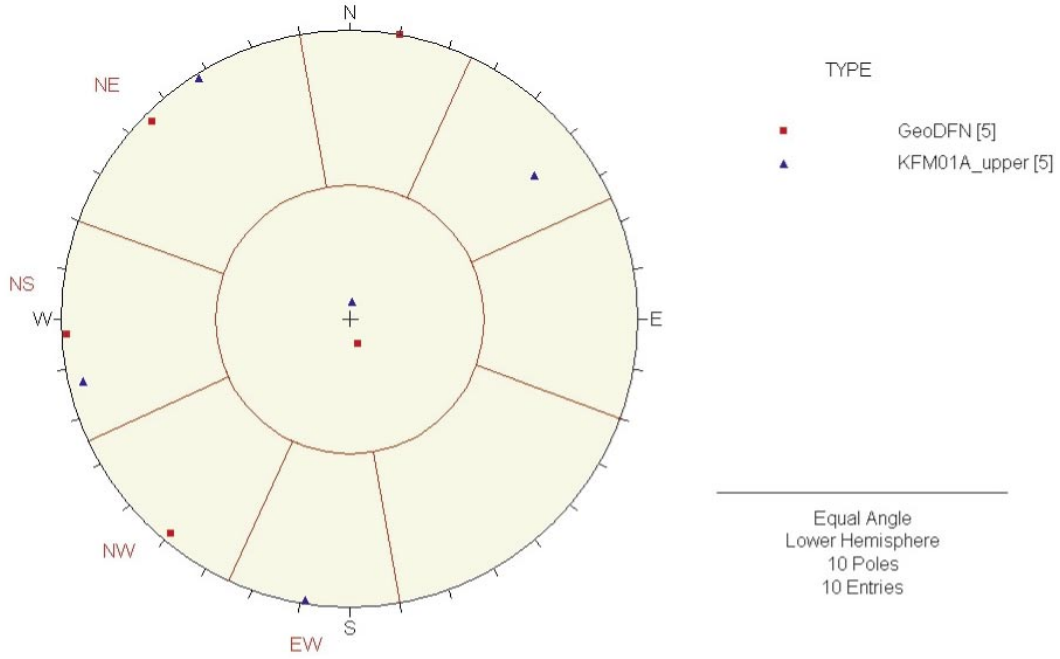

Figure B-7. *Summary of mean pole for each of the sets, calculated from open and partly-open fractures in the upper section (< 386 m) of KFM01A, compared to the mean pole of lineament-related fracture sets and the HZ set given in the Geo-DFN.*

Table B-5. Mean orientation of open and partly-open fractures for each set, calculated for the upper section of KFM01A.

Upper KFM01A	Strike (°)	Dip (°)	Fisher concentration
NS	347.97	86.84	12.5
NE	58.75	88.76	18.1
NW	142.21	77.11	10.5
EW	279.66	88.12	11.4
HZ	96.34	6.18	17.6

Table B-6. Mean orientations for the four sub-vertical lineament related fracture sets, and the sub-horizontal set, from the Geo-DFN (La Pointe and Staub, 2004 /1/).

Geo-DFN	Strike (°)	Dip (°)	Fisher concentration
NS	357.2	88.3	21.66
NE	45.2	87.3	21.54
NW	310.6	87.8	23.90
EW	100.4	89.3	30.63
HZ	252.9	9.7	8.18

B.1.3 KFM02A: Deformation zones and fracture intensities

KFM02A contains 9 Deformation Zones. The mean length, interval length and fracture intensity statistics in the borehole for each DZ is summarised in Table B-7. For the thicker zones, > 10 m, the fracture intensity is about $P10_{corr}$ = 2–3 m^{-1}. The orientations of fractures within all DZs are plotted as a stereonet in Figure B-8. There is no obvious overall pattern of DZ orientation in KFM02A, although ZFMNE00A2 (here a feature corresponding to DZ6, with DZ7 located immediately below ZFMNE00A2) dominates the borehole, and has an associated cluster of fractures dipping ESE that gives fractures in the HZ, NE and NS sets. A stereonet for the fractures in either DZ6 or DZ7 is shown in Figure B-9. This also shows that there is a secondary orthogonal cluster of fractures in the NW set dipping NE in DZ6 and SW in DZ7. KFM02A is a near–vertical borehole (mean trend = 299°, mean plunge = 84°), and has been approximated as a vertical borehole to calculate the Terzaghi weighting.

Table B-7. Positions‡, interval lengths and fracture intensity for Deformation Zones in KFM02A.

	HCD Domain	Mean length (m)	Interval (m)	all P10 (m^{-1})	open P10 (m^{-1})	open $P10_{corr}$ (m^{-1})
DZ2	ZFMNE00B6	115.92	11.67	7.3	5.74	7.53
DZ3	ZFMNE00A3	171.85	23.26	7.4	1.89	3.09
DZ4	ZFMNE00A3	266.54	0.14	21.4	14.29	16.48
DZ5	ZFMNE1189	306.82	6.25	5.8	1.44	2.59
DZ6	ZFMNE00A2	467.10	103.24	6.3	1.76	2.75
DZ7	Immediately below ZFMNE00A2	559.91	79.37	3.2	0.40	0.88
DZ8	ZFMNE1195	899.05	11.79	4.8	1.10	1.67
DZ9		924.16	1.61	19.3	6.83	7.69
DZ10	ZFMNE00B4	978.55	4.54	5.7	1.76	3.02

‡ The Position is expressed as mean length (m), which gives the length down the borehole to the centre of the DZ.

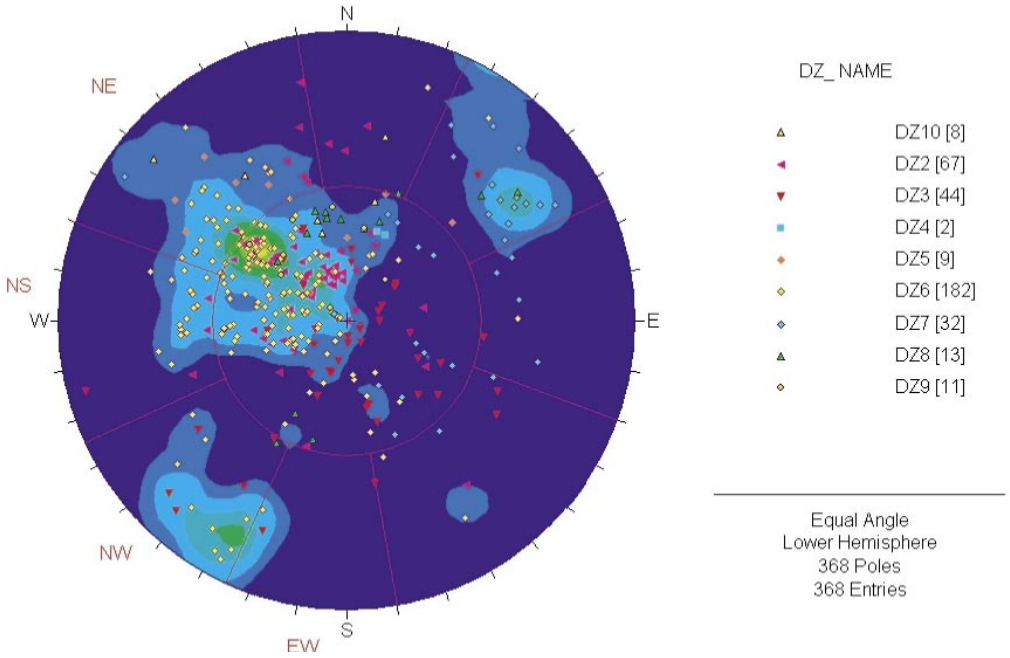

Figure B-8. *Poles of open and partly-open fractures associated with all Deformation Zones in KFM02A. The points show the poles to the individual fractures, and the coloured contours show a Terzaghi-corrected density plot.*

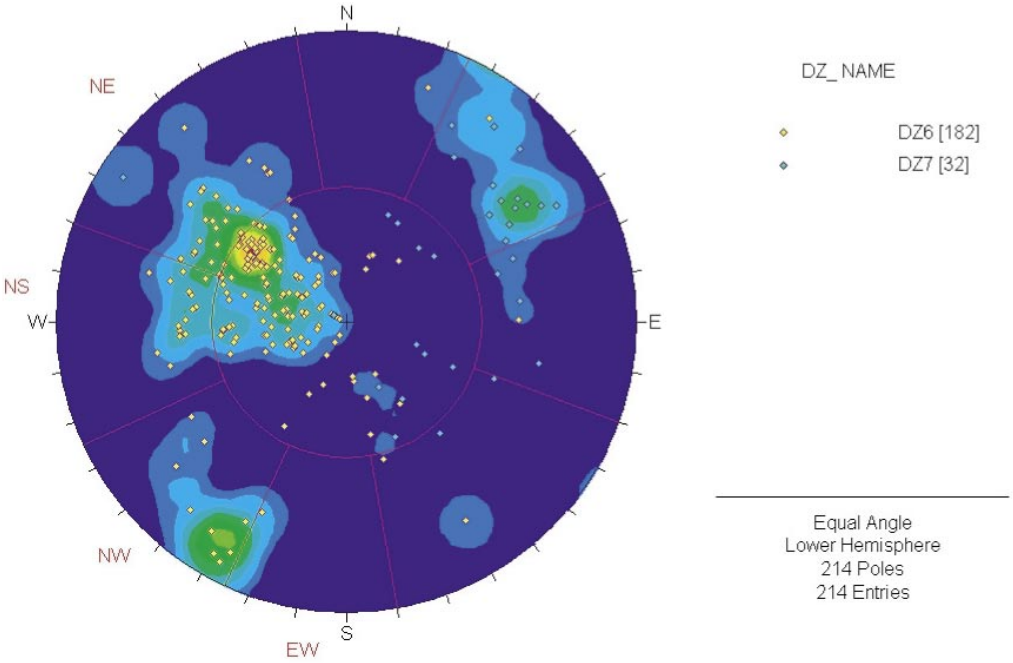

Figure B-9. *Poles of open and partly-open fractures associated with only DZ6 and DZ7 in KFM02A. (ZFMNE00A2 is represented by DZ6, with DZ7 located immediately below ZFMNE00A2) The points show the poles to the individual fractures, and the coloured contours show a Terzaghi-corrected density plot.*

B.1.4 KFM02A: Background fractures and fracture intensities

KFM02A has much lower fracture intensity in comparison to the other boreholes. Overall, there is a higher fracture intensity in the upper section of the borehole, above 415 m (open $P10_{corr}$ = 0.4 m^{-1}), and less at depth (open $P10_{corr}$ = 0.2 m^{-1}). Figure B-10 shows the cumulative P10 for sealed and open fractures down the borehole. KFM02A is cut by ZFMNE00A2 (corresponding to DZ6, with DZ7 located immediately below ZFMNE00A2). Hence, the fracture intensity has been considered separately above and below ZFMNE00A2 and associated fractures (i.e. DZ6 and DZ7). The fracture intensity statistics for each fracture set above 415 m are given in Table B-8. The corresponding statistics below 600 m are given in Table B-9. There is no overall dominant open fracture set, although the HZ and NE sets are more prevalent above ZFMNE00A2 and the NW and NS sets are more prevalent below ZFMNE00A2. This is confirmed visually by the stereonets shown in Figure B-11 and Figure B-12.

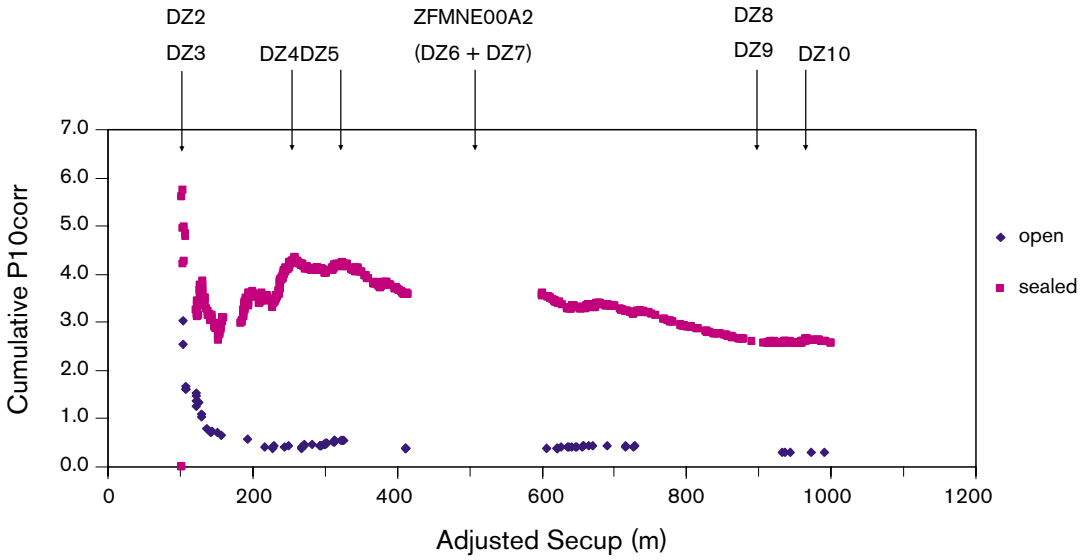

Figure B-10. *Cumulative $P10_{corr}$ (from the top) for open and partly-open fractures, and for sealed fractures for KFM02A.*

Table B-8. Fracture intensity for the upper section of KFM02A (< 415 m). The interval length is 272 m.

KFM02A_upper (< 416 m)	all P10 (m^{-1})	open P10 (m^{-1})	open $P10_{corr}$ (m^{-1})	open $P10_{corr}$ (%)
NS	0.169	0.011	0.034	8.80%
NE	0.404	0.029	0.100	26.14%
NW	0.118	0.022	0.065	16.87%
EW	0.077	0.015	0.056	14.65%
HZ	1.180	0.107	0.129	33.55%
Total	1.948	0.184	0.384	100.00%

Table B-9. Fracture intensity for the lower section of KFM02A (> 600 m). The interval length is 382 m.

KFM02A_lower (> 600 m)	all P10 (m^{-1})	open P10 (m^{-1})	open $P10_{corr}$ (m^{-1})	open $P10_{corr}$ (%)
NS	0.136	0.021	0.078	35.97%
NE	0.170	0.010	0.035	16.35%
NW	0.123	0.024	0.087	40.43%
EW	0.037	0.003	0.005	2.50%
HZ	0.447	0.008	0.010	4.75%
Total	0.913	0.065	0.216	100.00%

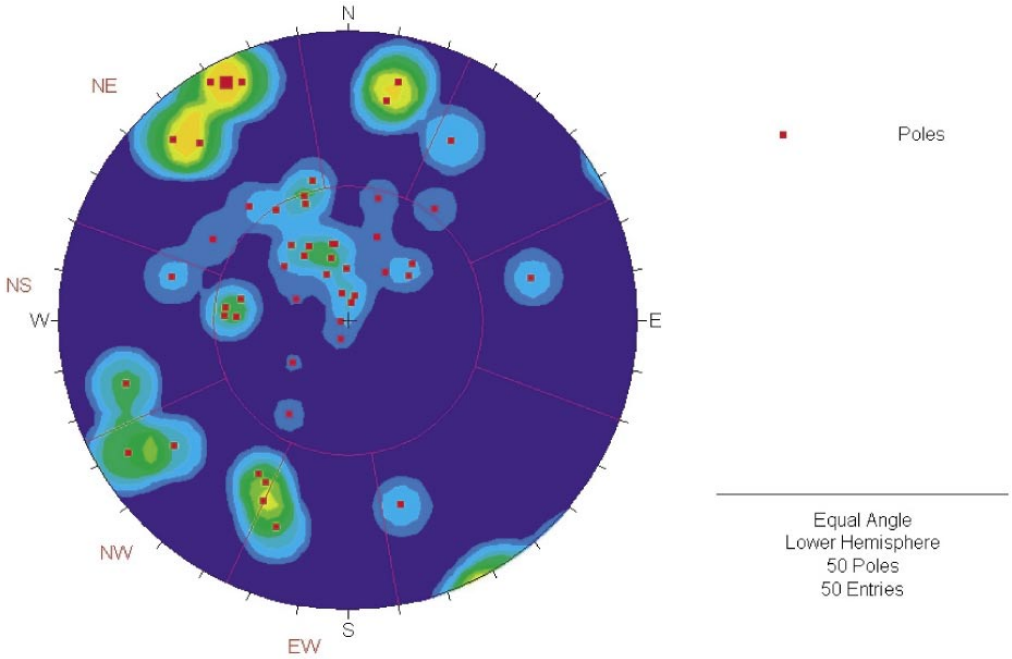

Figure B-11. *Open and partly-open background fractures in the upper section of KFM02A (above ZFMNE00A2, i.e. above DZ2 and DZ7, 415 m). The points show the poles to the individual fractures, and the coloured contours show a Terzaghi-corrected density plot.*

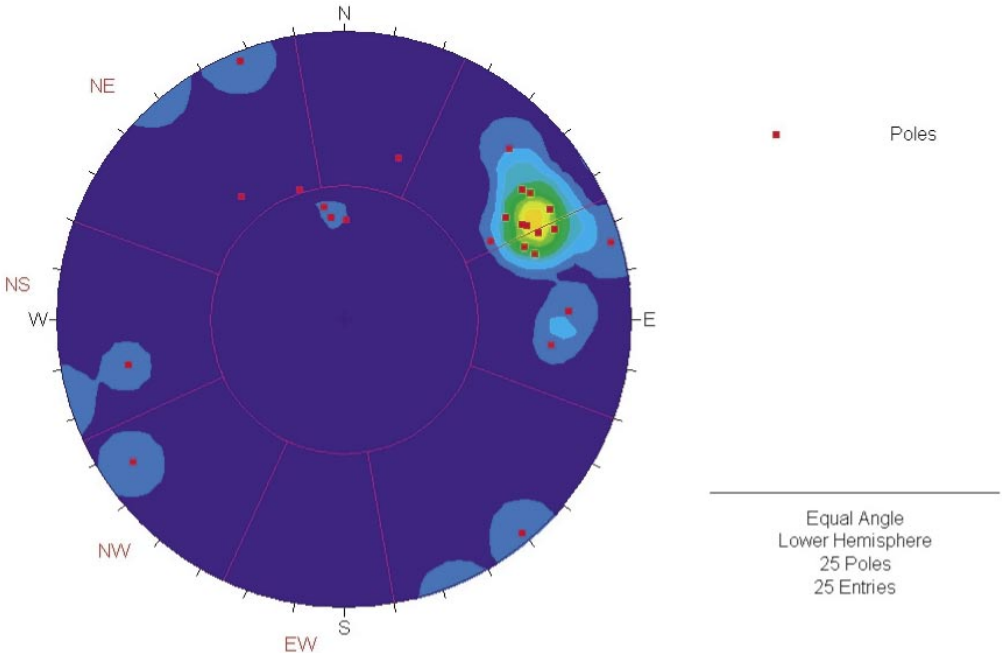

Figure B-12. *Open and partly-open background fractures in the lower section of KFM02A (below ZFMNE00A2 and associated fractures, i.e. below DZ2 and DZ7, 600 m). The points show the poles to the individual fractures, and the coloured contours show a Terzaghi-corrected density plot.*

B.1.5 KFM03A: Deformation zones and fracture intensities

There are 5 Deformation Zones within KFM03A. The mean length down the borehole for each DZ, interval length, mean orientations, and various fracture intensities are summarised in Table B-10. For the thicker zones, $P10_{corr}$ is about 2–3 m^{-1}. The orientations of fractures in the DZs are illustrated in Figure B-13. Overall, most open and partly-open features associated with DZs occur in the HZ set. KFM03A is a near–vertical borehole, and has been approximated as a vertical borehole to calculate the Terzaghi weighting. The mean trend of borehole KFM03A is 277° and the mean plunge is 85°.

Table B-10. Summary of Deformation Zones in KFM03A. The mean strike and dip of each DZ are Terzaghi weighted.

KFM03A	HCD name	Mean length‡ (m)	Interval length (m)	all P10 (m^{-1})	open P10 (m^{-1})	open $P10_{corr}$ (m^{-1})
DZ1	ZFMNE00A4	377.92	41.90	4.2	1.93	2.73
DZ2	ZFMNE00A7	451.57	6.24	7.7	0.48	0.60
DZ3	ZFMNE00B1	642.24	7.25	6.3	1.24	1.54
DZ4	ZFMNE00A3	809.23	12.33	4.1	2.27	3.33
DZ5		945.32	6.40	7.2	0.94	0.98

‡ The Position is expressed as mean length (m), which gives the length down the borehole to the centre of the DZ.

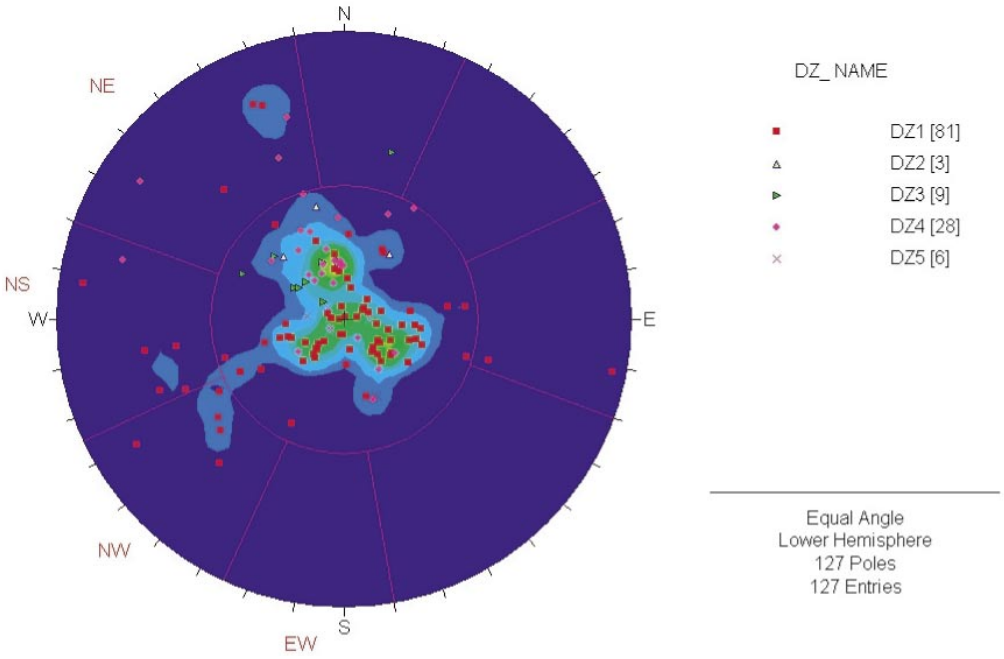

Figure B-13. *Poles of open and partly-open fractures associated with Deformation Zones in KFM03A. The points show the poles to the individual fractures, and the coloured contours show a Terzaghi-corrected density plot.*

B.1.6 KFM03A: Background fractures and fracture intensities

Figure B-14 shows the cumulative $P10_{corr}$ down borehole KFM03A indicating fairly homogeneous fracture intensity below the first 50 m of cored borehole, despite a small section of rock domain RFM017 intruded into RFM029. KFM03A is wholly above ZFMNE00A2. Flowing features are found throughout the whole length of KFM03A (see subsection B.2.3). Hence, the fracture intensity has been calculated for the complete borehole (see Table B-11). The total fracture intensity ($P10_{corr} = 0.7\ m^{-1}$) is less than that seen in the upper section of KFM01A, but is significantly higher than seen in the lower part of KFM01A and in KFM02A. The NE and HZ sets dominate, each having 29% of the total fracture count (see Table B-11 and Figure B-15).

Table B-11. Background fracture intensity for KFM03A. The interval length is 823 m.

KFM03A	all P10 (m^{-1})	open P10 (m^{-1})	open $P10_{corr}$ (m^{-1})	open $P10_{corr}$ (%)
NS	0.289	0.023	0.086	12.40%
NE	0.446	0.049	0.202	29.07%
NW	0.174	0.034	0.133	19.14%
EW	0.091	0.017	0.069	10.00%
HZ	0.765	0.179	0.204	29.39%
Total	1.765	0.301	0.695	100.00%

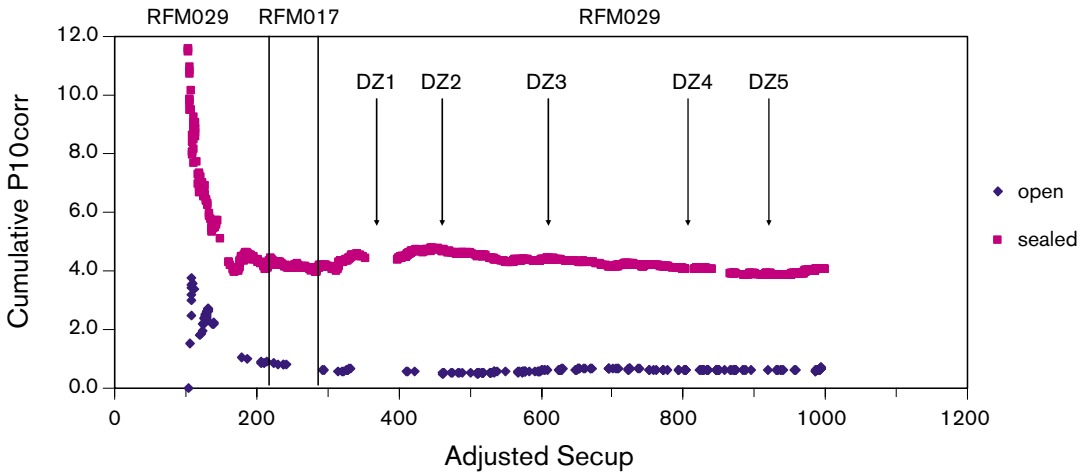

Figure B-14. *Cumulative $P10_{corr}$ (from the top) for open and partly-open fractures and for sealed fractures for KFM03A. DZ1 is shown as an apparent 'gap' in the data at ~ 378 m. DZ2 to DZ5 are smaller intervals (see Table B-10).*

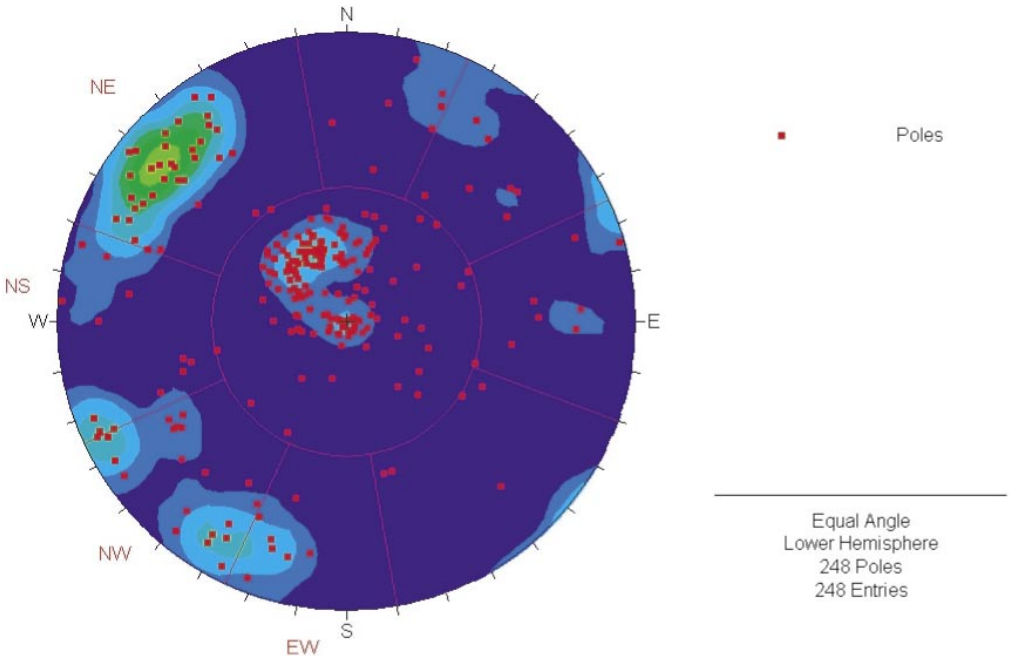

Figure B-15. *Open and partly-open background fractures of KFM03A. The points show the poles to the individual fractures, and the coloured contours show a Terzaghi-corrected density plot.*

B.1.7 KFM04A: Deformation zones and fracture intensities

KFM04A has 5 Deformation Zones. The mean length, interval length, and fracture intensity statistics in KFM04A for each DZ are summarised in Table B-12. The orientations of the features comprising each DZ are summarised in Figure B-16. The HZ and NW fracture sets dominate the DZs. ZFMNE00A2 is also splayed in this borehole and represented as DZ1, DZ2 and DZ3, while ZFMNE1188 is represented as DZ4 in the borehole. KFM04A is an inclined borehole (mean trend = 40°, mean plunge = 53°), and so the true trajectory of the borehole has been used to produce the Terzaghi weighting for each fracture, based on the inclination of the fracture relative to the borehole trajectory. From Table B-12 it can be seen that the fracture intensity tends to be higher in the shallower DZs.

Table B-12. Positions‡, interval lengths and fracture intensity for Deformation Zones in KFM04A.

KFM04A	HCD domain	Mean length (m)	Interval (m)	all P10 (m^{-1})	open P10 (m^{-1})	open $P10_{corr}$ (m^{-1})
DZ1	ZFMNE00A2	172.49	6.92	16.47	8.24	12.38
DZ2	ZFMNE00A2	207.49	10.89	15.89	7.25	10.94
DZ3	ZFMNE00A2	236.98	9.86	12.58	9.13	12.96
DZ4	ZFMNE1188	436.98	49.93	6.97	2.60	4.13
DZ5	ZFMNE1188	657.63	6.68	11.23	2.84	3.51

‡ The Position is expressed as mean length (m), which gives the length down the borehole to the centre of the DZ.

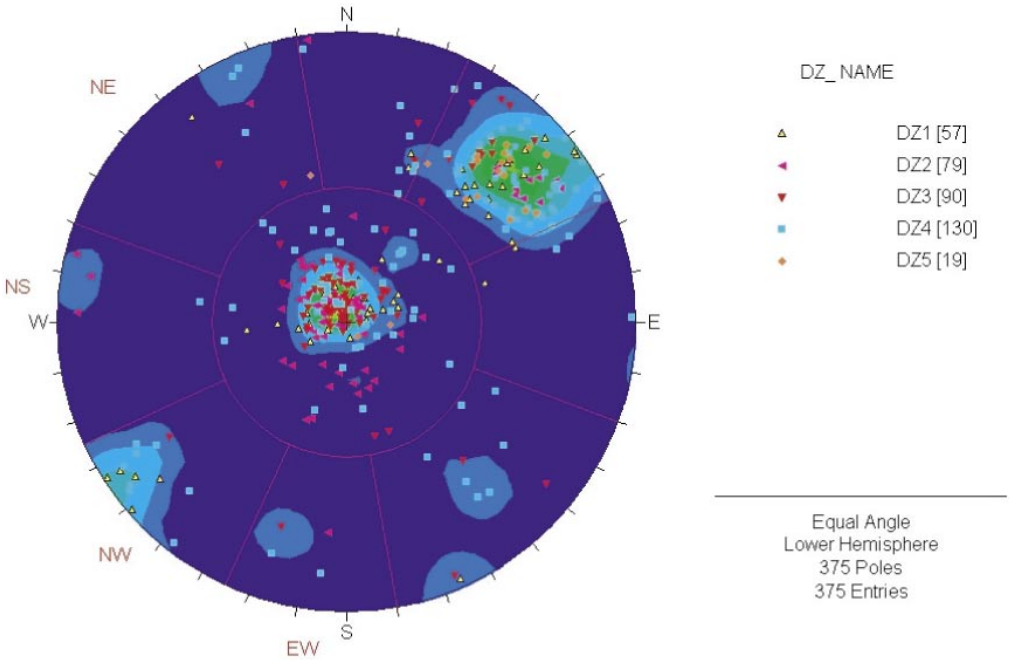

Figure B-16. *Poles of open and partly-open fractures associated with Deformation Zones in KFM04A. The points show the poles to the individual fractures, and the coloured contours show a Terzaghi-corrected density plot.*

B.1.8 KFM04A: Background fractures and fracture intensities

Figure B-17 shows the cumulative fracture intensity for sealed and open fractures down borehole KFM04A. The borehole intercepts three rock domains: RFM018, RFM012 and then RFM029. Overall, there is much higher fracture intensity above ZFMNE1188 (DZ4, 462 m) within rock domains RFM018 and RFM012 (open $P10_{corr} = 4.6\ m^{-1}$). Below ZFMNE1188, within rock domain RFM029, the fracture intensity drops to give an open $P10_{corr} = 0.7\ m^{-1}$. The fracture intensity statistics for each set within RFM029 are given in Table B-13. The open and partly-open fractures below ZFMNE1188 (462 m) are dominated by the HZ and NW sets. This is also illustrated by the stereonet shown in Figure B-18, which shows two dominant clusters around the horizontal and a near-vertical NW group.

Table B-13. Fracture intensity for the lower section of KFM04A (> 462 m, i.e. below DZ4). The interval length is 516 m.

KFM04A_lower (below 461.94 m)	all P10 (m^{-1})	open P10 (m^{-1})	open $P10_{corr}$ (m^{-1})	open $P10_{corr}$ (%)
NS	0.71	0.060	0.103	14.09%
NE	0.61	0.027	0.078	10.64%
NW	0.57	0.155	0.213	29.10%
EW	0.10	0.017	0.027	3.63%
HZ	0.69	0.250	0.312	42.54%
Total	2.68	0.509	0.733	100.00%

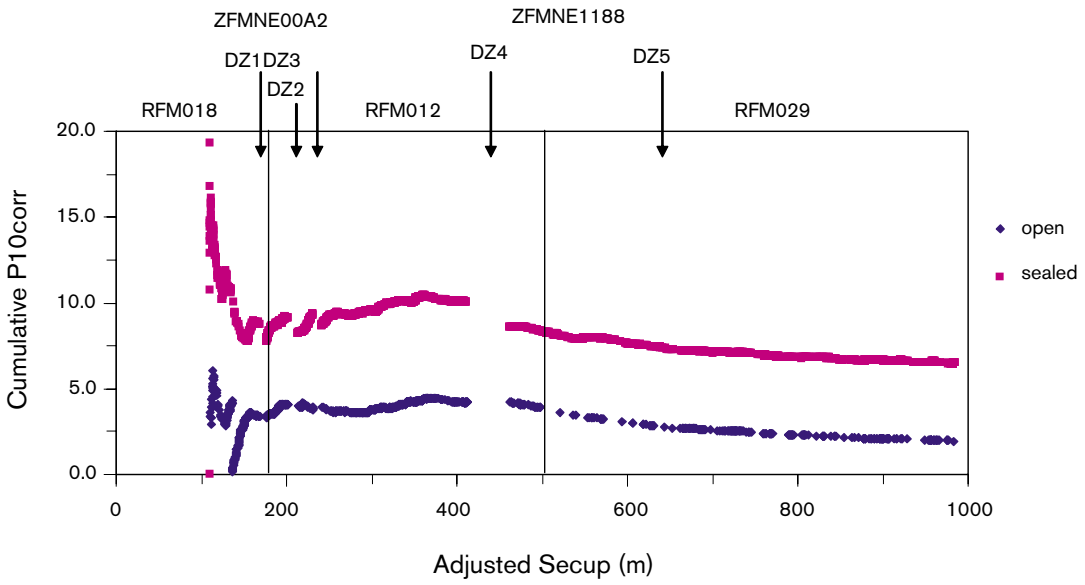

Figure B-17. *Cumulative $P10_{corr}$ (from the top) for open and partly-open fractures, and for sealed fractures for KFM04A. ZFMNE00A2 is represented by DZ1, DZ2 and DZ3 in KFM04A.*

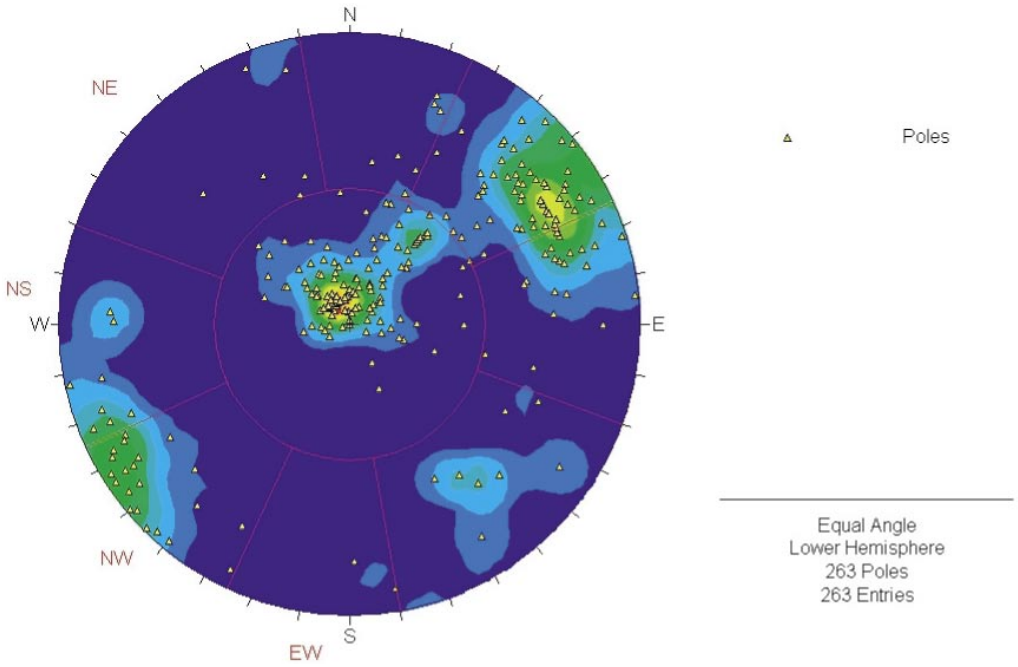

Figure B-18. *Open and partly-open background fractures in the lower section of KFM04A (below ZFMNE1188, i.e. below DZ4, 462 m). The points show the poles to the individual fractures, and the coloured contours show a Terzaghi-corrected density plot.*

B.1.9 KFM05A: Deformation zones and fracture intensities

KFM05A contains 6 Deformation Zones. The mean length, interval length, and fracture intensity statistics for each DZ are summarised in Table B-14. Fracture intensity is generally lower in the deeper DZs apart from DZ5, which has exceedingly high fracture intensity. The orientations of the features comprising each DZ are summarised in Figure B-19. The HZ and NE fracture sets dominate the DZs. The NE fractures dip NW, and there are few fractures in the NW set that dip SW. As for KFM01A, the complete length of KFM05A is below ZFMNE00A2. KFM05A is an inclined borehole (mean trend = 95°, mean plunge = 56°), and so the true trajectory of the borehole has been used to produce the Terzaghi weighting for each fracture, based on the inclination of the fracture relative to the borehole trajectory.

Table B-14. Positions‡, interval lengths and fracture intensity for Deformation Zones in KFM05A.

KFM05A	HCD domain	Mean length (m)	Interval (m)	all P10 (m^{-1})	open P10 (m^{-1})	open $P10_{corr}$ (m^{-1})
DZ1	ZFMNE00A2	107.80	11.05	9.23	7.96	10.67
DZ2	ZFMNE0401	426.02	19.57	7.41	1.94	4.40
DZ3-1	ZFMNE103A	612.58	6.67	8.55	2.25	3.88
DZ3-2	ZFMNE103B	716.50	6.56	6.86	0.46	0.90
DZ4	ZFMNE062A	904.04	23.71	6.66	0.42	1.17
DZ5	ZFMNE062B	942.56	13.11	6.56	0.76	21.02

‡ The Position is expressed as mean length (m), which gives the length down the borehole to the centre of the DZ.

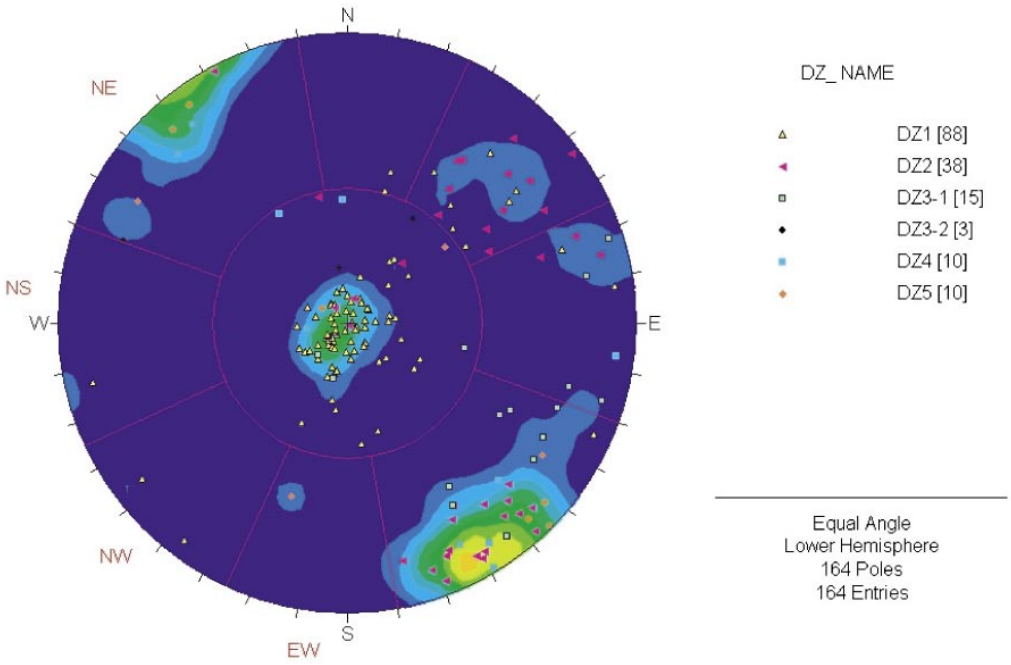

Figure B-19. *Poles of open and partly-open fractures associated with Deformation Zones in KFM05A. The individual features are plotted as points, and the coloured contours shows the Terzaghi-corrected density plot.*

B.1.10 KFM05A: Background fractures and fracture intensities

Figure B-20 shows the cumulative fracture intensity down KFM05A. There is a high fracture intensity in the top 50 m of the borehole, but overall there is little variation in open fracture intensity in KFM05A, giving an overall open $P10_{corr} = 1.0\ m^{-1}$. Fracture intensity statistics for each set are given in Table B-15. The open and partly-open fractures are dominated by the NE and HZ set. A stereonet plot for KFM05A (see Figure B-21) shows there is actually quite a spread of sub-vertical fractures in the NW and NS sets also, though more diffuse than in the HZ and NE sets.

Table B-15. Fracture intensity for KFM05A. The interval length is 804 m.

KFM05A	$P10_{all}$ (m^{-1})	$P10_{open}$ (m^{-1})	open $P10_{corr}$ (m^{-1})	open $P10_{corr}$ (%)
NS	0.46	0.082	0.159	14.8%
NE	1.21	0.152	0.436	40.5%
NW	0.37	0.092	0.154	14.3%
EW	0.12	0.012	0.033	3.1%
HZ	0.63	0.245	0.295	27.4%
Total	2.79	0.583	1.078	100.0%

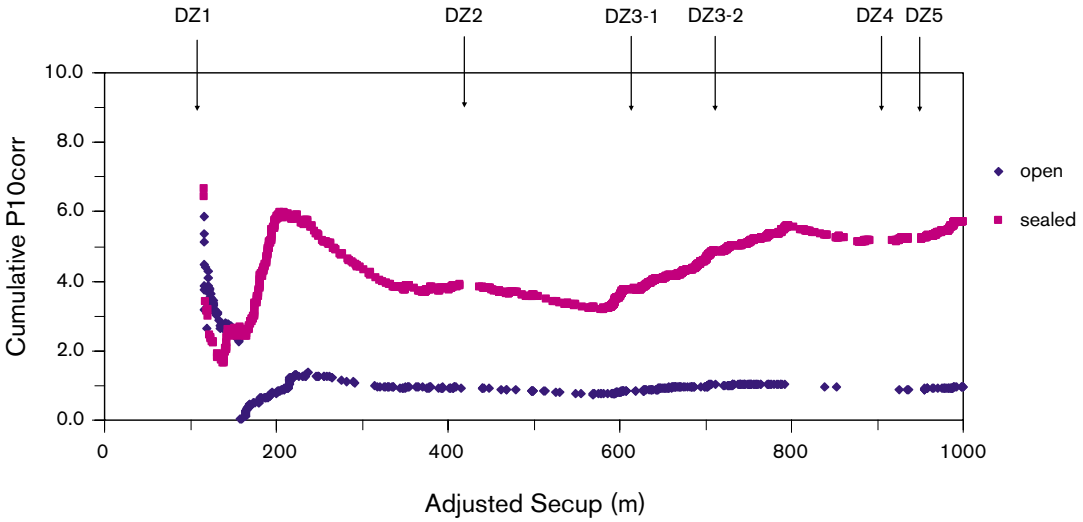

Figure B-20. *Cumulative $P10_{corr}$ (from the top) for open and partly-open fractures, and for sealed fractures for KFM05A.*

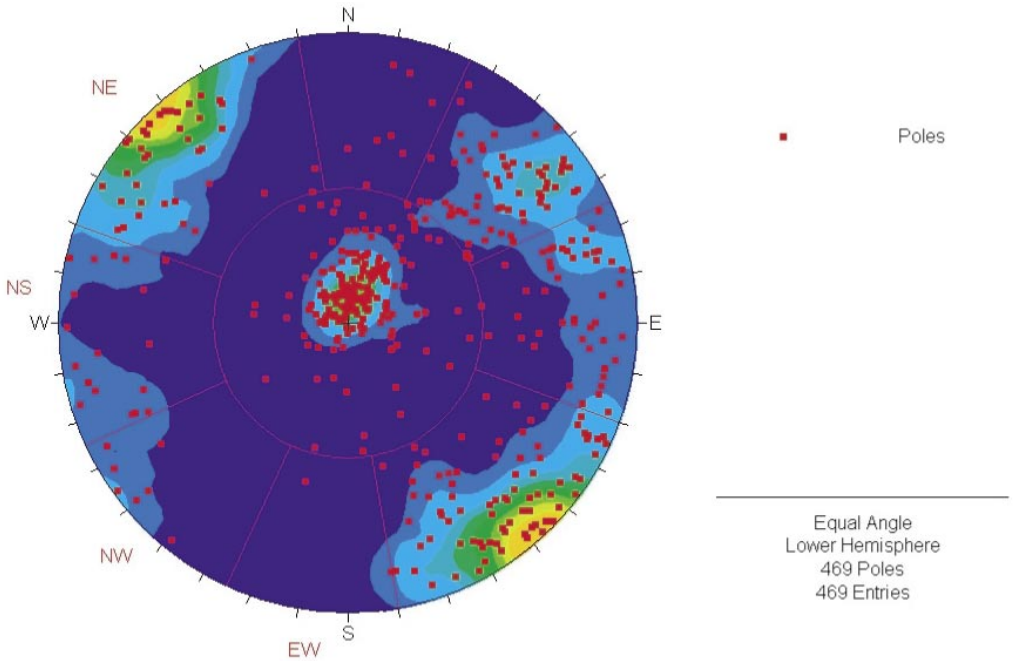

Figure B-21. *Open and partly-open background fractures in KFM05A. The plot shows the poles to the individual fractures and Terzaghi weighted Fisher concentrations as coloured contours.*

B.2 Analysis of hydrogeological data

B.2.1 KFM01A, orientation of flowing fractures

Flowing features in KFM01A are predominantly in the HZ and NE sets based on the PFL anomalies (see Figure B-22). This corresponds well with the dominant background fracture orientation. Comparing with Figure B-5 shows that only a small percentage of open fractures correspond with flowing features, and these are mainly in the sub-horizontal set and a few in the NE set. PSS flow is measured over 5 m intervals, in which there may be several fractures, and therefore it is difficult to match these to individual features. For KFM01A, no flowing features within DZs are recorded in either PFL or PSS data. In fact,

all flowing features are found within the top 400 m of KFM01A as shown in Figure B-23. Note that the transmissivity plotted here is for 5 m intervals for both PFL and PSS data, so that both sets of data can be compared in a consistent way. This is because the PSS data are given as the transmissivity of contiguous 5 m intervals whereas the PFL data are given as the transmissivity of individual fractures, and hence it is necessary to convert the PFL data into a compatible format. This is achieved by grouping the PFL anomalies according to the same 5 m intervals for which the PSS data are provided. In some instances there are a few anomalies in an interval, in others there are none. In KFM01A the detection limit is about 10^{-9} m^2s^{-1} for both PFL and PSS data, and so the PSS does not supplement the PFL data in this case.

It is useful to investigate the consistency between the transmissivities interpreted from the PFL and PSS anomalies. Figure B-24 shows a cross-plot of the PFL and PSS data for KFM01A. The agreement is generally good, though there are a few intervals with order of magnitude differences.

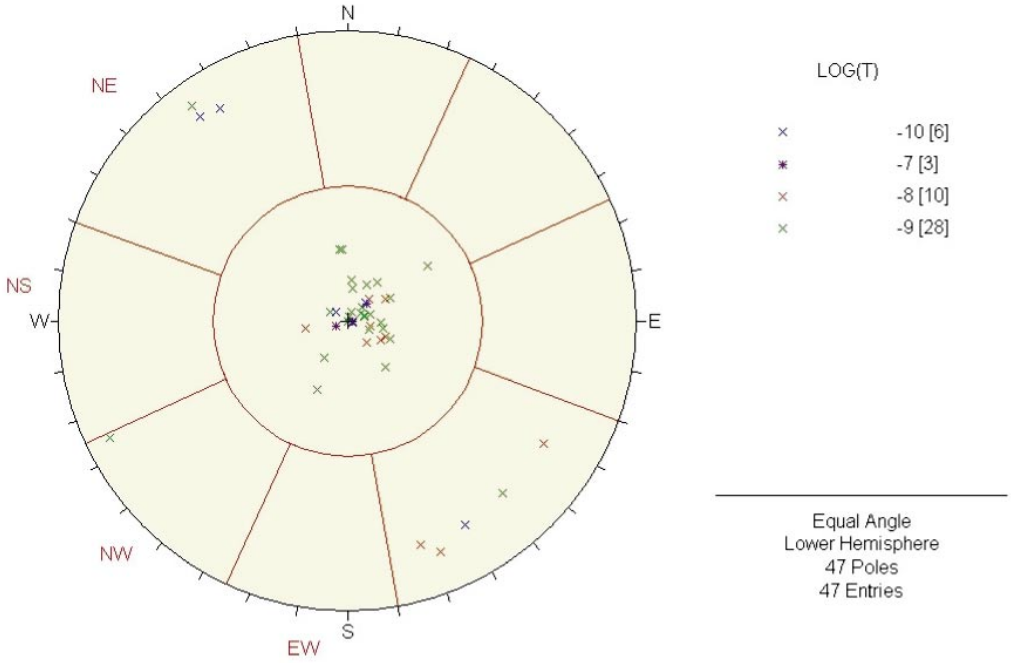

Figure B-22. *Orientations of the pole to fractures associated with PFL anomalies in KFM01A. Fractures are coloured by magnitude of the transmissivity of the PFL anomaly. The set divisions and the names of each set are superimposed in red.*

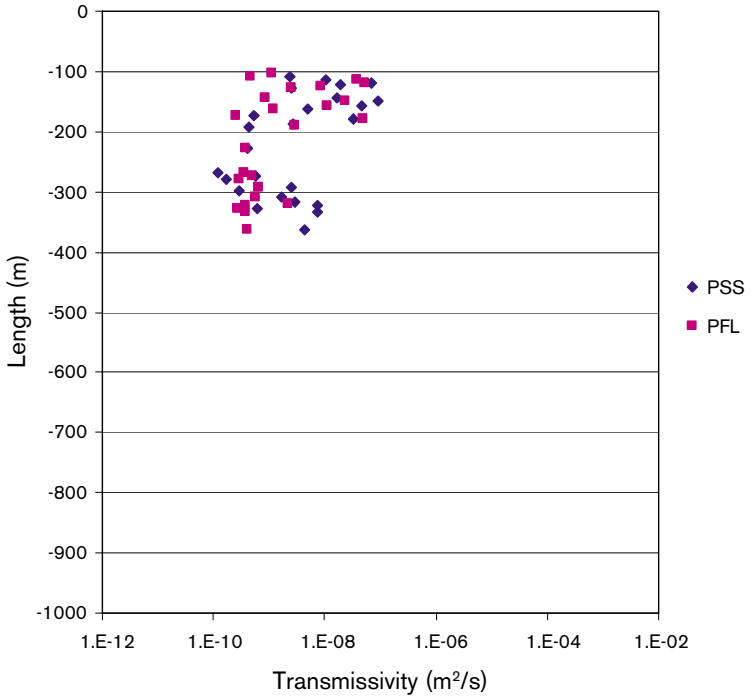

Figure B-23. *Transmissivity of 5 m borehole intervals with measurable flow recorded by PFL and PSS in KFM01A. The measurement limit is around 10^{-9} m^2s^{-1} for PFL and PSS.*

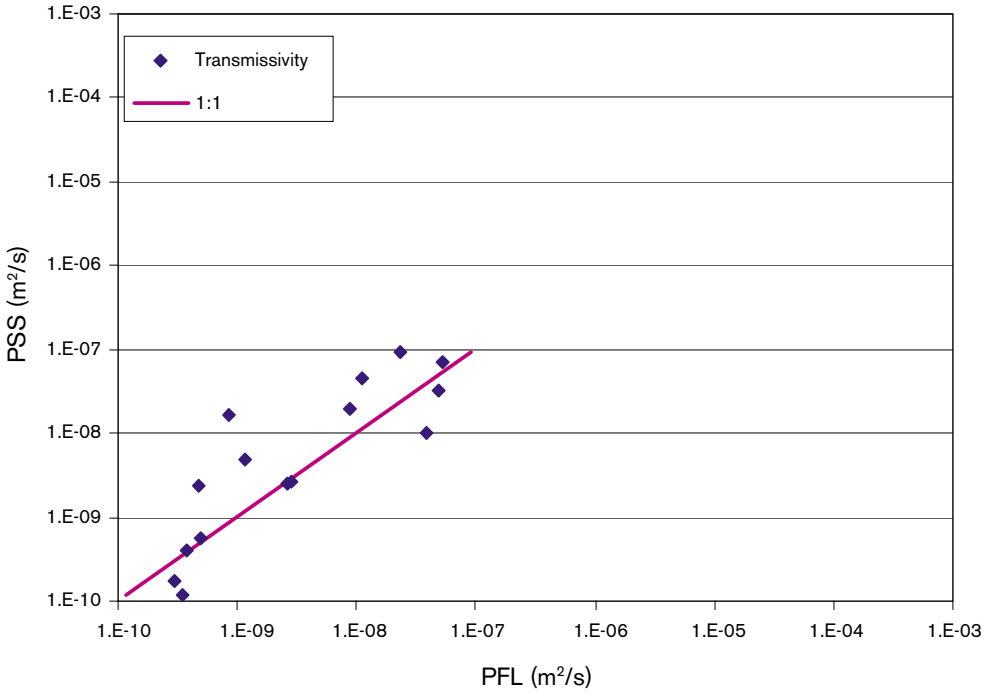

Figure B-24. *Cross-plot of PFL and PSS measurements for KFM01A. A 1:1 correlation is shown for comparison.*

B.2.2 KFM02A, Orientation of flowing fractures

In KFM02A, almost all flow in background rock is found above about 400 m. KFM02A has 10 DZs crossing the borehole. In particular, ZFMNE00A2 corresponds to DZ6, with DZ7 found immediately below ZFMNE00A2. Two main regions of flow are observed (see Figure B-28). Firstly above 314 m, and secondly between 414 m to 514 m, which corresponds to the upper part of ZFMNE00A2. The orientations of the flowing anomalies in DZs above 314 m are shown in Figure B-25, suggesting the flow anomalies are predominantly in the HZ set with a few high transmissivity fractures in the EW and NE sets. Flow anomalies outside of DZs above 314 m are plotted in Figure B-26, and again show the HZ set is dominant with a few fractures in the NW set. Comparing with Figure B-11 a high percentage of the open background fractures correspond to flow anomalies in this borehole. Figure B-27 shows the flow anomaly orientations between 414 m and 514 m, of which most anomalies belong to DZ6. Again, the HZ set is dominant, though there are SE dipping fractures that belong to NS and NE sets also, and some NW fractures dipping NE. Only one flow is measured at depth and is found within DZ8 (about 893 m). At all depths, flow anomalies coincide with the HZ set, and largely correspond to a DZ. There are relatively few flowing features that correspond to background fractures. This is consistent with the low open fracture intensity $P10_{corr}$ found in KFM02A (see subsection B.1.4). There is only one flowing feature below ZFMNE00A2, the base of which is around 600 m down the borehole.

Figure B-28 compares the distribution of measurable flow in 5 m intervals down KFM02A for the PFL and PSS data. The same flowing intervals are identified by both types of test, although in this case the detection limit on the PSS data is about $1/30^{th}$ of that for the PFL data and reveals some additional low flow intervals. Figure B-29 shows a cross-plot of the PFL and PSS data for KFM02A. Again, the agreement is generally good, although there is perhaps a slight bias toward higher transmissivities being interpreted from the PFL tests.

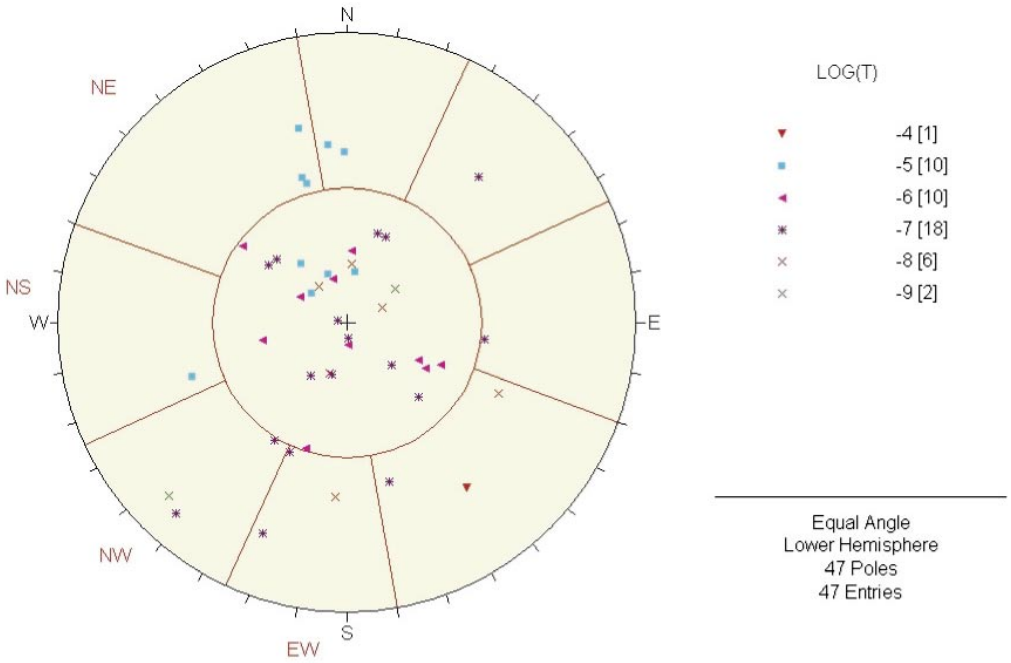

Figure B-25. *PFL anomalies from above 314 m in KFM02A. The stereonet shows the orientations of DZs that correspond to flow anomalies. The majority are in the HZ fracture set (central area of plot).*

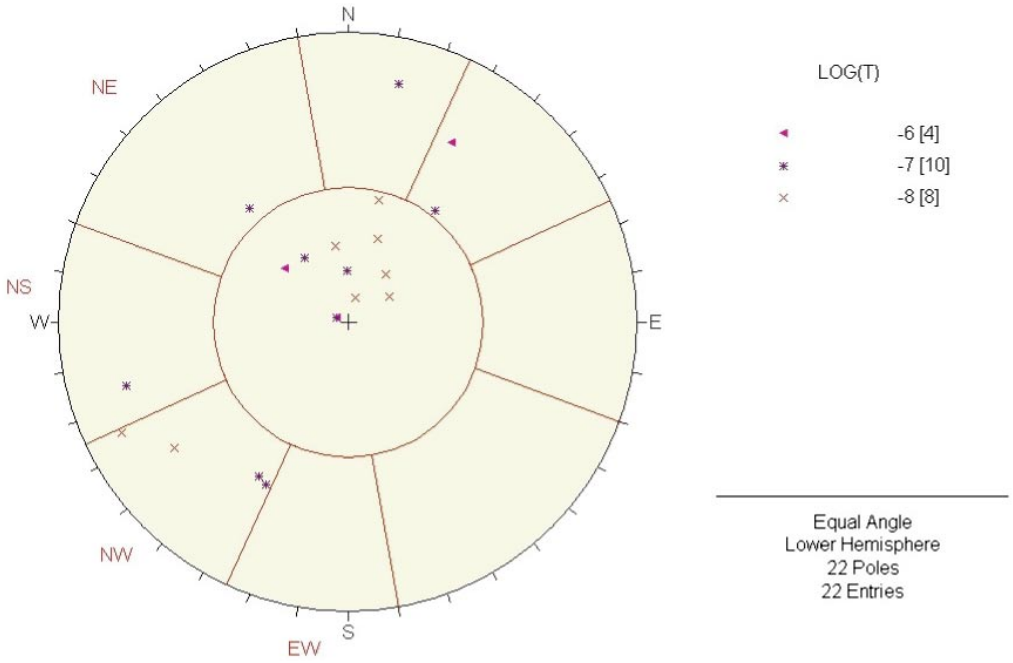

Figure B-26. *PFL anomalies from above 314 m in KFM02A. The stereonet shows the orientations of background fractures that correspond to flow anomalies. The majority are in the HZ fracture set (central area of plot).*

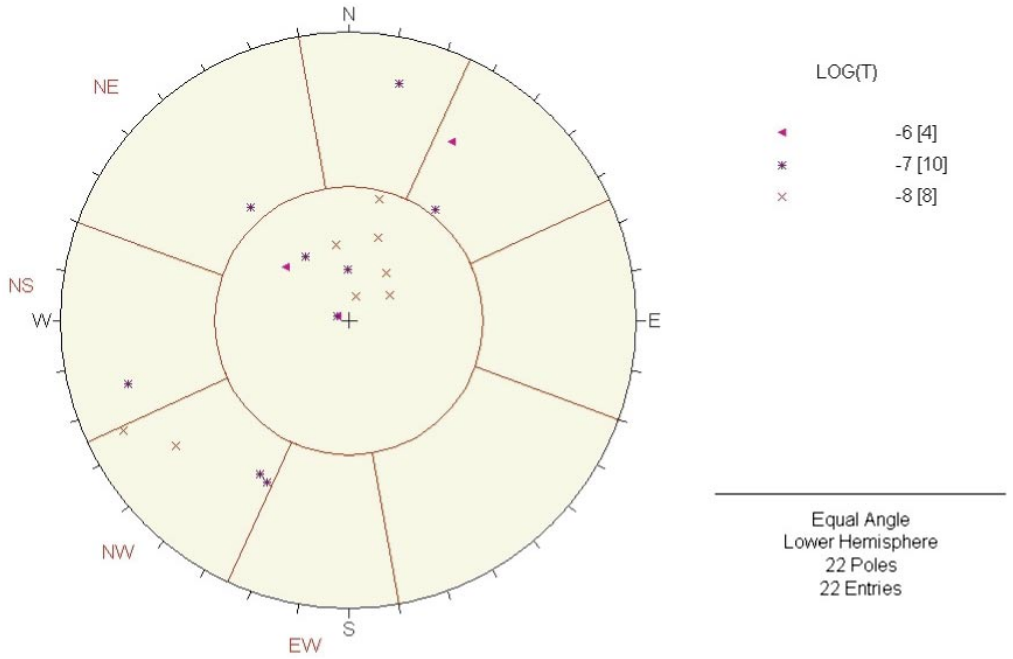

Figure B-27. *PFL anomalies from 414 m to 514 m in KFM02A. All PFL flow anomalies are matched to features within DZ6, except for 3 background fractures found within 3 m above DZ6. The stereonet shows the poles to all features, each feature matched with the flow anomalies.*

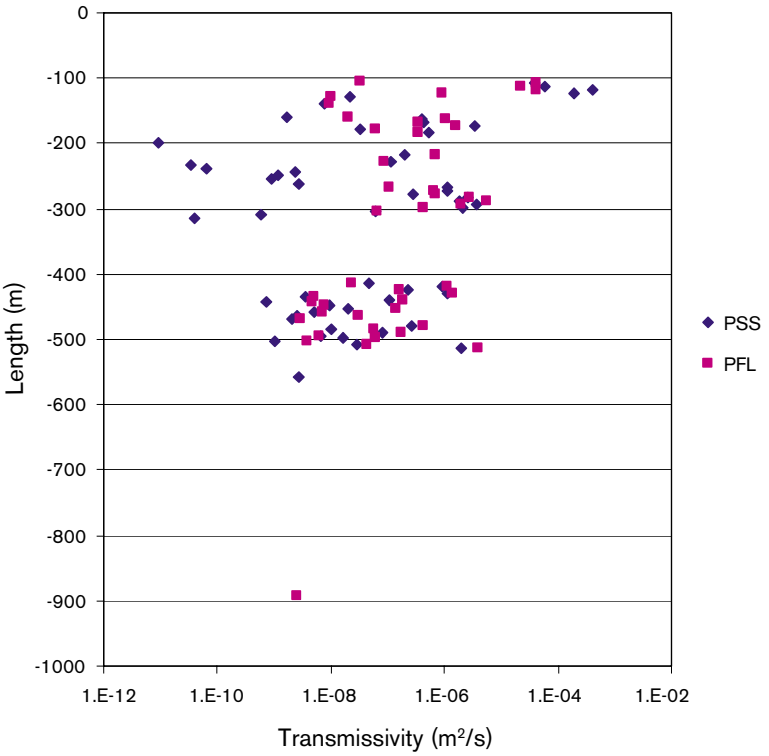

Figure B-28. *Transmissivity of 5 m borehole intervals with measurable flow recorded by PFL and PSS in KFM02A. The measurement limit is around 10^{-9} m^2s^{-1} for PFL data, and around 3 10^{-11} m^2s^{-1} for PSS data.*

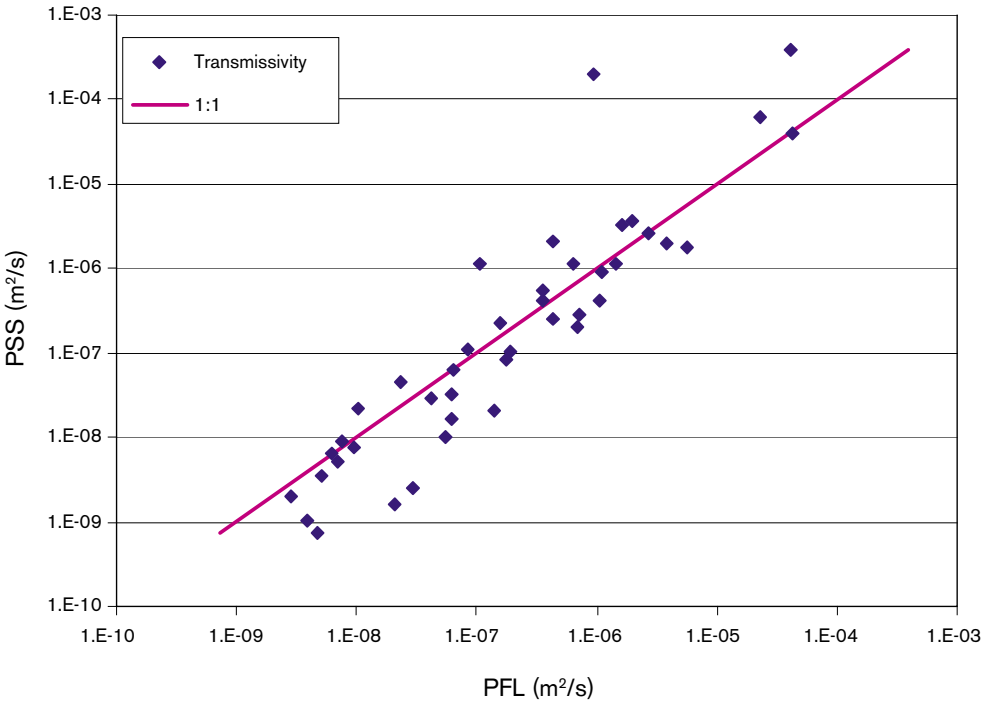

Figure B-29. *Cross-plot of PFL and PSS measurements for KFM02A. A 1:1 correlation is shown for comparison.*

B.2.3 KFM03A, Orientation of flowing fractures

Flow anomalies in KFM03A are predominantly in the HZ set, with a few anomalies in the NS and NE sets (see Figure B-30). This is consistent with major fracture sets seen in the KFM03A (see Figure B-13 and Figure B-15). The majority of the flowing features, and especially those with high transmissivity, are found within DZs, and belong to the HZ set. This is illustrated in Figure B-31. In addition, the flowing features found within background rock are illustrated in Figure B-32. These are associated with lower transmissivities than those in the DZs, but again fall mainly in the HZ set. Comparing with Figure B-15 only a small percentage of open fractures corresponds to flow anomalies here, and are in the HZ or Ne sets. This borehole is in contrast to boreholes KFM01A and KFM02A in that flows are measured throughout the full length of borehole.

Figure B-33 compares the distribution of measurable flow in 5 m intervals down KFM03A for the PFL and PSS data. Roughly the same intervals of high flows are identified by both tests and the values appear to be in good agreement, but again the lower detection limit on the PSS data (about 1/20th) reveals some additional flowing intervals not discerned by the PFL tests. Figure B-34 shows a cross-plot of the PFL and PSS data for KFM03A. Again, the agreement is generally good, probably the best of the three boreholes. The only significant differences are for low transmissivity intervals where the PFL data suggest a slight tendency to give a higher interpreted transmissivity than the PSS tests.

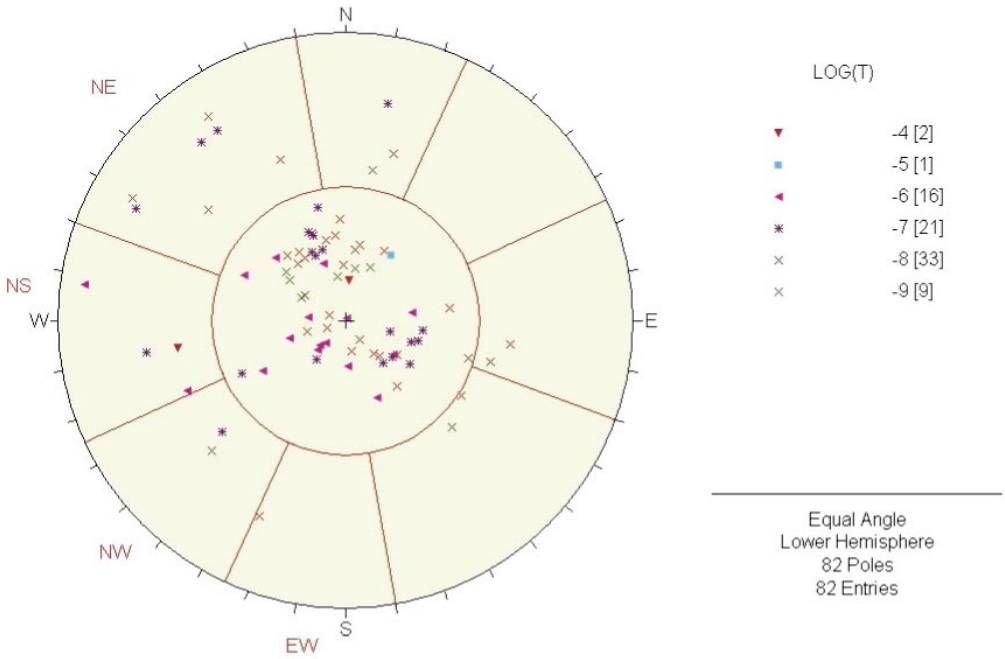

Figure B-30. *Orientations of the pole to background fractures and DZs associated with PFL anomalies in KFM03A. Fractures are coloured by magnitude of the transmissivity of the PFL anomaly. The set divisions and the names of each set are superimposed in red.*

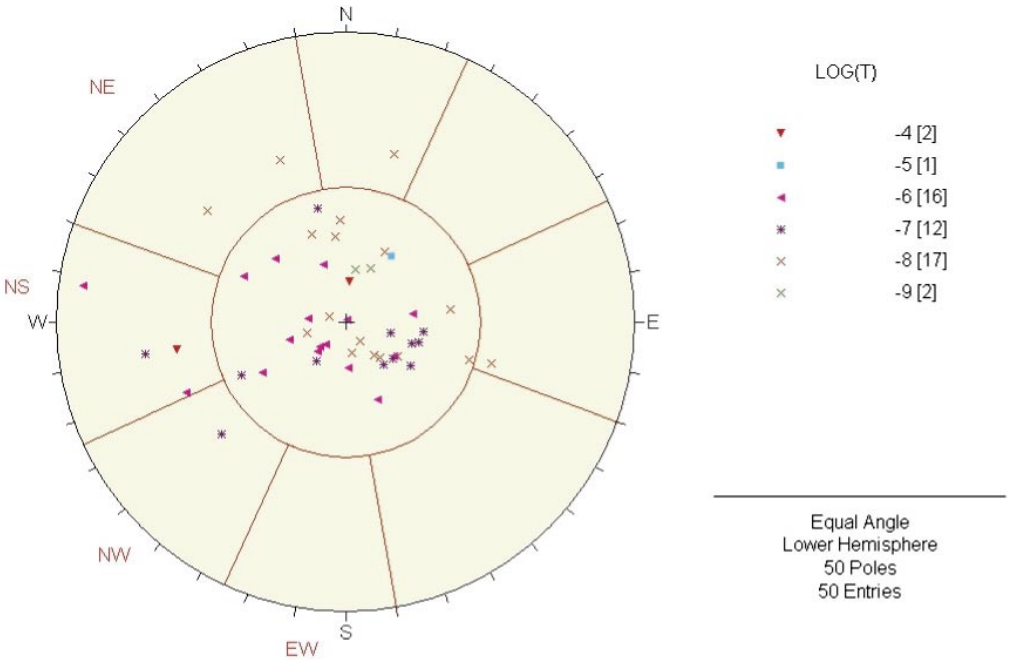

Figure B-31. *Orientations of the pole to DZs associated with PFL anomalies in KFM03A. Fractures are coloured by magnitude of the transmissivity of the PFL anomaly. The set divisions and the names of each set are superimposed in red.*

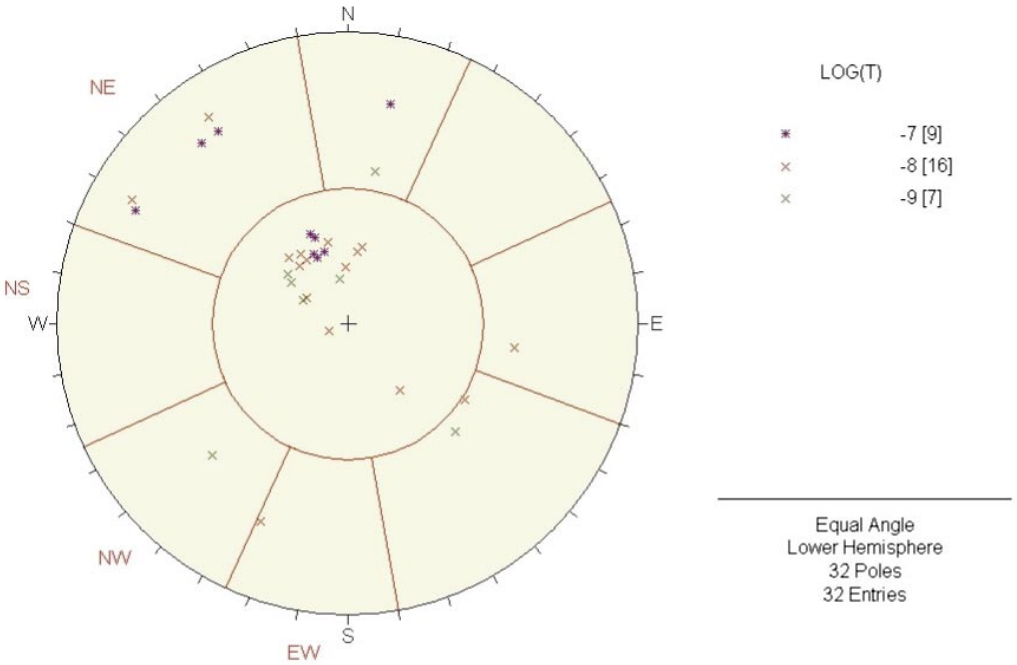

Figure B-32. *Orientations of the pole to background fractures associated with PFL anomalies in KFM03A. Fractures are coloured by magnitude of the transmissivity of the PFL anomaly. The set divisions and the names of each set are superimposed in red.*

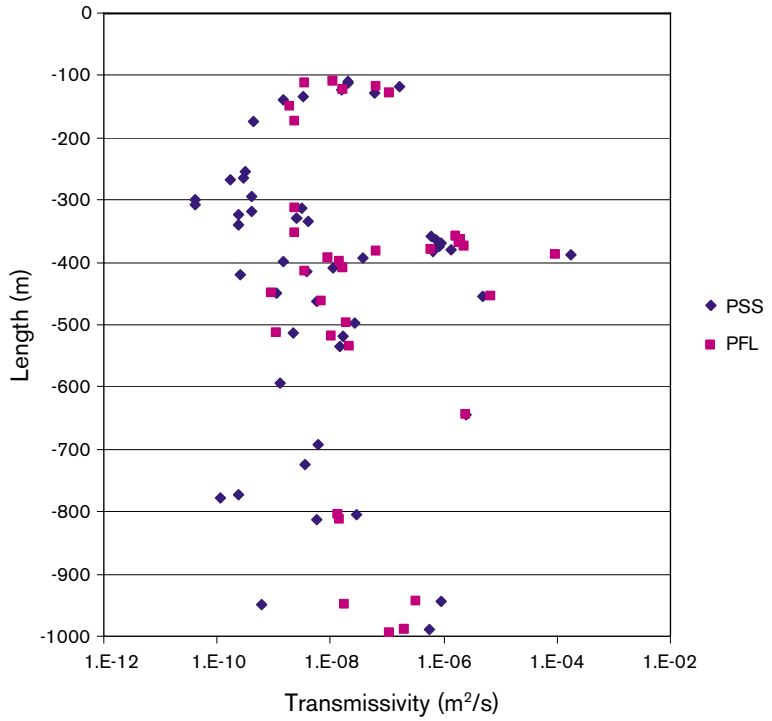

Figure B-33. *Transmissivity of 5 m borehole intervals with measurable flow recorded by PFL and PSS in KFM03A. The measurement limit is around 10^{-9} m^2s^{-1} for PFL data, and around 4 10^{-11} m^2s^{-1} for PSS data.*

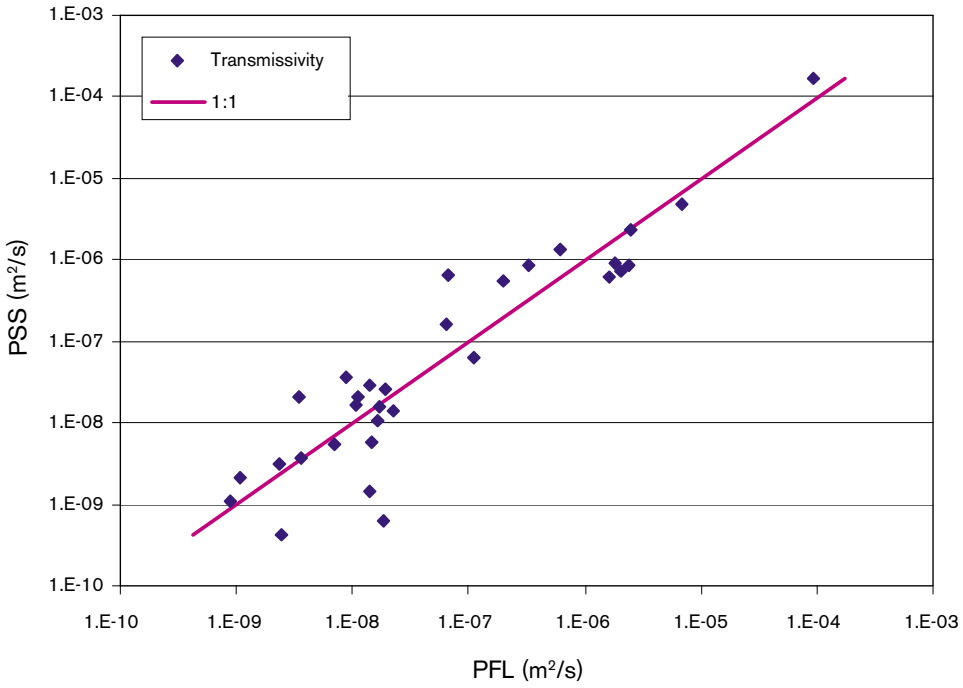

Figure B-34. *Cross-plot of PFL and PSS measurements for KFM03A. A 1:1 correlation is shown for comparison.*

B.2.4 KFM04A, Orientation of flowing fractures

Only PFL anomaly data are available for KFM04A (i.e. no PSS data). Figure B-35 shows logs of Boremap fracture confidence, crush-zones, the transmissivity of fractures interpreted from the PFL tests, rock domain, and DZs. The solid line on the PFL log indicates the interpreted detection limit. Flowing features are found almost entirely above 400 m. ZFMNE00A2 cuts KFM04A as a splayed structure composed of DZ1, DZ2 and DZ3 between 169 m to 242 m length down the borehole. The majority of flow is found above ZFMNE00A2, but there are a significant number of flowing features below ZFMNE00A2 also.

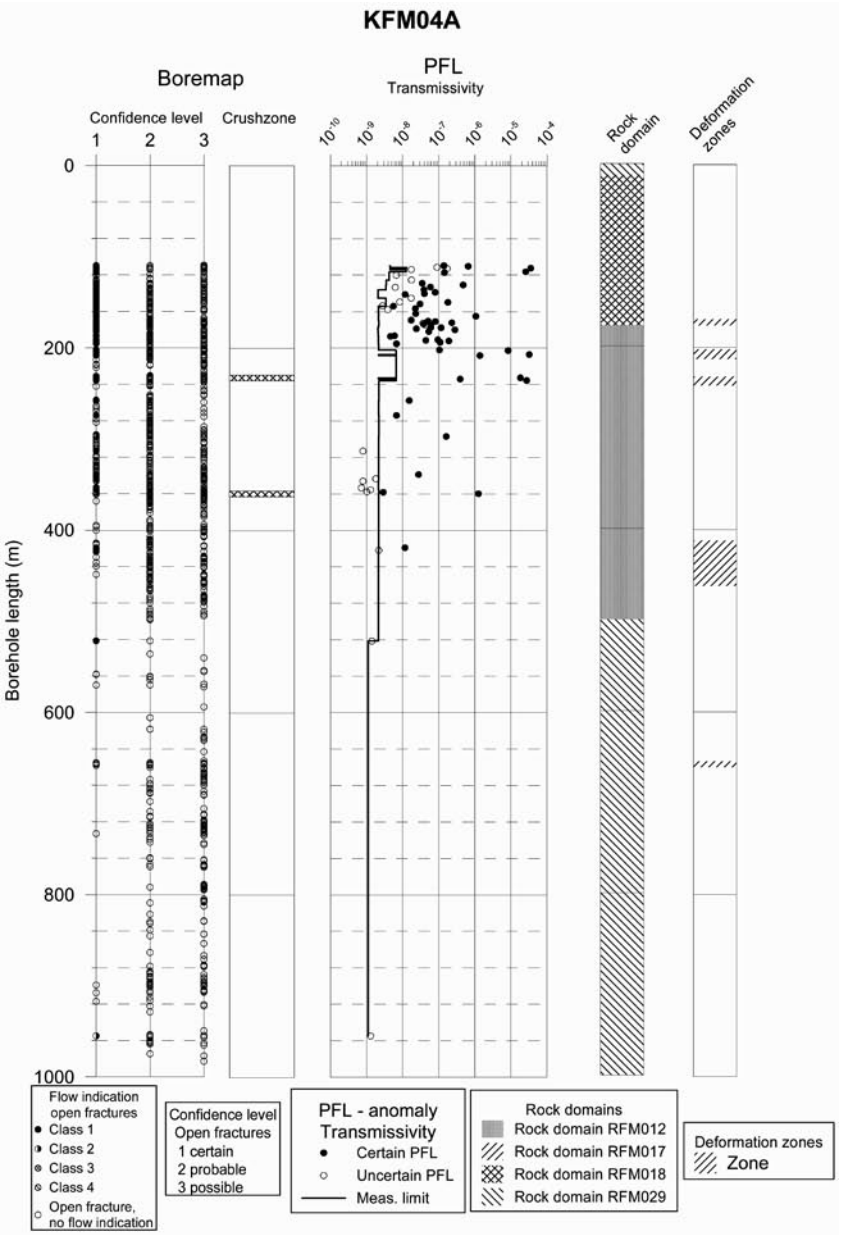

Figure B-35. *PFL flow anomalies in KFM04A. Note the detection limit (solid line on the PFL log) varies down KFM04A. (Plot provided as part of the Geo-DFN data delivery for Forsmark F1.2).*

The upper section of KFM04A (above ZFMNE00A2) shows that PFL flow anomalies with orientations in the HZ set dominate, with some flow in the NW and NE sets (see Figure B-36). (There are no DZs in this upper section.) Between 169 m and 242 m, ZFMNE00A2 cuts KFM04A. Within this section (ZFMNE00A2), all larger flow rates are found to match with DZ1, DZ2 and DZ3 and only flow anomalies with moderate transmissivity of order $10^{-7}\,m^2s^{-1}$ and $10^{-8}\,m^2s^{-1}$ match with background fractures (see Figure B-37). Again, flow is dominantly associated within the HZ set, with some flow in the NW set. Below ZFMNE00A2, the flow anomalies are more diffusely orientated, although most flow is observed in the NW set (see Figure B-38). Comparing with Figure B-18 an exceptionally small percentage of open fractures correspond to flow anomalies in KFM04A.

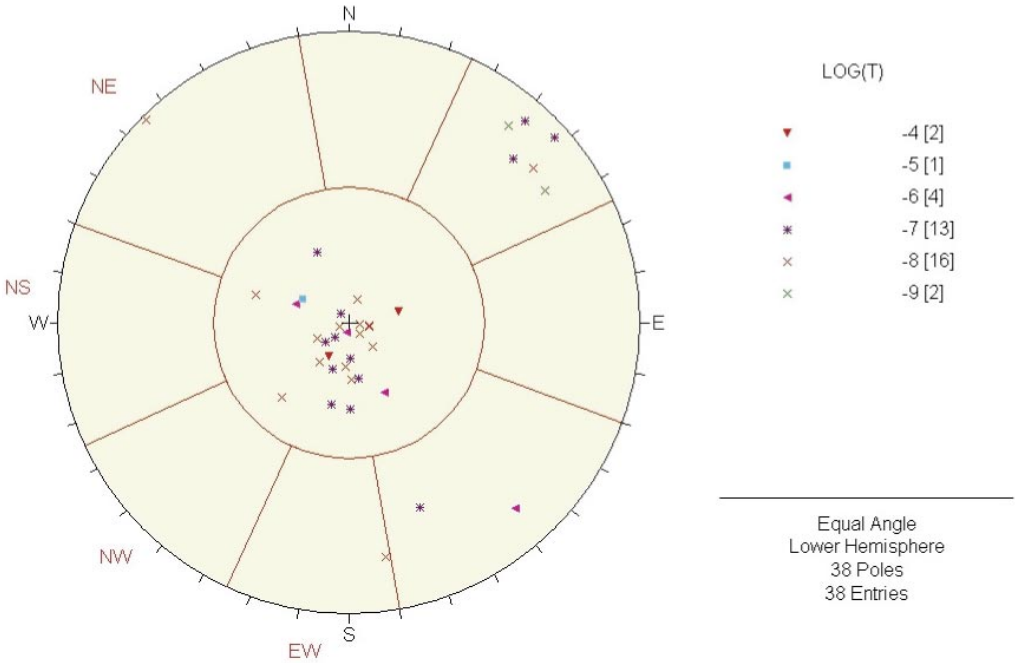

Figure B-36. *Orientations of the pole to fractures associated with PFL anomalies in the upper section of KFM04A (< 169 m, i.e. above ZFMNE00A2). Fractures are coloured by magnitude of the transmissivity of the PFL anomaly. There are no DZs within this section. The set divisions and the names of each set are superimposed in red.*

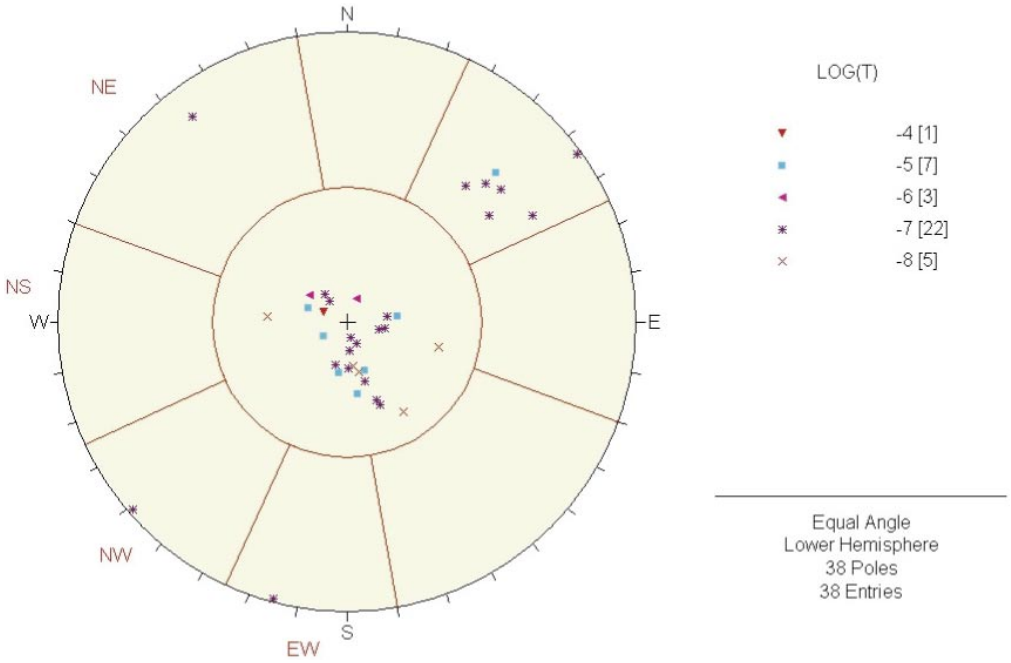

Figure B-37. *Orientations of the pole to features associated with PFL anomalies in ZFMNE00A2 as it cuts KFM04A on the boundary of the tectonic lens (169 m to 242 m length). Fractures are coloured by magnitude of the transmissivity of the PFL anomaly. Flow within DZ1, DZ2 and DZ3 as well as flow associated with background fractures between 169 m to 242 m length is shown. The set divisions and the names of each set are superimposed in red.*

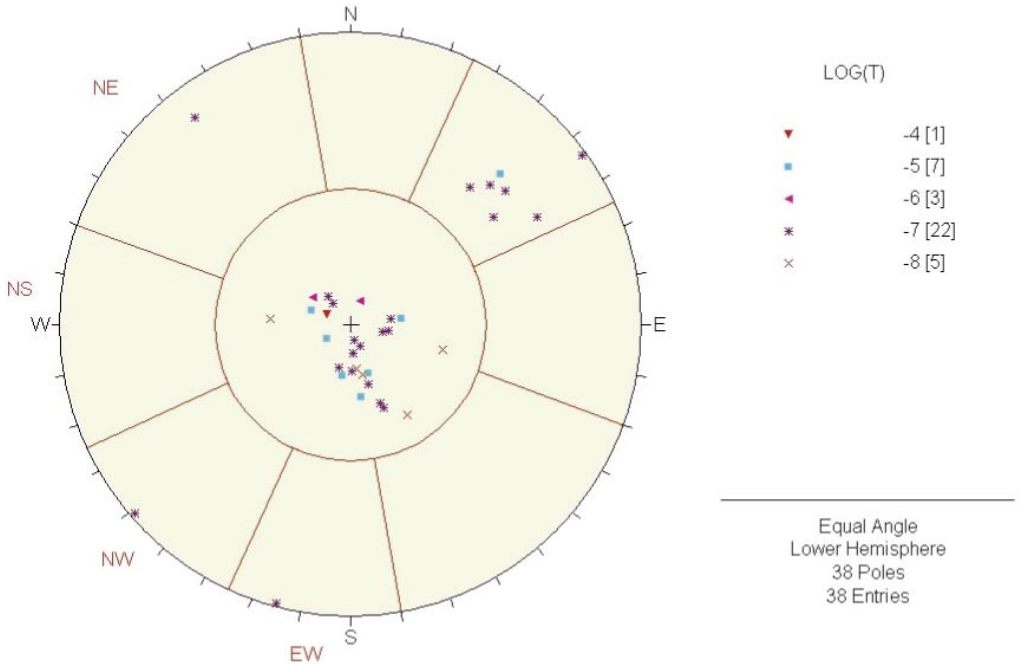

Figure B-38. *Orientations of the pole to features associated with PFL anomalies in the lower section of KFM04A (> 242 m length, i.e. below ZFMNE00A2). Features are coloured by magnitude of the transmissivity of the PFL anomaly. The set divisions and the names of each set are superimposed in red.*

B.2.5 KFM05A, orientation of flowing fractures

Only PFL anomaly data are available for KFM05A (i.e. no PSS data). Figure B-39 shows logs of Boremap fracture confidence, crush-zones, the transmissivity of fractures interpreted from the PFL tests, rock domain, and DZs. The solid line on the PFL log indicates the interpreted detection limit. (Note the broad DZ indicated in this figure between 600 m and 800 m is misleading. It was later re-interpreted into two narrow strands of the splayed DZ3 zone, see Table B-14.) Flowing features are found almost entirely above 200 m length down the borehole with only one additional feature at about 260 m. ZFMNE00A2 cuts KFM05A near the top, corresponding to DZ1 at 102 m to 113 m length and this coincides with some large transmissivities, of order $10^{-6}\,m^2s^{-1}$ to $10^{-4}\,m^2s^{-1}$. All other fractures in KFM05A are found below ZFMNE00A2 and flowing features in this section have transmissivities of order $10^{-7}\,m^2s^{-1}$ or less. There are two flow anomalies at depth on or just above the detection limit, one of which is associated with DZ3-2.

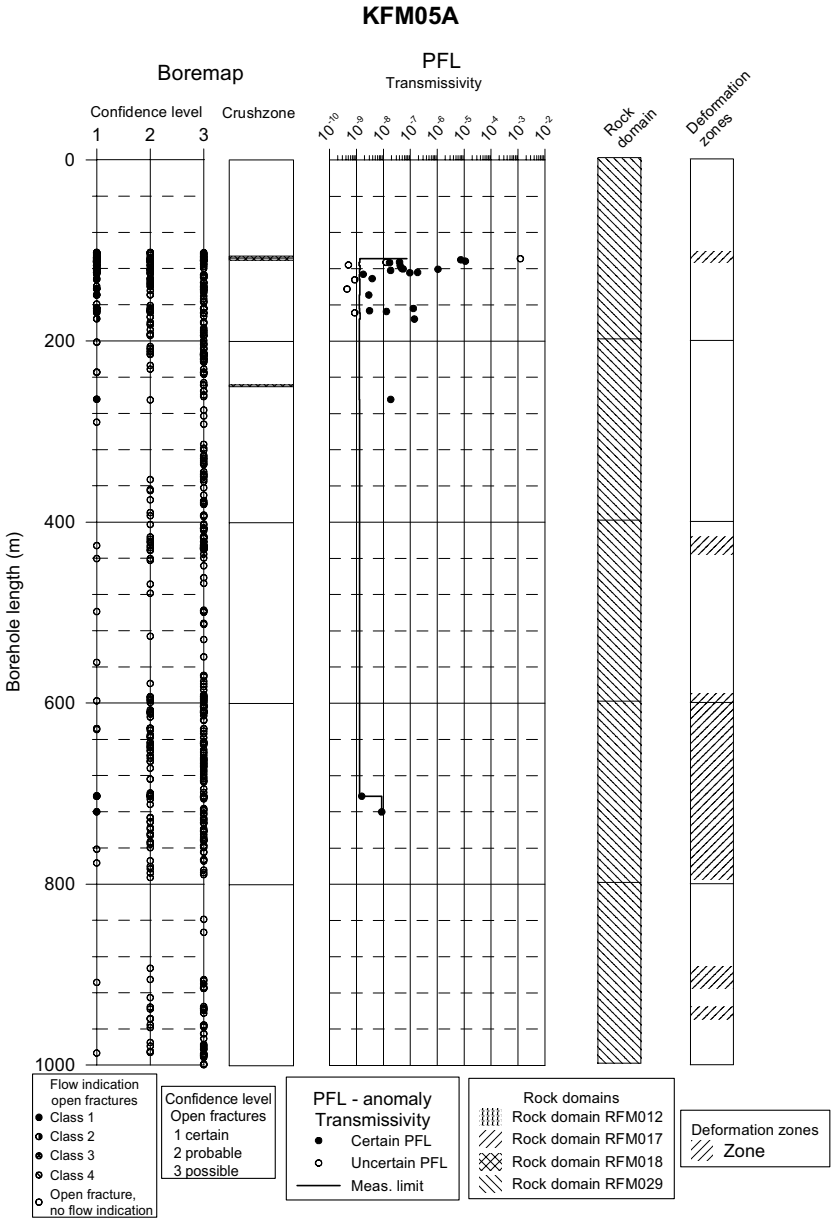

Figure B-39. *PFL flow anomalies in KFM05A. Note the detection limit (solid line on the PFL log) varies down KFM05A. (Plot provided as part of the Geo-DFN data delivery for Forsmark F1.2.)*

Figure B-40 demonstrates that the PFL flow anomalies are dominated by the HZ fracture set in both DZ1 and background fractures. Of these, the larger flows are found within DZ1 (ZFMNE00A2) and Figure B-41 shows that these correspond to fractures in the HZ set. Figure B-42 shows a stereonet for flow anomalies associated with background fractures.

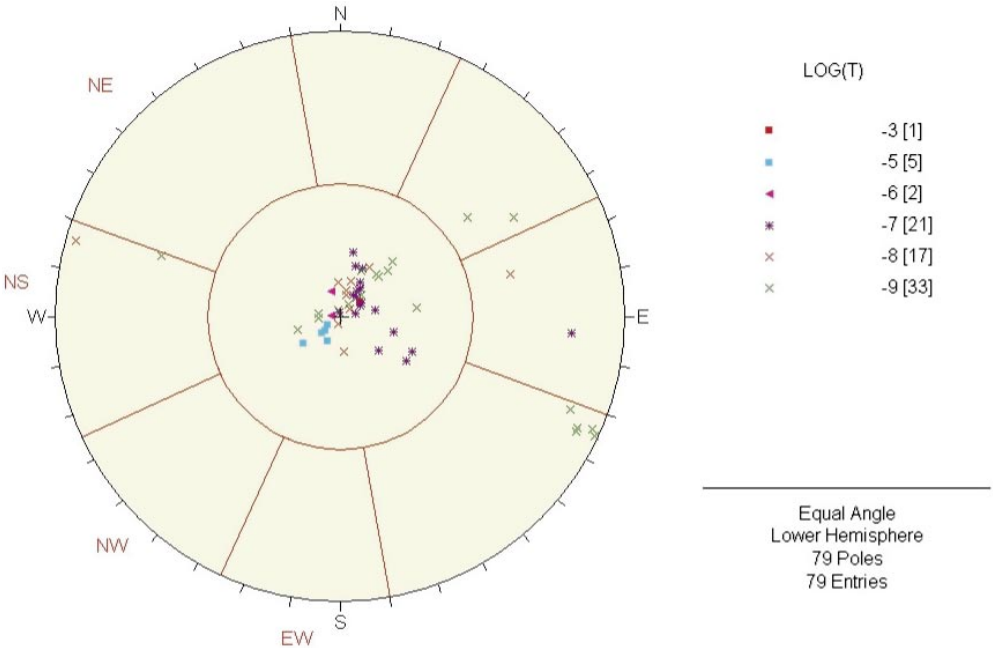

Figure B-40. *Orientations of the pole to all features associated with PFL anomalies in KFM05A. Both DZ1 and background fractures are plotted. Fractures are coloured by magnitude of the transmissivity of the PFL anomaly. The set divisions and the names of each set are superimposed in red.*

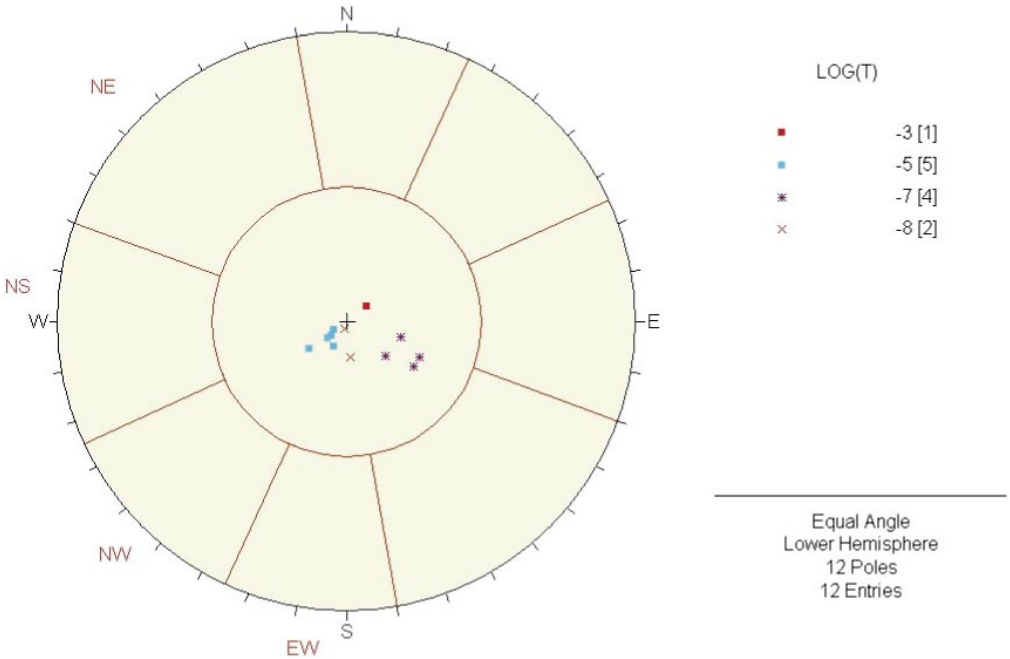

Figure B-41. *Orientations of the pole to fractures in DZ1 associated with PFL anomalies in KFM05A. Fractures are coloured by magnitude of the transmissivity of the PFL anomaly. The set divisions and the names of each set are superimposed in red.*

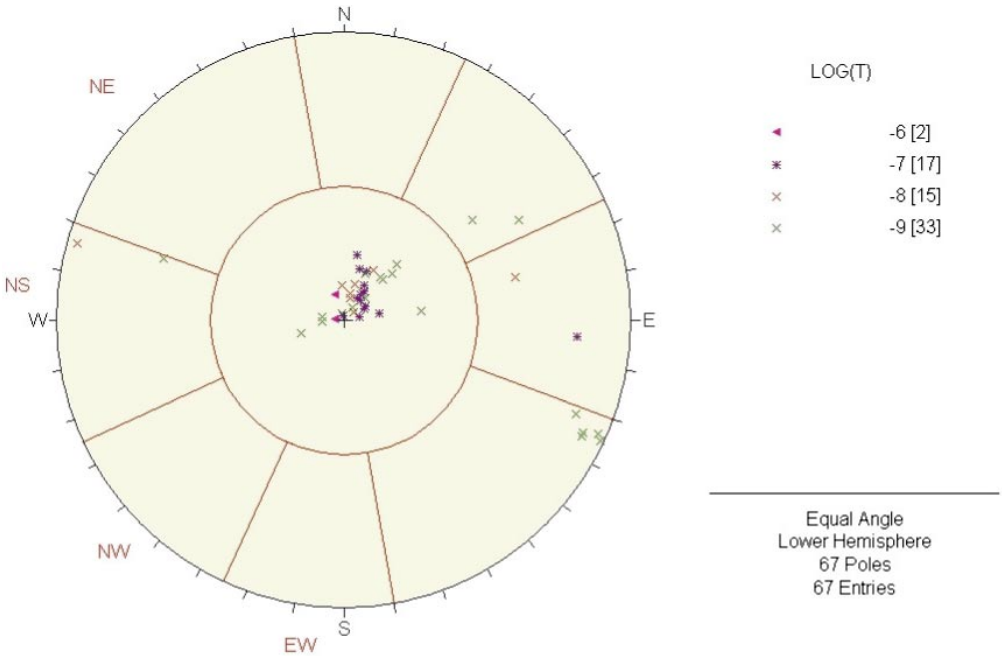

Figure B-42. *Orientations of the pole to background fractures associated with PFL anomalies in KFM05A. Fractures are coloured by magnitude of the transmissivity of the PFL anomaly. The set divisions and the names of each set are superimposed in red.*

Comparing with Figure B-21 a very small percentage of open fractures correspond with flow anomalies. Generally these have smaller transmissivities and are still dominated by the HZ set, though there are a few sub-vertical fractures mainly dipping W.

B.3 Simulations for assessment of DFN properties

As discussed in subsection 3.5 and Section B.2 of this Appendix, the distribution of flowing features varies greatly and it is difficult to come up with one model that describes the whole area. For example, flowing features are observed throughout the complete length of KFM03A (above ZFMNE00A2), whereas in KFM01A flow is only observed in the upper section (< 386 m) with no measurable flow in the lower section of KFM01A. KFM01A and KFM03 lay either side of the shallow ESE dipping ZFMNE00A2 DZ. Based on this and other considerations, a simple model was devised such that the rock is subdivided into volumes according to whether it is above or below ZFMNE00A2, and below ZFMNE00A2, the rock is further subdivided into an upper and lower volume. The different volumes of rock representing different regions of flowing and non-flowing features are summarised in Figure 3-5. In the DFN simulations, Volume E will be considered first (based on KFM03A, which shows flow throughout the total length of borehole), followed by Volume F (based on the upper section of KFM01A where there is flow) and then Volume G (based on the lower section of KFM01A where there is no observed flow).

B.3.1 DFN simulations for Volume E (based on the whole length of KFM03A)

For the simulations, KFM03A was modelled as vertical with length between 100 m and 1,000 m (the range over which fracture data was collected). Based on the Geo-DFN set classification, five sets of fractures were used to model the DFN, all having a range of lengths between 0.5 m and 1,000 m with a power-law distribution. The fracture sets were sub-divided into sets of smaller-scale (< 10 m) and larger-scale (> 10 m) length fractures.

Smaller-scale fractures were generated within a region around the borehole with a 10 m square horizontal cross-section, extending to 5 m above and below the top and bottom of the borehole. Larger-scale fractures were generated within a region around the borehole with a 1,200 m square horizontal cross-section, extending to 500 m above and below the top and bottom of the borehole. It was necessary to do this, as generating the small-scale fractures through the whole model domain would lead to an unnecessarily large model. The initial P32 estimated for each set was set to $P10_{corr}$ as calculated based on all open fractures in the boremap data, and was appropriately proportioned between the smaller- and larger-scale length fractures according to the parameters of the power-law distribution for the set. A summary of the DFN parameters used in the simulations is given in Table B-16.

Here, the mean pole orientation and Fisher concentration have been calculated for each fracture set based on the open fractures in KFM03A only. This choice has been made rather than using the global Geo-DFN statistics since there are such significant differences between the boreholes that it makes it very difficult to match the fracture intensity and relative intensity between the sets at a particular borehole using the Geo-DFN. (However, transmissivity matching in subsection 3.7 was carried out using the best fit fracture statistics, the global Geo-DFN parameters and the global variant Geo-DFN parameters.) To check the validity of the P32 values and relative intensities used for the fracture sets in the model, five DFN realisations were generated, and the P10 taken over the length of the borehole was compared with the observed value for KFM03A. The results are shown in Table B-17. The average P10 for the five realisations is only about 6% higher than the observed value. This shows that the using the $P10_{corr}$ values provides a good estimate of P32 since it reproduces the overall fracture statistics well.

A further, more in-depth, check was performed by comparing the relative intensity of fractures intersecting the borehole belonging to each set between the boremap data and each of five realisations, see Table B-18. The agreement between the proportions in the simulations and the observed proportions is reasonable. However, there is a consistent trend toward a slightly larger proportion of fractures in the sub-horizontal set in the simulations. However, this discrepancy is not considered significant enough to require any correction in the data used for the simulations. It is therefore concluded that the approach used to simulate the DFN around the KFM03A, and the DFN parameters in Table B-16, is reasonable and captures the boremap data.

As an example, one realisation of the DFN model is shown in Figure B-43 with all fractures included within a 1,000 m long and a 200 m diameter model domain surrounding KFM03A. The smaller-scale fractures (lengths between 0.5 m and 10 m), generated only within a region with a 10 m square horizontal cross-section around KFM03A, are shown in Figure B-44. Similar models were used to perform the flow simulations described in Section B.4.

Table B-16. Description of DFN parameters used for simulation of fractures in KFM03A. Note that these are the borehole specific mean pole orientations and Fisher concentrations.

Rock domain	Fracture set name	Orientation set pole: (trend, plunge), concentration	Length model Constants: power-law (L_0, k_r) (m)	Intensity, (P_{32}), valid length interval: L_0, L_{max} (m^2 m^{-3})	Relative intensity of P32	Transmissivity model Eq no, constants T (m^2 s^{-1})
RFM029 (177 m)	1: NS	(85, 0) 15.4	(0.5, 2.88)	0.695, (0.5, 1,000)	0.124	N/A
	2: NE	(131, 8) 26.1	(0.5, 3.02)		0.291	
RFM017 (68 m)	3: NW	(46, 4) 18.5	(0.5, 2.81)		0.191	
	4: EW	(197, 0) 27.0	(0.5, 2.95)		0.100	
RFM029 (707 m)	5: HZ	(156, 73) 11.3	(0.5, 2.92)		0.294	

Table B-17. Comparison of observed open fractures with predicted values in 900 m section of KFM03A for 5 realisations.

Case	Number of open fractures	P10 (m^{-1})	% of observation
Realisation 1	275	0.306	110.9%
Realisation 2	259	0.288	104.4%
Realisation 3	256	0.284	103.2%
Realisation 4	253	0.281	102.0%
Realisation 5	268	0.298	108.1%
Average modelled	262	0.291	105.7%
Observation	248	0.276	–

Table B-18. Comparison of relative $P10_{corr}$ density in borehole KFM03A between that observed and in the 5 realisations.

Set	Boremap data	Real 1	Real 2	Real 3	Real 4	Real 5	Average modelled
NS	7.7%	5.8%	6.6%	7.4%	3.6%	6.0%	5.9%
NE	16.1%	12.7%	10.8%	10.2%	16.2%	13.8%	12.7%
NW	11.3%	8.4%	10.0%	10.5%	11.9%	11.2%	10.4%
EW	5.6%	4.4%	4.6%	4.7%	2.0%	1.9%	3.5%
HZ	59.3%	68.7%	68.0%	67.2%	66.4%	67.2%	67.5%

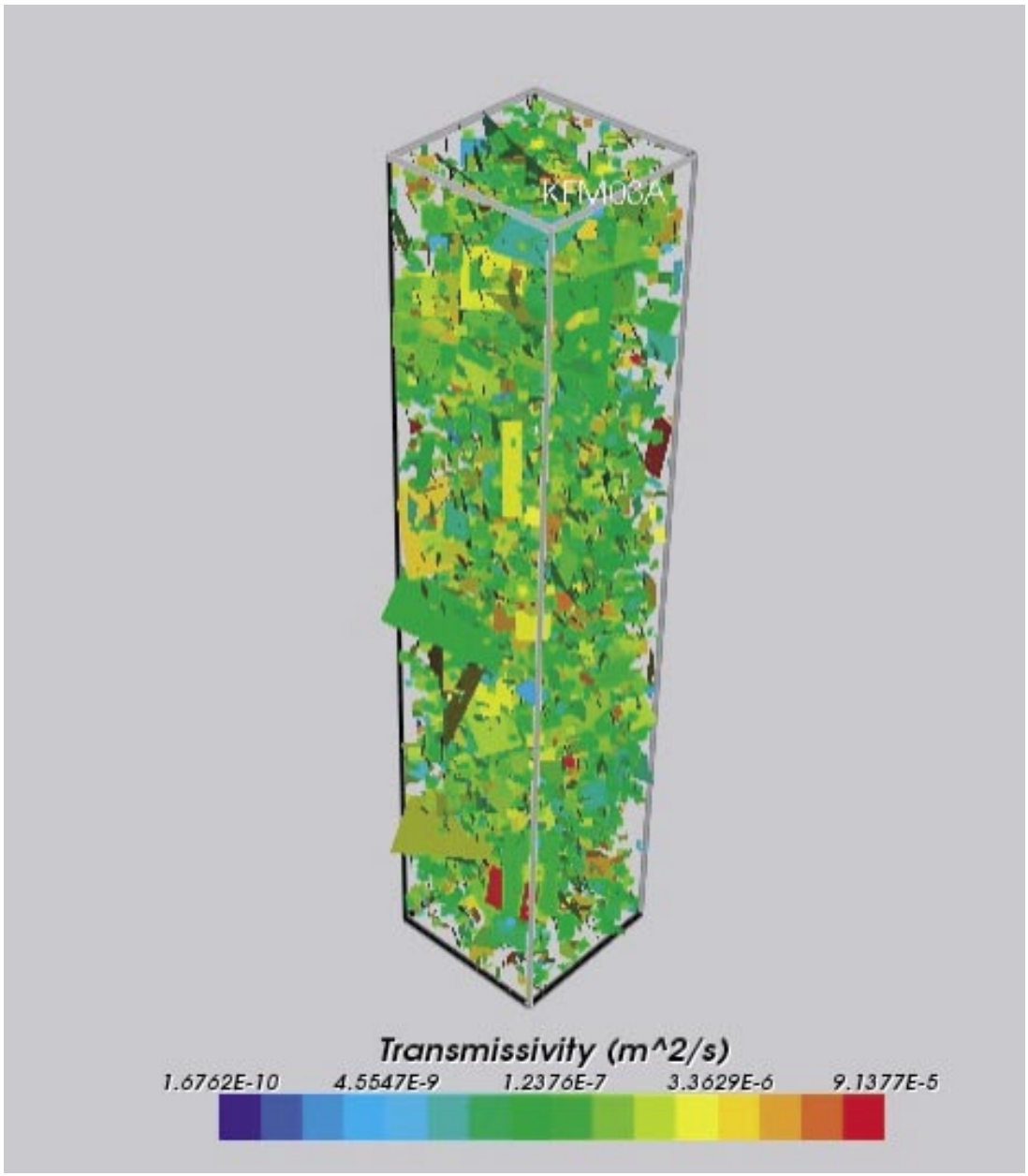

Figure B-43. *DFN realisation for a domain of 200 m square cross-section and 1,000 m length around borehole KFM03A. All fractures are shown and coloured by log(T) (in this case T is lognormally distributed and not correlated to L).*

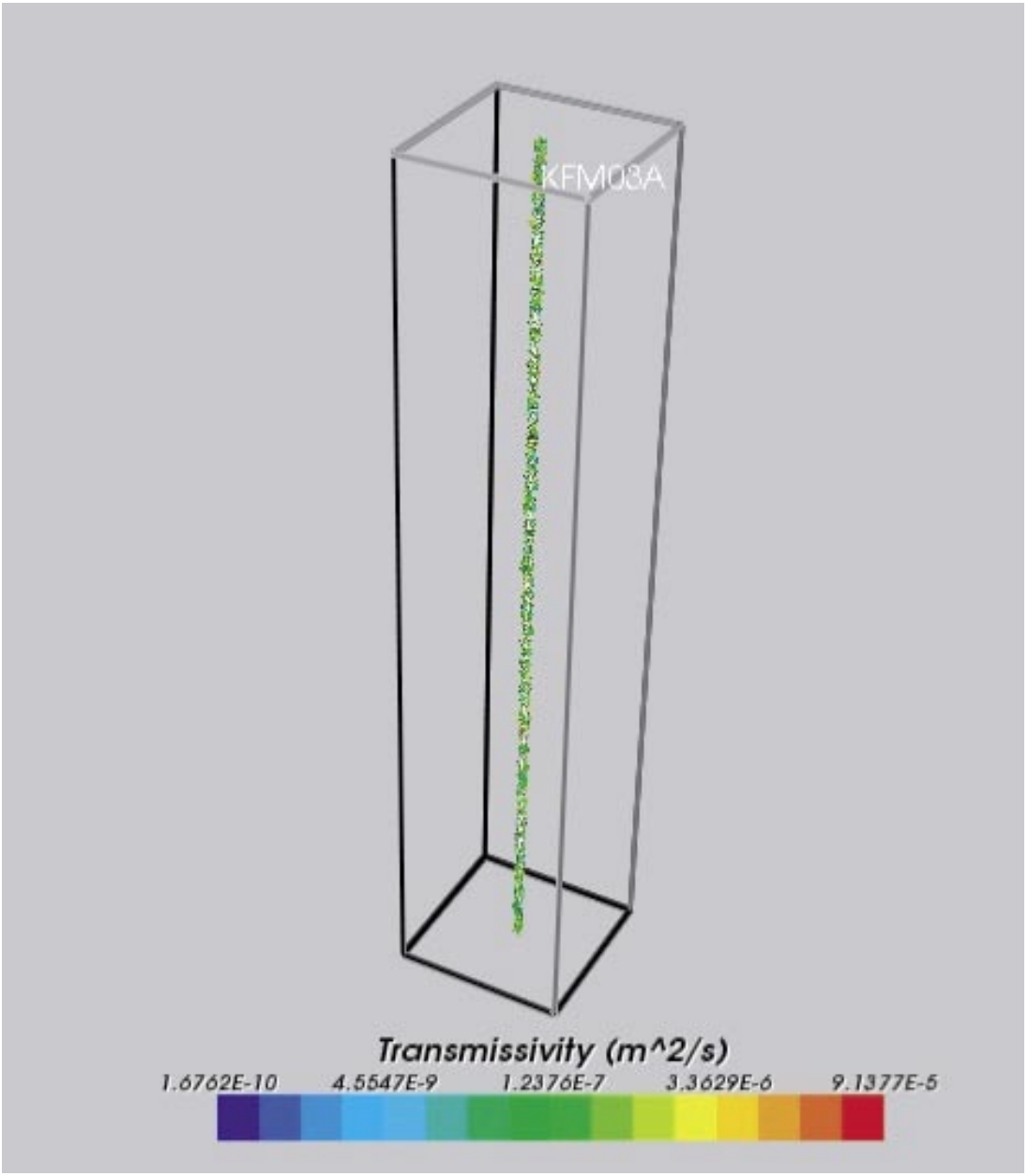

Figure B-44. *Small-scale fractures generated within a region of 10 m square cross-section around borehole KFM03A. Fractures are coloured by log(T) (in this case T is lognormally distributed and not correlated to L).*

B.3.2 DFN simulations for Volume E using variant Geo-DFN (based on whole length of KFM03A)

An alternative case for the Geo-DFN (termed 'variant Geo-DFN') was also proposed. This model, which used $k_r = 2.75$ for all fracture sets (Sven Follin, written communication, January 2005), shows a better match to the number of regional lineaments. The process of checking that the model matched the fracture intensity was repeated for Volume E, as was matching of transmissivity models to PSS and PFL data (subsection B.4.2). A summary of the variant Geo-DFN parameters is shown in Table B-19. As before, the validity of the P32 values and relative intensities used for the fracture sets in the model were checked using five DFN realisations, and the P10 taken over the length of the borehole was compared with the observed value for KFM03A. The results are shown in Table B-20. The average P10 for the five realisations is only about 6% lower than the observed value. In addition, the fracture set statistics are reproduced well. This shows that using the $P10_{corr}$ values provides a good estimate of P32 for the variant Geo-DFN.

Table B-19. Description of variant Geo-DFN parameters used for simulation of fractures in KFM03A.

Rock domain	Fracture set name	Orientation set pole: (trend, plunge), concentration	Length model, constants: power-law (L_0, k_r) (m)	Intensity, (P_{32}), valid length interval: L_0, L_{max} (m^2 m^{-3})	Relative intensity of P32	Transmissivity model Eq no, constants T (m^2 s^{-1})
RFM029 (177 m)	NS	(87, 2) 21.7	(0.5, 2.75)	0.75 (0.5, 1,000)	0.161	N/A
	NE	(135, 3) 21.5	(0.5, 2.75)		0.319	
RFM017 (68 m)	NW	(41, 2) 23.9	(0.5, 2.75)		0.164	
	EW	(190, 1) 30.6	(0.5, 2.75)		0.076	
RFM029 (707 m)	HZ	(343, 80) 8.2	(0.5, 2.75)		0.280	

Table B-20. Comparison of observed open fractures with predicted values using variant Geo-DFN, in 900 m section of KFM03A for 5 realisations.

Set	Observed open P10 (m^{-1})	Observed open N (fracts)	Open N (fracts) Real 1	Real 2	Real 3	Real 4	Real 5	Mean open P10 (m^{-1})	% of observation
NS	0.02	21	18	23	22	11	26	0.02	96.3%
NE	0.05	44	39	40	31	37	35	0.04	83.2%
NW	0.03	31	18	26	20	20	31	0.03	75.1%
EW	0.02	15	9	7	7	6	5	0.01	44.4%
HZ	0.18	161	159	159	162	181	183	0.19	105.0%
Total	0.30	271	243	255	242	255	280	0.28	94.0%

B.3.3 DFN simulations for Volume F (based on upper section of KFM01A)

Within KFM01A, flowing features are only observed in the upper section (< 386 m), hence a 300 m length of vertical borehole was used in the simulation since this is approximately the length of KFM01A for which there are measured flow anomaly data. The model domain is 400 m high, therefore extending 50 m above and below the vertical borehole. The model region has a 100 m radius.

As for Volume E, five sets of fractures were used to model the DFN, all having a range of lengths between 0.5 m and 1,000 m with a power-law distribution. The fracture sets were sub-divided into sets of smaller-scale (< 10 m) and larger-scale (> 10 m) length fractures. Smaller-scale fractures (0.5 to 10 m) were generated within a region around the borehole with a 10 m square horizontal cross-section, extending to 5 m above and below the top and bottom of the borehole. Larger-scale fractures (10 to 1,000 m) were generated within a region around the borehole of 1,200 m square horizontal cross-section, extending to 500 m above and below the top and bottom of the borehole (i.e. fracture centre limits were half the fracture length greater than the model domain). The initial P32 estimated for each set was set to $P10_{corr}$ as calculated based on all open fractures in the boremap data, and was appropriately proportioned between the smaller- and larger-scale length fractures according to the parameters of the power-law distribution for the set. The main fracture sets were generated on a range of scales with a power-law length distribution.

Initial matching of the measured open P10 gave a slight under-prediction by the model of about 6%. This is a reasonable match in terms of the overall fracture intensity. However, considering individual sets, the model performs poorly. For the sub-vertical sets, the model under-predicts P10 by about 30%, and over-predicts the HZ set by 6% of the measured open P10. Hence, it was felt necessary to adjust P32 for the fracture sets to correct for these differences so as to match both the total number of fractures and the proportions between the sets. This led to a total P32 of 4.7 m^2m^{-3} used in the model. The full set of parameters used for the upper section of KFM01A is given in Table B-21. Here, the mean pole orientation and Fisher concentration have been calculated for each fracture set based on the open fractures in KFM01A only. As before, this choice has been made rather than using the global Geo-DFN statistics since there are such significant differences between the boreholes that it makes it very difficult to match the fracture intensity and relative intensity between the sets at a particular borehole using the Geo-DFN. (Transmissivity matching in subsection 3.7 was carried out using the best fit fracture statistics and the global Geo-DFN parameters.

The results for five DFN realisations to match the measured open P10 are shown in Table B-22. After adjustment of P32 to correct for the proportions of open fractures in each set, the modelled open P10 matches the measured value very well.

Table B-21. Description of DFN parameters used for simulation of fractures in the upper section of KFM01A (< 400 m). The adjusted P32 (to match the proportions of fractures in each set) is shown, along with the adjusted set proportions. Note that these are the borehole specific mean pole orientations and Fisher concentrations.

Rock domain	Fracture set name	Orientation set pole: (trend, plunge), concentration	Length model, constants: power-law (L_0, k_r) (m)	Intensity, (P_{32}), valid length interval: L_0, L_{max} (m^2 m^{-3})	Relative intensity of P32	Transmissivity model Eq no, constants T (m^2 s^{-1})
RFM029	1: NS	(78, 3) 12.5	1: (0.5, 2.88)	4.7, (0.5, 1,000)	1: 0.110	N/A
	2: NE	(149, 1) 18.1	2: (0.5, 3.02)		2: 0.449	
	3: NW	(232, 13) 10.5	3: (0.5, 2.81)		3: 0.085	
	4: EW	(10, 2) 11.4	4: (0.5, 2.95)		4: 0.049	
	5: HZ	(186, 84) 17.6	5: (0.5, 2.92)		5: 0.306	

Table B-22. Matching of five realisation of modelled open P10 with that observed in the upper section of KFM01A. The modelled length is 300 m. The adjusted P32 used in the modelling is 4.7 m^2m^{-3}.

Set	Observed open P10 (m^{-1})	Observed open N (fracts)	open N (fracts)					Mean open P10 (m^{-1})	% of observation
			Real 1	Real 2	Real 3	Real 4	Real 5		
NS	0.10	31	31	27	38	26	37	0.11	103.5%
NE	0.35	106	105	113	82	127	99	0.35	99.3%
NW	0.11	32	44	44	33	27	42	0.13	119.6%
EW	0.06	17	18	17	17	15	17	0.06	99.1%
HZ	1.28	384	420	350	376	368	409	1.28	100.0%
Total	1.90	570	618	551	546	563	604	1.92	101.2%

B.4 Conditioning transmissivity against PFL and PSS data

Clearly the choice of statistical distribution used for transmissivity is a key assumption in interpreting the flow test-data. Three alternative transmissivity concepts were considered (as shown in Figure 3-4). For each of these concepts an associated set of parameters are required in the DFN simulations to give a match to the distribution of flow-rates, Q, seen in the PFL data. It would be preferable to match Q rather than T from the PFL data because, firstly, it is Q that is measured not T (T is inferred from Q based on the Dupuit formula /2/), and secondly, a fracture intersecting the borehole may have a substantial T value, but zero Q if it is not connected to the network. Matching Q necessitates performing flow calculations for flow to the borehole.

The approach of calibrating models against flow-rate data from PFL tests was followed in the Hydro-DFN modelling for Simpevarp 1.2 /15/. For Forsmark, the numbers of PFL anomalies above the measurement threshold is significantly lower than for Simpevarp, and hence gives fewer data with which to calibrate a model. This motivated making more use of the PSS hydraulic data that often have a lower measurement limit than the PFL method, and therefore in order to get a handle on the lower flow-rates, the model has been fitted against both PFL and PSS data. Since the PSS data are only available as transmissivity of 5 m intervals rather than flow-rates in individual fractures, it was necessary to compare simulated flow-rates in fractures in a consistent way. This was achieved by firstly inferring a transmissivity for each flowing fracture that intersects the borehole in the model using

Dupuit's formula and then grouping them according to the positions of the 5 m intervals for which PSS data were supplied. The transmissivity of PFL anomalies was converted in the same way for comparison. The models are then calibrated against both the total transmissivity of all features measured in the measurement interval, and against the statistical distribution of measured transmissivity values. Once the model had been calibrated against T values for PSS and PFL, then the calibration could be cross-checked on flow-rate, Q, of individual fractures from the PFL analyses.

For F1.2, PFL anomaly data were available for KFM01A to KFM05A, and also PSS packer-test data for KFM01A to KFM03A. The flow simulations were performed using the following assumptions:

- Zero head on the vertical and top boundaries. The vertical boundaries were 100 m away from the borehole. The top boundary was 50 m above the top of the borehole. A no-flow boundary was used on the base of the model, 50 m below the base of the borehole;
- A uniform drawdown of 10 m was specified throughout the length of the borehole;
- Fractures smaller than 1 m were discarded to make the flow calculations tractable;
- Small fractures less than 10 m in length were generated only within a 10 m diameter region surrounding the borehole;
- The modelled transmissivity (m^2s^{-1}) is calculated from the modelled flow rate Q (m^3s^{-1}) into the borehole, and hence the transmissivity can be compared with that calculated from the PFL differencing. The modelled T can be calculated using Dupuit's Formula /26/, assuming a radius of influence of 19 m and 0.038 m well radius, and a constant 10 m difference between the hydraulic head at the borehole and the hydraulic head at the radius of influence;
- Using the best-fit parameters determined by matching the transmissivity, the modelled flow-rate Q (m^3s^{-1}) into the borehole can be calculated and checked against Q from the PFL differencing (Section B.5);
- The measured and simulated transmissivities can be compared as simple distributions without concern for spatial bias.

Further, in matching T, the objective is only to match the total transmissivity and statistical distribution of T values, but not the actual intervals where the flows occur or to reproduce any clustering of flow anomalies such as may arise around DZs, for example. Also, the minimum flow-rate associated with a PSS flow interval is about $9\ 10^{-12}\ m^3s^{-1}$, which is a function of the detection limit, but it is assumed that perhaps there exist smaller fracture flows not detected by this equipment. (The minimum flow rate associated with a PFL flow anomaly is about $4\ 10^{-12}\ m^3s^{-1}$.) Hence, we will aim to match the part of the T distribution that has been measured, but not worry about the distribution of T below the detection limit. It should also be noted that several realisations of the DFN model are generated to test whether the chosen transmissivity values match in the average rather than fine-tuning each realisation to get a match, although comparisons are made between realisations to indicate the variability.

One important uncertainty that needs to be considered in matching the flow-tests is the percentage of open and partly-open fractures that contribute to flow given the uncertainties in their characterisation from the core. Hence, as well as varying the T parameters, we can also vary the percentage of open $P10_{corr}$ that is used.

B.4.1 Conditioning transmissivity for Volume E (complete length of KFM03A)

The modelling approach taken was to perform flow simulations in a DFN model using NAPSAC. In NAPSAC, the connectivity between fractures, boreholes and boundaries is established and then flow is calculated through each fracture connected to the network using the finite-element method and applying Darcy's law. The flow rate into the borehole from each connected fracture intersecting the borehole is then derived. The steady-state head distribution was calculated using a Pre-Conditioned Conjugate Gradient (PCCG) iterative solver with a low convergence criterion due to the large heterogeneity in the DFN models. This gave a relative mass balance of around 10^{-7}. Figure B–45 gives an example of the head distribution in a flow model. This is a case based on a correlated T distribution and with 100% of the open fractures. Here, fractures are coloured by the average head on the fracture. Most are red since we only see the fractures on the outside of the model and these are connected to the high head, 0 m, on the external boundaries. Fractures coloured grey are fractures that do not carry flow since they are isolated from the network or are dead-ends. They are coloured grey since there is no water in them, and hence no head can be calculated in them. The fractures connected to the borehole see the greatest drawdown, and Figure B-46 shows only the fractures connected to the borehole or that have a significant drawdown.

Parameters for the transmissivity models were fitted to both the PFL and the 5 m-interval PSS results by a trial and error process. Parameters were chosen to attempt to provide good fits to both the total transmissivity of flowing features in the borehole and a histogram of transmissivities (fitting above the detection limits for the flow tests). To allow comparison of the simulation results to the PSS and PFL data simultaneously, the results were converted into compatible formats. The transmissivities for the PFL anomalies were grouped into 5 m intervals and summed to match those of the PSS tests. Transmissivities for the simulated flow results were calculated following the same method used to calculate transmissivities from the flow-test data; these were then grouped and summed as for the PFL data. The transmissivity for each 5 m interval was plotted as a histogram. Since the number of intervals with flow above the detection limit was small for this borehole, the variability between realisations tended to be large and therefore five realisations were simulated for each fit to give a reasonable representation of the variability predicted.

Simulation results were initially fitted to all the PFL and PSS data and the P32 value used was based on 100% of all open and partly-open fractures. In this case the total transmissivity from the PFL data was $1.1\ 10^{-4}\ m^2s^{-1}$ and from the PSS data was $1.9\ 10^{-4}\ m^2s^{-1}$. Flows near to the detection limit resulted in transmissivities of 10^{-10}–$10^{-9}\ m^2s^{-1}$. This represents a very large range of values. A fit using a correlated transmissivity model is shown in Figure B–47. As can be seen, it proved difficult to find reasonable parameters for the transmissivity models that could reproduce such a large spread in the results while maintaining a fit to the distribution.

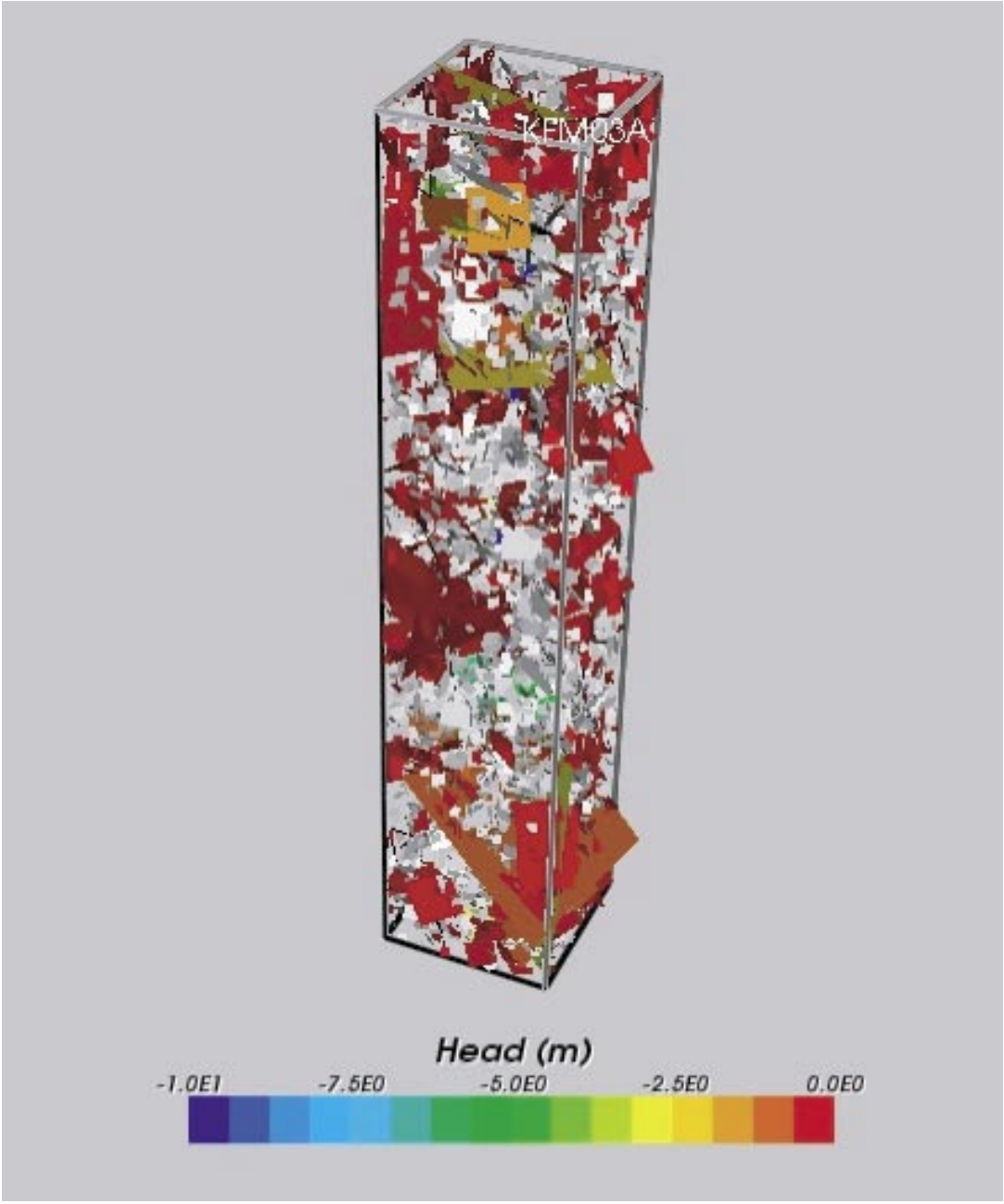

Figure B-45. *DFN realisation for a region of 200 m square cross-section around KFM03A used in the PFL/PSS simulation. For the case shown here, it is assumed that 100% of open and partly-open fractures are open. Also, only fractures with length greater than 1 m are used. Fractures are coloured by the average head on the fracture or grey where they are either isolated or dead-ends.*

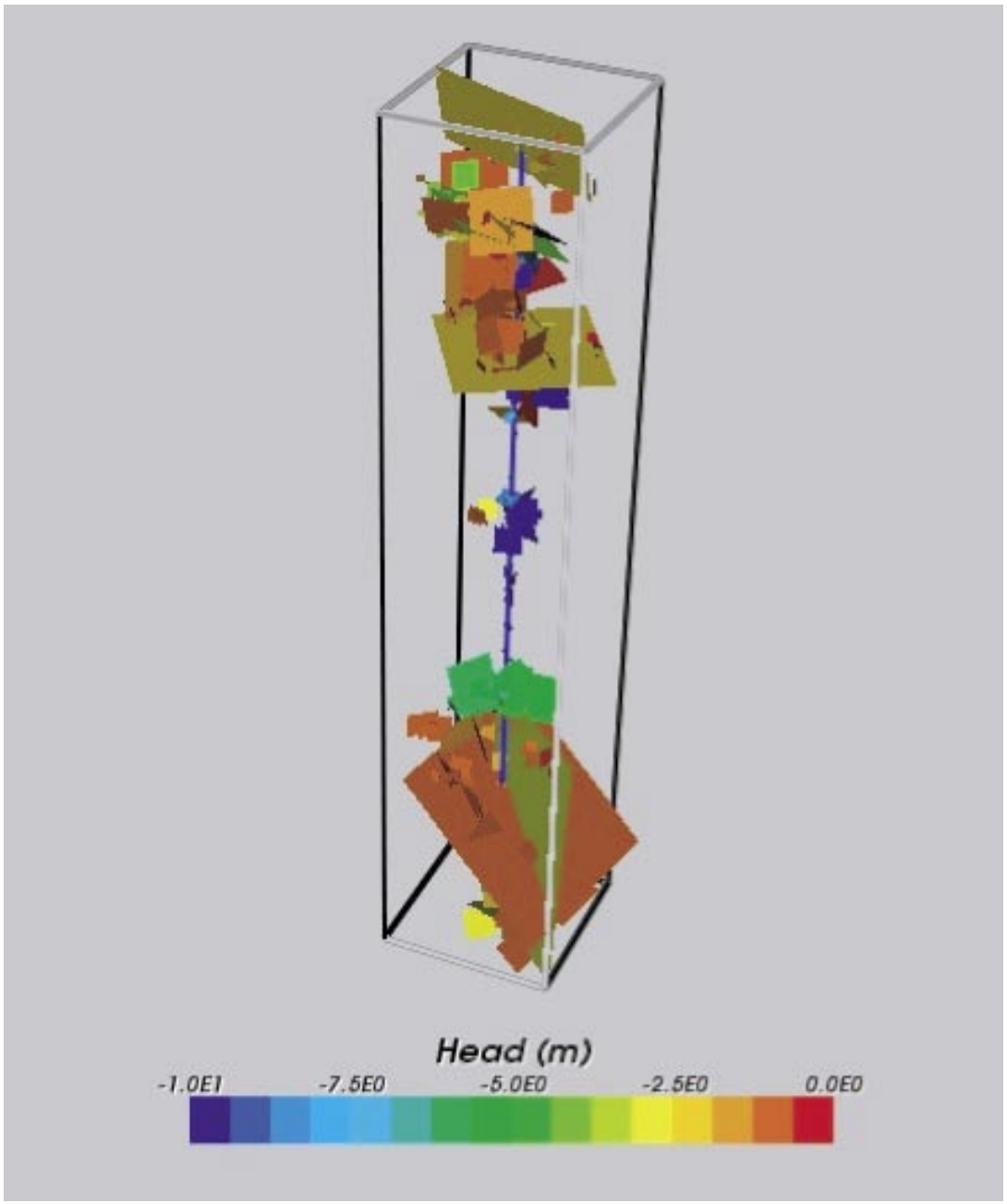

Figure B-46. *DFN realisation as for Figure B–45, but showing only the fractures around the borehole with a significant drawdown.*

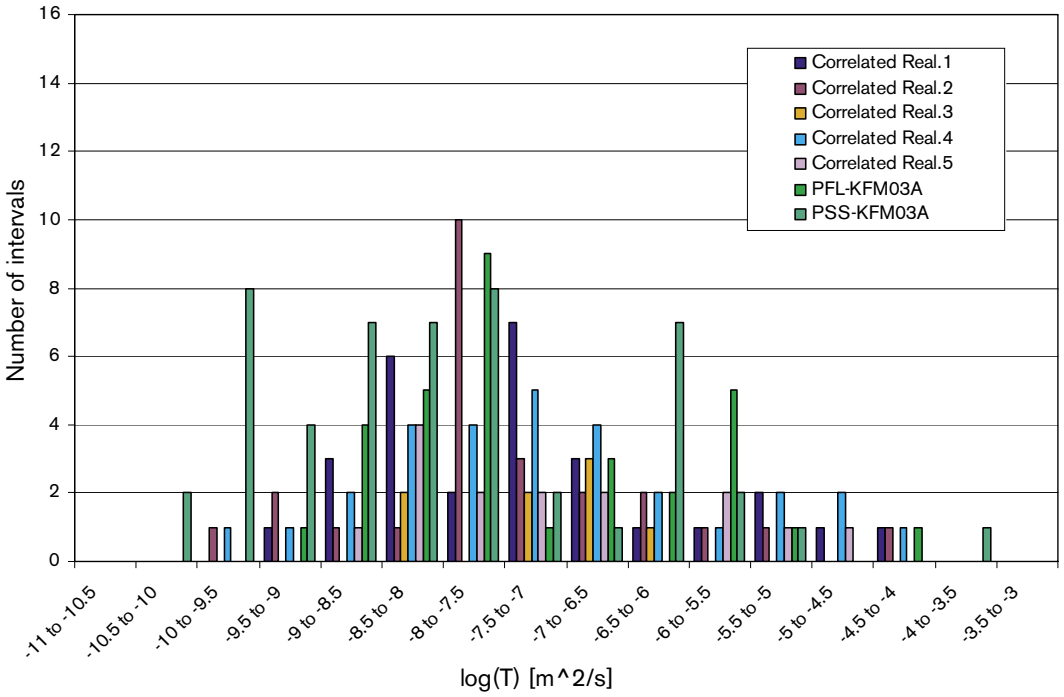

Figure B–47. *Histogram of Log(T) in 5 m intervals for 5 realisations of the correlated T distribution compared with the PFL anomaly and PSS data for KFM03A. All observed flows (both within and outside Deformation Zones) are shown. This preliminary case is based on 100% of open and partly-open fractures.*

Based on the difficulty of the initial fitting, it was decided that a more appropriate approach would be to determine suitable parameters to match only the smaller-scale transmissivities resulting from flows outside of DZs. Removing data corresponding to the DZs reduced the total transmissivity for the PFL flows to 6.0 10^{-7} m^2s^{-1} and for the PSS flows to 9.5 10^{-7} m^2s^{-1}. The power law distribution of fracture length provided by the Geo-DFN has a steep slope (k_r = 2.92 and 3.02 respectively for the dominant HZ and NE fracture sets). This results in a very large number of small fractures, and correspondingly very few large fractures, leading to poor connectivity. Hence, a good match to the observed PSS and PFL data requires that the P32 must be increased over and above the number of open and partly open fractures observed. Theoretically, it could be assumed that some of the features marked as sealed may be re-classified as open or partly open. From Table 3-7, 5% of sealed fractures are only possible, and 53% are probable. In the case of Volume E, the best match is seen with P32 of 130% of all open and partly open features for the correlated case (Figure B–48). Hence, this would require all of the possible sealed and about half the probable sealed fractures to be open. The transmissivity model parameters were adjusted to match both the total transmissivity for the PSS and PFL flows, and also the number of non-flowing intervals. Further fits, also using a P32 value of 130%, were produced for the uncorrelated and semi-correlated transmissivity models (Figure B–49 and Figure B–50).

Results for the correlated model are shown in Figure B–48. In this case, although the simulated results reproduce the total transmissivity and the required range of transmissivities well, is was difficult to reproduce the rather broad peak in the PSS data. Figure B–49 shows the uncorrelated model, which is reasonably well matched, although even using 130% of P32, the poor connectivity is shown by the variability in the five simulated realisations. A reasonable fit was produced for the semi-correlated (log(s.d.) = 1.0) case, as shown in Figure B–50.

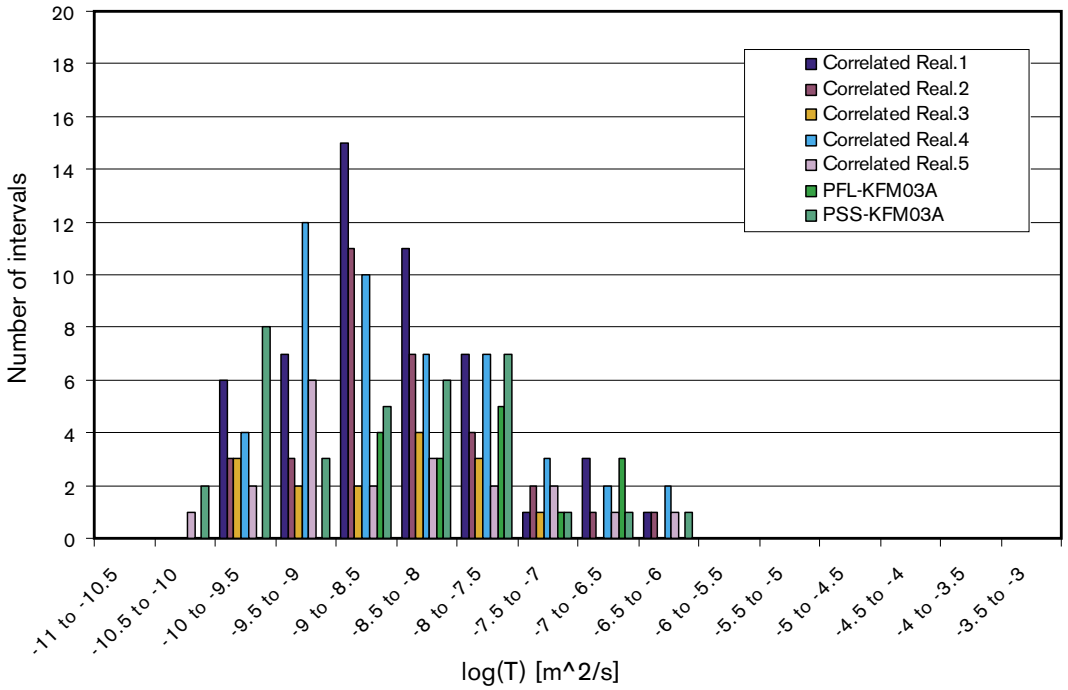

Figure B–48. *Histogram of Log(T) in 5 m intervals for 5 realisations of the correlated T distribution compared with the PFL anomaly and PSS data outside the DZs for KFM03A. This case is based on 130% of open and partly-open fractures.*

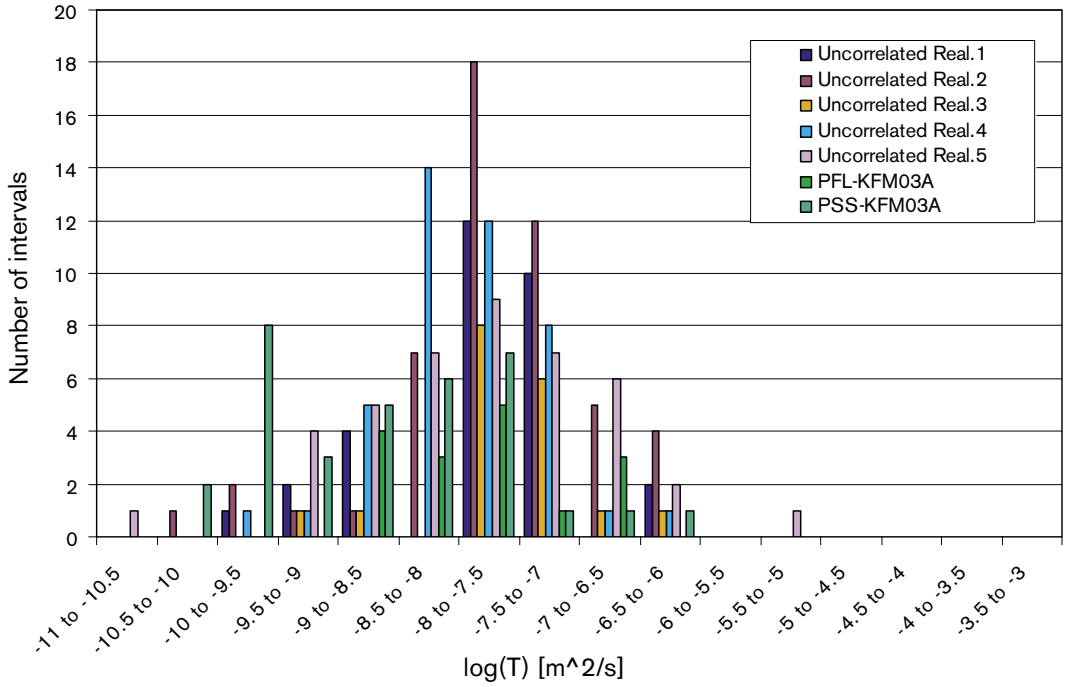

Figure B–49. *Histogram of Log(T) in 5 m intervals for 5 realisations of the uncorrelated T distribution compared with the PFL anomaly and PSS data outside the DZs for KFM03A. This case is based on 130% of open and partly-open fractures.*

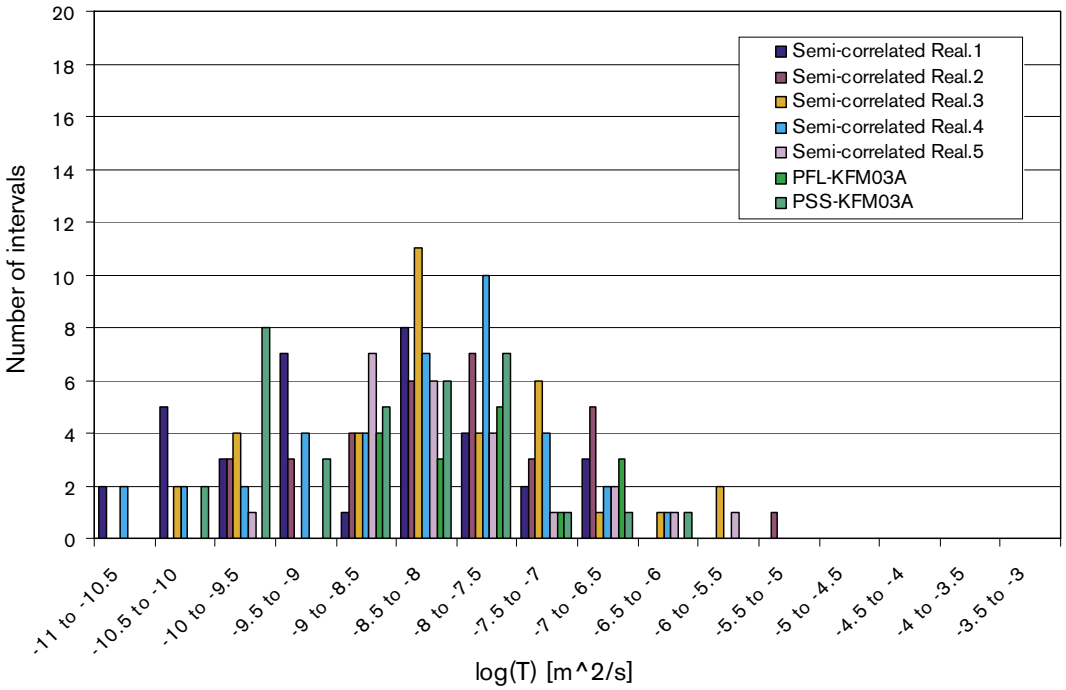

Figure B–50. *Histogram of Log(T) in 5 m intervals for 5 realisations of the semi-correlated T distribution compared with the PFL anomaly and PSS data outside the DZs for KFM03A. This case is based on 130% of open and partly-open fractures.*

As described above, the initial DFN modelling indicated that none of the transmissivity models could reproduce the full range of transmissivities determined from the PFL and PSS tests (i.e. with the DZs included) particularly well, irrespective of the parameter values assumed. To attempt to address this problem, a model was constructed in which separate transmissivity models were used for small- and large-scale fractures (the division between the scales was assumed to be at L = 100 m). With this additional flexibility in the model it may then be possible to reproduce transmissivities over the large range of values determined from the PFL and PSS measurements using reasonable values for the model parameters.

Results from simulations using two correlated transmissivity models and a P32 based on 130% of all open and partly-open fractures are shown in Figure B–51. The distribution of transmissivities below about 1 10^{-6} m^2 s^{-1} is reproduced reasonably well (although perhaps not quite as well as if this range is fitted in isolation). This improves the match to the number of 5 m flowing intervals overall (predicting 44 on average compared with an observed 50 flowing intervals in the PSS data) but still under-predicts the number of intervals with higher transmissivities.

The DFN model parameters used for each of the cases described in this section are given in Table B-23. Additional simulations were carried out using the Geo-DFN fracture set orientations, although the proportions of each fracture set were maintained from the fracture intensity analysis in subsection B.1.6. The parameters used in these Geo-DFN simulations are given in Table B-24. An alternative (variant) Geo-DFN was provided later in the project, and is described in subsection 3.7.2.

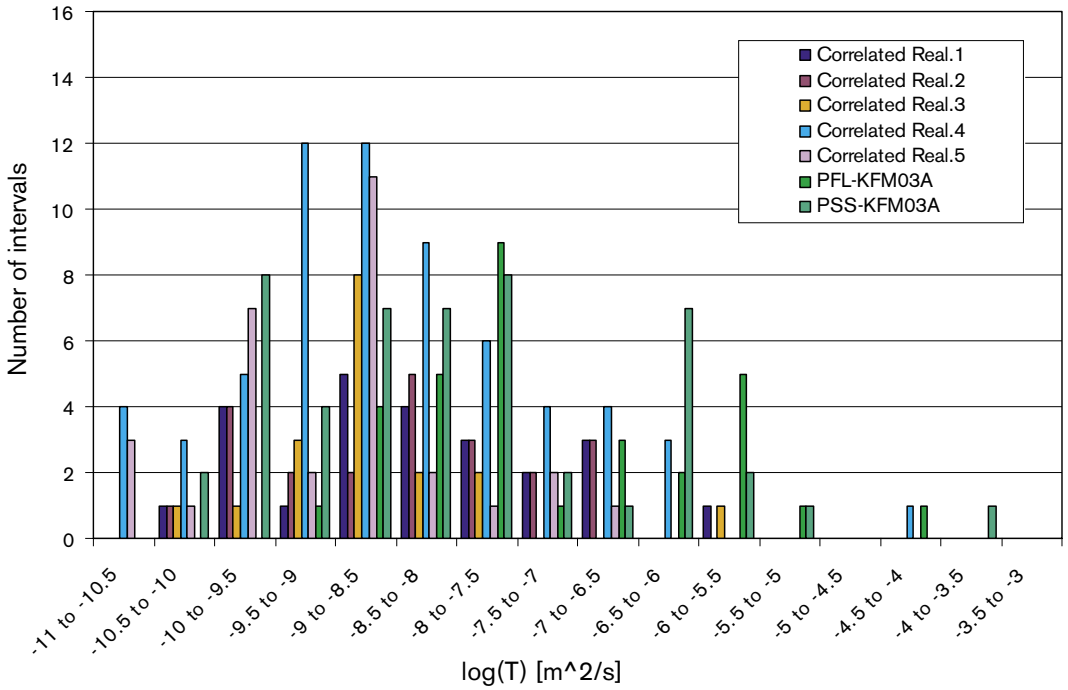

Figure B–51. *Histogram of Log(T) in 5 m intervals for 5 realisations of the correlated T distribution with separate correlations above and below L = 100 m compared with the PFL anomaly and PSS data for KFM03A. This case is based on 130% of open and partly-open fractures.*

Table B-23. Description of DFN parameters used for simulation of fractures to fit the PFL anomalies and PSS data for KFM03A. P32 and the transmissivity model parameters are given for each of the cases, denoted in italics. Borehole specific fracture set orientations and Fisher concentrations were used for this borehole (subsection B.1.6).

Rock domain	Fracture set name	Orientation set pole: (trend, plunge), concentration	Length model, constants: power-law (L_0, k_r) (m)	Intensity, (P_{32}), valid length interval: L_0, L_{max} (m^2 m^{-3})	Relative intensity of P32	Transmissivity model Eq no, constants T (m^2 s^{-1})
RFM029 (177 m)	NS	(85, 0) 15.4	(0.5, 2.88)	*130% of open:* 0.903, (0.5, 1,000)	0.124	*Correlated (excl DZs):* (a,b) (1.0 10^{-9}, 1.0)
	NE	(131, 8) 26.1	(0.5, 3.02)		0.291	
RFM017 (68 m)	NW	(46, 4) 18.5	(0.5, 2.81)		0.191	*Uncorrelated (excl DZs):* (μ,σ) (–6.5, 0.9)
	EW	(197, 0) 27.0	(0.5, 2.95)		0.100	*Semi-correlated (excl DZs):* (a,b,σ) (3.0 10^{-8}, 0.6, 1.0)
RFM029 (707 m)	HZ	(156, 73) 11.3	(0.5, 2.92)		0.294	*Alternative: Correlated, L < 100 m:* (a,b) (1.0 10^{-9}, 1.5); *L > 100 m:* (a,b) (1.0 10^{-10}, 2.0)

Table B-24. Description of DFN parameters and global Geo-DFN fracture set orientations used for simulation of fractures to fit the PFL anomalies and PSS data for KFM03A. P32 and the transmissivity model parameters are given for each of the cases, denoted in italics.

Rock domain	Fracture set name	Orientation set pole: (trend, plunge), concentration	Length model, constants: power-law (L_0, k_r) (m)	Intensity, (P_{32}), valid length interval: L_0, L_{max} (m^2 m^{-3})	Relative intensity of P32	Transmissivity model Eq no, constants T (m^2 s^{-1})
RFM029 (177 m)	NS	(87, 2) 21.7	(0.5, 2.88)	*130% of open:* 0.903, (0.5, 1,000)	0.124	*Correlated (excl DZs):* (a,b) (1.0 10^{-9}, 1.0)
	NE	(135, 3) 21.5	(0.5, 3.02)		0.291	*Uncorrelated (excl DZs):* (μ,σ) (–6.5, 0.9)
RFM017 (68 m)	NW	(41, 2) 23.9	(0.5, 2.81)		0.191	*Semi-correlated (excl DZs):* (a,b,σ) (3.0 10^{-8}, 0.6, 1.0)
	EW	(190, 1) 30.6	(0.5, 2.95)		0.100	*Alternative: Correlated, L < 100 m:* (a,b) (1.0 10^{-9}, 1.5); *L > 100 m:* (a,b) (1.0 10^{-10}, 2.0)
RFM029 (707 m)	HZ	(343, 80) 8.2	(0.5, 2.92)		0.294	

B.4.2 Conditioning transmissivity for Volume E using the variant Geo-DFN parameters (KFM03A)

Using the variant Geo-DFN parameters, transmissivity model parameters were fitted to both PFL and PSS data for Volume E. The transmissivities for PFL anomalies were grouped into 5 m intervals and summed, to match those of the PSS analyses. Five realisations were simulated to give a reasonable representation of the variability predicted.

Simulation results were fitted to the smaller flows in the PFL and PSS data. The best match was found using 70% of all open and partly-open fractures. This corresponds to the certain and probably open fractures. Examples of the correlated and uncorrelated cases are shown in Figure B-54 and Figure B-55. For the correlated case, 85% of 5 m intervals were modelled as non-flowing, in comparison to 81% and 91% of non-flowing intervals measured in the PSS and PFL data. Similarly, a good match to the average cumulative transmissivity (model showed 9.4 10^{-7} m^2s^{-1}, while the PSS data gave 9.5 10^{-7} m^2s^{-1}.

Overall, the variant Geo-DFN gave a good fit to the observed data, and it proved easier to match the transmissivity model parameters using the variant Geo-DFN. The model parameters used are shown in Table B-19.

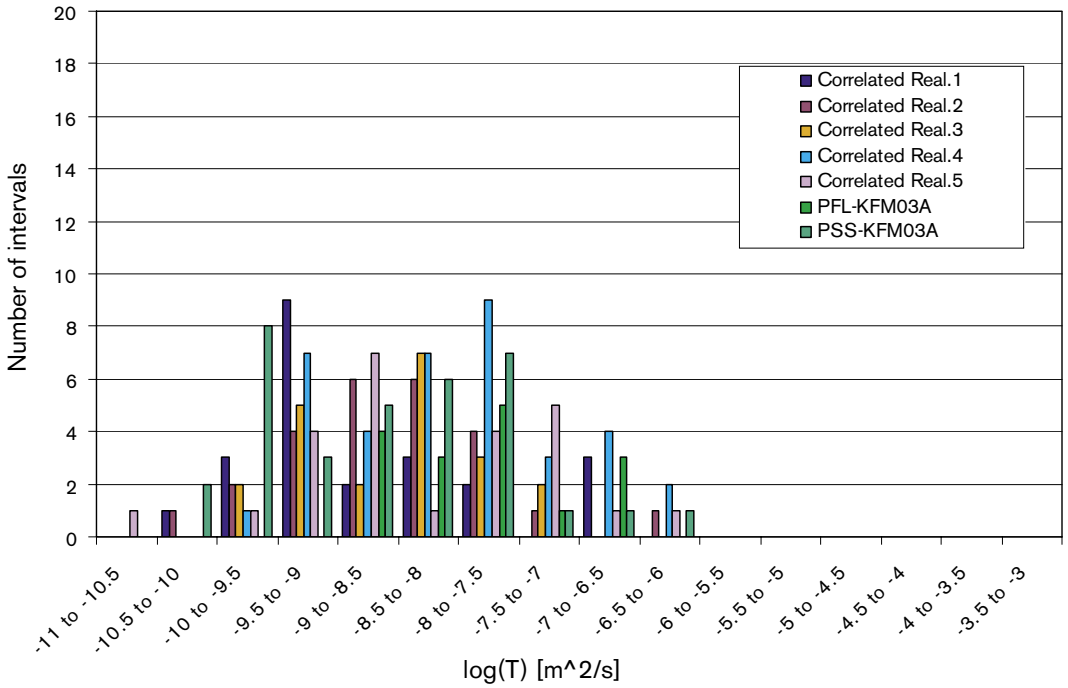

Figure B-52. *Histogram of Log(T) in 5 m intervals for 5 realisations of the correlated T distribution (using the variant Geo-DFN) compared with the PFL anomaly and PSS data for KFM03A. This case is based on 70% of open and partly-open fractures.*

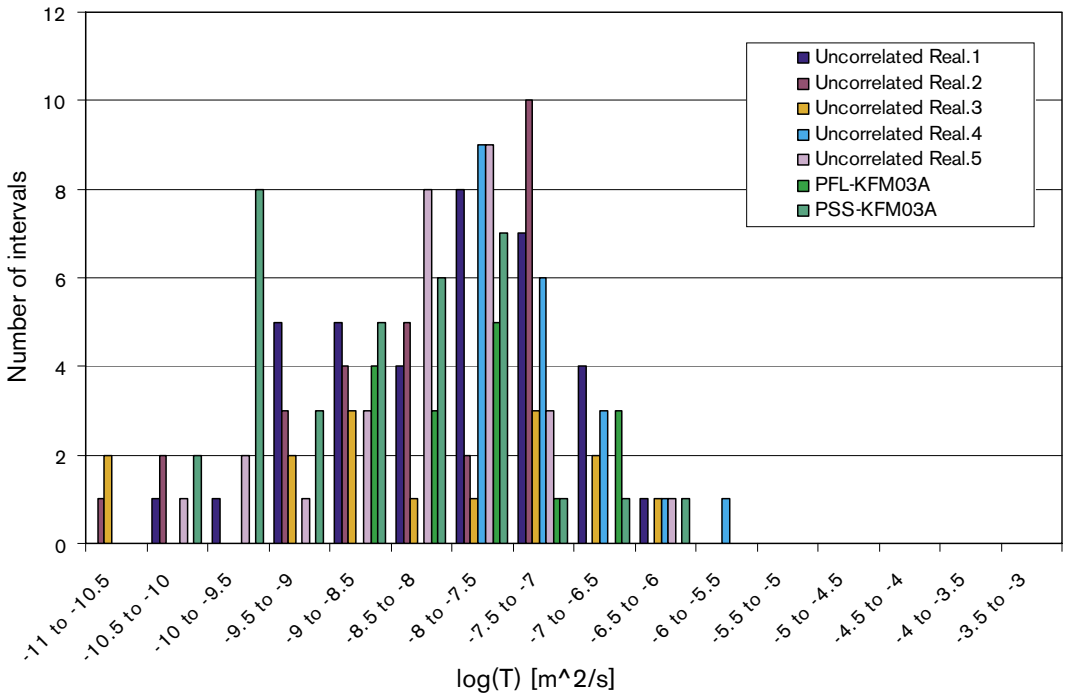

Figure B-53. *Histogram of Log(T) in 5 m intervals for 5 realisations of the uncorrelated T distribution (using the variant Geo-DFN) compared with the PFL anomaly and PSS data for KFM03A. This case is based on 70% of open and partly-open fractures.*

Table B-25. Description of variant Geo-DFN parameters used for simulation of fractures to fit the PFL anomalies and PSS data for Volume E (KFM03A). P32 and the transmissivity model parameters are given for each of the cases, denoted in italics.

Rock domain	Fracture set name	Orientation set pole: (trend, plunge), concentration	Length model, power-law (L_0, k_r) (m)	Intensity, (P_{32}), valid length interval: L_0, L_{max} (m^2 m^{-3})	Relative intensity of P32	Transmissivity model Eq no, constants T (m^2 s^{-1})
RFM029 (177 m)	NS	(87, 2) 21.7	(0.5, 2.75)	*70% of open:* 0.53, (0.5, 1,000)	0.161	*Correlated, (excl DZ):* (a,b) (1.0 10^{-9}, 1.0)
	NE	(135, 3) 21.5	(0.5, 2.75)		0.319	
RFM017 (68 m)	NW	(41, 2) 23.9	(0.5, 2.75)		0.164	*Uncorrelated (excl DZs):* (μ, σ) (–6.9, 0.9)
RFM029 (707 m)	EW	(190, 1) 30.6	(0.5, 2.75)		0.076	*Semi-correlated (excl DZs):* (a,b, σ) (1.0 10^{-8}, 0.3, 1.0)
	HZ	(343, 80) 8.2	(0.5, 2.75)		0.280	

B.4.3 Conditioning transmissivity for Volume F (upper section of KFM01A)

Transmissivity model parameters were fitted to both PFL and PSS data, in a similar way to Volume E (subsection B.4.1). The transmissivities for PFL anomalies were grouped into 5 m intervals and summed, to match those of the PSS analyses. Five realisations were simulated to give a reasonable representation of the variability predicted.

Simulation results were initially fitted to all the PFL and PSS data and the adjusted P32 value used was based on 100% of all open and partly-open fractures (subsection B.3.3). In this case the total transmissivity from the PFL data was 2.0 10^{-7} m^2s^{-1} and from the PSS data was 3.1 10^{-7} m^2s^{-1}. The PSS data show no flow in 56% of 5 m intervals over the 300 m simulated length, while the PFL data show 61% non-flowing 5 m intervals. Flows near to the detection limit resulted in transmissivities of 10^{-10}–10^{-9} m^2s^{-1}. Since the PSS tests can measure lower flows, one important criterion is to match the number of non-flowing intervals to the PSS data.

It is clear from the correlated transmissivity simulation, that 100% of open and partly-open fractures containing flow will significantly under-predict the measured number of non-flowing 5 m intervals (Figure B-54). The mean of the five simulated realisation gives 23% non-flowing intervals, compared with 56% observed in the PSS data. A simulated non-flowing interval is taken as a predicted flow with log(transmissivity) less than 10^{-10} m^2s^{-1} for KFM01A (i.e. less than any observed flow).

In the upper section of KFM01A, 26% of the open and partly-open fractures are regarded as certain (Table 3–5). Hence, the P32 was reduced to 26%, and the match of the correlated transmissivity model repeated (Figure B-55). The simulation shows a good match to the observed data, with a total simulated flow of 5 10^{-7} m^2s^{-1}, similar to the observed flow in the PSS tests. The simulated number of non-flowing features matches well (average of 60% simulated non-flowing features, in comparison to 56% non-flowing intervals in the PSS data and 60% non-flowing intervals in the PFL data).

The best-fit transmissivity parameters for Volume F (upper section of KFM01A) were seen to be similar to those used for Volume E, hence the simulation was re-run with identical parameters. This would help in consideration of a future cross-borehole ‘global’ Hydro-DFN model. The match for the correlated transmissivity case is shown in (Figure B-55).

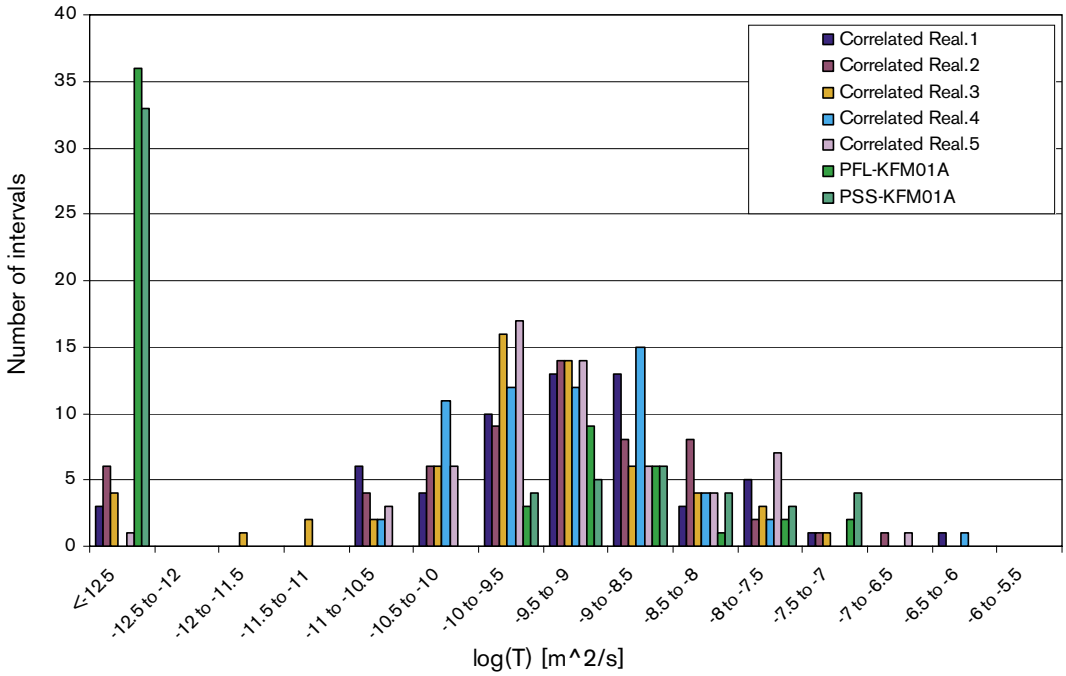

Figure B-54. *Histogram of Log(T) in 5 m intervals for 5 realisations of the correlated T distribution compared with the PFL anomaly and PSS data for the upper section of KFM01A. This case is based on 100% of open and partly-open fractures. The mean of the five realisations gives 23% non-flowing intervals, compared with 56% in the PSS data.*

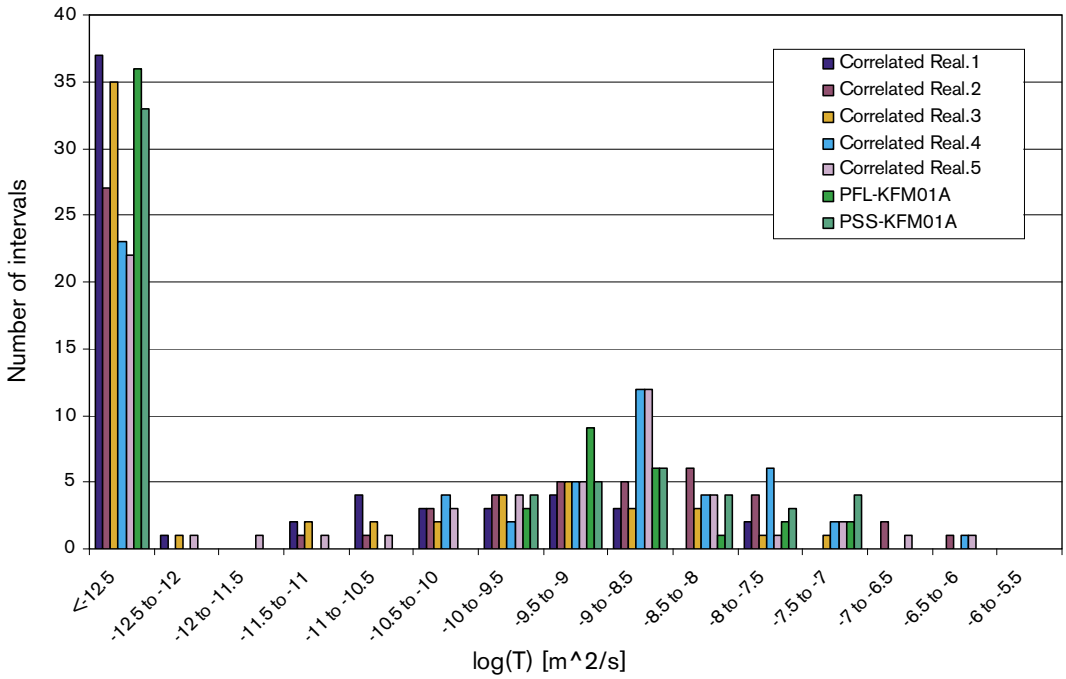

Figure B-55. *Histogram of Log(T) in 5 m intervals for 5 realisations of the correlated T distribution compared with the PFL anomaly and PSS data for the upper section of KFM01A. This case is based on 26% of open and partly-open fractures.*

The best matched transmissivity parameters for the uncorrelated transmissivity model are shown in Figure B-56. This case is based on 26% of open and partly-open fractures. The simulation shows a good match to the observed data, with a total simulated flow of $2\ 10^{-7}\ m^2s^{-1}$, similar to the observed flow in the PSS tests. The simulated number of non-flowing features matches well but is slightly high (average of 67% simulated non-flowing features, in comparison to 56% non-flowing intervals in the PSS data and 60% non-flowing intervals in the PFL data).

For the semi-correlated case, a log(σ) of 1.0 was used, and the a and b parameters adjusted to get the best match to the flow anomaly data. As before, an attempt was made to use the same transmissivity parameters as had been used for Volume E, to help with later production of a global Hydro-DFN model. 26% of the P32 for open fractures was used in the simulation, this matched the total flow rate reasonably well ($8\ 10^{-7}\ m^2s^{-1}$), and the average percentage of non-flowing intervals across the five realisations was 63%. A histogram for the semi-correlated T distribution is shown in Figure B-57.

The DFN model parameters used for each of the cases described in this section is given in Table B-26. For comparison, the global fracture set orientations from the Geo-DFN (as opposed to the calculated set orientations for the upper section of KFM01A) were used to simulate each of the three transmissivity models. The best-fit transmissivity parameters were used, and the simulation compared to the PSS and PFL flow anomaly data. In each case, the simulation matched well; an example for the correlated case is shown in Figure B-58. The DFN model parameters, and the global Geo-DFN fracture set parameters used are shown in Table B-27.

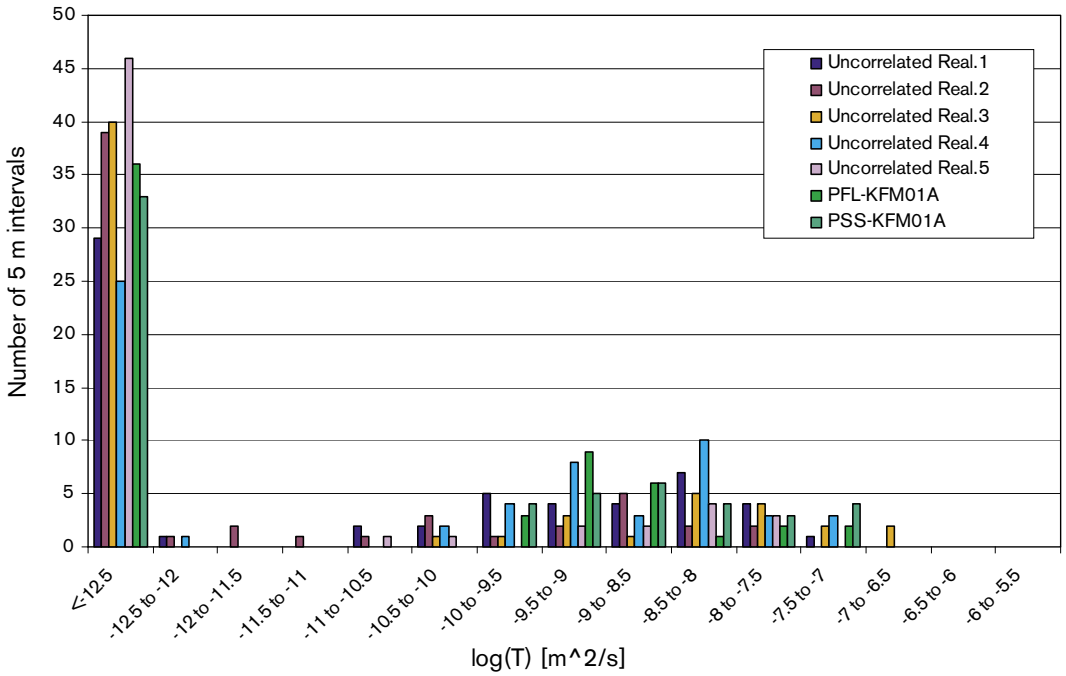

Figure B-56. *Histogram of Log(T) in 5 m intervals for 5 realisations of the uncorrelated T distribution compared with the PFL anomaly and PSS data for the upper section of KFM01A. This case is based on 26% of open and partly-open fractures.*

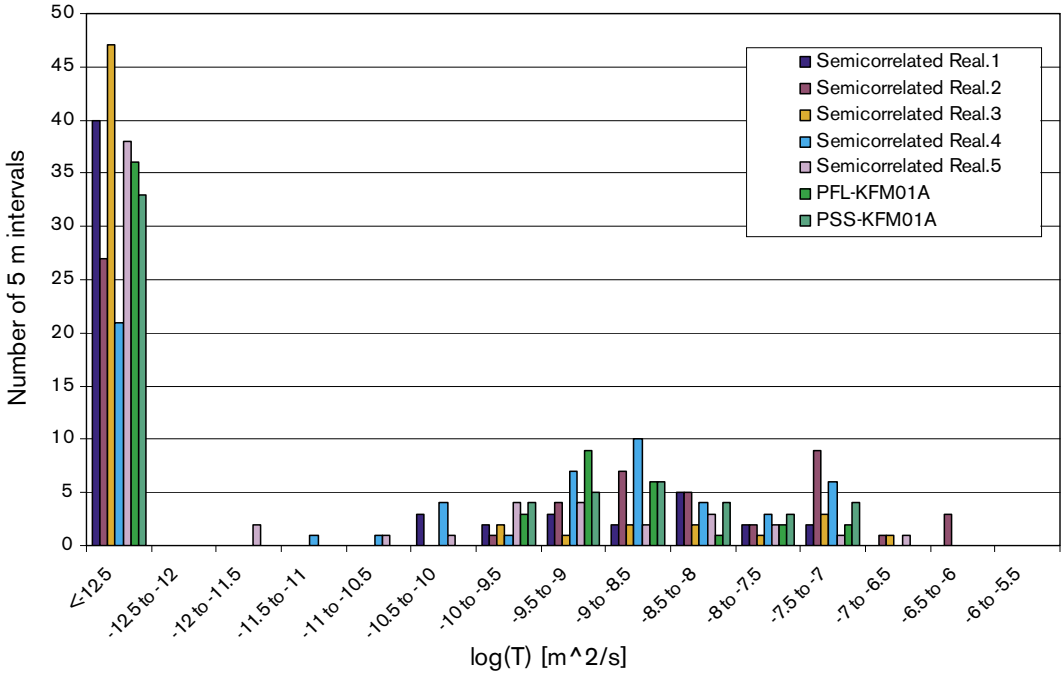

Figure B-57. *Histogram of Log(T) in 5 m intervals for 5 realisations of the semi-correlated T distribution compared with the PFL anomaly and PSS data for the upper section of KFM01A. This case is based on 26% of open and partly-open fractures.*

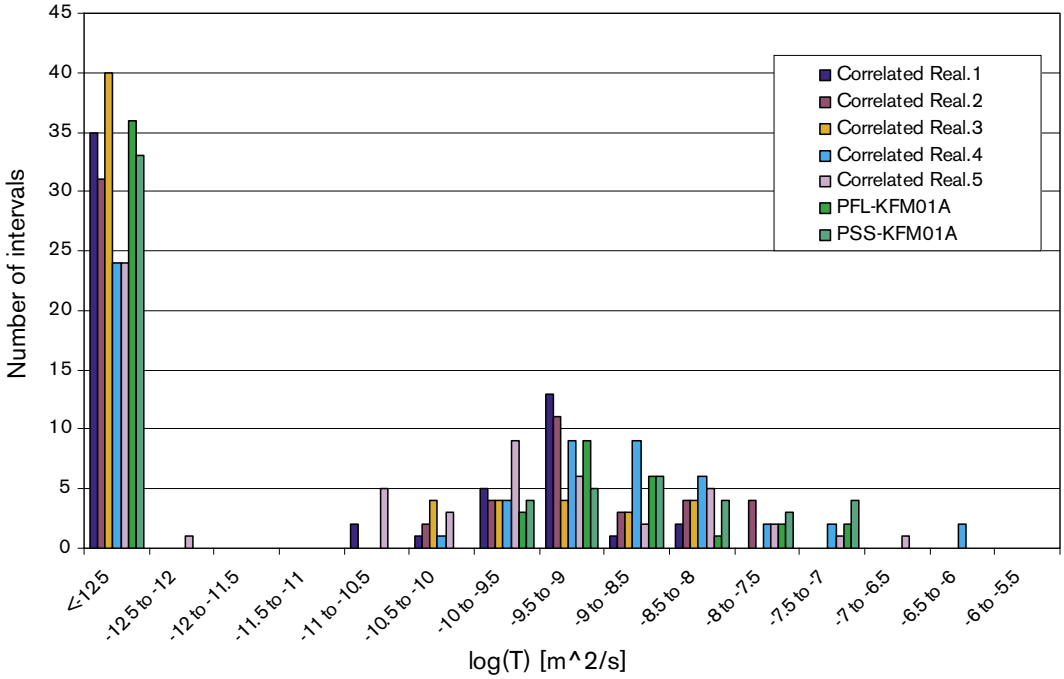

Figure B-58. *Histogram of Log(T) in 5 m intervals for 5 realisations of the correlated T distribution compared with the PFL anomaly and PSS data for the upper section of KFM01A. This case is based on 26% of open and partly-open fractures, and uses the global fracture set orientation from the Geo-DFN.*

Table B-26. Description of DFN parameters used for simulation of fractures to fit the PFL anomalies and PSS data for Volume F (upper section of KFM01A). P32 and the transmissivity model parameters are given for each of the cases, denoted in italics. (Borehole specific fracture set orientations and Fisher concentrations used from the upper section of KFM01A, subsection B.1.2).

Rock domain	Fracture set name	Orientation set pole: (trend, plunge), concentration	Length model, power-law (L_0, k_r) (m)	Intensity, (P_{32}), valid length interval: L_0, L_{max} (m^2 m^{-3})	Relative intensity of P32	Transmissivity model Eq no, constants T (m^2 s^{-1})
RFM029	NS	(78, 3) 12.5	(0.5, 2.88)	26% of open: 1.2 (0.5, 1,000)	0.110	*Correlated):* (a,b) (1 10^{-9}, 1.0)
	NE	(149, 1) 18.1	(0.5, 3.02)		0.449	*Uncorrelated:* (μ, σ) (–6.5, 0.9)
	NW	(232, 13) 10.5	(0.5, 2.81)		0.085	*Semi-correlated:* (a,b,σ) (3 10^{-8}, 0.6, 1)
	EW	(10, 2) 11.4	(0.5, 2.95)		0.049	
	HZ	(186, 84) 17.6	(0.5, 2.92)		0.306	

Table B-27. Description of DFN parameters and Geo-DFN set orientations used for simulation of fractures to fit the PFL anomalies and PSS data for Volume F (upper section of KFM01A). P32 and the transmissivity model parameters are given for each of the cases, denoted in italics.

Rock domain	Fracture set name	Orientation set pole: (trend, plunge), concentration	Length model, power-law (L_0, k_r) (m)	Intensity, (P_{32}), valid length interval: L_0, L_{max} (m^2 m^{-3})	Relative intensity of P32	Transmissivity model Eq no, constants T (m^2 s^{-1})
RFM029	NS	(87, 2) 21.7	(0.5, 2.88)	26% of open: 1.2 (0.5, 1,000)	0.110	*Correlated: (a,b) (1 10^{-9}, 1.0)*
	NE	(135, 3) 21.5	(0.5, 3.02)		0.449	*Uncorrelated: (μ, σ) (–6.5, 0.9)*
	NW	(41, 2) 23.9	(0.5, 2.81)		0.085	*Semi-correlated: (a,b,σ) (3 10^{-8}, 0.6, 1)*
	EW	(190, 1) 30.6	(0.5, 2.95)		0.049	
	HZ	(343, 80) 8.2	(0.5, 2.92)		0.306	

B.4.4 Conditioning transmissivity for Volume G (lower section of KFM01A)

Volume G is a region of no flow. It is as important to understand the characteristics of this volume of rock where no flow has been detected, as it is to consider the rock with groundwater flow. The lower section of KFM01A (below 412 m, i.e. below DZ2) has been considered as a region where no flow has been detected. The main question to answer is what minimum P32 is required to produce a volume of rock with no flow?

The transmissivities for PFL anomalies were grouped into 5 m intervals and summed, to match those of the PSS analyses. Best fit transmissivity model parameters from the correlated T model were used (coefficient a = 5 10^{-10}, exponent, b = 1). The measured open $P10_{corr}$ is 0.36 m^{-1} (below 412 m in KFM01A). Five realisations were simulated, using a P32 of 0.355 $m^2\,m^{-3}$, to give a reasonable representation of the variability predicted. Figure B-59 shows a good match, with two realisations predicting 100% non-flowing intervals, and the other three realisations predicting 93%, 94% and 98% non-flowing intervals. It is therefore suggested that a P32 of around 0.3 $m^2\,m^{-3}$ is the threshold below which the rock exhibits no flowing features.

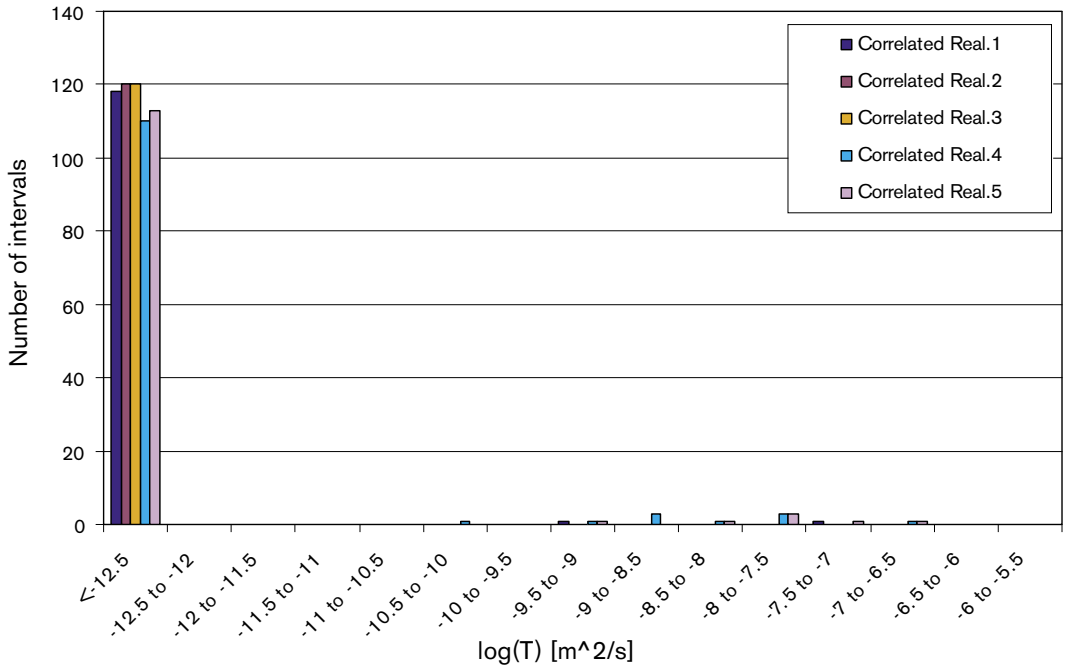

Figure B-59. *Histogram of Log(T) in 5 m intervals for 5 realisations of the correlated T distribution for Volume G, a region with no recorded flow (lower section of KFM01A). This case is based on 100 % of open and partly-open fractures below 412 m in KFM01A (measured* $P10_{corr} = 0.36\ m^{-1}$*, simulated P32 =* $0.355\ m^{-1}$*).*

B.5 Checking the simulated flow-rate distribution against PFL data

After the transmissivity has been matched to both PFL and PSS data (this allows a best fit to both the maximum number of data points and the lowest measurement limit), then the best case simulated flow rate, Q, is checked against the measured PFL flow anomalies. This has been considered firstly as a match of the simulated distribution of Q to the PFL flow anomalies, and secondly a few realisations have been plotted on a stereonet to check whether the simulated orientation of flowing fractures corresponds to the orientation of measured flow anomalies.

When checking the best fit T model parameters determined by matching the simulated T to PFL and PSS data, the flow anomaly data must be processed in two important ways:

1. Firstly, the actual drawdown in the boreholes is of the order of 10 m but varies considerably down the borehole, generally decreasing down the hole. Hence, the effective drawdown associated with the flow-rate measured from each anomaly is not constant, and so there is some bias. Since, we want to match Q as a distribution, it is important to remove this bias by renormalizing Q: $Q_{unbiased} = Q \times 10/\Delta h$, where Δh is the measured drawdown, and 10 m is the drawdown used in the simulations.
2. Secondly, for self-consistency, if several PFL anomalies are associated with a DZ, then the Q values for the anomalies are amalgamated into a single data point since the DFN model conceptualises the DZs as single large stochastic fractures.

B.5.1 Checking the simulated flow-rate against PFL data for Volume E (KFM03A)

The best fit parameters for each transmissivity model have been checked against the distribution of flow rate of individual features. Examples for the uncorrelated and correlated transmissivity models are shown in Figure B-60 and Figure B-61 (these examples use the borehole specific mean pole orientations and Fisher distributions, Table B-23). These show that the simulated flow rate distribution is reasonably well matched against the PFL flow anomalies, at least for a couple of realisations in each case.

For the correlated case for Volume E, the simulated flow for the best-fit correlated case excluding DZs (realisations 1 and 4) has been plotted on a stereonet (Figure B-62 and Figure B-63). This can be compared with the measured PFL matched to the orientation of individual features (Figure B-32). Realisations 1 and 4 show better matches to the PFL and PSS anomalies, hence these have been plotted. The simulated features with larger flow are found in the sub-HZ and possibly NE fracture sets, which corresponds well with the orientations of the measured flow anomalies in the background rock. However, the clustering of flow in a particular orientation, as seen in Figure B-32, is not reproduced due to the even spread of simulated fractures in the Fisher distribution.

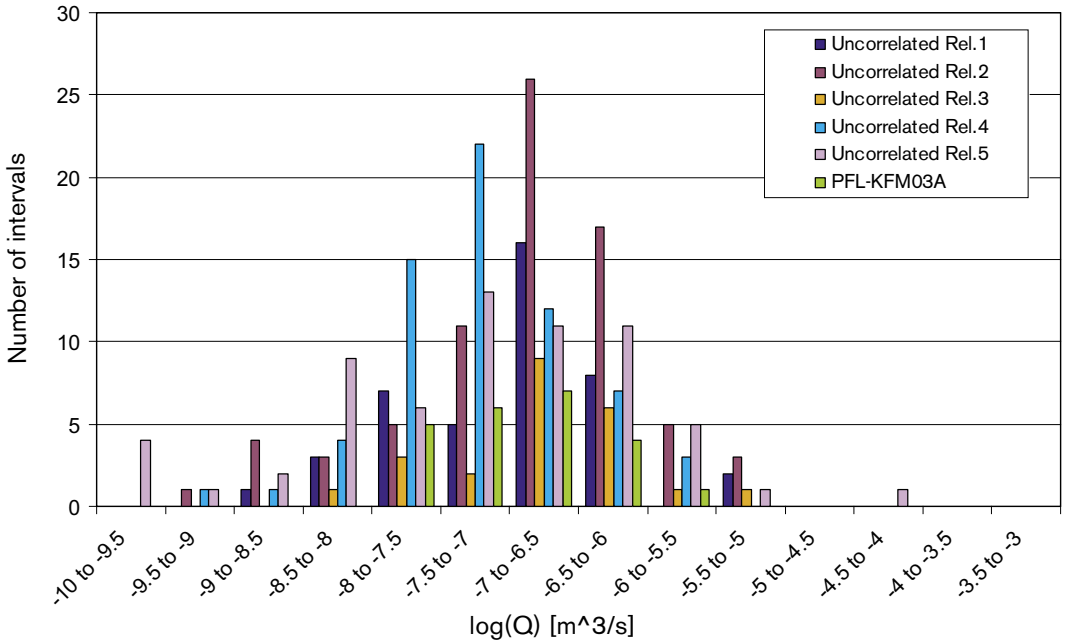

Figure B-60. *Histogram of Log(Q), flow-rate to borehole, for five realisations of the uncorrelated T distribution compared to the PFL anomaly data for Volume E (KFM03A). This case uses the best fit parameters from the matched PFL and PSS transmissivity for the 130% case, excluding DZs.*

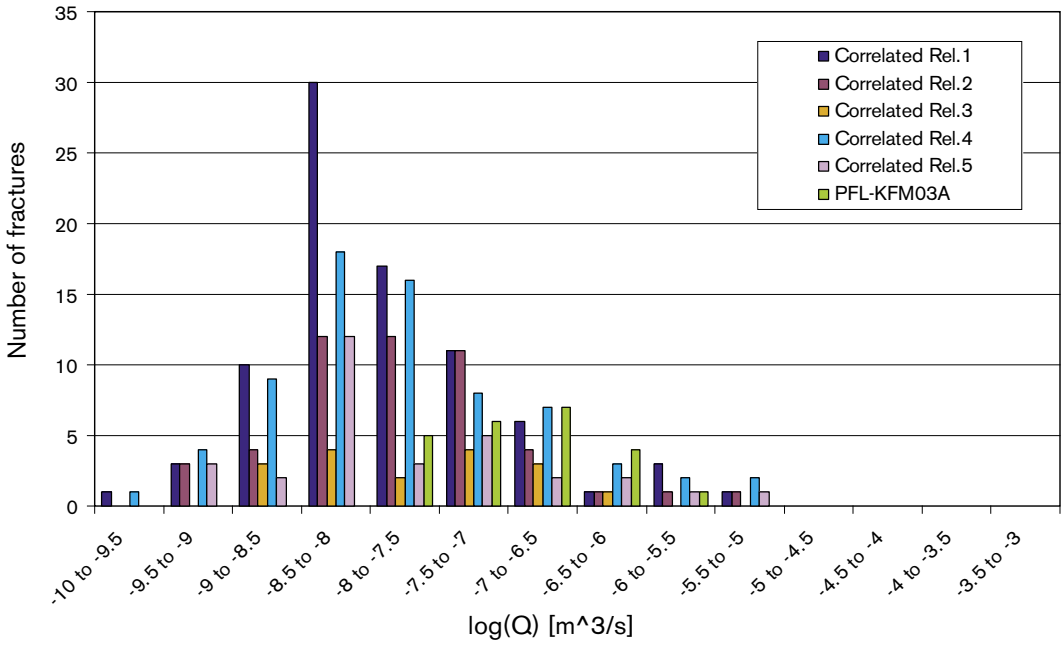

Figure B-61. *Histogram of Log(Q), flow-rate to borehole, for five realisations of the correlated T distribution compared to the PFL anomaly data for Volume E (KFM03A). This case uses the best fit parameters from the matched PFL and PSS transmissivity for the 130% case, excluding DZs.*

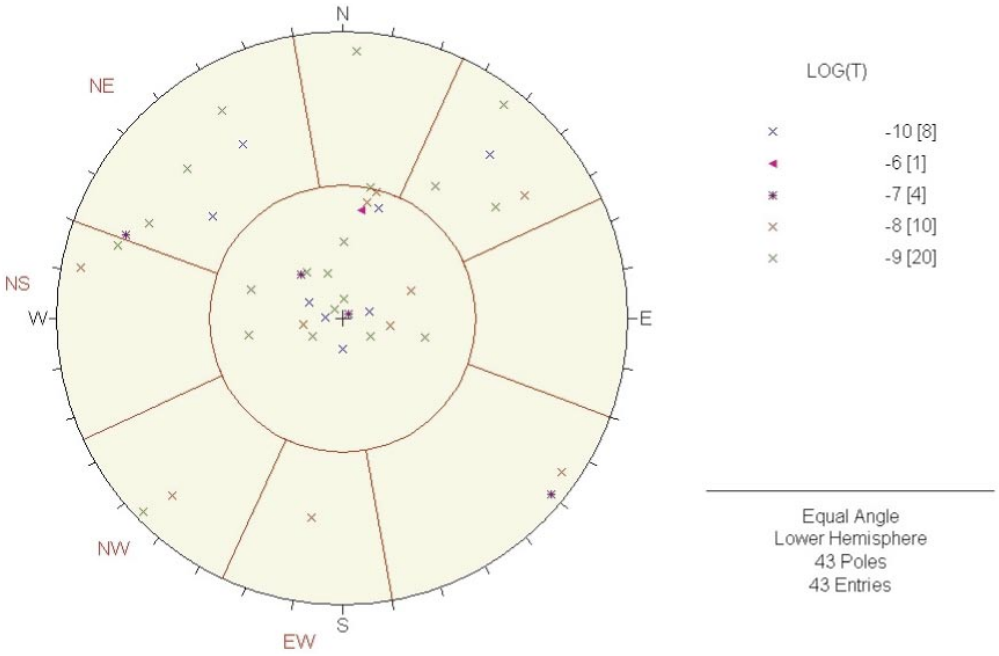

Figure B-62. *Orientations of the simulated flowing features for the best-fit correlated case for Volume E (KFM03A, excluding Deformation Zones, realisation 1). Compare with the measured PFL flow anomaly orientations in Figure B-32.*

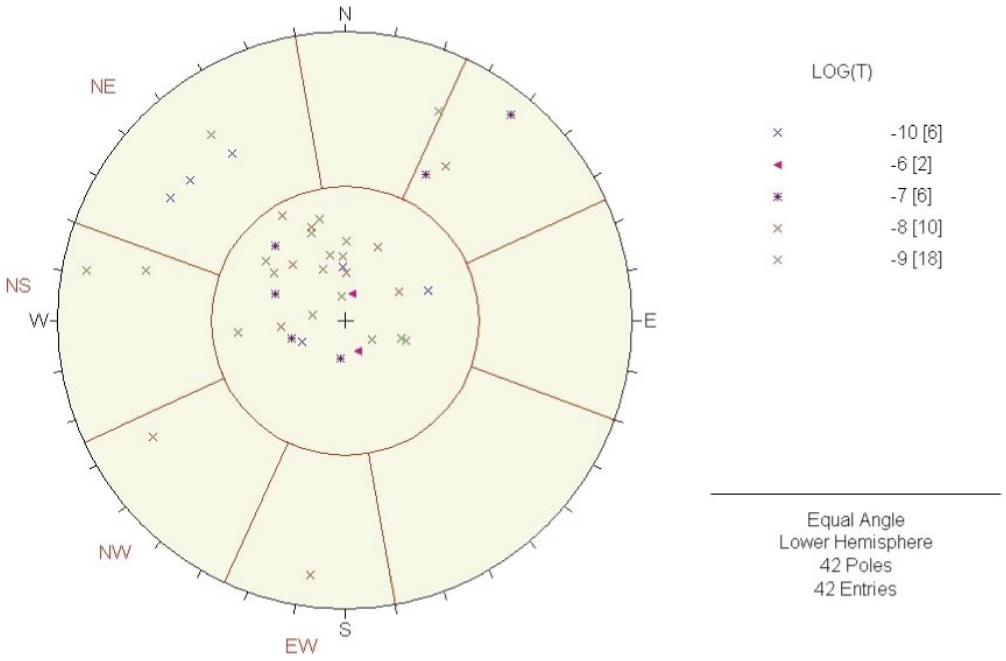

Figure B-63. *Orientations of the simulated flowing features for the best-fit correlated case for Volume E (KFM03A, excluding Deformation Zones, realisation 4). Compare with the measured PFL flow anomaly orientations in Figure B-32.*

B.5.2 Checking the simulated flow rate-against PFL data for Volume F (upper section of KFM01A)

The best-fit parameters for each transmissivity case have been checked against the distribution of flow rate of individual features. Examples are shown for the uncorrelated and correlated transmissivity models are shown in Figure B-64 and Figure B-65 (these examples use the borehole specific mean pole orientations and Fisher distributions, Table B-26). For the correlated case, the match is reasonable, particularly for realisations 1 and 3. This case uses the best-fit 'global' transmissivity model parameters, so a slightly greater simulated flow than the best overall match would be expected. Similarly, the uncorrelated case matches reasonably well to the measured flow rate data, bearing in mind that the minimum PFL measurement limit is around $10^{-9}\,m^3s^{-1}$.

For the correlated case for Volume F, the simulated flow for the best-fit correlated case (realisations 2 and 5) has been plotted on a stereonet (Figure B-66 and Figure B-67). This can be compared with the measured PFL matched to the orientation of individual features (Figure B-22). Realisations 2 and 5 are among the better matches to the PFL and PSS anomalies, hence these have been plotted. The simulated features with larger flow are found in the sub-HZ and possibly NE fracture sets, which corresponds well with the orientations of the measured flow anomalies in the background rock. However, the clustering of features containing flow in a particular orientation, as seen in Figure B-22, is not reproduced due to the even spread of simulated fractures in the Fisher distribution.

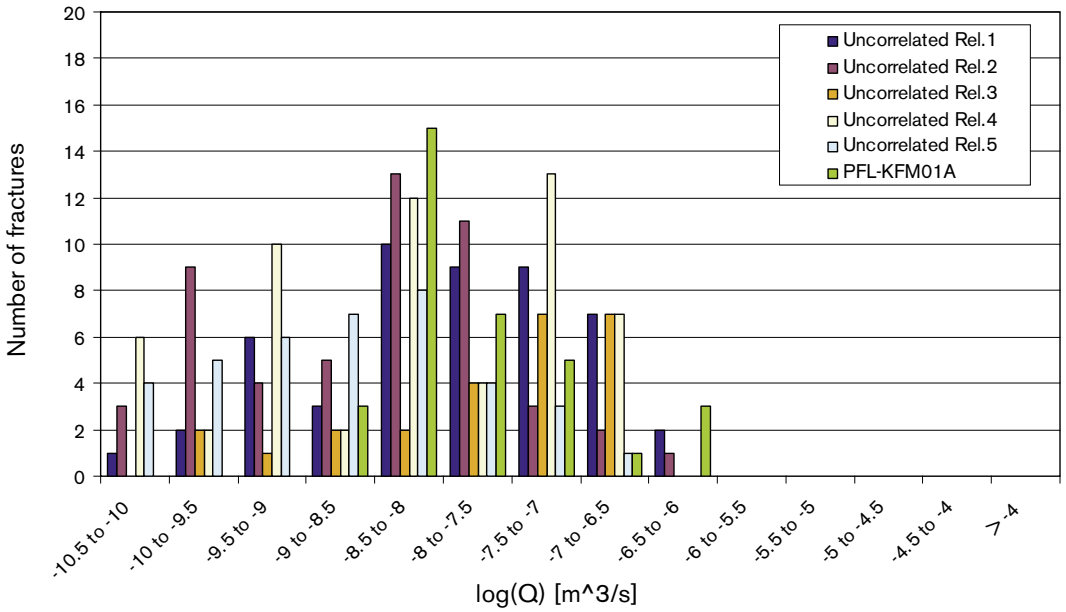

Figure B-64. *Histogram of Log(Q), flow-rate to borehole, for five realisations of the uncorrelated T distribution compared to the PFL anomaly data for Volume F (upper section of KFM01A). This case uses the best-fit parameters from the matched PFL and PSS transmissivity.*

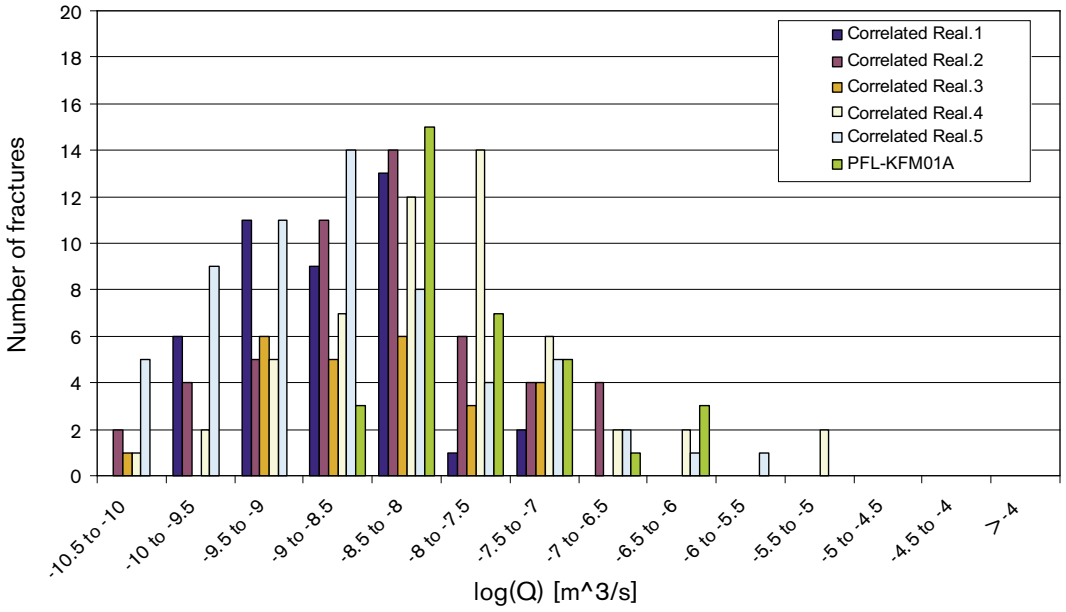

Figure B-65. *Histogram of Log(Q), flow-rate to borehole, for five realisations of the correlated T distribution compared to the PFL anomaly data for Volume F (upper section of KFM01A). This case uses the best-fit parameters from the matched PFL and PSS transmissivity (coefficient = 1 10^{-9}, exponent = 1).*

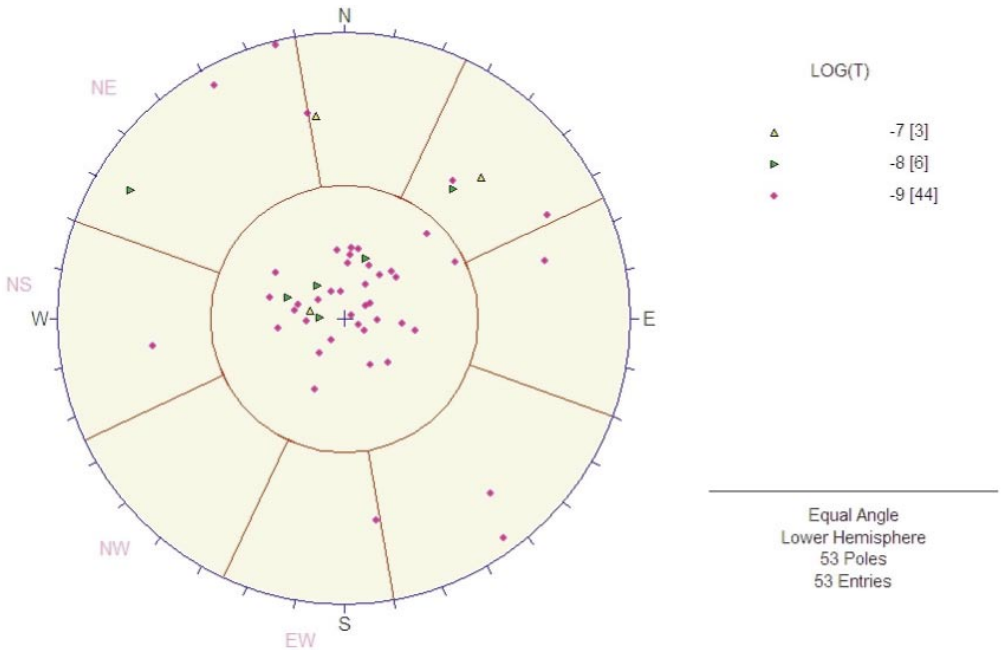

Figure B-66. *Orientations of the simulated flowing features for the best-fit correlated case for Volume F (upper section of KFM01A, realisation 2). Compare with the measured PFL flow anomaly orientations in Figure B-22.*

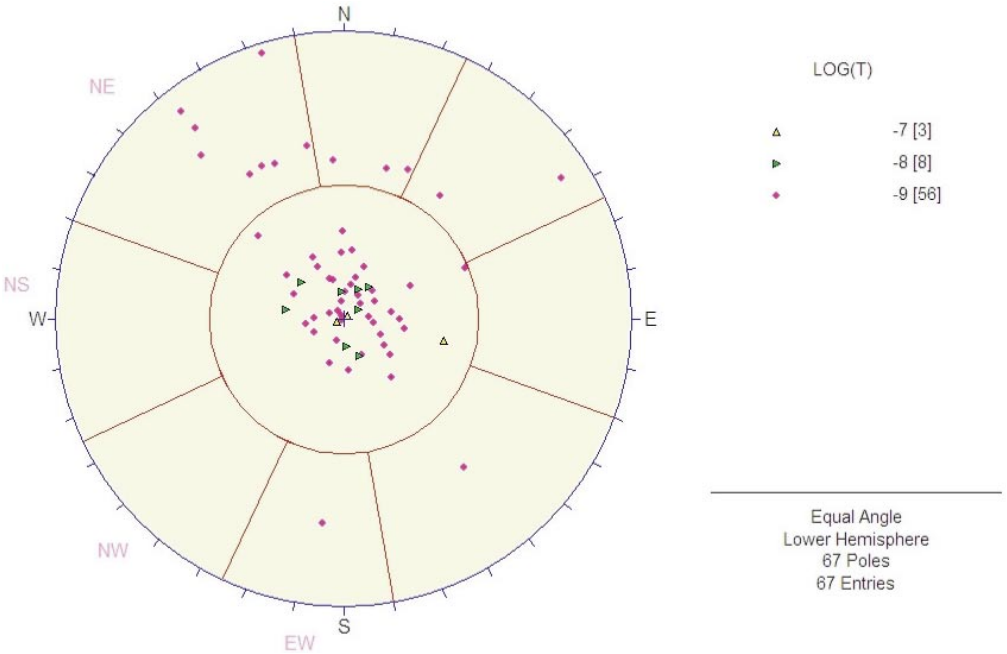

Figure B-67. *Orientations of the simulated flowing features for the best-fit correlated case for Volume F (upper section of KFM01A, realisation 5). Compare with the measured PFL flow anomaly orientations in Figure B-22.*

Appendix C

References for Appendix B

Description of transport properties of the present-day flow paths.

C.1 Methodology

The general approach to characterising transport properties is to track particles advected by the present-day flow-field and to record the initial Darcy-velocity (canister flux), travel time and F-quotient (see subsection 2.7). 2,000 particles are released at –400 m elevation and with a spacing of 50 m within a rectangle corresponding to the local-scale. Statistics are given as percentiles and the first four moments (Mean, Variance, Skewness and Kurtosis) to measure the shape of the distributions rather than just assume they are symmetric Gaussian.

As has already been concluded many of the cases give results very similar to the Base Case. Therefore the presented cases in the present chapter have been reduced to the cases that in any way significantly differ from the Base Case. For the rest of the cases it can just be stated that the varied physical property did not have any impact on the performance measures in the transport calculations.

C.2 Base Case (HCD3_BC_HRD3EC_HSD1_BC1)

In Figure C-1 and Figure C-2 the statistical results for the Base Case are shown as scatter plots and histograms for the four calculated performance measures travel time (t_w), canister flux (q_c, Darcy velocity), F-quotient (F) and path length (L). The results presented are based on the ensemble of particles released within the local-scale release-area. The results demonstrate a slight bi-modal behavior due to some particles starting in or near a fracture zone. Only a few particles have lengths greater than 4 km. However, these outliers are correspond to a very few particles that became stuck inside the model due to numerical problems.

The statistical summary is presented in Table C-1, where the statistics are calculated for numbers in $\log_{10}$ space. The median path length is 1 km and the 95th percentile 3.3 km.

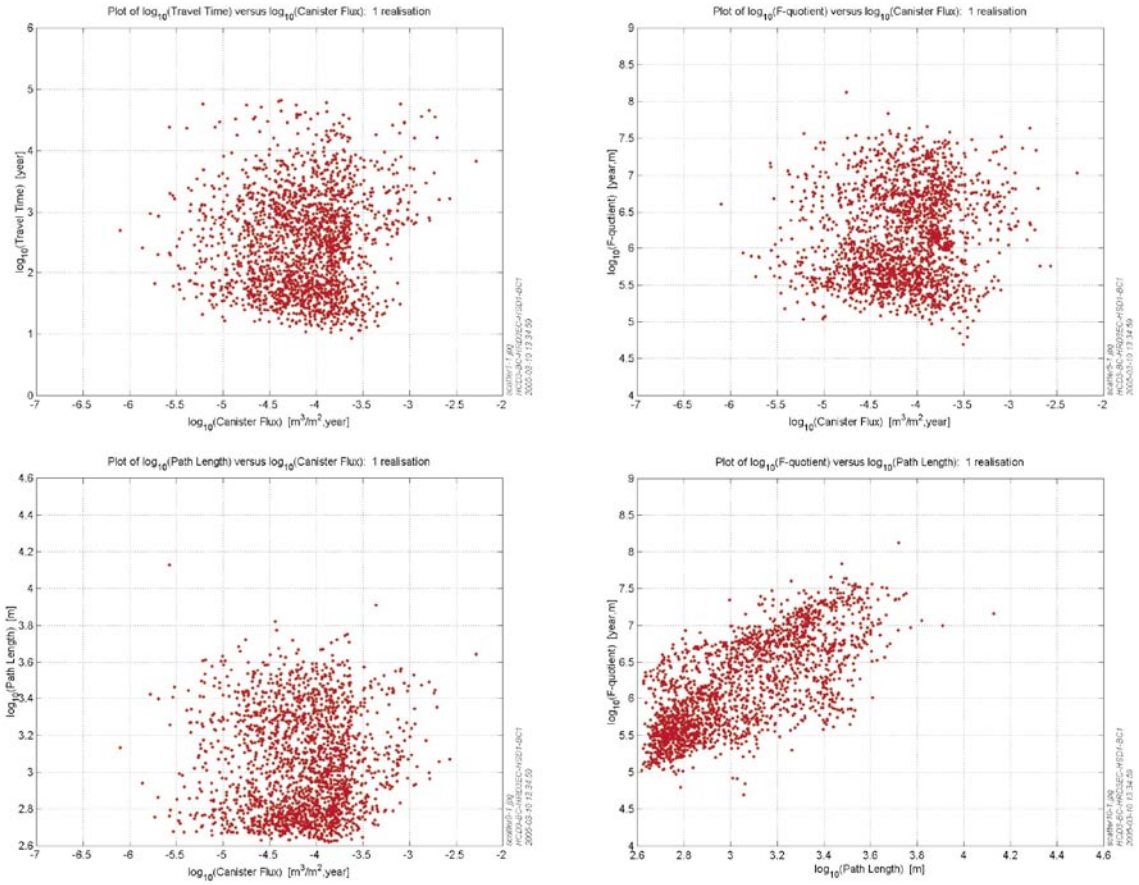

Figure C-1. *Scatter plots with different combinations of the calculated performance measures (t_w, q_c, F and L). Statistics shown for the ensemble of particles released in the local-scale release-area for the Base Case (HCD3_BC_HRD3EC_HSD1_BC1).*

Table C-1. Statistical summary of the calculated performance measures (t_w, q_c, F and L) for the ensemble of particles released in the local-scale release-area for the Base Case (HCD3_BC_HRD3EC_HSD1_BC1).

Statistical entity	Log_{10} (t_w) (y)	Log_{10} (q_c) (m y^{-1})	Log_{10} (F) (y m^{-1})	Log_{10} (L) (m)
Mean	2.482	–4.142	6.160	3.040
Median	2.454	–4.098	6.071	3.000
5th percentile	1.363	–5.023	5.280	2.687
25th percentile	1.790	–4.450	5.621	2.793
75th percentile	3.043	–3.810	6.696	3.268
95th percentile	3.851	–3.381	7.259	3.519
Std dev	0.803	0.497	0.629	0.274
Variance	0.644	0.247	0.396	0.075
Skewness	0.422	–0.267	0.300	0.449
Kurtosis	–0.482	0.407	–0.930	–0.836
Min value	0.928	–6.099	4.693	2.620
Max value	4.816	–2.280	8.122	4.130
Fraction OK	0.996	1.000	0.996	0.996

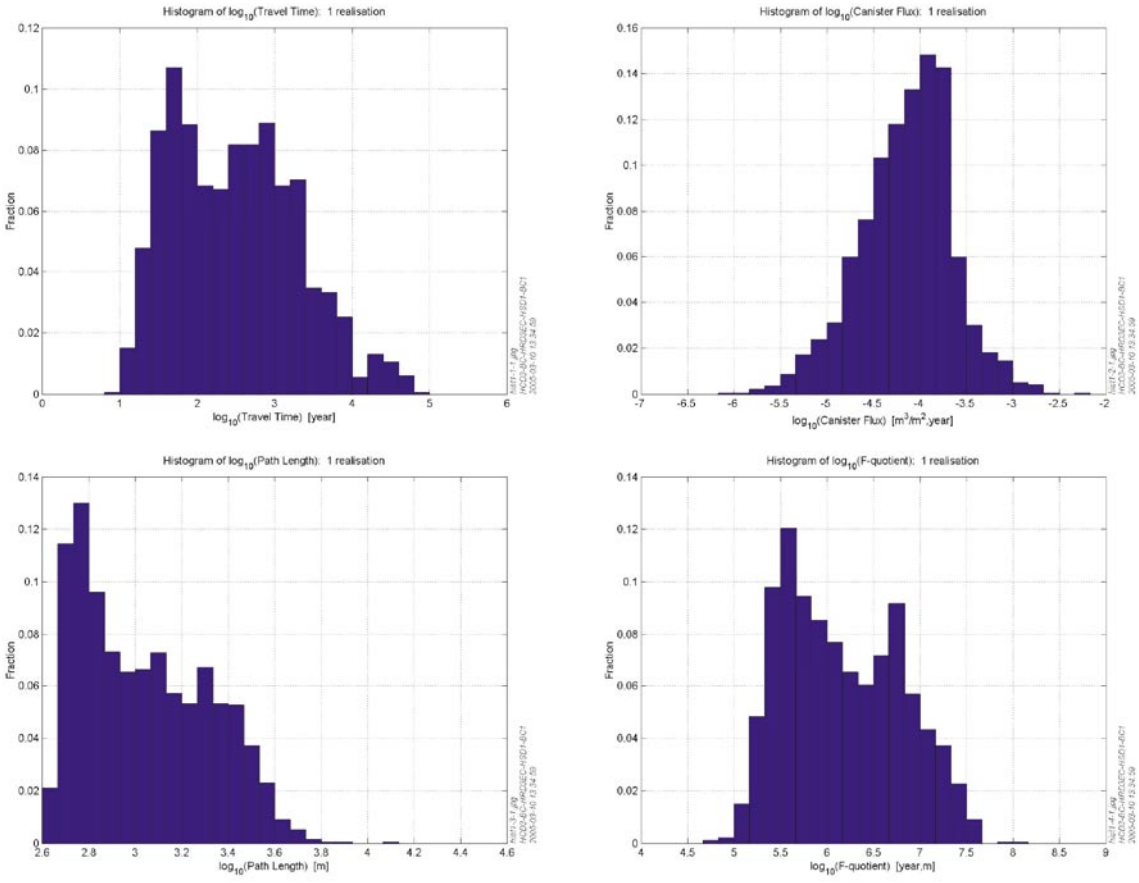

Figure C-2. *Histograms of the calculated performance measures (t_w, q_c, F and L). Statistics shown for the ensemble of particles released in the local-scale release-area for the Base Case (HCD3_BC_HRD3EC_HSD1_BC1).*

C.3 Uncorrelated transmissivity (HCD3_BC_HRD3EU_HSD1_BC1)

The conductivity generated with the uncorrelated transmissivity is slightly higher and smoother compared to the correlated case. This shows in the statistical results where the canister flow is higher for the uncorrelated case, see Figure C-3, Figure C-4 and Table C-2. In fact all four performance measures show slightly higher values compared to the correlated transmissivity case. The variance also changes somewhat. The median path length is about 1,300 m, which is 300 m longer than for the Base Case. This still suggests very localized flows and path ways.

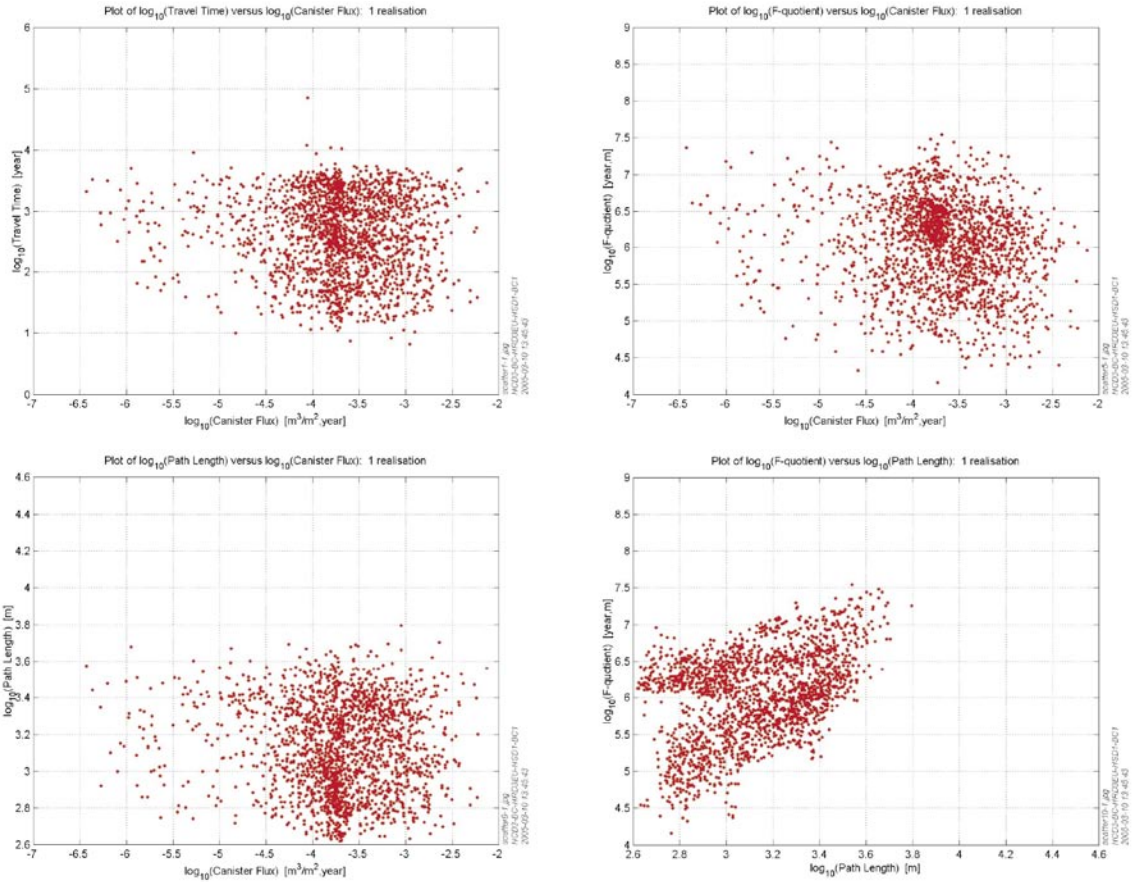

Figure C-3. *Scatter plots with different combinations of the calculated performance measures (t_w, q_c, F and L) for the ensemble of particles released in the local-scale release-area for the uncorrelated transmissivity (HCD3_BC_HRD3EU_HSD1_BC1).*

Table C-2. Statistical summary of the calculated performance measures (t_w, q_c, F and L) for the ensemble of particles released in the local-scale release-area for the uncorrelated transmissivity (HCD3_BC_HRD3EU_HSD1_BC1).

Statistical entity	Log_{10} (t_w) (y)	Log_{10} (q_c) (m y^{-1})	Log_{10} (F) (y m^{-1})	Log_{10} (L) (m)
Mean	2.617	–3.703	6.045	3.126
Median	2.674	–3.702	6.125	3.124
5th percentile	1.449	–4.827	4.979	2.749
25th percentile	2.105	–3.970	5.654	2.920
75th percentile	3.166	–3.313	6.467	3.326
95th percentile	3.523	–2.801	6.964	3.510
Std dev	0.661	0.618	0.591	0.245
Variance	0.436	0.381	0.349	0.060
Skewness	–0.317	–0.969	–0.361	0.028
Kurtosis	–0.806	2.218	–0.243	–0.972
Min value	0.825	–6.427	4.163	2.621
Max value	4.853	–2.124	7.540	3.797
Fraction OK	0.996	1.000	0.996	0.996

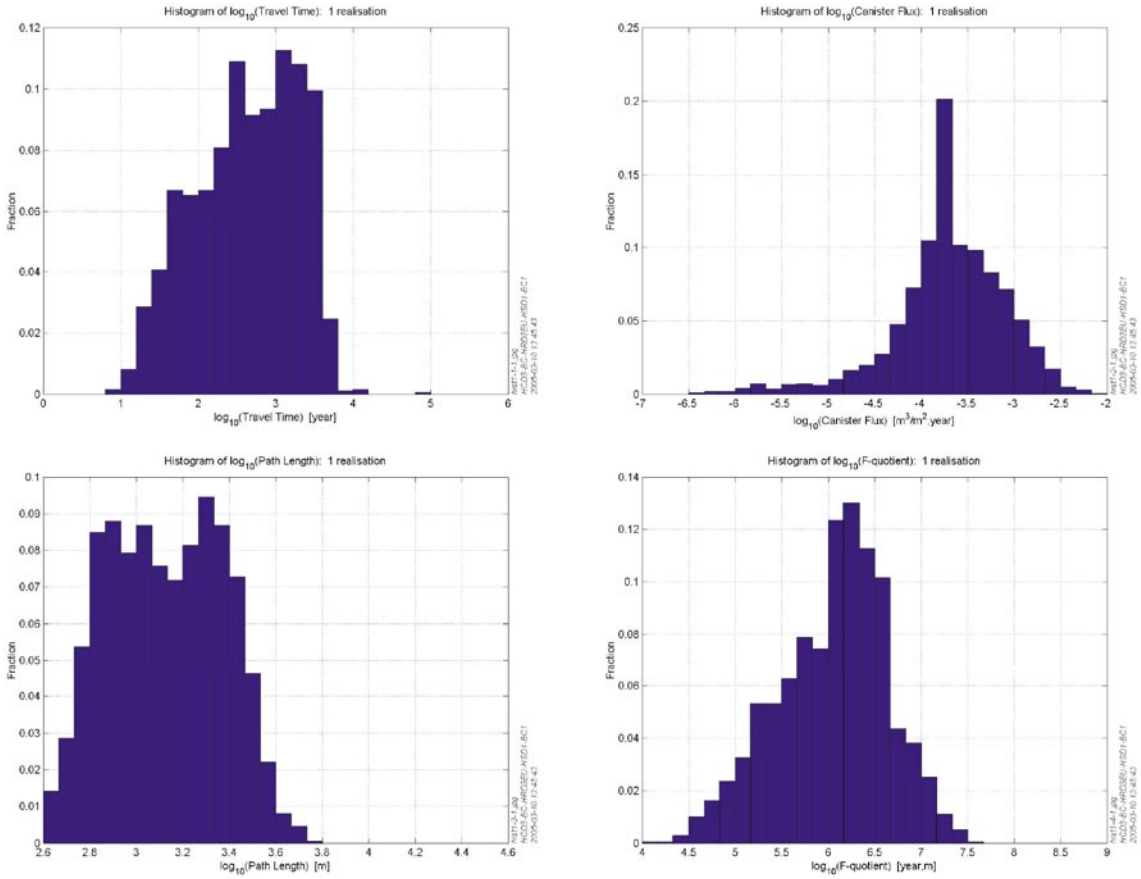

Figure C-4. *Histograms of the calculated performance measures (t_w, q_c, F and L) for the ensemble of particles released in the local-scale release-area for the uncorrelated transmissivity (HCD3_BC_HRD3EU_HSD1_BC1).*

C.4 Variant Geo-DFN with different power-law fracture length PDF (k_r = 2.75), uncorrelated transmissivity model (HCD3_BC_HRD3SFU_HSD1_BC1)

The results for the Variant Geo-DFN with uncorrelated transmissivity shows some differences compared to the Base Case at least with respect to the shape of the scatter plots and histograms, see Figure C-5, Figure C-6 and Table C-3. The median values of the calculated performance measures however do not differ much compared to the Base Case. The median path length stays around 1,000 m. The calculated higher moments (skewness and kurtosis) indicate that the distribution of four performance measures has changed slightly.

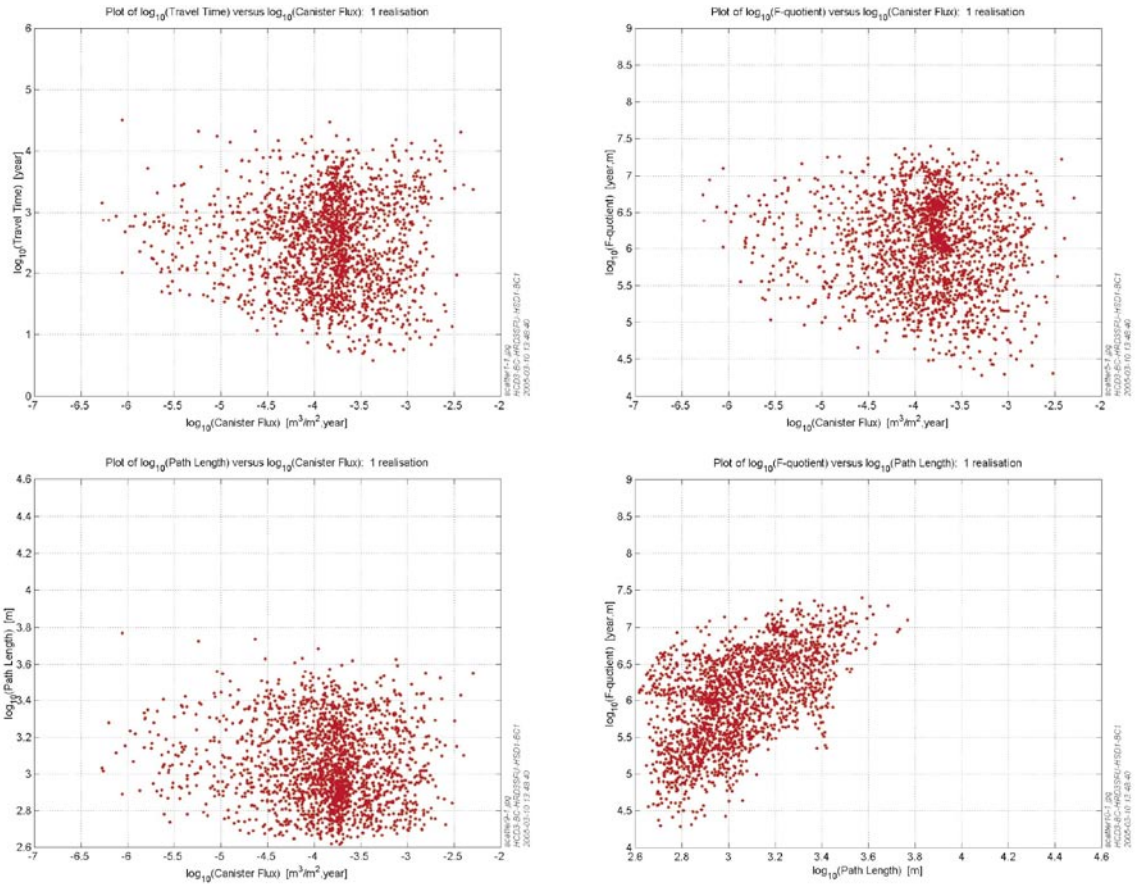

Figure C-5. *Scatter plots with different combinations of the calculated performance measures (t_w, q_c, F and L) for the ensemble of particles released in the local-scale release-area for the variant Geo-DFN with different power-law fracture length PDF (k_r = 2.75), uncorrelated transmissivity model (HCD3_BC_HRD3SFU_HSD1_BC1).*

Table C-3. Statistical summary of the calculated performance measures (t_w, q_c, F and L) for the ensemble of particles released in the local-scale release-area for the variant Geo-DFN (k_r = 2.75), uncorrelated T model (HCD3_BC_HRD3SFU_HSD1_BC1).

Statistical entity	Log_{10} (t_w) (y)	Log_{10} (q_c) (m y^{-1})	Log_{10} (F) (y m^{-1})	Log_{10} (L) (m)
Mean	2.475	–3.872	6.033	3.047
Median	2.500	–3.793	6.087	3.018
5th percentile	1.314	–5.036	4.993	2.725
25th percentile	1.914	–4.143	5.567	2.885
75th percentile	3.003	–3.534	6.514	3.210
95th percentile	3.657	–2.974	6.982	3.419
Std dev	0.733	0.599	0.614	0.217
Variance	0.537	0.358	0.377	0.047
Skewness	0.016	–0.829	–0.254	0.349
Kurtosis	–0.627	1.401	–0.598	–0.626
Min value	0.580	–6.273	4.283	2.617
Max value	4.502	–2.291	7.398	3.769
Fraction OK	0.998	1.000	0.998	0.998

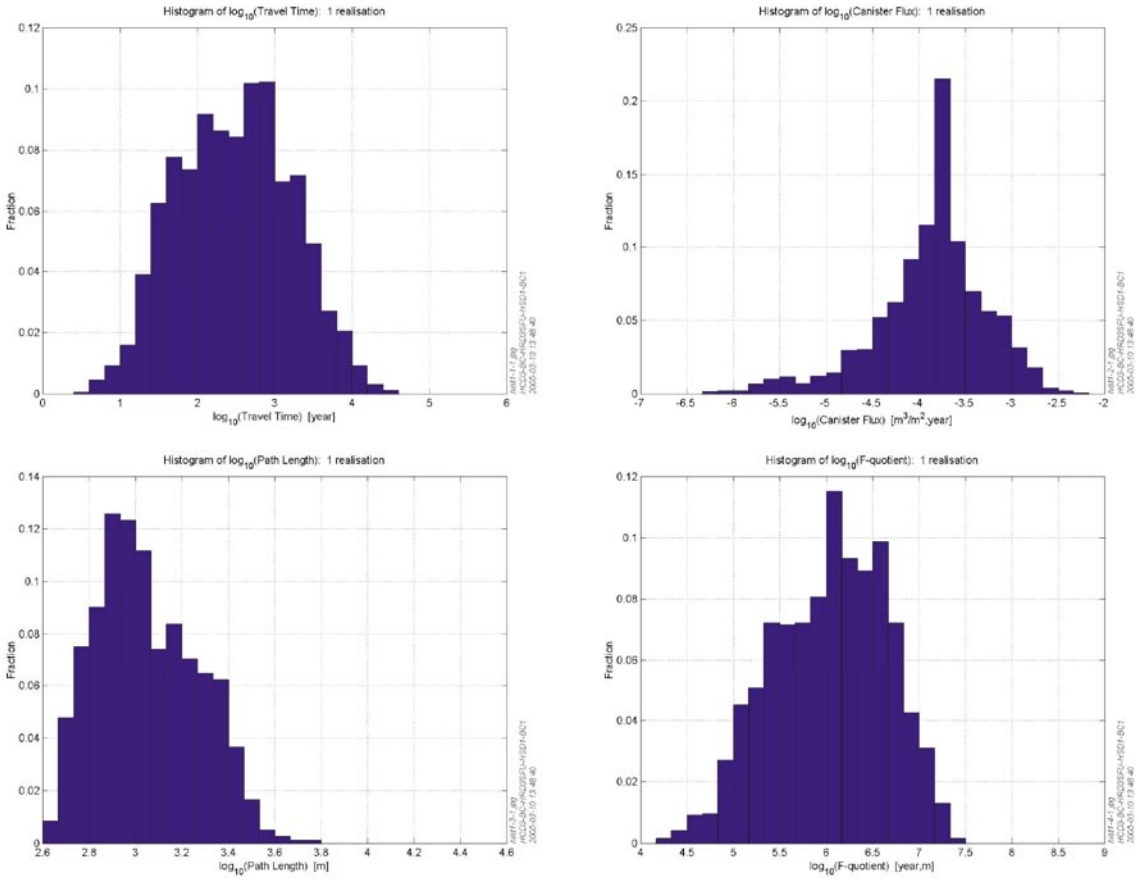

Figure C-6. *Histograms of the calculated performance measures (t_w, q_c, F and L) for the ensemble of particles released in the local-scale release-area for the Variant Geo-DFN (k_r = 2.75), uncorrelated T model (HCD3_BC_HRD3SFU_HSD1_BC1).*

C.5 Lower flow-wetted-surface, a_r = 0.25 m² m⁻³, for RMD (HCD3_BC_HRD3ECF1_HSD1_BC1)

As expected, changing the flow-wetted surface has an impact mainly on the F-quotient, see Figure C-7, Figure C-8 and Table C-4. The median and the 95th percentile of the F-quotient have decreased compared to the Base Case and the variance is less than half. For the other performance measures the difference is of less importance.

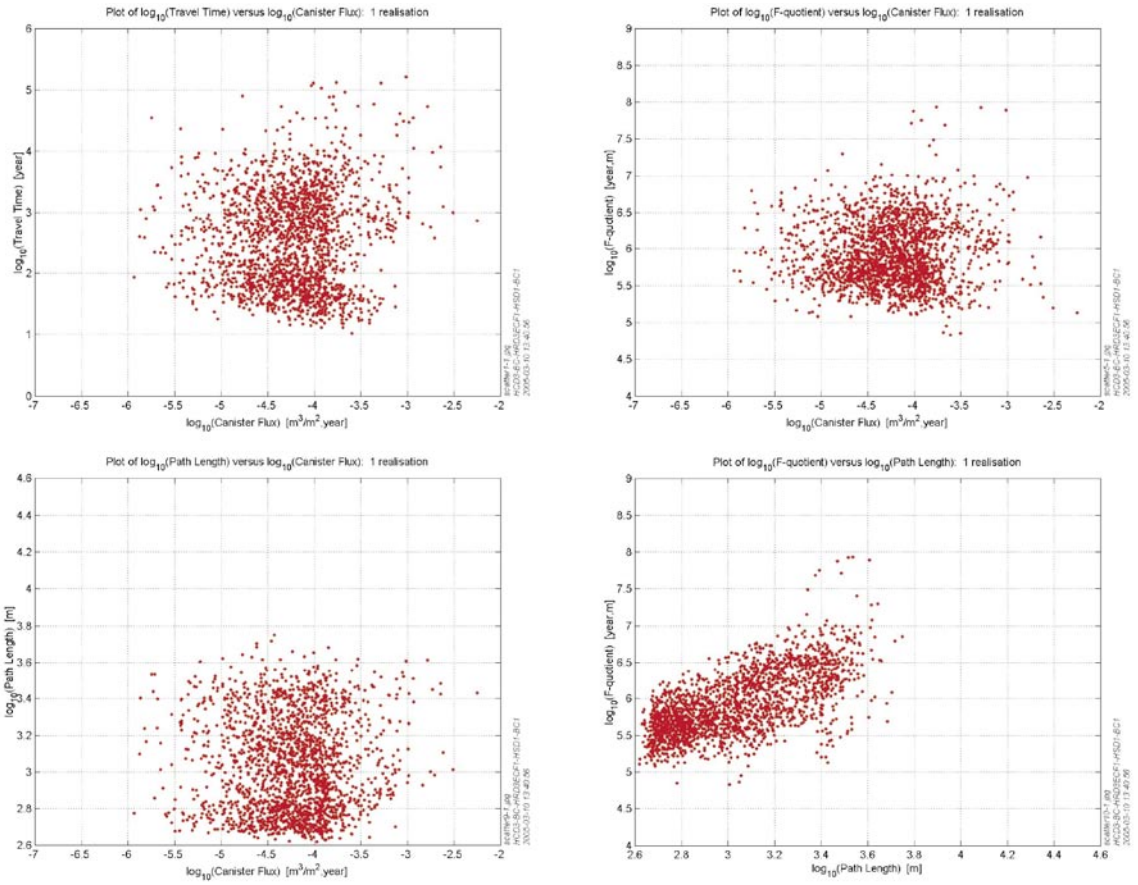

Figure C-7. *Scatter plots with different combinations of the calculated performance measures (t_w, q_c, F and L) for the ensemble of particles released in the local-scale release-area for the lower flow-wetted-surface, a_r = 0.25 m² m⁻³, for RMD (HCD3_BC_HRD3ECF1_HSD1_BC1).*

Table C-4. Statistical summary of the calculated performance measures (t_w, q_c, F and L) for the ensemble of particles released in the local-scale release-area for the lower flow-wetted-surface, a_r = 0.25 m² m⁻³, for RMD (HCD3_BC_HRD3ECF1_HSD1_BC1).

Statistical entity	Log_{10} (t_w) (y)	Log_{10} (q_c) (m y^{-1})	Log_{10} (F) (y m^{-1})	Log_{10} (L) (m)
Mean	2.551	–4.235	5.926	3.032
Median	2.564	–4.199	5.851	3.004
5th percentile	1.450	–5.124	5.330	2.689
25th percentile	1.860	–4.548	5.609	2.802
75th percentile	3.138	–3.926	6.225	3.231
95th percentile	3.811	–3.422	6.652	3.468
Std dev	0.782	0.497	0.428	0.257
Variance	0.612	0.247	0.183	0.066
Skewness	0.351	–0.156	0.671	0.370
Kurtosis	–0.497	0.635	0.697	–0.965
Min value	1.016	–5.934	4.829	2.621
Max value	5.211	–2.250	7.934	3.749
Fraction OK	0.995	1.000	0.995	0.995

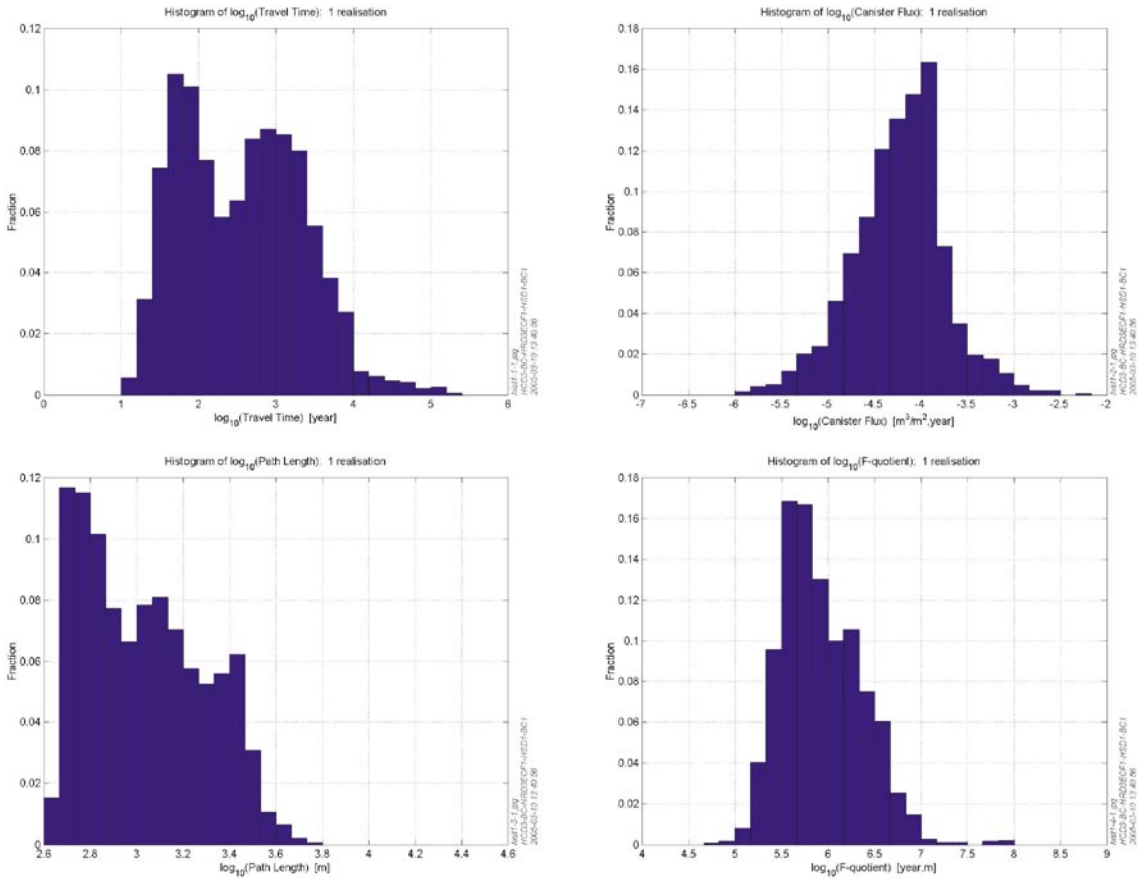

Figure C-8. *Histograms of the calculated performance measures (t_w, q_c, F and L) for the ensemble of particles released in the local-scale release-area for the Lower flow-wetted-surface, $a_r = 0.25\ m^2\ m^{-3}$, for RMD (HCD3_BC_HRD3ECF1_HSD1_BC1).*

C.6 Increased background conductivity outside RFM017/029 (HCD3_BC_HRD3ECK1_HSD1_BC1)

The increased conductivity outside RFM017/029 does not have a great impact on the transport results. This is expected since most of the released particles do not go very far (median path length is about 1 km). Only the particles that reach outside the candidate area are affected by the increased flow rates outside RFM017/029. The result is slightly lower 95th percentile for the travel time and F-quotient, see Figure C-9, Figure C-10 and Table C-5. This also results in a lower variance for the mentioned performance measures.

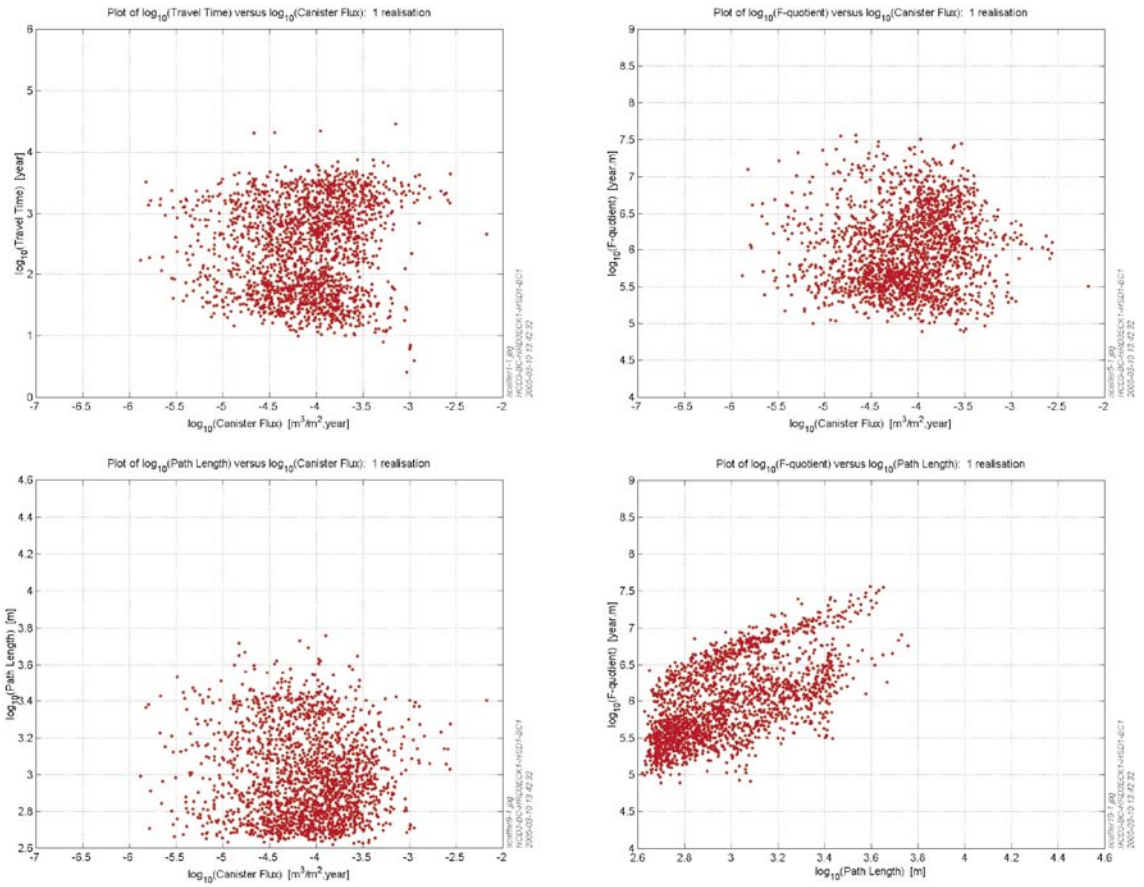

Figure C-9. *Scatter plots with different combinations of the calculated performance measures (t_w, q_c, F and L) for the ensemble of particles released in the local-scale release-area for the increased background conductivity outside RFM017/029 (HCD3_BC_HRD3ECK1_HSD1_BC1).*

Table C-5. Statistical summary of the calculated performance measures (t_w, q_c, F and L) for the ensemble of particles released in the local-scale release-area for increased background K outside RFM017/029 (HCD3_BC_HRD3ECK1_HSD1_BC1).

Statistical entity	Log_{10} (t_w) (y)	Log_{10} (q_c) (m y^{-1})	Log_{10} (F) (y m^{-1})	Log_{10} (L) (m)
Mean	2.419	–4.105	5.996	2.989
Median	2.462	–4.057	5.935	2.949
5th percentile	1.325	–5.032	5.254	2.684
25th percentile	1.743	–4.427	5.563	2.789
75th percentile	3.067	–3.754	6.366	3.150
95th percentile	3.500	–3.366	6.951	3.416
Std dev	0.738	0.512	0.532	0.236
Variance	0.545	0.262	0.283	0.056
Skewness	–0.026	–0.337	0.416	0.582
Kurtosis	–1.188	0.285	–0.564	–0.558
Min value	0.404	–5.881	4.889	2.621
Max value	4.455	–2.176	7.567	3.757
Fraction OK	0.996	1.000	0.996	0.996

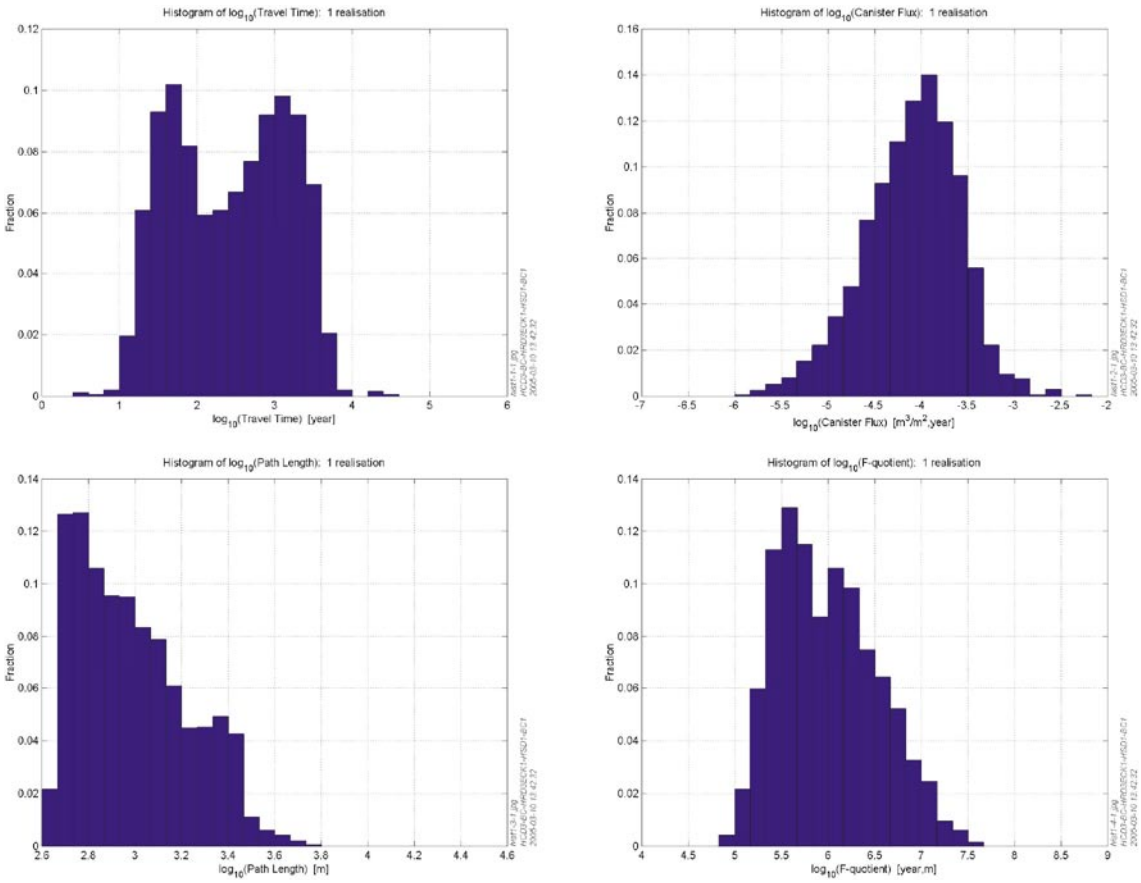

Figure C-10. *Histograms of the calculated performance measures (t_w, q_c, F and L) for the ensemble of particles released in the local-scale release-area for increased background K outside RFM017/029 (HCD3_BC_HRD3ECK1_HSD1_BC1).*

C.7 Alternative Case (AC) HCD model (HCD3_AC_HRD3EC_HSD1_BC1)

Both Alternative Case HCD models (unchanged and lowered porosity) give slightly lower canister flows and longer travel times. The F-quotient and the path length remain rather unchanged, see Figure C-11, Figure C-12 and Table C-6. Overall it can be concluded that due to the very localized flows in the model structural changes made to the region outside the candidate area have little effect on the flow and transport inside the area.

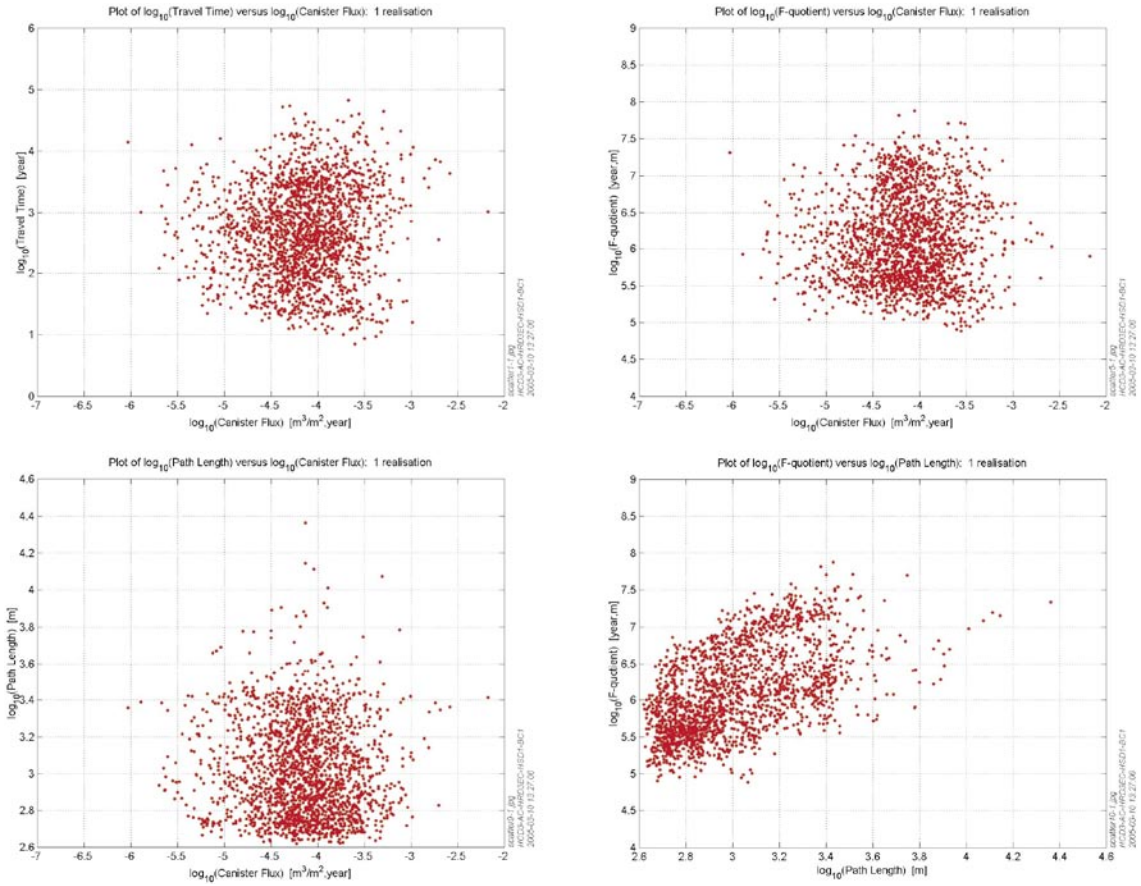

Figure C-11. *Scatter plots with different combinations of the calculated performance measures (t_w, q_c, F and L) for the ensemble of particles released in the local-scale release-area for the Alternative Case (AC) HCD model (HCD3_AC_HRD3EC_HSD1_BC1).*

Table C-6. Statistical summary of the calculated performance measures (t_w, q_c, F and L) for the ensemble of particles released in the local-scale release-area for the Alternative Case (AC) HCD model (HCD3_AC_HRD3EC_HSD1_BC1).

Statistical entity	Log_{10} (t_w) (y)	Log_{10} (q_c) (m y^{-1})	Log_{10} (F) (y m^{-1})	Log_{10} (L) (m)
Mean	2.692	–4.149	6.127	3.015
Median	2.690	–4.132	6.060	2.968
5th percentile	1.432	–5.009	5.300	2.689
25th percentile	2.144	–4.418	5.640	2.807
75th percentile	3.263	–3.841	6.558	3.193
95th percentile	3.848	–3.410	7.171	3.434
Std dev	0.746	0.477	0.586	0.253
Variance	0.557	0.227	0.343	0.064
Skewness	0.001	–0.293	0.369	0.772
Kurtosis	–0.597	0.588	–0.692	0.566
Min value	0.844	–6.027	4.883	2.620
Max value	4.821	–2.176	7.877	4.363
Fraction OK	0.988	1.000	0.988	0.988

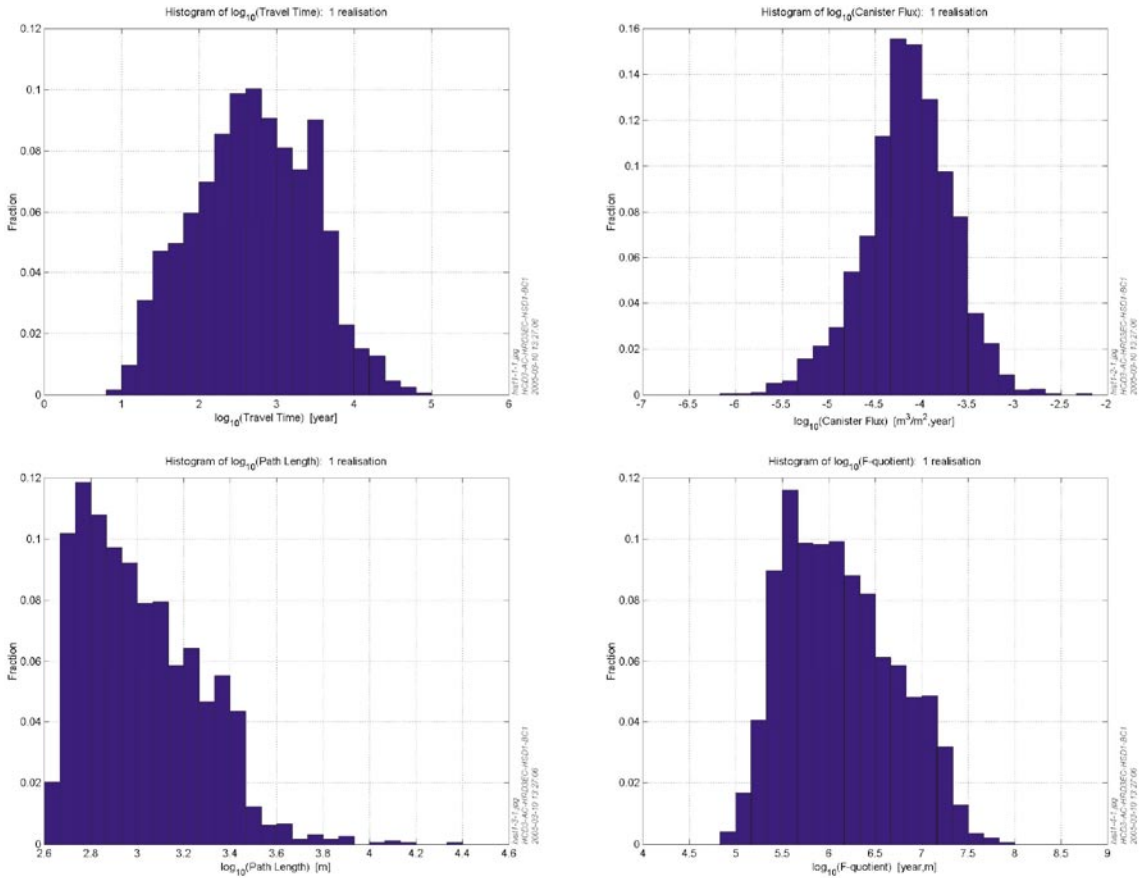

Figure C-12. *Histograms of the calculated performance measures (t_w, q_c, F and L) for the ensemble of particles released in the local-scale release-area for the Alternative Case (AC) HCD model (HCD3_AC_HRD3EC_HSD1_BC1).*

C.8 Conclusions

Transport calculations with present-day path lines have been performed using the derived model. Generally the sensitivity study shows that the model is not very sensitive to the changes considered and the differences compared to the Base Case are small. There are however a few parameters that clearly have significant effect on the results:

- The variations in the performance measures between the variants considered is generally low, around 5–10%. This perhaps should not be a surprise since all the cases considered have been calibrated against the same hydraulic data in the case of the Hydro-DFN variants, and against the same hydro-geochemistry data in the case of regional flow and solute transport.
- The F-quotient for most of the local-scale area is of order 10^6y m^{-1}, with the 5th percentile at about 10^5y m^{-1} and the 95th percentile at about 10^7y m^{-1}.
- The median path lengths stays around 1 km for all considered cases with only a few particles reaching further than 4 km. This indicates very localized flows in the modeled area.
- Changing the hydraulic properties of the rock volume outside RFM017/029 does not have a significant impact on the results (calibration of reference waters, transport calculations) for the candidate area.

- The uncertainties around the value of the flow-wetted surface should be addressed further since this has a significant impact mainly on the F-quotient.
- The cases using an uncorrelated transmissivity model show some differences compared to the Base Case. An explanation for this could be that we have a slight depth dependency. Further sensitivity studies are needed in order to investigate the impact of the hydraulic properties of the local-scale area on the calibration of the reference waters.

1 **La Pointe P R, Staub I, 2004.** Statistical Model of Fractures and Deformation Zones, Draft Report.

2 **De Marsily G, 1986.** Quantitative Hydrology, Groundwater Hydrology for Engineers, Academic Press, Inc., London.